

Non-destructive methods for monitoring plant health

Edited by

Nam-Hai Chua, Rajeev Ram and Michael S. Strano

Published in

Frontiers in Plant Science



FRONTIERS EBOOK COPYRIGHT STATEMENT

The copyright in the text of individual articles in this ebook is the property of their respective authors or their respective institutions or funders. The copyright in graphics and images within each article may be subject to copyright of other parties. In both cases this is subject to a license granted to Frontiers.

The compilation of articles constituting this ebook is the property of Frontiers.

Each article within this ebook, and the ebook itself, are published under the most recent version of the Creative Commons CC-BY licence. The version current at the date of publication of this ebook is CC-BY 4.0. If the CC-BY licence is updated, the licence granted by Frontiers is automatically updated to the new version.

When exercising any right under the CC-BY licence, Frontiers must be attributed as the original publisher of the article or ebook, as applicable.

Authors have the responsibility of ensuring that any graphics or other materials which are the property of others may be included in the CC-BY licence, but this should be checked before relying on the CC-BY licence to reproduce those materials. Any copyright notices relating to those materials must be complied with.

Copyright and source acknowledgement notices may not be removed and must be displayed in any copy, derivative work or partial copy which includes the elements in question.

All copyright, and all rights therein, are protected by national and international copyright laws. The above represents a summary only. For further information please read Frontiers' Conditions for Website Use and Copyright Statement, and the applicable CC-BY licence.

ISSN 1664-8714
ISBN 978-2-83251-626-3
DOI 10.3389/978-2-83251-626-3

About Frontiers

Frontiers is more than just an open access publisher of scholarly articles: it is a pioneering approach to the world of academia, radically improving the way scholarly research is managed. The grand vision of Frontiers is a world where all people have an equal opportunity to seek, share and generate knowledge. Frontiers provides immediate and permanent online open access to all its publications, but this alone is not enough to realize our grand goals.

Frontiers journal series

The Frontiers journal series is a multi-tier and interdisciplinary set of open-access, online journals, promising a paradigm shift from the current review, selection and dissemination processes in academic publishing. All Frontiers journals are driven by researchers for researchers; therefore, they constitute a service to the scholarly community. At the same time, the *Frontiers journal series* operates on a revolutionary invention, the tiered publishing system, initially addressing specific communities of scholars, and gradually climbing up to broader public understanding, thus serving the interests of the lay society, too.

Dedication to quality

Each Frontiers article is a landmark of the highest quality, thanks to genuinely collaborative interactions between authors and review editors, who include some of the world's best academicians. Research must be certified by peers before entering a stream of knowledge that may eventually reach the public - and shape society; therefore, Frontiers only applies the most rigorous and unbiased reviews. Frontiers revolutionizes research publishing by freely delivering the most outstanding research, evaluated with no bias from both the academic and social point of view. By applying the most advanced information technologies, Frontiers is catapulting scholarly publishing into a new generation.

What are Frontiers Research Topics?

Frontiers Research Topics are very popular trademarks of the *Frontiers journals series*: they are collections of at least ten articles, all centered on a particular subject. With their unique mix of varied contributions from Original Research to Review Articles, Frontiers Research Topics unify the most influential researchers, the latest key findings and historical advances in a hot research area.

Find out more on how to host your own Frontiers Research Topic or contribute to one as an author by contacting the Frontiers editorial office: frontiersin.org/about/contact

Non-destructive methods for monitoring plant health

Topic editors

Nam-Hai Chua — Temasek Life Sciences Laboratory, Singapore

Rajeev Ram — Massachusetts Institute of Technology, United States

Michael S. Strano — Massachusetts Institute of Technology, United States

Citation

Chua, N.-H., Ram, R., Strano, M. S., eds. (2023). *Non-destructive methods for monitoring plant health*. Lausanne: Frontiers Media SA.

doi: 10.3389/978-2-83251-626-3

Table of contents

- 05 **Fine-Grained Grape Leaf Diseases Recognition Method Based on Improved Lightweight Attention Network**
Peng Wang, Tong Niu, Yanru Mao, Bin Liu, Shuqin Yang, Dongjian He and Qiang Gao
- 17 **Detecting Plant Stress Using Thermal and Optical Imagery From an Unoccupied Aerial Vehicle**
Bonny Stutsel, Kasper Johansen, Yoann M. Malbêteau and Matthew F. McCabe
- 35 **Surface-Enhanced Raman Scattering Spectroscopy Combined With Chemical Imaging Analysis for Detecting Apple Valsa Canker at an Early Stage**
Shiyan Fang, Yanru Zhao, Yan Wang, Junmeng Li, Fengle Zhu and Keqiang Yu
- 47 **Handheld Multifunctional Fluorescence Imager for Non-invasive Plant Phenotyping**
Ruochong Zhang, Sally Shuxian Koh, Mark Ju Teng Teo, Renzhe Bi, Shuyan Zhang, Kapil Dev, Daisuke Urano, U. S. Dinish and Malini Olivo
- 56 **Non-destructive Plant Biomass Monitoring With High Spatio-Temporal Resolution via Proximal RGB-D Imagery and End-to-End Deep Learning**
Nicolas Buxbaum, Johann Heinrich Lieth and Mason Earles
- 71 **A Spatial-Temporal Analysis of Cellular Biopolymers on Leaf Blight-Infected Tea Plants Using Confocal Raman Microspectroscopy**
Alireza Sanaeifar, Dapeng Ye, Xiaoli Li, Liubin Luo, Yu Tang and Yong He
- 84 **Raman Spectroscopy Enables Non-invasive and Confirmatory Diagnostics of Aluminum and Iron Toxicities in Rice**
Samantha Higgins, Sudip Biswas, Nicolas K. Goff, Endang M. Septiningsih and Dmitry Kurouski
- 93 **Non-destructive Technologies for Plant Health Diagnosis**
Mervin Chun-Yi Ang and Tedrick Thomas Salim Lew
- 102 **Raman Spectroscopy Detects Changes in Carotenoids on the Surface of Watermelon Fruits During Maturation**
Tushar Dhanani, Tianyi Dou, Kishan Biradar, John Jifon, Dmitry Kurouski and Bhimanagouda S. Patil
- 111 **Raman Spectroscopy Applications in Grapevine: Metabolic Analysis of Plants Infected by Two Different Viruses**
Luisa Mandrile, Chiara D'Errico, Floriana Nuzzo, Giulia Barzan, Slavica Matić, Andrea M. Giovannozzi, Andrea M. Rossi, Giorgio Gambino and Emanuela Noris
- 125 **Novel Vegetation Indices to Identify Broccoli Plants Infected With *Xanthomonas campestris* pv. *campestris***
Mónica Pineda, María Luisa Pérez-Bueno and Matilde Barón

- 137 **Physiological Responses Manifested by Some Conventional Stress Parameters and Biophoton Emission in Winter Wheat as a Consequence of Cereal Leaf Beetle Infestation**
Helga Lukács, Ildikó Jócsák, Katalin Somfalvi-Tóth and Sándor Keszthelyi
- 148 **Benchmarking organic electrochemical transistors for plant electrophysiology**
Adam Armada-Moreira, Chiara Diacci, Abdul Manan Dar, Magnus Berggren, Daniel T. Simon and Eleni Stavrinidou



Fine-Grained Grape Leaf Diseases Recognition Method Based on Improved Lightweight Attention Network

Peng Wang^{1,2,3}, Tong Niu^{1,2,3}, Yanru Mao^{1,2,3}, Bin Liu^{2,3,4}, Shuqin Yang^{1,2,3*}, Dongjian He^{1,2,3*} and Qiang Gao^{1*}

¹ College of Mechanical and Electronic Engineering, Northwest Agriculture and Forestry (A&F) University, Yangling, China, ² Key Laboratory of Agricultural Internet of Things, Ministry of Agriculture and Rural Affairs, Xianyang, China, ³ Shaanxi Key Laboratory of Agricultural Information Perception and Intelligent Services, Xianyang, China, ⁴ College of Information Engineering, Northwest Agriculture and Forestry (A&F) University, Yangling, China

OPEN ACCESS

Edited by:

Nam-Hai Chua,
Temasek Life Sciences
Laboratory, Singapore

Reviewed by:

George Barbastathis,
Massachusetts Institute of
Technology, United States
Kevin Lim,
Wilmar International, Singapore

*Correspondence:

Shuqin Yang
yangshuqin1978@163.com
Dongjian He
hdj168@nwsuaf.edu.cn
Qiang Gao
hillfinder@163.com

Specialty section:

This article was submitted to
Technical Advances in Plant Science,
a section of the journal
Frontiers in Plant Science

Received: 08 July 2021

Accepted: 23 September 2021

Published: 22 October 2021

Citation:

Wang P, Niu T, Mao Y, Liu B, Yang S,
He D and Gao Q (2021) Fine-Grained
Grape Leaf Diseases Recognition
Method Based on Improved
Lightweight Attention Network.
Front. Plant Sci. 12:738042.
doi: 10.3389/fpls.2021.738042

Real-time dynamic monitoring of orchard grape leaf diseases can greatly improve the efficiency of disease control and is of great significance to the healthy and stable development of the grape industry. Traditional manual disease-monitoring methods are inefficient, labor-intensive, and ineffective. Therefore, an efficient method is urgently needed for real-time dynamic monitoring of orchard grape diseases. The classical deep learning network can achieve high accuracy in recognizing grape leaf diseases; however, the large amount of model parameters requires huge computing resources, and it is difficult to deploy to actual application scenarios. To solve the above problems, a cross-channel interactive attention mechanism-based lightweight model (ECA-SNet) is proposed. First, based on 6,867 collected images of five common leaf diseases of measles, black rot, downy mildew, leaf blight, powdery mildew, and healthy leaves, image augmentation techniques are used to construct the training, validation, and test set. Then, with ShuffleNet-v2 as the backbone, an efficient channel attention strategy is introduced to strengthen the ability of the model for extracting fine-grained lesion features. Ultimately, the efficient lightweight model ECA-SNet is obtained by further simplifying the network layer structure. The model parameters amount of ECA-SNet 0.5× is only 24.6% of ShuffleNet-v2 1.0×, but the recognition accuracy is increased by 3.66 percentage points to 98.86%, and FLOPs are only 37.4 M, which means the performance is significantly better than other commonly used lightweight methods. Although the similarity of fine-grained features of different diseases image is relatively high, the average F1-score of the proposed lightweight model can still reach 0.988, which means the model has strong stability and anti-interference ability. The results show that the lightweight attention mechanism model proposed in this paper can efficiently use image fine-grained information to diagnose orchard grape leaf diseases at a low computing cost.

Keywords: grape leaf diseases, diseases recognition, fine-grained image, attention mechanism, lightweight

INTRODUCTION

Grape leaf disease is the main factor that causes a large-scale reduction in orchards and restricts the healthy and stable development of the grape industry. Realizing real-time dynamic monitoring of orchard diseases is of great significance for the early prevention and control of orchard diseases and the cultivation of disease-resistant varieties. In recent years, with the development of computer vision technology and the continuous improvement of computing power, researchers have used deep learning methods in the field of crop disease diagnosis and have achieved remarkable results in general disease recognition tasks (Lu et al., 2017; Priyadharshini et al., 2019; Chen et al., 2020; Liu et al., 2020). For instance, Ma J. et al. (2018) proposed a deep convolutional neural network to identify three types of cucumber diseases and achieved an accuracy of 93.4%. Liu et al. (2018) proposed a network based on AlexNet and GoogLeNet, which used deep learning to diagnose apple leaf diseases for the first time. The accuracy on the test set reached 97.62%, which was better than traditional machine learning methods. Ferentinos (2018) tested five classical convolutional neural networks to identify plant leaf diseases, and the results showed that all of them can achieve ideal accuracy. Although the convolution neural network-based classification models mentioned above can achieve superior recognition results, it has the imperfection of highly dependent on the hardware performance of the device. The huge amount of network parameters leads to huge computational overhead, which cannot be afforded by ordinary devices, and it is difficult to deploy to the terminals for promotion.

In view of the high computational cost of large-scale models, many scholars have carried out pieces of lightweight model research. Xception (Chollet, 2017) was a lightweight model improved by Google based on the Inception-v3 (Szegedy et al., 2016). The deep separable convolution was used to reduce the parameters, but the computational cost was increased. Compared with traditional convolutional neural networks, while using deep separable convolution, MobileNet-v1 (Howard et al., 2017) introduces two hyperparameters that control the number of convolution kernels and the resolution of the input image. This model leveraged a stack layer structure; although the number of parameters was reduced, there still exists the model degradation problem. Sandler et al. (2018) suppressed the degradation of the model by introducing the Inverted Residuals structure. By using a linear activation function to effectively retain low-dimensional features, the parameters of the model were further reduced, and the accuracy was improved. Howard et al. (2019) added the Squeeze-Excitation module (Hu et al., 2018) to the Inverted Residual structure to endow the ability of the model to focus on key feature channels. The lightweight model structure was designed to be flexible and efficient, which may greatly reduce the calculation cost and easy to be applied on mobile terminals, including smartphones, embedded devices, etc. With its own advantages, the application of lightweight networks in the field of crop disease identification has also made some progress. Chao et al. (2020) combined DenseNet and Xception strategies and

proposed XDNet to identify five apple leaf diseases. The model recognition effect was preferable, and the amount of parameters was not high. Tang et al. (2020) introduced the SE module into the ShuffleNet network and proposed a lightweight convolutional neural network. The public data containing four types of grape diseases were used to evaluate the network performance; the accuracy of the training set can reach 99.14%. Bi et al. (2020) used the MobileNet network to identify two different apple diseases and compared with other models in terms of efficiency and accuracy to verify the effectiveness of the network. The above pieces of research have opened up a new way for the promotion of low-cost models; however, there are still problems that existing lightweight method cannot achieve pleasant and stable performance on a fine-grained image recognition task. Ramcharan et al. (2019) used a mobile device equipped with a lightweight model to diagnose cassava diseases in the field and found that the different angles, brightness, and changes in different diseases will affect the accuracy of the model.

Different from general image recognition tasks, the key information of the local area plays a decisive role in the classification decision in fine-grained image recognition. So, how to make full use of the effective information is the key to improve the performance on fine-grained recognition. Under the influence of many interference factors, the feature differences among different subclasses of a specific category of images may be small, or the feature differences among different objects in the same subclass may be large, which increases the difficulty of fine-grained image classification. Therefore, the fine-grained disease image recognition under the complex background has higher requirements for the comprehensive performance of the model. The fine-grained disease image identification method based on visual attention can effectively focus on the region of interest and improve the recognition performance of the model. In recent years, it has been widely used in image classification, object detection, and other fields and has achieved excellent results. Yang et al. (2020) proposed an attention mechanism that effectively used the key information of images and established the image classification model for 14 different crops based on transfer learning. The model was trained and tested with the PlantVillage public data set. The test results show that the F1-score of the proposed model can reach 0.93. Mi et al. (2020) introduced the attention mechanism into DenseNet to identify six different grades of wheat stripe rust and found that the performance of the model with attention mechanism can be significantly improved.

Inspired by the above research, a new lightweight model for fine-grained grape leaf disease recognition is proposed in this paper. The main innovations and contributions are summarized as below:

- (1) A new grape leaf disease data set is established, and the fine-grained grape leaf diseases image datasets (FGGLDIs, namely FGDs) are generated *via* image enhancement techniques. The image enhancement techniques are used to simulate grape leaf disease images collected under complex environment conditions, enhance the generalization performance of the

model, avoid over-fitting problems in the training process, and lay the foundation for the popularization of the model.

- (2) In this paper, the cross-channel interaction strategy without dimensionality reduction is introduced into the lightweight network, and a new fine-grained recognition model of grape disease images based on the attention mechanism is proposed. First, deep separable convolution is used to reduce the overall amount of parameters of the model. Second, the efficient channel attention (ECA) is embedded into the ShuffleNet infrastructure and implemented through one-dimensional convolution. Finally, a method of adaptive selection of the size of the one-dimensional convolution kernel is adopted to determine the coverage of the cross-channel interaction. The method proposed in this paper can effectively reduce the complexity while maintaining the performance of the model, realize the effective fusion of multichannel features, and strengthen the ability of the model to learn important and fine-grained information in the lesion area.

The remainder of the paper is organized as follows: In *Materials and Methods*, the structure information of the data set is introduced, and FGDs is generated by using data enhancement techniques. The model structure and the test process mentioned in this article are discussed in detail. *Results and Discussion* presents the test method to evaluate the performance of the model and analyzes the test results. The model attention and fine-grained feature learning are also displayed through heat maps and fine-grained feature maps, respectively. The *Conclusion* summarizes the work of this article.

MATERIALS AND METHODS

This section introduces the materials and methods used in the study, including the collected grape leaf disease image data, FGDs established through image enhancement techniques, relevant lightweight network, and detailed structure of the proposed model.

Data Acquisition

The original data set used in this study contains a total of 6,867 images of grape leaf disease from two parts. First, 3,388 images of powdery mildew, downy mildew, and healthy leaves are collected in the field of the grape planting experimental station of Northwest A&F University, Shaanxi Province, China. In different weather conditions and different time periods (sunny, cloudy, morning, noon, and evening), the MI 9 smartphone is used to shoot from different angles and directions. Then, a total of 3,479 black measles, black rot, and leaf blight are collected from the public data set. Through the above work, an original data set of common grape diseases is established.

Figure 1 shows a random sample of each category of the data set. It can be seen from the examples that there are a large amount of complex background (**Figures 1C,D,F**) and pure-color background (**Figures 1A,B,E**) images in the data set, which has high requirements for the comprehensive performance of the model. In **Figure 1**, black measles (**Figure 1A**), black rot (**Figure 1B**), and leaf blight spots (**Figure 1E**) have a high

degree of similarity. When the leaves are onset, brown spots are produced, which gradually expand into nearly circular spots with edges appearing dark brown. Downy mildew (**Figure 1C**) early disease spots are dense white frost-like objects, and the shape of the disease spots is usually irregular polygonal when restricted by leaf veins. When the disease is severe in the later stage, the leaves will fall off early. Powdery mildew (**Figure 1F**) leaves are covered with off-white powder, similar to downy mildew symptoms; both of which form clusters of lesions locally and are not easily distinguishable by the naked eye. Therefore, the above mentioned classification of different diseases can be expressed as a problem of fine-grained image classification.

Image Dataset Augmentation

In the orchards, grape leaves grow in different positions with different shapes, and there are interference factors such as weather and shooting angles. So, the data set need to be expanded to avoid over-fitting during the training process. Before performing image data augmentation, 100 images were randomly selected from each category in the original data set, a total of 600 images, and then, adding Gaussian noise, rotated left 90°, rotated right 90°, vertically flipped, and weakened sharpness, respectively, forming an enhanced robustness test data set (RTD), containing 3,000 images. Gaussian blur, contrast enhancement by 30% and decrease by 30%, and brightness enhancement by 30% and decrease by 30% are adopted to the remaining images in the original data set to simulate weather interference. Then, rotating the image by 90°, 270°, horizontal flip, and vertical flip to simulate the disturbance of different shooting angles and the FGDs is established. **Table 1** shows the detailed structure information of FGDs. After the model was trained, RTD was used to test the model to verify the effect of model training. The above work provides a data basis for model training.

ECA-SNet Network

Relevant Lightweight Network

With the development of computer vision technology, there is an increasing demand for running high-quality deep neural networks on mobile devices. Limited by the level of computing power, it is difficult for mobile devices to carry conventional convolution neural networks (CNNs) to deal with complete various tasks. In order to meet the requirements of applying deep neural networks on embedded and mobile terminals and maintaining superior performance, the MobileNet-v2 endows the model with remarkable feature extraction capabilities by stacking the Inverted Residual Block feature extraction structure. The specific method is to increase the dimensionality of input feature matrix through 1×1 convolution, and then use 3×3 deep separable convolution for feature learning, reduce the amount of model calculations, and, finally, decrease the dimensionality through 1×1 convolution and output after linear activation function. In order to give the model attention mechanism, MobileNet-v3 uses the Squeeze-and-Excitation module on the basis of MobileNet-v2 to optimize the feature learning ability of deep separable convolution. By assigning different weights to different channel features, the adaptability of the model to complex backgrounds is enhanced. Zhang et al. (2018)

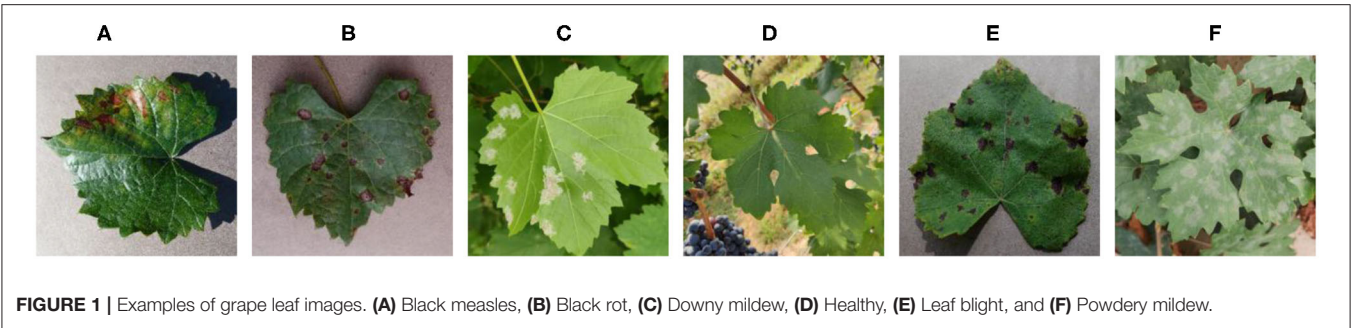
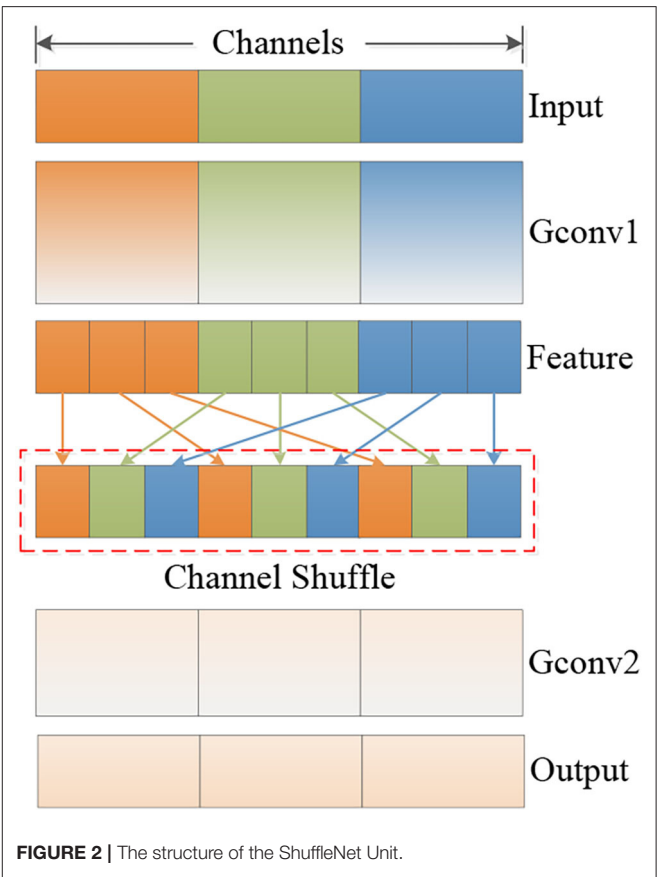


TABLE 1 | The structure of FGDs.

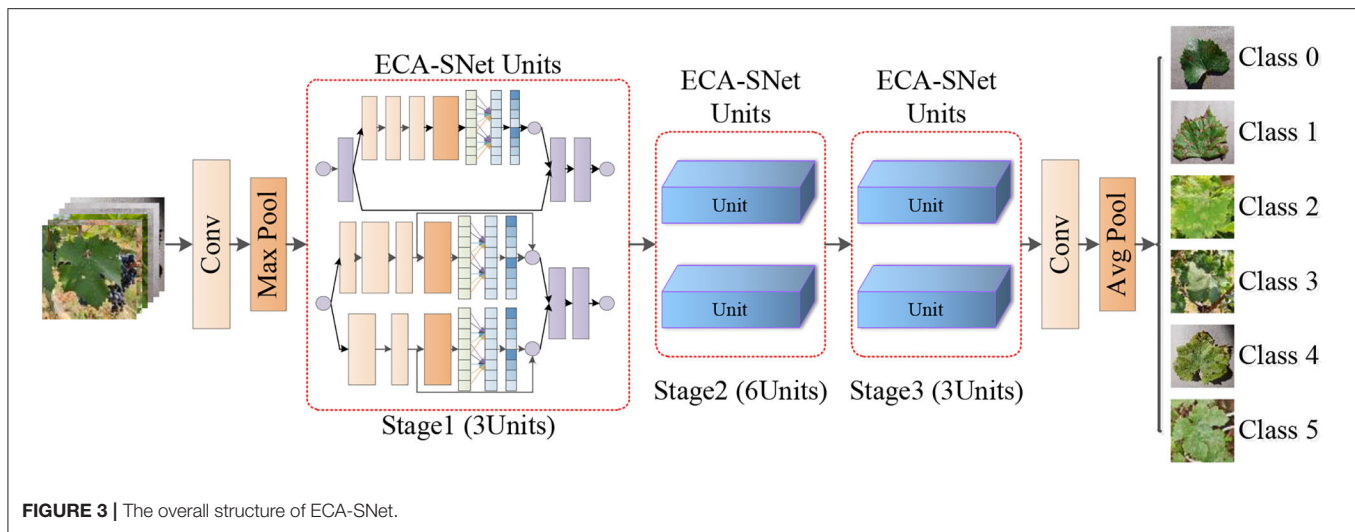
Categories	Black measles	Black rot	Downy mildew	Healthy	Leaf blight	Powdery mildew
Training set	8,664	8,640	8,080	8,112	8,128	8,512
Validation set	2,166	2,160	2,020	2,028	2,032	2,128
Total	10,830	10,800	10,100	10,140	10,160	10,640
Proportion	0.1728	0.1723	0.1612	0.1618	0.1621	0.1698

proposed ShuffleNet network to solve the problems of computing resources wasting and information interaction choked between group convolutions, and greatly reduce computational costs. The model mainly includes point-wise group convolution and channel shuffle operation, as is shown in **Figure 2**. Mobile terminal devices emphasize real-time, so it is necessary to speed up the inference process while maintaining the final accuracy. Commonly used inference acceleration methods, such as pruning existing models to reduce connection redundancy, quantification, and factorization, to reduce computational redundancy, and knowledge distillation of large models into small models are all accelerating and transforming existing models. ShuffleNet focuses on structural design to directly improve performance, and the core structure is more efficient.

In ShuffleNet-v1, floating-point operations per second (FLOPs) was used to measure the multiplication operation of convolution, and the design of this structure aims at reducing FLOPs. However, many factors that affect the model speed also include indicators, such as the memory access cost (MAC) and the level of parallelism. Other operations, such as data reading and writing, channel shuffling, etc., also consume certain time and affect the model inference speed. A large amount of point-wise group convolutions was used in ShuffleNet-v1, which increases MAC and reduces computational parallelism. In addition, a high degree of model fragmentation will significantly affect the speed of inference. The excessive use of element-wise operations, such as activation function, tensor addition, and offset addition, are not conducive to speed improvement. Based on the above criteria, Ma N. et al. (2018) redesigned the ShuffleNet Unit and proposed the idea of channel separation to replace the group convolution. The input feature is equally divided into two branches, and each branch maintains the same identity after separation. The 1×1 convolution is used to, instead, point-wise group convolution and maintained the same



channel depth in a single branch. The reasoning speed is further improved by reducing element-wise operations, and channel shuffling is used to realize information interaction. Furthermore,



the network structure can be scaled by controlling the number of convolution kernels, which could adjust the network width.

Structure of Proposed Model

In recent years, some progress has been made in the research of crop disease recognition based on attention mechanism (Karthik et al., 2020; Zeng and Li, 2020). The attention mechanism assigns high-contribution information to the larger weights while suppressing other irrelevant information through weights distribution, which is an effective method for model performance optimization. Different types of grape leaf diseases have relatively small differences, and the distinguishable fine-grained features are difficult to capture. Therefore, the effective attention mechanism to the characteristics of fine-grained lesions is the key to solving this problem.

Inspired by the above work, a fine-grained image recognition network for grape leaf diseases with a lightweight attention mechanism, namely ECA-SNet, is proposed in this paper. The main structure of the model includes three stages and a total of 12 ECA-SNet Units as is shown in **Figure 3**. First, the conventional convolution is implemented on the input image, and the Max pooling operation is used to reduce the size of output feature matrix to 1/4 of the input image, and then the characteristic information is learned through 12 ECA-SNet Units. Finally, the output features of the conventional convolutional layer and the pooling layer are sent to the fully connected layer for classification.

Wang et al. (2020) analyzed the conventional channel attention mechanism and found that the dimensionality reduction operation affects the performance of channel attention, and proper cross-channel interaction can significantly reduce the complexity of the model while maintaining efficient performance. Therefore, this paper adopts the strategy without dimensionality reduction in the design of basic structure of ECA-SNet Unit, as shown in **Figure 4**. There are two types of ECA-SNet Units. The module shown in **Figure 4A** (Unit 1) is the first unit of each Stage. The input feature matrix passing

through two non-interacting branches and concatenating the two output feature matrices to doubled their depth. The ECA strategy is used in two branch structures, respectively. **Figure 4B** (Unit 2) module is the subsequent structure of each stage. First, the input feature matrix is equally divided into two groups. The main branch undergoes a series of operations and uses the ECA strategy, another branch output directly without operation and concatenating with the output of the main branch, and the depth of the feature matrix remain unchanged.

The strategy without dimensionality reduction of cross-channel interaction that increases the revenue of the channel attention mechanism is shown in **Figure 5**. By considering each channel and its n neighborhoods, cross-channel interaction information is captured. The size of the convolution kernel n represents the coverage of cross-channel interaction, that is, the number of neighborhoods that participate in the attention prediction of a specific channel.

In order to avoid manual tuning, the method of adaptively selecting the one-dimensional convolution kernel size is used to determine the value of n . Conv1D is used to capture the cross-channel interaction; the size of n determines the coverage of the interaction. The number of n is related to the channel dimension C , and, in the case of fixed number group convolutions, the high-dimensional (low-dimensional) channel is proportional to the long-distance (short-distance) convolution. In the same way, the coverage of n of the cross-channel information interaction is also proportional to the channel dimension C , that is, the mapping relationship between n and C is shown in Equation (1):

$$C = \phi(n) \quad (1)$$

Based on the above analysis, it can be seen that n and C are in a non-linear proportion. As a kernel function, exponential family functions are widely used to deal with unknown mapping problems. So, the exponential function is used to approximate the mapping ϕ as shown in Equation (2). In addition, since the

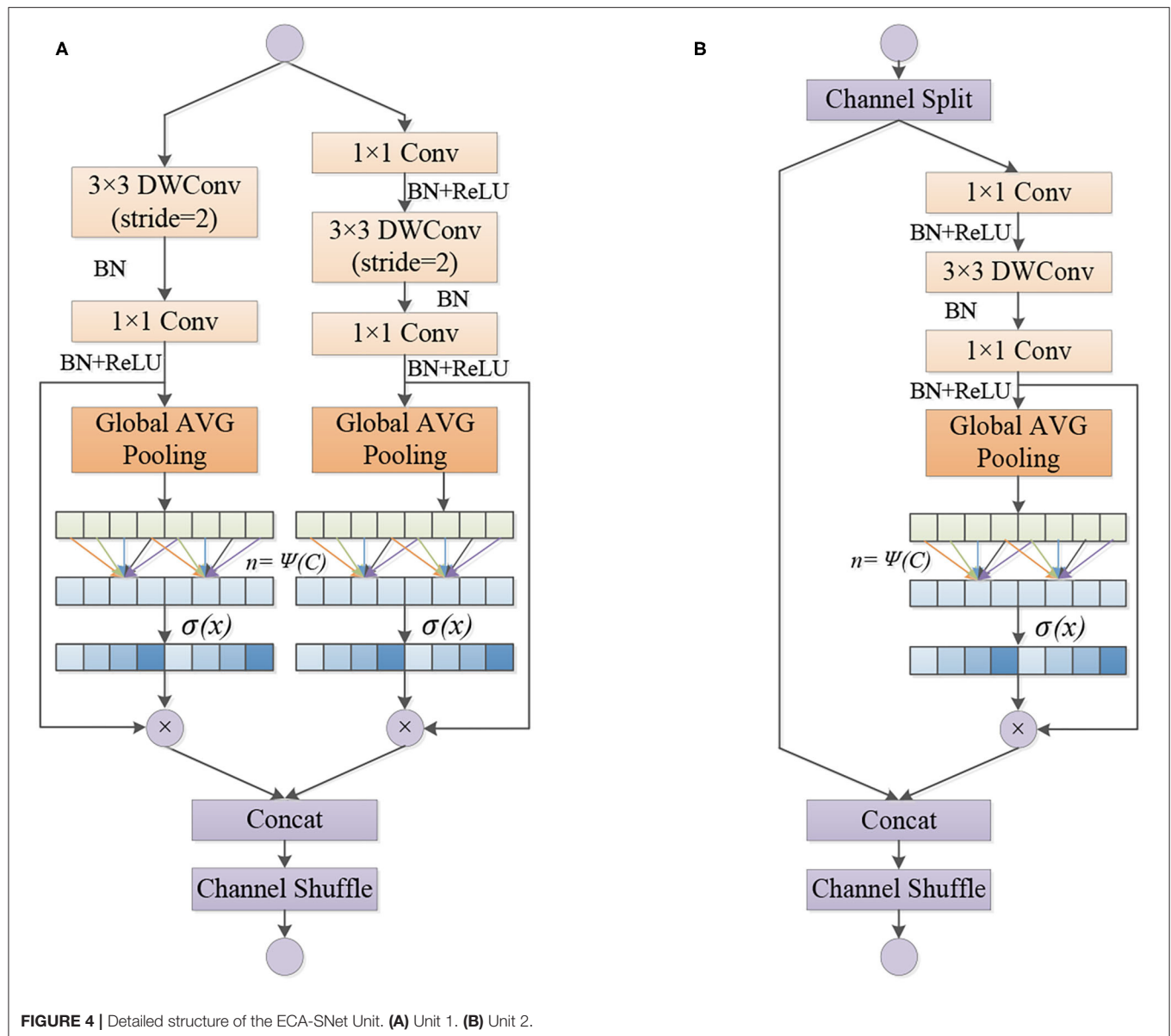


FIGURE 4 | Detailed structure of the ECA-SNet Unit. (A) Unit 1. (B) Unit 2.

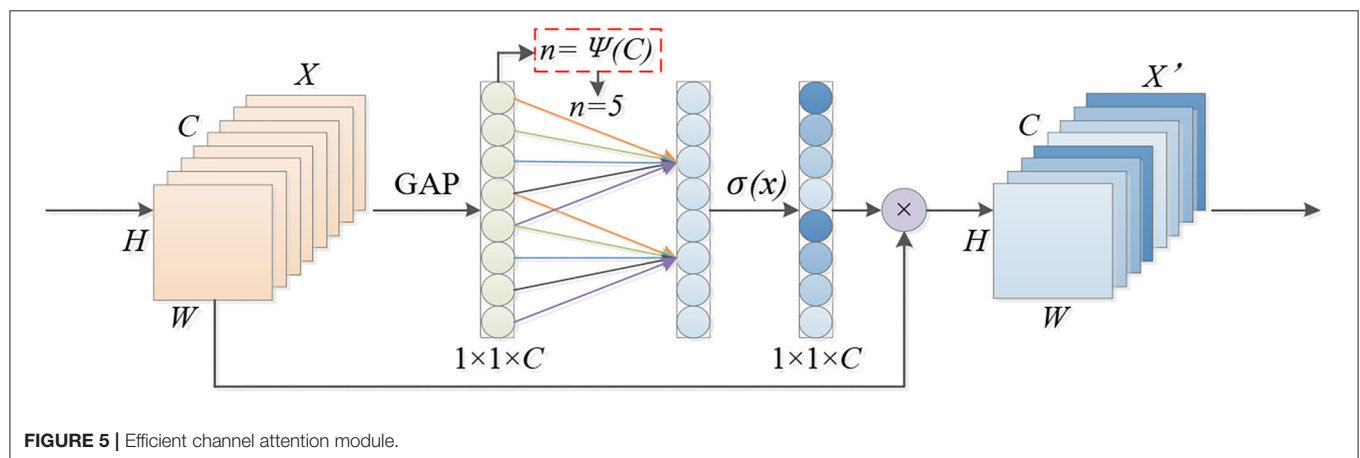


FIGURE 5 | Efficient channel attention module.

TABLE 2 | Detailed structural information of ECA-SNet.

Layer	Output size	Kernel size	Repeat	Output channel	
				0.5×	1.0×
Input	224 × 224	–	–	3	3
Conv	112 × 112	3 × 3	1	24	24
MaxPool	56 × 56	3 × 3	1		
Stage1	28 × 28	–	3	48	116
Stage2	14 × 14	–	6	96	232
Stage3	7 × 7	–	3	192	464
Conv	7 × 7	1 × 1	1	1,024	1,024
avg pool	1 × 1	7 × 7	1	–	–
FC	–	–	1	6	6

channel dimension is usually set to an integer power of 2, $2^{(\gamma^*n-b)}$ is used instead of $\exp(\gamma^*n-b)$, and the mapping relationship of Equation (3) was obtained. In this paper, in order to reduce the time and computational costs of the training process and improve the friendliness of model training, the hyperparameters γ and b were set to 2 and 1, respectively. It can be seen that the function ϕ enables long-range interactions for large-sized channels.

$$C=\varphi(n) \approx \exp(\gamma^*n-b) \quad (2)$$

$$C=\varphi(n)=2^{(\gamma^*n-b)} \quad (3)$$

Finally, given the channel dimension C , the size of convolution kernel n can be determined according to Equation (4), where $|m|_{\text{odd}}$ represents the odd number closest to m .

$$n=\Psi(C)=\left\lceil \frac{\log_2(C)}{\gamma} + \frac{b}{\gamma} \right\rceil_{\text{odd}} \quad (4)$$

The detailed structure information of the model is shown in **Table 2**. Two different versions of networks, 0.5× and 1.0×, are designed according to the depth of the output feature matrix. Repeat represents the number of repetitions of a specific operation; multiple ECA-SNet Units are repeated in Stage1–Stage3. It should be noted that the first operation of each stage is Unit 1, which doubled the feature dimension, and is only used for the first layer in each stage, and Unit 2 is used for subsequent operations.

EXPERIMENTAL RESULTS AND DISCUSSION

Parameters Setting

In order to verify the performance of the ECA-SNet network, the Python language is used to build a model based on the Pytorch 1.7.1 deep learning framework, and the model is trained and tested on a GPU-equipped server. The detailed equipment configuration information of the test is shown in **Table 3**.

TABLE 3 | Hardware and software environment.

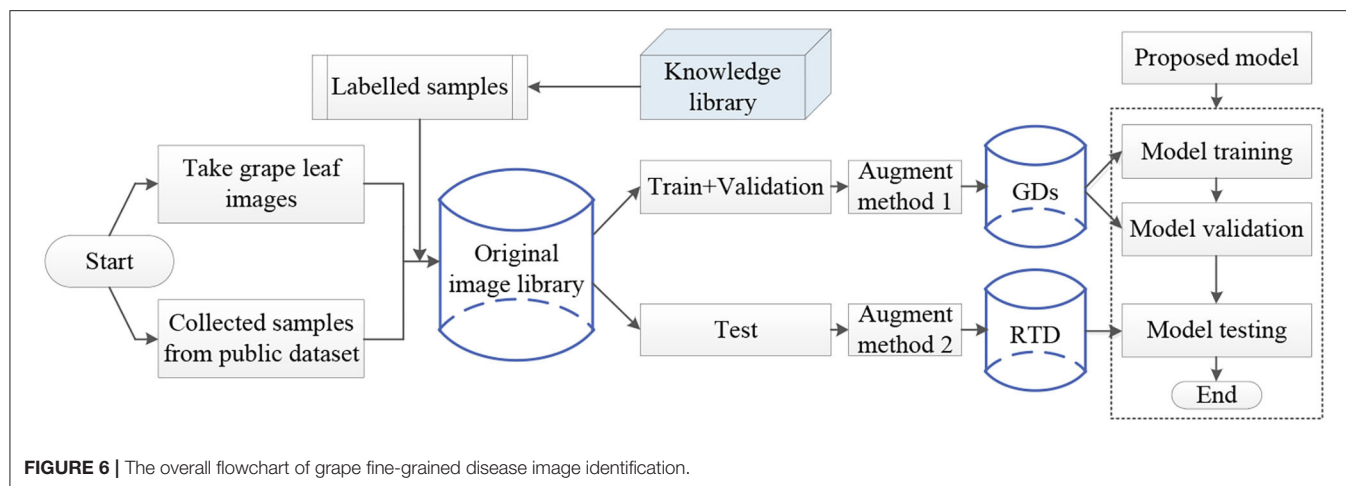
Configuration item	Value
CPU	Intel® Xeon(R) Gold 5217 CPU@3.00 GHz
GPU	NVIDIA Tesla V100 (32GB)
Operating system	Ubuntu 18.04.5 LTS 64
RAM	251.4GB
Hard disk	8TB

Model Training Process

The experiment process of fine-grained image recognition of the grape disease is shown in **Figure 6**. First, images of grape leaves are collected from orchards and public data set, and disease categories are labeled based on expert experience and then, standardized the annotated disease images and divided the original image library into the training set, the validation set, the test set, and different methods are used to enhance the training set and the test set. Finally, the model is trained with FGDs and tested with RTD to identify the type of each disease.

Weights Information Iterate Process

In order to visualize the optimization process of the numerical distribution of the convolutional layer, the histogram of weight value distribution of part convolutional layers is drawn, which is shown in **Figure 7**. **Figure 7A** shows the iterative process of the weights information of the first convolutional layer of the network. The abscissa is the numerical change of the convolutional layer during the iteration process, and the ordinate is the number of iterations. It can be seen that the weights information with large contribution is gradually highlighted, indicating that the model has been continuously optimized during the training process. When iterating to the 25th epoch, the weights value basically no longer changes, indicating that the network training has tended to be saturated. **Figure 7B** is the tiled form of histogram of the last convolutional layer in the network. The abscissa represents the numerical information of the convolutional layer, and the ordinate represents the number



of times the corresponding numerical value appears. With the training process proceeds, the data distribution tends to be concentrated. In order to keep the training process stable and convergent, the learning rate decays according to the cosine curve.

Performance of Proposed Model

In order to evaluate the performance of the model, the proposed model is tested with RTD, and the confusion matrix of the 0.5× version and 1.0× version of ECA-SNet is shown in **Figures 8A,B**. **Figures 8A,B** show the classification performance of ECA-SNet, and the accuracy reached 98.86 and 99.66%, respectively. Among them, the main misclassification of 0.5× version of the model is misidentification of the Black rot as Black measles, and there is also a little misidentification between Downy mildew, Powdery mildew, and Healthy leaves. Compared with 0.5× version, ECA-SNet 1.0× has a higher recognition performance, and the error is further reduced. Accurate recognition of fine-grained images in a complex background poses a great challenge, but the false recognition of each category of the model in this paper is steadily maintained at a low level. The test results show that ECA-SNet can accurately perceive key areas and has strong robustness and stability for fine-grained image recognition of grape diseases in complex environments.

Comparison of Proposed Model With Traditional Lightweight CNNs

In order to clarify the performance level of the model, the comparative test is conducted with multiple lightweight networks. Based on the confusion matrix, indicators, such as accuracy, precision, recall, and F1-score, are used to measure the comprehensive recognition performance of different grape diseases in each network. Accuracy, precision, recall, and F1-score are calculated from true positive (TP), false positive (FP), true negative (TN), and false negative (FN) results. The calculation of these indicators is shown in Equations (5–8):

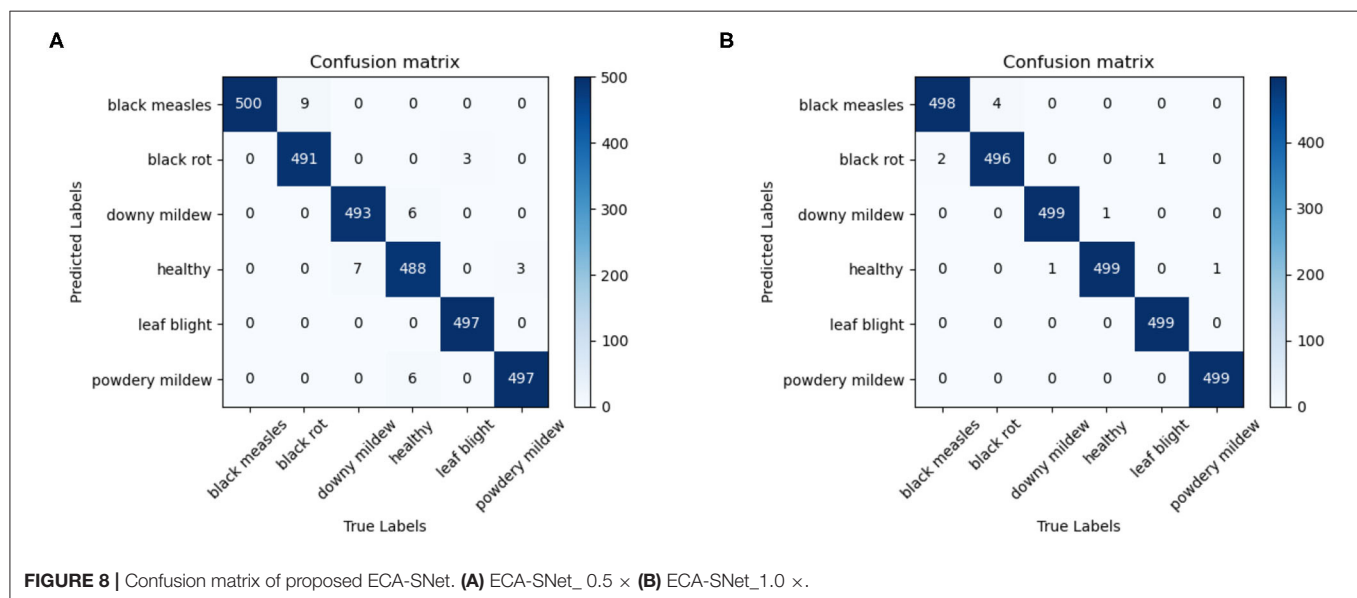
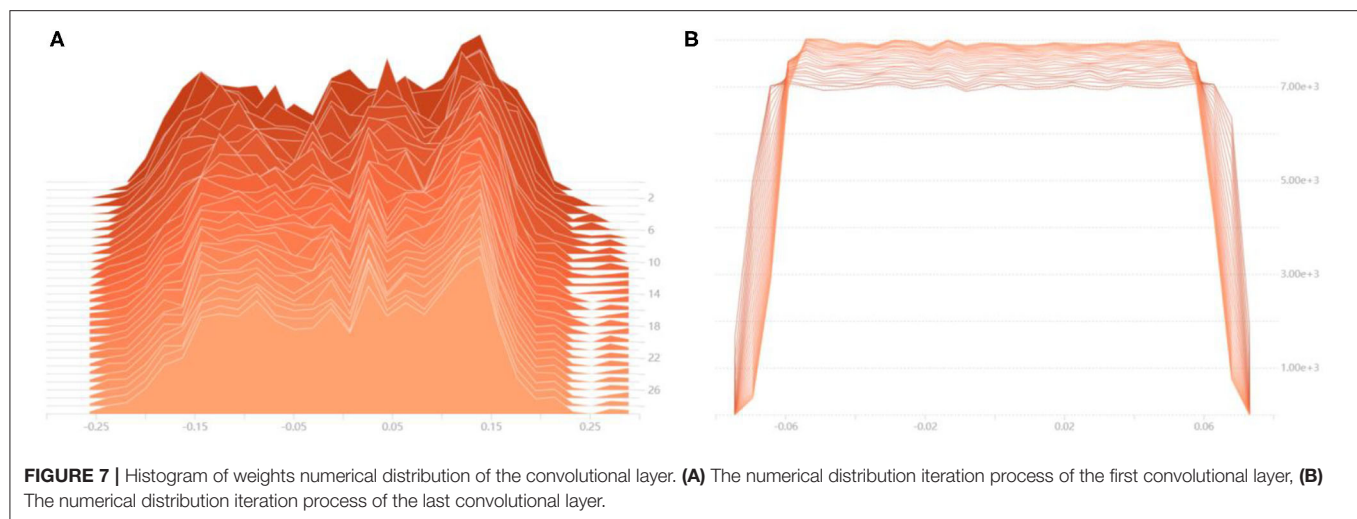
$$\text{Accuracy} = \frac{TP + TN}{TP + FP + TN + FN} \quad (5)$$

$$\text{Precision} = \frac{TP}{TP + FP} \quad (6)$$

$$\text{Recall} = \frac{TP}{TP + FN} \quad (7)$$

$$\text{F1 - score} = 2 \times \frac{\text{Precision} \times \text{Recall}}{\text{Precision} + \text{Recall}} \quad (8)$$

The performance indicators of ECA-SNet and other commonly used lightweight networks are compared, and the statistical results are shown in **Table 4**. MobileNet-v2 adopts the inverted residual structure, which effectively avoids the problem of model degradation. Deep separable convolution, the core of feature extraction, can greatly reduce the amount of parameters and calculations while ensuring accuracy. The RTD accuracy of MobileNet-v2 0.4× can reach 95.23%, which proves that the bottleneck structure has a strong feature learning ability. It is worth noting that, although both the 0.4× and 0.7× versions of MobileNet-v2 can achieve acceptable recognition accuracy, they need more calculations compared with other lightweight networks, which has a certain impact on the running speed of the model. By introducing the channel attention mechanism and redesigning the time-consuming layer structure, MobileNet-v3 greatly reduces the amount of calculations and achieves an average F1-score slightly higher than MobileNet-v2. However, due to the adoption of the channel attention strategy that included the dimensionality reduction layer, it inevitably leads to the increases of the parameters. The ShuffleNet-v2 network optimized the ShuffleNet structure based on criteria, such as optimal MAC, reduced network fragmentation, and reduced element-wise operations. Since the network failed to pay attention on the fine-grained information of the key areas of grape leaves when extracting features, the ShuffleNet-v2 test results performed poorly. Additionally, it can be seen from **Table 4** that the higher complexity of the relevant network has a certain improvement in the effect of disease identification. It is



because the increase of feature extraction layer structure enables the network to learn more relevant features, but this also leads to a rapid increase of model volume.

ECA-SNet generates high-efficiency channel attention by adaptively selecting the size of a one-dimensional convolution kernel on the basis of ShuffleNet-v2 and avoiding dimensionality reduction operations. The channel interaction strategy greatly improved the performance of channel attention, making ECA-SNet have the accurate recognition performance. The test accuracy of ECA-SNet 0.5× and ECA-SNet 1.0× with the RTD reaches 98.86 and 99.66%, respectively, which are higher than other networks of the same magnitude and have the least amount of parameters and computational costs. The test results show that avoiding dimensionality reduction and proper cross-channel interaction is very important for learning efficient channel attention.

Network Attention and Fine-Grained Visualization


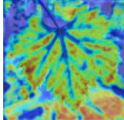
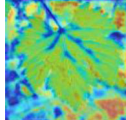
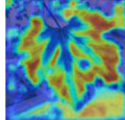
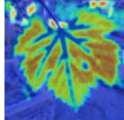

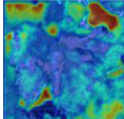
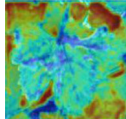
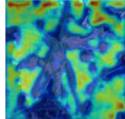
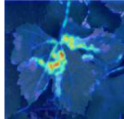

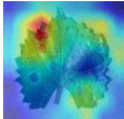
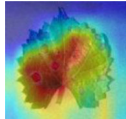
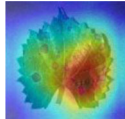
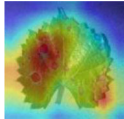

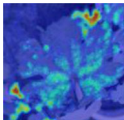
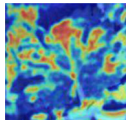
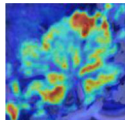
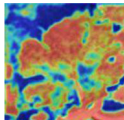

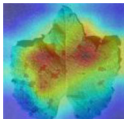
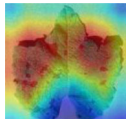
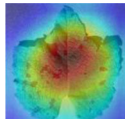
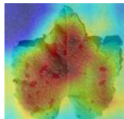
The evaluation of model performance through common indicators lacks intuitive display, and it is difficult to understand which part of the input image the model relies on to make decisions. In order to understand and analyze the network structure and visually display the model decision-making basis, the attention heat map visualization method is used to display the attention area. **Table 5** shows the attention heat map of ECA-SNet and other commonly used lightweight models. Sample images of healthy, downy mildew, black rot, powdery mildew, and leaf blight are randomly selected for testing. The red mark in the original image in **Table 5** is the annotation information of the diseased area on the grape leaves by the expert. According to the visualization results, it can be seen that the location of the key fine-grained features of grape disease images in a complex

TABLE 4 | Performance comparison of the proposed ECA-SNet against the classical lightweight CNNs.

Model	Accuracy/%	Average Precision/%	Average Recall/%	Average F1-score	FLOPs/M	Params/M
MobileNet-v3 small_0.75x	94.76	95.28	94.76	0.950	40.7	0.89
ShuffleNet-v2_0.5x	92.46	92.81	92.46	0.926	41.5	0.35
MobileNet-v2_0.4x	95.23	92.25	95.23	0.937	81.5	0.39
ECA-SNet_0.5x	98.86	98.86	98.86	0.988	37.4	0.31
MobileNet-v3 large_0.75x	96.70	96.83	96.70	0.967	146.1	2.42
ShuffleNet-v2_1.0x	95.20	95.30	95.20	0.952	147.8	1.26
MobileNet-v2_0.7x	95.93	96.03	95.93	0.959	178.6	1.12
ECA-SNet_1.0x	99.66	99.66	99.66	0.996	125.6	1.08

Bold values indicate best results under each index.

TABLE 5 | Visualization of attention heat map of grape leaf diseases.


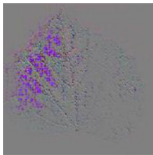
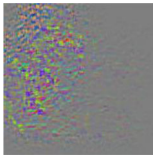
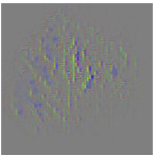
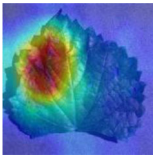
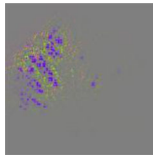

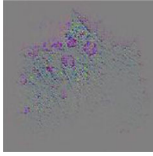
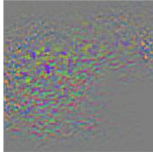
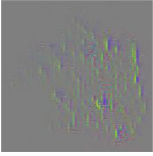
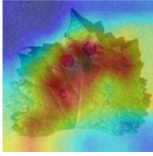
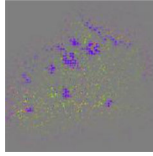

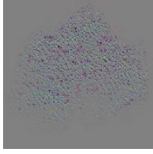
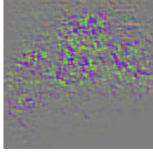
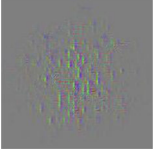
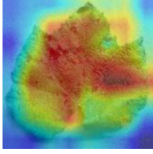
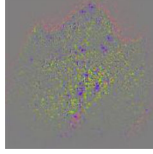
Class	Original image	ShuffleNet-v2 0.5x	MobileNet-v2 small 0.4x	MobileNet-v3 small 0.75x	ECA-SNet 0.5x
Healthy					
Downy mildew					
Black rot					
Powdery mildew					
Leaf blight					

background is difficult to determine, and neither ShuffleNet nor MobileNet can accurately focus on the key feature regions. The MobileNet-v2 network pays attention to much background information, which leads to insufficient feature learning. On account of MobileNet-v3 introduction of a channel attention mechanism, it plays a certain role in the key area of feature learning and reduces the attention of background information, but the effect is still poor. The ECA-SNet proposed in this paper can distinguish the foreground and the background and accurately locate the key areas. The leaf diseased area is strongly activated as the decision-making basis. In the recognition of diseased leaves with a purity background, each network can focus on the diseased area to varying degrees and has remarkable recognition ability. Compared with other networks, ECA-SNet can more comprehensively focus on lesion areas in different locations and has more superior decision-making capability.

The diseased spots of grape leaves are usually scattered randomly in different positions on the leaves; the shape, size,

and density of the diseased spots will affect Grad-CAM++ (Chattopadhyay et al., 2017). Therefore, in order to further display the fine-grained information of the network focus area, the guided back propagation and Grad-CAM++ were dot multiplication to obtain visual feature maps. The feature maps obtained above have both high resolution and category separability. Some example image test results are shown in Table 6. The red mark in the original image in Table 6 is the annotation information of the region of interest (diseased area) on the grape leaves by the expert. The feature maps of ShuffleNet-v2 are sensitive to large areas of lesions and can accurately locate the area of lesions. When the lesions become smaller and their locations gradually disperse, the fine-grained information extraction capability of the model is greatly declined. The fine-grained information extracted by MobileNet-v2 has much redundancy, which affects the accurate judgment of the model. MobileNet-v3 reduces redundancy, but the richness of fine-grained information is also reduced and fails to accurately

TABLE 6 | Fine-Grained feature visualization of grape leaf diseases.

Class	Original image	ShuffleNet-v2 0.5×	MobileNet-v2 small 0.4×	MobileNet-v3 small 0.75×	ECA-SNet heatmap	ECA-SNet 0.5×
Black measles						
						
						
Black rot						
Leaf blight						

locate the key information for classification decisions. According to **Table 6**, it can be found that ECA-SNet has excellent adaptability to lesion features; the key fine-grained information is comprehensive, and the information redundancy is low. The model in this paper can accurately locate different lesion shapes, positions, and densities and can make accurate classification decisions accordingly. The above test results show that the model in this paper fully considers the characteristics of disease spots and model structure, and the performance of grape leaf disease recognition is improved significantly.

CONCLUSION

A fine-grained image recognition model for grape diseases with an improved lightweight channel attention mechanism is proposed in this paper, which provides technical support for dynamic and efficient management of orchard grape diseases. Based on mobile devices, 3,388 images of grape leaf diseases are collected in the field, and 3,479 images are obtained from public data sets. By using image-enhancement techniques, the FGDs containing 62,670 images are generated. First, on the basis of ShuffleNet, a cross-channel interaction strategy without dimensionality reduction is used to make the model have efficient channel attention. Second, the layer structure is reduced in different stages to build an efficient ECA-SNet with a less parameter. Ultimately, the cross-channel coverage is determined by adaptively selecting the one-dimensional convolution kernel, which reduces the calculation costs while maintaining efficient channel attention performance. The proposed model is trained with FGDs and has been tested with RTD. The comparative experiments, including various performance evaluation indicators and process visualization, are carried out.

Through the experimental results, it can be seen that the model proposed in this paper achieves the best recognition

effect under the condition of extremely low calculation and parameters, with an accuracy of 98.86% and the F1-score of 0.988. Means, such as visualization, also show the superior performance of the model and realize the efficient performance of fine-grained disease images identification of grape leaves. The above work laid the theoretical foundation for the next development of automatic inspection equipment for disease identification and real-time orchard grape disease information acquisition.

DATA AVAILABILITY STATEMENT

The raw data supporting the conclusions of this article will be made available by the authors, without undue reservation.

AUTHOR CONTRIBUTIONS

PW, YM, and TN collected data. PW designed and performed the experiment, analyzed data, trained algorithms, and wrote the manuscript. BL, SY, DH, and QG conceived the study and participated in its design. All the authors contributed to the article and approved the submitted version.

FUNDING

This work was funded by the Key Research and Development Program of Shaanxi under Grants Nos. 2021NY-138 and 2019ZDLNY07-06-01.

ACKNOWLEDGMENTS

We would like to thank the reviewers for their valuable suggestions on this manuscript.

REFERENCES

- Bi, C., Wang, J., Duan, Y., Fu, B., Kang, J., and Shi, Y. (2020). MobileNet Based Apple Leaf diseases identification. *Mobile. Netw. Appl.* doi: 10.1007/s11036-020-01640-1
- Chao, X., Sun, G., Zhao, H., Li, M., and He, D. (2020). Identification of apple tree leaf diseases based on deep learning models. *Symmetry* 12:1065. doi: 10.3390/sym12071065
- Chattopadhyay, A., Sarkar, A., Howlader, P., and Balasubramanian, V. N. (2017). Grad-CAM++: improved visual explanations for deep convolutional networks. *arXiv* 1710.11063. doi: 10.1109/WACV.2018.00097
- Chen, J., Zhang, D., and Nanekharan, Y. A. (2020). Identifying plant diseases using deep transfer learning and enhanced lightweight network. *Multimed. Tools Appl.* 79, 31497–31515. doi: 10.1007/s11042-020-09669-w
- Chollet, F. (2017). Xception: deep learning with depthwise separable convolutions. *IEEE Conf. Comput. Vis. Patt. Recogn.* 2017, 1800–1807. doi: 10.1109/CVPR.2017.195
- Ferentinos, K. P. (2018). Deep learning models for plant disease detection and diagnosis. *Comput. Electron. Agric.* 145, 311–318. doi: 10.1016/j.compag.2018.01.009
- Howard, A., Sandler, M., Chen, B., Wang, W., Chen, L., Tan, M., et al. (2019). “Searching for MobileNetV3,” in *IEEE Conference Computation Vision Pattern Recognition* (Seoul), 1314–1324. doi: 10.1109/ICCV.2019.00140
- Howard, A. G., Zhu, M., Chen, B., Kalenichenko, D., Wang, W., Weyand, T., et al. (2017). Mobilenets: efficient convolutional neural networks for mobile vision applications. *arXiv* 1704.04861.
- Hu, J., Shen, L., Albanie, S., Sun, G., and Wu, E. (2018). “Squeeze-and-Excitation networks,” in *IEEE Transaction Pattern Analysis Machine Intelligence* (Salt Lake City, UT), 2011–2023. doi: 10.1109/CVPR.2018.00745
- Karthik, R., Hariharan, M., Anand, S., Mathikshara, P., Johnson, A., and Menaka, R. (2020). Attention embedded residual CNN for disease detection in tomato leaves. *Appl. Soft Comput.* 86:105933. doi: 10.1016/j.asoc.2019.105933
- Liu, B., Ding, Z., Tian, L., He, D., Li, S., and Wang, H. (2020). Grape leaf disease identification using improved deep convolutional neural networks. *Front. Plant Sci.* 11:1082. doi: 10.3389/fpls.2020.01082
- Liu, B., Zhang, Y., He, D., and Li, Y. (2018). Identification of apple leaf diseases based on deep convolutional neural networks. *Symmetry* 10:1. doi: 10.3390/sym10010011
- Lu, J., Hu, J., Zhao, G., Mei, F., and Zhang, C. (2017). An in-field automatic wheat disease diagnosis system. *Comput. Electron. Agric.* 142, 369–379. doi: 10.1016/j.compag.2017.09.012
- Ma, J., Du, K., Zheng, F., Zhang, L., Gong, Z., and Sun, Z. (2018). A recognition method for cucumber diseases using leaf symptom images based on deep convolutional neural network. *Comput. Electron. Agric.* 154, 18–24. doi: 10.1016/j.compag.2018.08.048
- Ma, N., Zhang, X., Zheng, H., and Sun, J. (2018). ShuffleNet V2: practical guidelines for efficient CNN architecture design. *arXiv* 1807.11164. doi: 10.1007/978-3-030-01264-9_8
- Mi, Z., Zhang, X., Su, J., Han, D., and Su, B. (2020). Wheat stripe rust grading by deep learning with attention mechanism and images from mobile devices. *Front. Plant Sci.* 11:558126. doi: 10.3389/fpls.2020.558126
- Priyadarshini, R. A., Arivazhagan, S., Arun, M., and Mirnalini, A. (2019). Maize leaf disease classification using deep convolutional neural networks. *Neural. Comput. Appl.* 31:8887–8895. doi: 10.1007/s00521-019-04228-3
- Ramcharan, A., McCloskey, P., Baranowski, K., Mbilinyi, N., Mrisho, L., Ndalahwa, M., et al. (2019). A mobile-based deep learning model for cassava disease diagnosis. *Front. Plant Sci.* 10:272. doi: 10.3389/fpls.2019.00272
- Sandler, M., Howard, A., Zhu, M., Zhmoginov, A., and Chen, L. (2018). “Mobilenetv2: inverted residuals and linear bottlenecks,” in *IEEE Conference Computation Vision Pattern Recognition* (Salt Lake City, UT), 4510–4520. doi: 10.1109/CVPR.2018.00474
- Szegedy, C., Vanhoucke, V., Ioffe, S., Shlens, J., and Wojna, Z. (2016). “Rethinking the inception architecture for computer vision. *IEEE Conference Computation Vision Pattern Recognition* (Las Vegas, NV), 2818–2826. doi: 10.1109/CVPR.2016.308
- Tang, Z., Yang, J., Li, Z., and Qi, F. (2020). Grape disease image classification based on lightweight convolution neural networks and channelwise attention. *Comput. Electron. Agric.* 178:105735. doi: 10.1016/j.compag.2020.105735
- Wang, Q., Wu, B., Zhu, P., Li, P., Zuo, W., and Hu, Q. (2020). “ECA-Net: efficient channel attention for deep convolutional neural networks,” in *IEEE Conference Computation Vision Pattern Recognition* (Seattle, WA), 11531–11539. doi: 10.1109/CVPR42600.2020.01155
- Yang, G., He, Y., Yang, Y., and Xu, B. (2020). Fine-Grained image classification for crop disease based on attention mechanism. *Front. Plant Sci.* 11:854. doi: 10.3389/fpls.2020.600854
- Zeng, W., and Li, M. (2020). Crop leaf disease recognition based on self-attention convolutional neural network. *Comput. Electron. Agric.* 172:105341. doi: 10.1016/j.compag.2020.105341
- Zhang, X., Zhou, X., Lin, M., and Sun, J. (2018). “ShuffleNet: an extremely efficient convolutional neural network for mobile devices,” in *IEEE Conference Computation Vision Pattern Recognition* (Salt Lake City, UT), 6848–6856. doi: 10.1109/CVPR.2018.00716

Conflict of Interest: The authors declare that the research was conducted in the absence of any commercial or financial relationships that could be construed as a potential conflict of interest.

Publisher’s Note: All claims expressed in this article are solely those of the authors and do not necessarily represent those of their affiliated organizations, or those of the publisher, the editors and the reviewers. Any product that may be evaluated in this article, or claim that may be made by its manufacturer, is not guaranteed or endorsed by the publisher.

Copyright © 2021 Wang, Niu, Mao, Liu, Yang, He and Gao. This is an open-access article distributed under the terms of the Creative Commons Attribution License (CC BY). The use, distribution or reproduction in other forums is permitted, provided the original author(s) and the copyright owner(s) are credited and that the original publication in this journal is cited, in accordance with accepted academic practice. No use, distribution or reproduction is permitted which does not comply with these terms.



Detecting Plant Stress Using Thermal and Optical Imagery From an Unoccupied Aerial Vehicle

Bonny Stutsel*, Kasper Johansen, Yoann M. Malbêteau† and Matthew F. McCabe

Hydrology, Agriculture and Land Observation, Water Desalination and Reuse Center, King Abdullah University of Science and Technology, Thuwal, Saudi Arabia

OPEN ACCESS

Edited by:

Rajeev Ram,
Massachusetts Institute of
Technology, United States

Reviewed by:

Ali Parsaeimehr,
Delaware State University,
United States
Giovanni Avola,
National Research Council (CNR),
Italy

*Correspondence:

Bonny Stutsel
bonnystutsel@gmail.com

†Present address:

VanderSat,
Haarlem, Netherlands

Specialty section:

This article was submitted to
Technical Advances in Plant Science,
a section of the journal
Frontiers in Plant Science

Received: 01 July 2021

Accepted: 14 September 2021

Published: 25 October 2021

Citation:

Stutsel B, Johansen K,
Malbêteau YM and McCabe MF (2021)
Detecting Plant Stress Using Thermal
and Optical Imagery From an
Unoccupied Aerial Vehicle.
Front. Plant Sci. 12:734944.
doi: 10.3389/fpls.2021.734944

Soil and water salinization has global impact on the sustainability of agricultural production, affecting the health and condition of staple crops and reducing potential yields. Identifying or developing salt-tolerant varieties of commercial crops is a potential pathway to enhance food and water security and deliver on the global demand for an increase in food supplies. Our study focuses on a phenotyping experiment that was designed to establish the influence of salinity stress on a diversity panel of the wild tomato species, *Solanum pimpinellifolium*. Here, we explore how unoccupied aerial vehicles (UAVs) equipped with both an optical and thermal infrared camera can be used to map and monitor plant temperature (T_p) changes in response to applied salinity stress. An object-based image analysis approach was developed to delineate individual tomato plants, while a green-red vegetation index derived from calibrated red, green, and blue (RGB) optical data allowed the discrimination of vegetation from the soil background. T_p was retrieved simultaneously from the co-mounted thermal camera, with T_p deviation from the ambient temperature and its change across time used as a potential indication of stress. Results showed that T_p differences between salt-treated and control plants were detectable across the five separate UAV campaigns undertaken during the field experiment. Using a simple statistical approach, we show that crop water stress index values greater than 0.36 indicated conditions of plant stress. The optimum period to collect UAV-based T_p for identifying plant stress was found between fruit formation and ripening. Preliminary results also indicate that UAV-based T_p may be used to detect plant stress before it is visually apparent, although further research with more frequent image collections and field observations is required. Our findings provide a tool to accelerate field phenotyping to identify salt-resistant germplasm and may allow farmers to alleviate yield losses through early detection of plant stress via management interventions.

Keywords: unoccupied aerial vehicle, unmanned aerial vehicle, thermal infrared, salt tolerance, phenotyping, tomato, plant stress, accessions

INTRODUCTION

The area of agricultural land impacted by salinization and sodification is increasing globally, with more than 50% of arable land predicted to be affected by 2050 (Wang et al., 2003; Jamil et al., 2011). Concurrently, it is anticipated that crop production will need to more than double to meet the demands of a projected 10 billion people by 2050 (Ray et al., 2013). Furthermore, increasing affluence and shifting diets toward greater meat consumption mean that without improvements in productivity, water consumption in agriculture will increase by a further 70–90% over the same period (Molden, 2013; Pittock et al., 2016). Global freshwater supplies are under extreme pressure, with agricultural production already accounting for more than two-thirds of freshwater use (Famiglietti, 2014; Brauman et al., 2016; Pastor et al., 2019). Therefore, irrigation with brackish water presents as an enticing option, as the targeted application of water is an effective way to close the yield gap (Licker et al., 2010; Mueller et al., 2012). The identification and breeding of cultivars with increased resilience to salt stress would provide an effective twofold solution to ensuring future food security by enabling production on marginal land and the potential to irrigate with brackish water (Morton et al., 2018).

Salt stress in plants results in complex physiology and morphometric changes that occur in two distinct phases (Munns and Tester, 2008). The first phase occurs rapidly (minutes to days) as the plant responds to the buildup of salt in the roots, which leads to reduced osmotic potential and hence water uptake. This phase is referred to as ion-independent and causes stomatal closure and a reduction in new shoot growth. The second ionic phase occurs more slowly (days to weeks) once salt concentration in the leaves reaches cytotoxic levels, resulting in senescence of mature leaves (Munns and Tester, 2008; Isayenkov and Maathuis, 2019). A plant's response to salt stress also varies with the growing environment (Maas, 1993), making field trials necessary to assess stress in agronomically important traits such as yield quantity and quality. Despite focused research efforts, there has been little progress in identifying salt-tolerant genes. Researchers attribute this lack of progress to the genetic complexity of salt tolerance (Morton et al., 2018) and the limitations of manual field phenotyping (Araus and Cairns, 2014). New tools and approaches are required to bridge this phenotype-to-genotype divide (McCabe and Tester, 2021).

Recent advances in remote sensing technologies offer a means to overcome some of the limitations of traditional field phenotyping. Unpiloted aerial vehicles (UAVs) mounted with multispectral, hyperspectral, and thermal sensors have proven particularly useful for phenotyping due to their ability to capture plant data at unprecedented spatial (sub-cm), temporal (on-demand), and spectral resolutions. Laborious and often subjective manual measurements of plant phenotypic traits can now be augmented by consistent information derived for an entire field in a single flight and with repeatability across the growth cycle (Araus and Cairns, 2014; Holman et al., 2016). For example, UAV-captured data can provide insights on plant nitrogen status (Perry et al., 2018), height (Ziliani et al., 2018),

biomass (Bendig et al., 2014; Johansen et al., 2020), and temperature (Deery et al., 2016; Malbêteau et al., 2018) at the field scale and on demand, which is accelerating field screening and selection of germplasm for agronomically important traits to guide breeding programs and optimize commercial cultivars (Hickey et al., 2019).

The last decade has seen a rapid expansion in the application of UAVs for field phenotyping (Yang et al., 2017; Xie and Yang, 2020). However, applications of UAV-based sensing in salinized environments for rapid identification of salt-tolerant germplasm are relatively unexplored, despite research showing that wild-growing relatives (e.g., *Solanum pimpinellifolium*) of cultivated crops (e.g., *Solanum lycopersicum*) have increased salt tolerance (Zuriaga et al., 2009; Rao et al., 2013; Bolger et al., 2014; Razali et al., 2018). Johansen et al. (2019, 2020) addressed this gap by assessing phenotypic traits, including tomato plant area, plant cover, growth rate, condition, biomass, and yield from UAV-based multispectral imagery to discriminate plant performance under salt stress and control conditions. They identified distinct differences in phenotypic traits between control and salt-treated plants and found the traits suitable for identifying most of the highest yield-producing plant accessions. They also incorporated these traits into a random forest approach to predicting yield before harvest. Overall, their results indicated that salt tolerance is evident in many phenotypic expressions and is best discriminated from other abiotic and biotic stresses by incorporating UAV measurements of multiple traits.

Extending on these prior studies, we investigate the collection of plant temperature measurements (T_p) derived from UAV-based thermal infrared (TIR) cameras to screen for salt stress. T_p is commonly used as a surrogate for stomatal conductance, as stomatal closure results in reduced transpiration, which in turn leads to an increase in T_p (Tanner, 1963; Jones, 2013). However, TIR-based T_p is also influenced by environmental factors such as net radiation, vapor pressure deficit (VPD), and wind speed (Jackson et al., 1988). Therefore, researchers commonly use T_p measurements in combination with air temperature (T_a) for TIR indices such as the crop water stress index (CWSI) (Idso et al., 1981; Jackson et al., 1981) to normalize data and compare plant stress across multiple days. T_p and its use *via* the CWSI have been explored in broad-acre crops (Bian et al., 2019; Gracia-Romero et al., 2019; Zhang et al., 2019), tree crops (Gonzalez-Dugo et al., 2012, 2014; Park et al., 2017), and vineyards (Baluja et al., 2012; Bellvert et al., 2016; Sepúlveda-Reyes et al., 2016; Kustas et al., 2018). From an analysis of the recent literature, an examination of T_p retrievals in annual vegetable crops seems to be limited to potato plants (Rud et al., 2014). The ability to detect salinity-induced stress in tomato plants *via* remotely sensed T_p in the initial ion-independent phase would be particularly helpful in providing an early detection method of stress before changes in plant color or shape occur.

Using remotely sensed T_p as an indicator of stress requires its accurate retrieval from UAV TIR imagery, which remains challenging (Aragon et al., 2020; Döpper et al., 2020; Perich et al., 2020). First, UAV TIR cameras use lightweight uncooled

microbolometers, making them prone to thermal drift (Gómez-Candón et al., 2016; Mesas-Carrascosa et al., 2018; Döpfer et al., 2020). Second, the impact of vignetting and dead pixels in the focal plane array needs to be accounted for (Kelly et al., 2019; Aragon et al., 2020). Third, the methods used to generate the orthomosaic from which T_p is retrieved will also influence the apparent temperature (Perich et al., 2020). Fourth, shadowing within the plant canopy can lead to large temperature differences between sunlit and shaded components, which may require consideration (Jones et al., 2002). Fifth, the soil background temperature integration can bias the retrieved T_p (Jones and Sirault, 2014). Finally, the sensitivity of T_p to environmental variation means that weather changes such as wind speed, wind direction, or cloud cover across a flight can introduce uncertainty (Maes et al., 2017).

Overcoming the low radiometric accuracy of UAV-based TIR cameras has led to the development of laboratory-based and vicarious calibration procedures to improve temperature retrievals (see Jensen et al., 2014; Khanal et al., 2017; Maes et al., 2017; Ribeiro-Gomes et al., 2017; Torres-Rua, 2017; Aragon et al., 2020). Even though calibration procedures are employed, research to date demonstrates the need to carefully consider how data are captured, processed, and ultimately used to retrieve T_p . Researchers have employed many methods to identify vegetation pixels from which to retrieve T_p in coarse TIR imagery. Researchers interested in bulk canopy temperature have previously used simple polygons to delineate plots (Deery et al., 2016; Gracia-Romero et al., 2019; Perich et al., 2020). However, this method only works for crops with canopy closure, which precludes the impact of the background soil temperature on T_p retrievals. Therefore, TIR imagery is commonly co-registered to red, green, and blue (RGB), multispectral, or hyperspectral imagery so that vegetation indices or classification algorithms can be applied to identify pixels representing vegetation (Rud et al., 2014; Zhang et al., 2019; Maimaitijiang et al., 2020). To prevent reliance on other data sources, a number of approaches have been developed based solely on TIR imagery for T_p retrieval (Meron et al., 2010, 2013; Cohen et al., 2017; Park et al., 2017; Bian et al., 2019). Often, such approaches delineate canopy extent using edge detection methods, from which they can then retrieve T_p from pixels.

For a method to be adopted in precision agriculture workflows, it needs to be farmer-friendly and as straightforward as possible (Cohen et al., 2017). Based on the reviewed literature, there is currently a significant knowledge gap and disconnect between obtaining and extracting UAV-based TIR information and then ensuring this information can be translated into meaningful biological understanding at the individual plant scale (Kellner et al., 2019). Our research presents an approach for retrieving T_p from UAV-based TIR and RGB imagery, with an experimental focus on a diversity panel of tomato plants undergoing drip-irrigation in both control and salt water conditions. The retrieved T_p is interrogated to understand its response to plants experiencing salt stress and establish if TIR-based indices can identify differences in plant stress between control and salt-treated plants, and the optimum time during the growing season to detect plant stress using multi-temporal UAV-based TIR data.

MATERIALS AND METHODS

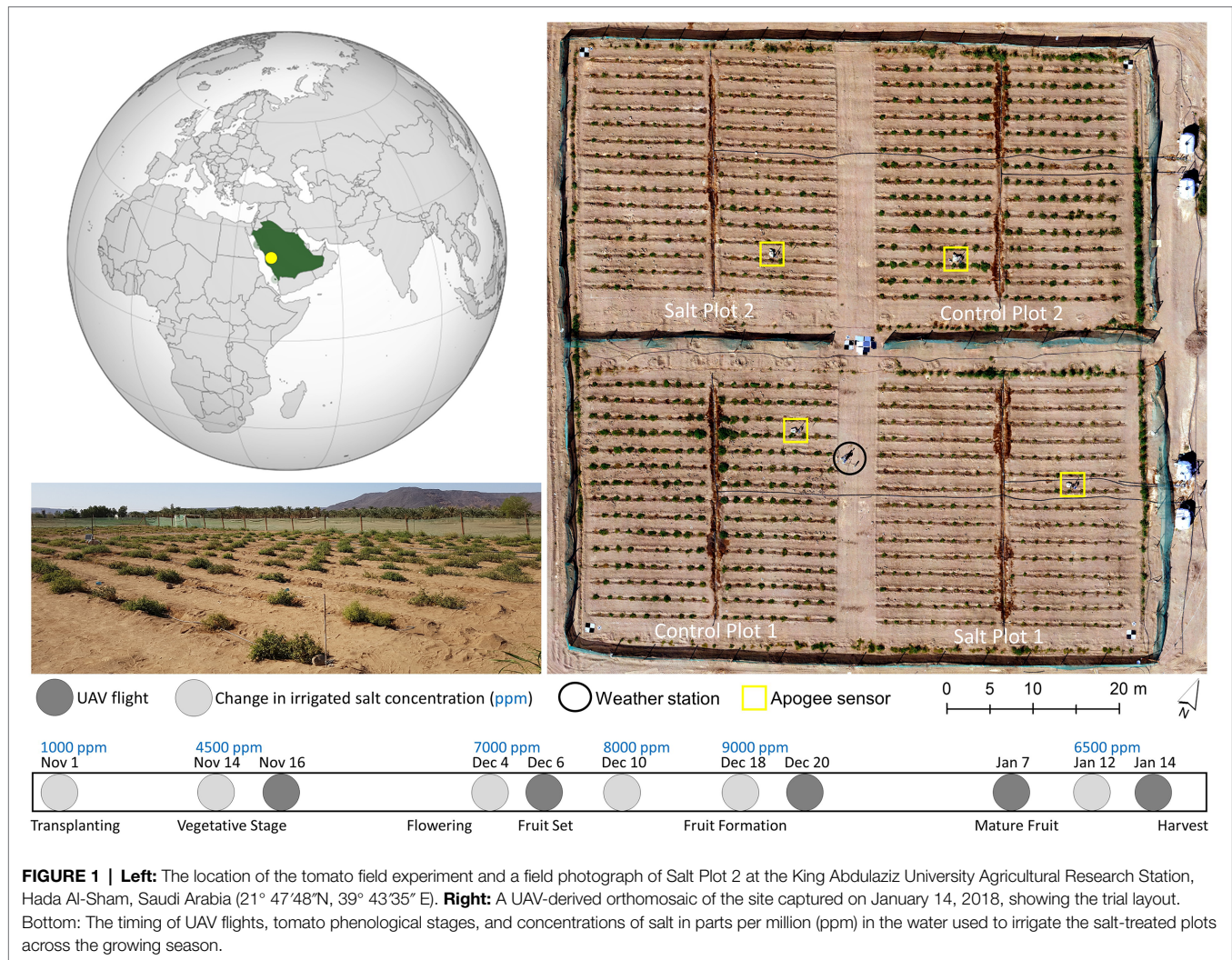
Description of Study Site

The study took place during the 2017–2018 growing season (November–January) at a field located within the King Abdulaziz University Agricultural Research Station in Hada Al-Sham, Saudi Arabia (21° 47'48"N, 39° 43'35"E, **Figure 1**). The field was divided into four separate plots, each approximately 40 m x 40 m, with 15 rows of 20 tomato plants. Two plots were established as controls, with freshwater irrigation (approx. 900–1,000 ppm NaCl). The other two plots were irrigated twice daily (except Fridays) with saline water of increasing concentrations (**Figure 1**). In developing the diversity panel, 200 accessions (199 wild *Solanum pimpinellifolium* and one commercial *S. lycopersicum*) were screened for salt tolerance via randomized planting of three replications of each accession for each treatment (i.e., three salt-treated and three control plants per accession, producing a total of 1,200 plants). At the beginning of November, 1,200 seedlings were transplanted into the field (after 1 month of greenhouse growth), with harvesting taking place between 16 and 26 January (**Figure 1**). Additional details of the site and trial design information can be found in Aragon et al. (2020) and Johansen et al. (2019). The focus of this study was to understand whether TIR data can identify differences in plant stress between control and salt-treated *Solanum pimpinellifolium* plants.

A weather station was installed toward the middle of the field (**Figure 1**) to collect meteorological data throughout the growing season. T_a and relative humidity (RH) were recorded every minute at 2.3 m above ground level (AGL) using an HMP155 humidity and temperature probe (Vaisala, Helsinki, Finland), from which the VPD was calculated (May et al., 2008). Wind speed and direction were also recorded every minute at 2.2 m AGL with a WindSonic anemometer (Gill, Hampshire, United Kingdom). Meteorological data were augmented by four distributed stations in each of the plots that measured point-scale thermal infrared temperature via an Apogee radiometer (SI-111, Apogee, Logan, United States), which facilitates interpretation of the UAV-collected TIR data (see locations in **Figure 1**). The Apogee sensors were installed in each plot approximately 1 m above a plant, representing a footprint of around 0.40 m². As our study occurred in an arid desert environment, sandstorms impacted the site on December 8 and 16, 2017, and January 4 and 8–10, 2018. To combat the impact of the sandstorms on results, field staff washed the plants with non-saline water after each event.

Thermal Infrared and Optical RGB Data Collection and Processing

Thermal Infrared Image Collection and Processing
TIR images were captured using a gimbal-stabilized FLIR Tau 2 core with a ThermalCapture 2.0 capture system (TeAx, Wilnsdorf, Germany) mounted on a DJI Matrice 100 quadcopter (Da Jiang Innovations, Shenzhen, China). The camera has a broadband spectral range across 7.5–13.5 μ m with a resolution of 640 x 512 pixels and a focal length of 13 mm. Manufacturer



guidelines indicate temperature retrievals with a specified accuracy of $\pm 5^{\circ}\text{C}$ and sensitivity of 0.04°C . Flying height was 13 m AGL at a speed of $2\text{ m}\cdot\text{s}^{-1}$ for a total flight duration of approximately 17 min, with flight times shown in **Table 1**. The imagery was collected from a nadir view, with around 60% sidelap and 93% forward overlap. Five large circular aluminum trays that can be easily distinguished in the TIR data (due to their low emissivity) were deployed at both the center and each corner of the field as ground control points (GCPs) (**Figure 1**). Each GCP's location was surveyed using a Leica AS10 Real-Time Kinematic Global Navigation Satellite System and base station (Leica Geosystems, St. Gallen, Switzerland).

Before deploying the TeAx 640 camera, a temperature-dependent radiometric calibration matrix was applied to correct ambient temperature dependency, vignette effects, and other non-uniformity noise (Aragon et al., 2020). The multilinear regression matrix from Aragon et al. (2020) was applied to the collected thermal data before subsequent processing. In this correction, the mean T_a acquired during each flight was used for the temperature-dependent radiometric calibration to remove any influence of ambient temperature dependency.

Geo-referencing and orthorectification of the TIR imagery were performed using Agisoft PhotoScan (Agisoft LLC, St. Petersburg, Russia). Before image alignment and scene reconstruction based on matched feature points, the calibrated radiance values were linearly stretched to the full dynamic range to improve feature identification. The image alignment step also performs a bundle adjustment to estimate the camera positions, orientations, and lens calibration parameters. Hence, to recalculate the camera positions, the self-calibrating bundle adjustment computes three-dimensional point clouds from which thermal orthophotos were built (Malbêteau et al., 2021).

For each of the five UAV campaigns, approximately 150 individual geo-referenced and orthorectified images were collected across each of 18 flight lines. Due to the forward overlap of 93% and the near-identical acquisition time of neighboring overlapping images, an averaging approach was applied to each pixel in the overlapping areas of each swath. The averaging method was applied to each swath due to the rapid changes in surface temperature and the impact of environmental conditions on the uncooled (unstabilized) sensor, which is often a significant challenge for UAV-based TIR processing (Aragon

TABLE 1 | UAV data collection date, start time and coincident mean air temperature (T_a), relative humidity (RH), wind speed (WS), and vapor pressure deficit (VPD) for the 17-min flights.

UAV Flight Date	Start Time	Ta (°C)	RH (%)	WS (ms ⁻¹)	VPD (kPa)
November 16, 2017	13:33	32.83	38.78	4.02	3.05
December 06, 2017	11:00	32.48	22.89	2.85	3.77
December 20, 2017	11:56	32.14	14.39	2.29	4.11
January 07, 2018	12:42	29.79	15.85	1.44	3.53
January 14, 2018	12:47	30.11	27.76	2.43	3.09

et al., 2020). To alleviate the influence of flight orientation relative to the wind direction and to ensure normalization of neighboring swaths, a flight direction correction method was also applied. The correction method normalized the pixel values within the neighboring swaths by assuming a 0°C difference between the overlapping (60% sidelap) areas. Initially, the first swath of the flight survey was used for correcting the second swath. Then, the second corrected swath was used for correcting the third swath and so forth. Adjusting the temperatures of each swath one by one and starting with the first swath of the flight survey ensured that all swaths were also corrected for temperature variability experienced during the 17 min of flight time (Malbêteau et al., 2021). The normalization process of individual swaths allowed them to be merged to form an orthomosaic.

Optical RGB Image Collection and Processing

RGB data were collected with a Zenmuse X3 camera (Dà-Jiāng Innovations, Shenzhen, China) concurrently with the TIR data, except on December 6, 2017, when RGB data were collected at 11:44 (approximately 44 min after the TIR data collection). The RGB image collection occurred with 82% sidelap and 93% along-track overlap, with a photograph captured every 3 s. All UAV data were collected under clear sky conditions and close to solar noon to reduce sun angle impacts on the RGB data (Table 1). RGB imagery was processed in Agisoft PhotoScan (Agisoft LLC, St. Petersburg, Russia) to construct a geometrically corrected orthomosaic, which was then radiometrically corrected using calibration panels and the empirical line method (Smith and Milton, 1999). Additional information regarding the collection, processing, and calibration of the RGB imagery is outlined in Johansen et al. (2019).

The processed RGB orthomosaics had a GSD of 0.005 m. The RGB orthomosaics were resampled to the same resolution as the TIR orthomosaics (0.015 m) using nearest-neighbor resampling in the rasterio.warp module. The resampling was undertaken to ensure that the RGB data could be used to determine each plant's extent for T_p retrieval from the TIR data (Figure 2). To ensure accurate co-registration of the TIR and RGB datasets, the RGB orthomosaics were manually geo-referenced in QGIS (QGIS Development Team, 2021) to

the TIR data using the five GCPs with a polynomial transformation, resulting in a mean square error between the centers of each GCP across all campaigns of approximately 0.01 m.

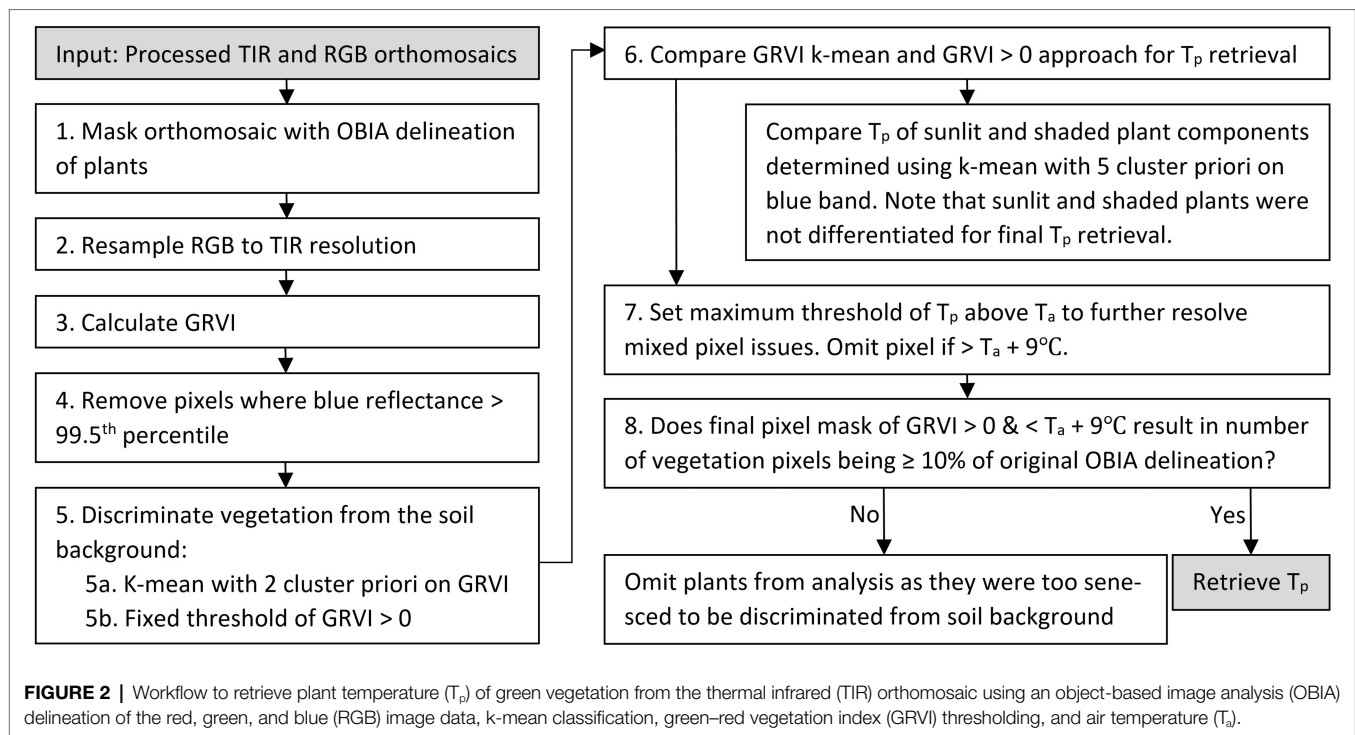
Retrieving Plant Temperature From the Thermal Infrared Orthomosaics

An object-based image analysis (OBIA) approach was applied to the RGB orthomosaics to identify each plant's extent in the TIR orthomosaic (Figure 2, Step 1). A full description of the workflow used to create the OBIA RGB delineations can be found in Johansen et al. (2019). In order to omit pixels within the delineated plants that were associated with white identification tags (attached to individual plants), pixels with blue reflectance above the 99.5th percentile were removed. Next, green vegetation was discriminated within the delineated objects by applying a k-means clustering to the green-red vegetation index (GRVI) (Motohka et al., 2010). The GRVI was calculated as per Eq. 1 using the collected RGB data, as this index produced good results in Johansen et al. (2019; Figure 2, Step 5a). We applied a k-mean unsupervised approach run with two clusters, k-means++ initialization, ten different centroid seeds, and a maximum iteration of 300 in the scikit-learn package of the Python 3.5 software (Pedregosa et al., 2011). We set two clusters since the plants had already been delineated with the OBIA approach, and we were merely interested in discriminating vegetation from the sandy background, which had distinct spectral characteristics. For the classification of vegetation, a threshold value of $GRVI > 0$ was also used (Motohka et al., 2010). The distribution of temperature for vegetation classified with both the k-means approach and the GRVI threshold was subsequently compared to determine the most suitable approach (Figure 2, Step 6).

$$\text{Green-red vegetation index (GRVI)} = \frac{\text{Green} - \text{Red}}{\text{Green} + \text{Red}} \quad (1)$$

Even after the GRVI mask was applied, there were a number of pixels with T_p that was considerably higher than that expected for vegetation, indicating mixed pixel or classification issues. Therefore, the approach of Rud et al. (2014) was adopted to determine a realistic estimate for the maximum deviation of T_p from T_a . In this case, a threshold of $T_a + 9^\circ\text{C}$ was used after analyzing both the field-installed Apogee radiometer and UAV data for the growing season. Subsequently, any pixels that had positive GRVI values but were warmer than $T_a + 9^\circ\text{C}$ were removed to allow the formation of the final vegetation mask, from which T_p was ultimately retrieved (see Figures 2, 3).

Following Poblete et al. (2018), a k-mean clustering using a five-cluster *a priori* and k-means++ initialization was also applied on the blue band in order to differentiate sunlit and shaded areas of the tomato plants. The selection of a five-cluster *a priori* was also verified by applying the elbow method to identify the optimum number of clusters (Thorndike, 1953). The maximum blue reflectance value of the first cluster was used as the threshold above which vegetation was identified as sunlit. From the final vegetation mask (Figure 2), we retrieved



descriptive statistics of T_p (minimum, maximum, mean, median, standard deviation, and pixel count). If the vegetation mask had a pixel count of <10% of the original number of pixels in the OBIA delineation, we removed the plant from further analysis, assuming the plant was dead or that the canopy had senesced and was thus too sparse for accurate T_p retrieval.

Identifying Plant Stress and Calculating Thermal Indices

To consistently compare plant temperature across the five flights, we calculated the deviation of T_p from ambient temperature ($dT_p = T_p - T_a$), a measure often used in field phenotyping studies of heat tolerance (Balota et al., 2007). To further normalize for meteorological conditions, we calculated the CWSI using Eq (2) (Idso et al., 1981; Jackson et al., 1981), where dT_p is the actual difference between T_p and T_a , $dT_{p_{LL}}$ is the lower limit that represents transpiration at the maximum rate (theoretically a non-stressed plant cooled *via* latent heat exchange), and $dT_{p_{UL}}$ is the upper limit that represents a halt in transpiration (theoretically a stressed plant, where sensible heat exchange determines T_p).

$$CWSI = \frac{dT_p - dT_{p_{LL}}}{dT_{p_{UL}} - dT_{p_{LL}}} \quad (2)$$

Traditionally, there have been two ways to derive these transpiration baselines: empirically ($CWSI_E$) and theoretically ($CWSI_T$), with many researchers reviewing and debating the various limitations of each (Gardner et al., 1992; Maes and

Steppe, 2012; Gerhards et al., 2019). The main limitation of the $CWSI_T$ is the complex meteorological data required to solve the energy balance equation. $CWSI_E$ has seen broad application, as it only needs three variables (T_a , T_p , and RH) to be calculated. However, the $CWSI_E$ approach requires dT_p and VPD measurements to be collected across an entire growing season to calculate robust baselines (Gardner et al., 1992). More recently, UAV studies have proposed a simplified statistical method ($CWSI_S$) using the temperature distribution in the image scene to set the baselines (Gonzalez-Dugo et al., 2013; Rud et al., 2014; Bian et al., 2019). This simplified approach is appealing, as it only requires measurements of T_a , which facilitates applications in precision agriculture (Cohen et al., 2017). However, both stressed and non-stressed plants need to be present in the imagery using the simplified approach.

As our study occurred in Saudi Arabia, where there is a paucity of studies applying the CWSI, we tested all three approaches. For $CWSI_E$, we calculated the baselines using the intercept and slope values for tomato plants in Idso (1982). For $CWSI_T$, we calculated $dT_{p_{LL}}$ as presented in O'Shaughnessy et al. (2011). As the calculation of $dT_{p_{UL}}$ in $CWSI_T$ is error-prone due to the estimation requirements of aerodynamic resistance and roughness length (Idso et al., 1981), we did not calculate it. Instead, we adopted $T_a + 9^\circ\text{C}$ as an estimate for $dT_{p_{UL}}$ (see **Retrieving Plant Temperature**). For the simplified statistical approach ($CWSI_S$), we examined the T_p histogram distribution and set $dT_{p_{LL}}$ as the mean of the lowest 5% of plant temperatures in the control plots, while $dT_{p_{UL}}$ was set as $T_a + 9^\circ\text{C}$. (Meron et al., 2013; Rud et al., 2014; Bian et al., 2019). We applied a standard independent two-sample T-test ($\alpha = 0.01$) in the SciPy package of the Python 3.5 software language

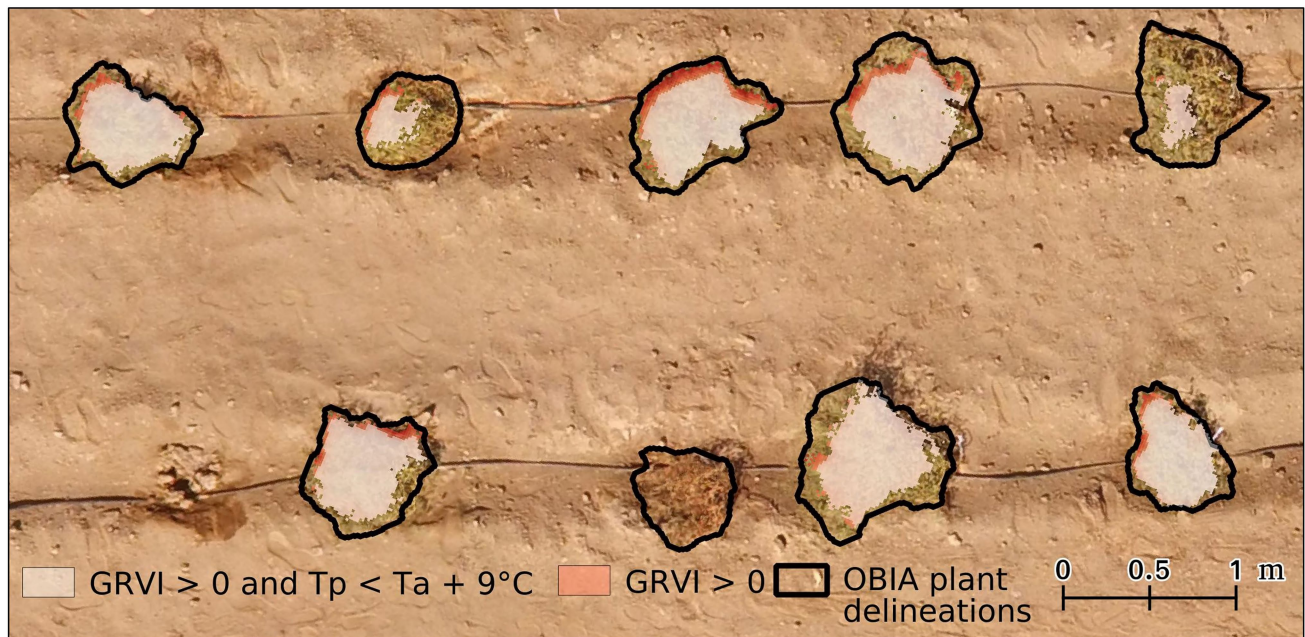


FIGURE 3 | An example of the vegetation mask where the GRVI was greater than 0 (i.e., indicating vegetation) and with pixels greater than air temperature (T_a) + 9°C dropped. Data are overlaid on a red, green, and blue image of six plants in a range of conditions in control plot 2 on January 14, 2018. Note light red on the edge plant corresponds to GRVI > 0 pixels warmer than T_a + 9°C.

(Virtanen et al., 2020) to assess whether there was a difference in thermal indices between salt-treated and control plots. To understand the change in thermal indices across the season, we calculated the percentage difference between the treatments and plotted the thermal indices as a box plot for each treatment to determine the optimum time to detect stress.

A field-based visual assessment of plants in poor condition was performed on January 4, which identified 30 dead plants. To assess whether T_p could be used to identify the dead plants earlier in the season and prior to senescence, 30 healthy plants were also selected from a visual assessment of the January 7 RGB data, with those plants distributed across the two control and two salt plots. That allowed comparison of the plants from the two groups, i.e., healthy and dead in the beginning of January, to determine whether T_p could be used for early detection of plant stress, while all plants were still green in December.

RESULTS

Discriminating Plant From Soil Temperature in the Thermal Infrared Orthomosaics

To determine the best approach to discriminate vegetation in the TIR orthomosaics to retrieve T_p , pixel-based temperature distributions within all tomato plants in the field trial were plotted. The presence of pixel-based temperatures >50°C (i.e., approximately T_a + 20°C) within the OBIA delineations (Figure 4)

indicated that some pixels represented soil or non-photosynthetic vegetation. When pixel-based temperature was retrieved using k-means clustering of the GRVI with a two-cluster *a priori* to separate background and vegetation, the frequency of pixels with temperatures >40°C reduced significantly (Figure 4). Therefore, it was assumed that this method was predominantly retrieving temperature from pixels representing vegetation rather than a mixed pixel response. A limitation of the k-means classification was attributed to vegetation being discriminated with a dynamic threshold of the GRVI value for the different campaigns to separate the two classes (Table 2), making a multi-temporal comparison of T_p challenging. Using a fixed threshold of GRVI > 0 to discriminate vegetation produced a similar temperature distribution across the five campaigns to that of the k-mean approach (Figure 4). However, the frequency of pixels with positive GRVI values decreased as the percentage of senesced vegetation increased. For example, the k-mean threshold for GRVI that separates vegetation and background was 0.02 on December 6. However, as non-photosynthetic vegetation increased, the threshold became -0.04 by January 14, which was the date exhibiting the largest difference between the two approaches in the number of retrieved vegetation pixels (Table 2). As a consistent comparison across the five flight dates was of most interest, a fixed threshold of GRVI > 0 was adopted for the final mask to retrieve T_p . However, a flexible clustering approach may produce better discrimination for single campaigns, which can be seen in the reduced number of pixels >40°C in the k-mean approach on December 6 (Figure 4).

As shown in Figure 4, the number of plant pixels increased through the growing season, peaking on January 7 with a subsequent

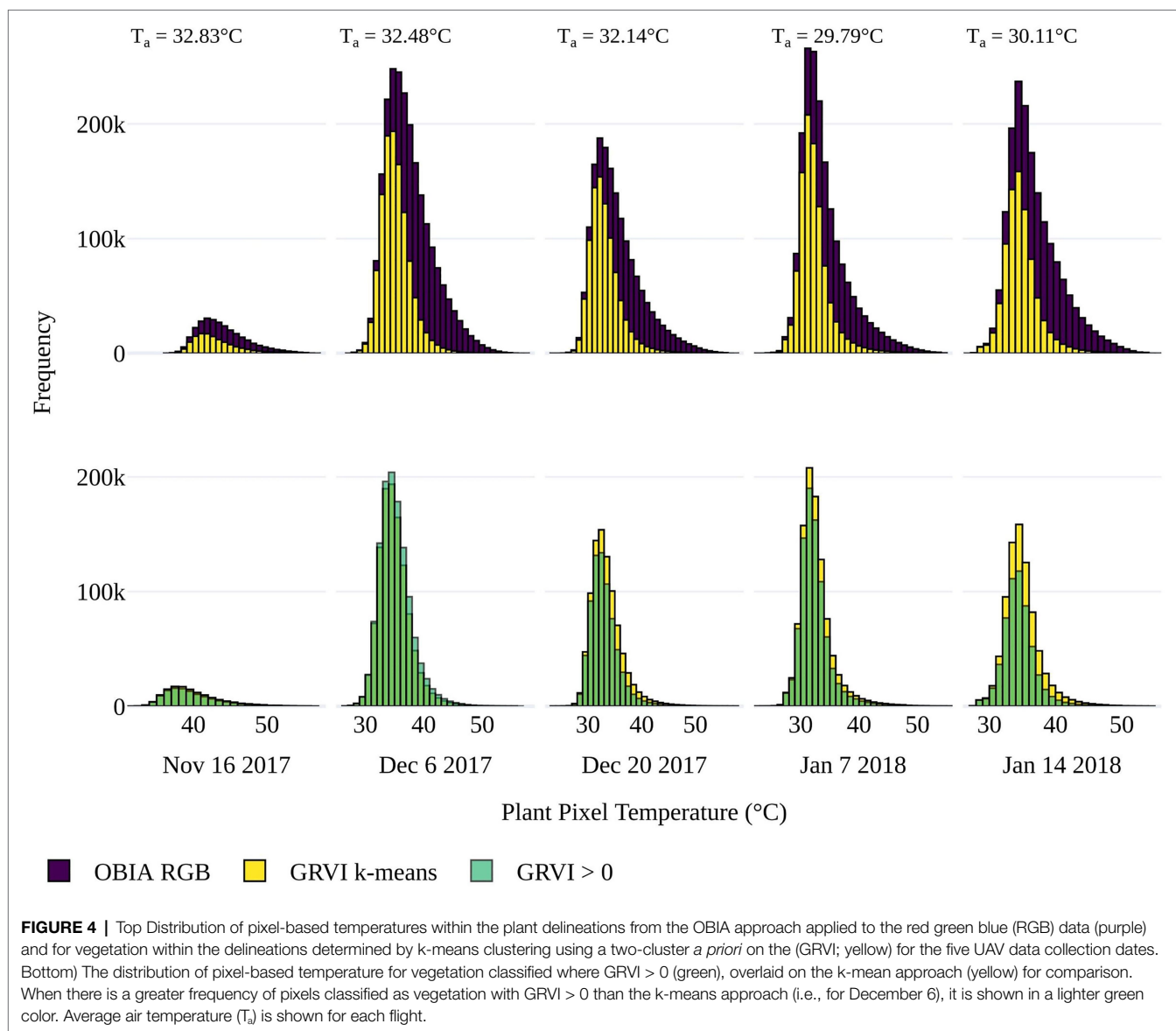


FIGURE 4 | Top Distribution of pixel-based temperatures within the plant delineations from the OBIA approach applied to the red green blue (RGB) data (purple) and for vegetation within the delineations determined by k-means clustering using a two-cluster *a priori* on the (GRVI; yellow) for the five UAV data collection dates. Bottom) The distribution of pixel-based temperature for vegetation classified where GRVI > 0 (green), overlaid on the k-mean approach (yellow) for comparison. When there is a greater frequency of pixels classified as vegetation with GRVI > 0 than the k-means approach (i.e., for December 6), it is shown in a lighter green color. Average air temperature (T_a) is shown for each flight.

TABLE 2 | The GRVI k-mean thresholds separating vegetation and the soil background across the five UAV data collection dates, as well as standard deviation (σ) of plant temperature (T_p) in the field trial for vegetation masks using GRVI > 0 and GRVI > 0 in combination with $T_p < T_a + 9^\circ\text{C}$.

Flight date	Nov 16, 2017	Dec 06, 2017	Dec 20, 2017	Jan 07, 2018	Jan 14, 2018
GRVI k-mean threshold	-0.02	0.02	-0.03	-0.02	-0.04
Max σ of T_p @ GRVI > 0	6.0	7.1	7.8	9.2	4.9
Mean σ of T_p @ GRVI > 0	2.3	2.2	2.0	2.1	1.8
Max σ of T_p @ GRVI > 0 + $T_p < T_a + 9^\circ\text{C}$	2.6	3.2	3.3	2.7	2.5
Mean σ of T_p @ GRVI > 0 + $T_p < T_a + 9^\circ\text{C}$	1.3	1.8	1.6	1.5	1.2

reduction due to increasing plant senescence prior to harvest. Counter to this trend was the reduction in the number of vegetation pixels on December 20. The fact that this occurred in both the OBIA and GRVI retrievals suggests that the decline may be attributed

to the plant damage and decrease in plant area caused by a sandstorm before the UAV capture (Johansen et al., 2019). There is a tendency toward a negative relationship between GRVI and T_p , as increased GRVI values (greenness) result

in T_p decreases due to latent heat exchange during transpiration. In our study, this trend held within the OBIA delineations, which included background soil and non-photosynthetic vegetation (**Figure 5**). However, there was no clear relationship between T_p and GRVI for $GRVI > 0$. The large range in T_p values for pixels with $GRVI > 0$ and the fact that there were pixels with positive GRVI values that have unrealistically high temperatures for vegetation demonstrated that the GRVI co-registration method did not fully resolve mixed pixel issues. Therefore, we set a more realistic threshold of $T_a + 9^\circ\text{C}$ for the maximum deviation of T_p from T_a to mask pixels further. The need for the $T_a + 9^\circ\text{C}$ threshold is shown with the reduction in the maximum standard deviation (σ) of T_p before and after the threshold was applied (**Table 2**). The mean of the maximum σ of T_p was 7°C for the five dates with $GRVI > 0$ but decreased to 2.9°C with the $GRVI > 0$ and $T_p < T_a + 9^\circ\text{C}$ (**Table 2**). The drop in the σ of T_p indicates that $GRVI > 0$ and $T_p < T_a + 9^\circ\text{C}$ effectively classified vegetation pixels and omitted background and mixed pixels, which is essential to ensure confidence that changes in T_p are an indication of a response to salt stress.

The number of plants from which T_p was able to be retrieved with the final vegetation mask ($GRVI > 0$ and $T_p < T_a + 9^\circ\text{C}$) compared to the number of plants as identified with the initial OBIA RGB delineation is shown in **Table 3**. As the growing season progressed, the sample size of the salt and control plots started to differ due to increased deterioration of plant condition in the salt plots based on the $GRVI < 0$ and $T_p > T_a + 9^\circ\text{C}$ thresholds. Note also that T_p was extracted from more plants on December 6 than November 16, due to the small plant size of the initial vegetative growth stage, as well as and soil background effects (i.e., the $T_a + 9^\circ\text{C}$ threshold).

Examining the Influence of Sunlit and Shaded Components of Tomato Plants

While separating vegetation and soil temperatures is important to minimize mixed pixel responses (McCabe et al., 2008), high-resolution TIR sensing also allows for the discrimination of sunlit and shaded elements within the instrument's field of view. To assess whether large temperature differences existed between sunlit and shaded vegetation components, the distributions of the sunlit (high reflectance) and shaded (low reflectance) components within the tomato plants (as determined by $GRVI > 0$) were compared to that of the whole plant, i.e., sunlit and shaded components combined. As shown in **Figure 6**, the plants had a relatively homogenous temperature range between sunlit and shaded plant components. The largest difference in shaded and sunlit temperatures occurred on December 6, 2017, which coincided with the date of the greenest vegetation (highest GRVI values) and earliest data collection time of 11:00h. The denser, more developed canopy and lower sun angle likely increased the impact of shading on this date. However, as there was no distinct temperature range between sunlit and shaded components, subsequent analysis of retrieved T_p of salt stress was based on both sunlit and shaded vegetation, defined by $GRVI > 0$ and $T_p < T_a + 9^\circ\text{C}$.

Can UAV Thermal Infrared Data Identify Stressed Tomato Plants?

To determine differences in plant response to either fresh or saline water irrigation, we assessed the deviation of T_p from the ambient temperature in both the salt and control plots. As shown in **Figure 7**, the mean temperature of tomato plants in the salt-treated plots consistently deviated from the ambient temperature more than the control plots across all five collection dates. The mean dT_p was above 5°C in both the salt-treated

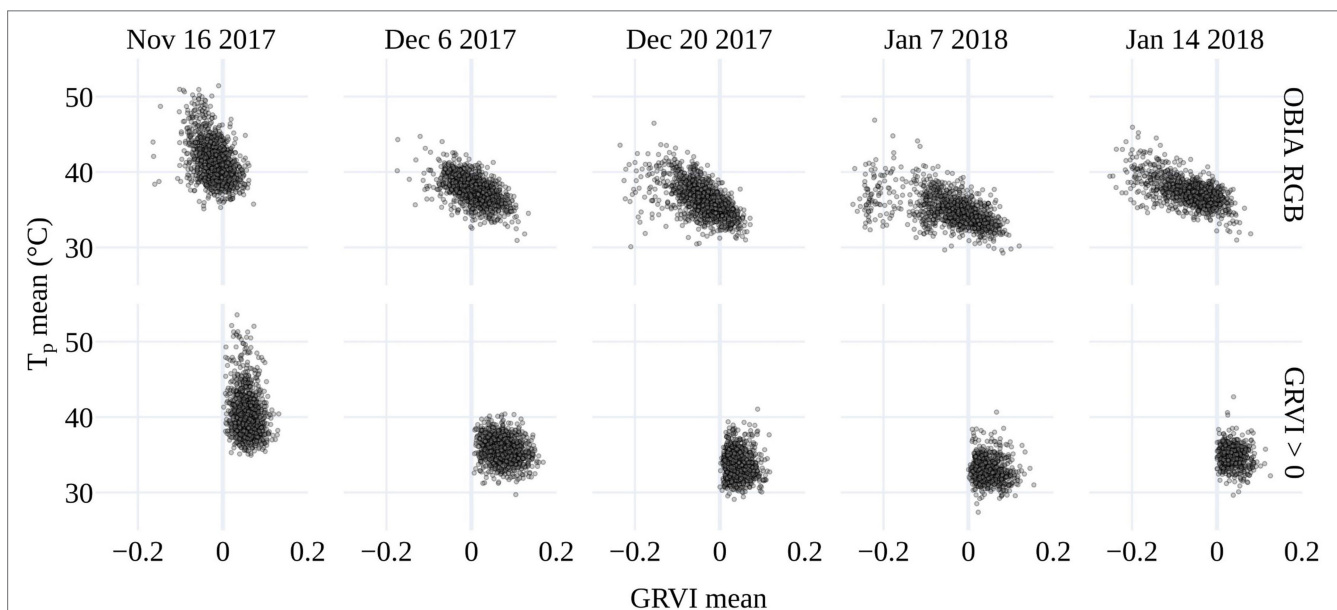
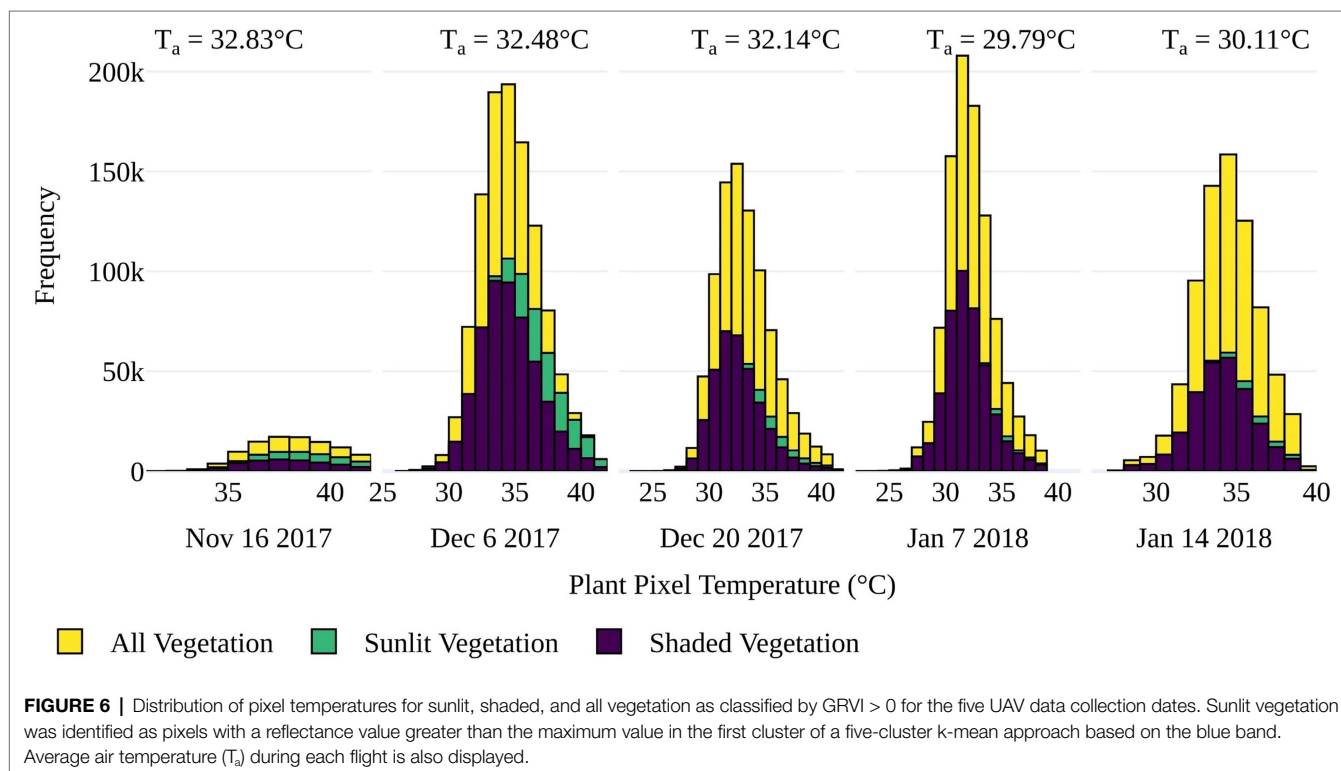


FIGURE 5 | The relationship between mean plant temperature (T_p) and the mean GRVI for the OBIA delineations (top) and $GRVI > 0$ retrieval.

TABLE 3 | Number of plants for which plant temperature (T_p) was retrieved in each of the thermal infrared orthomosaics.

UAV flight date	OBIA delineation			OBIA masked for $GRVI > 0$ & $T_p < T_a + 9^\circ\text{C}$		
	Control	Salt	Total	Control	Salt	Total
November 16, 2017	587	585	1,172	470	464	934
December 06, 2017	587	586	1,173	575	555	1,130
December 20, 2017	583	582	1,165	531	394	925
January 07, 2018	561	566	1,127	490	361	851
January 14, 2018	524	521	1,045	449	251	700

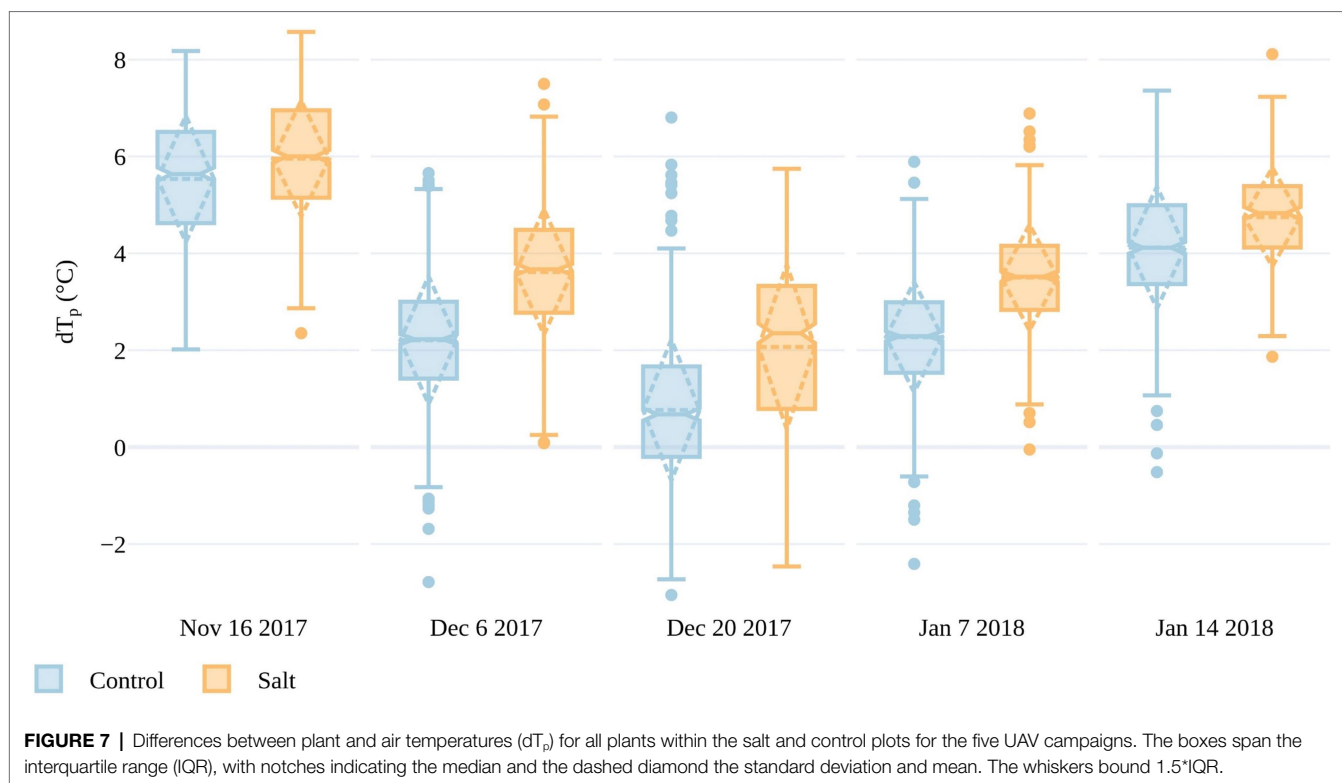
The number of plants is calculated based on: (1) the delineations of the OBIA approach and (2) the OBIA approach combined with the application of $GRVI > 0$ and $T_p < T_a + 9^\circ\text{C}$.



and control plots during the first collection on November 16, indicating that the plants may have been too small or sparse for accurate T_p retrieval. For instance, the mean plant area based on the OBIA RGB delineation was 0.06m^2 on November 16, but increased to 0.42m^2 by December 6. From December 6 to January 14, mean dT_p increased from 2.2 to 4.1°C in the control plots and from 3.6 to 4.7°C in the salt plots, demonstrating that the salt treatment led plants to have a higher T_p above the ambient temperature (Figure 7). The biggest difference in dT_p between salt and control plots occurred on December 20, with a difference of 1.3°C . Interestingly, on this day, plants also had the smallest deviation from T_a , with only one outlier in the control plot exceeding 6°C . The UAV flight on December 20 had a higher VPD (atmospheric demand for water) than on December 6 and January 7 and 14. Often, increasing VPD can lead to an initial increase in stomatal conductance, which decreases as the plant regulates its water exchange (Damour et al., 2010). The influence of VPD on

tomato stomatal conductance may have caused the smaller dT_p values for this date and may also be contributing to the larger dT_p difference between salt-treated and control plants (Patanè, 2011). The difference in dT_p between treatments was less apparent on January 14 (4 days before harvest), which may have been the result of plant aging and senescence being a larger factor in determining T_p than salt stress, as will be discussed in **UAV-Derived Plant Temperature**.

In order to compare results across the data collections, T_p had to be normalized for the variable weather conditions. To do this, the CWSI was calculated in three ways, as presented in **Identifying Plant Stress and Calculating Thermal Indices** (also see **Supplementary Figure S1**). Here, we only discuss $CWSI_s$, as it only required measurements of T_a and showed similar characteristics to $CWSI_e$ and $CWSI_t$ (Also, a full season of accurate daily dT_p was not available to calculate robust local transpiration baselines.) A smaller difference in $CWSI_s$ between the control and salt-treated plots occurred on January

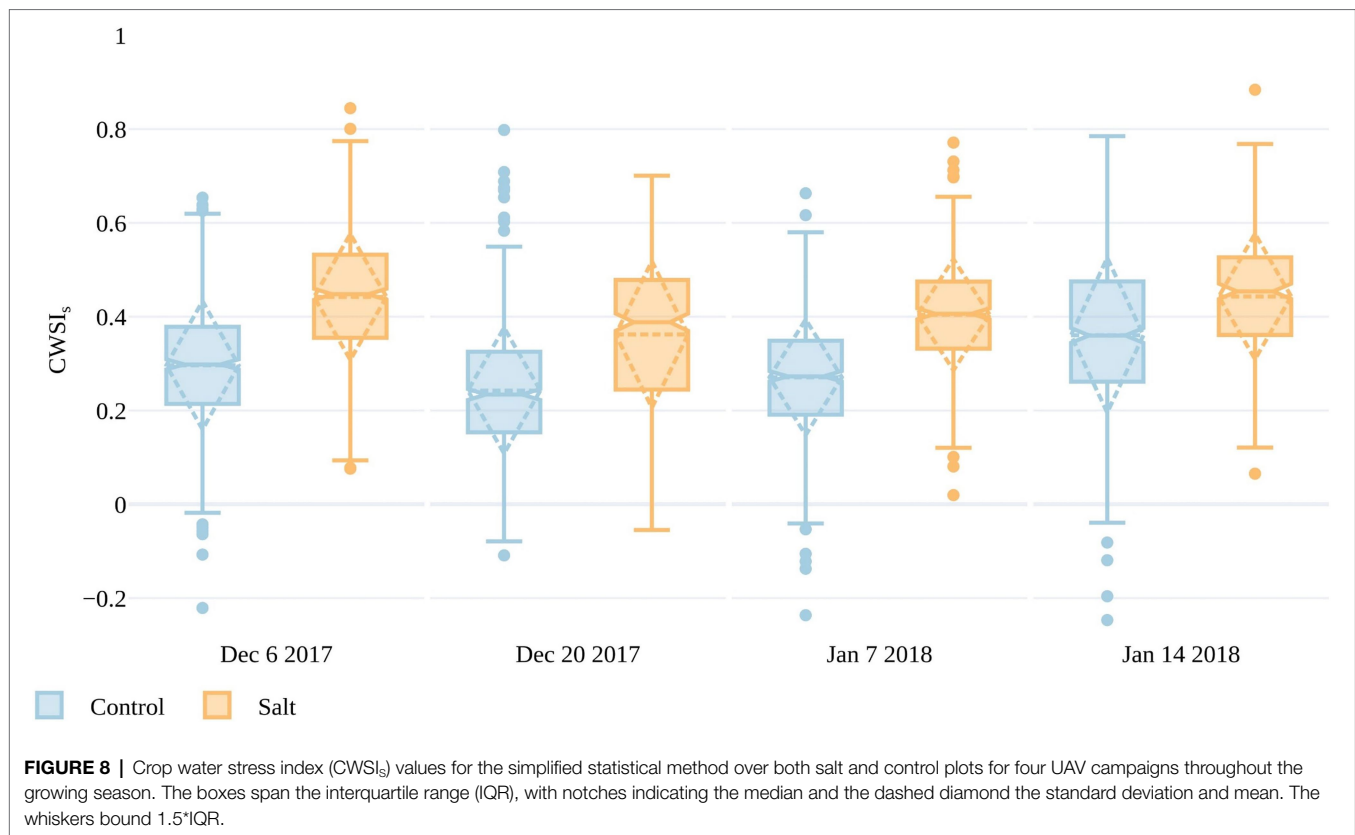


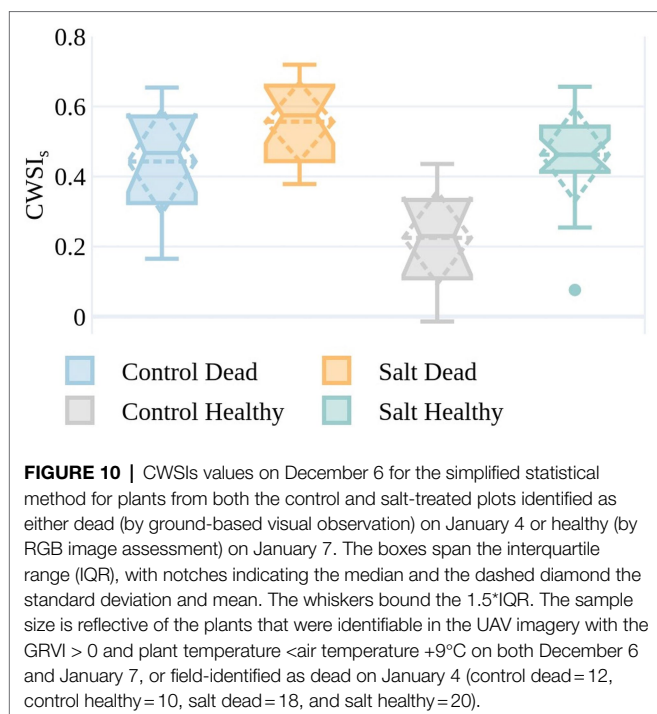
14 compared to the preceding dates. The smaller difference in CWSI_s between treatments closer to harvest suggests that T_p was better at discriminating stress between the fruit formation and ripening/mature stages (Figure 1), when plants in both plots had more developed canopies. From December 6 to January 7, mean CWSI_s in the control plots ranged between 0.23 and 0.27, whereas the salt plots ranged from 0.36 to 0.44, indicating that $\text{CWSI}_s > \sim 0.36$ may be an indicator of stress. It is worth noting that CWSI_s values < 0 represent plants that are cooler than the mean of the lowest 5% of plant temperatures in the control plots, which was used to set the lower limit in the CWSI that represents transpiration at the maximum rate. As CWSI_s was overestimated if T_p was retrieved from non-vegetation surfaces (Irmak et al., 2000), we omitted CWSI_s values for November 16 due to large dT_p values on that date, which represented T_p retrievals integrated the soil background. It is apparent from Figures 7, 8 that there is a large range in T_p (and consequently dT_p) and CWSI_s values within both the control and salt plots, which may be due to different stomatal responses to stress in each of the 200 accessions, as well as spatial variations within the trial. The spatial variations are plotted in Figure 9, with individual CWSI_s shown for both the control and salt treatment for December 20, 2017, and January 7, 2018, which represented the time from fruit formation to mature, ripe fruit. As can be seen, there is a clear tendency for higher CWSI_s values in the two salt treatments, relative to the control, with a larger number of plants with CWSI_s values > 0.35 in the salt-treated plots. For instance, on December 20, only 19% of control plants had a $\text{CWSI}_s > 0.35$, compared to 57% for the salt-treated plants. On January 7,

the proportion of plants with $\text{CWSI}_s > 0.35$ for the control and salt plots increased to 24 and 68%, respectively (Figure 9). It is, of course, important to recognize that spatial variability in real-world trials is more than just a function of plant stress, with other soil and environmental factors playing a role. However, while not all aspects of the spatial variation (e.g., the December sandstorms with northeasterly winds) in CWSI_s observed in Figure 8 can be attributed to salt-induced stress alone, Figure 9 provides some additional insights to help interpret the influence of irrigation treatments.

A field-based assessment of plant condition was undertaken on January 4, with 30 plants identified as dead. An equivalent number of healthy plants were separately identified from the RGB imagery collected on January 7. The CWSI_s values for plants in the healthy and dead categories are shown on December 6 in Figure 10 to understand whether CWSI_s values measured earlier in the season were indicative of the plant condition in early January.

Plants in the salt plots that were dead by January 4, but in good condition on December 6, generally had higher CWSI_s values than those control plants that were still healthy at the beginning of January (Figure 10). Of the plants that were classified as healthy, the ones in the control plots exhibited lower CWSI_s values than in the salt plots (median = 0.46 and 0.23, respectively). Interestingly to note is that for salt-irrigated plants on December 6, the difference in median CWSI_s values between plants that were dead and healthy by the beginning of January (0.57 and 0.46, respectively) is much smaller than for the control plants (0.47 and 0.23, respectively). This is most likely because the salt irrigation caused some level of





plant stress early in the growing season, i.e., December 6, irrespective of plant appearance. These differences in CWSI_s values on December 6 indicate that at least some plants that appeared green and visibly healthy with GRVI > 0 and $T_p < T_a + 9^\circ\text{C}$ showed early stress warning signs with high CWSI_s values almost a month prior to plant death.

DISCUSSION

Identifying salt-resistant germplasm in field trials is challenging for a number of reasons, not the least being that plant response to stress is complex and manual field methods to screen germplasm are onerous and often subjective (Araus and Cairns, 2014; Morton et al., 2018). UAV remote sensing has emerged to phenotype plants and provides a way to derive an additional understanding of stress responses. Previous research has explored the morphometric detection of salt stress in tomatoes through RGB and multispectral UAV data (Johansen et al., 2019, 2020). While data collection and processing workflows for such approaches are comparatively well developed, the retrieval of accurate T_p from UAV TIR data remains challenging (Ribeiro-Gomes et al., 2017; Torres-Rua, 2017; Kelly et al., 2019; Aragon et al., 2020; Perich et al., 2020).

Challenges in the Retrieval of Plant Temperature From Thermal Infrared Imagery

Here, we explored the retrieval of T_p from a UAV TIR camera in a tomato field trial, demonstrating that it is possible to detect differences between salt-treated and control plants, which may help identify salt-tolerant tomato germplasm in future

research. In our study, T_p was retrieved where GRVI > 0 and setting a maximum pixel threshold of $T_a + 9^\circ\text{C}$. The latter condition was required because the presence of pixels with $T_p > T_a + 20^\circ\text{C}$ in the OBIA plant delineation showed that object-based methods alone are insufficient to retrieve accurate T_p , at least from the tomato plants explored herein. This finding aligns with Cohen et al. (2017), who also suggest that while object-based approaches work well for tree crops, they fail to retrieve T_p from field crops due to their less defined canopy structure. We observed that even when T_p is extracted from pixels with GRVI > 0, temperatures that are unrealistically high for vegetation still occurred, demonstrating that the use of GRVI alone does not fully resolve mixed pixel issues. Our findings align with recent UAV TIR studies that could not eliminate all mixed pixels. For example, Zhang et al. (2019) used red and green reflectance together with TIR data to retrieve T_p for a maize crop and concluded that better methods for eliminating mixed pixels are required to facilitate accurate extraction.

In our study, the mixed pixel issues were alleviated by combining RGB data with this empirical method (i.e., $T_a + 9^\circ\text{C}$), which estimates the maximum temperature possible for non-transpiring vegetation. Researchers commonly report this empirical upper baseline in studies of drought stress for inclusion in CWSI calculations, e.g., $T_a + 5^\circ\text{C}$ in cotton (Cohen et al., 2005), $T_a + 7^\circ\text{C}$ in potato (Rud et al., 2014), and $T_a + 5^\circ\text{C}$ in wheat (Jackson, 1982) have all been used. The fact that our upper baseline was larger than those published could be attributed to the higher solar radiation and T_a of the arid field site or potentially an extreme isohydric behavior (Han et al., 2020), with closed stomata required to maintain turgor. As the field installed Apogee TIR radiometers used for setting the $T_a + 9^\circ\text{C}$ threshold make an integrated measurement of T_p from their field of view, vegetation movement driven by wind may have occasionally led to the integration of soil temperature, but it was not possible to fully resolve or remove the impact of soil background (Aubrecht et al., 2016).

The successful retrieval of T_p using a co-registration approach between the RGB and TIR imagery was dependent on good pixel alignment of the whole study area (Meron et al., 2013). While the datasets in the study were collected with two different sensors (Zenmuse X3 and TeAx 640) having differing resolutions and viewing geometries, they showed good alignment at the GCPs. Future research could identify whether the processing of RGB and TIR data together, as in Javadnejad et al. (2020), leads to better T_p retrieval than processing datasets separately with co-registration to GCPs. While new strategies for processing TIR data and identifying vegetation within the orthomosaic would likely improve results, research advances are inevitably constrained by available UAV TIR camera resolutions (640 × 480 pixels) and precision (Aragon et al., 2020). Although lower flying heights can increase pixel resolution, the downwash from a multirotor UAV may influence measured T_p (Tang et al., 2020). Lower flying height also increases flying time to cover the site, increasing the chance of temperature changes occurring during a flight, which could further influence results. The precision of uncooled microbolometers, together with the

potential impact of adjacency effects from background scattering (Aragon et al., 2020), adds further uncertainty to derived T_p measurements. While the adjacency effect on high-resolution satellite data has recently been explored (Zheng et al., 2019; Duan et al., 2020), the influence on UAV-based data remains under-explored and should be the focus of future work, especially in regard to phenotyping studies, where sub-degree accuracies may be required.

The detection of plant stress *via* UAV TIR data can be sensitive to the level of solar radiation due to its influence on stomatal conductance, with many studies showing the need to consider variation between sunlit and shaded plant components (Jones et al., 2002; Meron et al., 2013; Poblete et al., 2018; Zhang et al., 2019). However, these studies predominately occur in tree or vineyard crops with developed canopies where intra- and inter-plant shading can be significant compared to low profile well-spaced tomato plants. Nonetheless, we examined the temperature difference between high (sunlit) and low (shaded) blue reflectance areas of the plants and found, as opposed to Poblete et al. (2018), that shadowing did not increase the range in T_p . Therefore, the separation of sunlit and shaded plant components did not improve results in our study. It also meant that methods incorporating the standard deviation of T_p as a proxy for transpiration differences between sunlit and shaded areas to detect stress such as in Han et al. (2016), could not be applied to our study.

UAV-Derived Plant Temperature Can Be Used to Identify Plant Stress

While there are many unresolved questions and inherent sensor limitations for T_p retrievals from UAV TIR data, our research demonstrates a detectable difference in T_p between the salt-treated and control plots. Differences are apparent across all data collections following the initial salt application on November 14, 2017. Results suggest that T_p best discerns plant stress between the stages of fruit formation and ripening (i.e., between December 20 and January 7), an outcome most likely related to canopy cover, which was shown to peak approximately a month before harvest (Johansen et al., 2019). Increased canopy closure reduces soil background influence and increases the plant area over which transpiration is occurring. Once senescence begins, and photosynthesis reduces, and so too does transpiration and canopy cover. This result aligns with Perich et al. (2020), which, although based on a wheat crop, also showed that the optimal time to make TIR measurements is before the onset of senescence. The smaller difference in TIR indices (dT_p and CWSIs) between salt and control plots on January 14, together with the broad range in plant condition in both treatments, demonstrates that the morphometric methods of Johansen et al. (2019) present a better approach for identifying stress-tolerant germplasm close to harvest.

Our results suggest that a threshold of CWSIs >0.36 may indicate stress, based on mean differences between salt-treated and control plants and the fact that this threshold applied to 57 and 68% of plants in the salt plot, but only 19 and 24% in the control plots on December 20 and 7 January, respectively.

While studies applying CWSI to tomato plants are limited, our results are similar to Anconelli et al. (1993), where CWSI >0.35 led to yield reduction in processing tomatoes (i.e., tomatoes that are canned and machine harvested). Many studies have suggested that CWSI values around 0.3 represent an optimum threshold for commencing irrigation in response to water stress (Reginato, 1983; da Silva and Rao, 2005; González-Dugo et al., 2006). While there are observable differences between the salt and control plots, there is a broad range of dT_p and consequently CWSIs values in both treatments. This range may be inherent to the data collection method due to thermal drift or the creation of the orthomosaic. However, compared to previous research we applied a novel orthomosaic generation method by Malbêteau et al. (2021), wherein the temperature of overlapping pixels was averaged along each swath and normalized between-swath temperatures to reduce the impact of standard orthomosaic generation approaches (which integrate overlapping flight lines collected minutes apart and exposed to different wind directions). Presuming the ranges in CWSIs are reflective of real temperature differences between plants, we suggest that these differences are due to the 200 accessions exhibiting a range of stomatal conductance responses to salt stress. While T_p has been used to detect plant stress since the 1960s (Fuchs and Tanner, 1966), it is based on the assumption that plants show an isohydric reaction to stress, reducing stomatal conductance to limit transpiration. A growing body of evidence suggests that plants within the same species exhibit both isohydric and anisohydric responses to stress (Sade et al., 2012). The mechanism employed by tomato varieties with different salt tolerance levels to regulate water use is also unclear (Han et al., 2020). For example, the commercial variety “Moneymaker” (*Lycopersicon esculentum* Mill., cv) is anisohydric and maintains stomatal conductance in response to stress (Sade et al., 2012). The domesticated variety “Brigade” (*Lycopersicon esculentum* Mill.) reduces stomatal conductance under drought stress. However, it also opens stomata within a day of irrigation (Patanè, 2011). In comparison, wild types of tomato plants can keep stomata closed for up to 6 days after irrigation to maintain turgor (Torrecillas et al., 1995). The variation in stomatal conductance response among the 200 wild genotypes in our trial is still to be determined. Therefore, even with very accurate T_p retrievals, cooler plants may not necessarily be the least stressed in terms of agronomically desirable traits such as yield. Plants that had a higher temperature soon after salt application may maintain turgor and produce comparatively higher yields. Resolving this complexity and determining whether T_p can be used to differentiate the performance of accessions in our trial are the focus of ongoing research. Identification of inter-accession differences was not the intent of the research presented herein, as the combination of accuracy limitations in current TIR cameras (Kelly et al., 2019; Aragon et al., 2020), the complex role of environmental interactions with plant response, and the uncertainty and complexity in the mechanism employed by *Solanum pimpinellifolium* plants in response to salt stress are all aspects that impact the discrimination of accession-based behavior. Ongoing work will seek to explore some of the genotype–phenotype interactions, and the thermal infrared

data may provide some insights into this effort. As UAV-based T_p results are confounded by a plant's morphology (canopy density, leaf inclination), there also needs to be focused research into how to account for morphological variation to increase confidence in the association between observed T_p and stomatal conductance (Perich et al., 2020).

The fusion of TIR information with broadband spectral (Johansen et al., 2019) or hyperspectral data will likely provide more in-depth insight than TIR data alone to elucidate the challenges in observed T_p associated with plant physiological response (Hernández-Clemente et al., 2019). Building upon the results herein and integrating TIR data into the development of turnkey UAV phenotyping solutions could provide a method to enable the early detection of salt impacts by detecting changes in T_p in the initial ion-independent response to stress. While our study would have been improved by ground-based visual scoring of plant health during November and December (after the initial salt application), our results showed that CWSI_s values were higher in salt-treated than control plants from December 6. Early detection of stress before observed changes in plant form would enable breeders to select germplasm for future breeding studies rapidly and farmers to balance irrigation with brackish water while maintaining yields.

CONCLUSION

Salinization is increasingly impacting agricultural land around the world, and available freshwater water resources are increasingly under sustained pressures. Identifying new plant varieties that can either thrive on salinized land or tolerate irrigation with brackish water is crucial to ensuring future water and food security. UAV-based remote sensing has emerged as an effective means to phenotype field plants rapidly. Combining TIR imagery with multispectral data may enable the detection of plant stress before visible symptoms become apparent. Here, we retrieved T_p from UAV-based TIR data using concurrently collected RGB data to identify vegetation pixels ($GRVI > 0$) and an empirical estimate of the maximum possible vegetation temperature ($T_p < T_a + 9^\circ\text{C}$) to alleviate mixed pixels with background contamination. Results demonstrated measurable differences in T_p between salt-treated and control plants across five UAV campaigns performed during the growing season, with analysis suggesting that CWSI_s > 0.36 was indicative of stress. The reduction in CWSI_s differences between treatments toward the end of the growing season demonstrates that the optimum time to use T_p for identifying salt stress is between the fruit formation and ripening stages. T_p and CWSI_s differences between salt and control plots were detectable from December 6, indicating that TIR data may provide a means of early detection of salt stress before visible impacts are discernable. Further research with more frequent image and field data around the initial salt treatment is required to identify the exact time between salt application and a measurable T_p response to stress. T_p and CWSI_s differences were also identified not just between control and salt-treated plants, but between control plants that went on to either die or sustain their plant health

a month later. While our analyses provide new insights into the use of UAV-based TIR sensing for the early detection of plant stress, additional research is required to explain both the observed spatial variation and the processes behind stomatal conductance regulation in individual accessions.

DATA AVAILABILITY STATEMENT

The original contributions presented in the study are included in the article/**Supplementary Material**, further inquiries can be directed to the corresponding author.

AUTHOR CONTRIBUTIONS

BS, YM, and KJ undertook all UAV image processing and analysis. BS led the writing of the manuscript, with KJ, YM, and MM, also contributing. KJ, YM, and MM coordinated field and UAV data collection. KJ carried out the object-based plant delineations. MM designed the UAV-based experiment, including RGB, multispectral, thermal, and hyper-spectral data collection, and was involved in all aspects of the project. All authors contributed to the article and approved the submitted version.

FUNDING

MT and his team undertook the tomato plant experiment and were supported by the King Abdullah University of Science and Technology (KAUST) Office of Sponsored Research (OSR) under Award No. 2302-01-01 for undertaking the plant experiments. MM and his team were supported by Competitive Research Grant Nos. URF/1/2550-1 and URF/1/3413-01 for undertaking the UAV-based component of this research.

ACKNOWLEDGMENTS

We would like to thank all the workers and specially Prof. Magdi Mousa, at the King Abdulaziz University Agricultural Research Station in Hada Al-Sham for their extensive help with removing weeds, plant maintenance, and harvesting. Khadija Zemmouri and Dinara Utarbayeva prepared plots and undertook sowing of all plants. Dr. Mitchell Jack Love Moreton designed the plant experiment. Prof. Magdi Mousa led the team of workers to undertake planting, irrigation, fertilization, observation, and washing of plants after sandstorms. Prof. Mark Tester conceived the whole plant experiment.

SUPPLEMENTARY MATERIAL

The Supplementary Material for this article can be found online at: <https://www.frontiersin.org/articles/10.3389/fpls.2021.734944/full#supplementary-material>

REFERENCES

- Anconelli, S., Mannini, P., and Battilani, A. (1993). CWSI and baseline studies to increase quality of processing tomatoes *Acta Hortic.* 376, 303–306. doi: 10.17660/ActaHortic.1994.376.40
- Aragon, B., Johansen, K., Parkes, S., Malbetéau, Y., Al-Mashharawi, S., Al-Amoudi, T., et al. (2020). A calibration procedure for field and Uav-based uncooled thermal infrared instruments. *Sensor* 20:3316. doi: 10.3390/s20113316
- Araus, J. L., and Cairns, J. E. (2014). Field high-throughput phenotyping: the new crop breeding frontier. *Trends Plant Sci.* 19, 52–61. doi: 10.1016/j.tplants.2013.09.008
- Aubrecht, D. M., Helliker, B. R., Goulden, M. L., Roberts, D. A., Still, C. J., and Richardson, A. D. (2016). Continuous, long-term, high-frequency thermal imaging of vegetation: uncertainties and recommended best practices. *Agric. For. Meteorol.* 228, 315–326. doi: 10.1016/j.agrformet.2016.07.017
- Balota, M., Payne, W. A., Evett, S. R., and Lazar, M. D. (2007). Canopy temperature depression sampling to assess grain yield and genotypic differentiation in winter wheat. *Crop Sci.* 47, 1518–1529. doi: 10.2135/cropsci2006.06.0383
- Baluja, J., Diago, M. P., Balda, P., Zorer, R., Meggio, F., Morales, F., et al. (2012). Assessment of vineyard water status variability by thermal and multispectral imagery using an unmanned aerial vehicle (UAV). *Irrig. Sci.* 30, 511–522. doi: 10.1007/s00271-012-0382-9
- Bellvert, J., Zarco-Tejada, P. J., Marsal, J., Girona, J., González-Dugo, V., and Fereres, E. (2016). Vineyard irrigation scheduling based on airborne thermal imagery and water potential thresholds. *Aust. J. Grape Wine Res.* 22, 307–315. doi: 10.1111/ajgw.12173
- Bendig, J., Bolten, A., Bennertz, S., Broscheit, J., Eichfuss, S., and Bareth, G. (2014). Estimating biomass of barley using crop surface models (CSMs) derived from UAV-based RGB imaging. *Remote Sens.* 6, 10395–10412. doi: 10.3390/rs61110395
- Bian, J., Zhang, Z., Chen, J., Chen, H., Cui, C., Li, X., et al. (2019). Simplified evaluation of cotton water stress using high resolution unmanned aerial vehicle thermal imagery. *Remote Sens.* 11:267. doi: 10.3390/rs11030267
- Bolger, A., Scossa, F., Bolger, M. E., Lanz, C., Maumus, F., Tohge, T., et al. (2014). The genome of the stress-tolerant wild tomato species *Solanum pennellii*. *Nat. Genet.* 46, 1034–1038. doi: 10.1038/ng.3046
- Brauman, K. A., Richter, B. D., Postel, S., Malsy, M., and Flörke, M. (2016). Water depletion: An improved metric for incorporating seasonal and dry-year water scarcity into water risk assessments. *Elem. Sci. Anth.* 4:000083. doi: 10.12952/journal.elementa.000083
- Cohen, Y., Alchanatis, V., Meron, M., Saranga, Y., and Tsipris, J. (2005). Estimation of leaf water potential by thermal imagery and spatial analysis. *J. Exp. Bot.* 56, 1843–1852. doi: 10.1093/jxb/eri174
- Cohen, Y., Alchanatis, V., Saranga, Y., Rosenberg, O., Sela, E., and Bosak, A. (2017). Mapping water status based on aerial thermal imagery: comparison of methodologies for upscaling from a single leaf to commercial fields. *Precis. Agric.* 18, 801–822. doi: 10.1007/s11119-016-9484-3
- da Silva, B. B., and Rao, T. R. (2005). The CWSI variations of a cotton crop in a semi-arid region of Northeast Brazil. *J. Arid Environ.* 62, 649–659. doi: 10.1016/j.jaridenv.2005.01.017
- Damour, G., Simonneau, T., Cochard, H., and Urban, L. (2010). An overview of models of stomatal conductance at the leaf level. *Plant Cell Environ.* 33, 1419–1438. doi: 10.1111/j.1365-3040.2010.02181.x
- Deery, D. M., Rebetzke, G. J., Jimenez-Berni, J. A., James, R. A., Condon, A. G., Bovill, W. D., et al. (2016). Methodology for high-throughput field phenotyping of canopy temperature using airborne thermography. *Front. Plant Sci.* 7:1808. doi: 10.3389/fpls.2016.01808
- Döpfer, V., Gränzig, T., Kleinschmit, B., and Förster, M. (2020). Challenges in UAS-based TIR imagery processing: image alignment and uncertainty quantification. *Remote Sens.* 12:1552. doi: 10.3390/rs12101552
- Duan, S.-B., Li, Z.-L., Gao, C., Zhao, W., Wu, H., Qian, Y., et al. (2020). Influence of adjacency effect on high-spatial-resolution thermal infrared imagery: implication for radiative transfer simulation and land surface temperature retrieval. *Remote Sens. Environ.* 245:111852. doi: 10.1016/j.rse.2020.111852
- Famiglietti, J. S. (2014). The global groundwater crisis. *Nat. Clim. Chang.* 4, 945–948. doi: 10.1038/nclimate2425
- Fuchs, M., and Tanner, C. B. (1966). Infrared thermometry of vegetation. *Agron. J.* 58:597. doi: 10.2134/agronj1966.00021962005800060014x
- Gardner, B. R., Nielsen, D. C., and Shock, C. C. (1992). Infrared thermometry and the crop water stress index. I. History, theory, and baselines. *J. Prod. Agric.* 5, 462–466. doi: 10.2134/jpa1992.0462
- Gerhards, M., Schlerf, M., Mallick, K., and Udelhoven, T. (2019). Challenges and future perspectives of multi-/hyperspectral thermal infrared remote sensing for crop water-stress detection: A review. *Remote Sens.* 11:1240. doi: 10.3390/rs11101240
- Gómez-Candón, D., Virlet, N., Labbé, S., Jolivet, A., and Regnard, J.-L. (2016). Field phenotyping of water stress at tree scale by UAV-sensed imagery: new insights for thermal acquisition and calibration. *Precis. Agric.* 17, 786–800. doi: 10.1007/s11119-016-9449-6
- González-Dugo, M. P., Moran, M. S., Mateos, L., and Bryant, R. (2006). Canopy temperature variability as an indicator of crop water stress severity. *Irrig. Sci.* 24, 233–240. doi: 10.1007/s00271-005-0022-8
- Gonzalez-Dugo, V., Zarco-Tejada, P., Berni, J. A., Suárez, L., Goldhamer, D., and Fereres, E. (2012). Almond tree canopy temperature reveals intra-crown variability that is water stress-dependent. *Agric. For. Meteorol.* 154–155, 156–165. doi: 10.1016/j.agrformet.2011.11.004
- Gonzalez-Dugo, V., Zarco-Tejada, P. J., and Fereres, E. (2014). Applicability and limitations of using the crop water stress index as an indicator of water deficits in citrus orchards. *Agric. For. Meteorol.* 198, 94–104. doi: 10.1016/j.agrformet.2014.08.003
- Gonzalez-Dugo, V., Zarco-Tejada, P., Nicolás, E., Nortes, P. A., Alarcón, J. J., Intrigliolo, D. S., et al. (2013). Using high resolution UAV thermal imagery to assess the variability in the water status of five fruit tree species within a commercial orchard. *Precis. Agric.* 14, 660–678. doi: 10.1007/s11119-013-9322-9
- Gracia-Romero, A., Kefauver, S. C., Fernandez-Gallego, J. A., Vergara-Díaz, O., Nieto-Taladriz, M. T., and Araus, J. L. (2019). UAV and ground image-based phenotyping: a proof of concept with durum wheat. *Remote Sens.* 11:1244. doi: 10.3390/rs11101244
- Han, W., Jia, J., Hu, Y., Liu, J., Guo, J., Shi, Y., et al. (2020). Maintenance of root water uptake contributes to salt-tolerance of a wild tomato species under salt stress. *Arch. Agron. Soil Sci.* 67, 205–217. doi: 10.1080/03650340.2020.1720911
- Han, M., Zhang, H., DeJonge, K. C., Comas, L. H., and Trout, T. J. (2016). Estimating maize water stress by standard deviation of canopy temperature in thermal imagery. *Agric. Water Manag.* 177, 400–409. doi: 10.1016/j.agwat.2016.08.031
- Hernández-Clemente, R., Hornero, A., Mottus, M., Penuelas, J., González-Dugo, V., Jiménez, J. C., et al. (2019). Early diagnosis of vegetation health From high-resolution hyperspectral and thermal imagery: lessons learned From empirical relationships and radiative transfer modelling. *Curr. For. Rep.* 5, 169–183. doi: 10.1007/s40725-019-00096-1
- Hickey, L. T., Hafeez, A. N., Robinson, H., Jackson, S. A., Leal-Bertioli, S. C. M., Tester, M., et al. (2019). Breeding crops to feed 10 billion. *Nat. Biotechnol.* 37, 744–754. doi: 10.1038/s41587-019-0152-9
- Holman, F., Riche, A., Michalski, A., Castle, M., Wooster, M., and Hawkesford, M. (2016). High throughput field phenotyping of wheat plant height and growth rate in field plot trials using UAV based remote sensing. *Remote Sens.* 8:1031. doi: 10.3390/rs8121031
- Idso, S. B. (1982). Non-water-stressed baselines: a key to measuring and interpreting plant water stress. *Agric. Meteorol.* 27, 59–70. doi: 10.1016/0002-1571(82)90020-6
- Idso, S. B., Jackson, R. D., Pinter, P. J., Reginato, R. J., and Hatfield, J. L. (1981). Normalizing the stress-degree-day parameter for environmental variability. *Agric. Meteorol.* 24, 45–55. doi: 10.1016/0002-1571(81)90032-7
- Irmak, S., Haman, D. Z., and Bastug, R. (2000). Determination of crop water stress index for irrigation timing and yield estimation of corn. *Agron. J.* 92, 1221–1227. doi: 10.2134/agronj2000.9261221x
- Isayenkov, S. V., and Maathuis, F. J. M. (2019). Plant salinity stress: Many unanswered questions remain. *Front. Plant Sci.* 10:80. doi: 10.3389/fpls.2019.00080
- Jackson, R. D. (1982). “Canopy temperature and crop water stress,” in *Advances in Irrigation, Vol. 1*. ed. D. Hillel (New York: Academic Press, INC.), 43–85.
- Jackson, R. D., Idso, S. B., Reginato, R. J., and Pinter, P. J. (1981). Canopy temperature as a crop water stress indicator. *Water Resour. Res.* 17, 1133–1138. doi: 10.1029/WR017i004p01133

- Jackson, R. D., Kustas, W. P., Choudhury, B. J., and Reginato, R. J. (1988). A reexamination of the crop water stress index. *Irrig. Sci.* 9, 309–317. doi: 10.1007/BF00296705
- Jamil, A., Riaz, S., Ashraf, M., and Foolad, M. R. (2011). Gene expression profiling of plants under salt stress. *Crit. Rev. Plant Sci.* 30, 435–458. doi: 10.1080/07352689.2011.605739
- Javadnejad, F., Gillins, D. T., Parrish, C. E., and Slocum, R. K. (2020). A photogrammetric approach to fusing natural colour and thermal infrared UAS imagery in 3D point cloud generation. *Int. J. Remote Sens.* 41, 211–237. doi: 10.1080/01431161.2019.1641241
- Jensen, A. M., McKee, M., and Chen, Y. (2014). “Procedures for processing thermal images using low-cost microbolometer cameras for small unmanned aerial systems,” in *2014 IEEE Geoscience and Remote Sensing Symposium* (Piscataway: IEEE), 2629–2632.
- Johansen, K., Morton, M. J., Malbêteau, Y., Aragon, B. J. L., Al-Mashharawi, S., Ziliani, M., et al. (2020). Predicting biomass and yield in a tomato phenotyping experiment using UAV imagery and machine learning. *Front. Artif. Intell.* 3:28. doi: 10.3389/frai.2020.00028
- Johansen, K., Morton, M. J. L., Malbêteau, Y. M., Aragon, B., Al-Mashharawi, S. K., Ziliani, M. G., et al. (2019). Unmanned aerial vehicle-based phenotyping using morphometric and spectral analysis can quantify responses of wild tomato plants to salinity stress. *Front. Plant Sci.* 10:370. doi: 10.3389/fpls.2019.00370
- Jones, H. G., 2013. *Plants and Microclimate: A Quantitative Approach to Environmental Plant Physiology*. Cambridge: Cambridge University Press.
- Jones, H. G., and Sirault, X. (2014). SCALING of thermal images at different spatial resolution: The mixed pixel problem. *Agronomy* 4, 380–396. doi: 10.3390/agronomy4030380
- Jones, H. G., Stoll, M., Santos, T., de Sousa, C., Chaves, M. M., and Grant, O. M. (2002). Use of infrared thermography for monitoring stomatal closure in the field: Application to grapevine. *J. Exp. Bot.* 53, 2249–2260. doi: 10.1093/jxb/erf083
- Kellner, J. R., Albert, L. P., Burley, J. T., and Cushman, K. (2019). The case for remote sensing of individual plants. *Am. J. Bot.* 106, 1139–1142. doi: 10.1002/ajb2.1347
- Kelly, J., Kljun, N., Olsson, P.-O., Mihai, L., Liljeblad, B., Weslien, P., et al. (2019). Challenges and best practices for deriving temperature data from an uncalibrated UAV thermal infrared camera. *Remote Sens.* 11:567. doi: 10.3390/rs11050567
- Khanal, S., Fulton, J., and Shearer, S. (2017). An overview of current and potential applications of thermal remote sensing in precision agriculture. *Comput. Electron. Agric.* 139, 22–32. doi: 10.1016/j.compag.2017.05.001
- Kustas, W. P., Anderson, M. C., Alfieri, J. G., Knipper, K., Torres-Rua, A., Parry, C. K., et al. (2018). The grape remote sensing atmospheric profile and evapotranspiration experiment. *Bull. Am. Meteorol. Soc.* 99, 1791–1812.
- Licker, R., Johnston, M., Foley, J. A., Barford, C., Kucharik, C. J., Monfreda, C., et al. (2010). Mind the gap: how do climate and agricultural management explain the ‘yield gap’ of croplands around the world? *Glob. Ecol. Biogeogr.* 19, 769–782. doi: 10.1111/j.1466-8238.2010.00563.x
- Maas, E. (1993). “Plant growth response to salt stress,” in *Towards the Rational Use of High Salinity Tolerant Plants. Tasks for Vegetation Science*, Vol. 27. eds. H. Leith and A. A. Masoom (Dordrecht: Springer), pp. 279–291.
- Maes, W., Huete, A., and Steppe, K. (2017). Optimizing the processing of UAV-based thermal imagery. *Remote Sens.* 9:476. doi: 10.3390/rs9050476
- Maes, W., and Steppe, K. (2012). Estimating evapotranspiration and drought stress with ground-based thermal remote sensing in agriculture: a review. *J. Exp. Bot.* 63, 4671–4712. doi: 10.1093/jxb/ers165
- Maimaitijiang, M., Sagan, V., Sidike, P., Hartling, S., Esposito, F., and Fritsch, F. B. (2020). Soybean yield prediction from UAV using multimodal data fusion and deep learning. *Remote Sens. Environ.* 237:111599. doi: 10.1016/j.rse.2019.111599
- Malbêteau, Y., Johansen, K., Aragon, B., Al-Mashharawi, S. K., and McCabe, M. F. (2021). Overcoming the challenges of thermal infrared orthomosaics using a swath-based approach to correct for dynamic temperature and wind effects. *Remote Sens.* 13:3255. doi: 10.3390/rs13163255
- Malbêteau, Y., Parkes, S., Aragon, B., Rosas, J., and McCabe, M. F. (2018). Capturing the diurnal cycle of land surface temperature using an unmanned aerial vehicle. *Remote Sens.* 10:1407. doi: 10.3390/rs10091407
- May, R.M., Arms, S.C., Marsh, P., Bruning, E., Leeman, J.R., Goebbert, K., et al. 2008. *MetPy: A Python Package for Meteorological Data*. Unidata, Boulder, Colorado.
- McCabe, M. F., Balick, L. K., Theiler, J., Gillespie, A. R., and Mushkin, A. (2008). Linear mixing in thermal infrared temperature retrieval. *Int. J. Remote Sens.* 29, 5047–5061. doi: 10.1080/01431160802036474
- McCabe, M. F., and Tester, M. (2021). Digital insights: bridging the phenotype-to-genotype divide. *J. Exp. Bot.* 72, 2807–2810. doi: 10.1093/jxb/erab108
- Meron, M., Sprints, M., Tsipris, J., Alchanatis, V., and Cohen, Y. (2013). Foliage temperature extraction from thermal imagery for crop water stress determination. *Precis. Agric.* 14, 467–477. doi: 10.1007/s11119-013-9310-0
- Meron, M., Tsipris, J., Orlov, V., Alchanatis, V., and Cohen, Y. (2010). Crop water stress mapping for site-specific irrigation by thermal imagery and artificial reference surfaces. *Precis. Agric.* 11, 148–162. doi: 10.1007/s11119-009-9153-x
- Mesas-Carrascosa, F.-J., Pérez-Porras, F., Meroño de Larriva, J. E., Mena Frau, C., Agüera-Vega, F., Carvajal-Ramírez, F., et al. (2018). Drift correction of lightweight microbolometer thermal sensors on-board unmanned aerial vehicles. *Remote Sens.* 10:615. doi: 10.3390/rs10040615
- Molden, D., 2013. *Water for Food Water for Life: A Comprehensive Assessment of Water Management in Agriculture*. London: Routledge.
- Morton, M. J. L., Awlia, M., Al-Tamimi, N., Saade, S., Pailles, Y., Negrão, S., et al. (2018). Salt stress under the scalpel – dissecting the genetics of salt tolerance. *Plant J.* 97:tpj.14189. doi: 10.1111/tpj.14189
- Motohka, T., Nasahara, K. N., Oguma, H., and Tsuchida, S. (2010). Applicability of green-red vegetation index for remote sensing of vegetation phenology. *Remote Sens.* 2, 2369–2387. doi: 10.3390/rs2102369
- Mueller, N. D., Gerber, J. S., Johnston, M., Ray, D. K., Ramankutty, N., and Foley, J. A. (2012). Closing yield gaps through nutrient and water management. *Nature* 490, 254–257. doi: 10.1038/nature11420
- Munns, R., and Tester, M. (2008). Mechanisms of salinity tolerance. *Annu. Rev. Plant Biol.* 59, 651–681. doi: 10.1146/annurev.arplant.59.032607.092911
- O’Shaughnessy, S. A., Evett, S. R., Colaizzi, P. D., and Howell, T. A. (2011). Using radiation thermography and thermometry to evaluate crop water stress in soybean and cotton. *Agric. Water Manag.* 98, 1523–1535. doi: 10.1016/j.agwat.2011.05.005
- Park, S., Ryu, D., Fuentes, S., Chung, H., Hernández-Montes, E., and O’Connell, M. (2017). Adaptive estimation of crop water stress in nectarine and peach orchards using high-resolution imagery from an unmanned aerial vehicle (UAV). *Remote Sens.* 9:828. doi: 10.3390/rs9080828
- Pastor, A., Palazzo, A., Havlik, P., Biemans, H., Wada, Y., Obersteiner, M., et al. (2019). The global nexus of food–trade–water sustaining environmental flows by 2050. *Nat. Sustain.* 2, 499–507. doi: 10.1038/s41893-019-0287-1
- Patané, C. (2011). Leaf area index, leaf transpiration and stomatal conductance as affected by soil water deficit and VPD in processing tomato in semi arid Mediterranean climate. *J. Agron. Crop Sci.* 197, 165–176. doi: 10.1111/j.1439-037X.2010.00454.x
- Pedregosa, F., Varoquaux, G., Gramfort, A., Michel, V., Thirion, B., Grisel, O., et al. (2011). Scikit-learn: machine learning in python. *J. Mach. Learn. Res.* 12, 2825–2830.
- Perich, G., Hund, A., Anderegg, J., Roth, L., Boer, M. P., Walter, A., et al. (2020). Assessment of multi-image unmanned aerial vehicle based high-throughput field phenotyping of canopy temperature. *Front. Plant Sci.* 11:150. doi: 10.3389/fpls.2020.00150
- Perry, E.M., Goodwin, I., and Cornwall, D., 2018. Remote sensing using canopy and leaf reflectance for estimating nitrogen status in red-blush pears. *HortScience* 53, 78–83. doi: 10.21273/HORTSCI12391-17
- Pittock, J., Hussey, K., and Stone, A. (2016). “Groundwater management under global change: Sustaining biodiversity, energy and food supplies,” in *Integrated Groundwater Management: Concepts, Approaches and Challenges*. eds. A. J. Jakeman, O. Barreteau, R. J. Hunt, J.-D. Rinaudo and A. Ross (Cham: Springer International Publishing), 75–96.
- Poblete, T., Ortega-Farías, S., and Ryu, D. (2018). Automatic coregistration algorithm to remove canopy shaded pixels in UAV-borne thermal images to improve the estimation of crop water stress index of a drip-irrigated cabernet sauvignon vineyard. *Sensors* 18:397. doi: 10.3390/s18020397
- QGIS Development Team (2021). *QGIS Geographic Information System*. Open Source Geospatial Foundation Project. Available at: <http://qgis.org.osgeo.org>
- Rao, E. S., Kadirvel, P., Symonds, R. C., and Ebert, A. W. (2013). Relationship between survival and yield related traits in *Solanum pimpinellifolium* under salt stress. *Euphytica* 190, 215–228. doi: 10.1007/s10681-012-0801-2

- Ray, D. K., Mueller, N. D., West, P. C., and Foley, J. A. (2013). Yield trends are insufficient to double global crop production by 2050. *PLoS One* 8:e66428. doi: 10.1371/journal.pone.0066428
- Razali, R., Bougouffa, S., Morton, M. J. L., Lightfoot, D. J., Alam, I., Essack, M., et al. (2018). The genome sequence of the wild tomato *Solanum pimpinellifolium* provides insights into salinity tolerance. *Front. Plant Sci.* 9:1402. doi: 10.3389/fpls.2018.01402
- Reginato, R. J. (1983). Field quantification of crop water stress. *Trans. ASAE* 26, 772–775. doi: 10.13031/2013.34021
- Ribeiro-Gomes, K., Hernández-López, D., Ortega, J., Ballesteros, R., Poblete, T., and Moreno, M. (2017). Uncooled thermal camera calibration and optimization of the photogrammetry process for UAV applications in agriculture. *Sensors* 17:2173. doi: 10.3390/s17102173
- Rud, R., Cohen, Y., Alchanatis, V., Levi, A., Brikman, R., Shenderoy, C., et al. (2014). Crop water stress index derived from multi-year ground and aerial thermal images as an indicator of potato water status. *Precis. Agric.* 15, 273–289. doi: 10.1007/s11119-014-9351-z
- Sade, N., Gebremedhin, A., and Moshelion, M. (2012). Risk-taking plants: anisohydric behavior as a stress-resistance trait. *Plant Signal. Behav.* 7, 767–770. doi: 10.4161/psb.20505
- Sepúlveda-Reyes, D., Ingram, B., Bardeen, M., Zúñiga, M., Ortega-Farías, S., and Poblete-Echeverría, C. (2016). Selecting canopy zones and thresholding approaches to assess grapevine water status by using aerial and ground-based thermal imaging. *Remote Sens.* 8:822. doi: 10.3390/rs8100822
- Smith, G. M., and Milton, E. J. (1999). The use of the empirical line method to calibrate remotely sensed data to reflectance. *Int. J. Remote Sens.* 20, 2653–2662. doi: 10.1080/014311699211994
- Tang, Q., Zhang, R., Chen, L., Xu, G., Deng, W., Ding, C., et al. (2020). High-accuracy, high-resolution downwash flow field measurements of an unmanned helicopter for precision agriculture. *Comput. Electron. Agric.* 173:105390. doi: 10.1016/j.compag.2020.105390
- Tanner, C. B. (1963). Plant temperatures. *Agron. J.* 55, 210–211. doi: 10.2134/agronj1963.00021962005500020043x
- Thorndike, R. L. (1953). Who belongs in the family? *Psychometrika* 18, 267–276. doi: 10.1007/BF02289263
- Torrecillas, A., Guillaume, C., Alarcón, J. J., and Ruiz-Sánchez, M. C. (1995). Water relations of two tomato species under water stress and recovery. *Plant Sci.* 105, 169–176. doi: 10.1016/0168-9452(94)04048-6
- Torres-Rua, A. (2017). Vicarious calibration of sUAS microbolometer temperature imagery for estimation of radiometric land surface temperature. *Sensors* 17:1499. doi: 10.3390/s17071499
- Virtanen, P., Gommers, R., Oliphant, T. E., Haberland, M., Reddy, T., Cournapeau, D., et al. (2020). SciPy 1.0: fundamental algorithms for scientific computing in python. *Nat. Methods* 17, 261–272. doi: 10.1038/s41592-019-0686-2
- Wang, W., Vinocur, B., and Altman, A. (2003). Plant responses to drought, salinity and extreme temperatures: towards genetic engineering for stress tolerance. *Planta* 218, 1–14. doi: 10.1007/s00425-003-1105-5
- Xie, C., and Yang, C. (2020). A review on plant high-throughput phenotyping traits using UAV-based sensors. *Comput. Electron. Agric.* 178:105731. doi: 10.1016/j.compag.2020.105731
- Yang, G., Liu, J., Zhao, C., Li, Z., Huang, Y., Yu, H., et al. (2017). Unmanned aerial vehicle remote sensing for field-based crop phenotyping: current status and perspectives. *Front. Plant Sci.* 8:1111. doi: 10.3389/fpls.2017.01111
- Zhang, L., Niu, Y., Zhang, H., Han, W., Li, G., Tang, J., et al. (2019). Maize canopy temperature extracted from UAV thermal and RGB imagery and its application in water stress monitoring. *Front. Plant Sci.* 10:1270. doi: 10.3389/fpls.2019.01270
- Zheng, X., Li, Z.-L., Zhang, X., and Shang, G. (2019). Quantification of the adjacency effect on measurements in the thermal infrared region. *IEEE Trans. Geosci. Remote Sens.* 57, 9674–9687. doi: 10.1109/TGRS.2019.2928525
- Ziliani, M. G., Parkes, S. D., Hoteit, I., and McCabe, M. F. (2018). Intra-season crop height variability at commercial farm scales using a fixed-wing UAV. *Remote Sens.* 10:2007. doi: 10.3390/rs10122007
- Zuriaga, E., Blanca, J. M., Cordero, L., Sifres, A., Blas-Cerdán, W. G., Morales, R., et al. (2009). Genetic and bioclimatic variation in *Solanum pimpinellifolium*. *Genet. Resour. Crop. Evol.* 56, 39–51. doi: 10.1007/s10722-008-9340-z

Conflict of Interest: The authors declare that the research was conducted in the absence of any commercial or financial relationships that could be construed as a potential conflict of interest.

Publisher's Note: All claims expressed in this article are solely those of the authors and do not necessarily represent those of their affiliated organizations, or those of the publisher, the editors and the reviewers. Any product that may be evaluated in this article, or claim that may be made by its manufacturer, is not guaranteed or endorsed by the publisher.

Copyright © 2021 Stutsel, Johansen, Malbêteau and McCabe. This is an open-access article distributed under the terms of the Creative Commons Attribution License (CC BY). The use, distribution or reproduction in other forums is permitted, provided the original author(s) and the copyright owner(s) are credited and that the original publication in this journal is cited, in accordance with accepted academic practice. No use, distribution or reproduction is permitted which does not comply with these terms.



Surface-Enhanced Raman Scattering Spectroscopy Combined With Chemical Imaging Analysis for Detecting Apple Valsa Canker at an Early Stage

Shiyan Fang^{1,2,3}, Yanru Zhao^{1,2,3}, Yan Wang⁴, Junmeng Li^{1,2,3}, Fengle Zhu⁵ and Keqiang Yu^{1,2,3*}

OPEN ACCESS

Edited by:

Nam-Hai Chua,
Temasek Life Sciences Laboratory,
Singapore

Reviewed by:

Gajendra Pratap Singh,
Singapore-MIT Alliance for Research
and Technology (SMART), Singapore
Dmitry Kourouski,
Texas A&M University, United States

*Correspondence:

Keqiang Yu
keqiang_yu@nwfau.edu.cn

Specialty section:

This article was submitted to
Technical Advances in Plant Science,
a section of the journal
Frontiers in Plant Science

Received: 29 October 2021

Accepted: 14 January 2022

Published: 04 March 2022

Citation:

Fang S, Zhao Y, Wang Y, Li J,
Zhu F and Yu K (2022)
Surface-Enhanced Raman Scattering
Spectroscopy Combined With
Chemical Imaging Analysis
for Detecting Apple Valsa Canker
at an Early Stage.
Front. Plant Sci. 13:802761.
doi: 10.3389/fpls.2022.802761

¹ College of Mechanical and Electronic Engineering, Northwest A&F University, Yangling, China, ² Key Laboratory of Agricultural Internet of Things, Ministry of Agriculture and Rural Affairs, Yangling, China, ³ Shaanxi Key Laboratory of Agricultural Information Perception and Intelligent Service, Yangling, China, ⁴ College of Plant Protection, Northwest A&F University, Yangling, China, ⁵ School of Computer and Computing Science, Zhejiang University City College, Hangzhou, China

Apple Valsa canker (AVC) with early incubation characteristics is a severe apple tree disease, resulting in significant orchards yield loss. Early detection of the infected trees is critical to prevent the disease from rapidly developing. Surface-enhanced Raman Scattering (SERS) spectroscopy with simplifies detection procedures and improves detection efficiency is a potential method for AVC detection. In this study, AVC early infected detection was proposed by combining SERS spectroscopy with the chemometrics methods and machine learning algorithms, and chemical distribution imaging was successfully applied to the analysis of disease dynamics. Results showed that the samples of healthy, early disease, and late disease sample datasets demonstrated significant clustering effects. The adaptive iterative reweighted penalized least squares (air-PLS) algorithm was used as the best baseline correction method to eliminate the interference of baseline shifts. The BP-ANN, ELM, Random Forest, and LS-SVM machine learning algorithms incorporating optimal spectral variables were utilized to establish discriminative models to detect of the AVC disease stage. The accuracy of these models was above 90%. SERS chemical imaging results showed that cellulose and lignin were significantly reduced at the phloem disease-health junction under AVC stress. These results suggested that SERS spectroscopy combined with chemical imaging analysis for early detection of the AVC disease was feasible and promising. This study provided a practical method for the rapidly diagnosing of apple orchard diseases.

Keywords: apple Valsa canker, early detection, Surface-Enhanced Raman Scattering, chemical imaging, machine learning

INTRODUCTION

Apple Valsa canker (AVC), caused by fungus *Valsa mali*, is a severe apple tree disease resulting in serious economic losses in Southeast Asia and China (Wang et al., 2011). Commonly, AVC is mainly found by the characteristics of canker, infected tissue softening, outflowed light brown water stain, sunken or cracked on trunks at the early infected stage (Zang et al., 2012). The fungal pathogen mainly infected the subcutaneous phloem through the wounded bark tissue at the initial infected stage. After infection, fungus hypha colonized the phloem tissues, leading to severe tissue cell death (Suzaki, 2008). What's more, plant protection experts have proved that the fungus *Valsa mali* can survive in weak and dead tissues of the apple trees for more than 1 year before appearing visible symptoms (Meng et al., 2019). For example, Zang et al. (2012) found that more than 50% of apple orchards existed fungus *Valsa mali* in symptomless apple tree tissues. However, when visible symptoms appear, it is challenging to prevent AVC from spreading throughout the orchard by conventional treating methods such as spraying fungicides, manually removing the diseased areas, and pruning the dead branches. Unfortunately, there were no adequate methods for AVC treatment due to the complicated pathogenic mechanism so far. Thus, early detection of the infected trees is necessary to prevent the rapid development of the disease in orchards.

There are various molecular biology methods, including Enzyme-Linked ImmunoSorbent Assay (ELISA) and Polymerase Chain Reaction (PCR), were developed for the isolation and identification of pathogenic (Liu et al., 2015; Golhani et al., 2018). ELISA kits have been widely utilized thanks to the low cost, but are ineffective for detecting symptomless tissue (Fang and Ramasamy, 2015), while PCR is an effective detection method. Zang et al. (2012) developed a nested PCR assay to detect the presence of *Valsa mali* in apple trees and achieved an accuracy of 64.7%. However, DNA deriving from the woody plant tissues contained PCR inhibiting compounds and could affect the accuracy of PCR reaction (Martinelli et al., 2015). What's worse, a well-equipped laboratory and experienced personnel are also required, which was not feasible for on-site detection using the PCR (Okiro et al., 2019). Therefore, it is of great significance to develop a fast, non-destructive and economical method for accurate detection of AVC.

Reported studies have demonstrated that advanced non-invasive measuring technologies, such as RGB image processing (Cruz et al., 2019; Hu et al., 2020), dielectric spectrum (Khaled et al., 2018), laser scanning (Khairunniza and Vong, 2014), and spectroscopic methods (Ranulfi et al., 2016; Dou et al., 2021) have a massive amount of potential for diagnosing tree diseases. Among them, the spectroscopy technique is powerful for quality and safety inspection due to the character of simplicity, rapidity, and affordability, which makes it indispensable in tree disease detection. Raman spectroscopy (RS) is a non-invasive, rapid, and high throughput spectroscopic technique (Farber et al., 2020; Huang et al., 2020; Zhao et al., 2021). Raman shift is only related to the vibration frequency of the molecular functional group, but not to the incident light.

Therefore, each sample's the Raman "fingerprint" of each sample is unique (Fang et al., 2021). Significantly, RS could provide essential information related to the biochemical composition of the tree tissue cell, such as protein, polysaccharide, and lipid. Neither symptomatic nor asymptomatic trees, these biochemical compositions are significantly different between diseased and healthy tissue. These compositions changes can be reflected in Raman shifts or intensity changes of specific Raman bands assigned to those molecules. Therefore, RS provides an accessible way to identify subtle changes in the molecular compounds, which offers theoretical evidence for detecting tree diseases. Vallejo et al. (2016) investigated the application of RS combined with statistical analysis for detecting citrus Huanglongbing (HLB) infection in the field, and a good result was obtained with an overall classification accuracy of about 89.2%. Sanchez et al. (2019b) readily distinguished between healthy and early-HLB citrus trees using a handheld Raman system and achieved an accuracy of 94%. In their following study, Sanchez et al. (2019a) demonstrated that utilizing a handheld Raman spectrometer in combined with chemometric analyses enabled the detection and identification of the secondary disease on HLB-infected orange trees. Those researches indicated that the RS technique combined with chemometrics methods could detect diseased trees.

However, RS is frequently interfered by fluorescence caused by chromophores in plant tissue, and compositional changes under disease stress may lead to Raman band broadening or drift (Mukherjee et al., 2017; Petrov, 2017). This drawback may lead to significant deviations in the biochemical composition analysis of RS data. Surface enhanced Raman scattering (SERS) spectroscopy, based on the improvement of traditional RS, uses certain metallic nano-substrates such as gold or silver nanoparticles (AgNPs) to enhance signals under low laser powers, which maximizes fluorescence suppression. Meanwhile, the Raman system combined with the micro-imaging technology allows for scanning micron-scale Raman collection points (e.g., one-micron pixel) (Li X. L. et al., 2019), which offers chemical information on the constituents at a high spatial resolution *in situ*. Qin et al. (2011) developed a Raman chemical imaging system to visualize the internal distribution of lycopene in postharvest tomatoes and established a Raman chemical image to visualize the spatial distribution of lycopene at different stages of maturity. Yang et al. (2018) used a Raman imaging system to detect the spatial distribution of chemical components in maize seeds. These studies manifested that Raman chemical imaging has great potential in the visualizing of plant tissue components.

Therefore, this study aimed to develop a fast, non-invasive, and *in situ* diagnosis method for detecting AVC at early infection stages using SERS combined with micro-imaging technology. The main objectives are to: (1) Optimize experimental conditions (i.e., laser intensity and exposure time) for obtaining valid SERS micro-imaging data, including Synthesis and SERS AgNPs characterization; (2) Establish optimal discriminative models for detecting AVC in early infection stages based on machine learning algorithms; (3) Generate micro-distribution maps of cellulose and lignin at the disease-health junction of the tree phloem tissues to reveal the dynamic development characteristics of the disease.

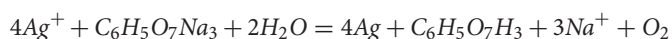
MATERIALS AND METHODS

Fungal Culture and Sample Inoculation

The fungus *Valsa mali* stored at -80°C in an ultra-low temperature refrigerator were inoculated onto potato dextrose agar (PDA) medium. The 2-year-old apple branches (*Malus domestica* cv. Fuji) were collected from the Economic Tree Garden of Northwest A&F University. The selected branches were pruned into 15 cm segments, and the surface of the branches was disinfected with 75% alcohol for 15 min. Then, they were cleaned with sterile water three times until there was no odor. The ends of the branches were sealed with a wet skimmed cotton to keep them fresh, followed by punching holes in the branches with a hole puncher (hole diameter 5 mm). The activated *Valsa mali* fungus was inoculated on the wounds of apple branches with two points on each branch. After inoculation, the branches were transferred to a 25°C incubator for further incubation.

Synthesis and Surface-Enhanced Raman Scattering Silver Nanoparticles Characterization

In the present research, AgNPs were synthesized by using the Lee–Meisel method. The synthesis steps were as follows: AgNO_3 (36 mg) was dissolved in 200 ml of ultrapure water and boiled quickly. A solution of 1 wt.% trisodium citrate (6 mL) was charged to the reaction solution and was held on boiling for 25 min accompanied by stirring at 200 rpm. After cooling to room temperature, we pour the AgNPs solution into a centrifuge tube and store it away from light. The chemical reaction equation is as follows:



Subsequently, the prepared AgNPs were characterized to verify their validity. The morphology of the AgNPs was measured by Tecnai G2 transmission electron microscopy (FEI Inc., Hillsboro, OR, United States). The UV-Vis absorption spectra of the AgNPs were measured using Lambda 35 Spectrophotometer (PerkinElmer Inc., Waltham, MA, United States). The Raman spectra of the AgNPs were collected by DXR3xi Raman micro-imaging spectrometer (Thermo Fisher Scientific Inc., Waltham, MA, United States).

Surface-Enhanced Raman Scattering Spectroscopy Acquisition

First, branches were removed from the incubator, and the inoculation points on the phloem were scraped with a knife as the samples. Each sample placed on a glass slide was dripped with the AgNPs. Then, each sample was placed on the automatic stage and aligned with a Raman laser using a 10x/0.25 NA magnification objective lens for SERS imaging collection using a DXR3xi Raman micro-imaging system (Thermo Fisher Scientific Inc., Waltham, MA, United States). Specific parameters were to: the excitation wavelength was 785 nm; the collected spectral range was 300–3,000 $\text{shift}/\text{cm}^{-1}$; the laser intensity was 2.6 mW; the exposure time was 0.00285 s (350 Hz); the number of scanning was 40.

For spectral imaging in the x and y directions, the samples were scanned point by point in 2 μm steps. It should be noted that no destructive effects of the laser on the samples were observed. Routinely, before starting the Raman measurements, the calibration procedure that came with the instrument was executed automatically. At this time, the software interface displayed “Performing automatic X axis calibration.” The data acquisition software OMNICxi v1.6 was used to adjust the acquisition parameters.

Spectral Data Processing and Analysis Spectra Preprocessing

Background noises and baselines were generated during the acquisition of the SERS spectra, which seriously impaired the interpretability of the spectra. Meanwhile, these noises and baselines would also reduce the simplicity and robustness of the calibration model built on these spectra. Therefore, selecting the optimal pretreatment method was necessary to improve the spectral quality. In this study, spectral curves were first extracted for each pixel point of the imaging data before spectra preprocessing. Then, the spectral data were preprocessed with three algorithms to eliminate noise and correct the baseline background. These three algorithms include the multiple spectral baseline correction (MSBC), the asymmetric least squares (AsLS), and the adaptive iterative reweighted penalized least squares (air-PLS). Subsequently, the advantages and disadvantages of the three algorithms were compared using the correlation analysis method.

The AsLS method, proposed by Eilers (2003, 2004), is a classical baseline correction algorithm that combined a smoother with the asymmetric weighting of deviations from the smoothed trend to form an effective baseline estimation method. The MSBC method, proposed by Peng et al. (2010), is an improved approach based on the AsLS algorithm. The MSBC method learns baselines that perform well on the corresponding spectra and then “co-regularize” the selection by correcting inconsistencies between the spectra. Air-PLS is an improvement approach based on the weighting of the original model by the weighted least squares method. The light environment is automatically subtracted by meaning the iterative regression, and the background is deducted (Baek et al., 2015).

Optimal Variables Selection and Dimension Reduction

Multivariate calibration methods in chemometrics aim to construct relationships between variables and properties of interest to make a classification model. However, with the redundant spectral variables, data usually included some noise and unnecessary information, which rendering unreliable predictive properties. Therefore, optimal variables selection and dimension reduction have been used to address these problems.

Principal component analysis (PCA) can replace the original variables with a few principal components with significant deviation to reduce the original high-dimensional variable space (Dong et al., 2014). In addition, competitive adaptive reweighted sampling (CARS) and random frog (RFrog) algorithms were combined to select the optimal variables associated with the

predicted properties and exclude the interference of unrelated variables. The CARS algorithm used exponentially decreasing function (EDF) as a selection strategy to select critical variables based on adaptive reweighted sampling competitively (Li et al., 2009; Li Q. Q. et al., 2019). The RFrog algorithm calculated the selection probability of each variable by moving across trans-dimensions between models, enabling the search for the optimal variable (Li et al., 2012).

Classification Models

BP artificial neural network (BP-ANN) (Zhang et al., 2018) is the most classical and successful neural network commonly utilized for non-linear fitting and pattern recognition. BP-ANN is a one-way multi-layer feedforward network composed of an input, hidden, and output layer. The learning process is composed of forwarding propagation of signals and back-propagation of errors.

The random forest (RForest) is a widely used machine learning algorithm, which has been successfully applied to pattern recognition (Lussier et al., 2020), and the choice appropriate number of decision trees is crucial in RForest. When the test data entered the classifier, each decision tree classified the data. Finally, the class with the most classification results from all decision trees was taken as the result.

The least squares support vector machine (LS-SVM) is a machine learning method that emerged from the statistical learning theory. LS-SVM divides the data samples into multi classes by determining a hyperplane in the input space, maximizing the separation between the classes (Lucay et al., 2020). Its vital parameter indexes are the kernel function and the corresponding parameters of this function.

Extreme learning machine (ELM) is one of the practical training algorithms for single-layer feedforward neural networks (Qiu et al., 2015). ELM has a faster training and better generalization performance than traditional machine learning algorithms and could overcome issues such as the local minimum, inappropriate learning rate, and overfitting (Wu et al., 2021). Therefore, it is widely used in the condition of classification and regression.

In summary, **Figure 1** demonstrated Key steps for detecting apple Valsa canker at an early stage based on SERS spectroscopy combined with chemical imaging analysis. All procedures were written in MATLAB R2018b (The MathWorks, Natick, MA, United States) and ran on a personal computer with an Intel Core i5-9400F CPU, 16GB RAM, and a Windows 10 operating system.

RESULTS AND DISCUSSION

Phenotypic Development of Healthy and Inoculated Branch

Figure 2a demonstrated the strains of the fungus *Valsa mali* on the PDA medium. The junctions of diseased and healthy tissues in the inoculated branch samples were assessed visually in the early stage of AVC disease. The bark surface of inoculated branch samples showed no visible symptoms during the first 7 days. However, the phloem inside the bark appeared with

early infection symptoms. **Figure 2b** demonstrated the dynamic process of the diseased phloem in the first 7 days. The healthy phloem (the first 3 days) had a smooth surface and displayed tender green. The diseased phloem became rough and showed pale brown when the symptoms of mild infection were visible on the 5th day. Subsequently, the diseased phloem appeared dark brown, and the tissue was rotten on the 7th day. The infected area of the diseased phloem, centered on the inoculation site, was continuously extended outward with time. Most notably, the infection symptoms remained in the phloem and did not appear on the bark surface in the first 7 days. The phloem regions were manually labeled as healthy, disease-1 (the disease-health intersection), and disease-2 (late-disease) according to the infection progression of the pathogen. The purpose of dividing the region into three categories is to simulated the time-series dynamic process of pathogen infection (i.e., pathogen infection spread outward around the center point). In **Figure 2c**, the disease-health intersection of the diseased phloem was presented using optical microscopy. It can be observed that the healthy tissue appeared green with intact cellular tissue structure; The disease-1 tissue appeared dark brown, and the infected tissue outflowed light brown water stain; The disease-2 tissue was mainly characterized by canker and softened tissue.

Surface-Enhanced Raman Scattering Silver Nanoparticles and Its Characterization

The microstructure, UV-Vis spectrum, and Raman spectrum of AgNPs were analyzed to investigate the enhancement effects of the synthesized AgNPs. **Figure 3A** is the transmission electron microscopy (TEM) image of AgNPs, **Figure 3B** displays the UV-Vis spectra, and **Figure 3C** shows the Raman spectra.

In **Figure 3A**, it could be seen that the morphological character of AgNPs was very uniform in a monodisperse spherical shape. In addition, the average diameter of AgNPs was about 50 nm. As shown in **Figure 3B**, only one UV-Vis characteristic absorption peak (at 410 nm) corresponding to the single plasmon resonance mode was observed, and the half-peak breadth was only 90 nm. These features further indicated that the shape and size of the synthesized AgNPs were very uniform. In **Figure 3C**, the Raman spectrum had a faint signal, suggesting that the synthesized AgNPs themselves had no strong Raman characteristic peaks and did not have an interferential effect on experimental results. Therefore, the synthesized AgNPs were suitable as SERS substrate to detect branch samples in this research.

Overview of Surface-Enhanced Raman Scattering Spectra

Spectral imaging is capable of acquiring the spectra from a specified point at the sample surface. By adjusting the *x*, *y* position, acquisitions of the spectra from multiple points on the sample surface can be performed, assembling a spectral image of the sample. **Figure 4** clearly showed the spectrum of healthy tissue samples, with and without AgNPs, respectively. Raman spectra peaks of healthy samples without AgNPs did not appear. The SERS characteristic peaks of healthy samples were obvious,

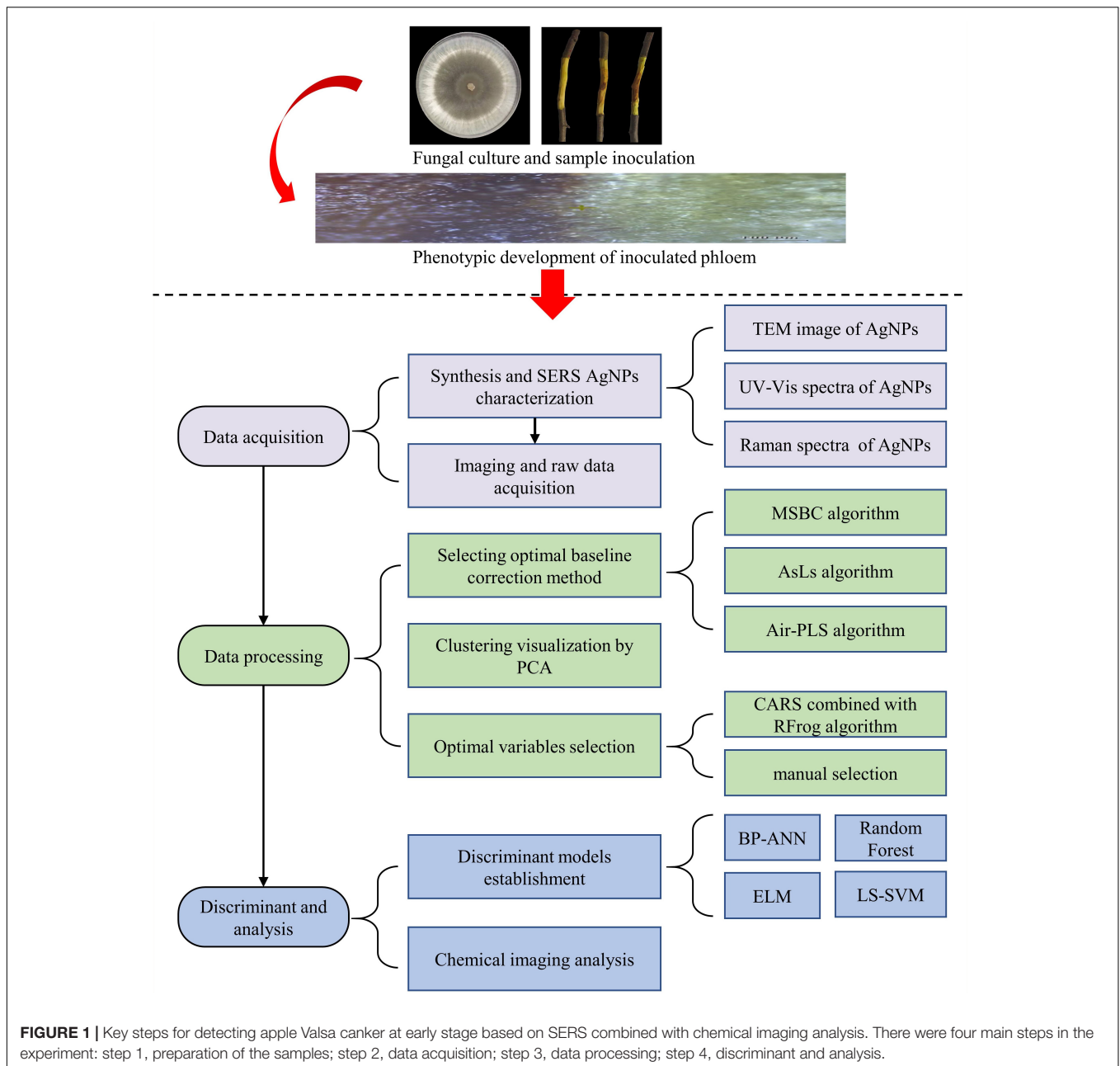


FIGURE 1 | Key steps for detecting apple Valsa canker at early stage based on SERS combined with chemical imaging analysis. There were four main steps in the experiment: step 1, preparation of the samples; step 2, data acquisition; step 3, data processing; step 4, discriminant and analysis.

which further proved that AgNPs were effective. **Figure 5** showed the micro-spectral image of diseased phloem through pointwise scanning by Raman micro-imaging system. The spectral data were obtained by splitting each pixel point of the spectral image. All the original SERS spectra were also shown in **Figure 5**. The pathogenic mechanism of AVC remains poorly understood (Wang et al., 2021). On the one hand, cell wall degrading enzymes (e.g., pectinases) played an important role in the infection process (Yin et al., 2013). On the other hand, studies have shown that phloridzin in apple tissues can be degraded by AVC, and the metabolites have toxic effects on apple tissue cells (Feng et al., 2020). These researches explained why the vibration band of disease-2 is weaker than the health spectrum.

There was an obvious baseline offset in the disease-1 and disease-2 even after dropwise addition of the AgNPs to suppress fluorescence. Therefore, the MSBC, AsLS, and air-PLS algorithms were adopted to eliminate the disturbances of the baseline offset. The parameters for these methods were manually set to obtain the best result. For the MSBC algorithm, the parameters were set to $\lambda = 150$, $\mu = 8 \times 10^7$, and $\rho = 0$. For AsLS algorithm, the parameters were set to $\lambda = 5,000$, and $\rho = 0.0001$. For the air-PLS algorithm, the parameters were set to $\lambda = 150$, and $\rho = 0.01$. The corrected spectra and the predicted fluorescence baselines were plotted in **Figures 6A–C**. As shown in **Figure 6**, the curved baselines were well-fitted and subtracted by the three algorithms. The corrected spectra showed that the baselines were pulled

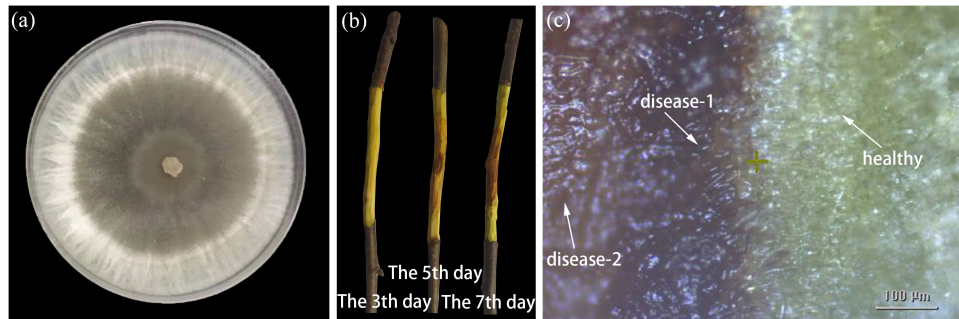


FIGURE 2 | Phenotypic development of healthy and inoculated branch. **(a)** The strains of the fungus *Valsa mali* on PDA medium. **(b)** The dynamic process of the diseased phloem in the first 7 days. **(c)** Optical micrograph of the disease-health junction.

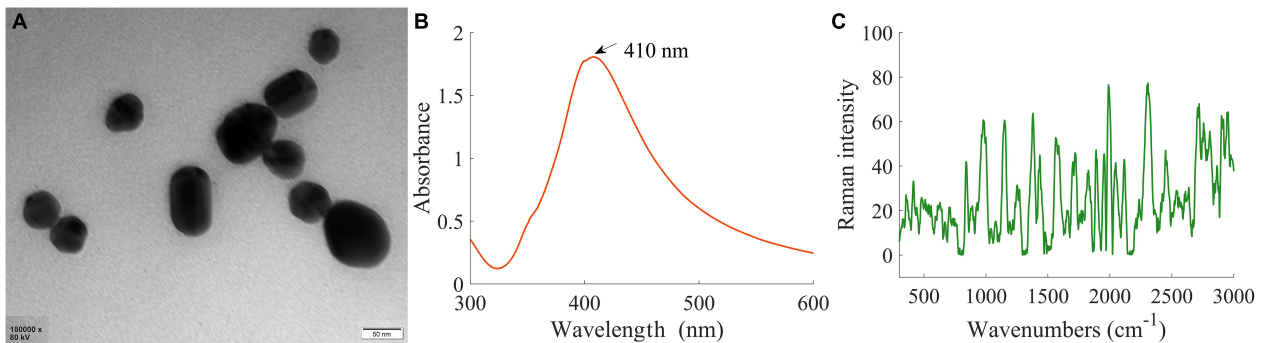


FIGURE 3 | SERS AgNPs and its characterization. **(A)** Transmission electron microscopy image of AgNPs. **(B)** The UV-Vis spectra of AgNPs. **(C)** Raman spectrum of AgNPs.

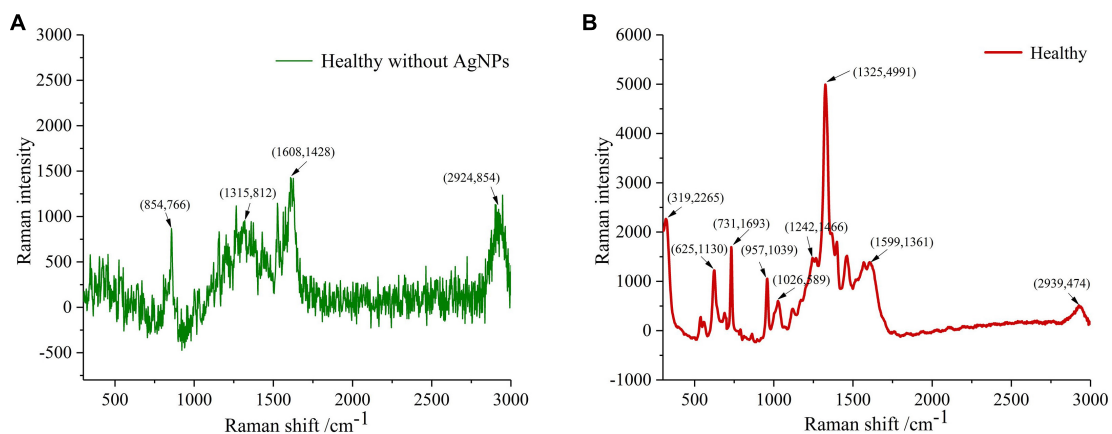


FIGURE 4 | The spectrum of healthy tissue samples, with and without AgNPs, respectively. **(A)** Raman spectra peaks of healthy samples without AgNPs did not appeared. **(B)** The SERS characteristic peaks of healthy samples were obvious, which further proved that AgNPs was effective.

back to zero absorbance, the peak locations remained unchanged, and the peak shapes were more prominent, which indicated the effectiveness of the baseline correction methods.

As shown in **Figure 6**, many SERS peaks can be clearly observed. In detail, the peaks at 319, 957, 1,026, 1,165, 1,242, and 1,325 cm^{-1} were indicators of cellulose, corresponding to C-C-C or C-O-C skeletal bending (Szymanska et al., 2011), C-C

or C-O stretching vibration (Beć et al., 2020), C-C or C-O stretching vibration (Beć et al., 2020), H-C-C or H-C-O skeletal bending (Edwards et al., 1997), C = O stretching vibration (Beć et al., 2020), and C-H bending vibration (Edwards et al., 1997), respectively. The peaks at 625, 731, 1,599, and 2,939 cm^{-1} were indicators of lignin, corresponding to skeletal bending (Agarwal et al., 2011), skeletal bending (Agarwal et al., 2011), C-C

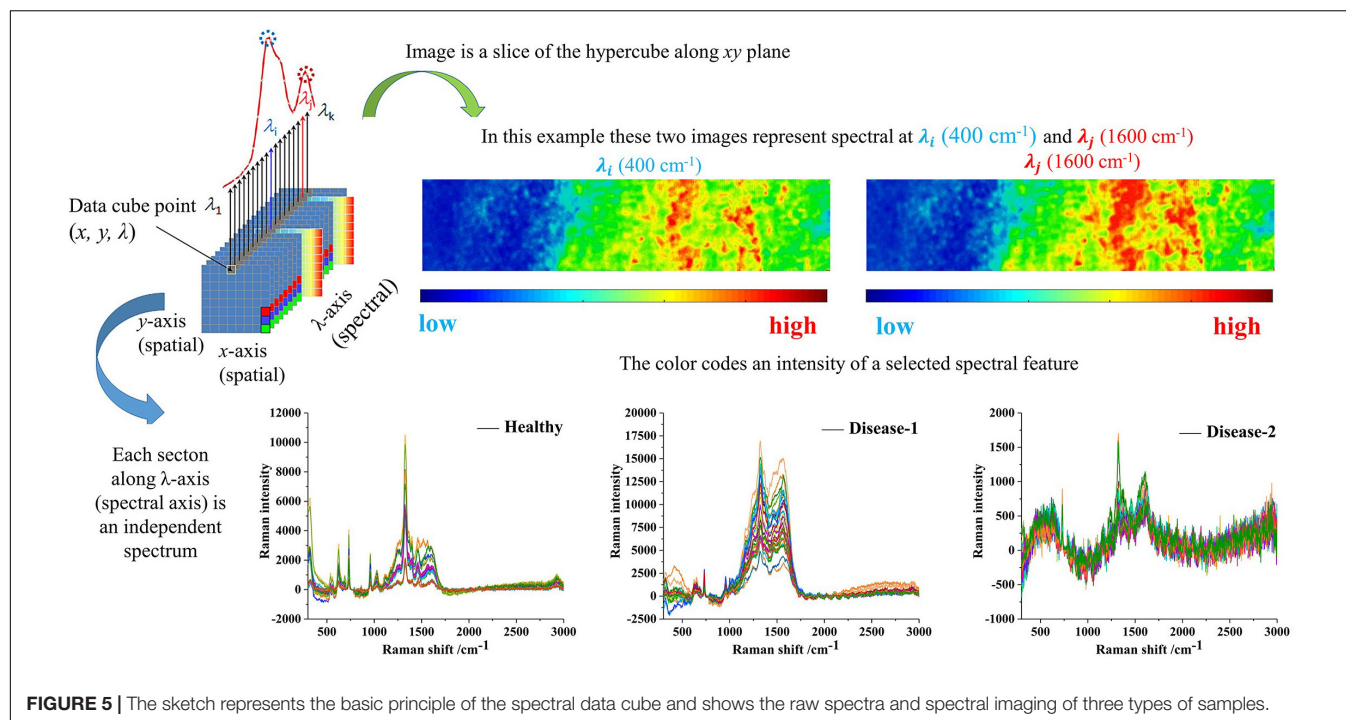


FIGURE 5 | The sketch represents the basic principle of the spectral data cube and shows the raw spectra and spectral imaging of three types of samples.

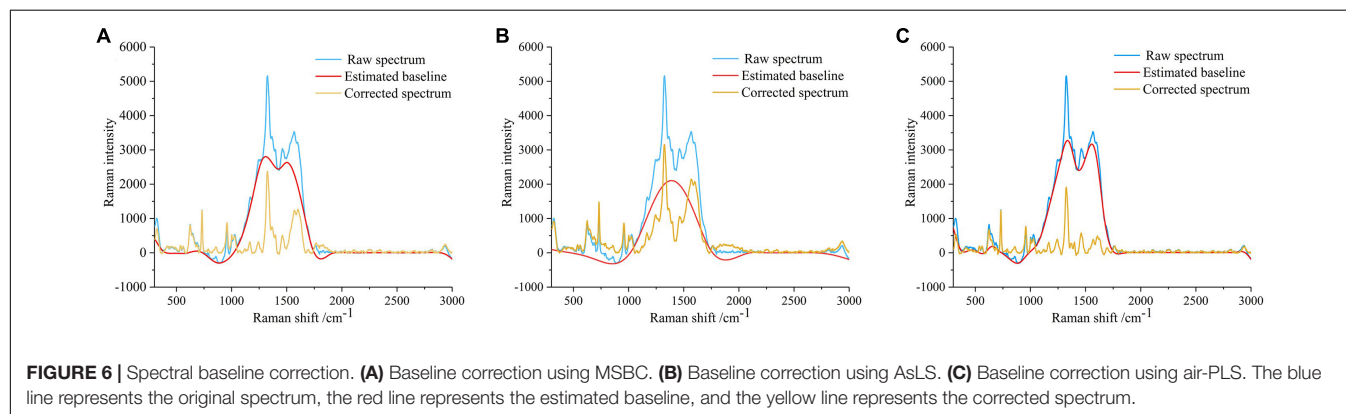


FIGURE 6 | Spectral baseline correction. (A) Baseline correction using MSBC. (B) Baseline correction using AsLS. (C) Baseline correction using air-PLS. The blue line represents the original spectrum, the red line represents the estimated baseline, and the yellow line represents the corrected spectrum.

aromatic ring (Agarwal, 2006), and C-H asymmetric stretching vibration (Gierlinger and Schwanninger, 2007), respectively. The assignment of characteristic wavenumbers was presented in Table 1.

Selecting Optimal Preprocessing Method

The correlation analysis method was adopted to select the best preprocessing algorithms. The correlation between the corrected variables was plotted in Figure 7. Significantly, the regions close to the line $y = x$ had a correlation coefficient of 1, indicating that the original spectra were greatly disturbed by the baseline offset. This high degree of collinearity would cause adverse effects on classification analysis. Comparing Figures 7B–D with Figure 7A, the regions with a high degree of collinearity have a noticeable decrease, and most of the spectral variables had low correlation with others except in the spectral ranges of 300–400, 640–880, and 1,490–1,970 cm^{-1} . In addition, the proportion of pixel

points with values greater than 0.6 to the total pixel points was calculated, and the proportions were 0.35, 0.09, 0.24, and 0.07, respectively. The AsLS method failed to effectively fit the baseline at 1,200–1,600 cm^{-1} , resulting in a relatively poor result of baseline correction. This result indicated that the MSBC and air-PLS baseline offset elimination strategies could greatly reduce the high correlation levels among spectral variables, and especially, the air-PLS algorithm had the best elimination effect. Therefore, the spectra corrected by the air-PLS algorithm were used for further analysis.

Clustering Visualization by Principal Component Analysis

As an unsupervised learning strategy, PCA was often used to demonstrate the clustering effect based on the samples' similarity of samples in the feature space. In the present research, PCA was performed on the raw spectra of the total sample set to visualize

TABLE 1 | Assignment of characteristic wavenumbers.

Wavenumber	Assignment	Biological components	References
319	C-C-C or C-O-C skeletal bending	Cellulose	Szymanska et al. (2011)
625	Skeletal bending	Lignin	Agarwal et al. (2011)
731	Skeletal bending	Lignin	Agarwal et al. (2011)
957	C-C or C-O stretching vibration	Cellulose	Beć et al. (2020)
1,026	C-C or C-O stretching vibration	Cellulose	Beć et al. (2020)
1,165	H-C-C or H-C-O skeletal bending	Cellulose	Edwards et al. (1997)
1,242	C = O stretching vibration	Cellulose	Beć et al. (2020)
1,325	C-H bending vibration	Cellulose	Edwards et al. (1997)
1,599	C-C aromatic ring	Lignin	Agarwal (2006)
2,939	C-H asymmetric stretching vibration	Lignin	Gierlinger and Schwanninger (2007)

the distribution of healthy, disease-1, and disease-2 samples. The score scatters plot of clustering analysis were shown in **Figure 8**. PC1, PC2, and PC3 provided 51.74, 15.01, and 11.56% of the variations among samples, respectively. The cumulative contribution of the first three PCs achieved 78.31%. **Figure 8**

demonstrated that the healthy, disease-1, and disease-2 samples had obvious clustering effects. Therefore, the three types of samples had distinct spectral characteristics.

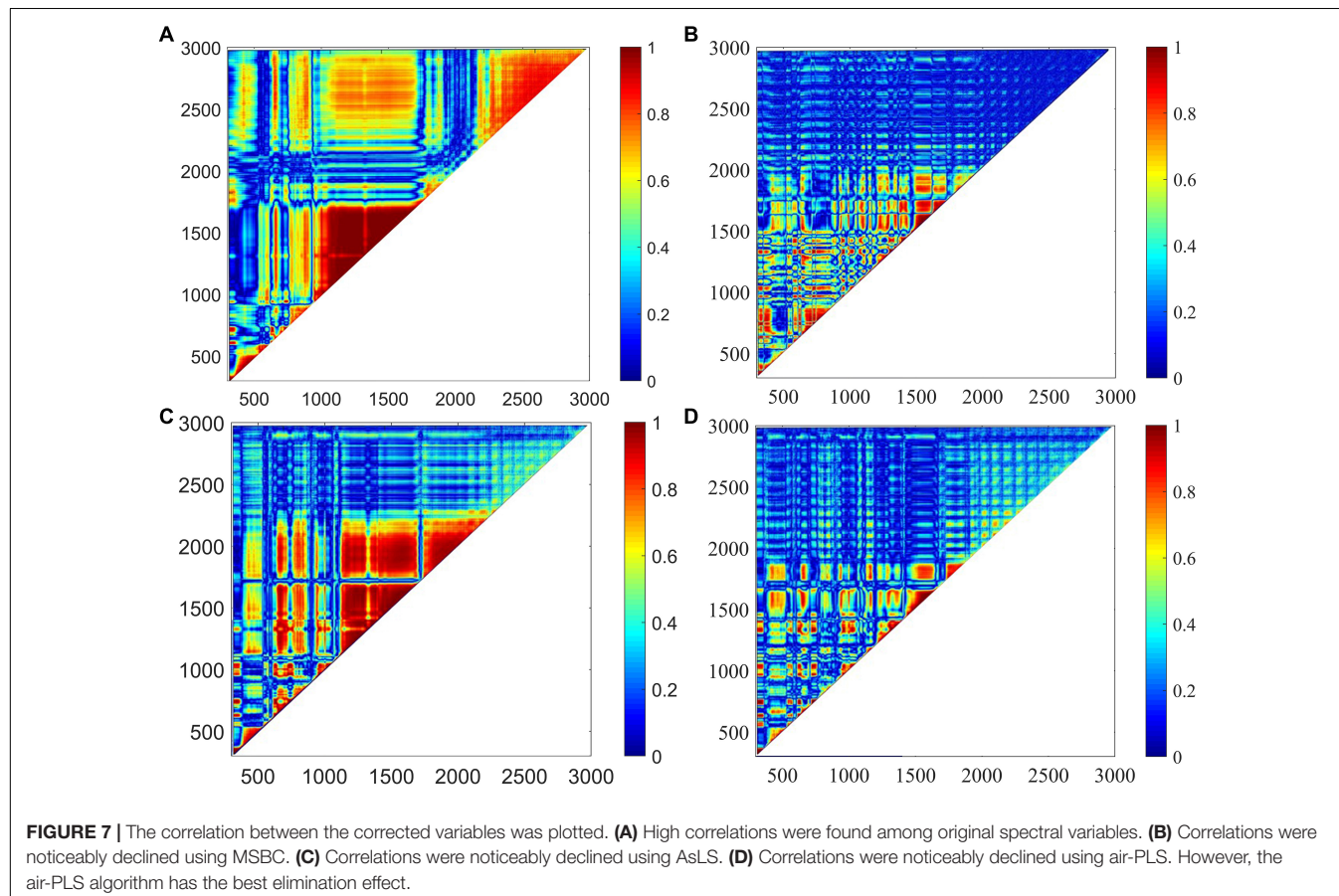
Optimal Variables Selection

There were 1,401 variables in the SERS spectra. However, spectral data contained many non-critical variables, which might reduce the accuracy and stability of subsequent discriminant models. Therefore, selecting optimal variables was essential for better choices of discriminant models. In the present research, two strategies were used to select characteristic variables: algorithm selection (CARS combined with RFrog) and manual selection.

Important variables were extracted from the total 1,401 spectral variables in the full range of 300–3,000 cm^{-1} , as shown in **Figure 9**. The selected optimal variable subsets were set to subset-1 and subset-2, respectively. In the algorithm selection method, 10 wavenumbers at 448, 536, 667, 1,165, 1,211, 1,312, 1,314, 1,412, 1,707, and 2,951 cm^{-1} in the subset-1 were identified. In the manual selection method, 10 wavenumbers at 319, 625, 731, 957, 1,026, 1,165, 1,325, 1,460, 1,570, and 2,939 cm^{-1} in the subset-2 were identified.

Discriminant Models Establishment

Before establishing discriminant models, SERS spectral data were divided into a calibration set and a prediction set at the ratio



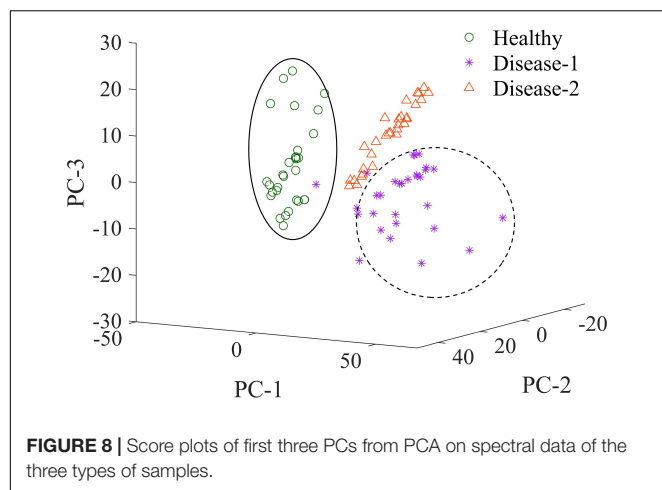


FIGURE 8 | Score plots of first three PCs from PCA on spectral data of the three types of samples.

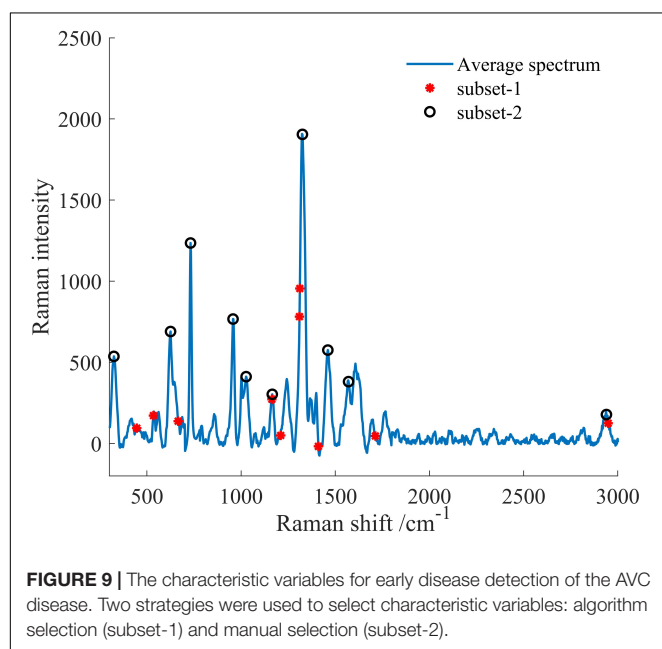


FIGURE 9 | The characteristic variables for early disease detection of the AVC disease. Two strategies were used to select characteristic variables: algorithm selection (subset-1) and manual selection (subset-2).

of 3:1. Generally, the independent variable (x) represented the spectral matrix of samples, and labeled grades (y) stood for the AVC infection severities. Therefore, the labels for healthy, disease-1, and disease-2 were 1, 2, and 3, respectively. BP-ANN, ELM, RForest, and LS-SVM models were established using four variable matrices (x) to classify the healthy, disease-1, and disease-2 samples. These four variable matrices (x) included the full SERS spectra, the subset-1, the subset-2, and the predicted fluorescence baselines.

After formula calculation and experience screening, the learning rate of the BP-ANN model was set uniformly to 0.1, and the number of neurons in the hidden layers were 10, 3, 3, and 10, respectively. The number of neurons in the hidden layer of the ELM model was determined by comparing the performances of the ELM model using different numbers of neurons from 1 to 100 with a step of 1. The ELM with 34 neurons was selected as the optimal model. The number of decision trees in the RForest

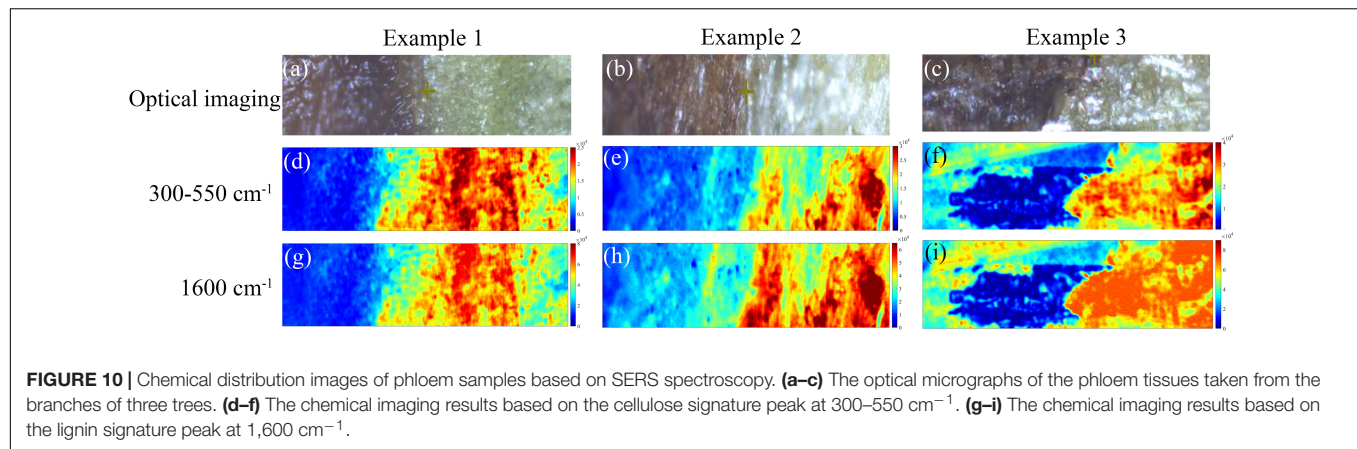
model was determined by comparing the model performances using different numbers of decision trees from 1 to 500 with a step of 1. The RForest with 100 decision trees was selected as the optimal model. The LS-SVM model used RBF as the kernel function, and the optimal penalty coefficient (c) and the kernel function parameter gamma (g) were obtained by a grid search procedure. Finally, the best- c was 379, and the best- g was 45.

The discriminant accuracy of the models was presented in **Table 2**. There were significant differences in the classification results of the four models on the full spectra dataset. The classical BP-ANN model learned complex relationships between data, thus improving the analytical performance (such as high sensitivity and specificity) of classification. However, the BP-ANN model had the regrettable tendency to train toward a local optimal rather than a global optimal (Lussier et al., 2020). This also explained why the BP-ANN model had the lowest classification accuracy on the full spectra dataset compared to the other three models. As opposed to the BP-ANN model, the LS-SVM model was deterministic and its solution was global and unique. As a result, the classification accuracy of the LS-SVM model improved significantly compared to the BP-ANN model. In the present case of the RForest model, each tree selected features maximize the separation of the dataset into three classes. The output of each decision tree was then pooled, leading to the final optimal classification result. Therefore, the RForest model also exhibited excellent analytical performance comparable to the LS-SVM model.

Compared with the full spectra dataset, over 99% of non-critical input variables (10 vs. 1401) were removed in subset-1 and subset-2. Meanwhile, the classification accuracy of the subset models was not decreased significantly, which demonstrated the superiority of the optimal variable selection strategies. Generally, the fluorescence baselines reduced the simplicity and robustness of a calibration model built on the raw spectra. The existing studies by other scholars had removed the fluorescence baseline from the raw data. However, the classification accuracy of the models based on the fluorescence dataset was surprisingly excellent in the present research. When infesting the phloem tissue, fungus *Valsa mali* produced various chemical substances such as protocatechuic acid, isocoumarin, and phlorizin. Although these chemical substances produced fluorescence interference, the baseline reflected the chemical composition and content information. Thus, the fluorescence baseline became available as valid information. This innovative discovery will guide our subsequent research.

TABLE 2 | The discriminant accuracy of the models.

Models	Discriminant accuracy (%)				Running time (s)
	Full SERS spectra	Subset-1	The subset-2	Predicted fluorescence baselines	
BP-ANN	86.22	93.17	92.42	91.80	0.28
ELM	92.36	85.35	88.93	95.39	0.01
RForest	98.46	96.67	95.87	99.57	0.15
LS-SVM	98.86	94.49	95.48	98.04	0.91



However, the above three methods mainly focused on feature extraction, optimal parameters, and optimal variables selection without considering the model runtime, which was also crucial for intelligent online detection, were not investigated. Furthermore, the intelligent online detection would be an important research direction in plant disease detection fields. The ELM model randomly generated the hidden node parameters and then analytically determined the output weights instead of iterative tuning (Huang et al., 2006). Thus, the ELM model runs quickly and lends itself to real application scenarios, which is very important for intelligent online detection. As seen in Table 2, the ELM model ran as fast as 0.01 s, far better than the other three methods. The LS-SVM model first used the grid search method to select the best- c and best- g , severely delaying the discriminatory efficiency and making the run time as high as 0.91 s. Therefore, the ELM algorithm can be considered as the detection model in the subsequent online detection study.

Chemical Imaging Analysis of the Disease-Health Junction

The SERS micro-spectral image data cube of each phloem sample was processed by the air-PLS algorithm to eliminate fluorescence baseline, and the parameter values were consistent with section “Overview of Surface-Enhanced Raman Scattering Spectra.” Then the processed micro-spectral cube in a pixel-wise manner generated chemical distribution images in Figure 10. The symmetric tensile vibration at 1,600 cm^{-1} in lignin was identified as the characteristic peak of lignin components, while the bands at 300–550 cm^{-1} were contributed by cellulose. Therefore, these images were constructed based on the cellulose signature peak at 300–550 cm^{-1} and lignin signature peak at 1,600 cm^{-1} .

Due to the fact that cell walls were probed in phloem tissues, the spectra collected did not contain any intracellular signals. Figures 10a–c showed the optical micrographs of the phloem tissues taken from the branches of three trees. The chemical imaging results based on the cellulose signature peak at 300–550 cm^{-1} were shown in Figures 10d–f. The redder-colored the pixels, the stronger the spectral signals of the chemical component. Meanwhile, the bluer-colored the pixels,

the weaker the spectral signals. It can be noticed that the SERS signal at the healthy tissue exhibited high intensity with red, bright yellow, and green pixel colors. The diseased phloem tissue exhibited low intensity with blue and green pixel colors, and the disease-health junction exhibited green pixel colors. These differences in SERS imaging of different regions can be attributed to differences in cell wall components. The chemical imaging results based on the lignin signature peak at 1,600 cm^{-1} were shown in Figures 10g–i, showing a similar pattern as the cellulose distribution. The different regions of the phloem tissue shown a distinct distribution of cellulose and lignin, and the observations here were in good agreement with optical micrographs. The results suggested that cellulose and lignin in the cell walls of infected tissues reduced significantly. It also confirmed previous research (Ke et al., 2013) that cell wall degrading enzymes were considered to play an important role in fungal infection. Therefore, Raman microimaging was capable of detecting AVC at early infection stages. It is worth noting that Raman microimaging can visualize the intensity and distribution of components of the cell walls *in situ* through cytological observations. Meanwhile, this rapid and non-invasive chemical imaging strategy is superior to the other methods, such as the reagent staining method and transmission electron microscopy.

CONCLUSION

In this study, SERS spectroscopy combined with chemometric methods was applied for early detection of the AVC disease. Firstly, three spectral preprocessing algorithms were compared, and the air-PLS algorithm was considered effective in removing the spectra fluorescence background. Thereafter, PCA provided a good clustering effect to visualize the distribution of samples in three classes. Two strategies selected optimal variables to develop machine learning models for detecting AVC disease, and these models exhibited excellent analytical performance. Meanwhile, the classification accuracy of the models based on the fluorescence dataset was surprisingly excellent, which was a great inspiration. Besides, this study proposed a new strategy for SERS chemical imaging of the diseased apple phloem tissues using

a non-destructive, label-free method. This chemical imaging provided the spatiotemporal dynamic characteristics of changes in the cellulose and lignin of the phloem disease-health junction under fungus stress, which would be helpful in the early AVC detection and analysis of disease dynamics.

DATA AVAILABILITY STATEMENT

The original contributions presented in the study are included in the article/supplementary material, further inquiries can be directed to the corresponding author/s.

AUTHOR CONTRIBUTIONS

SF: writing – original draft and writing – review and editing. JL: investigation, resources, writing – review and editing, and revision. YW, FZ, and YZ: investigation and resources. KY: conceptualization, investigation, resources, and writing – review and editing. All authors contributed to the article and approved the submitted version.

REFERENCES

- Agarwal, U. P. (2006). Raman imaging to investigate ultrastructure and composition of plant cell walls: distribution of lignin and cellulose in black spruce wood (*Picea mariana*). *Planta* 224, 1141–1153. doi: 10.1007/s00425-006-0295-z
- Agarwal, U. P., James, D. M., and Sally, A. R. (2011). FT-Raman investigation of milled-wood lignins: softwood, hardwood, and chemically modified black spruce lignins. *J. Wood Chem. Technol.* 31, 324–344. doi: 10.1080/02773813.2011.562338
- Baek, S. J., Aaron, P., Young, J. A., and Jaebum, C. (2015). Baseline correction using asymmetrically reweighted penalized least squares smoothing. *Analyst* 140, 250–257. doi: 10.1039/c4an01061b
- Beć, K., Justyna, G., Günther, B., Michael, P., and Christian, H. (2020). Principles and applications of vibrational spectroscopic imaging in plant science: a review. *Front. Plant Sci.* 11:1226. doi: 10.3389/fpls.2020.01226
- Cruz, A., Yiannis, A., Roberto, P., Alberto, M., Alessandra, P., Luigi, D. B., et al. (2019). Detection of grapevine yellows symptoms in *Vitis vinifera* L. with artificial intelligence. *Comput. Electron Agric.* 157, 63–76.
- Dong, C. W., Yang, Y., Zhang, J. Q., Zhu, H. K., and Liu, F. (2014). Detection of thrips defect on green-peel citrus using hyperspectral imaging technology combining PCA and B-spline lighting correction method. *J. Integr. Agric.* 13, 2229–2235. doi: 10.1016/s2095-3119(13)60671-1
- Dou, T. Y., Lee, S., Sonia, I., Nicolas, G., Prakash, N., Kranthi, M., et al. (2021). Biochemical origin of Raman-based diagnostics of Huanglongbing in grapefruit trees. *Front. Plant Sci.* 12:680991. doi: 10.3389/fpls.2021.680991
- Edwards, H. G. M., Farwell, D. W., and Webster, D. (1997). FT Raman microscopy of untreated natural plant fibres. *Spectrochim. Acta A Mol. Biomol. Spectrosc.* 53, 2383–2392. doi: 10.1016/s1386-1425(97)00178-9
- Eilers, P. H. C. (2003). A perfect smoother. *Anal. Chem.* 75, 3631–3636. doi: 10.1021/ac034173t
- Eilers, P. H. C. (2004). Parametric time warping. *Anal. Chem.* 76, 404–411.
- Fang, S. Y., Cui, R. Y., Wang, Y., Zhao, Y. R., Yu, K. Q., and Jiang, A. (2021). Application of multiple spectral systems for the tree disease detection: a review. *Appl. Spectrosc. Rev.* doi: 10.1080/05704928.2021.1930552
- Fang, Y., and Ramasamy, P. R. (2015). Current and prospective methods for plant disease detection. *Biosensors* 5, 537–561. doi: 10.3390/bios5030537
- Farber, C., Rebecca, B., Li, P., Charles, R., and Dmitry, K. (2020). Non-invasive characterization of single-, double- and triple-viral diseases of wheat with a

FUNDING

This work was supported by the National Natural Science Foundation of China (Program Nos. 31901403 and 61705188), Natural Science Basic Research Plan in Shaanxi Province of China (Program No. 2020JQ-267), China Postdoctoral Science Foundation (Program No. 2018M641023), Shaanxi Province Postdoctoral Science Foundation (Program No. 2017BSHYDZZ61), Science and Technology Innovation and Achievement Transformation Project of Experimental Demonstration Station (Program No. TGZX2019-10), and Key Laboratory of Agricultural Internet of Things, Ministry of Agriculture and Rural Affairs, China.

ACKNOWLEDGMENTS

We would like to thank Guangyu Sun (Northwest A&F University) for providing the experimental materials. We would also like to thank Life Science Large Instrument Sharing Platform (Northwest A&F University) for its support for TEM experiments.

- hand-held Raman spectrometer. *Front. Plant Sci.* 11:1300. doi: 10.3389/fpls.2020.01300
- Feng, Y. Q., Yin, Z. Y., Wu, Y. M., Xu, L. S., Du, H. X., Wang, N. N., et al. (2020). LaeA controls virulence and secondary metabolism in apple canker pathogen *Valsa mali*. *Front. Plant Sci.* 11:581203. doi: 10.3389/fmicb.2020.581203
- Gierlinger, N., and Schwanninger, S. (2007). The potential of Raman microscopy and Raman imaging in plant research. *Spectrosc. Int. J.* 21, 69–89.
- Golhani, K., Siva, K. B., Ganesan, V., and Biswajeet, P. (2018). A review of neural networks in plant disease detection using hyperspectral data. *Information Processing Agric.* 5, 354–371.
- Hu, G. S., Yin, C. G., Wan, M. Z., Zhang, Y., and Fang, Y. (2020). Recognition of diseased Pinus trees in UAV images using deep learning and AdaBoost classifier. *Biosystem Eng.* 194, 138–151.
- Huang, C. H., Gajendra, P. S., Su, H. P., Chua, N. H., Rajeev, J. R., and Bong, S. P. (2020). Early diagnosis and management of nitrogen deficiency in plants utilizing Raman spectroscopy. *Front. Plant Sci.* 11:663. doi: 10.3389/fpls.2020.00663
- Huang, G. B., Zhu, Q. Y., and Siew, C. K. (2006). Extreme learning machine: theory and applications. *Neurocomputing* 70, 489–501.
- Ke, X. W., Huang, L. L., Han, Q. M., Gao, X. N., and Kang, Z. S. (2013). Histological and cytological investigations of the infection and colonization of apple bark by *Valsa mali* var. *mali*. *Australas Plant Pathol.* 42, 85–93.
- Khairunniza, B. S., and Vong, N. V. (2014). Detection of basal stem rot (BSR) infected oil palm tree using laser scanning data. *Agric. Agric. Sci. Procedia.* 2, 156–164.
- Khaled, A. Y., Samsuzana, A. A., Siti, K. B., Nazmi, M. N., and Idris, A. S. (2018). Spectral features selection and classification of oil palm leaves infected by Basal Stem Rot (BSR) disease using dielectric spectroscopy. *Comput. Electron Agric.* 144, 297–309.
- Li, H. D., Liang, Y. Z., Xu, Q. S., and Cao, D. S. (2009). Key wavelengths screening using competitive adaptive reweighted sampling method for multivariate calibration. *Anal. Chim. Acta* 648, 77–84. doi: 10.1016/j.aca.2009.06.046
- Li, H. D., Qing, S. X., and Liang, Y. Z. (2012). Random frog: an efficient reversible jump Markov Chain Monte Carlo-like approach for variable selection with applications to gene selection and disease classification. *Anal. Chim. Acta* 740, 20–26. doi: 10.1016/j.aca.2012.06.031
- Li, Q. Q., Yue, H., Song, X. Z., Zhang, J. X., and Min, S. G. (2019). Moving window smoothing on the ensemble of competitive adaptive reweighted sampling algorithm. *Spectrochim. Acta A Mol. Biomol. Spectrosc.* 214, 129–138. doi: 10.1016/j.saa.2019.02.023

- Li, X. L., Sha, J. J., Chu, B. Q., Wei, Y. Z., Huang, W. H., Zhou, H., et al. (2019). Quantitative visualization of intracellular lipids concentration in a microalgae cell based on Raman micro-spectroscopy coupled with chemometrics. *Sensor Actuat B Chem.* 292, 7–15. doi: 10.1016/j.snb.2019.04.048
- Liu, M., Elisa, M., Julie, T. C., Julie, C., Sylvia, K. W., Raymond, T., et al. (2015). Detection and identification of selected cereal rust pathogens by TaqMan® real-time PCR. *Can. J. Plant Pathol.* 37, 92–105. doi: 10.1080/07060661.2014.999123
- Lucay, F. A., Luis, A. C., and Edelmira, D. G. (2020). An LS-SVM classifier based methodology for avoiding unwanted responses in processes under uncertainties. *Comput. Chem. Eng.* 138:106860. doi: 10.1016/j.compchemeng.2020.106860
- Lussier, F., Vincent, T., Benjamin, C., Gregory, Q. W., and Jean, F. M. (2020). Deep learning and artificial intelligence methods for Raman and surface-enhanced Raman scattering. *TrAC Trend Anal. Chem.* 124:115796.
- Martinelli, F., Riccardo, S., Salvatore, D., Stefano, P., Giuseppe, S., Paolo, R., et al. (2015). Advanced methods of plant disease detection. a review. *Agron. Sustain. Dev.* 35, 1–25.
- Meng, X. L., Xing, H. Q., Han, Z. Y., Guo, Y. B., Wang, Y. N., Hu, T. L., et al. (2019). Latent infection of valsa mali in the seeds, seedlings and twigs of crabapple and apple trees is a potential inoculum source of valsa canker. *Sci. Rep.* 9:7738. doi: 10.1038/s41598-019-44228-w
- Mukherjee, D., Bolla, G. R., and Benjaram, M. R. (2017). Characterization of ceria-based nano-oxide catalysts by raman spectroscopy. *Top Catal.* 60, 1673–1681.
- Okiro, L. A., Matthew, A. T., Steven, G. N., Christine, D. S., and Monica, L. P. (2019). Comparative evaluation of LAMP, qPCR, conventional PCR, and ELISA to detect ralstonia solanacearum in Kenyan potato fields. *Plant Dis.* 103, 959–965. doi: 10.1094/PDIS-03-18-0489-RE
- Peng, J. T., Peng, S. L., Jiang, A., Wei, J. P., Li, C. W., and Tan, J. (2010). Asymmetric least squares for multiple spectra baseline correction. *Anal. Chim. Acta* 683, 63–68. doi: 10.1016/j.aca.2010.08.033
- Petrov, D. V. (2017). Pressure dependence of peak positions, half widths, and peak intensities of methane Raman bands (v2, 2v4, v1, v3, and 2v2). *J. Raman Spectrosc.* 48, 1426–1430. doi: 10.1002/jrs.5141
- Qin, J. W., Chao, K. L., and Moon, S. K. (2011). Investigation of Raman chemical imaging for detection of lycopene changes in tomatoes during postharvest ripening. *J. Food Eng.* 107, 277–288. doi: 10.1016/j.jfoodeng.2011.07.021
- Qiu, S. S., Gao, L. P., and Wang, J. (2015). Classification and regression of ELM, LVQ and SVM for E-nose data of strawberry juice. *J. Food Eng.* 144, 77–85.
- Ranulfi, A. C., Marcelo, C. B. C., Thiago, M. K. K., Juliana, F. A., Ednaldo, J. F., Barbara, S. B., et al. (2016). Laser-induced fluorescence spectroscopy applied to early diagnosis of citrus Huanglongbing. *Biosyst. Eng.* 144, 133–144.
- Sanchez, L., Shankar, P., Mike, I., Kranthi, M., and Dmitry, K. (2019a). Detection and identification of canker and blight on orange trees using a hand-held Raman spectrometer. *J. Raman Spectrosc.* 50, 1875–1880. doi: 10.1002/jrs.5741
- Sanchez, L., Shankar, P., Xing, Z. L., Kranthi, M., and Dmitry, K. (2019b). Rapid and noninvasive diagnostics of Huanglongbing and nutrient deficits on citrus trees with a handheld Raman spectrometer. *Anal. Bioanal. Chem.* 411, 3125–3133. doi: 10.1007/s00216-019-01776-4
- Suzaki, K. (2008). Population structure of *Valsa ceratosperma*, causal fungus of Valsa canker, in apple and pear orchards. *J. Gen. Plant Pathol.* 74, 128–132.
- Szymanska, C., Monika, J. C., and Artur, Z. (2011). Sensing the structural differences in cellulose from apple and bacterial cell wall materials by raman and FT-IR spectroscopy. *Sensors* 11, 5543–5560. doi: 10.3390/s110605543
- Vallejo, P., Moises, R., Maria, G. G. M., Miguel, G. R. E., Francisco, J. G., Hugo, R. N. C., et al. (2016). Raman spectroscopy an option for the early detection of citrus huanglongbing. *Appl. Spectrosc.* 70, 829–839. doi: 10.1177/0003702816638229
- Wang, W. D., Nie, J. J., Lv, L. Q., Gong, W., Wang, S. L., Yang, M. M., et al. (2021). A *Valsa mali* effector Protein 1 targets apple (*Malus domestica*) pathogenesis-related 10 Protein to promote virulence. *Front. Plant Sci.* 12:741342. doi: 10.3389/fpls.2021.741342
- Wang, X. L., Wei, J. L., Huang, L. L., and Kang, Z. S. (2011). Re-evaluation of pathogens causing Valsa canker on apple in China. *Mycologia* 103, 317–324. doi: 10.3852/09-165
- Wu, D. M., Wang, X. L., and Wu, S. C. (2021). A hybrid method based on extreme learning machine and wavelet transform denoising for stock prediction. *Entropy* 23:440. doi: 10.3390/e23040440
- Yang, G. Y., Wang, Q. Y., Liu, C., Wang, X. B., Fan, S. X., and Huang, W. Q. (2018). Rapid and visual detection of the main chemical compositions in maize seeds based on Raman hyperspectral imaging. *Spectrochim. Acta A Mol. Biomol. Spectrosc.* 200, 186–194. doi: 10.1016/j.saa.2018.04.026
- Yin, Z. Y., Ke, X. W., and Huang, L. L. (2013). Validation of reference genes for gene expression analysis in Valsa mali var. mali using real-time quantitative PCR. *World J. Microb. Biot.* 29, 1563–1571. doi: 10.1007/s11274-013-1320-6
- Zang, R., Yin, Z. Y., Ke, X. W., Wang, X. J., Li, Z. L., Kang, Z. S., et al. (2012). A nested PCR assay for detecting Valsa mali var. mali in different tissues of apple trees. *Plant Dis.* 96, 1645–1652. doi: 10.1094/PDIS-05-11-0387-RE
- Zhang, L., Wang, F. L., Sun, T., and Xu, B. (2018). A constrained optimization method based on BP neural network. *Neural Comput. Appl.* 29, 413–421.
- Zhao, Y. R., Fang, S. Y., Ye, Y. K., and Yu, K. Q. (2021). Chemometric development using portable molecular vibrational spectrometers for rapid evaluation of AVC (*Valsa mali* Miyabe et Yamada) infection of apple trees. *Vib. Spectrosc.* 114:103231. doi: 10.1016/j.vibspec.2021.103231

Conflict of Interest: The authors declare that the research was conducted in the absence of any commercial or financial relationships that could be construed as a potential conflict of interest.

Publisher's Note: All claims expressed in this article are solely those of the authors and do not necessarily represent those of their affiliated organizations, or those of the publisher, the editors and the reviewers. Any product that may be evaluated in this article, or claim that may be made by its manufacturer, is not guaranteed or endorsed by the publisher.

Copyright © 2022 Fang, Zhao, Wang, Li, Zhu and Yu. This is an open-access article distributed under the terms of the Creative Commons Attribution License (CC BY). The use, distribution or reproduction in other forums is permitted, provided the original author(s) and the copyright owner(s) are credited and that the original publication in this journal is cited, in accordance with accepted academic practice. No use, distribution or reproduction is permitted which does not comply with these terms.



Handheld Multifunctional Fluorescence Imager for Non-invasive Plant Phenotyping

Ruochong Zhang¹, Sally Shuxian Koh^{2,3}, Mark Ju Teng Teo¹, Renzhe Bi¹, Shuyan Zhang¹, Kapil Dev¹, Daisuke Urano^{2,3*}, U. S. Dinish^{1*} and Malini Olivo^{1*}

¹ Translational Biophotonic Laboratory, Institute of Bioengineering and Bioimaging, A*STAR, Singapore, Singapore,

² Temasek Life Sciences Laboratory, Singapore, Singapore, ³ Department of Biological Sciences, National University of Singapore, Singapore, Singapore

OPEN ACCESS

Edited by:

Yuzhen Lu,
Mississippi State University,
United States

Reviewed by:

Lingfeng Duan,
Huazhong Agricultural University,
China
Giovanni Agati,
Nello Carrara Institute of Applied
Physics (IFAC), Italy

*Correspondence:

Daisuke Urano
Daisuke@till.org.sg
U. S. Dinish
Dinish@ibb.a-star.edu.sg
Malini Olivo
Malini_Olivo@ibb.a-star.edu.sg

Specialty section:

This article was submitted to
Technical Advances in Plant Science,
a section of the journal
Frontiers in Plant Science

Received: 26 November 2021

Accepted: 09 March 2022

Published: 08 April 2022

Citation:

Zhang R, Koh SS, Teo MJT, Bi R,
Zhang S, Dev K, Urano D, Dinish US
and Olivo M (2022) Handheld
Multifunctional Fluorescence Imager
for Non-invasive Plant Phenotyping.
Front. Plant Sci. 13:822634.
doi: 10.3389/fpls.2022.822634

Fluorescence imaging has shown great potential in non-invasive plant monitoring and analysis. However, current systems have several limitations, such as bulky size, high cost, contact measurement, and lack of multifunctionality, which may hinder its applications in a wide range of settings including indoor vertical farming. Herein, we developed a compact handheld fluorescence imager enabling multipurpose plant phenotyping, such as continuous photosynthetic activity monitoring and non-destructive anthocyanin quantification. The compact imager comprises of pulse-amplitude-modulated multi-color light emitting diodes (LEDs), optimized light illumination and collection, dedicated driver circuit board, miniaturized charge-coupled device camera, and associated image analytics. Experiments conducted in drought stressed lettuce proved that the novel imager could quantitatively evaluate the plant stress by the non-invasive measurement of photosynthetic activity efficiency. Moreover, a non-invasive and fast quantification of anthocyanins in green and red Batavia lettuce leaves had excellent correlation (>84%) with conventional destructive biochemical analysis. Preliminary experimental results emphasize the high throughput monitoring capability and multifunctionality of our novel handheld fluorescence imager, indicating its tremendous potential in modern agriculture.

Keywords: fluorescence, multifunctional, handheld, non-invasive plant phenotyping, photosynthetic activity, anthocyanin

INTRODUCTION

Effective plant monitoring techniques are critical in gaining insights on plant health, allowing for improved decision-making and a more streamlined workflow in modern agriculture. Most land plants produce their own food by chlorophyll, a group of green pigments. Part of the ambient light absorbed by chlorophyll are used to produce carbohydrates through photochemistry and the unused parts are either dissipated as heat or re-emitted as longer wavelength fluorescence. These three processes are in competition and chlorophyll fluorescence emission was found to be dynamic and complex with a plenty of information (Kautsky, 1960). Hence, chlorophyll fluorescence

has been widely used as an indicator of photosynthetic activity (PSA) and plant self-protection mechanism. Modulated chlorophyll fluorescence measurement methods (Quick and Horton, 1984; Schreiber et al., 1986) became more popular than non-modulated methods as they can be used in the presence of ambient light in the field and do not require a dark environment. More interestingly, chlorophyll fluorescence was found to be related to the amount of phenolic compound in the epidermis of leaves and fruit peels (Cerovic et al., 2002; Hagen et al., 2006; Agati et al., 2007). Anthocyanin, as an important part of phenolic compound, attracts much attention due to its antioxidant effects and health benefits (Khoo et al., 2017). Besides, anthocyanin content can help to assess quality, maturity stage, and also in determining the harvesting time of a plant (Christian and Jackson, 2009). The conventional destructive biochemical analysis of anthocyanin is discontinuous, time-consuming, and costly since it involves harvesting, multiple extraction steps before reaching the quantification stage (Nakata and Ohme-Takagi, 2014). Thus, there is a great demand for an advanced device that can be used for both PSA monitoring and fast non-destructive anthocyanin quantification to improve agricultural efficiency and productivity.

Nowadays, several fluorescence imagers and sensors are commercially available for non-invasive PSA monitoring, such as Walz Imaging-PAM, Photon Systems Instrument FluorCams, and LI-COR (Cen et al., 2017; van Tol et al., 2017; Wang et al., 2017; Backes et al., 2021; Linn et al., 2021). However, none of the above-mentioned imaging devices can be used to quantify anthocyanin content. Moreover, they are relatively bulky and expensive. Apart from the above mentioned devices, Force A founded in 2004 developed Dualex and Multiplex which have been used to quantify anthocyanin content through fluorescence emission (Hagen et al., 2006; Agati et al., 2007; Steele et al., 2009), but they are point sensors without imaging capability. Besides, they cannot quantitate plants' PSA parameters that requires pulse-amplitude modulated (PAM) excitation. Hence, there is an unmet need for a compact and high-throughput fluorescence imager for multi-purpose applications. Technical challenges in developing such a system include combining multiple functions in single device, maintaining system performance, size, and cost reduction. Herein, we overcame these challenges and developed a compact handheld multifunctional and multi-spectral fluorescence imager with the following advantages: (1) it combines non-invasive and continuous PSA monitoring and anthocyanin distribution quantification in a single device; (2) it is a high-resolution imaging device, which inherently has high throughput measurement capability and can provide morphological information; (3) it is compact and low-cost by incorporating dedicated optoelectronics design. The study was divided into two parts to verify the functions of the self-developed device: PSA monitoring and non-invasive anthocyanin quantification. In the first part, the PSA of drought and control plants were measured by the imager to quantify the stress condition based on obtained fluorescence images. In the second part, non-invasive anthocyanin measurement was carried out and results were correlated with biochemical analysis to assess the quantification accuracy of our device.

MATERIALS AND METHODS

Instrument Design

The developed compact fluorescence imager mainly consists of multi-spectral light emitting diode (LED panel, LED driver board, CCD camera with IMX273 sensor, imaging lenses, and filters. Its photo and overall schematic are shown in **Figures 1A,B**. The size reduction was achieved by using a customized board-level driver circuit and all-in-one multi-spectral LED (Cree XLamp XM-L) that provide high-intensity RGB output in a small package (5 mm × 5 mm). Each package contains 625 (± 5), 528 (± 8), and 458 (± 8) nm LED diodes and each of them can be controlled independently. A total of 12 RGB LEDs are connected in series and arranged in the groups of 3 on 4 LED blocks. Individual LED block was tilted by 30 degrees for better illumination. RGB color channels are controlled by three independent LED drivers (AP8802H, Diodes Incorporated). In this study, the LED was operated in PAM mode with different widths and amplitudes of pulse light to achieve dynamic illumination (Schreiber et al., 1986). The dimming of LEDs was adjusted by the 0–5 V analog output signal from the data acquisition (DAQ) card (USB-6003, NI). A board level mono color charge-coupled device (CCD) camera (A15S, Alkeria) was fixed in the center and employed as an image detector, together with an imaging lens and 695 nm long-pass filter (LPF). The working distance is adjustable from 25 mm to infinity and the resolution is $1,088 \times 1,456$.

Fluorescence Data Acquisition and Processing

The device provides two operating modes, which can be used to monitor the PSA and measure anthocyanin content, non-invasively and continuously. Under PSA monitoring mode, the measuring light (ML), saturation pulse (SP), and actinic light (AL) in blue (465 nm) with different intensity and period are shined at a specific sequence. The modulation of various LED beams was controlled by analog output from DAQ card with different pulse widths and voltages. ML is a weak and short pulse used to measure the minimal fluorescence without causing any photosynthesis. It was set to be 1 ms with 3 s pulse interval and $< 1 \mu\text{mol photons m}^{-2}\text{s}^{-1}$. SP is a strong pulse that makes all photosystem II reaction centers closed, which is used to determine the maximal fluorescence yield. It was set at 200 ms with intensity of $> 3,000 \mu\text{mol photons m}^{-2}\text{s}^{-1}$. AL refers to the continuous light to drive the photosynthetic activity with intensity of $\sim 300 \mu\text{mol photons m}^{-2}\text{s}^{-1}$. The illumination sequence of different pulses and the corresponding camera shutter signal are shown in **Figure 1C**. After 3-h dark adaption, the ML was applied to measure minimal fluorescence F_0 pixel-wisely, followed by a SP to get maximal fluorescence F_m . Then, 5 MLs were shined to measure the fluorescence response after SP. Note that the number of MLs is adjustable. The AL was turned on after that and together with sequential MLs and SPs, steady state fluorescence F (after photosynthesis is stable) and maximal fluorescence after light adaption F_m' were obtained. The camera shutter was fixed at 980 μs to acquire the images

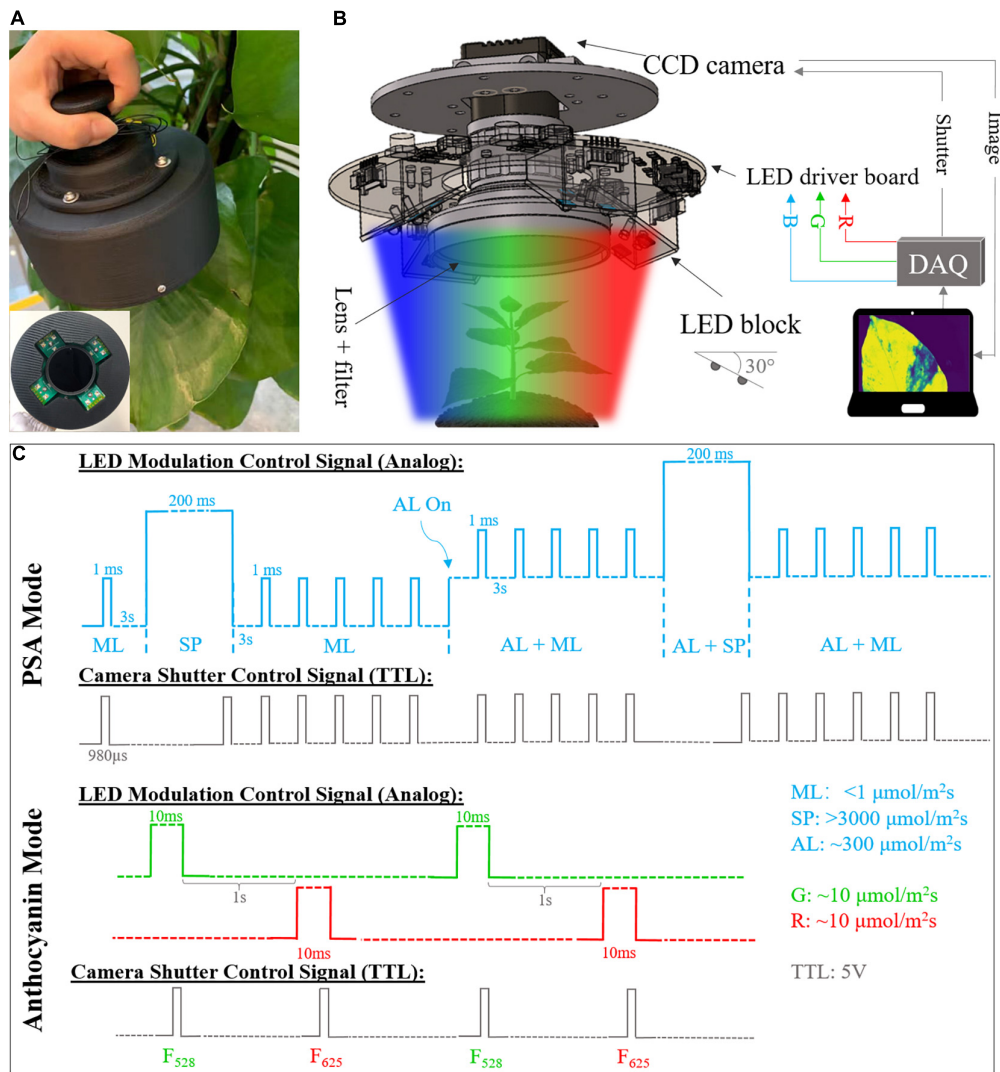


FIGURE 1 | (A) Photograph of the developed compact fluorescence imager. Side view and front view (inset). **(B)** System diagram and inner structure of fluorescence imager. DAQ, data acquisition. **(C)** Timing diagram of light emitting diode (LED) modulation and camera shutter control signals for photosynthetic activity monitoring with blue LEDs. ML, measuring light; SP, saturation pulse; AL, actinic light; TTL, transistor–transistor logic. Note that the timing diagram is for illustration purpose only. The pulse widths and amplitudes are not presented in right scale due to limited space.

at the end of ML and SP. Fluorescence images were saved real-time for post-processing. The maximum efficiency and operating efficiency of photosystem II (PSII) for each pixel can be calculated as (Kitajima and Butler, 1975; Genty et al., 1989):

$$F_v/F_m = \frac{F_m - F_0}{F_m} \quad (1)$$

$$\phi_{PSII} = \frac{F'_m - F}{F'_m} \quad (2)$$

For anthocyanin measurement, the green (528 nm) and red (625 nm) LEDs were shined sequentially with 10 ms pulse width and 1 s interval. The illumination intensity for both colors were adjusted and measured by a commercial photoactive radiation

(PAR) meter (Apogee SQ-500) to ensure the same PAR output according to photosynthetic photon flux (Barnes et al., 1993). Anthocyanins are usually located in the epidermis of plant leaves to absorb light and protect plants from harmful radiation (Hughes et al., 2007; Zhu et al., 2018). The green and red LED induced images were acquired at the steady state. Thus, based on chlorophyll screening effect and Beer-Lambert Law, the pixel-wise anthocyanin index was estimated by the following formula (Agati et al., 2007):

$$Anth_Index = \log \left(\frac{F_{625}}{F_{528}} \right) \quad (3)$$

where F_{625} and F_{528} are steady state fluorescence images excited by red and green LEDs.

Plant Preparation for Photosynthetic Activity Measurement

Drought treatment was planned for PSA monitoring. Lettuce seeds (*Lactuca sativa* var. Little Gem) were surface sterilized using a 10% bleach solution containing Triton X-100, and then plated on Murashige and Skoog (1962) basal media with 1% agar. Plants were germinated and grown in a growth chamber at 22°C under 24 h continuous light and $\sim 90 \mu\text{mol m}^{-2} \text{s}^{-1}$ light intensity. After 4 days, lettuce seedlings were transferred to soil containing a 10:1 ratio of BVB peatmoss (BVB substrates, Netherlands) and sand. Plants were grown at 22 °C under a 16 h light/8 h dark cycle, $\sim 150 \mu\text{mol m}^{-2} \text{s}^{-1}$ light intensity, and 70% relative humidity. Before drought treatment, all plants were watered daily to keep the soil wet. When the plants were 23 days old, watering was withheld. Then, 64 equally sized lettuce plants were randomly divided into control and drought groups. At days 3 and 5 after the start of drought treatment, water was added to control plants (till soil was saturated with water), and relevant non-invasive PSA measurements were taken in the afternoon about 4–6 h after watering. On day 3, 16 plants of each group were measured. The same procedure was repeated on day 5 and the remaining 32 plants of the two groups were measured. The whole process is illustrated in **Figure 2A**.

Biochemical Analysis for Anthocyanin Content

For anthocyanin measurement, mixed salad leaves (Farmers' Pick) were purchased from a supermarket. Then, 22 leaves including 5 green, 12 red, and 5 intermediate Batavia leaves (**Supplementary Figure 1**) were measured non-invasively by the developed fluorescence imager. Following non-invasive measurements, the biochemical quantification of total anthocyanins was carried out. The anthocyanin extraction was based on the procedure described by Neff and Chory (1998). The fresh weights of each sample were measured. Samples were placed in microfuge tubes and snap frozen in liquid nitrogen, then ground using a mortar and pestle. The extraction protocol is designed as follows where the volumes described in the following steps (except microplate reader measurements) were used for every 100 mg of fresh weight measured (total volumes were scaled according to the fresh weight of each sample). After grinding plant samples, 300 μl of methanol (containing 1% HCl) was added. Samples were incubated overnight in a dark refrigerator. On the next day, 200 μl water was added to each tube, followed by 500 μl chloroform. Then, samples were spun down in a centrifuge at $21,000 \times g$ for 5 min. Furthermore, 400 μl of the supernatant (top methanol and water) phase was transferred into a new microfuge tube. Another 400 μl of 60% methanol (containing 1% HCl):40% water solution was added into the new microfuge tube. Two replicates of 200 μl per sample were pipetted in a 96-well microplate. Total anthocyanins were determined by measuring the A_{530} and A_{657} using a Spark multimode microplate reader (Tecan, Switzerland). Total anthocyanin content of the entire leaf sample in relative units was calculated based on the formula

in Laby et al. (2000), except that the fresh weight was not divided:

$$\text{Total anthocyanins} = [\text{OD}_{530} - (0.25 \times \text{OD}_{657})] \times \text{total extraction volume (mL)} \quad (4)$$

Statistical Analysis

For the obtained Φ_{PSII} and F_v/F_m fluorescence images, 5,000 pixels out of the non-zero pixels (effective pixels) for each plant were randomly selected and averaged. Background pixels with zero values were excluded. Then, the mean fluorescence intensities of the 16 plants in each group at days 3 and 5 were plotted in boxplots. The mean values and standard deviations (SDs) are calculated over the 16 plants for each group at each time point and summarized in **Supplementary Table 1**. The box was defined by the minimum, 25th percentile, median, 75th percentile, and the maximum of pixel intensities. Difference between the means of drought and control plants was compared by two-tail Student's *t*-test using Python 3.7, SciPy toolbox.

Total anthocyanin index was calculated as the sum of every pixel's value of anthocyanin image. Then, Random sample consensus (RANSAC), a robust regression algorithm was executed in Python to determine the correlation between non-invasively measured total anthocyanin index and destructive biochemical analysis result, as described in Equation 4. RANSAC can automatically exclude outliers during regression to enhance the overall predication accuracy. Data points whose residuals are out of the threshold (median absolute deviation (MAD) by default) are classified as outliers.

RESULTS

High Throughput Plant Photosynthetic Activity Monitoring Under Drought Treatment

During PSA measurement, blue output from RGB LEDs was triggered and the fluorescence imager was fixed on the top of plants with fully opened aperture. The working distance was adjusted to ~ 20 cm with the field of view (FOV) of $\sim 23 \text{ cm} \times 17 \text{ cm}$ throughout the experiment to cover most part of the plants. The acquired series of fluorescence images were calculated pixel-wise based on Equations 1, 2 to obtain Φ_{PSII} and F_v/F_m images on days 3 and 5. Representative images are shown in **Figures 2B,C** and the remaining images are provided in the **Supplementary Figures 2, 3**. From the images, the difference between control and drought groups can be clearly seen. At day 3, control group fluorescence images showed slightly higher values than drought group, especially for F_v/F_m . The difference between treatments became more pronounced at day 5. To better quantify these differences, statistical analysis mentioned in the section "Statistical Analysis" was performed and result is shown in **Figure 2D** and **Supplementary Table 1**. It can be calculated that at day 3, the Φ_{PSII} and F_v/F_m mean values of control group are 0.46 and 0.61% higher than drought group, respectively. For Φ_{PSII} , the value of *p* is 0.7 indicating that there

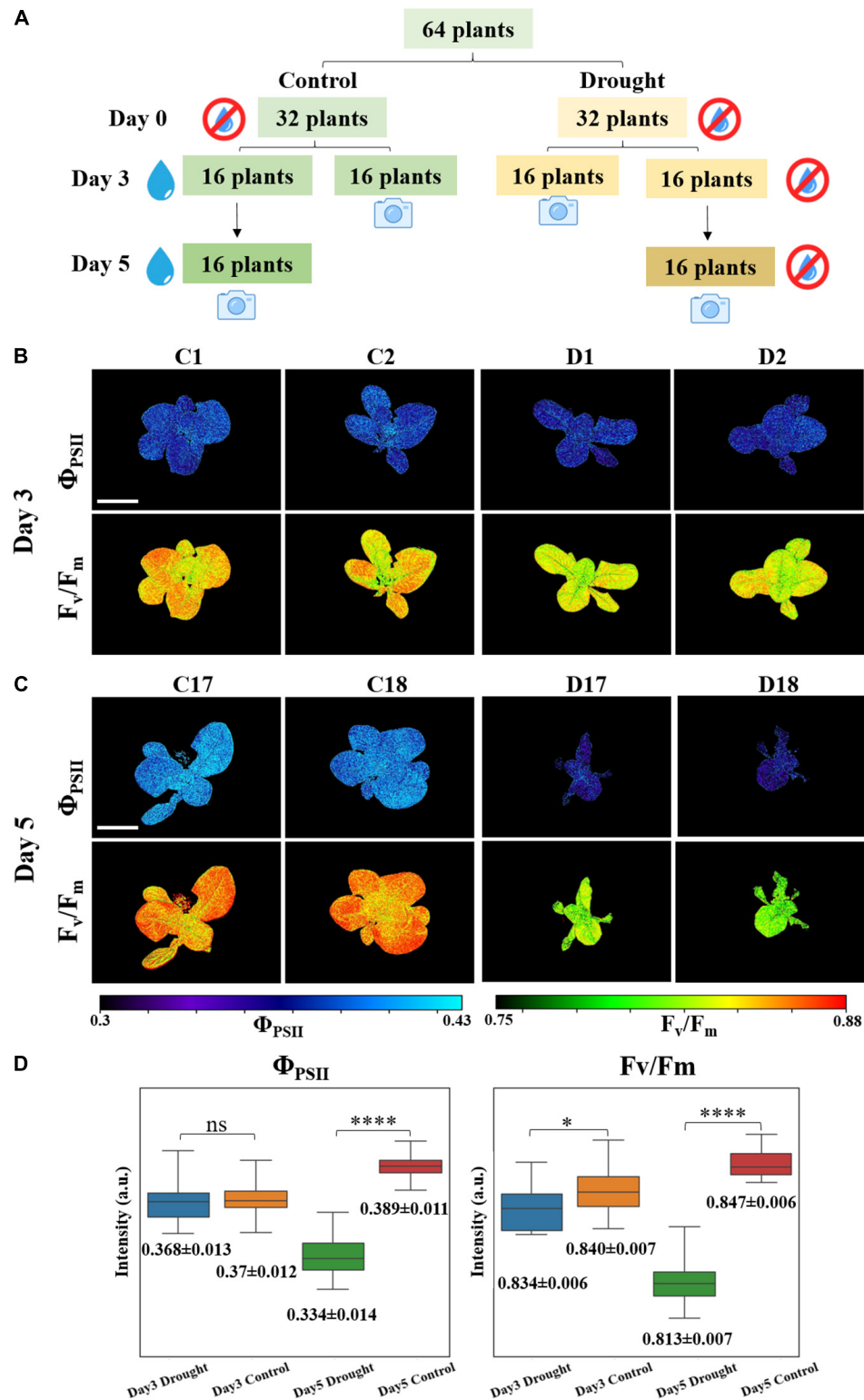


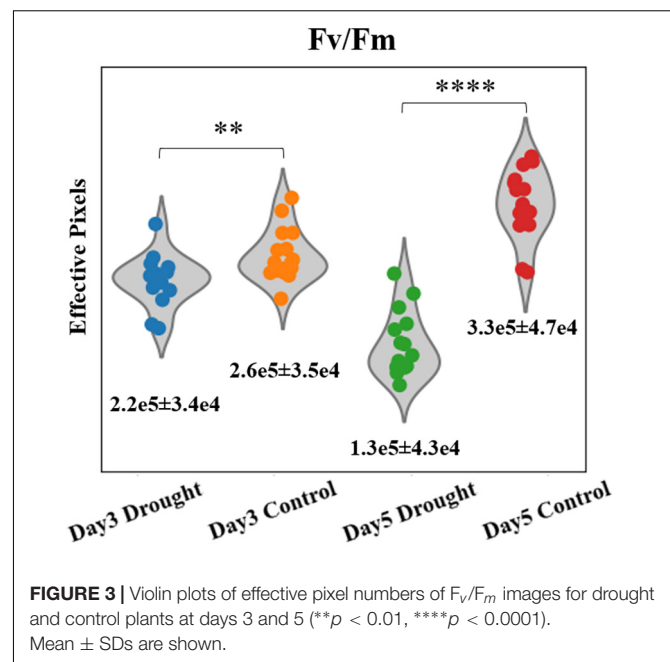
FIGURE 2 | (A) Plants drought treatment for photosynthetic activity measurement. Examples of **(B)** day 3 and **(C)** day 5 fluorescence images of Φ_{PSII} and F_v/F_m . C represents for control group and D represents for drought group. The scale bar represents 5 cm. **(D)** Boxplots: mean values of 5,000 effective pixels randomly selected from Φ_{PSII} and F_v/F_m images of the 16 plants in drought and control groups at days 3 and 5. Box is defined by 25th, 50th, and 75th percentiles. Top and bottom bars are maximum and minimum pixel intensities. Numbers below are mean values \pm standard deviations (SDs). Student's *t*-test were conducted to compare the difference of drought and control groups based on the values of *p* (*n* = 16, ns: *p* > 0.05, **p* < 0.05, *****p* < 0.0001).

is no statistically significant difference between the two groups. Nevertheless, F_v/F_m appears to be a better indicator to detect plant stress at early stage, since $p < 0.05$ showing the difference between two groups is statistically significant. At day 5, mean values of Φ_{PSII} and F_v/F_m increased by 5.3 and 0.96% for control group but decreased by 9.1 and 2.6% for drought group, with respect to day 3. Φ_{PSII} and F_v/F_m of control group are 16.4 and 4.3% higher than drought group. Moreover, the values of p are almost 0 indicating that the stressed plants can be well distinguished at day 5 either by Φ_{PSII} or F_v/F_m . It is also worth noting that the spread, interquartile range (IQR), and SD of drought group at day 5 are larger than those in the control group, indicating that higher photosynthetic heterogeneity is present in the stressed plants. Successful identification of such heterogeneity by fluorescence imaging can assist in predicting plant response to environment (Bresson et al., 2015).

Unlike point sensors, which can only provide conventional photosynthetic parameters, such as Φ_{PSII} and F_v/F_m etc., the homemade fluorescence imager can simultaneously provide morphological information to monitor plant canopy cover size using the single device, which is useful in studying the effect of stress on crop yields (Osborne, 2016; Anda et al., 2021). Since the whole plants' canopies were imaged in the PSA experiment, the size can be easily quantified from any of the corresponding fluorescence images as an additional parameter. To estimate the plant size, we counted the number of effective pixels (non-zero) of F_v/F_m images for individual plant, and are presented in **Figure 3**. The mean and SDs are summarized in **Supplementary Table 2**. At day 3 when water was added to the control group, the effective numbers of pixels of F_v/F_m images is 18.1% higher for the control group, based on their mean values. The value of p of these two groups are 0.009. At day 5, the significant difference between drought and control groups can be seen. By counting the leaf area in F_v/F_m images, the differences in mean effective pixels is $\sim 154\%$. The Student's t -test of drought and control groups gave $p < 0.0001$ for F_v/F_m images. Moreover, stressed plants decreased 41% in canopy size while control plants grew $> 27\%$ from day 3–5, according to F_v/F_m effective pixels. The preliminary result proved that the fluorescence imager can provide both photosynthetic and morphological parameters simultaneously to monitor the plant condition, which is an advantage over normal cameras or point sensors.

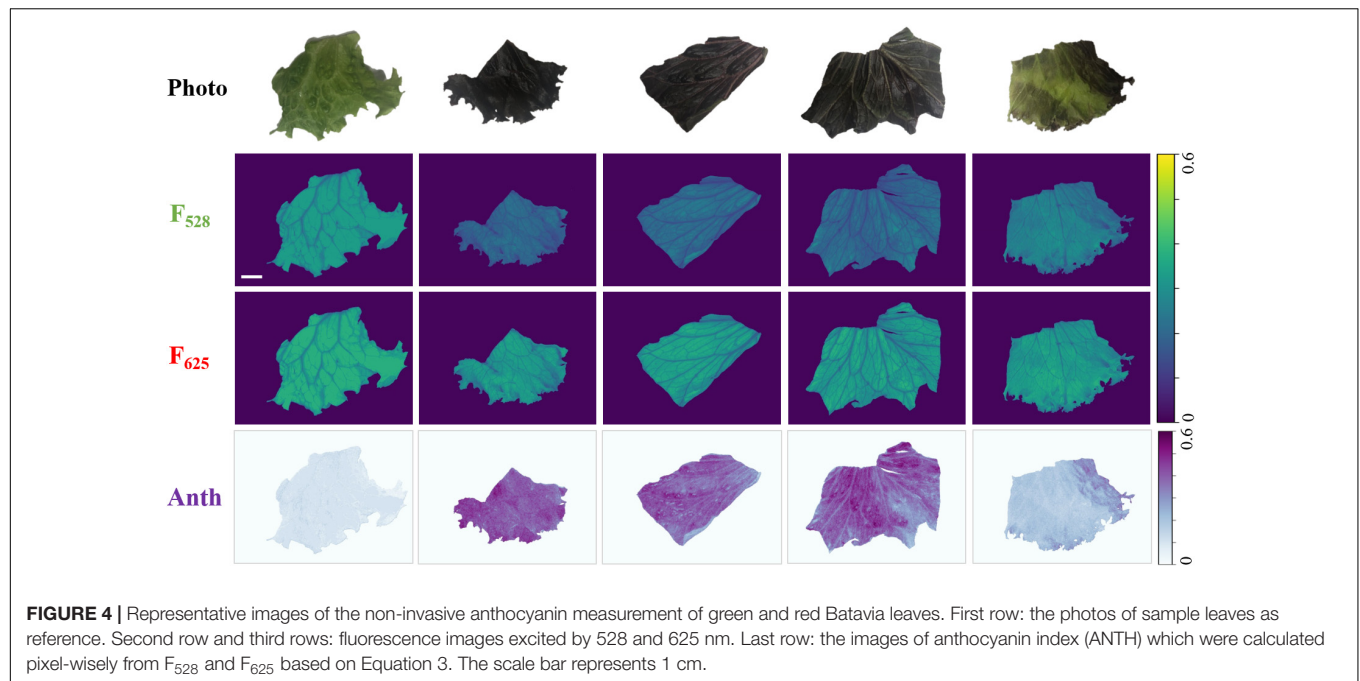
Non-invasive Anthocyanin Measurement vs. Biochemical Analysis

A non-invasive anthocyanin measurement was conducted using red and green output from RGB LEDs as excitations. Working distance was adjusted to be ~ 9 cm in this experiment and the corresponding FOV ($8.5 \text{ cm} \times 6 \text{ cm}$) was enough to cover the entire leaf sample. **Figure 4** shows the examples of non-invasive anthocyanin measurement done by the developed fluorescence imager. The first row shows photos taken by mobile phone camera as a reference. The second and third rows are the fluorescence images generated by 528 and 625 nm illumination, respectively. It should be noted that F_{528} and F_{625} are shown using the same colormap (viridis) and dynamic range for direct



visualization and comparison. The anthocyanin distribution images calculated from F_{528} and F_{625} based on Equation 3 are drawn in Python BuPu colormap and shown in the last row. It can be clearly seen that for red Batavia, F_{528} is much lower than F_{625} resulting in the higher anthocyanin index. This is because anthocyanins absorb green light while transmits red light. More anthocyanins distributed in epidermis leads to the stronger attenuation of green light (Agati et al., 2007). Therefore, the amount of 528 nm photons that reached the mesophyll to excite chlorophyll fluorescence decreases. On the contrary, green Batavia leaf with extremely low or no anthocyanin content shows smaller difference between F_{528} and F_{625} , since less green light is absorbed by the epidermis. The amount of red and green photons passing through epidermis to excite chlorophyll are similar, resulting in lower anthocyanin index, as expected. It can be considered that the anthocyanin index of green Batavia leaf is much lower than red one for every pixel, which is closer to the background signal. Hence, it looks light-colored and even “disappeared” in the anthocyanin distribution plot. Results for other samples can be found in **Supplementary Figures 1, 4–6**.

To validate the non-invasive anthocyanin index measurement using a fluorescence imager, anthocyanin content from the leaf extracts was quantitated and correlated using a biochemical method. Results from biochemical measurements are presented in **Supplementary Table 3**. The regression and fitting were performed as described in section “Statistical Analysis.” The correlation results of destructive biochemical analysis and anthocyanin index are shown in **Figure 5**. Despite two outliers (sample 15 and 18) were spotted, the final coefficients of determination R^2 are 0.8404 and 0.8420, respectively, indicating an excellent linear correlation and validating the effectiveness and accuracy of our compact fluorescence imager in the non-invasive anthocyanin measurement.

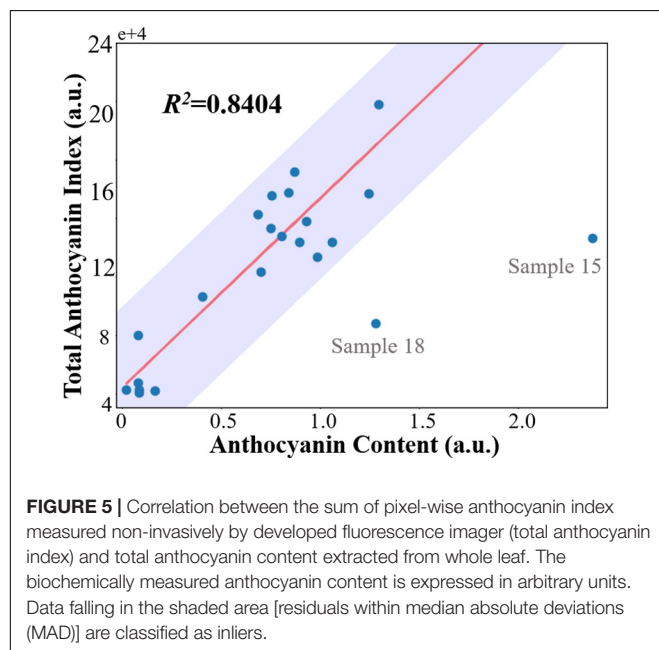


DISCUSSION

Our compact handheld fluorescence imager realized the non-invasive monitoring and quantification of PSA and anthocyanin content in plants and leaves, emphasizing its multifunctionality. First, with a series of blue pulse illuminations under PSA mode, the home-built fluorescence imager was able to continuously acquire fluorescence images and form fluorescence induction kinetic curves (Supplementary Figure 7), which reflect the plant

transient response to the ambient light and energy transfer efficiencies. Φ_{PSII} and F_v/F_m values were used to identify plant stress in drought experiment that showed similar values and trend as reported before (Wang et al., 2018; Shin et al., 2020). Apart from Φ_{PSII} and F_v/F_m demonstrated in this work, more photochemical and non-photochemical quenching parameters can be also calculated from the curve (Maxwell and Johnson, 2000) that will be carried out in the planned future work. In addition, we demonstrated that plant canopy cover can be calculated from fluorescence images, so that both photosynthetic and morphological parameters can be obtained simultaneously, which makes it superior to normal cameras and fluorescence point sensors.

In addition, conventional destructive anthocyanin quantification by the biochemical analysis requires tedious procedures, which is time consuming and manpower intense. Our fluorescence imager with alternate red and green illuminations, can display anthocyanin content distribution fast and non-invasively in the FOV, for plant maturity stage determination (Ahmadiani et al., 2014) or quality evaluation. Zivcak et al. (2017) named fluorescence signal $\log(F_{635}/F_{516})$ as ANTH index and they conducted a study to non-invasively quantify the total flavonoid content in lettuce using ANTH index measured by a single-point detector. They correlated it with total flavonoids measured by an aluminum chloride colorimetric method with quercetin calibration and obtained a coefficient of determination of $R^2 = 0.5356$. In our study, $\log(F_{625}/F_{528})$ was correlated with total anthocyanin content, the correlation was significantly improved to $R^2 = 0.84$. Better correlation may owe to anthocyanin's dominant absorption of red light among flavonoids. Additionally, thanks to its imaging capability, the entire leaf could be covered. Every pixel of leaf was counted, instead of a rough estimation based on a small area average.



Supplementary Figure 8 shows correlation between average anthocyanin index and anthocyanin content per gram fresh weight (total anthocyanins/FW), where average anthocyanin index was calculated as the mean value of randomly selected 1,000 non-zero pixels for each sample. In this case, a power function was used for fitting, according to Agati et al. (2007) and achieved $R^2 = 0.8420$. However, average anthocyanin index obtained by optical method is area based and expressed per pixel. On the other hand, biochemically-measured anthocyanin content is normalized to leaf weight and expressed per gram fresh weight. Hence, this correlation is the lack of validity without considering leaf fresh weight per area, which is not recommended. Overall, the imaging capability of our device will contribute to high throughput screening, detailed spatial heterogeneity detection and high spatial resolution etc., bringing in more convenience and possibilities for plant phenotyping and quality checks.

However, there are a few aspects that need to be considered in the operation of the system. First, the PAR illumination is only uniform at a certain distance, meaning that the leaves at different heights may undergo different illumination intensity. However, it will not affect the final result, since both PSA and anthocyanin measurement are based on the relative ratio or dynamic change of fluorescence signals during different illuminations. Second, for anthocyanin measurement, Equation 3 is only valid when anthocyanins are distributed in the epidermis of plants. Moreover, calibration curves may be different for different species. This could be addressed by calibrating the system with large datasets, which will be validated in our ongoing study in an indoor vertical farm. The purpose of this study was to introduce the tremendous capability of the system. In the future applications, the calibration and limit of detection need to be carried out and determined accordingly. Last, in the current study, a PC was used for real-time data transfer and processing. In future, powerful microcontroller and LCD screen will be incorporated for real-time on-board image processing and display, to make the fluorescence imager a stand-alone device toward commercialization.

CONCLUSION

In conclusion, we have developed a multifunctional compact handheld fluorescence imager for non-invasive and high throughput plant phenotyping. Preliminary PSA measurement was conducted and plants under drought stress were successfully differentiated by photosynthetic and morphological

indicators. Anthocyanin content in Batavia lettuce leaves was quantified non-invasively and showed good correlation with biochemical analysis. Being different from commercially available fluorescence imaging and sensing devices, our fluorescence imager utilizes all-in-one RGB LEDs, a dedicated driver circuit, and a method to achieve multifunction capability and compact size. To the best of our knowledge, it is the first-of-its-kind compact fluorescence imaging device for both the non-invasive PSA monitoring and anthocyanin distribution measurement. These features will help to significantly reduce manpower and cost in various applications to improve agricultural efficiency. We envision that this system has great potential in modern agriculture for both in-field and indoor farm settings.

DATA AVAILABILITY STATEMENT

The original contributions presented in the study are included in the article/**Supplementary Material**, further inquiries can be directed to the corresponding author/s.

AUTHOR CONTRIBUTIONS

RZ, UD, and DU conceived and designed the study. SK prepared the plant for PSA study and also carried out biochemical analysis. RZ, MT, and RB developed the device. RZ and MT conducted the fluorescence experiment. RZ and SK analyzed the data and wrote the manuscript. SZ and KD provided input and also revised the manuscript. DU, UD, and MO supervised the project. All authors contributed to the article and approved the submitted version.

FUNDING

This work was supported by Agency of Science, Technology and Research (A*STAR), under its Industry Alignment Fund Pre-positioning Program, Award H19E4a0101 (HiPPA) and BMRC Central Research Fund (UIBR) 2021.

SUPPLEMENTARY MATERIAL

The Supplementary Material for this article can be found online at: <https://www.frontiersin.org/articles/10.3389/fpls.2022.822634/full#supplementary-material>

REFERENCES

- Agati, G., Meyer, S., Matteini, P., and Cerovic, Z. G. (2007). Assessment of anthocyanins in grape (*Vitis vinifera* L.) berries using a noninvasive chlorophyll fluorescence method. *J. Agric. Food Chem.* 55, 1053–1061. doi: 10.1021/jf062956k
- Ahmadiani, N., Robbins, R. J., Collins, T. M., and Giusti, M. M. (2014). Anthocyanins contents, profiles, and color characteristics of red cabbage extracts from different cultivars and maturity stages. *J. Agric. Food Chem.* 62, 7524–7531. doi: 10.1021/jf501991q
- Anda, A., Simon, B., Soós, G., da Silva, J. A. T., and Menyhárt, L. (2021). Water stress modifies canopy light environment and qualitative and quantitative yield components in two soybean varieties. *Irrig. Sci.* 39, 549–566.
- Backes, A., Vaillant-Gaveau, N., Esmaeel, Q., Barka, E. A., and Jacquard, C. (2021). A biological agent modulates the physiology of barley infected with *Drechslera teres*. *Sci. Rep.* 11:8330. doi: 10.1038/s41598-021-87853-0
- Barnes, C., Tibbitts, T., Sager, J., Deitzer, G., Bubenheim, D., Koerner, G., et al. (1993). Accuracy of quantum sensors measuring yield photon flux and photosynthetic photon flux. *HortScience* 28, 1197–1200.

- Bresson, J., Vasseur, F., Dauzat, M., Koch, G., Granier, C., and Vile, D. (2015). Quantifying spatial heterogeneity of chlorophyll fluorescence during plant growth and in response to water stress. *Plant Methods* 11:23. doi: 10.1186/s13007-015-0067-5
- Cen, H., Weng, H., Yao, J., He, M., Lv, J., Hua, S., et al. (2017). Chlorophyll fluorescence imaging uncovers photosynthetic fingerprint of citrus Huanglongbing. *Front. Plant Sci.* 8:1509. doi: 10.3389/fpls.2017.01509
- Cerovic, Z. G., Ounis, A., Cartelat, A., Latouche, G., Goulas, Y., Meyer, S., et al. (2002). The use of chlorophyll fluorescence excitation spectra for the non-destructive in situ assessment of UV-absorbing compounds in leaves. *Plant. Cell Environ.* 25, 1663–1676.
- Christian, K. R., and Jackson, J. C. (2009). Changes in total phenolic and monomeric anthocyanin composition and antioxidant activity of three varieties of sorrel (*Hibiscus sabdariffa*) during maturity. *J. Food Compos. Anal.* 22, 663–667.
- Genty, B., Briantais, J.-M., and Baker, N. R. (1989). The relationship between the quantum yield of photosynthetic electron transport and quenching of chlorophyll fluorescence. *Biochim. Biophys. Acta (BBA)-General Subj.* 990, 87–92.
- Hagen, S. F., Solhaug, K. A., Bengtsson, G. B., Borge, G. I. A., and Bilger, W. (2006). Chlorophyll fluorescence as a tool for non-destructive estimation of anthocyanins and total flavonoids in apples. *Postharvest Biol. Technol.* 41, 156–163.
- Hughes, N. M., Morley, C. B., and Smith, W. K. (2007). Coordination of anthocyanin decline and photosynthetic maturation in juvenile leaves of three deciduous tree species. *New Phytol.* 175, 675–685. doi: 10.1111/j.1469-8137.2007.02133.x
- Kautsky, H. (1960). Chlorophyll-fluorescenz und Kohlensäureassimilation. XIII. mitteilung, die fluoreszenzkurve und die photochemie der pflanze. *Biochem. Z.* 332, 277–292.
- Khoo, H. E., Azlan, A., Tang, S. T., and Lim, S. M. (2017). Anthocyanidins and anthocyanins: colored pigments as food, pharmaceutical ingredients, and the potential health benefits. *Food Nutr. Res.* 61:1361779. doi: 10.1080/16546628.2017.1361779
- Kitajima, M., and Butler, W. L. (1975). Quenching of chlorophyll fluorescence and primary photochemistry in chloroplasts by dibromothymoquinone. *Biochim. Biophys. Acta (BBA)-Bioenergetics* 376, 105–115. doi: 10.1016/0005-2728(75)90209-1
- Laby, R. J., Kincaid, M. S., Kim, D., and Gibson, S. I. (2000). The Arabidopsis sugar-insensitive mutants *sis4* and *sis5* are defective in abscisic acid synthesis and response. *Plant J.* 23, 587–596. doi: 10.1046/j.1365-313x.2000.00833.x
- Linn, A. I., Zeller, A. K., Pfündel, E. E., and Gerhards, R. (2021). Features and applications of a field imaging chlorophyll fluorometer to measure stress in agricultural plants. *Precis. Agric.* 22, 947–963.
- Maxwell, K., and Johnson, G. N. (2000). Chlorophyll fluorescence—a practical guide. *J. Exp. Bot.* 51, 659–668. doi: 10.1093/jxb/51.345.659
- Murashige, T., and Skoog, F. (1962). A revised medium for rapid growth and bio assays with tobacco tissue cultures. *Physiol. Plant.* 15, 473–497.
- Nakata, M., and Ohme-Takagi, M. (2014). Quantification of anthocyanin content. *Bio-protocol* 4:1098. doi: 10.1007/s00438-018-1464-z
- Neff, M. M., and Chory, J. (1998). Genetic interactions between phytochrome A, phytochrome B, and cryptochrome 1 during *Arabidopsis* development. *Plant Physiol.* 118, 27–35. doi: 10.1104/pp.118.1.27
- Osborne, C. P. (2016). Crop yields: CO₂ fertilization dries up. *Nat. Plants* 2:16138. doi: 10.1038/nplants.2016.138
- Quick, W. P., and Horton, P. (1984). Studies on the induction of chlorophyll fluorescence in barley protoplasts. I. factors affecting the observation of oscillations in the yield of chlorophyll fluorescence and the rate of oxygen evolution. *Proc. R. Soc. London. Ser. B. Biol. Sci.* 220, 361–370.
- Schreiber, U., Schliwa, U., and Bilger, W. (1986). Continuous recording of photochemical and non-photochemical chlorophyll fluorescence quenching with a new type of modulation fluorometer. *Photosynth. Res.* 10, 51–62. doi: 10.1007/BF00024185
- Shin, Y. K., Bhandari, S. R., Jo, J. S., Song, J. W., Cho, M. C., Yang, E. Y., et al. (2020). Response to salt stress in lettuce: changes in chlorophyll fluorescence parameters, phytochemical contents, and antioxidant activities. *Agronomy* 10:1627.
- Steele, M. R., Gitelson, A. A., Rundquist, D. C., and Merzlyak, M. N. (2009). Nondestructive estimation of anthocyanin content in grapevine leaves. *Am. J. Enol. Vitic.* 60, 87–92.
- van Tol, N., Rolloos, M., Augustijn, D., Alia, A., de Groot, H. J., Hooykaas, P. J. J., et al. (2017). An Arabidopsis mutant with high operating efficiency of photosystem II and low chlorophyll fluorescence. *Sci. Rep.* 7:3314. doi: 10.1038/s41598-017-03611-1
- Wang, H., Qian, X., Zhang, L., Xu, S., Li, H., Xia, X., et al. (2017). Detecting crop population growth using chlorophyll fluorescence imaging. *Appl. Opt.* 56, 9762–9769. doi: 10.1364/AO.56.009762
- Wang, H., Qian, X., Zhang, L., Xu, S., Li, H., Xia, X., et al. (2018). A method of high throughput monitoring crop physiology using chlorophyll fluorescence and multispectral imaging. *Front. Plant Sci.* 9:407. doi: 10.3389/fpls.2018.00407
- Zhu, H., Zhang, T.-J., Zheng, J., Huang, X.-D., Yu, Z.-C., Peng, C.-L., et al. (2018). Anthocyanins function as a light attenuator to compensate for insufficient photoprotection mediated by nonphotochemical quenching in young leaves of *Acmena acuminatissima* in winter. *Photosynthetica* 56, 445–454.
- Zivcak, M., Brückova, K., Sytar, O., Brestic, M., Olsovska, K., and Allakhverdiev, S. I. (2017). Lettuce flavonoids screening and phenotyping by chlorophyll fluorescence excitation ratio. *Planta* 245, 1215–1229. doi: 10.1007/s00425-017-2676-x

Conflict of Interest: The authors declare that the research was conducted in the absence of any commercial or financial relationships that could be construed as a potential conflict of interest.

Publisher's Note: All claims expressed in this article are solely those of the authors and do not necessarily represent those of their affiliated organizations, or those of the publisher, the editors and the reviewers. Any product that may be evaluated in this article, or claim that may be made by its manufacturer, is not guaranteed or endorsed by the publisher.

Copyright © 2022 Zhang, Koh, Teo, Bi, Zhang, Dev, Urano, Dinish and Olivo. This is an open-access article distributed under the terms of the Creative Commons Attribution License (CC BY). The use, distribution or reproduction in other forums is permitted, provided the original author(s) and the copyright owner(s) are credited and that the original publication in this journal is cited, in accordance with accepted academic practice. No use, distribution or reproduction is permitted which does not comply with these terms.



Non-destructive Plant Biomass Monitoring With High Spatio-Temporal Resolution via Proximal RGB-D Imagery and End-to-End Deep Learning

Nicolas Buxbaum^{1*}, Johann Heinrich Lieth^{2†} and Mason Earles^{1,3†}

¹Department of Biological and Agricultural Engineering, University of California, Davis, Davis, CA, United States, ²Department of Plant Sciences, University of California, Davis, Davis, CA, United States, ³Department of Viticulture and Enology, University of California, Davis, Davis, CA, United States

OPEN ACCESS

Edited by:

Nam-Hai Chua,
Temasek Life Sciences Laboratory,
Singapore

Reviewed by:

LiuJun Li,
Missouri University of Science
and Technology, United States
Ahmad Al-Mallahi,
Dalhousie University, Canada

*Correspondence:

Nicolas Buxbaum
nrbuxbaum@ucdavis.edu

[†]These authors have contributed
equally to this work and share last
authorship

Specialty section:

This article was submitted to
Technical Advances in Plant Science,
a section of the journal
Frontiers in Plant Science

Received: 15 August 2021

Accepted: 21 March 2022

Published: 13 April 2022

Citation:

Buxbaum N, Lieth JH and
Earles M (2022) Non-destructive
Plant Biomass Monitoring With High
Spatio-Temporal Resolution via
Proximal RGB-D Imagery and
End-to-End Deep Learning.
Front. Plant Sci. 13:758818.
doi: 10.3389/fpls.2022.758818

Plant breeders, scientists, and commercial producers commonly use growth rate as an integrated signal of crop productivity and stress. Plant growth monitoring is often done destructively via growth rate estimation by harvesting plants at different growth stages and simply weighing each individual plant. Within plant breeding and research applications, and more recently in commercial applications, non-destructive growth monitoring is done using computer vision to segment plants in images from the background, either in 2D or 3D, and relating these image-based features to destructive biomass measurements. Recent advancements in machine learning have improved image-based localization and detection of plants, but such techniques are not well suited to make biomass predictions when there is significant self-occlusion or occlusion from neighboring plants, such as those encountered under leafy green production in controlled environment agriculture. To enable prediction of plant biomass under occluded growing conditions, we develop an end-to-end deep learning approach that directly predicts lettuce plant biomass from color and depth image data as provided by a low cost and commercially available sensor. We test the performance of the proposed deep neural network for lettuce production, observing a mean prediction error of 7.3% on a comprehensive test dataset of 864 individuals and substantially outperforming previous work on plant biomass estimation. The modeling approach is robust to the busy and occluded scenes often found in commercial leafy green production and requires only measured mass values for training. We then demonstrate that this level of prediction accuracy allows for rapid, non-destructive detection of changes in biomass accumulation due to experimentally induced stress induction in as little as 2 days. Using this method growers may observe and react to changes in plant-environment interactions in near real time. Moreover, we expect that such a sensitive technique for non-destructive biomass estimation will enable novel research and breeding of improved productivity and yield in response to stress.

Keywords: controlled environment agriculture, deep learning, biomass, monitoring, lettuce, computer vision, artificial intelligence, phenotyping algorithms

INTRODUCTION

Plant growth is a foundational biological process that underlies both agricultural and ecological productivity. Biomass accumulation is the final product of photosynthetic CO₂ assimilation and its rate is closely tied to traits such as productivity and stress response (Muchow, 1988; Scully and Wallace, 1990). Growth rate is linked to crop productivity and yield for grain, fruit, and vegetable crops. Vegetative crop growth rate, for example, is a strong predictor of final grain production in rice, soybean, wheat, and maize (Egli and Zhen-wen, 1991; Karimi and Siddique, 1991; Takai et al., 2006; Egli, 2019). Among leafy vegetables, growth rate is even more directly tied to yield as the leaves, and often stems, are harvested as the final product. Due to its close link to yield, growth rate is commonly measured in response to limitation and excess application of inputs such as light (Zhou et al., 2019), temperature (Zhou et al., 2019), nutrients (Sapkota et al., 2019), and water (Gallardo et al., 1996). Consequently, growth rate in response to variable inputs provides an optimization criterion for breeding higher input efficiency crops (e.g., nitrogen and water use efficiency; Zotarelli et al., 2009). Beyond breeding, growth rate monitoring provides commercial agricultural producers a means for detecting stress and understanding growth over time, both of which can lead to more precise planning and optimization of management practices (Kacira et al., 2005). Thus, plant growth monitoring is a critical tool for breeders, scientists, and commercial producers in their efforts to manage and develop more productive and stress tolerant crops.

The most direct method of determining plant biomass growth is *via* destructive sampling, which requires harvesting and weighing each individual (Catchpole and Wheeler, 1992). The destructive nature of this method reduces its utility in breeding and commercial settings as it often necessitates prohibitive numbers of individuals to generate the representative samples required for daily or sub-daily population biomass estimates. On the other hand, non-destructive biomass estimation allows for continuous measurement of individual plants which substantially reduces plant number requirements for effective experimentation and monitoring. Hand-gathered allometric methods that relate volume and height data to biomass are time-consuming, laborious, and may generalize poorly (Pottier and Jabot, 2017). The recent development of proximal and remote sensing-based approaches offers the promise of lower data acquisition cost and increased throughput and accuracy. Such methods generally involve computer vision-based analysis of color (Jung et al., 2015; Jiang et al., 2018) and 3D data modalities (Mortensen et al., 2018; Hu et al., 2018; Jin et al., 2020). Data is typically acquired from one or more viewpoints using color sensors, RGB-D cameras, or LiDAR systems. Then, plant pixels (or in the case of 3D data, voxels or 3D points) are segmented from the background *via* either classical or machine learning methods (Jung et al., 2015; Jiang et al., 2018; Mortensen et al., 2018; Loresco et al., 2019; Jin et al., 2020). The segmented data is used to generate features that can serve as predictors of biomass such as pixel counts (Jiang et al., 2018), 3D volume (Mortensen et al., 2018; Jin et al., 2020),

plant height (Hu et al., 2018; Jin et al., 2020), projected leaf area (Mortensen et al., 2018; Jin et al., 2020), and other color and structural features (Hu et al., 2018; Jin et al., 2020). More recently, promising results have been achieved with deep learning methods which do not rely on initial scene segmentation, but instead estimate biomass by directly mapping input images to biomass (Zhang et al., 2020).

Of these prior works, most rely on idealized scene conditions containing isolated individuals within field-of-view of the image. Only the methods of Jin et al. (2020) and Mortensen et al. (2018) are designed to estimate individual plant biomass within scenes containing the dense plant canopies typical of commercial agricultural settings. In commercial agriculture, high planting densities result in neighboring plants that create occlusions with each other, significantly increasing the complexity of the segmentation task. Furthermore, even with an effective segmentation algorithm, occlusions can cause large holes within the resulting segmented plant pixels, potentially reducing the accuracy of calculated biomass predictors. These problems are greatly exacerbated in leafy green production, where canopies can become near continuous (Figures 1A–C). While both works developed effective plant-from-plant segmentation schemes, neither tested their methods on extremely high density continuous canopies (Mortensen et al., 2018; Jin et al., 2020). Further, both methods rely to some degree on human input, greatly reducing the throughput and advantage of remote sensing based biomass estimation.

To solve the challenge of accurate and autonomous individual plant biomass estimation within high density canopies, we propose an end-to-end deep learning approach. Our end-to-end approach eliminates the need to perform explicit individual plant segmentation and instead allows a deep convolutional neural network (DCNN) to implicitly perform segmentation by learning a mapping from input image space to individual plant biomass. Motivated by previous biomass estimation work that relies on 3D data as well as the ability of DCNNs to jointly learn from color and depth imagery (Gupta et al., 2014; Eitel et al., 2015; Ophoff et al., 2019; Ward et al., 2019), our model incorporates both color and depth data as provided by an inexpensive and commercially available stereovision RGB-D camera. We hypothesize that DCNNs are well suited to understanding not only plant structure and size, but the influence of neighboring plant occlusion on the resulting view presented in overhead imagery of dense plant canopies.

In this work we develop a novel approach to non-destructively monitor crops by estimating the fresh biomass of individual lettuce plants grown in a typical commercial hydroponic cropping system from a proximal overhead viewpoint. By combining RGB-D sensing with a deep learning regression approach, we demonstrate state-of-the-art performance for quantifying biomass across the entire range of the lettuce growth cycle, from transplant (< 1g) through maturity (> 30g). Our approach and results not only have implications for leaf lettuce but can more broadly be applied to estimate biomass and other phenotypic traits of crops grown in occluded environments. To validate our model's ability to function as a crop monitoring system, we perform an additional experiment which subjects plants to various heterogeneously

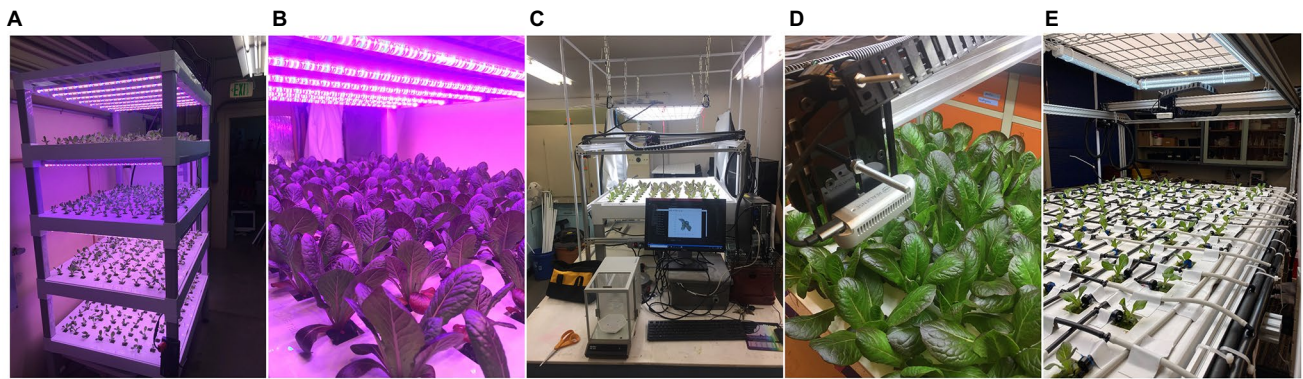


FIGURE 1 | (A,B) The SananBio vertical cultivation system with individual lettuce plants at various growth stages. **(C,D)** The 2-axis imaging system equipped with an RGB-depth camera that was used to image lettuce plants and weigh destructively weigh individual plant mass values. **(E)** Our modified top fed drip system for growth monitoring under controlled nutrient stress.

applied nutrient stresses. This rigorously tests the model's ability to capture varying trends in growth between neighboring individuals and shows that monitoring growth dynamics at the individual plant scale is possible under non-idealized cropping conditions.

MATERIALS AND METHODS

Dataset for Deep Learning Model Creation

Our dataset used in model creation is composed of pairs of overhead images and biomass values of the baby leaf lettuce cultivar *Lactuca sativa* var. Powerhouse grown in a high density hydroponic cropping system. Every image was centered upon a unique individual lettuce plant and the associated biomass value was the measured fresh above ground biomass of the corresponding center plant in the image.

Cultivation System

Plants used in this work were grown indoors within a laboratory facility at the University of California, Davis campus. Plants were grown in continuously recirculating nutrient film technique hydroponic systems (SananBio, Xiamen, Fujian, China; **Figure 1A**). The systems were composed of four vertical tiers, with each tier holding two growing trays. One growing tray contained 54 plants arranged in a nine by five grid pattern with an approximate spacing of three inches. Seeds were germinated in one-inch rockwool cubes and transplanted into the SananBio system growing trays after first emergence of true leaves. Plants were grown until imaging and destructive measurement of fresh biomass was performed. Each rockwool cube contains the plant's root system which is free to grow beyond the cube into a drainage channel. Photosynthetic photon flux was maintained continuously at an average of $135 \mu\text{mol}\cdot\text{s}^{-1}\cdot\text{m}^{-2}$ over the canopy area. Temperature was maintained between 72 and 85°F.

Imaging System

The chosen imaging system utilized an Intel RealSense d435i (Intel Corp., Santa Clara, CA, United States) camera mounted

vertically over the imaging bay at a height of 37 cm (**Figures 1C,D**). It was actuated to positions directly above each plant by a stepper motor and belt driven positioning system. While the theoretical tolerances of the positioning system are on the order of 1 mm, inaccuracies due to deformations of the plastic trays and alignment with the imaging system resulted in observed positional tolerances of approximately 1 cm. Images were always taken while the camera was not in motion. Data collected consisted of an 848 pixel by 480 pixel 8-bit color RGB image as well as an associated depth image. The depth image is a 2D image, where each pixel represents the distance between the sensor and the in-scene object with a precision of 0.1 mm. No filtering was applied to the depth images. We chose to utilize a depth to color image alignment scheme with the Intel RealSense 435i, which involves a transformation of the depth image centered at one monochromatic sensor origin to the designated color sensor origin. The result was a depth image aligned to the color image (i.e., they share a coordinate system).

Data Collection

Data collection was performed on single trays, which correspond to a 54 plant subsample of the growth trial. During each data collection event a tray was removed from the cultivation system and placed under the imaging system. The illumination within the imaging system was maintained at approximately 100 lux and 6,500 K. Immediately after imaging, fresh above ground biomass was recorded. This was accomplished by severing the plants directly below the cotyledon and weighing them to a precision of 0.001 g or 0.1 g, depending upon the plant's size and ability to fit within an analytical balance chamber. Each data collection event therefore yielded 54 RGB images, 54 aligned depth images, and 54 plant biomass values.

Growth Trials for Destructive Biomass Measurements

Six growth cycles were conducted sequentially over a 5 months period. Each cycle featured a varying number of total trays

and plant count, although individual trays always contained a full 54 plants. During each growth cycle, data collection events started 1 week after transplant at a rate of three to four events per week and continued until all trays were harvested. This resulted in plants with a harvest date between 7–30 days after transplant. A total of 3,888 plants were harvested and their biomass values destructively measured.

Non-destructive Growth Monitoring in Response to Stress Induction

After achieving satisfactory biomass prediction accuracy, we implemented the model in a plant monitoring application to track growth over time from transplant to harvest. We modified our previous hydroponic system from nutrient film technique, where every plant received the same fertigation solution, to a top-fed drain to waste system (**Figure 1E**). This allows for the application of unique fertigation solution to four subsets of plants in a random spatial arrangement. Each plant site was fertigated by a single 0.5 gallon per hour pressure compensating emitter for 1 min every 7 h. Four separate pumps supply the system, each connected to drip lines arranged in an alternating pattern along each axis. By supplying each pump with a certain fertigation solution, we can dynamically select the fertigation solution experienced by any particular subset of the plants. The entire growing system was canted to facilitate draining and reduce the uptake of shared leachate by plant roots. We maintain equivalent lighting and transplanting conditions as the original dataset.

Experimental Design

Our experiment consisted of 108 plants that were completely randomly distributed into four groups of 27 plants ($n=27$; **Figure 1E**). Each group was subjected to a different schedule of nutrient stress inductions and reductions designed to dynamically modify the growth rate of each treatment group over time (**Table 1**). Since the plants were grown hydroponically, nutrient stress was induced by providing pure distilled water through the irrigation system. To return to non-stress conditions, fertigation was resumed with half strength Hoagland solution. We composed a schedule of nutrient stress applications for each of three treatments and a control (**Table 1**). For each treatment we indicate the number of days after transplant (rounded to the nearest imaging date) that stress conditions were induced or reduced. All treatments started with Hoagland solution after transplant (Day 0). The “control” treatment receives no stress induction and is provided Hoagland solution for the entire growth period.

Data Collection

We utilized the same imaging system as in the original model training dataset. The only modification made was within our software to allow for automated image capture according to a set interval. Images were taken every 8 h for the duration of the experiment, with each imaging event consisting of 108 images. This resulted in a sequential representation of plant growth composed of 96 images per plant over the 32-day experiment (a total of 10,368 sets of RGB and depth images). Imaging of the entire tray of 108 plants required 5 min to complete.

In addition to the collected image data, we measure per-plant width (defined as the largest horizontal extent of the plant) and height (distance from the top of the growth tray to the tallest portion of the plant) at three separate dates (day 12, 16, and 23 from transplant). These non-destructive measurements provide us with some understanding of ground-truth plant growth, helping verify that our stress treatments truly induce the changes in plant growth that our model illustrates.

Model Detection of Stress Treatments

As the purpose of this work is to evaluate the suitability of a deep learning-based biomass estimation model as a crop monitoring technique, we evaluate how well the model predictions can capture changes in growth induced by controlled nutrient stresses applied heterogeneously over time and space. We approach this by examining the per-treatment model predicted mass, as well as the derived metrics growth rate (GR) and relative growth rate (RGR; Equation 1). For each metric we test for treatment effects by determining when the per-treatment means become statistically separable from each other over time. Based on our understanding of expected treatment effects, we can utilize the results of our statistical tests to determine which growth metrics are the most responsive determinants of nutrient stress.

Our test consists of applying Tukey's HSD test (Tukey, 1949) for multiple pairwise comparisons to determine whether the treatment means are distinguishable at $p \leq 0.05$ between any two treatments. We calculate this for each growth trait across the entire time series. RGR is calculated for each plant within a given data collection event by first applying a backwards looking moving-average with a window size of 3, followed by a gradient based RGR calculation given by Equation 1.

$$RGR_t = \frac{GR}{m_t} \text{ with } GR = \frac{m_t - m_{t-1}}{\Delta t} \quad (1)$$

where m_t = moving average biomass at time t and Δt = difference in time between t and $t-1$ (units are 8 h). Boundary cases in the moving average and RGR calculations are dropped.

TABLE 1 | Treatment schedules as begun on particular days (“Solution” = half strength Hoagland solution; “Water” = De-ionized distilled water).

Treatment	<i>n</i>	Day 0	Day 6	Day 11.7	Day 15.7	Day 15.7
A	27	Solution	Water	Solution	Solution	Solution
B	27	Solution	Solution	Water	Water	Solution
C	27	Solution	Solution	Water	Solution	Water
D (control)	27	Solution	Solution	Solution	Solution	Solution

RGB-D Regression Network Architecture

Our choice of architecture is modeled from successful work in RGB-D object detection and classification utilizing feedforward neural networks (Eitel et al., 2015; Ward et al., 2019). We utilize a dual-branch architecture for each input data modality along with feature map fusion (Figure 2). In particular, Ophoff et al. (2019) empirically demonstrated that a mid to late fusion architecture performs best for real-time object detection when utilizing YOLOv2 as the feature extraction network for each branch. We utilize ResNet-50 for feature extraction and retain the final $1,000 \times 1$ fully connected layer from ImageNet's 1,000 classes while removing the softmax activation function. The fully connected layer from each branch is then end to end concatenated into a feature vector of 2000×1 . This feature vector is passed to the regression head, which consists of one fully connected $1,000 \times 1$ layer and one 1×1 layer. Rectified linear unit functions are utilized as the activation function between all layers besides the final, which is simply a linear activation. In testing we found no benefit to increased depth of the regression head. The resulting late fusion network can leverage transfer learning with ImageNet pretrained weights for fast convergence with our relatively small dataset (Figure 2).

Model Loss Function

We train the network to minimize a mean average percent error (MAPE) loss function (Equation 2). While known to produce biased under estimations in statistical prediction problems, in our testing an MAPE loss function resulted in more even model performance across the entire range of possible plant sizes than either L1 or L2 loss functions. We speculate that this is due to the MAPE loss function driving model learning as a function of relative, rather than absolute, difference between the model predictions and ground truth. This phenomenon is especially pronounced in our dataset, which features a range of plant mass values in the order of 300x—from 0.1g to more than 30g. It should be noted that we favor relative error and consistent model performance across all plant sizes as it better pertains to our goal of utilizing plant mass estimation models to inform crop status across the entire growth cycle.

$$MAPE = \left(\frac{1}{n} \sum_{i=1}^n \left| \frac{A_i - F_i}{A_i} \right| \right) \quad (2)$$

where n = number of samples, A_i = i -th sample ground truth mass, and F_i = i -th predicted mass.

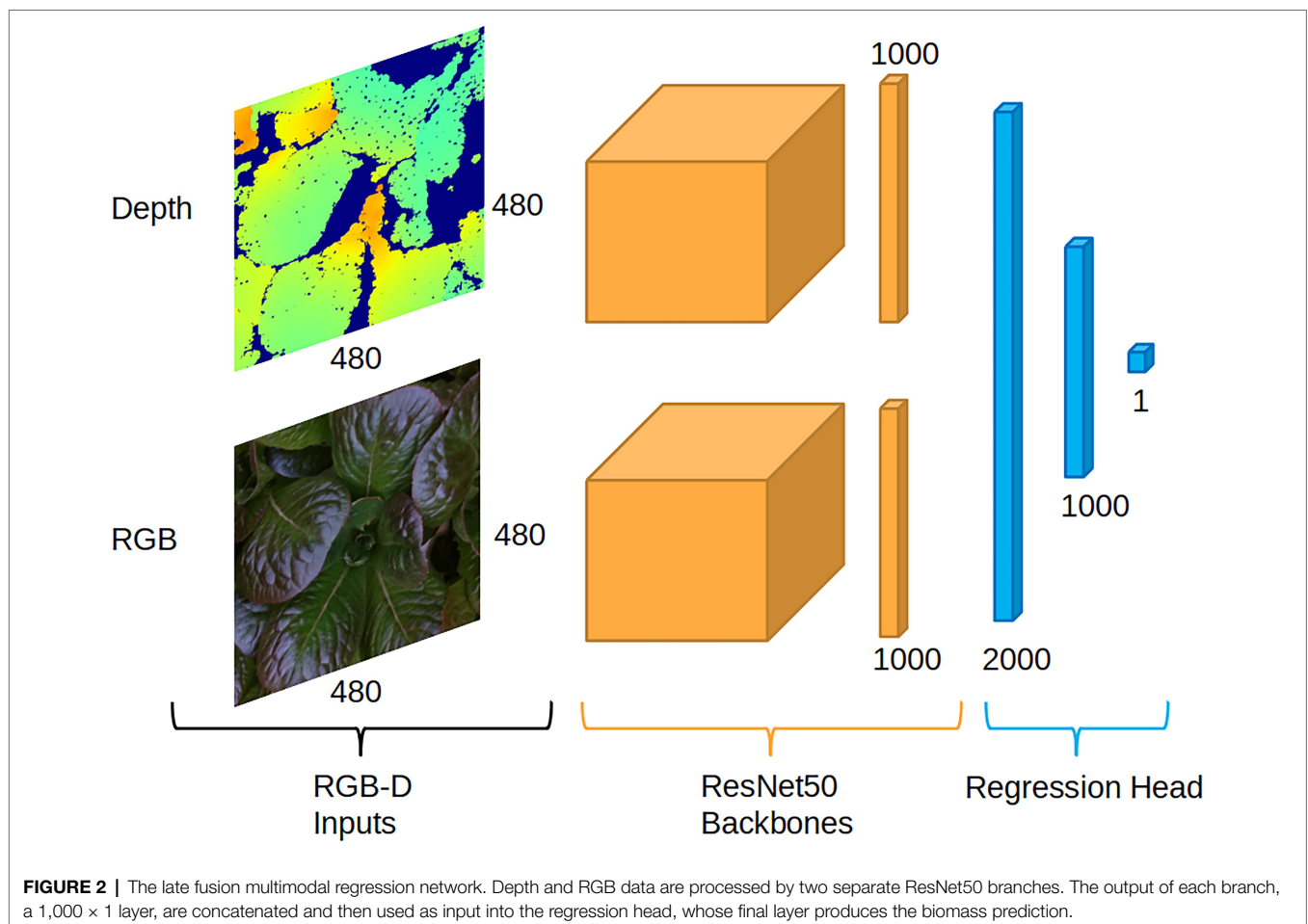


FIGURE 2 | The late fusion multimodal regression network. Depth and RGB data are processed by two separate ResNet50 branches. The output of each branch, a $1,000 \times 1$ layer, are concatenated and then used as input into the regression head, whose final layer produces the biomass prediction.

Model Input Preprocessing

While our color data may be utilized directly by the RGB branch of the model, the single channel depth data lacks the 3-channel dimension expected by the first layer of the pre-trained Resnet50 depth branch. Possible solutions of adapting non 3-channel input data for use with RGB pre-trained networks generally fall into two distinct pre-processing schemes: (1) Expanding the third dimension of the input data to 3 channels or (2) replacing the first layer of the network with a new convolutional kernel that expects a different size channel dimension. The former solution allows for full retention of pre-trained weights, while the second requires a new, untrained weight initialization for the first convolutional layer. We find that encoding of the single channel depth input to three channel RGB, as proposed by Eitel et al. (2015), results in improved learning compared with other pre-processing schemes tested: (1) single channel depth combined with a new, randomly initialized first convolutional layer and (2) three times replicated depth channel input with pretrained first convolutional layer. We follow a “jet” color scheme that maps the depth output of the RealSense camera to RGB color. The depth and corresponding color images are linearly normalized to [0, 1] and maintain their precision *via* a 32-bit floating-point number. Normalization is achieved by first filtering out large depth data values corresponding to the non-plant scene, defined as any depth value larger than 380 mm (a number arrived at by taking into account the camera field of view and height from the growing tray). This reduces the range of depth values from [0, 12,000] (the maximum distance possible in the scene) to [0, 3,800] while maintaining all relevant scene information. Reducing the depth data range increases the contrast of the resulting RGB mapping. Finally, both color and depth images are center cropped to 480 by 480 pixels.

Model Training Details

The model is implemented using the PyTorch framework within Python (Paszke et al., 2019). Each branch of the RGBD network is initialized from modality-specific pre-trained weights. This is achieved by first training each branch separately as its own model to predict lettuce biomass. Those branches are initialized *via* ImageNet pre-trained weights available from the PyTorch’s model zoo and are trained with a regression head consisting of a single 1000×1 fully connected layer. The regression head is then removed and the remaining branch weights used to initialize the weights for final fine-tuning of the RGBD model. All relevant training parameters are kept consistent across the RGB, depth, and RGBD networks.

The training dataset is composed of 2,484 plants, corresponding to the remaining data from the validation and test sets as described in Section 2.4. (Figure 3A) The weights and biases of the network are learned using the AdamW optimizer with a weight decay of 0.001. The learning rate is set to 0.0001 and is decreased by 50 percent at epochs 20, 40, 60, 80, and 100. We use a mini batch size of 16 on a single Nvidia Titan RTX GPU. Training is terminated at

convergence, defined as when no decrease in epoch validation loss is observed for 60 continuous epochs.

Training Data Augmentation

We apply regularization by utilizing several problem and data appropriate data augmentation schemes at train time; all of which were done using PyTorch Torchvision augmentation functions (Paszke et al., 2019). The first is a random, image center-based rotation of both depth and color images from 0 to 360 degrees. We speculate that this is an effective augmentation strategy that preserves the input data distribution due to the symmetrical nature of lettuce plant growth combined with the location of the plant apex at the image center. The second is a random manipulation of brightness, contrast, saturation, and hue by a factor of 0.5–1.5. The third is a grayscale transformation of the color image applied with a probability of 0.1. The second and third augmentation schemes are applied to the color input image only and serve to reduce model dependency on color. The color images in our dataset are not of uniform quality due to unaccounted for changes in scene brightness relative to camera exposure time. We choose not to apply similar augmentation schemes to the depth data, as the mapped RGB channel distribution and intensity values are directly related to scene geometry as a result of their encoding from depth information.

Model Selection and Evaluation

For the purpose of model selection, we created a validation set that better represents all possible plant conditions than the overall dataset (Figure 3B). This involved sampling from the overall dataset such that the validation set achieved a more, although not perfectly, uniform distribution across biomass values. We selected eight trays (378 plants) that represent harvest times from 14 to 35 days since germination. From this distribution, we subsample 100 individual data points *via* a weighted sampling scheme: biomass values are discretized into 35 bins corresponding to 1 g increments, and then are sampled by weighing each bin inversely to its count. Best performing models were selected based upon the lowest loss achieved on the validation dataset at model convergence.

Model evaluation criteria is an important factor for determining model performance in regression tasks. Common criterion for biomass estimates include MAPE (Equation 2) and root mean squared error (RMSE; Equation 3). However, for the problem of plant mass estimation, single value summary statistics give incomplete insight into model performance as they mask potential heteroscedasticity as well as imbalances in dataset distribution. The nature of our problem changes significantly over the range of biomass values and corresponding stage of development of the plants in the scene. Plant structure and size varies significantly over time, while larger neighboring plants introduce increasing occlusions. Additionally, the end user of such a model may have varying use cases and accuracy requirements.

$$RMSE = \sqrt{\frac{1}{n} \sum_{i=1}^n (A_i - F_i)^2} \quad (3)$$

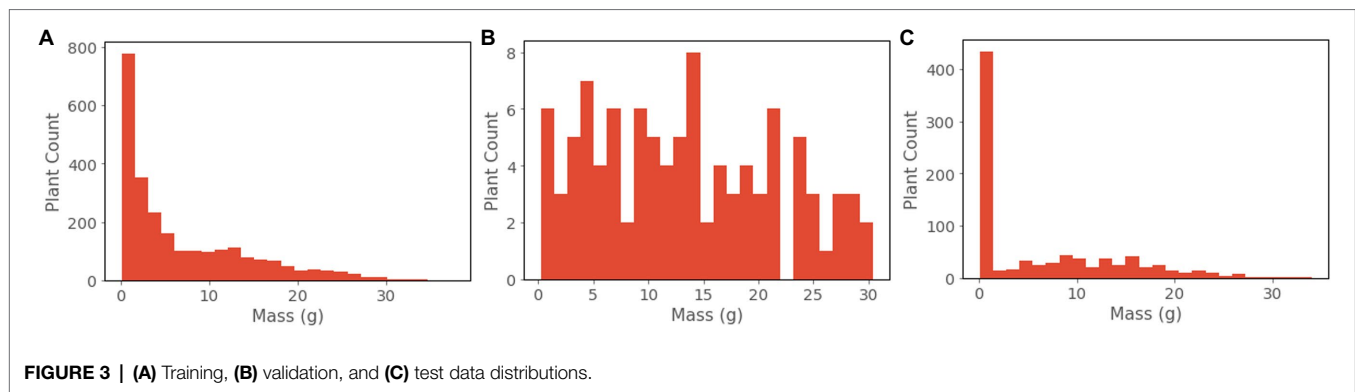


FIGURE 3 | (A) Training, **(B)** validation, and **(C)** test data distributions.

Where n = number of samples, A_i = i -th sample ground truth mass, and F_i = i -th predicted mass.

For these reasons, during model evaluation we report RMSE and MAPE on a per-group basis for ranges of ground truth mass values. These groups were chosen based upon the relative levels of occlusion experienced by plants of those mass values on average. We present the results of all models evaluated on the unseen test dataset. Our test set was composed of 864 plants sourced from a single growth cycle not present in either the training or validation sets (Figure 3C). Sourcing all test data from a separate growth cycle reduces the possibility of overfitting to variations in phenotypic expression within the different growth trials.

Model Ablation Study

The rationale for utilizing joint RGB and depth data modalities as predictor variables in a biomass estimation model centered on three facets: (1) the current state of the art detection and semantic segmentation models utilize RGB data, (2) many current biomass estimation methods utilize 3D representations, and (3) DCNNs can effectively learn jointly from each modality. However, we find it worthwhile to further investigate whether the combined data modalities truly result in superior predictive performance over either modality individually. We conduct an ablation study which tests the ability of each data modality to predict plant biomass. In this study, we present the predictive results of the RGB and depth only networks that also form the weights used during the initialization of the RGBD network. Each network mirrors the RGB-D regression network, with identical training parameters as well as input preprocessing, pretraining, and similar regression head.

Model Interpretation *via* Gradient Class Activation Mapping

Intuitively, the problem of individual plant biomass estimation requires an understanding of the extent and physical characteristics of the plant of interest in the scene, including an approximation of any occluded or out of scene portions. Due to the nature of our loss function, there is no strict enforcement of localization, leaving us unsure as to whether the model is in fact learning center plant mass, or simply some other mapping of common scene features of the dataset to biomass. This limits our trust in the model—and its broader applicability to problems involving individual plant mass estimation—by potentially reducing its

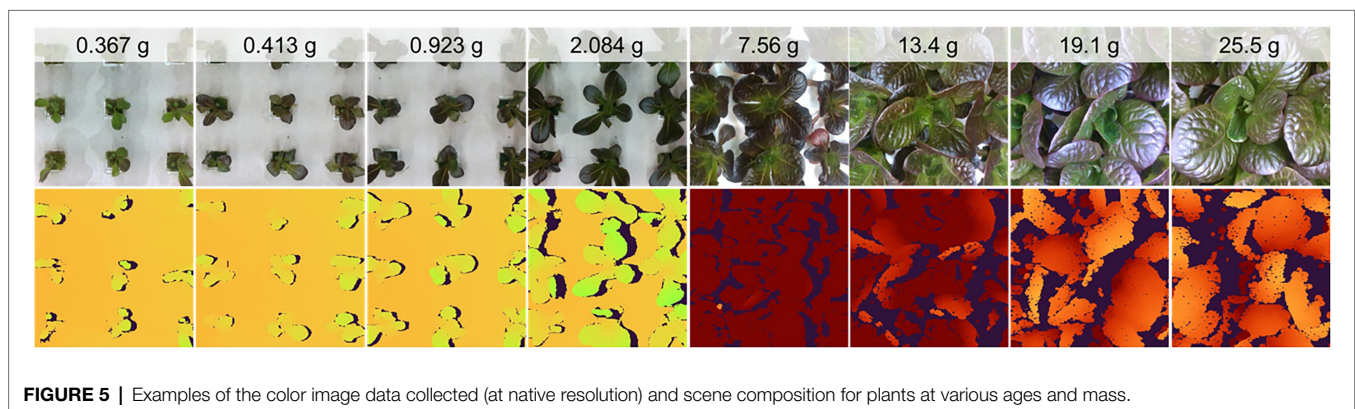
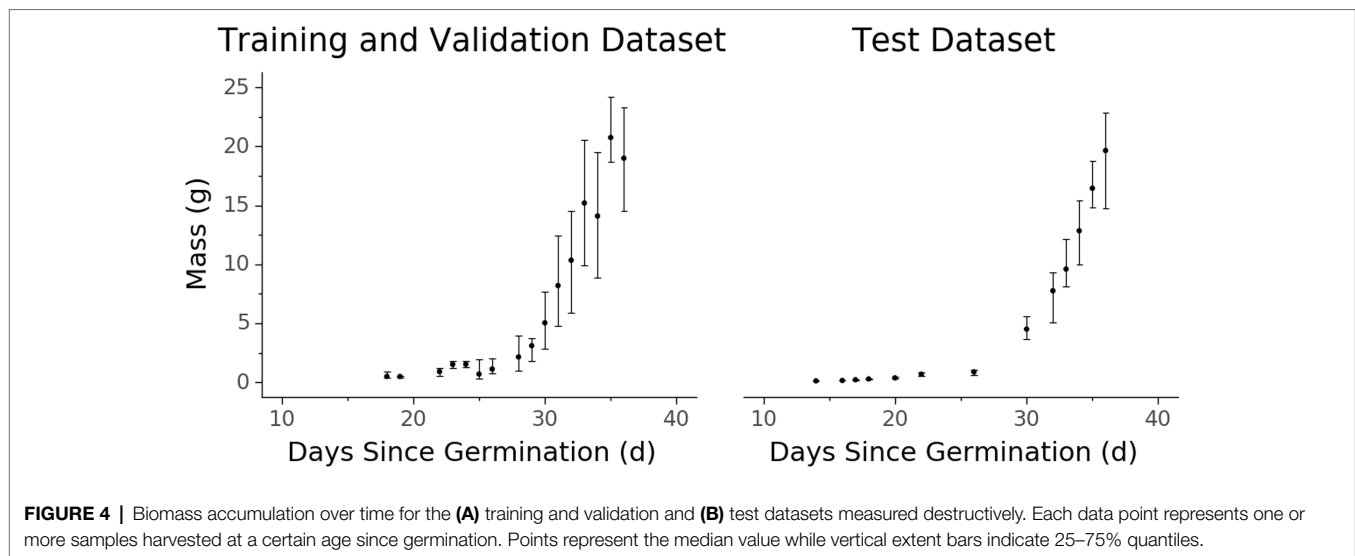
generalizability outside of the dataset distribution. Due to our homogenous environmental conditions, our dataset generally features scenes of plants of similar size and age. An ability to generalize outside of this distribution becomes important when considering certain applications of the model, such as growth rate abnormality detection where estimation of unlike neighbors may become important. While one could answer the question of generalizability through extensive testing within a target distribution, we forgo that additional expense and explore the question instead by investigating model decision making and predictive behavior. In particular, we utilize Gradient Class Activation Mapping (GradCAM; Selvaraju et al., 2016) to explore model localization *via* the latent space as well as examine examples of the success and failure modes of the model. GradCAM is a generalization of the class activation map method (Zhou et al., 2015) that allows for visualization of important latent space features in pixel space. We apply GradCAM to the final block of the RGB Resnet50 branch of our RGBD network, ignoring the depth branch contribution in favor of simplicity in understanding model localization. We report the visualizations of Guided GradCAM for the top five best and worst predictions over four different binned ranges of plant mass.

In addition to GradCAM, we explore the model prediction success and failure modes by visually examining the best and worst predictions. We hypothesize that a model that has truly learned center plant mass is likely to succeed and fail under different scene conditions than a model that has learned an unrelated mapping. For instance, the former might succeed when the center plant is less occluded, while the latter might succeed under scene conditions where plants are relatively similar (i.e., median of dataset distribution). Similarly, failure modes are likely to differ, such as when the center plant is under heavy occlusion, or when the center plant is of greatly different size than its neighbors (dataset distribution outlier). While this analysis is speculative in nature, we found it worthwhile to publish some best and worst case examples that may help illustrate what mapping the model has learned.

RESULTS

Lettuce Image and Biomass Dataset

The resulting dataset contains comprehensive representations of the lettuce cultivar ‘Powerhouse’ over its entire life cycle,



totaling 3,888 RGB images, 3,888 aligned depth images, and 3,888 plant biomass values (Figure 4). Due to its size, a variety of phenotypic expressions are present, including variations in leaf color from green to dark purple. Some trays also exhibited stem elongation, likely a physical response to either shade condition or low air temperature.

There are some qualities of the dataset that are worth noting. Due to the exponential nature of plant growth, the dataset distribution is skewed towards smaller and younger plants (Figures 3, 4). Additionally, the plants were grown under well-watered and adequate nutritional conditions, and therefore the dataset contains no representations of plants under water stress or severe nutritional stress. A variety of possible environmental parameters exist that could result in phenotypic responses that are not represented in the dataset.

Lettuce Image Data

In their native resolution of 848 by 480, the images contain up to 15 plant sites, although this is reduced to nine plant sites at a resized 480 by 480 resolution for model use (Figure 5). At larger plant sizes, the scene changes significantly, with far

fewer plants represented. In fact, the center plant's full extent is often not completely represented in the resized images (Figure 5).

The color data were well focused and generally of high quality, although issues related to the RealSense camera's automatic exposure algorithm resulted in some over- (low contrast, larger average pixel values) and under- (low contrast, smaller average pixel values) exposed images. Depth images contained some missing pixels due to errors in stereo matching due to occlusion and specular effects. The extent of missing data was generally greater for larger plants (Figure 5). The depth data were not evaluated for absolute measurement accuracy, although visualizations of the depth data show good representation of the scene despite missing data.

RGBD Model

The model shows strong predictive performance over the entire 854 plant test set, achieving an RMSE of 1.13 g, a MAPE of 7.3%, and a Pearson's correlation coefficient of 0.989 (Figure 6A). Some heteroscedasticity can be observed, and the greatest average relative errors occurred on the smallest and largest of

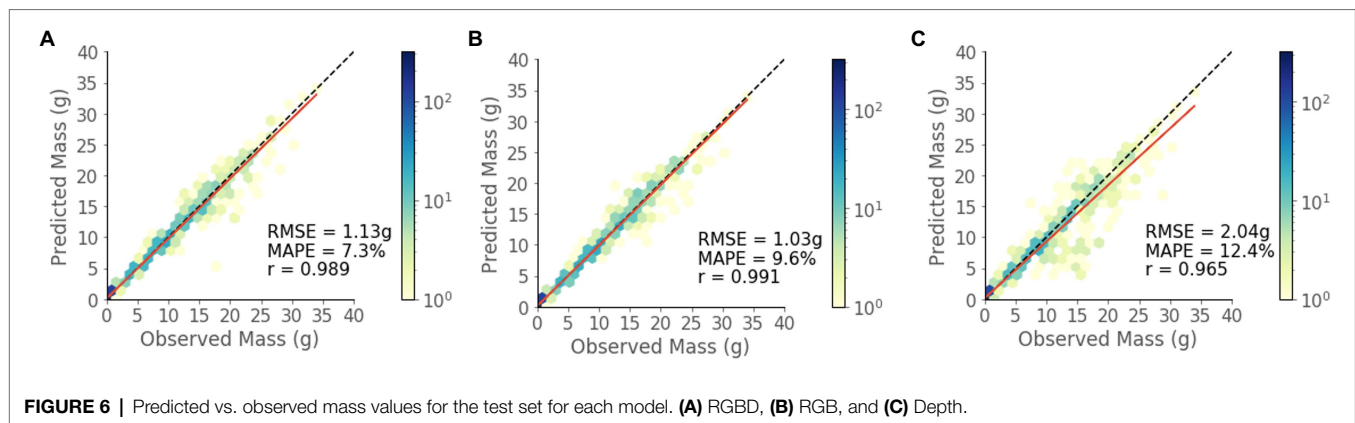


FIGURE 6 | Predicted vs. observed mass values for the test set for each model. (A) RGBD, (B) RGB, and (C) Depth.

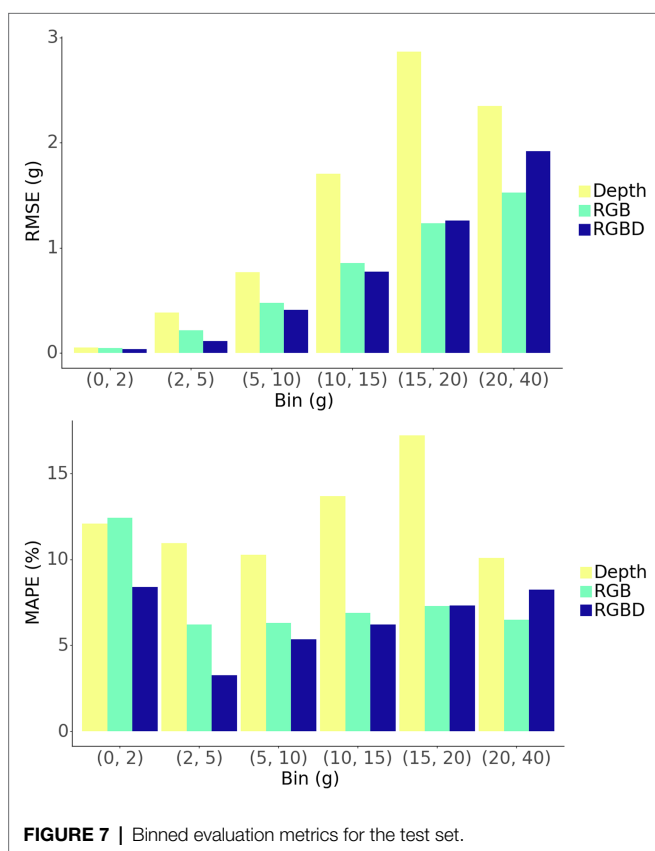


FIGURE 7 | Binned evaluation metrics for the test set.

plant masses, in addition to some variability in predictive power between that ranges (Figure 7).

Model Data Modality Comparison

The RGBD model outperforms both RGB and depth only models in MAPE while the RGB model outperforms in RMSE (Figures 6B,C). Among the smallest plants, RGBD significantly outperforms each modality separately while the RGB and depth models achieve very similar relative and absolute error (Figure 7). As the plants increase in mass, the RGBD model generally outperforms the RGB and depth models while RGB outperforms

depth. However, for plants between 10–15 g and 15–25 g, RGB shows comparable performance and even outperforms the combined RGBD modality in both MAPE and RMSE metrics.

Model Prediction Performance Examination

Among the best predictions, the model shows strong localization of the center plant (Figure 8). This tends to hold true across plant sizes, with important activations indicated along occlusion boundaries for larger plants. We notice a similar outcome among the worst predictions, although some cases show activations that are not centered on the center plant or appear to contain additional activations of neighboring plants that are not part of an occlusion boundary.

Examining the best and worst case model predictions reveals a nuanced relationship between prediction error and scene composition. We notice that in comparison to the high error predictions, low error predictions generally involve less occluded scenes. However, some examples of high error scenes show similar levels of occlusion to their low error counterparts, especially among examples of bins [2, 5] (Figure 8). In this bin, the worst performing cases do not appear contain stronger occlusion, but rather the center plant is significantly smaller than its neighbors.

Model Predicted Biomass Response to Stress Treatments

The control (Treatment D) exhibits an expected sigmoidal biomass accumulation pattern approaching an asymptote after day 30 (Figure 9). All other treatments resulted in less biomass accumulation over the experimental period compared with the control.

Starting after the stress induction of treatment A on day 6, the mean biomass accumulation decreases. The mean separation (as calculated *via* Tukey HSD test) between treatment A and the other treatments occurs on day 9.3, approximately 3.3 days after the stress induction. No mean separation occurs before this day. At day 11.7, treatment A begins to receive nutrient solution, removing the nutrient stress and increasing biomass accumulation until day 24.3. Here, a malfunction

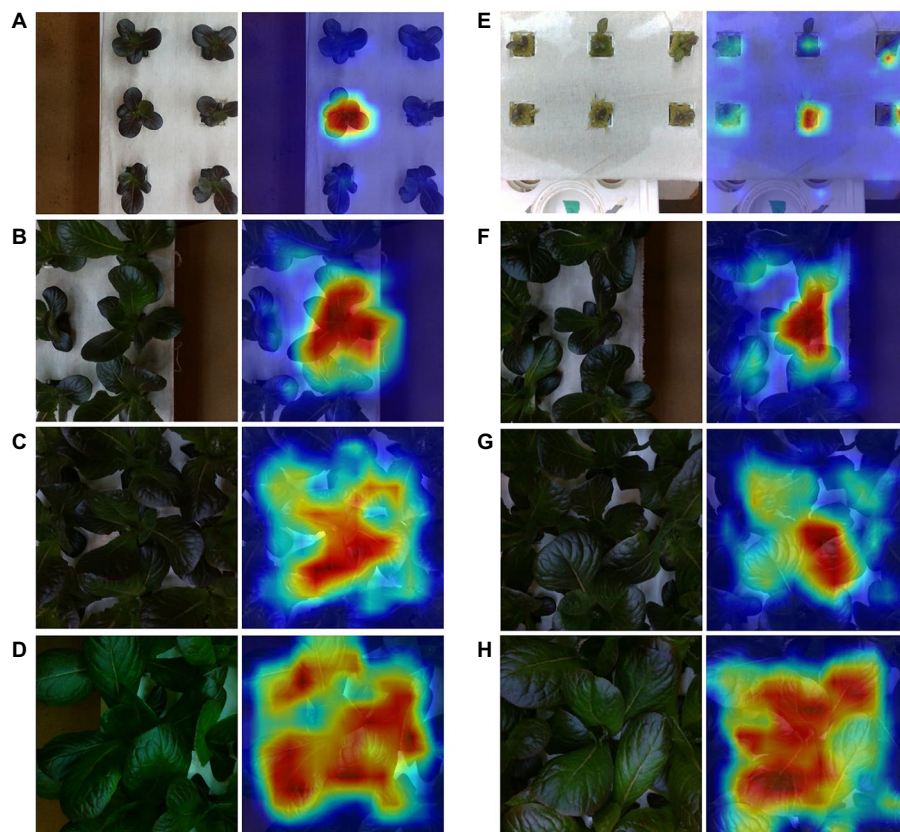


FIGURE 8 | Sample best (A–D) and worst (E–H) predictions from the test set along with GradCam output for varying mass ranges. Each represents a mass range. Starting from the top are [0, 2] (A,E), [2, 5] (B,F), [5, 10] (C,G), and [10, 25] (D,H).

of the irrigation system caused extensive wilting in some of the individuals within the treatment. This was remediated on day 26, and recovery can be seen at that time in the wilted plants (Supplementary Figure S1), as well is in the biomass predictions (Figure 9). After this recovery, the confidence interval associated with treatment A mean biomass estimation increases dramatically.

The response of biomass accumulation to the nutrient stress applied simultaneously to treatments B and C on day 11.7 is evident by their decrease in biomass accumulation compared with treatment D (control). There is a delay in the separation of the means between treatments C and D of 2.3 days after stress induction (day 14), and of 3 days between treatments B and D (day 14.7). No mean separation between these treatments occurs before day 14.

The response to the nutrient stress reduction applied to treatment C on day 15.7 is evident in the increase of biomass accumulation of treatment C compared with treatment B (Figure 9). Treatment C's mean biomass becomes significantly larger than treatment B's on day 20.7 (5 days after stress reduction).

The final scheduled stress event occurs on day 21, when treatment C begins to receive water and treatment B receives Hoagland solution. This results in the treatment means becoming

inseparable at day 26, where it remains as such for the remaining duration of the trial.

Model Predicted Growth Rate and Relative Growth Rate as Stress Response Indicators

In contrast with the model predicted biomass accumulation, the derived growth metrics GR and RGR exhibit significantly more daily fluctuation (Figures 10, 11). A result of this variation is the potential for mean separation between treatments that are experiencing identical growing conditions. Because of this, a simple difference in treatment mean GR or RGR is not a suitable metric for stress detection. Instead, we propose a criterion of two consecutive differences in GR or RGR means to indicate a significant change in growth dynamics between treatments. Stress response detection based on this criterion for GR is indicated at day 8.7 for treatment A compared with treatments B, C, and D; day 13.7 for treatments B and C compared with treatment D (control), and day 18.3 for treatment B compared with treatment C. Stress response detection for RGR is indicated at day 8.7 for treatment A compared with treatments B, C, and D; day 13.3 for treatments B and C compared with treatment D (control), and day 17.7 for treatment B compared with treatment C (Table 2).

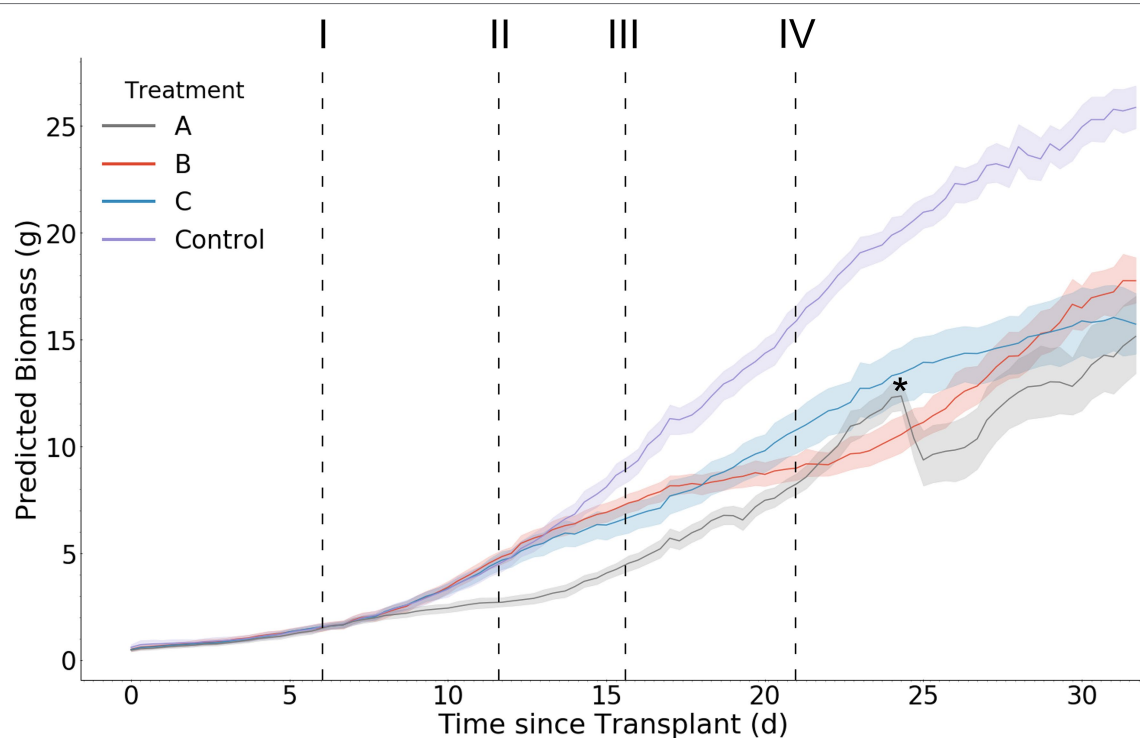


FIGURE 9 | Mean per treatment predicted biomass with 95% confidence interval. Dark vertical lines and roman numerals indicate when treatments were applied. (I) Treatment A begins to receive pure water, (II) Treatment A begins to receive Hoagland solution and Treatments B and C begin to receive water, (III) Treatment C begins to receive Hoagland solution, and (IV) Treatment B begins to receive Hoagland solution and Treatment C begins to receive water. An asterisk marks where wilting in Treatment A was visually noticed in the image data (day 24.3).

DISCUSSION

In this study we present a powerful technique for accurate non-destructive plant biomass prediction in visually occluded environments. While direct performance comparisons with prior studies are difficult due to a general lack of benchmark datasets for plant biomass estimation, we believe that our method represents state-of-the-art for the proximal non-destructive individual biomass estimation task. Moreover, we show that deep learning models can learn individual plant traits under heavy occlusion without explicit localizing annotations. The ability for deep learning models to implicitly learn occlusion lowers data labelling costs and allows for the potential to solve complicated tasks in agriculture that are challenging to solve *via* hand engineered computer vision algorithms. As data quantity can be large in agricultural systems, our method's reliance on relatively inexpensive supervision in the form of biomass measurements allows for scalability that likely will only improve prediction accuracy. Finally, we have shown that it is possible to achieve high predictive performance on plant biomass estimation solely from color data acquired *via* readily available and low cost RGB sensors.

Comparison With Prior Non-destructive Lettuce Biomass Estimation Efforts

The results presented here demonstrate a substantial advancement in our capacity to non-destructively estimate individual plant

biomass under occluded growth conditions. In comparison with the results obtained by Mortensen et al. (2018), our model demonstrates substantially lower relative error at 7.3% compared to 40%. While the cropping system is not identical between this study and that of Mortensen et al. (2018), our work maintains lower relative error even under much greater occlusion and planting density. It should be noted that while the author's field-based data acquisition system allowed for good control of lighting conditions, the scene background conditions are busier than our indoor acquisition system due to irregular soil and weed presence. Similarly, to our work, the authors' method relies on images taken above the plant to be estimated. However, their method additionally requires the xy-coordinates of the stem emergence point to be known, as well as segmentation masks for validation of the underlying segmentation algorithm used to generate the fresh weight predictors. While our method relies on a far larger dataset, each data annotation is less expensive as we require only a single measured fresh weight value per plant.

In another study, Zhang et al. (2020) used a convolutional neural network approach to single plant biomass estimation but did so only on isolated plants lacking occlusion. While an RGBD camera was also used in their work, depth data was used only for an initial preprocessing segmentation step and not as model input. Despite a lack of occlusion from neighboring plants, their segmented RGB-only model appears to underperform both our RGB and RGBD models through

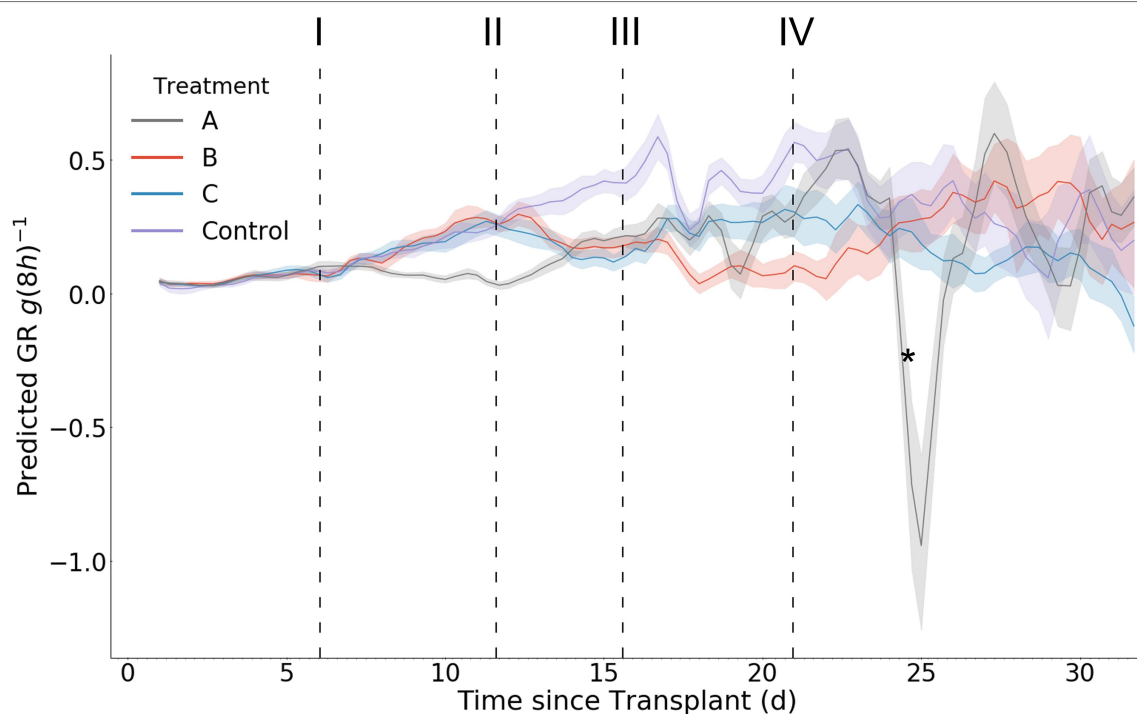


FIGURE 10 | Mean per treatment predicted growth rate with 95% confidence interval. Y axis units are $g(8h)^{-1}$. Dark vertical lines and roman numerals indicate when treatments were applied. (I) Treatment A begins to receive pure water, (II) Treatment A begins to receive Hoagland solution and Treatments B and C begin to receive water, (III) Treatment C begins to receive Hoagland solution, and (IV) Treatment B begins to receive Hoagland solution and Treatment C begins to receive water. An asterisk marks where wilting in Treatment A was visually noticed in the image data (day 24.3).

visual comparison of the predicted versus observed scatter plots. However, a quantitative comparison between our studies is difficult to make due to missing information on the normalizing unit in the normalized RMSE performance metric used by the authors. If we do indeed achieve higher performance, we speculate that this is due to the use of a larger training dataset along with a DCNN regression architecture that leverages a pre-trained ResNet backbone.

Learned Model Features and Generalizability

Perhaps one of the more powerful aspects of our modeling approach is the ability to implicitly learn to localize the center plant during training without explicit annotation. This localization is evident in the visualizations of feature map activations provided by GradCAM in both best and worst case prediction examples (Figure 8). Similar visualizations provided by GradCAM of the depth modality also show similar trends between the best and worst case predictions, including strong localization. However, it is evident that model starts to fail when the center plant is of lesser size than its neighbors. This is likely a result of two conditions: increased occlusion under these conditions and overfitting to the training dataset. In particular, the latter condition is due to the uniform nature of the cultivation practices used to generate the dataset, which resulted in scenes containing neighboring plants that generally (but not always) are of similar size and mass. Therefore, our

model has likely learned to estimate center plant mass while also overfitting to some degree to common scene features of the training data distribution. Our plant monitoring experiment further supports this, as those scenes contained neighboring plants with significant variation in size and mass. The model's ability to capture, in aggregate, expected changes in growth under such conditions suggests that it has learned to predict center plant mass. The model could be made more robust to variable sized plants by training with a more heterogeneous dataset; a hypothesis which warrants further investigation in future studies.

Another notable phenomenon is the relative lack of contribution of the depth data modality to model predictive performance. It is possible that our use of depth data is suboptimal for model learning. For instance, the pre-trained weights are tuned for feature extraction of color, and not depth, images. To allow for the use of pre-trained weights we map the depth data to a 3-channel color image, allowing the model to directly use its pre-trained feature extraction capabilities on the depth data. This mapping scheme imbues color data with a direct relationship to absolute distance from the sensor (e.g., red is farthest away while blue closest). While this does allow the model to learn biomass estimation to some extent, it is unknown whether it has maintained a strong understanding of absolute scene size and shape after this mapping due to the pre-training of the initial convolutional layer. Additionally, as our image capture height is fixed, the real world area represented by each pixel is essentially constant, allowing relative plant size to be estimated

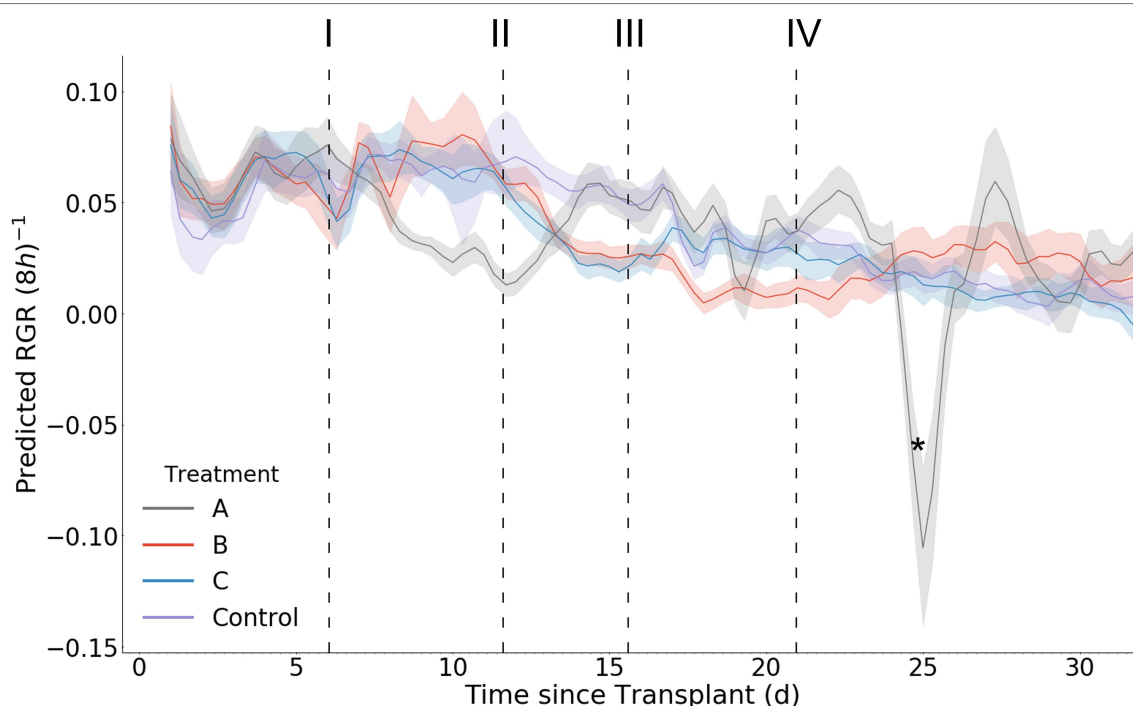


FIGURE 11 | Mean per treatment predicted relative growth rate with 95% confidence interval. Y axis units are in $(8h)^{-1}$. Dark vertical lines and roman numerals indicate when treatments were applied. (I) Treatment A begins to receive pure water, (II) Treatment A begins to receive Hoagland solution and Treatments B and C begin to receive water, (III) Treatment C begins to receive Hoagland solution, and (IV) Treatment B begins to receive Hoagland solution and Treatment C begins to receive water. An asterisk marks where wilting in Treatment A was visually noticed in the image data (day 24.3).

TABLE 2 | A summary of time until statistically significant treatment mean metric differences are observed for each stress event.

Metric	Stress event response time		
	Day 6	Day 11.7	Day 15.7
Biomass	3.3 d	3 d	5 d
GR	2.7 d	2 d	2.3 d
RGR	2.7 d	1.7 d	1.7 d

The stress events occurred on days 6, 11.7, and 15.7, and the times indicated for each metric are the number of days from each event until the time of data capture indicating treatment separation as provided by Tukey HSD test.

in the scene *via* RGB only. It may be the case that had image acquisition height been variable, depth data may have had an increased importance and outperformed color as the relative size of plants in each scene could no longer be directly tied to their absolute size in world space. We suspect that a modified architecture that can more directly utilize depth data would outperform, such as models that utilize 3D representations of the scene such as meshes or point clouds (Qi et al., 2017).

Model Predictions for Plant Growth Monitoring

We have shown that our model is able to predict individual plant biomass with enough accuracy to capture the effects of

nutrient stress on biomass accumulation within 2 days, even when those effects are applied with spatial heterogeneity. This illustrates model robustness to heterogeneous plant size in the scene despite having been trained on more homogenous conditions. We further validate the response of the model by showing through hand collected measurement that our treatments had real effect on plant size, and by extension, in biomass accumulation (Supplementary Figure S2). However, it is difficult to quantify the true accuracy of the biomass, GR, and RGR calculations, as we have no ground truth for each treatment. Further, there are sources of variation in the response of each plant to the treatments, such as genotypic and block effects, which are not easily separable from model prediction error when examining the data in aggregate. Potential sources of block effects in include variations in lighting intensity, as well cross treatment contamination from plant roots which extend into the common drainage channels of the hydroponic system. As such, we do not have an exact understanding of the how our model's predicted stress induction response time differs from the true stress induction response time.

While we do not know the true model biomass prediction error for this experiment, we do know that larger prediction errors would likely lead to a longer time before significant treatment effects can be determined by the Tukey HSD test. In a soilless top-fed hydroponic system such as ours, we would expect a significant change in fertigation solution (such as our nutrient stress treatments) to result in a close to immediate

change to RGR. This is due to both the lack of cation exchange capacity of the stone wool medium and the ratio of medium volume to irrigation volume, likely resulting in a rapid change in concentration of nutrient ions in the root zone (Silber, 2008). Without access to nutrient ions, the plant's biomass accumulation rate slows over time as it must rely only upon existing nutrient stores in its tissues to support cell growth and function. Our model required between 1.7 and 2.7 days to determine a significant treatment effect *via* RGR, which we believe is consistent with expected RGR of typical lettuce cultivars, the expected effect of complete nutrient deprivation on RGR, and our originally published model test error of 7.3% (Holsteijn, 1980).

The predicted RGR curves generally follow the expected shape as previously seen in the literature (Holsteijn, 1980). RGR decreases with time for all treatments as well as the control. During stress induction the RGR decreases, and then increases during stress reduction (Figure 11). An interesting phenomenon can be seen after stress reduction: a treatment's RGR may rejoin that of the control provided no additional stress is introduced or sustained (Figure 11). The variance of the predictions within each treatment increases with time, as evidenced by larger mean confidence intervals. This is consistent with the expected model error as determined during our model validation. It should be noted that the ability to detect significant treatment effects was maintained beyond day 17, at which point plants of up to 15g existed and contained significant occlusion. In addition to predicting RGR response between the comparable treatments *via* analysis of variance, by examining the graphs of RGR, GR, and biomass over time we can see that the effects of stress reduction (Treatment A on day 12) and stress induction (Treatment C on day 21) that occurred without a directly comparable treatment (Figures 9–11). The effect of Treatment C's day 21 stress induction can be seen through day 32, revealing that our model maintains general accuracy even when neighboring plants (in particular, Treatment D) are large (Figure 9).

An unintended irrigation malfunction caused some individuals (approximately 15) within treatment A to experience water stress starting at approximately day 24. While we do not know exactly when water stress began for those individuals, it becomes visually noticeable in the image data at day 24.7 (Supplementary Figure S1). A reduction in predicted biomass is observed during this water stress period (Figure 9). That our model indicates a sudden change in biomass may practically be quite valuable and supports its sensitivity to changes in growth rate. While reduced predicted biomass is consistent with reduced plant water content under drought conditions, we exercise caution in concluding that our model can accurately extrapolate to individuals that are experiencing less than well-watered conditions, as such conditions are not represented in either the training or test datasets used to create and evaluate the model. This does leave open the possibility, however, that our model can serve as an indicator of crop response to environmental parameters that result in morphological change beyond biomass accumulation. Such sensitivity also allows

for the future possibility of fine-tuning the model with data that includes plants experiencing wilting or other stress conditions, furthering the use of the model as a non-destructive plant stress detector.

CONCLUSION

Our work introduces a novel technique that applies proximal vision based plant trait estimation models to the problem of stress detection and growth monitoring with high spatial and temporal resolution over the entire lettuce cropping cycle. By utilizing highly accurate biomass estimation models, short-term plant-environment interactions within cropping systems can be better monitored and quantified. Our brief exploration of the response in biomass accumulation to nutrient stress is far from exhaustive. Improvements could result from implementations featuring models with lower prediction error and more frequent data acquisition. To further determine the utility and ability of such sensing methods at scale, an implementation into a commercial facility should be conducted. This would help answer questions such as which stresses are best predicted by short term changes in biomass accumulation, on what basis do we make comparison of individuals for the purpose of stress or abnormality detection, and where do these methods fail in real world settings.

DATA AVAILABILITY STATEMENT

The raw data supporting the conclusions of this article will be made available by the authors, without undue reservation. Code available at <https://github.com/NicoBux/Plant-Biomass-Monitoring>.

AUTHOR CONTRIBUTIONS

NB, ME, and JL: conceptualization, performance evaluation, visualization, and review and editing. NB: data collection, model generation and testing, and writing—original draft. All authors contributed to the article and approved the submitted version.

FUNDING

This project was partly supported by USDA AI Institute for Next Generation Food Systems (AIFS), USDA award number 2020-67021-32855.

SUPPLEMENTARY MATERIAL

The Supplementary Material for this article can be found online at: <https://www.frontiersin.org/articles/10.3389/fpls.2022.758818/full#supplementary-material>

REFERENCES

- Catchpole, W. R., and Wheeler, C. J. (1992). Estimating plant biomass: A review of techniques. *Aust. J. Ecol.* 17, 121–131. doi: 10.1111/j.1442-9993.1992.tb00790.x
- Egli, D. B. (2019). Crop growth rate and the establishment of sink size: a comparison of maize and soybean. *J. Crop Improv.* 33, 1–17. doi: 10.1080/15427528.2019.1597797
- Egli, D. B., and Zhen-wen, Y. (1991). Crop growth rate and seeds per unit area in soybean. *Crop Sci.* 31, 439–442. doi: 10.2135/cropsci1991.0011183X003100020043x
- Eitel, A., Springenberg, J. T., Spinello, L., Riedmiller, M., and Burgard, W. (2015). “Multimodal deep learning for robust RGB-D object recognition.” in *2015 IEEE/RSJ International Conference on Intelligent Robots and Systems (IROS)*; September 28, 2015.
- Gallardo, M., Jackson, L. E., Schulbach, K., Snyder, R. L., Thompson, R. B., and Wyland, L. J. (1996). Production and water use in lettuces under variable water supply. *Irrig. Sci.* 16, 125–137. doi: 10.1007/bf02215620
- Gupta, S., Girshick, R., Arbeláez, P., and Malik, J. (2014). “Learning rich features from RGB-D images for object detection and segmentation,” in *Computer Vision – ECCV 2014. ECCV 2014. Lecture Notes in Computer Science. Vol. 8695*. eds. D. Fleet, T. Pajdla, B. Schiele and T. Tuytelaars (Cham: Springer).
- Holsteijn, H. M. C. V. (1980). *Growth of Lettuce II. Quantitative Analysis of Growth*. Netherlands: Veenman.
- Hu, Y., Wang, L., Xiang, L., Wu, Q., and Jiang, H. (2018). Automatic non-destructive growth measurement of leafy vegetables based on kinect. *Sensors* 18:806. doi: 10.3390/s18030806
- Jiang, J. S., Kim, H. J., and Cho, W. J. (2018). On-the-go image processing system for spatial mapping of lettuce fresh weight in plant factory. *IFAC* 51, 130–134. doi: 10.1016/j.ifacol.2018.08.075
- Jin, S., Su, Y., Song, S., Xu, K., Hu, T., Yang, Q., et al. (2020). Non-destructive estimation of field maize biomass using terrestrial lidar: an evaluation from plot level to individual leaf level. *Plant Methods* 16:69. doi: 10.1186/s13007-020-00613-5
- Jung, D.-H., Park, S. H., Han, X. Z., and Kim, H.-J. (2015). Image processing methods for measurement of lettuce fresh weight. *J. Biosyst. Eng.* 40, 89–93. doi: 10.5307/jbe.2015.40.1.089
- Kacira, M., Sase, S., Okushima, L., and Ling, P. P. (2005). Plant response-based sensing for control strategies in sustainable greenhouse production. *J. Agric. Meteorol.* 61, 15–22. doi: 10.2480/agrm.61.15
- Karimi, M. M., and Siddique, K. H. M. (1991). Crop growth and relative growth rates of old and modern wheat cultivars. *Aust. J. Agric. Res.* 42, 13–20. doi:10.1071/AR9910013
- Loresco, P. J. M., Vicerra, R. R., and Dadios, E. (2019). “Segmentation of lettuce plants using super pixels and thresholding methods in smart farm hydroponics setup,” in *Lecture Notes in Engineering and Computer Science: Proceedings of the World Congress on Engineering 2019*; July, 3–5 2019, London.
- Mortensen, A. K., Bender, A., Whelan, B., Barbour, M. M., Sukkarieh, S., Karstoft, H., et al. (2018). Segmentation of lettuce in coloured 3D point clouds for fresh weight estimation. *Comput. Electron. Agric.* 154, 373–381. doi: 10.1016/j.compag.2018.09.010
- Muchow, R. C. (1988). Effect of nitrogen supply on the comparative productivity of maize and sorghum in a semi-arid tropical environment grain yield and nitrogen accumulation. *F. Crop. Res.* 18, 31–43. doi: 10.1016/0378-4290(88)90057-3
- Ophoff, T., Van Beeck, K., and Goedemé, T. (2019). Exploring Rgb+depth fusion for real-time object detection. *Sensors* 19:866. doi: 10.3390/s19040866
- Paszke, A., Gross, S., Massa, F., Lerer, A., Bradbury, J., Chanan, G., et al. (2019). “Pytorch: An imperative style, high-performance deep learning library.” *Advances in Neural Information Processing Systems* 32; December 3, 2019.
- Pottier, J., and Jabot, F. (2017). Non-destructive biomass estimation of herbaceous plant individuals: a transferable method between contrasted environments. *Ecol. Indic.* 72, 769–776. doi: 10.1016/j.ecolind.2016.08.030
- Qi, C. R., Su, H., Mo, K., and Guibas, L. J. (2017). Pointnet: deep learning on point sets for 3D classification and segmentation. *CVPR* 2017, 77–85. doi: 10.1109/cvpr.2017.16
- Sapkota, S., and Sapkota, S., and Liu, Z. (2019). Effects of nutrient composition and lettuce cultivar on crop production in hydroponic culture. *Horticulturae* 5:72. doi:10.3390/horticulturae5040072
- Scully, B. T., And Wallace, D. H. (1990). Variation in and relationship of biomass, growth rate, harvest index, and phenology to yield of common bean. *J. Am. Soc. Hortic. Sci.* 115, 218–225. doi:10.21273/jashs.115.2.218
- Selvaraju, R. R., Cogswell, M., Das, A., Vedantam, R., Parikh, D., and Batra, D. (2016). Grad-CAM: visual explanations from deep networks via gradient-based localization. *Int. J. Comput. Vis.* 128, 336–359. doi: 10.1007/s11263-019-01228-7
- Silber, A. (2008). *6 – Chemical Characteristics of Soilless Media*. Amsterdam: Elsevier.
- Takai, T., Matsuura, S., Nishio, T., Ohsumi, A. K., Tatsuhiko, S., and Horie, T. (2006). Rice yield potential is close related to crop growth rate during late reproductive period. *Field Crops Res.* 96, 328–335. doi: 10.1016/j.fcr.2005.08.001
- Tukey, J. W. (1949). Comparing individual means in the analysis of variance. *Biometrics* 5, 99–114. doi: 10.2307/3001913
- Ward, I. R., Laga, H., and Bennamoun, M. (2019). “RGB-D image-based object detection: from traditional methods to deep learning techniques,” in *Advances in Computer Vision and Pattern Recognition*. eds. P. L. Rosin, Y.-K. Lai, L. Shao and Y. Liu (London: Springer), 169–201.
- Zhang, L., Xu, Z., Xu, D., Ma, J., Chen, Y., and Fu, Z. (2020). Growth monitoring of greenhouse lettuce based on a convolutional neural network. *Hortic. Res.* 7:124. doi: 10.1038/s41438-020-00345-6
- Zhou, B., Khosla, A., Lapedriza, A., Oliva, A., and Torralba, A. (2015). “Learning deep features for discriminative localization.” in *2016 IEEE Conference on Computer Vision and Pattern Recognition (CVPR)*; June 1, 2015.
- Zhou, J., Li, P. P., Wang, J. Z., and Fu, W. (2019). Growth, photosynthesis, and nutrient uptake at different light intensities and temperatures in lettuce. *HortScience* 54, 1925–1933. doi: 10.21273/hortsci14161-19
- Zotarelli, L., Scholberg, J. M., Dukes, M. D., Muñoz-Carpena, R., and Icerman, J. (2009). Tomato yield, biomass accumulation, root distribution And irrigation water use efficiency On A Sandy soil, As affected By nitrogen rate And irrigation scheduling. *Agric. Water Manag.* 96, 23–34. doi: 10.1016/j.agwat.2008.06.007

Conflict of Interest: The authors declare that the research was conducted in the absence of any commercial or financial relationships that could be construed as a potential conflict of interest.

Publisher’s Note: All claims expressed in this article are solely those of the authors and do not necessarily represent those of their affiliated organizations, or those of the publisher, the editors and the reviewers. Any product that may be evaluated in this article, or claim that may be made by its manufacturer, is not guaranteed or endorsed by the publisher.

Copyright © 2022 Buxbaum, Lieth and Earles. This is an open-access article distributed under the terms of the Creative Commons Attribution License (CC BY). The use, distribution or reproduction in other forums is permitted, provided the original author(s) and the copyright owner(s) are credited and that the original publication in this journal is cited, in accordance with accepted academic practice. No use, distribution or reproduction is permitted which does not comply with these terms.



A Spatial-Temporal Analysis of Cellular Biopolymers on Leaf Blight-Infected Tea Plants Using Confocal Raman Microspectroscopy

Alireza Sanaeifar^{1,2}, Dapeng Ye¹, Xiaoli Li^{1,2*}, Liubin Luo², Yu Tang³ and Yong He²

¹ Fujian Colleges and Universities Engineering Research Center of Modern Agricultural Equipment, Fujian Agriculture and Forestry University, Fuzhou, China, ² College of Biosystems Engineering and Food Science, Zhejiang University, Hangzhou, China, ³ Academy of Interdisciplinary Studies, Guangdong Polytechnic Normal University, Guangzhou, China

OPEN ACCESS

Edited by:

Nam-Hai Chua,
Temasek Life Sciences Laboratory,
Singapore

Reviewed by:

Wei Zeng,
Zhejiang Agriculture and Forestry
University, China
Gajendra Pratap Singh,
Singapore-MIT Alliance for Research
and Technology (SMART), Singapore

*Correspondence:

Xiaoli Li
xiaolili@zju.edu.cn

Specialty section:

This article was submitted to
Technical Advances in Plant Science,
a section of the journal
Frontiers in Plant Science

Received: 31 December 2021

Accepted: 25 March 2022

Published: 18 April 2022

Citation:

Sanaeifar A, Ye D, Li X, Luo L,
Tang Y and He Y (2022) A
Spatial-Temporal Analysis of Cellular
Biopolymers on Leaf Blight-Infected
Tea Plants Using Confocal Raman
Microspectroscopy.
Front. Plant Sci. 13:846484.
doi: 10.3389/fpls.2022.846484

The objective of the present study was to characterize the temporal and spatial variation of biopolymers in cells infected by the tea leaf blight using confocal Raman microspectroscopy. We investigated the biopolymers on serial sections of the infection part, and four sections corresponding to different stages of infection were obtained for analysis. Raman spectra extracted from four selected regions (circumscribing the vascular bundle) were analyzed in detail to enable a semi-quantitative comparison of biopolymers on a micron-scale. As the infection progressed, lignin and other phenolic compounds decreased in the vascular bundle, while they increased in both the walls of the bundle sheath cells as well as their intracellular components. The amount of cellulose and other polysaccharides increased in all parts as the infection developed. The variations in the content of lignin and cellulose in different tissues of an individual plant may be part of the reason for the plant's disease resistance. Through wavelet-based data mining, two-dimensional chemical images of lignin, cellulose and all biopolymers were quantified by integrating the characteristic spectral bands ranging from 1,589 to 1,607 cm^{-1} , 1,087 to 1,100 cm^{-1} , and 2,980 to 2,995 cm^{-1} , respectively. The chemical images were consistent with the results of the semi-quantitative analysis, which indicated that the distribution of lignin in vascular bundle became irregular in sections with severe infection, and a substantial quantity of lignin was detected in the cell wall and inside the bundle sheath cell. In serious infected sections, cellulose was accumulated in vascular bundles and distributed within bundle sheath cells. In addition, the distribution of all biopolymers showed that there was a tylose substance produced within the vascular bundles to prevent the further development of pathogens. Therefore, confocal Raman microspectroscopy can be used as a powerful approach for investigating the temporal and spatial variation of biopolymers within cells. Through this method, we can gain knowledge about a plant's defense mechanisms against fungal pathogens.

Keywords: leaf blight disease, tea, confocal Raman microspectroscopy, wavelet transform, chemical imaging

INTRODUCTION

Almost every country in the world consumes tea on a daily basis, making it one of the top three most popular beverages in the world. There are many diseases affecting tea crops, and one of the most serious is tea leaf blight, caused by *Colletotrichum camelliae* Massee (Wang et al., 2016). Typically, anthracnose appears 5–18 days after infection and the affected leaves wither as a result of the damage caused by the development of the lesion (He et al., 2019). Plants that are infected with a pathogen take numerous protective measures to protect themselves. A plant disease resistance can be divided into two categories: organizational structure resistance and chemical resistance. The organizational structure resistance includes the cuticular layers, cork layers, abscission layers, tylose, gum, and so on, while the chemical resistance includes phenolic compounds, phytoalexins, hypersensitive reactions, pathogenesis-related proteins, and so forth (Lu et al., 2018).

In the prevention of fungal diseases, phenolic compounds play a vital role as a kind of chemical resistance. These compounds have the ability to kill pathogens and postinfection productions. The antimicrobial properties of certain phenolic compounds were highlighted recently in a number of studies (Korukluoglu et al., 2008; Mikulic-Petkovsek et al., 2013). Lignin is one of the most significant phenolic compounds. Plant lignins are primarily involved in supporting organs, transmitting sap through lignified parts of the plant's vascular system, and serving as defensive compounds (Etesami and Jeong, 2018; Soderberg et al., 2021). A reduction in lignin content in crop plants can adversely impact lodging resistance and disease resistance (Pedersen et al., 2005). It has been reported that both abiotic and biotic stresses stimulate some defense genes, including peroxidase, polyphenol oxidase, and phenylalanine aminoamylase, which together are responsible for the formation of lignin within plants (Anand et al., 2009; Shinde et al., 2018). To prevent pathogens from progressing further, lignin forms cork layers around the site of infection. Additionally, tylose is also an important structure found in the infected tissues of the vascular bundle, which consists of hemicellulose, cellulose, and pectin (Pegg et al., 2020; Kashyap et al., 2021). Tylose can affect the vascular bundle by blocking it, thereby preventing infection. Additionally, gum can also provide some resistance to infection by acting on the site of infection (Kashyap et al., 2021). Several studies have demonstrated that biopolymers such as lignin or other phenolic compounds, as well as cellulose or other polysaccharides are adapted to the process of disease resistance in plants. However, the temporal and spatial changes of these biopolymers at the cellular level as a result of infective development are unclear. As a result, further studies are necessary in order to clarify the role of these biopolymers in disease resistance.

There are many conventional chemical analyses that are routinely performed on certain biopolymers, such as high performance liquid chromatography (Mikulic-Petkovsek et al., 2013), but these methods are in most cases invasive and use a large quantity of chemical reagents in order to determine the results (Bellaloui et al., 2012). It should be noted that all of these methods require disintegration of the plant tissues, so

only information about composition can be determined, not micromolecular structure and distribution. Also, the distribution of lignin can be determined using an electron microscope (Kiyoto et al., 2018; Polo et al., 2020). The problem is that no domain information can be collected simultaneously, and staining technology must be used in conjunction with microscopes in order to get distribution information. Therefore, a quantitative and qualitative analysis technology should be developed for future research.

Raman microspectroscopy technique has shown a great deal of promise in finding out compositional, structural and spatial information about cellular polymers, due to its high spatial resolution and spectral fingerprint response characteristics (Zhao et al., 2019; Mateu et al., 2020; Saletnik et al., 2021). A remarkable perspective on visualizing cellular walls can be gained by Raman microspectroscopy, which provides detailed information about the physical properties and chemical composition of the cell wall in plants (Pohling et al., 2014). It has also been used to investigate the structure of different types of vascular cells in plants, which are highly complex tissues subject to substantial changes during growth (Jin et al., 2018). This technique has been successful in revealing the spatial and structural characteristics of lignin and cellulose (Ji et al., 2013; Kanbayashi et al., 2019). The Raman peak associated with lignin appears approximately at $1,600\text{ cm}^{-1}$ since the lignin molecule is composed of aromatic ring vibrations which are in symmetry (Gierlinger and Schwanninger, 2006). Furthermore, Raman microspectroscopy can be used to assess changes in lignin composition during plant lignification (Littlejohn et al., 2015), as well as assess differences in lignin distribution and intensity within the walls of different types of xylem cells (Wang et al., 2021). However, there has been no research to our knowledge that has utilized Raman spectroscopy to investigate the time and spatial variations of lignin and cellulose in cells infected with fungal pathogens.

Raman spectroscopy of biological tissues typically produces low-energy signals that are disturbed by noise and fluorescence background. The background-signal contribution is usually reduced by hardware methods at the stage of detection or numerical methods at the stage of data processing (Zeng et al., 2021). However, hardware techniques tend to be inconvenient and costly (Adami and Kiefer, 2013). There are several ways to eliminate background noise, such as direct or modified polynomial fitting and subtraction (Beier and Berger, 2009), rolling-circle spectral filtering (Brandt et al., 2006) and so forth. However, all of these methods of background data reduction are not capable of handling large amounts of data. In order to perform each spectroscopy correction, a special polynomial or circle radius is required, which leads to large mathematical calculations and a disunity calibration reference. Wavelet transform (WT) has been widely used for the denoising and background removal in Raman spectroscopy (Ma et al., 2018; Chi et al., 2019). In general, the WT process is a mathematical algorithm that is capable of localizing signals both on a time and frequency scale. It is also possible for part of the inherent information to be found within a particular sub-space of WT. There is a kind of WT called the discrete wavelet transform (DWT) in which the wavelets are discretely sampled. DWT is

a well-established method for improving resolution via spectral denoising and baseline removal (Chen et al., 2011). Researchers in the field of Raman spectroscopy have recently suggested the use of DWT as an ideal strategy for denoising and removing background noise. It has the greatest advantage that bulk data can be processed according to a unified wavelet structure (Tavassoli et al., 2020; Sharan et al., 2021).

It was the objective of the present study to demonstrate the potential of confocal Raman microspectroscopy and the data mining method DWT for the detection of temporal and spatial variation of biopolymers in tea cells induced by leaf blight infection along with the time period of infection for determining the causes of this variation. It is a cutting-edge analytical tool which is capable of imaging lignin and cellulose *in situ*. Our research opens up a novel way of studying plant disease resistance at the cellular scale without involving destruction of the plants.

MATERIALS AND METHODS

Preparation of Tea Samples

We grew tea seedlings [*Camellia sinensis* (L.) O. Kuntze] of the variety Longjing 43 in pots under natural light, temperature, and manual water conditions for nearly 1 year. In order to confirm that the chosen tea was healthy and free from any fungus infection, the samples were cultivated in a climate incubator (DRX-1200, Hangzhou Runbo Experimental Equipment Co. Ltd., Hangzhou, China) at a fixed temperature (25°C) and humidity (90%) for 10 days. If the plant showed no signs of disease, the plant was chosen for the subsequent infection experiment; otherwise, this procedure was repeated until the plant was healthy. This procedure was followed in order to select healthy tea plants. The fungus (*Colletotrichum camelliae* Massee) was supplied by the Agricultural Experiment Station of Zhejiang University. The mycelium block was inoculated on the tea leaf 4 days after activation. Afterward, the inoculated tea was grown in an incubator for 10 days at a temperature of 28°C and with a relative humidity of 90%.

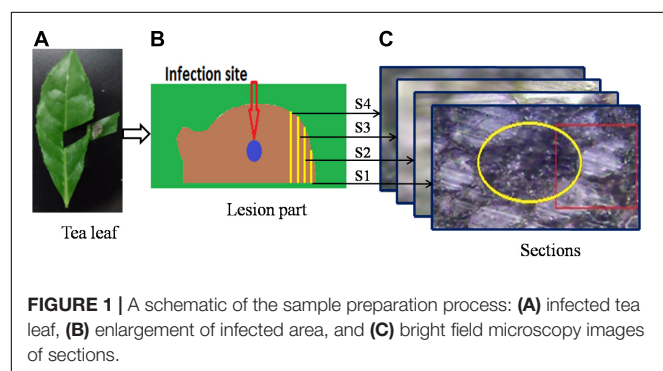
The lesion part (Figure 1B) was then cut from the tea leaf (Figure 1A), and prepared for resin embedding in accordance with the following steps. (1) Double fixation: first, the specimen was fixed with 2.5% glutaraldehyde in phosphate buffer (pH 7.0) for more than 4 h, and then it was washed three times in the

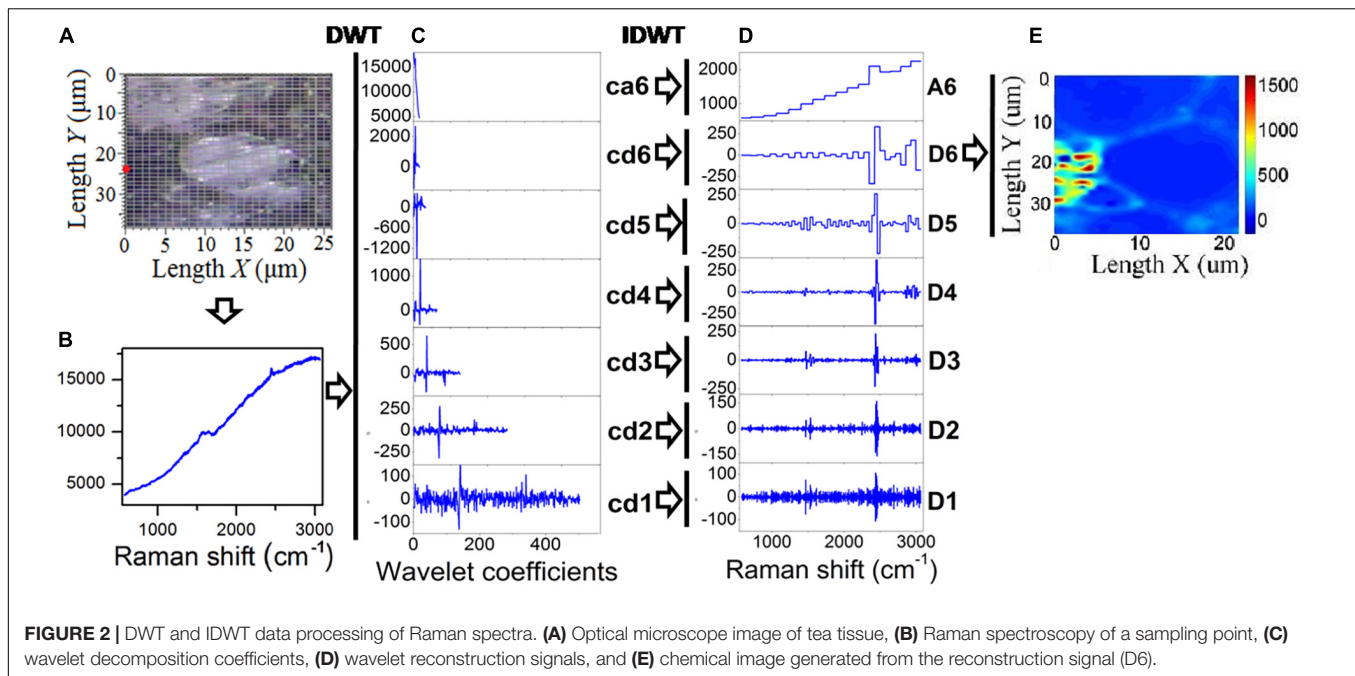
phosphate buffer after it had been fixed; finally, the specimen was postfixed with 1% OsO₄ in phosphate buffer (pH 7.0) for an hour. (2) Dehydration: a series of increasing concentrations of ethanol was used to dehydrate the specimen (50, 70, 80, 90, 95, and 100%). About 15–20 min were spent in each step, then the solution was transferred to absolute acetone. (3) Infiltration: in a 1:1 mixture of absolute acetone and the final spurr resin mixture, the specimen was dissolved for 1 hour at room temperature. Afterward, the mixture was treated with acetone-resin (1:3) for 3 h and left overnight. (4) Embedding and semithin sectioning: in capsules containing embedding medium, specimens were heated at 70°C for approximately 9 h. A microtome (Thermo Fisher Finesse 325 paraffin) was used to cut sections of 5 µm thick without further processing. The cutting direction was edge toward the infection site. Four sections were selected for Raman spectroscopy, and each section was separated by about 50 µm. Figure 1 illustrates the process of sample preparation. The schematic diagram of the infected part and the locations of four sections are shown in Figure 1B. The infection site was at the center of the lesion part (represented with a blue circle in Figure 1B). The sectioning was done from the edge to the center. Accordingly, S1 was designated as the first section, namely the shortest infection time and the slightest extent of infection. The second, third, and fourth sections were labeled S2, S3, and S4, respectively. Within these four sections, S4 had the longest infection period and the most serious degree of infection.

Spectroscopy Acquisition

A confocal Raman microspectrometer (Renishaw, United Kingdom/Via-Reflex 532/XYZ) equipped with a diode-pumped solid state laser (50 mW at 532 nm) was applied to collect the spectra. The use of 532 nm wavelength excitation to analyze cellulose and lignin contributions has demonstrated that the signal from these biomolecules can be used for detailed analysis of the cell wall, despite the non-bleaching selectivity. The comparative analysis of NIR (785 nm)-excited versus 532 nm-excited Raman spectra of the same samples indicated that imaging and characterization of cellular walls may yield greater advantages from high scattering at the visible wavelength, rather than from low bleaching at the NIR wavelength (Heiner et al., 2018; Zeise et al., 2018).

The laser power applied to the sample was 0.5 mW, and the incident laser beam was focused onto the sample surface with a 50× objective lens at 0.75 numerical aperture. During the mapping process, an integration time of 10 s and steps of 1 µm were assigned, and every pixel was represented by a single scan. The four sections were scanned near the vascular bundle, which can be seen in Figure 1C, where the yellow circle represents the vascular bundle and the red rectangle represents the scanning area. The Raman spectrometer was configured to map the Raman spectral data with a spatial resolution of 1 µm in both horizontal and vertical directions. Due to the differences in tissue types, the scanning extent varied for the different sections, with 1,053, 735, 936, and 780 points for the S1, S2, S3, and S4 sections, respectively. For the purpose of removing background, a Raman spectroscopy of pure spurr resin was also performed.





Discrete Wavelet Transform

As explained in the introduction, DWT provides an extremely useful method to remove Raman background information. In wavelet analysis, signals are decomposed into discrete levels of resolution, which is known as multi-resolution. Due to the fact that the background consists primarily of low-frequency features, this background is removed from the spectrum. To denoise a specific Raman signal, in addition to the DWT for decomposition (analysis), an inverse DWT (IDWT) is also applied for reconstruction (synthesis; Li et al., 2020). Sub-band filters can be used to decompose and reconstruct wavelets. A schematic view of a WT used in the present study for minimizing the effects of fluorescence in Raman chemical imaging is shown in **Figure 2**. **Figure 2A** illustrates the Raman spectral scanning region of healthy tea tissue, where each grid point represents a sampling point. **Figure 2B** shows a Raman spectral response curve for a sample circled with a red line in **Figure 2A**, and this sample is taken as an example to illustrate the inhibition of fluorescence by WT. The Daubechies 1 wavelet was adopted for decomposition and reconstruction in this study, and then seven wavelet decomposition coefficients were calculated as a_6 , d_6 , d_5 , d_4 , d_3 , d_2 , and d_1 , as seen in **Figure 2C**. Following this, seven wavelet reconstruction signals (A_6 , D_6 , D_5 , D_4 , D_3 , D_2 , and D_1) were computed by IDWT from the corresponding wavelet decomposition coefficients, as shown in **Figure 2D**. As illustrated in **Figure 2E**, the Raman chemical image can finally be derived from the wavelet reconstructed signal (D_6) for all sampling points.

The optimization approach for chemical imaging was implemented in three steps in this study. The first step involved wavelet decomposition of the signal, followed by wavelet reconstruction, and the third step involved

integrating the biopolymer feature bands based on the reconstruction structure D_6 .

RESULTS

Raman Spectrum of Leaf Blight-Infected Tea Tissue

Raman spectral scanning includes the vascular system, and vascular bundles are tightly surrounded with bundle sheath cells as shown in **Figure 1C**. The details of the scanning regions of the four sections and their typical Raman spectral responses are shown in **Figure 3**.

Figures 3A,C,E,G show the bright-field microscopy images of scanning areas of the S1, S2, S3, and S4, respectively, the tissues within the yellow ellipse represent the vascular bundles, whereas the tissues within the red ellipse represent the bundle sheath cells. Also, **Figures 3B,D,F,H** show the Raman spectra of the sampling points along the horizontal black line in each scanning area. It is important to note that these black lines traverse both vascular bundles and bundle sheath cells. According to **Figure 3B**, the Raman intensity of the vascular bundle lying on the black line is much larger, up to 3.5×10^4 . However, the Raman intensities of the other sampling points are almost equal to zero. Accordingly, it is concluded that there is a substantial difference between the Raman spectral response of vascular bundle and bundle sheath cells in the S1 section. The Raman spectral intensity of the vascular bundle is still higher than that of the bundle sheath cell in the S2 section, although the difference is less than that of the S1 section (**Figure 3D**). The Raman spectral intensity of the vascular bundle is shown in **Figure 3F** to be greatly reduced, while the Raman spectral intensity of the bundle sheath cell is highly increased, and the difference

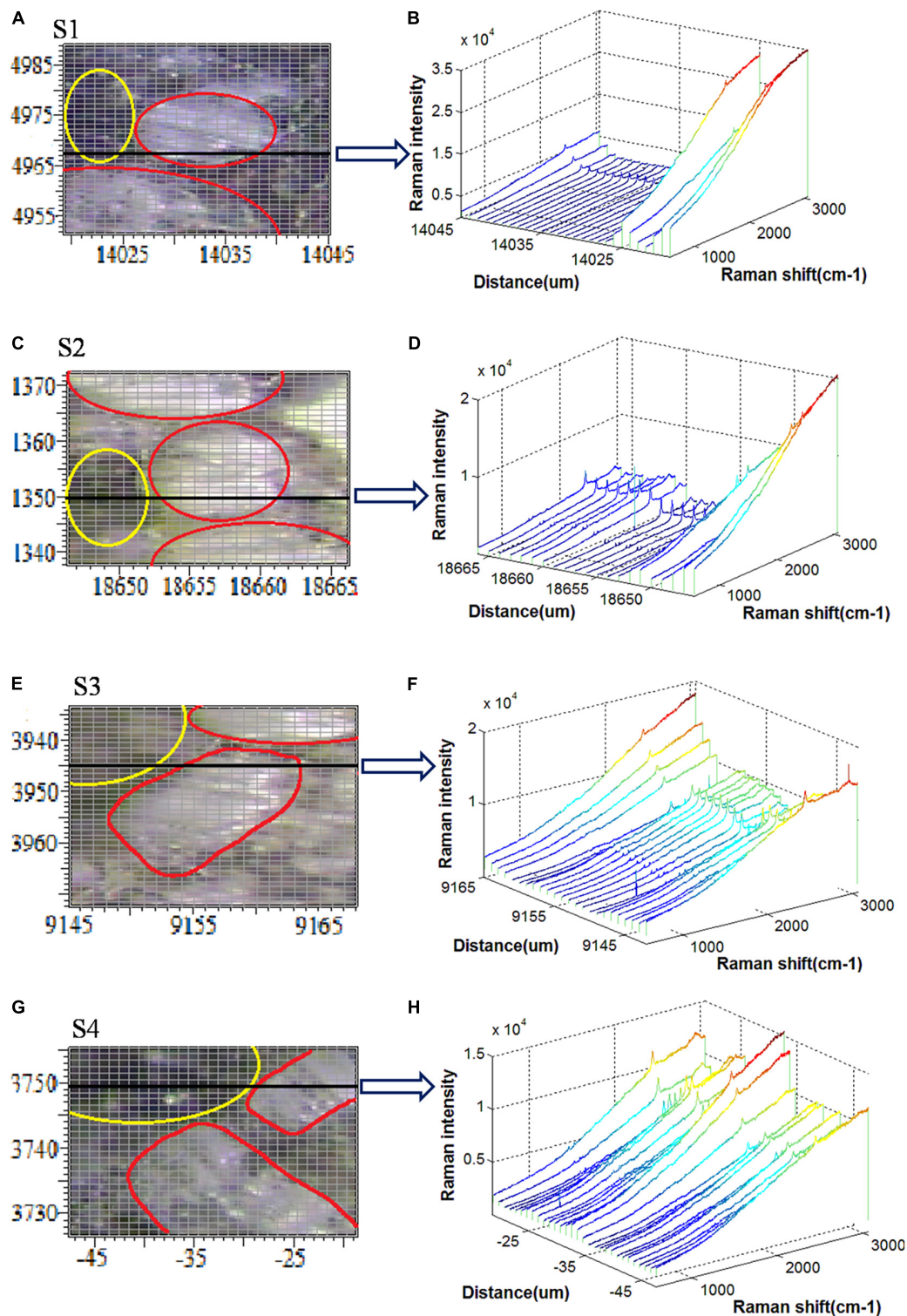


FIGURE 3 | Raman spectral scanning regions and spectral responses for (A,B) S1, (C,D) S2, (E,F) S3, and (G,H) S4.

between the two is further reduced in the S3 section. As shown in **Figure 3H**, the Raman spectral intensities in the bundle sheath cell and the vascular bundle are comparable in the S4 section.

Generally, the Raman intensity of the vascular bundles in the four sections is relatively high, which may be attributed to the high lignin content of the vascular bundles (Richter et al., 2011).

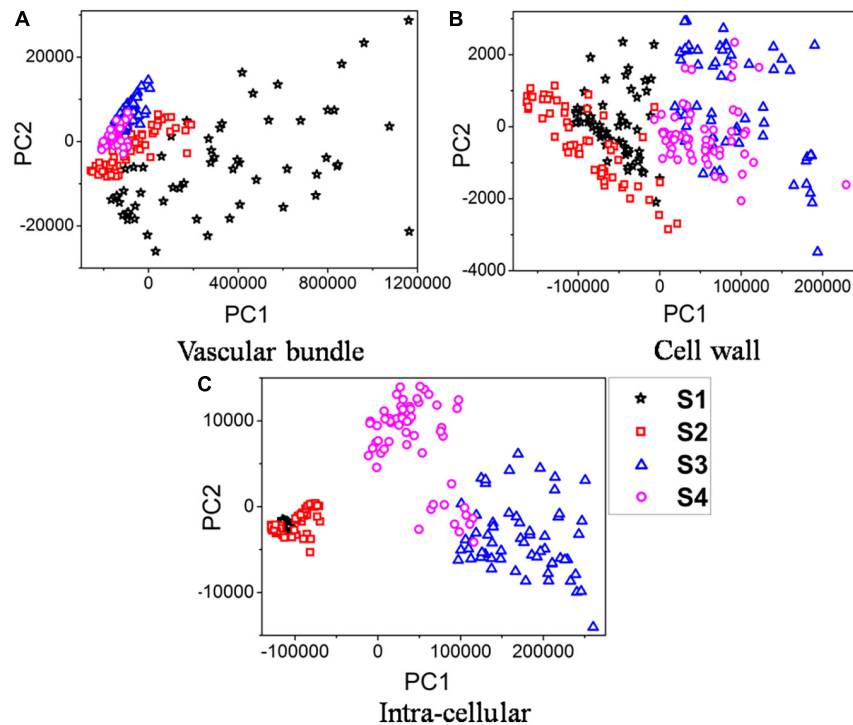


FIGURE 4 | PCA plots of samples infected over time. **(A)** Vascular bundle. **(B)** Cell wall. **(C)** Intra-cellular.

Also, the Raman intensities of vascular bundles are ranked in descending order as S1, S2, S3, and S4 indicating that the lignin and other biopolymers decreased from S1 to S4 along with an increase in infection severity. In addition, it is noteworthy that the Raman spectral response differences of the vascular bundle and bundle sheath cells gradually decrease from S1 to S4, indicating that the differences in structure and composition between these two types of tissues are gradually diminishing as the disease severity increases. It may be because the pathogen destroys the ordered structure of these tissues and decomposes many of the biopolymers that compose their cell walls.

Principal Component Analysis-Based Temporal Classification of Infection

An overview of the temporal and spatial comparisons of four sections was presented in the previous section. In order to have a detailed temporal analysis of these sections, Raman spectra of the same tissue in four different sections were selected. There are two parts to the bundle sheath cell, namely, the cell wall and the inside of the cell. As the proportion of vascular bundles was small in the scanning region, the analysis was conducted on the whole bundle. In this regard, three different parts were distinguished: the cell wall of the bundle sheath cell, the inside of the bundle sheath cell, and the vascular bundle. As shown in **Figure 3**, 60 points were recorded for each part. Sample points for the vascular bundle were selected within the yellow circles, samples for the cell wall were selected along the edge of the red lines, and samples for intracellular were selected within the red areas.

To simplify the data visualization process, principal component analysis (PCA) was first used to re-express the original Raman signals. In three different parts, 240 Raman spectral samples in sections S1, S2, S3, and S4 were analyzed using PCA. The PCA was applied to the Raman spectral region of $579\text{--}3,062\text{ cm}^{-1}$. **Figures 4A–C** illustrate the results of PCA analyses for the first two principal components (PC1, PC2) of the vascular bundle, cell wall, and intracellular components, respectively.

Results indicated that the first two components, in three separate parts, contained over 99% of the data variance in classification based on four different stages of infection. **Figure 4A** indicates that the vascular bundle signal in S1 is quite different from that in the other three sections, with a more scattered distribution. The reason is that the Raman spectra of vascular bundles in S1 were significantly higher than those of S2, S3, and S4 (see **Figure 3**). Additionally, since the vascular bundle itself is composed of xylem and phloem, these 60 spectra are scattered throughout due to the fact that the vascular bundle itself is composed of various structures and substances. However, the vascular bundle spectra of S2, S3, and S4 were more concentrated, indicating that the structures of the bundle were not greatly different. It is possible that the structure has been damaged in these sections. This conclusion is in accordance with the results in the previous section. According to **Figure 4B**, the boundary between these four sections was not clearly defined, there were some overlaps. Specifically, the S1 overlapped the S2 and the S3 overlapped the S4. However, the boundary of S1 and S2 was clearly distinct from S3 and S4,

indicating the composition of the cell wall in S3 and S4 was clearly different from S1 and S2. Also, in **Figure 4C**, the boundary was clearly defined, except in S1 and S2. The analysis revealed the components of S1 and S2 inside the cell were similar, but they differed greatly in S3 and S4. In spite of overlaps in the PCA score plots, the clustering results were satisfactory. Thus, the extracted two principal components were able to reveal Raman spectral features in the vascular bundle, cell wall, and intracellular structures of the four sections, ensuring effective identification. Furthermore, the principal component distribution indicates that Raman spectroscopy can reflect differences in four sections, i.e., Raman spectroscopy is capable of recognizing four sections.

Analysis of Raman Spectra Based on Characteristic Peaks

It is essential to determine the characteristic peaks of the background before analyzing the distribution of biopolymer in tea cells. Due to the presence of spurr resin in a semi-thin transverse section of the tea tissue, background disturbance from the spurr resin must be removed. **Figure 5** shows representative Raman spectra of vascular tissue and its background. The spectrum of the vascular tissue is randomly selected from the vascular bundle on the first section in **Figure 3A** marked with a yellow circle, while the spectrum of the background comes from the pure spurr resin. For removing fluorescence interference and highlighting the signal, polynomial fitting and subtracting were employed. There were six main peaks in the resin, which could interfere with the analysis of the sample. Especially the peak at $1,664\text{ cm}^{-1}$, which is also included in the sample. The spectroscopy of the vascular bundle generated a strong and broad peak at $1,600\text{ cm}^{-1}$. This peak may be comprised of four peaks: $1,570$, $1,600$, $1,630$, and $1,660\text{ cm}^{-1}$. These last three peaks were related to lignin. The $1,600\text{ cm}^{-1}$ was assigned to aromatic ring mode, the $1,630\text{ cm}^{-1}$ to ring conjugated C=C stretching of coniferaldehyde, and the $1,660\text{ cm}^{-1}$ to ring conjugated C=C stretching of coniferyl alcohol (Hänninen et al., 2011; Mateu et al., 2020). It is noteworthy that these three peaks appeared in all phenolic compounds. There was also a peak at

$1,214\text{ cm}^{-1}$ corresponding to aryl-O of aryl-OH and aryl-O-CH₃ and guaiacyl ring mode (with C=O group) that was related to lignin. The peak at 900 cm^{-1} was associated with bending of HCC and HCO at C6, and the signal around $1,000\text{ cm}^{-1}$ was associated with heavy atom stretching (CC and CO; Adapa et al., 2009). The two peaks were related to cellulose. The peak at $1,110\text{ cm}^{-1}$ may consist of two peaks ($1,095$ and $1,123\text{ cm}^{-1}$), which were related to cellulose as well. Additionally, these peaks corresponded to the highest polysaccharide levels. Signals at $1,335\text{ cm}^{-1}$ were caused by HCC and HCO bending or by aliphatic O-H bending. Both lignin and cellulose showed signals at this wavelength (Adapa et al., 2009). Since the resin possesses a peak at $1,660\text{ cm}^{-1}$ as well, it was selected as a standard peak for semi-quantitative comparisons. It should also be mentioned that the sharp peak around $2,400\text{ cm}^{-1}$ that was caused by noise has been removed as it represents a spurious peak from the spectrometer.

Following this, biopolymer analysis was conducted on three positions, namely the vascular bundle, the cell wall, and the intracellular. According to the results of the PCA, Raman spectroscopy can demonstrate differences in the four sections. Raman spectroscopy was averaged to simplify the analysis, and then polynomial fitting and subtracting were implemented to eliminate fluorescence interference and highlight the signal.

Figure 6A shows the spectrum of the vascular bundle from S1 to S4. In **Figure 6B**, a semi-quantitative analysis was performed and a standard peak at $1,660\text{ cm}^{-1}$ was chosen as a baseline in order to make an accurate comparison. From S1 to S4, the Raman intensity of $1,600$ and $1,630\text{ cm}^{-1}$ that corresponded to lignin decreased. This finding revealed that the more severe infection within the vascular bundle resulted in less lignin content. In this case, it may be because the structure of the vascular bundle was damaged by the pathogen, causing the lignin to be distributed irregularly. A small amount of lignin might be expelled from the vascular bundle; therefore, the content of lignin in the vascular bundle was reduced. The decomposition of lignin caused by fungi is another cause for the reduction of lignin. Research has previously revealed that certain fungi have the capacity to decompose lignin (Wei, 2012). In contrast, the peaks relating to cellulose, such as 900 and $1,000\text{ cm}^{-1}$, were increased from S1 to S4. In other words, the maximum cellulose content was located in the most serious section. This was due to the fact that, when a pathogen invades the vascular bundle, the xylem will produce a substance called tylose, consisting of cellulose, hemicellulose, and pectin. The vascular bundle was damaged by the pathogen, thus the defense structure tylose was produced to block the vessels and prevent the spread of the invasion.

The spectrum of the cell wall from S1 to S4 is shown in **Figure 7A**, and the semi-quantitative analysis is shown in **Figure 7B**. It was shown that the Raman intensities of $1,630$ and $1,600\text{ cm}^{-1}$ increased first and then decreased slightly, which was different from the variation trend in vascular bundles. This may be due to the plant's inherent resistance to stress. To avoid further damage, the plant may increase its lignin content (Chérif et al., 1991). The Raman intensities of cellulose were initially decreased and then increased. The reduction of cellulose in cell walls may be a result of pathogen decomposition. In S3 and S4, however,

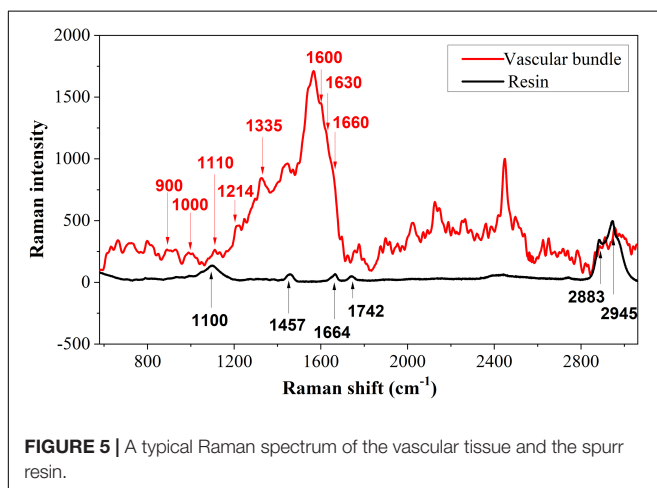
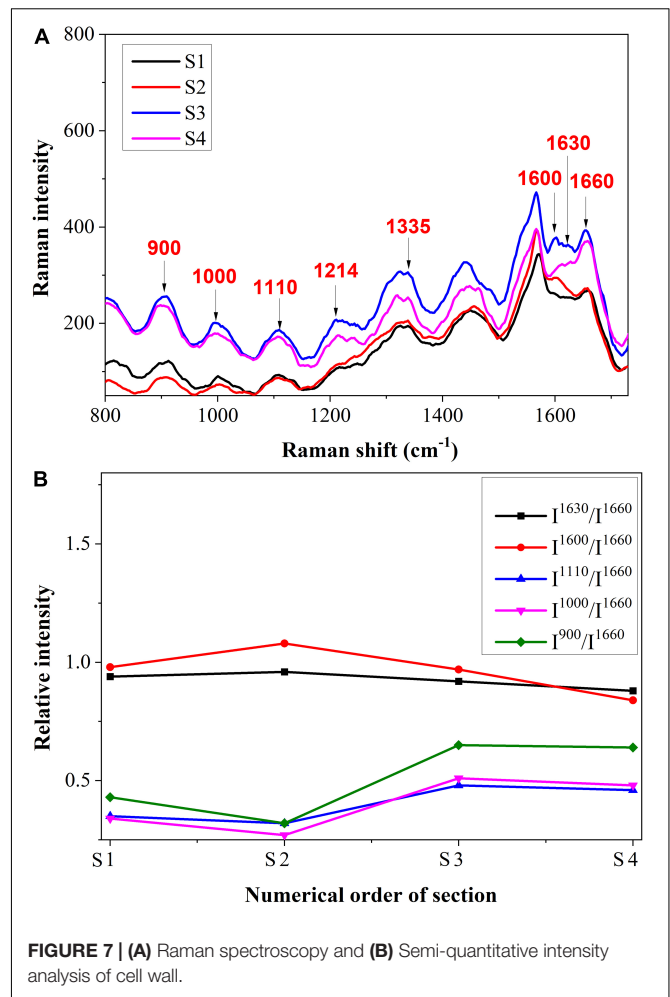
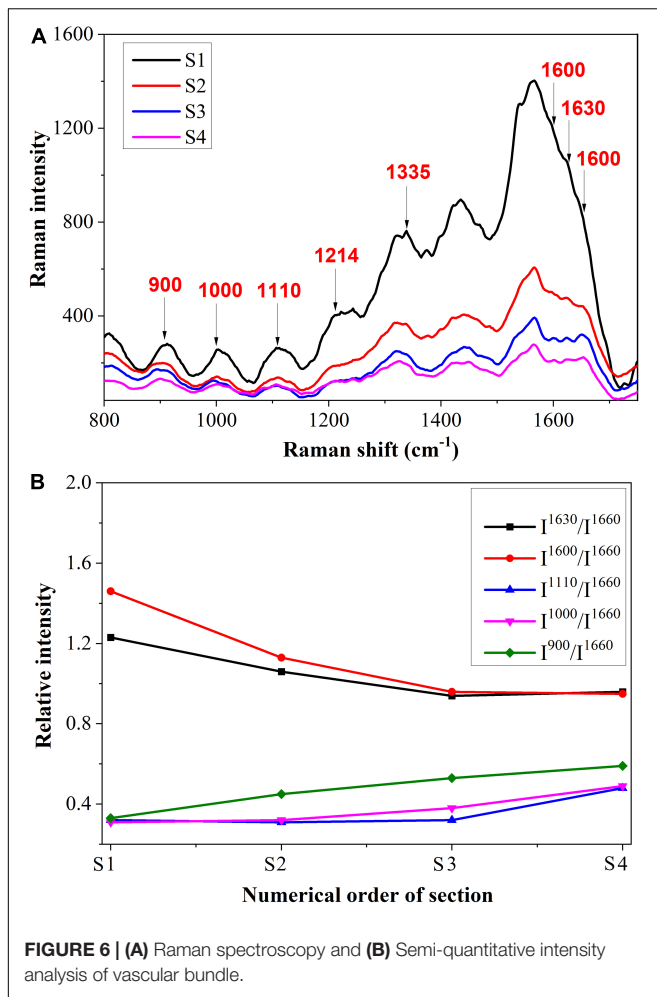


FIGURE 5 | A typical Raman spectrum of the vascular tissue and the spurr resin.

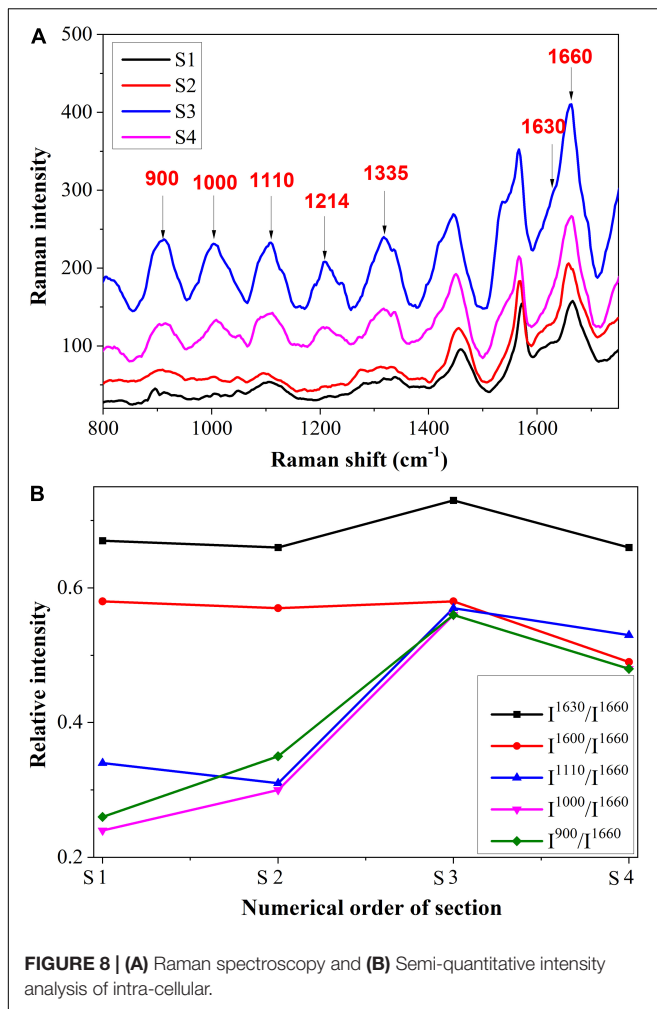


the content increased, which may be due to the emergence of some new substances. In previous research, it was reported that hydroxylproline-rich glycoproteins are present in cell walls to protect them against pathogens (Deepak et al., 2008).

In **Figure 8A**, we present the intracellular spectrum from S1 to S4, and **Figure 8B** shows the semi-quantitative analysis. As can be observed, there was a similar variation trend in Raman intensity between the intracellular and the cell wall. There was an increase in intensity at 1,600 and 1,630 cm^{-1} , followed by a decrease. As the Raman shifts at these two peaks are observed in all phenolic compounds, this may indicate that the amount of phenolic compounds within the cell was increased. In addition to their role in the prevention of fungal diseases, phenolic compounds also exert toxic effects on pathogens and their postinfection activities (Korukluoglu et al., 2008; Mikulic-Petkovsek et al., 2013). Thus, the presence of phenolic compounds also contributed to the plant's active resistance. In addition, the Raman bands at 900, 1,000, and 1,110 cm^{-1} increased first and then decreased. This may be due to another organizational structure resistance, namely gum, which contains substances such as cellulose, semi-cellulose, lignin, etc. Gum also functions to prevent pathogens from spreading further (Kashyap et al., 2021).

Raman Chemical Imaging of Biopolymers

As the scanning regions contain thousands of Raman spectra, DWT was applied to remove the noise and fluorescence interference from the spectra. The chemical images of lignin and cellulose were reconstructed using DWT. The lignin band of 1,600 cm^{-1} which was assigned to aromatic ring mode was used to establish chemical images. In order to visualize the chemical image of lignin, spectral intensity from 1,589 to 1,607 cm^{-1} was integrated. Furthermore, the chemical image of cellulose was produced with a range of intensities from 1,087 to 1,100 cm^{-1} . Also, the CH-stretching region between 2,980 and 2,995 cm^{-1} , which was assigned to all polymers, such as cellulose, hemicellulose, pectin and lignin, was used to establish chemical images (Gierlinger and Schwanninger, 2006). The chemical images of the four sections are illustrated in **Figure 9**, and the white arrowheads indicate the vascular bundles. The distribution of lignin in the slightest infected area is almost limited to the vascular bundles and the corner of the bundle sheath cell wall (**Figure 9B**). As shown in **Figure 9C**, there is a distribution of cellulose in the vascular bundle as well as in the entire bundle sheath cell wall. Additionally, the distribution



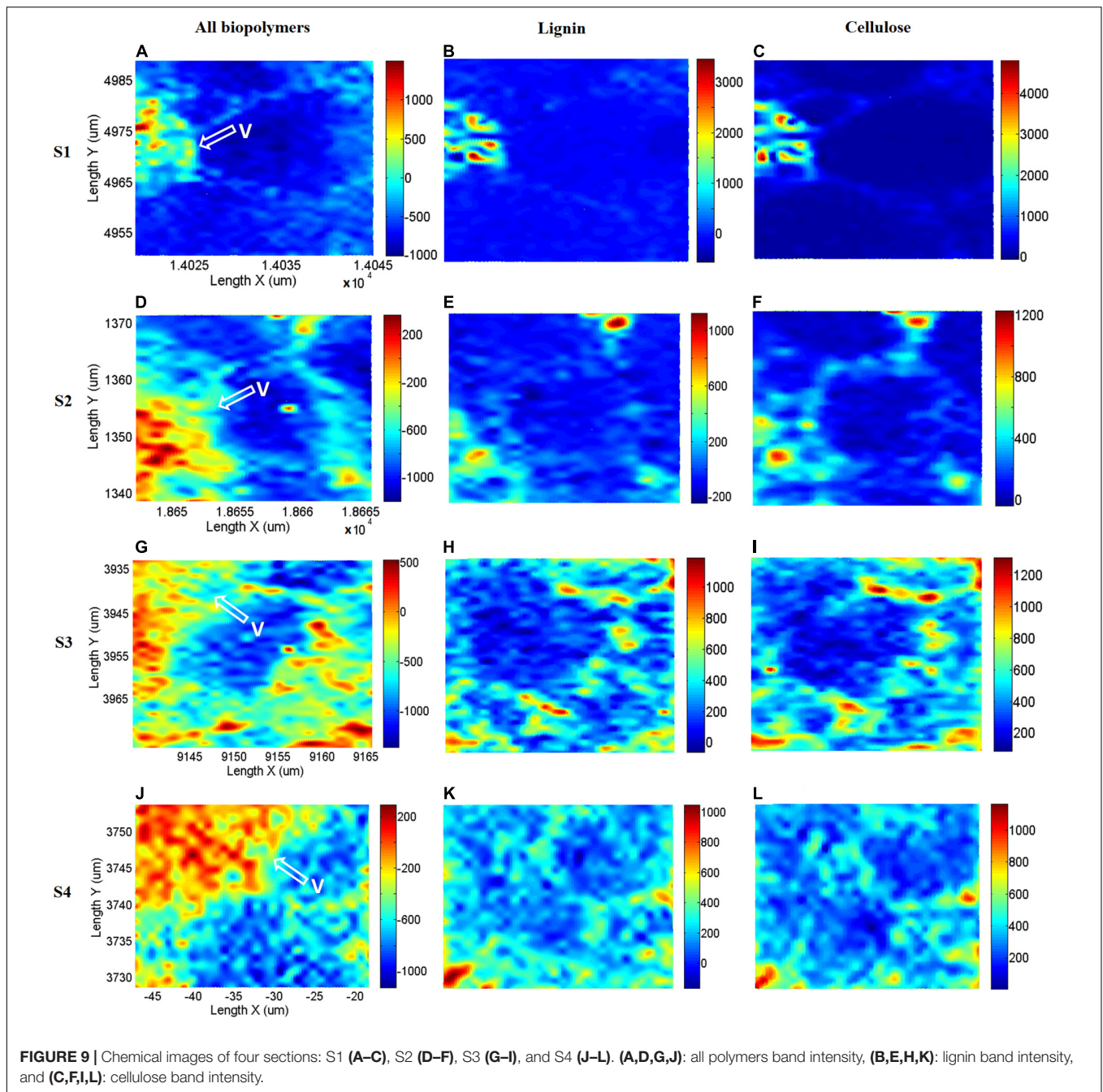
area of all biopolymers (**Figure 9A**) was greater than that of lignin and cellulose due to the presence of hemicellulose and pectin. As the extent of infection was increased in **Figure 9E**, the distribution of lignin in the vascular bundle became irregular. In addition to the corner of the bundle sheath cell, lignin is produced throughout the entire cell wall. **Figure 9F** shows that the distribution of cellulose was similar to that of lignin. The distribution of all biopolymers (**Figure 9D**) revealed that there was an accumulation in the vascular bundle. It is shown in **Figure 9H** that most lignin is distributed in the cell wall, and the structure of the vascular bundle is damaged, therefore the amount of lignin in the bundle is reduced as compared to **Figures 9B,E**. In addition, an abundance of lignin or phenolic compounds accumulated inside the cell. The distribution of cellulose (**Figure 9I**) was also extended to the intracellular space. As shown in **Figure 9G**, the photochemical image of biopolymers shows cellulose, hemicellulose, pectin, and lignin are abundantly produced. Lastly, in the most seriously infected section, lignin or other phenolic compounds (**Figure 9K**), as well as cellulose (**Figure 9L**) were scattered throughout the scanning region. Moreover, a significant amount of biopolymers were accumulated

(**Figure 9J**) in the vascular bundle, which was associated with the formation of tylose.

DISCUSSION

While it is known that lignin, phenolic compounds, tylose, and other biopolymers contribute substantially to plant disease resistance, their temporal and spatial variations with the development of infection have not been well investigated. Confocal Raman microscopy was used in this study for the analysis of biopolymers on a micrometer scale. There was a clear visualization of the spatial distribution of the lignin. Using semi-quantitative analysis, it was found that the Raman intensities of lignin decrease gradually from S1 to S4, while cell wall and intracellular Raman intensities increase. There was also an increase in cellulose content in the vascular bundle as well as in the cell wall and intracellular spaces. This may be due to the fact that in the vascular bundle, there is primarily resistance provided by hemicellulose, cellulose or pectin, specifically by tylose. In the bundle sheath cell, both biopolymers contribute to the resistance factor. There was a rising trend in both **Figures 7B, 8B**. Variations can be caused by antimicrobial polymers such as phenolic compounds, hydroxyproline-rich glycoproteins, gum, etc. It should be noted that the semi-quantitative analysis has confirmed the chemical images. The lignin distribution in the vascular bundle has become increasingly irregular from S1 to S4. In this case, the pathogens have caused damage to the structure of the vascular bundle, which has led to a loss of rigidity in the vascular, eventually degenerating and collapsing. The lignin content of the vascular bundle was reduced as a result. Using the CH-stretching region between 2,980 and 2,995 cm^{-1} , the chemical image of all biopolymers containing hemicellulose, cellulose, and pectin determined that these polymers were gradually accumulated in the vascular bundle. In addition, the distribution of lignin in bundle sheath cells demonstrated that in sections where the infection was severe, like S3 or S4, the cells were thick with lignin or phenolic compounds in order to resist pathogen invasion. These results are consistent with previous research. Researchers discovered that phenolic compounds show defense responses characterized by rapid and early accumulation at the infection site, which prevents the pathogen from spreading (Chérif et al., 1991). The formation of lignin was one of the responses to these conditions (Zhao et al., 2019; Mateu et al., 2020; Saletnik et al., 2021). In bundle sheath cells, cellulose was distributed similarly to lignin. This occurred due to the synthesis of various polysaccharides to combat the pathogen, such as hydroxyproline-rich glycoproteins.

It has been shown in our study that the wavelet transform can be highly efficient in reducing low-frequency fluorescence signals that accompanied and interfered with the Raman spectra of plant tissues. This finding was also consistent with other studies that have shown that the wavelet transform eliminates the low-frequency fluorescence signal. Using wavelet coefficients at level 6, the Raman spectral difference between untreated samples and alkali-treated samples of rice straw was quantitatively assessed after residual noise and fluorescent background was removed



(Li et al., 2020). In support of our findings, researchers have indicated that spectroscopic methods combined with DWT analysis offered a rapid and non-destructive approach for estimating integral chemical information (Wang et al., 2018; Yao et al., 2018; Li et al., 2019; Liu et al., 2021). It was possible to perform wavelet transform on spectra using a formula which involves manipulating and adjusting the wavelet function to generate values that distinguish various frequencies. DWT analysis was therefore able to access a larger amount of information embedded within the plant spectrum resulting in an advanced ability to extract information from it.

Although imaging techniques are widely used to analyze cell walls, a thorough understanding of their structure is still lacking. The classic methods for imaging cell walls are to stain or label their chemical components (e.g., using immunolabeling); however, such analyses rely on the results of a large number of mixed samples obtained from enzyme-isolated or pulverized plant tissues (Zhao et al., 2019). Imaging of plant cell walls is performed using classical methods to determine the spatial and temporal changes in polysaccharides within cell walls during the growth process (Hervé et al., 2011; Tobimatsu et al., 2013). However, these techniques have limitations due to

their expense, depth of penetration and spatial resolution, and some of them use fluorescent imaging, which poses challenges due to photobleaching and genetic modifications. In addition, these microscopy approaches are non-quantitative for analyzing cell walls. Confocal Raman microspectroscopy, which does not require stains or fluorescent indicators to operate, has greatly improved label-free imaging and enabled more in-depth and detailed study of the plant cell wall. In addition to measuring cell wall components simultaneously, it also allows observing changes in cell wall morphology (Wu et al., 2016).

It should be noted that this paper has some limitations that can be improved in future research. Increasing the number of sections in this article would provide a comprehensive description of the entire infection process. Furthermore, the scanning area can be large enough to allow for the representation of the entire cell. It is demonstrated in this paper that a novel approach is used to examine the mechanism of plant resistance, which contributes to a better comprehension of biopolymer variations in the process of fungal infection. This is the first time that confocal Raman microspectroscopy has been applied to study the time and spatial variation of damage to the cell wall in fungal-host interactions. The method proposed in this paper is potentially applicable for the *in situ* quantification of polymers in the cell wall structure as well as composition. Researchers can evaluate the damage to the cell walls directly from epidermal tissue using Raman microspectroscopy in the future with the help of laser penetration of microdots infected by pathogens. It has been demonstrated that the microspectroscopy method can provide real-time monitoring of the structure of the poplar cell wall during the process of ethyl-3-methylimidazolium acetate solubilization (Zhang et al., 2014). Accordingly, in this non-destructive *in situ* method, there is no requirement for samples to be cut or significantly altered in order to be measured, thus preserving the integrity of samples.

CONCLUSION

This study used confocal Raman microspectroscopy for the first time to further investigate the temporal and spatial variations of biopolymers observed in tea leaf blight-infected cells. We analyzed the Raman spectra of four sections that show progression of infection in order to conduct a semi-quantitative Raman intensity analysis of biopolymers. PCA was able to reveal Raman spectral signatures in the vascular bundle, cell wall, and intracellular structures of each of the four sections, which enabled Raman spectroscopy to be used to differentiate between the four

sections. A semi-quantitative analysis revealed that the Raman intensities of lignin gradually declined as infection progressed, whereas those of the cell wall and intracellular regions increased. As well, cellulose quantities increased in three parts with infection severity. It was proposed that the wavelet transform could be used for *in situ* Raman chemical imaging. With its excellent multiscale analysis capability, wavelet transform was able to exclude low-frequency fluorescence interference as well as high-frequency cosmic rays from the image. It was found that the two-dimensional chemical images of lignin, cellulose, and all biopolymers are analyzed via wavelet-based data mining based on the acquisition of the characteristic wavelengths ranging from 1,589 to 1,607 cm^{-1} , 1,087 to 1,100 cm^{-1} , and 2,980 to 2,995 cm^{-1} , respectively. The semi-quantitative analysis results were completely consistent with the chemical images that were obtained. Therefore, confocal Raman microspectroscopy can be considered a powerful tool that can be used to analyze cellular biopolymers to identify changes occurring due to fungal infection.

DATA AVAILABILITY STATEMENT

The raw data supporting the conclusions of this article will be made available by the authors, without undue reservation.

AUTHOR CONTRIBUTIONS

AS: writing—original draft, investigation, conceptualization, visualization, formal analysis, and software. DY: methodology and funding acquisition. XL: conceptualization, validation, writing—review and editing, supervision, project administration, and funding acquisition. LL: resources and data curation. YT: data curation. YH: writing—review and editing, supervision, project administration, and funding acquisition. All authors contributed to the article and approved the submitted version.

FUNDING

The research was funded by the National Natural Science Foundation of China (Project No: 31771676, 32171889, and 32071895), Key R&D Projects in Zhejiang Province (Project No: 2022C02044), and Open Research Fund Program of Fujian Colleges and Universities Engineering Research Center of Modern Agricultural Equipment, Fujian Agriculture and Forestry University (Grant No. MAE-201901).

REFERENCES

- Adami, R., and Kiefer, J. (2013). Light-emitting diode based shifted-excitation raman difference spectroscopy (LED-SERDS). *Analyst* 138, 6258–6261. doi: 10.1039/c3an01367g
- Adapa, P. K., Karunakaran, C., Tabil, L. G., and Schoenau, G. J. (2009). *Potential Applications of Infrared and Raman Spectromicroscopy for Agricultural Biomass*. Available online at: <https://cigrjournal.org/index.php/Ejournal/article/view/1081> [Accessed December 23, 2021].
- Anand, T., Bhaskaran, R., Raguchander, T., Samiyappan, R., Prakasam, V., and Gopalakrishnan, C. (2009). Defence responses of chilli fruits to *Colletotrichum capsici* and *Alternaria alternata*. *Biol. Plant.* 53, 553–559. doi: 10.1007/s10535-009-0100-5
- Beier, B. D., and Berger, A. J. (2009). Method for automated background subtraction from raman spectra containing known contaminants. *Analyst* 134, 1198–1202. doi: 10.1039/b821856k
- Bellaloui, N., Mengistu, A., Zobiolo, L. H. S., and Shier, W. T. (2012). Resistance to toxin-mediated fungal infection: role of lignins, isoflavones, other seed

- phenolics, sugars, and boron in the mechanism of resistance to charcoal rot disease in soybean. *Toxin Rev.* 31, 16–26. doi: 10.3109/15569543.2012.691150
- Brandt, N. N., Brovko, O. O., Chikishev, A. Y., and Paraschuk, O. D. (2006). Optimization of the rolling-circle filter for raman background subtraction. *Appl. Spectrosc.* 60, 288–293. doi: 10.1366/000370206776342553
- Chen, D., Chen, Z., and Grant, E. (2011). Adaptive wavelet transform suppresses background and noise for quantitative analysis by raman spectrometry. *Anal. Bioanal. Chem.* 400, 625–634. doi: 10.1007/s00216-011-4761-5
- Chérif, M., Benhamou, N., and Bélanger, R. R. (1991). Ultrastructural and cytochemical studies of fungal development and host reactions in cucumber plants infected by *Pythium ultimum*. *Physiol. Mol. Plant Pathol.* 39, 353–375. doi: 10.1016/0885-5765(91)90017-C
- Chi, M., Han, X., Xu, Y., Wang, Y., Shu, F., Zhou, W., et al. (2019). An Improved background-correction algorithm for raman spectroscopy based on the wavelet transform. *Appl. Spectrosc.* 73, 78–87. doi: 10.1177/0003702818805116
- Deepak, S., Shailasree, S., Sujeeth, N., Kini, R. K., Mithöfer, A., and Shetty, S. H. (2008). Serodiagnosis of pearl millet resistance to downy mildew by quantitating cell wall P/HRGP using polyclonal antiserum Pab-P/HRGP. *Eur. J. Plant Pathol.* 121, 77–85. doi: 10.1007/s10658-007-9246-1
- Etesami, H., and Jeong, B. R. (2018). Silicon (Si): review and future prospects on the action mechanisms in alleviating biotic and abiotic stresses in plants. *Ecotoxicol. Environ. Saf.* 147, 881–896. doi: 10.1016/j.ecoenv.2017.09.063
- Gierlinger, N., and Schwanninger, M. (2006). Chemical imaging of poplar wood cell walls by confocal raman microscopy. *Plant Physiol.* 140, 1246–1254. doi: 10.1104/pp.105.066993
- Hänninen, T., Kontturi, E., and Vuorinen, T. (2011). Distribution of lignin and its coniferyl alcohol and coniferyl aldehyde groups in *Picea abies* and *Pinus sylvestris* as observed by raman imaging. *Phytochemistry* 72, 1889–1895. doi: 10.1016/j.phytochem.2011.05.005
- He, S., An, T., Runa, A., and Liu, S. (2019). Validation of reliable reference genes for RT-qPCR Studies of target gene expression in *colletotrichum camelliae* during spore germination and mycelial growth and interaction with host plants. *Front. Microbiol.* 10:2055. doi: 10.3389/fmicb.2019.02055
- Heiner, Z., Zeise, I., Elbaum, R., and Kneipp, J. (2018). Insight into plant cell wall chemistry and structure by combination of multiphoton microscopy with raman imaging. *J. Biophotonics* 11:e201700164. doi: 10.1002/jbio.201700164
- Hervé, C., Marcus, S. E., and Knox, J. P. (2011). Monoclonal antibodies, carbohydrate-binding modules, and the detection of polysaccharides in plant cell walls. *Methods Mol. Biol.* 715, 103–113. doi: 10.1007/978-1-61779-008-9_7
- Ji, Z., Ma, J. F., Zhang, Z. H., Xu, F., and Sun, R. C. (2013). Distribution of lignin and cellulose in compression wood tracheids of *Pinus yunnanensis* determined by fluorescence microscopy and confocal Raman microscopy. *Ind. Crops Prod.* 47, 212–217. doi: 10.1016/j.indcrop.2013.03.006
- Jin, K., Liu, X., Wang, K., Jiang, Z., Tian, G., Yang, S., et al. (2018). Imaging the dynamic deposition of cell wall polymer in xylem and phloem in *Populus × euramericana*. *Planta* 248, 849–858. doi: 10.1007/s00425-018-2931-9
- Kanbayashi, T., Ishikawa, A., Matsunaga, M., Kobayashi, M., and Kataoka, Y. (2019). Application of confocal raman microscopy for the analysis of the distribution of wood preservative coatings. *Coatings* 9:621. doi: 10.3390/coatings9100621
- Kashyap, A., Planas-Marquès, M., Capellades, M., Valls, M., and Coll, N. S. (2021). Blocking intruders: inducible physico-chemical barriers against plant vascular wilt pathogens. *J. Exp. Bot.* 72, 184–198. doi: 10.1093/jxb/eraa444
- Kiyoto, S., Yoshinaga, A., Fernandez-Tendero, E., Day, A., Chabbert, B., and Takabe, K. (2018). Distribution of lignin, hemicellulose, and arabinogalactan protein in hemp phloem fibers. *Microsc. Microanal.* 24, 442–452. doi: 10.1017/S1431927618012448
- Korukluoglu, M., Sahan, Y., and Yigit, A. (2008). Antifungal properties of olive leaf extracts and their phenolic compounds. *J. Food Saf.* 28, 76–87. doi: 10.1111/j.1745-4565.2007.00096.x
- Li, F., Wang, L., Liu, J., Wang, Y., and Chang, Q. (2019). Evaluation of leaf n concentration in winter wheat based on discrete wavelet transform analysis. *Remote Sens.* 11:1331. doi: 10.3390/rs11111331
- Li, X., Sha, J., Xia, Y., Sheng, K., Liu, Y., and He, Y. (2020). Quantitative visualization of subcellular lignocellulose revealing the mechanism of alkali pretreatment to promote methane production of rice straw. *Biotechnol. Biofuels* 13:8. doi: 10.1186/s13068-020-1648-8
- Littlejohn, G. R., Mansfield, J. C., Parker, D., Lind, R., Perfect, S., Seymour, M., et al. (2015). In vivo chemical and structural analysis of plant cuticular waxes using stimulated raman scattering microscopy. *Plant Physiol.* 168, 18–28. doi: 10.1104/pp.15.00119
- Liu, J., Ding, J., Ge, X., and Wang, J. (2021). Evaluation of total nitrogen in water via airborne hyperspectral data: potential of fractional order discretization algorithm and discrete wavelet transform analysis. *Remote Sens.* 13:4643. doi: 10.3390/rs13224643
- Lu, Q., Wang, Y., Li, N., Ni, D., Yang, Y., and Wang, X. (2018). Differences in the characteristics and pathogenicity of *colletotrichum camelliae* and *C. Fructicola* isolated from the tea plant [*Camellia sinensis* (L.) O. Kuntze]. *Front. Microbiol.* 9:3060. doi: 10.3389/fmicb.2018.03060/BIBTEX
- Ma, X., Sun, X., Wang, H., Wang, Y., Chen, D., and Li, Q. (2018). Raman spectroscopy for pharmaceutical quantitative analysis by low-rank estimation. *Front. Chem.* 6:400. doi: 10.3389/fchem.2018.00400
- Mateu, B. P., Bock, P., and Gierlinger, N. (2020). “Raman imaging of plant cell walls BT,” in *The Plant Cell Wall: Methods and Protocols*, ed. Z. A. Popper (New York, NY: Springer), 251–295. doi: 10.1007/978-1-0716-0621-6_15
- Mikulic-Petkovsek, M., Schmitzer, V., Jakopic, J., Cunja, V., Veberic, R., Munda, A., et al. (2013). Phenolic compounds as defence response of pepper fruits to *Colletotrichum coccodes*. *Physiol. Mol. Plant Pathol.* 84, 138–145. doi: 10.1016/j.pmpp.2013.09.003
- Pedersen, J. F., Vogel, K. P., and Funnell, D. L. (2005). Impact of reduced lignin on plant fitness. *Crop Sci.* 45, 812–819. doi: 10.2135/cropsci2004.0155
- Pegg, T., Edelmann, R. R., and Gladish, D. K. (2020). Immunoprofiling of cell wall carbohydrate modifications during flooding-induced aerenchyma formation in fabaceae roots. *Front. Plant Sci.* 10:1805. doi: 10.3389/fpls.2019.01805
- Pohling, C., Brackmann, C., Duarte, A., Buckup, T., Enejder, A., and Motzkus, M. (2014). Chemical imaging of lignocellulosic biomass by CARS microscopy. *J. Biophotonics* 7, 126–134. doi: 10.1002/jbio.201300052
- Polo, C. C., Pereira, L., Mazzafera, P., Flores-Borges, D. N. A., Mayer, J. L. S., Guizara-Sicaire, M., et al. (2020). Correlations between lignin content and structural robustness in plants revealed by X-ray ptychography. *Sci. Rep.* 10, 1–11. doi: 10.1038/s41598-020-63093-6
- Richter, S., Müssig, J., and Gierlinger, N. (2011). Functional plant cell wall design revealed by the raman imaging approach. *Planta* 233, 763–772. doi: 10.1007/s00425-010-1338-z
- Saletnik, A., Saletnik, B., and Puchalski, C. (2021). Overview of popular techniques of raman spectroscopy and their potential in the study of plant tissues. *Molecules* 26:1537. doi: 10.3390/molecules26061537
- Sharan, T. S., Sharma, S., and Sharma, N. (2021). Denoising and spike removal from raman spectra using double density dual-tree complex wavelet transform. *J. Appl. Spectrosc.* 88, 117–124. doi: 10.1007/s10812-021-01149-9
- Shinde, S. D., Meng, X., Kumar, R., and Ragauskas, A. J. (2018). Recent advances in understanding the pseudo-lignin formation in a lignocellulosic biorefinery. *Green Chem.* 20, 2192–2205. doi: 10.1039/c8gc00353j
- Soderberg, D. N., Kyre, B., Bonello, P., and Bentz, B. J. (2021). Lignin concentrations in phloem and outer bark are not associated with resistance to mountain pine beetle among high elevation pines. *PLoS One* 16:e0250395. doi: 10.1371/journal.pone.0250395
- Tavassoli, N., Poursorkh, Z., Bicho, P., and Grant, E. (2020). TOGA feature selection and the prediction of mechanical properties of paper from the raman spectra of unrefined pulp. *Anal. Bioanal. Chem.* 412, 8401–8415. doi: 10.1007/s00216-020-02978-x
- Tobimatsu, Y., Wagner, A., Donaldson, L., Mitra, P., Niculaes, C., Dima, O., et al. (2013). Visualization of plant cell wall lignification using fluorescence-tagged monolignols. *Plant J.* 76, 357–366. doi: 10.1111/tpj.12299
- Wang, B., Luo, M., Liu, Y., Guo, X., Liu, X., Zhang, C., et al. (2021). Improving sample preparation to investigate lignin intensity of xylem at the cellular level by confocal raman microspectroscopy of *Populus tomentosa*. *J. For. Res.* 32, 2135–2142. doi: 10.1007/s11676-020-01244-1
- Wang, J., Chen, Y., Chen, F., Shi, T., and Wu, G. (2018). Wavelet-based coupling of leaf and canopy reflectance spectra to improve the estimation accuracy of foliar nitrogen concentration. *Agric. For. Meteorol.* 248, 306–315. doi: 10.1016/j.agrformet.2017.10.017
- Wang, Y. C., Hao, X. Y., Wang, L., Xiao, B., Wang, X. C., and Yang, Y. J. (2016). Diverse *Colletotrichum* species cause anthracnose of tea plants (*Camellia sinensis* (L.) O. Kuntze) in China. *Sci. Rep.* 6, 1–13. doi: 10.1038/srep35287

- Wei, X. (2012). "Degradation of soybean stalk lignin with white-rot fungus and sem characterization of surface structure BT," in *Information Technology and Agricultural Engineering*, eds E. Zhu and S. Sambath (New York, NY: Springer), 479–484. doi: 10.1007/978-3-642-27537-1_59
- Wu, H., Xu, H., Li, H., Wei, D., Lin, J., and Li, X. (2016). Seasonal development of cambial activity in relation to xylem formation in Chinese fir. *J. Plant Physiol.* 195, 23–30. doi: 10.1016/j.jplph.2015.12.013
- Yao, X., Si, H., Cheng, T., Jia, M., Chen, Q., Tian, Y. C., et al. (2018). Hyperspectral estimation of canopy leaf biomass phenotype per ground area using a continuous wavelet analysis in wheat. *Front. Plant Sci.* 9:1360. doi: 10.3389/fpls.2018.01360
- Zeise, I., Heiner, Z., Holz, S., Joester, M., Büttner, C., and Kneipp, J. (2018). Raman imaging of plant cell walls in sections of cucumis sativus. *Plants* 7:7. doi: 10.3390/plants7010007
- Zeng, J., Ping, W., Sanaeifar, A., Xu, X., Luo, W., Sha, J., et al. (2021). Quantitative visualization of photosynthetic pigments in tea leaves based on raman spectroscopy and calibration model transfer. *Plant Methods* 17:4. doi: 10.1186/s13007-020-00704-3
- Zhang, X., Ma, J., Ji, Z., Yang, G. H., Zhou, X., and Xu, F. (2014). Using confocal raman microscopy to real-time monitor poplar cell wall swelling and dissolution during ionic liquid pretreatment. *Microsc. Res. Tech.* 77, 609–618. doi: 10.1002/jemt.22379
- Zhao, Y., Man, Y., Wen, J., Guo, Y., and Lin, J. (2019). Advances in Imaging Plant Cell Walls. *Trends Plant Sci.* 24, 867–878. doi: 10.1016/j.tplants.2019.05.009
- Conflict of Interest:** The authors declare that the research was conducted in the absence of any commercial or financial relationships that could be construed as a potential conflict of interest.
- Publisher's Note:** All claims expressed in this article are solely those of the authors and do not necessarily represent those of their affiliated organizations, or those of the publisher, the editors and the reviewers. Any product that may be evaluated in this article, or claim that may be made by its manufacturer, is not guaranteed or endorsed by the publisher.
- Copyright © 2022 Sanaeifar, Ye, Li, Luo, Tang and He. This is an open-access article distributed under the terms of the Creative Commons Attribution License (CC BY). The use, distribution or reproduction in other forums is permitted, provided the original author(s) and the copyright owner(s) are credited and that the original publication in this journal is cited, in accordance with accepted academic practice. No use, distribution or reproduction is permitted which does not comply with these terms.



Raman Spectroscopy Enables Non-invasive and Confirmatory Diagnostics of Aluminum and Iron Toxicities in Rice

Samantha Higgins¹, Sudip Biswas², Nicolas K. Goff¹, Endang M. Septiningsih² and Dmitry Kurouski^{1,3*}

¹ Department of Biochemistry and Biophysics, Texas A&M University, College Station, TX, United States, ² Department of Soil and Crop Sciences, Texas A&M University, College Station, TX, United States, ³ Institute for Quantum Science and Engineering, Texas A&M University, College Station, TX, United States

OPEN ACCESS

Edited by:

Nam-Hai Chua,
Temasek Life Sciences Laboratory,
Singapore

Reviewed by:

Chenliang Yu,
Zhejiang A&F University, China
Gajendra Pratap Singh,
Singapore-MIT Alliance for Research
and Technology (SMART), Singapore

*Correspondence:

Dmitry Kurouski
dkurouski@tamu.edu

Specialty section:

This article was submitted to
Technical Advances in Plant Science,
a section of the journal
Frontiers in Plant Science

Received: 06 August 2021

Accepted: 28 March 2022

Published: 16 May 2022

Citation:

Higgins S, Biswas S, Goff NK,
Septiningsih EM and Kurouski D
(2022) Raman Spectroscopy Enables
Non-invasive and Confirmatory
Diagnostics of Aluminum and Iron
Toxicities in Rice.
Front. Plant Sci. 13:754735.
doi: 10.3389/fpls.2022.754735

Metal toxicities can be detrimental to a plant health, as well as to the health of animals and humans that consume such plants. Metal content of plants can be analyzed using colorimetric, atomic absorption- or mass spectroscopy-based methods. However, these techniques are destructive, costly and laborious. In the current study, we investigate the potential of Raman spectroscopy (RS), a modern spectroscopic technique, for detection and identification of metal toxicities in rice. We modeled medium and high levels of iron and aluminum toxicities in hydroponically grown plants. Spectroscopic analyses of their leaves showed that both iron and aluminum toxicities can be detected and identified with ~100% accuracy as early as day 2 after the stress initiation. We also showed that diagnostics accuracy was very high not only on early, but also on middle (day 4–day 8) and late (day 10–day 14) stages of the stress development. Importantly this approach only requires an acquisition time of 1 s; it is non-invasive and non-destructive to plants. Our findings suggest that if implemented in farming, RS can enable pre-symptomatic detection and identification of metallic toxins that would lead to faster recovery of crops and prevent further damage.

Keywords: metal toxicity, rice, Raman spectroscopy, non-invasive diagnostics, plants

HIGHLIGHTS

- We show that Raman spectroscopy can be used for confirmatory pre-symptomatic diagnostics of high and medium levels of iron and aluminum toxicities in rice.

INTRODUCTION

Continuous improvement in crop yield is critically important to address the growing problem of food security (Ingram and Maye, 2020; Payne and Kurouski, 2021). Biotic and abiotic stresses can substantially reduce crop yield. Biotic stresses caused by viruses, fungi, and bacteria can reduce up to 30% of the crop yield (Ingram and Maye, 2020; Payne and Kurouski, 2021), whereas abiotic stresses such as drought, flood, extreme temperatures, nutritional deficiencies, and metallic toxicities can

be more detrimental (Mantri et al., 2012; Waqas et al., 2019; Angulo-Bejarano et al., 2021). These stresses can reduce up to 70% of the crop yield (Farber et al., 2019a; Lew et al., 2020; Payne and Kurouski, 2021). Some efforts have been made to subsequently reduce the impacts of various abiotic stresses in rice crops, through genetics, genomics, and breeding programs (Thomson et al., 2009; Chin et al., 2011; Jagadish et al., 2012; Hasanuzzaman et al., 2013; Kumar et al., 2014; Li et al., 2014; Matthus et al., 2015; Gonzaga et al., 2017; Singh et al., 2017; Septiningsih and Mackill, 2018; Thapa et al., 2020; Ignacio et al., 2021; Liang et al., 2021; Tnani et al., 2021).

Metal toxicities can damage the plant directly, as well as cause substantial health issues if such plants are consumed by animals and humans. For instance, aluminum (Al) toxicity is a major issue for crop production in numerous countries with acidic soils [soils with pHs of 5.5 and lower; (Barabasz et al., 2002)]. Such soils take over 50% of the arable land in the world. Al ions inhibit elongation and division of cells in the root tip, decelerating root development, which results in a substantial decrease in water and nutrient uptake by plants (Bojórquez-Quintal et al., 2017). This results in a substantial change in the plant metabolism and may cause the death of the plant (Farber et al., 2019a). Consumption of such Al-rich plants is also associated with dementia and other neurodegenerative disorders. Iron (Fe) is an essential element for all living organisms. However, if it accumulated in plants, Fe promotes Fenton reaction that generates hydroxyl radicals, which in turn damage lipids, proteins, and DNA (Sahrawat, 2005). Fe also inhibits cell division and elongation of plant roots. As a result, plants grown on Fe-rich soils demonstrate suppressed vegetation and lower crop yield compared to plants cultivated on soils with a low Fe content. These pieces of evidence demonstrate an urgent need for timely detection and identification of such metal toxicities in plants.

Conventionally, metal toxicities are diagnosed via colorimetric, atomic absorption or mass spectroscopy analyses (Sáez-Plaza et al., 2013). The colorimetric approaches are based on thiocyanates and a Prussian Blue dye (Woods and Mellon, 1941; Gitz et al., 2018). Such colorimetric approaches are routinely used for qualitative metal ion staining in animal and plant histological sections (Johnson et al., 2012; Roschztardtz et al., 2013; Grillet et al., 2014; De la Fuente et al., 2017). However, these methods are laborious, lacks precision and fail to detect small variations of metals between samples. Atomic absorption spectroscopy is a highly accurate technique that is based on the electromagnetic emission of the individual elements that are converted into ions by flame-heating of the sample (Wachasunder and Nafade, 2001). Together with inductively coupled plasma-mass spectroscopy (ICP-MS), atomic absorption spectroscopy is frequently used for highly accurate identification of metal content of both plants and soils (Masson et al., 2010; Tokaloğlu, 2013). However, these spectroscopy approaches are laborious and costly; they also require sample shipment to a laboratory, which typically cannot be afforded by most farmers in developing countries. These limitations of traditional techniques for plant and soil analyses catalyzed a search for inexpensive, fast, and portable analogs that can be used for confirmatory diagnosis of metal toxicities in plants.

Our own results, as well as experimental findings reported by other groups, show that Raman spectroscopy (RS) can be used to detect both biotic and abiotic stresses in plants (Altangerel et al., 2017; Egging et al., 2018; Farber and Kurouski, 2018; Farber et al., 2019b, 2021; Mandrile et al., 2019; Sanchez et al., 2019b, 2020a,b; Gupta et al., 2020). RS is based on a phenomenon of inelastic light scattering that was experimentally demonstrated by C.V. Raman at the beginning of the 20th century. These inelastically scattered photons provide information about the structure and composition of analyzed specimens (Kurouski et al., 2015). Biotic and abiotic stresses drastically alter plant metabolism (Payne and Kurouski, 2021). Such changes can be detected using RS, which allows for confirmatory, non-invasive, and non-destructive diagnostics of both biotic and abiotic stresses. For instance, Farber and Kurouski (2018) showed that RS could detect and identify different fungal pathogens in corn. Sanchez et al. (2019a,b, 2020c) discovered that RS could be used to detect Huanglongbing (HLB) or Citrus Greening Disease in oranges and grapefruits. Furthermore, using RS, HLB could be distinguished from nutritional deficiencies with 100% accuracy. Recently reported experimental findings show that RS can also detect and identify nutritional deficiencies caused by a lack of nitrogen, phosphorus, and potassium in soil (Sanchez et al., 2020a). These results show that RS be used to probe changes in plant biochemistry associated with a lack of macronutrients. Based on these findings, we hypothesized that RS may have similar sensitivity for diagnostics of changes associated with microelements, such as Al and Fe.

In this study, we aim to determine the extent to which RS can be used to detect Al and Fe toxicities in rice (*Oryza sativa*). For this, we performed a growth chamber experiment in which rice plants were exposed to medium and high levels of Al and Fe toxicities (**Supplementary Figure 1**). Using a hand-held Raman spectrometer, we collected spectra from leaves of these plants starting at day 2 (D2) after stresses were induced. These spectra were used to determine changes in plant biochemistry that are likely to be associated with both Al and Fe toxicities.

We also used Partial Least Squares-Discriminant Analysis (PLS-DA) to determine the accuracy of Raman-based diagnostics of metal toxicities. Our finding shows that RS coupled to PLS-DA can detect pre-systematic Al and Fe toxicities with high accuracies. These findings suggest that RS can be used for screening metal toxicities in plants. This information can be used to mitigate the stresses on the early stages of plant vegetation and minimize the consumption of such toxin-contaminated crops by animals and humans.

MATERIALS AND METHODS

Plant Materials and Experimental Design

Presidio rice was grown in bins that contained Styrofoam with pads. The pads were covered by a mesh grid as described by Samonte et al. (2013) and Sanchez et al. (2020a). One pre-germinated seedling was placed in the mesh in each hole resulting in a total of 24 seedlings per bin. The seedlings were first soaked in water for the

first 24 h to initiate seed germination (Sanchez et al., 2020a). Next, germinated plants were grown in a Yoshida solution consisting of macronutrients (114.30 mg/L NH_4NO_3 , 50.40 mg/L $\text{NaH}_2\text{PO}_4 \cdot 2\text{H}_2\text{O}$, 89.30 mg/L K_2SO_4 , 108.25 mg/L CaCl_2 and 405 mg/L $\text{MgSO}_4 \cdot 7\text{H}_2\text{O}$), and micronutrients [1.875 mg/L $\text{MnCl}_2 \cdot 4\text{H}_2\text{O}$, 0.093 mg/L $(\text{NH}_4)_6\text{Mo}_7\text{O}_{24} \cdot 4\text{H}_2\text{O}$, 1.09 mg/L H_3BO_3 , 0.038 mg/L $\text{CuSO}_4 \cdot 5\text{H}_2\text{O}$, 9.62 mg/L $\text{FeCl}_3 \cdot 6\text{H}_2\text{O}$, 14.88 mg/L $\text{C}_6\text{H}_8\text{O}_7 \cdot \text{H}_2\text{O}$ and 0.043 mg/L $\text{ZnSO}_4 \cdot 7\text{H}_2\text{O}$] for 4 weeks. Next, plants were exposed to medium and high Fe and Al stresses. For Al stress, 0.042 mg/L or 314 μM of AlCl_3 was used in the high-stress bin and 0.021 mg/L or 157 μM of AlCl_3 was used in the medium stress bin. For Fe stress, the high-stress bin contained 2.196 g/L or 8.12 mM $\text{FeCl}_3 \cdot 6\text{H}_2\text{O}$ solution, and the medium stress bin contained 1.098 g/L or 4.06 mM $\text{FeCl}_3 \cdot 6\text{H}_2\text{O}$ solution. During the 2-week period in which plants were under metallic stress, height measurements, photographs, and Raman spectra were collected at D2, D4, D6, D8, D10, D12, and D14, **Supplementary Figure 1**. The pH was checked every day during stress conditions to ensure that the solution remained at a pH of 5. Every 3 days, a new hydroponic solution was created, the old stress solution was discarded, and fresh stress solutions were added at the same concentrations for each medium stress and high stress. The growth of the rice occurred in a controlled growth chamber with a day/night setting on a 12 h/12 h, humidity set to 55%, and a day/night temperature set to 29°C/26°C (Sanchez et al., 2020a). The experiment was repeated twice for this work.

Raman Spectroscopy

Agilent Resolve hand-held Raman spectrometer was used to collect spectra from plants. For each spectral acquisition, the plant leaf was gently positioned at the nozzle of the spectrometer. Acquisition time was 1 s; laser power was 495 mW. Baseline correction was performed automatically by the spectrometer. These conditions were found to be non-destructive as no visual damage of plant leaves was evident after spectral acquisition (Sanchez et al., 2019a). A total of 50 spectra were collected from each group of plants (50 for control, 50 for Al high, 50 for Al medium, 50 for Fe high, and 50 for Fe medium). Next, spectra were exported from the spectrometer and analyzed using PLS Toolbox (Eigenvector Research Inc., Wenatchee, WA, United States).

Data Analysis

First, multiplicative signal correction based on the mean was applied to all data. Next, the second derivative was taken of the Raman spectra with a filter width of 51 and polynomial order 3. Finally, the spectra were smoothed with a 15-point window then area normalized. A partial least squares-discriminant analysis (PLS-DA) was performed for all data presented in the results and discussion of this manuscript. The imported spectra wavenumbers that were analyzed were included from 300 cm^{-1} to 2,000 cm^{-1} which includes all important spectra characteristics of rice plants and metallic stress. Each spectrum was area normalized at 1,440 cm^{-1} and mean-centered. Every PLS model statistically analyzed the level of metallic stress to sort the significant differences between Al and Fe metallic toxicities, **Supplementary Figure 2**. PLS-DA results are summarized in

Tables 2, 3. For instance, Al high stress plants were compared to the control group (healthy plants) on D2 using the PLS-DA binary model in which the Cross Validation matrix ranked the accuracy of the ability for the Raman spectrometer to distinguish between the two data sets. The confusion matrix of Al high versus healthy on D2 gave a true prediction rate (TPR) of 1 (100%) for distinguishing Al High stress plants from healthy plants. The same method was used for the other experimental groups and following days (see **Supplementary Figures 1, 2**).

RESULTS AND DISCUSSION

Spectra collected from leaves of healthy rice plants exhibited vibrational bands that could be assigned to pectin (747 cm^{-1}), cellulose (915 and 1,048 cm^{-1}), carotenoids (1,000, 1,155, 1,185, 1,218, and 1,525 cm^{-1}), phenylpropanoids (1,601–1,630 cm^{-1}), protein (1,674 cm^{-1}), and aliphatic vibrations (1,218, 1,288, 1,326, 1,382, 1,440, and 1,488 cm^{-1}) that cannot be assigned to a particular class of compounds (**Figure 1** and **Table 1**).

We found that spectra collected from leaves of rice exposed to both medium and high Fe toxicities demonstrate an increase in the intensities of phenylpropanoid vibrations (1,601–1,630 cm^{-1}), as well as a decrease in the intensities of carotenoids (1,000, 1,155, 1,184, 1,218, and 1,525 cm^{-1}). These spectral changes suggest that Fe toxicity is associated with an increase in the concentration of phenylpropanoids and a decrease in the concentration of carotenoids.

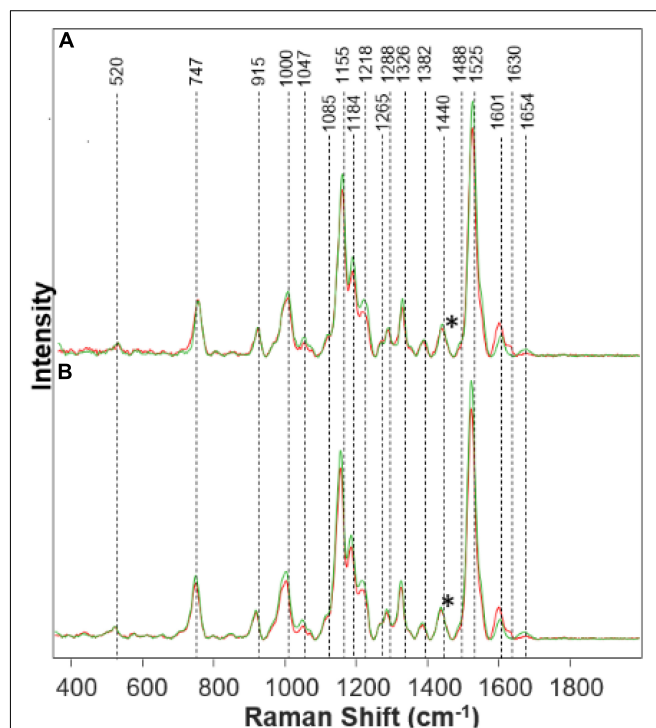


FIGURE 1 | Raman spectra collected from leaves of healthy (green) and Fe stressed (red) at day 10 with high (A) and medium (B) levels of Fe. Spectra normalized on CH_2 vibrations (1,440 cm^{-1}) present in nearly all classes in biological molecules [marked by asterisks (*)].

TABLE 1 | Vibrational bands and their assignments for spectra collected from rice leaves.

Band (cm ⁻¹)	Vibrational mode	Assignment
520	$\nu(\text{C-O-C})$ Glycosidic	Carbohydrates (Edwards et al., 1997; Pan et al., 2017)
747	$\gamma(\text{C-O-H})$ of COOH	Pectin (Synytsya et al., 2003)
915	$\nu(\text{C-O-C})$ In-plane, symmetric	Cellulose, phenylpropanoids (Edwards et al., 1997)
1,000	In-plane CH ₃ rocking of polyene aromatic ring of phenylalanine	Carotenoids (Schulz et al., 2005); protein
1,047	$\nu(\text{C-O})+\nu(\text{C-C})+\delta(\text{C-O-H})$	Cellulose, phenylpropanoids (Edwards et al., 1997)
1,085	$\nu(\text{C-O})+\nu(\text{C-C})+\delta(\text{C-O-H})$	Carbohydrates (Almeida et al., 2010)
1,155	C-C Stretching; $\nu(\text{C-O-C})$, $\nu(\text{C-C})$ in glycosidic linkages, asymmetric ring breathing	Carotenoids (Schulz et al., 2005), carbohydrates (Wiercigroch et al., 2017)
1,184	$\nu(\text{C-O-H})$ Next to aromatic ring+ $\sigma(\text{CH})$	Carotenoids (Schulz et al., 2005)
1,218	$\delta(\text{C-C-H})$	Carotenoids (Schulz et al., 2005), xylan (Agarwal, 2014)
1,265	Guaiacyl ring breathing, C-O stretching (aromatic); -C=C-	Phenylpropanoids (Cao et al., 2006), unsaturated fatty acids (Jamieson et al., 2018)
1,288	$\delta(\text{C-C-H})$	Aliphatics (Yu et al., 2007)
1,326	δCH_2 Bending	Aliphatics, cellulose, phenylpropanoids (Edwards et al., 1997)
1,382	δCH_2 Bending	Aliphatics (Yu et al., 2007)
1,440–1,488	$\delta(\text{CH}_2)$	Aliphatics (Yu et al., 2007)
1,525	-C=C- (in-plane)	Carotenoids (Rys et al., 2014; Adar, 2017; Devitt et al., 2018)
1,601–1,630	$\nu(\text{C-C})$ Aromatic ring+ $\sigma(\text{CH})$	Phenylpropanoids (Agarwal, 2006; Kang et al., 2016)
1,654	-C=C-, C=O Stretching, amide I	Proteins (Devitt et al., 2018)

Our own results, as well as experimental findings reported by other groups, show that on the molecular level, an increase in the intensity of phenylpropanoid vibrations is due to an increase in the concentration of low molecular weight aromatic compounds, such as p-coumaric acid. These molecules are also directly involved in the plant response against biotic and abiotic stresses such as bacteria and nutritional deficiencies.

A decrease in the carotenoid content has strong physiological relevance to plant defense mechanisms (Havaux, 2014). Specifically, Fe ions activate enzymatic oxidation of neoxanthin, one of the plant carotenoids, that yields abscisic acid, a hormone that enhances plant resistance to such stresses (Nambara and Marion-Poll, 2005). Reactive oxygen species (ROS) produced by Fenton reaction can also oxidize β -carotenes producing β -ionone, β -cyclocitral that aim to protect the plant against various biotic and abiotic stresses (Nambara and Marion-Poll, 2005; Havaux, 2014). Thus, reduction in the concentration of carotenoids by ROS can be considered to be a hallmark of Fe toxicity (Yu et al., 2007).

We have also observed a decrease in the intensity of cellulose (1,047 cm⁻¹) and protein (1,654 cm⁻¹) bands (Figure 1). These spectral changes that Fe toxicities are associated

with cellulose degradation in plants, as well as the strong transformation of plant enzymes. More detailed elucidation of direct biochemical changes requires the use of high-performance liquid chromatography (HPLC) and its mass spectroscopy (HPLC-MS) analogs. These studies are beyond the scope of the current work.

The physiological effects of Fe on plant health corresponds with what is shown on the Raman spectra in Figure 1. The increased peak in the phenylpropanoid band region corresponds to an increase in phenylpropanoids within the plant. Phenylpropanoids play a key role in plant development and cell division. Thus, when metal toxicity such as Fe is present, there is an increase in phenylpropanoids to defend itself against abiotic stresses (Cheynier et al., 2013). These phenolics can be detrimental to the plant when released as a defense mechanism due to the toxicity of some phenols in great quantities, which causes harm to plant growth (Cheynier et al., 2013). Visual evidence is seen in the **Supplementary Material** of Fe stressed plants that they died the quickest. Carotenoids are partly responsible for plant color and photosynthesis. We see that the Fe stress plants quickly lost their color, turning brown rapidly. A decrease in the carotenoid band region corresponds to a decrease in carotenoids in the Fe stressed plants, leading to a lack of healthy color. Without carotenoids, the plant will lose molecules for maintaining normal plant health. Carotenoids are a predecessor to abscisic acid (ABA) which is involved in a defense mechanism (Stanley and Yuan, 2019). Since carotenoids play a role in the photosynthetic process, it is evident that with a decrease in carotenoids, the plant will become extremely sick or die (as we see in both Fe medium stress and Fe high-stress plants). Proteins and

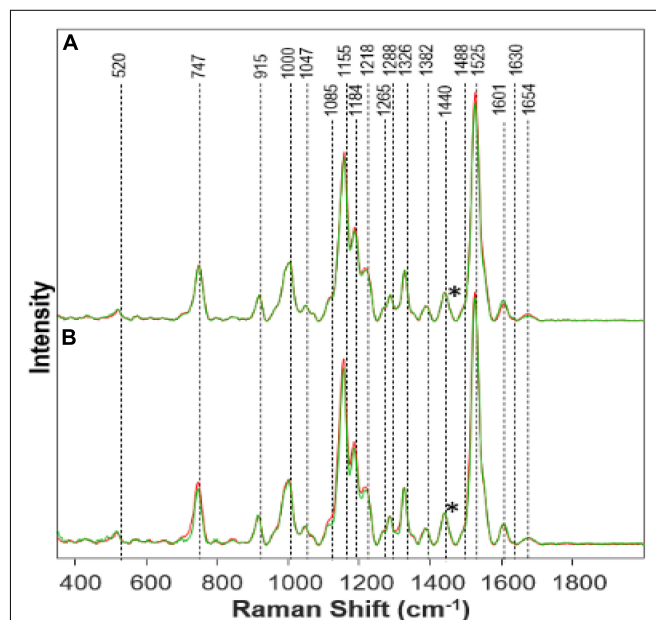


FIGURE 2 | Raman spectra collected from leaves of (A) Al High (red) vs. Healthy (green) on day 14; (B) Al Medium (red) vs. Healthy (green) on day 14. Spectra normalized on CH₂ vibrations (1,440 cm⁻¹) present in nearly all classes in biological molecules [marked by asterisks (*)].

TABLE 2 | Percent accuracy of stress vs. healthy over 2 weeks.

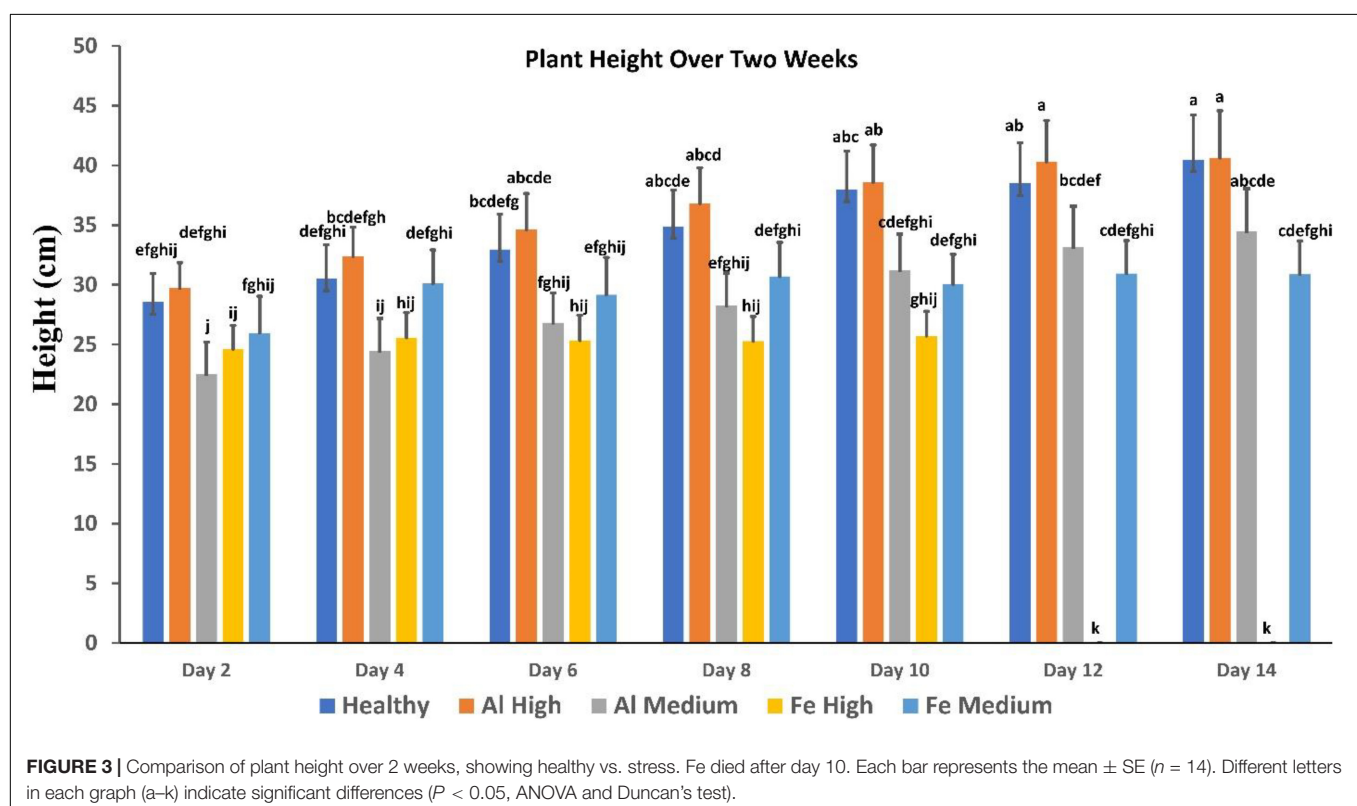
Accuracy of stress vs. Healthy each day							
	D2	D4	D6	D8	D10	D12	D14
Al High	100%	82%	100%	92%	94%	90%	96%
Al Medium	100%	94%	100%	100%	74%	100%	94%
Fe High	92%	82%	100%	100%	100%	–	–
Fe Medium	100%	74%	100%	100%	100%	100%	92%

pectin are integral components for the strength and structure of the plant. Pectin is responsible for cell wall strength (Wu et al., 2018). Moreover, we see a decrease in the protein and pectin band intensities corresponding to the reduction in pectin and protein concentration within the Fe stressed plants also leading to degraded plants shown visually from the **Supplementary Material**.

We found that Al toxicities cause nearly opposite changes in plant biochemistry. Specifically, we have observed an increase in the intensities of carotenoid and protein vibrations in the spectra collected from plants exposed to Al stresses (**Figure 2**). We also found that the intensity of phenylpropanoid vibrations decreased in the spectra collected from Al-stressed plants. Importantly, if the magnitude of these changes for medium and high Fe stresses were nearly the same, the magnitude of stresses for high (**Figure 2A**) vs. medium (**Figure 2B**) Al stresses is different. As expected, we have observed greater changes upon stronger (high vs. medium) stresses.

Visually the Al stressed plants appeared healthier and grew taller while keeping the healthy green color for a longer time. Much is still to be learned from Al stress and why an opposite effect was shown comparatively with Fe stress. This is quite interesting because the phenylpropanoid band intensity decreases as a representation of the decrease in phenylpropanoids under Al stress. This, in turn, should mean that the root elongation would also decrease rapidly, and the Al stress plants would die quickly. However, we see that the Al high-stress plants grew the most in comparison to the other stressed plants. It is possible that Presidio may possess some degree of tolerance to Al toxicity. It is known that Al will affect different varieties of plants in different ways (Bojórquez-Quintal et al., 2017). Therefore, further research needs to be done especially on the physiological effects of Al toxicity in plants.

Other studies have shown that Al can induce a more efficient nutrient uptake mechanism which would lead to faster growth (Bojórquez-Quintal et al., 2017). This may explain the reason we see rapid growth yet a decrease in the phenylpropanoid band because the efficiency of nutrient uptake is combatting the decrease in phenylpropanoids. The pectin band increased while the concentration of Al increased, suggesting an increase of pectin within the plant. Another study also found an increase of pectin by 50% in Al stress plants (Nagayama et al., 2019). Pectin is responsible for cell wall strength (Wu et al., 2018). Pectin can be linked to increased plant growth (Hassan et al., 2019). Due to Al influencing pectin increase within the plant, and pectin aiding in growth, we see an increase in the height of the Al high-stress plants. With the increase in the carotenoid band intensity,



as Al concentration increases, an inference can be made that Al has caused an increase in the concentration of carotenoids within the plant. Carotenoids are linked to plant growth and are also produced as part of a defense mechanism when certain biotic and abiotic stresses are present (Swapnil et al., 2021). Since carotenoids are an integral part of photosynthesis, it can be stated that the increase in Al causing an increase in carotenoids has led to faster growth. Higher carotenoid concentration will allow for more efficient photosynthesis and thus plant growth. We also see that the protein band has an increased intensity, meaning an increased concentration in protein within Al stress plants. Previous studies have also found that Al can increase a variety of proteins within a plant (Chen and Lin, 2010). Proteins also aid in plant growth, as we see in the Al high-stress plants. Again, further study should investigate the effects of Al on plant growth and toxicity.

Next, we used PLS-DA to investigate the accuracy of identifying both Al and Fe stresses at different states of plant vegetation (Table 2). We found that both Al and Fe stresses (high and medium levels) can be diagnosed as accurately as 98% at D2. This accuracy slightly decreases at D4 (83%), then reaching 100% at D6. These findings suggest that once the stress is induced, it causes drastic changes in plant biochemistry (D2). However, aiming to mitigate such stresses, plants try to level off Al- and Fe- induced changes in plant biochemistry, which reduces the accuracy of their diagnostics at D4. The magnitude of such efforts is reduced at D6, which results in highly accurate differentiation between the biochemistry of a healthy plant and plants exposed to both Fe and Al toxicities.

We also investigated the extent to which spectroscopic libraries can be used for robust and reliable identification of these stresses in plants. For this, we used spectra collected at different time points to build a model that can be used for the identification of high and medium Al and Fe stresses (Figure 3). We found that high Al stress can be diagnosed with 88.6% accuracy, whereas high Fe stress can be detected and identified with 88.3% accuracy (Table 3). Interestingly, the accuracy of diagnostics of medium levels of stresses is higher and is equal to 94.9% and 88%, respectively. Finally, we found that the absence of metal stresses healthy plants can be diagnosed with ~90% accuracy.

It is important to note that conventionally used parameters, such as plant height, cannot be used for the identification of such changes (Figure 3). Specifically, we found that plants exposed to high Al stresses are taller than healthy plants, whereas analogous medium Al stresses result in substantial deceleration of the plant growth. High Fe stresses cause substantial impairment to the plant vegetation that results in substantial deceleration of the plant growth. However, plants exposed to medium Fe

stress, although they experience some impairment in the plant growth typically only incrementally behind healthy plants at the corresponding vegetation state.

It is important to note that this work is a first proof-of-principle study that reflects the potential of RS in confirmatory diagnostics of plant stresses caused by metal toxicities. Additional work is required to verify these findings on other crops, such as sorghum, wheat and corn. It is also important to investigate the extent to which a spectroscopic library developed for one plant variety in one geographic area can be used for the accurate stress determination in other varieties and other geographic areas. Finally, it is critically important to determine the extent to which other abiotic stresses, as well as biotic stresses that can be simultaneously present in plants that experience metallic toxicities can alter the accuracy of detection of individual stresses. These studies are currently in progress in our laboratory.

CONCLUSION

Our findings show that RS can be used for a label-free, fast and confirmatory diagnostics of plant stresses caused by Al and Fe toxicities. Although such diagnostics can be performed by atomic absorption spectroscopy and ICP-MS, RS requires no sample modification which drastically limits direct costs of such testing. Our results show that already at D2, one can detect and identify medium when referring to the stress levels and high Al and Fe toxicities with ~100% accuracy. Our findings demonstrate that not only at early but also at middle and late stages, both middle and high Al and Fe toxicities can be correctly detected and identified. One can expect that a hand-held Raman spectrometer equipped with such libraries and chemometric models can be used directly in the field for timely assessment of the plant health. We also expect that such devices can be used in grocery stores for label-free, non-invasive and non-destructive control of plant products.

This work also expanded the potential of RS in digital farming. Our findings together with experimental results reported by other groups demonstrate that this innovative spectroscopic technique can be used to transform agricultural approaches in the United States and overseas (Altangerel et al., 2017; Egging et al., 2018; Farber and Kurouski, 2018; Farber et al., 2019b, 2021; Mandrile et al., 2019; Sanchez et al., 2019b, 2020a,b; Gupta et al., 2020).

DATA AVAILABILITY STATEMENT

The original contributions presented in the study are included in the article/**Supplementary Material**, further inquiries can be directed to the corresponding author/s.

AUTHOR CONTRIBUTIONS

SH: investigation, data curation, and methodology. SB: methodology. NG: investigation. ES: methodology and supervision. DK: methodology, funding acquisition, and

TABLE 3 | Percent accuracy from binary model to distinguish between stressed plant and healthy plants.

Stress vs. Healthy	Stress vs. Healthy		
	Al	Fe	Healthy Avg.
High stress	88.60%	87.23%	88.29%
Medium stress	94.90%	88.03%	91.00%

supervision. All authors contributed to the article and approved the submitted version.

FUNDING

We are grateful to the AgriLife Research of Texas A&M for provided financial support. We also acknowledge the Governor's University Research Initiative (GURI) grant program of Texas A&M University, GURI Grant Agreement Nos. 12-2016 and M1700437.

REFERENCES

- Adar, F. (2017). Carotenoids – their resonance Raman spectra and how they can be helpful in characterizing a number of biological systems. *Spectroscopy* 32, 12–20.
- Agarwal, U. P. (2006). Raman imaging to investigate ultrastructure and composition of plant cell walls: distribution of lignin and cellulose in black spruce wood (*Picea mariana*). *Planta* 224, 1141–1153. doi: 10.1007/s00425-006-0295-z
- Agarwal, U. P. (2014). 1064 nm FT-Raman spectroscopy for investigations of plant cell walls and other biomass materials. *Front. Plant Sci.* 5:490. doi: 10.3389/fpls.2014.00490
- Almeida, M. R., Alves, R. S., Nascimbem, L. B., Stephani, R., Poppi, R. J., and de Oliveira, L. F. (2010). Determination of amylose content in starch using Raman spectroscopy and multivariate calibration analysis. *Anal. Bioanal. Chem.* 397, 2693–2701. doi: 10.1007/s00216-010-3566-2
- Altangerel, N., Ariunbold, G. O., Gorman, C., Alkahtani, M. H., Borrego, E. J., Bohlmeyer, D., et al. (2017). In vivo diagnostics of early abiotic plant stress response via Raman spectroscopy. *Proc. Natl. Acad. Sci. U.S.A.* 114, 3393–3396. doi: 10.1073/pnas.1701328114
- Angulo-Bejarano, P. I., Puente-Rivera, J., and Cruz-Ortega, R. (2021). Metal and metalloid toxicity in plants: an overview on molecular aspects. *Plants (Basel, Switzerland)* 10:635. doi: 10.3390/plants10040635
- Barabasz, W., Albinska, D., Jaskowska, M., and Lipiec, J. (2002). Ecotoxicology of aluminium. *Pol. J. Environ. Stud.* 11, 199–204.
- Bojórquez-Quintal, E., Escalante-Magaña, C., Echevarría-Machado, I., and Martínez-Estévez, M. (2017). Aluminum, a friend or foe of higher plants in acid soils. *Front. Plant Sci.* 8:1767. doi: 10.3389/fpls.2017.01767
- Cao, Y., Shen, D., Lu, Y., and Huang, J. (2006). A Raman-scattering study on the net orientation of biomacromolecules in the outer epidermal walls of mature wheat stems (*Triticum aestivum*). *Ann. Bot.* 97, 1091–1094. doi: 10.1093/aob/mcl059
- Chen, J.-H., and Lin, Y.-H. (2010). Effect of aluminum on variations in the proteins in pineapple roots. *Soil Sci. Plant Nutr.* 56, 438–444. doi: 10.1111/j.1747-0765.2010.00479.x
- Cheyrier, V., Comte, G., Davies, K. M., Lattanzio, V., and Martens, S. (2013). Plant phenolics: recent advances on their biosynthesis, genetics, and ecophysiology. *Plant Physiol. Biochem.* 72, 1–20. doi: 10.1016/j.plaphy.2013.05.009
- Chin, J. H., Gamuyao, R., Dalid, C., Bustamam, M., Prasetyono, J., Moeljopawiro, S., et al. (2011). Developing rice with high yield under phosphorus deficiency: Pup1 sequence to application. *Plant Physiol.* 156, 1202–1216. doi: 10.1104/pp.111.175471
- De la Fuente, V., Rufo, L., Rodríguez, N., Franco, A., and Amils, R. (2017). Comparison of iron localization in wild plants and hydroponic cultures of *Imperata cylindrica* (L.) P. Beauv. *Plant Soil* 418, 25–35. doi: 10.1007/s11104-017-3251-8
- Devitt, G., Howard, K., Mudher, A., and Mahajan, S. (2018). Raman spectroscopy: an emerging tool in neurodegenerative disease research and diagnosis. *ACS Chem. Neurosci.* 21, 404–420. doi: 10.1021/acscchemneuro.7b00413
- Edwards, H. G., Farwell, D. W., and Webster, D. (1997). FT Raman microscopy of untreated natural plant fibres. *Spectrochim. Acta A* 53, 2383–2392. doi: 10.1016/S1386-1425(97)00178-9

ACKNOWLEDGMENTS

We thank Rohini Morey for provided help with the collection of spectral data and height measurements.

SUPPLEMENTARY MATERIAL

The Supplementary Material for this article can be found online at: <https://www.frontiersin.org/articles/10.3389/fpls.2022.754735/full#supplementary-material>

- Egging, V., Nguyen, J., and Kourouski, D. (2018). Detection and identification of fungal infections in intact wheat and sorghum grain using a hand-held Raman spectrometer. *Anal. Chem.* 90, 8616–8621. doi: 10.1021/acs.analchem.8b01863
- Farber, C., and Kourouski, D. (2018). Detection and identification of plant pathogens on maize kernels with a hand-held Raman spectrometer. *Anal. Chem.* 90, 3009–3012. doi: 10.1021/acs.analchem.8b00222
- Farber, C., Mahnke, M., Sanchez, L., and Kourouski, D. (2019a). Advanced spectroscopic techniques for plant disease diagnostics. a review. *Trends Analyt. Chem.* 118, 43–49. doi: 10.1016/j.trac.2019.05.022
- Farber, C., Sanchez, L., Pant, S., Scheuring, D. C., Vales, M. I., Mandadi, K., et al. (2021). Potential of spatially offset Raman spectroscopy for detection of zebra chip and potato virus Y diseases of potatoes (*Solanum tuberosum*). *ACS Agric. Sci. Technol.* 1, 211–221. doi: 10.1021/acscagstech.1c00024
- Farber, C., Shires, M., Ong, K., Byrne, D., and Kourouski, D. (2019b). Raman spectroscopy as an early detection tool for rose rosette infection. *Planta* 250, 1247–1254. doi: 10.1007/s00425-019-03216-0
- Gitz, J. C., Sadot, N., Zaccari, M., and Zarivach, R. (2018). A colorimetric method for measuring iron content in plants. *J. Vis. Exp.* 139:57408. doi: 10.3791/57408
- Gonzaga, Z. J. C., Carandang, J., Singh, A., Collard, B. C., Thomson, M. J., and Septiningsih, E. M. (2017). Mapping QTLs for submergence tolerance in rice using a population fixed for SUB1A tolerant allele. *Mol. Breed.* 37, 1–10.
- Grillet, L., Ouerdane, L., Flis, P., Hoang, M. T., Isaure, M. P., Lobinski, R., et al. (2014). Ascorbate efflux as a new strategy for iron reduction and transport in plants. *J. Biol. Chem.* 289, 2515–2525. doi: 10.1074/jbc.M113.514828
- Gupta, S., Huang, C. H., Singh, G. P., Park, B. S., Chua, N.-H., and Ram, R. J. (2020). Portable Raman leaf-clip sensor for rapid detection of plant stress. *Sci. Rep.* 10:20206. doi: 10.1038/s41598-020-76485-5
- Hasanuzzaman, M., Nahar, K., and Fujita, M. (2013). “Extreme temperature responses, oxidative stress and antioxidant defense in plants,” in *Abiotic Stress-Plant Responses and Applications in Agriculture*, Vol. 13, eds K. Vahdati and C. Leslie (London: IntechOpen), 169–205.
- Hassan, M. K., Mcinroy, J. A., Jones, J., Shantharaj, D., Liles, M. R., and Kloepper, J. W. (2019). Pectin-Rich amendment enhances soybean growth promotion and nodulation mediated by *Bacillus velezensis* strains. *Plants* 8:120. doi: 10.3390/plants8050120
- Havaux, M. (2014). Carotenoid oxidation products as stress signals in plants. *Plant J.* 79, 597–606. doi: 10.1111/tpj.12386
- Ignacio, J. C. I., Zaidem, M., Casal, C., Dixit, S., Kretschmar, T., Samaniego, J. M., et al. (2021). Genetic mapping by sequencing more precisely detects loci responsible for anaerobic germination tolerance in rice. *Plants* 10:705. doi: 10.3390/plants10040705
- Ingram, J., and Maye, D. (2020). What are the implications of Digitalisation for agricultural knowledge? *Front. Sustain. Food Syst.* 4:66. doi: 10.3389/fsufs.2020.00066
- Jagadish, S., Septiningsih, E., Kohli, A., Thomson, M., Ye, C., Redona, E., et al. (2012). Genetic advances in adapting rice to a rapidly changing climate. *J. Agron. Crop Sci.* 198, 360–373. doi: 10.1111/j.1439-037x.2012.00525.x
- Jamieson, L. E., Li, A., Faulds, K., and Graham, D. (2018). Ratiometric analysis using Raman spectroscopy as a powerful predictor of structural properties of fatty acids. *R. Soc. Open Sci.* 5:181483. doi: 10.1098/rsos.181483

- Johnson, D. B., Kanao, T., and Hedrich, S. (2012). Redox transformations of iron at extremely low pH: fundamental and applied aspects. *Front. Microbiol.* 3:96. doi: 10.3389/fmicb.2012.00096
- Kang, L., Wang, K., Li, X., and Zou, B. (2016). High pressure structural investigation of benzoic acid: Raman spectroscopy and X-ray diffraction. *J. Phys. Chem. C* 120, 14758–14766.
- Kumar, A., Dixit, S., Ram, T., Yadaw, R., Mishra, K., and Mandal, N. (2014). Breeding high-yielding drought-tolerant rice: genetic variations and conventional and molecular approaches. *J. Exp. Bot.* 65, 6265–6278. doi: 10.1093/jxb/eru363
- Kurouski, D., Van Duyne, R. P., and Lednev, I. K. (2015). Exploring the structure and formation mechanism of amyloid fibrils by Raman spectroscopy: a review. *Analyst* 140, 4967–4980. doi: 10.1039/c5an00342c
- Lew, T. T. S., Sarojam, R., Jang, I. C., Park, B. S., Naqvi, N. I., Wong, M. H., et al. (2020). Species-independent analytical tools for next-generation agriculture. *Nat. Plants* 6, 1408–1417. doi: 10.1038/s41477-020-00808-7
- Li, J.-Y., Liu, J., Dong, D., Jia, X., Mccouch, S. R., and Kochian, L. V. (2014). Natural variation underlies alterations in Nramp aluminum transporter (NRAT1) expression and function that play a key role in rice aluminum tolerance. *Proc. Natl. Acad. Sci. U.S.A.* 111, 6503–6508. doi: 10.1073/pnas.1318975111
- Liang, Y., Tabien, R. E., Tarpley, L., Mohammed, A. R., and Septiningsih, E. M. (2021). Transcriptome profiling of two rice genotypes under mild field drought stress during grain-filling stage. *AoB Plants* 13:lab043. doi: 10.1093/aobpla/plab043
- Mandriale, L., Rotunno, S., Miozzi, L., Vaira, A. M., Giovannozzi, A. M., Rossi, A. M., et al. (2019). Nondestructive Raman spectroscopy as a tool for early detection and discrimination of the infection of tomato plants by two economically important viruses. *Anal. Chem.* 91, 9025–9031. doi: 10.1021/acs.analchem.9b01323
- Mantri, N., Patade, V., Penna, S., Ford, R., and Pang, E. (2012). “Abiotic stress responses in plants: present and future,” in *Abiotic Stress Responses in Plants*, eds P. Ahmad and M. Prasad (New York, NY: Springer), 1–19. doi: 10.1007/978-1-4614-0634-1_1
- Masson, P., Dalix, T., and Bussière, S. (2010). Determination of major and trace elements in plant samples by inductively coupled plasma–mass spectrometry. *Commun. Soil Sci. Plant Anal.* 41, 231–243.
- Matthus, E., Wu, L.-B., Ueda, Y., Höller, S., Becker, M., and Frei, M. (2015). Loci, genes, and mechanisms associated with tolerance to ferrous iron toxicity in rice (*Oryza sativa* L.). *Theor. Appl. Genet.* 128, 2085–2098. doi: 10.1007/s00122-015-2569-y
- Nagayama, T., Nakamura, A., Yamaji, N., Satoh, S., Furukawa, J., and Iwai, H. (2019). Changes in the distribution of pectin in root border cells under aluminum stress. *Front. Plant Sci.* 10:1216. doi: 10.3389/fpls.2019.01216
- Nambara, E., and Marion-Poll, A. (2005). ABCISIC ACID BIOSYNTHESIS AND CATABOLISM. *Annu. Rev. Plant Biol.* 56, 165–185. doi: 10.1146/annurev.arplant.56.032604.144046
- Pan, T.-T., Pu, H., and Sun, D.-W. (2017). Insights into the changes in chemical compositions of the cell wall of pear fruit infected by *Alternaria alternata* with confocal Raman microspectroscopy. *Postharv. Biol. Technol.* 132, 119–129. doi: 10.1016/j.postharvbio.2017.05.012
- Payne, W. Z., and Kourouski, D. (2021). Raman-based diagnostics of biotic and abiotic stresses in plants. A review. *Front. Plant Sci.* 11:616672. doi: 10.3389/fpls.2020.616672
- Roschztardt, H., Conejero, G., Divol, F., Alcon, C., Verdeil, J. L., Curie, C., et al. (2013). New insights into Fe localization in plant tissues. *Front. Plant Sci.* 4:350. doi: 10.3389/fpls.2013.00350
- Rys, M., Juhasz, C., Surowka, E., Janeczko, A., Saja, D., Tobias, I., et al. (2014). Comparison of a compatible and an incompatible pepper-tobamovirus interaction by biochemical and non-invasive techniques: chlorophyll a fluorescence, isothermal calorimetry and FT-Raman spectroscopy. *Plant Physiol. Biochem.* 83, 267–278. doi: 10.1016/j.plaphy.2014.08.013
- Sáez-Plaza, P., Navas, M. J., Wybraniec, S., Michałowski, T., and Asuero, A. G. (2013). An overview of the Kjeldahl method of nitrogen determination. Part II. Sample preparation, working scale, instrumental finish, and quality control. *Crit. Rev. Anal. Chem.* 43, 224–272. doi: 10.1080/10408347.2012.751787
- Sahrawat, K. L. (2005). Iron toxicity in wetland rice and the role of other nutrients. *J. Plant Nutr.* 27, 1471–1504. doi: 10.1081/pln-200025869
- Samonte, S. O. P. B., Tabien, R. E., and Wilson, L. T. (2013). Parental selection in rice cultivar improvement. *Rice Sci.* 20, 45–51. doi: 10.1016/s1672-6308(13)60107-9
- Sanchez, L., Ermolenkov, A., Biswas, S., Septiningsih, E. M., and Kourouski, D. (2020a). Raman spectroscopy enables non-invasive and confirmatory diagnostics of salinity stresses, nitrogen, phosphorus, and potassium deficiencies in rice. *Front. Plant Sci.* 11:573321. doi: 10.3389/fpls.2020.573321
- Sanchez, L., Ermolenkov, A., Tang, X. T., Tamborindeguy, C., and Kourouski, D. (2020b). Non-invasive diagnostics of *Liberibacter* disease on tomatoes using a hand-held Raman spectrometer. *Planta* 251:64. doi: 10.1007/s00425-020-03359-5
- Sanchez, L., Pant, S., Mandadi, K., and Kourouski, D. (2020c). Raman spectroscopy vs quantitative polymerase chain reaction in early stage Huanglongbing diagnostics. *Sci. Rep.* 10:10101. doi: 10.1038/s41598-020-67148-6
- Sanchez, L., Pant, S., Irely, M., Mandadi, K., and Kourouski, D. (2019a). Detection and identification of canker and blight on orange trees using a hand-held Raman spectrometer. *J. Raman Spectrosc.* 50, 1875–1880. doi: 10.1002/jrs.5741
- Sanchez, L., Pant, S., Xing, Z., Mandadi, K., and Kourouski, D. (2019b). Rapid and noninvasive diagnostics of Huanglongbing and nutrient deficits on citrus trees with a handheld Raman spectrometer. *Anal. Bioanal. Chem.* 411, 3125–3133. doi: 10.1007/s00216-00019-01776-00214
- Schulz, H., Baranska, M., and Baranski, R. (2005). Potential of NIR-FT-Raman spectroscopy in natural carotenoid analysis. *Biopolymers* 77, 212–221. doi: 10.1002/bip.20215
- Septiningsih, E. M., and Mackill, D. J. (2018). “Genetics and breeding of flooding tolerance in rice,” in *Rice Genomics, Genetics and Breeding*, eds T. Sasaki and M. Ashikari (Singapore: Springer), 275–295. doi: 10.1007/978-981-10-7461-5_15
- Singh, A., Carandang, J., Gonzaga, Z. J. C., Collard, B. C., Ismail, A. M., and Septiningsih, E. M. (2017). Identification of QTLs for yield and agronomic traits in rice under stagnant flooding conditions. *Rice* 10, 1–18. doi: 10.1186/s12284-017-0154-5
- Stanley, L., and Yuan, Y.-W. (2019). Transcriptional regulation of carotenoid biosynthesis in plants: so many regulators, so little consensus. *Front. Plant Sci.* 10:1017. doi: 10.3389/fpls.2019.01017
- Swapnil, P., Meena, M., Singh, S. K., Dhuldhaj, U. P., Harish, and Marwal, A. (2021). Vital roles of carotenoids in plants and humans to deteriorate stress with its structure, biosynthesis, metabolic engineering and functional aspects. *Curr. Plant Biol.* 26, 100203. doi: 10.1016/j.cpb.2021.100203
- Synysya, A., Čopíková, J., Matijka, P., and Machoví, V. (2003). Fourier transform Raman and infrared spectroscopy of pectins. *Carbohydr. Polym.* 54, 97–106. doi: 10.1016/S0144-8617(03)00158-9
- Thapa, R., Tabien, R. E., Thomson, M. J., and Septiningsih, E. M. (2020). Genome-wide association mapping to identify genetic loci for cold tolerance and cold recovery during germination in rice. *Front. Genet.* 11:22. doi: 10.3389/fgene.2020.00022
- Thomson, M. J., Ismail, A. M., Mccouch, S. R., and Mackill, D. J. (2009). “Marker assisted breeding,” in *Abiotic Stress Adaptation in Plants*, eds A. Pareek, S. Sopory, and H. Bohnert (Dordrecht: Springer), 451–469.
- Tnani, H., Chebotarov, D., Thapa, R., Ignacio, J. C. I., Israel, W. K., Quilloy, F. A., et al. (2021). Enriched-GWAS and transcriptome analysis to refine and characterize a major QTL for anaerobic germination tolerance in rice. *Int. J. Mol. Sci.* 22:4445. doi: 10.3390/ijms22094445
- Tokaloğlu, S. (2013). Determination of trace elements in commonly consumed medicinal herbs by ICP-MS and multivariate analysis. *Food Chem.* 134, 2504–2508. doi: 10.1016/j.foodchem.2012.04.093
- Wachasunder, S. D., and Nafade, A. (2001). Precision and accuracy control in the determination of heavy metals by atomic absorption spectrometry. *Science* 58, 517–528. doi: 10.1080/00207230108711348
- Waqas, M. A., Kaya, C., Riaz, A., Farooq, M., Nawaz, I., Wilkes, A., et al. (2019). Potential mechanisms of abiotic stress tolerance in crop plants induced by Thiourea. *Front. Plant Sci.* 10:1336. doi: 10.3389/fpls.2019.01336
- Wiercigroch, E., Szafraniec, E., Czamara, K., Pacia, M. Z., Majzner, K., Kochan, K., et al. (2017). Raman and infrared spectroscopy of carbohydrates: a review. *Spectrochim. Acta A* 185, 317–335. doi: 10.1016/j.saa.2017.05.045

- Woods, J. T., and Mellon, M. G. (1941). Thiocyanate method for iron. A spectrophotometric study. *Ind. Eng. Chem. Anal. Ed.* 13, 551–554. doi: 10.1021/i560096a013
- Wu, H.-C., Bulgakov, V. P., and Jinn, T.-L. (2018). Pectin methylesterases: cell wall remodeling proteins are required for plant response to heat stress. *Front. Plant Sci.* 9:1612. doi: 10.3389/fpls.2018.01612
- Yu, M. M. L., Schulze, H. G., Jetter, R., Blades, M. W., and Turner, R. F. B. (2007). Raman microspectroscopic analysis of triterpenoids found in plant cuticles. *Appl. Spectrosc.* 61, 32–37. doi: 10.1366/000370207779701352

Conflict of Interest: The authors declare that the research was conducted in the absence of any commercial or financial relationships that could be construed as a potential conflict of interest.

Publisher's Note: All claims expressed in this article are solely those of the authors and do not necessarily represent those of their affiliated organizations, or those of the publisher, the editors and the reviewers. Any product that may be evaluated in this article, or claim that may be made by its manufacturer, is not guaranteed or endorsed by the publisher.

Copyright © 2022 Higgins, Biswas, Goff, Septiningsih and Kurouski. This is an open-access article distributed under the terms of the Creative Commons Attribution License (CC BY). The use, distribution or reproduction in other forums is permitted, provided the original author(s) and the copyright owner(s) are credited and that the original publication in this journal is cited, in accordance with accepted academic practice. No use, distribution or reproduction is permitted which does not comply with these terms.



Non-destructive Technologies for Plant Health Diagnosis

Mervin Chun-Yi Ang¹ and Tedrick Thomas Salim Lew^{2,3*}

¹ Disruptive and Sustainable Technologies for Agricultural Precision IRG, Singapore-MIT Alliance for Research and Technology, Singapore, Singapore, ² Department of Chemical and Biomolecular Engineering, National University of Singapore, Singapore, Singapore, ³ Institute of Materials Research and Engineering, Agency for Science, Technology and Research (A*STAR), Singapore, Singapore

OPEN ACCESS

Edited by:

Nam-Hai Chua,
Temasek Life Sciences
Laboratory, Singapore

Reviewed by:

Kanchan Vishwakarma,
Swedish University of Agricultural
Sciences, Sweden

*Correspondence:

Tedrick Thomas Salim Lew
tedrick@nus.edu.sg
orcid.org/0000-0002-4815-9921

Specialty section:

This article was submitted to
Technical Advances in Plant Science,
a section of the journal
Frontiers in Plant Science

Received: 26 February 2022

Accepted: 29 April 2022

Published: 27 May 2022

Citation:

Ang MC-Y and Lew TTS (2022)
Non-destructive Technologies for
Plant Health Diagnosis.
Front. Plant Sci. 13:884454.
doi: 10.3389/fpls.2022.884454

As global population grows rapidly, global food supply is increasingly under strain. This is exacerbated by climate change and declining soil quality due to years of excessive fertilizer, pesticide and agrichemical usage. Sustainable agricultural practices need to be put in place to minimize destruction to the environment while at the same time, optimize crop growth and productivity. To do so, farmers will need to embrace precision agriculture, using novel sensors and analytical tools to guide their farm management decisions. In recent years, non-destructive or minimally invasive sensors for plant metabolites have emerged as important analytical tools for monitoring of plant signaling pathways and plant response to external conditions that are indicative of overall plant health in real-time. This will allow precise application of fertilizers and synthetic plant growth regulators to maximize growth, as well as timely intervention to minimize yield loss from plant stress. In this mini-review, we highlight *in vivo* electrochemical sensors and optical nanosensors capable of detecting important endogenous metabolites within the plant, together with sensors that detect surface metabolites by probing the plant surface electrophysiology changes and air-borne volatile metabolites. The advantages and limitations of each kind of sensing tool are discussed with respect to their potential for application in high-tech future farms.

Keywords: nanosensors, wearable sensors, volatiles, plant health, non-destructive

INTRODUCTION

Plant health monitoring is an attractive and sustainable strategy that could be used for optimization of crop growth practices. It complements popular agricultural techniques used by farmers to maximize yield including crop rotation, intercropping and genetic modification (Uzogara, 2000; Wang et al., 2014; Yang et al., 2020). It also allows the precise calibration of optimal dosage and application of agrichemicals such as pesticides, herbicides or plant growth regulators (Ang et al., 2021; Roper et al., 2021). However, current chromatography-based analytical techniques are limiting the potential of plant health monitoring in influencing farm management decisions on a day-to-day basis (Pan et al., 2010; Balcke et al., 2012). Though highly sensitive and quantitative, these techniques are destructive and highly labor-intensive, requiring laboratory-based extraction and processing of multiple plant samples for every data point.

The emergence of non-destructive sensors is critical in supporting more efficient plant health monitoring. These sensors transduce plant signals into digital signals to establish direct communication between plants and growers (Qu et al., 2021). By tapping into plants' physiological events in real time, non-destructive sensors enable prompt adjustment of environmental conditions to augment crop productivity while minimizing resource use (Xi et al., 2021). In this mini-review, the focus is on sensors that detect endogenous metabolites, phytohormones and signaling molecules within the plant itself, and sensors that detect surface or air-borne volatile metabolites. Dynamic changes in internal plant metabolites or signaling molecules often influence various aspects of plant growth and development, as well as plant acclimation responses to external stresses. The *in vivo* sensors are based on either electrochemical sensors or plant nanobionic sensors. Both sensing platforms have shown enhancements in sensitivity and selectivity driven by recent advances in nanotechnology which conferred unique electrocatalytic and optical properties to the sensors (Kwak et al., 2017; Li et al., 2021). **Table 1** compares the various *in vivo* electrochemical and plant nanobionic sensors, plant metabolites it detects, nanomaterial-based sensor design, detection method and plant species that the sensors were demonstrated in. Besides internal signaling molecules and plant phytohormones, plants also emit surface metabolites in the form of electrical signals, and air-borne metabolites in the form of volatile organic compounds (VOCs) serving as chemical signals that mediate inter-plant communication, and trigger defense responses of neighboring receiver plants (Erb, 2018; Hu et al., 2021). This forms the basis of crop yield enhancement through intercropping. Hence, non-destructive sensors that capture and monitor the emission of VOCs in real-time would also be indicative of plant health, enabling early diagnosis of plant diseases.

ELECTROCHEMICAL SENSORS FOR *IN PLANTA* MONITORING OF HORMONES AND SIGNALING MOLECULES

Electrochemical sensing technology is a promising strategy for detection of plant hormones and signaling molecules in living plants. The key advantages of electrochemical sensing technologies include good repeatability and accuracy, high sensitivity, portability due to ease of miniaturization, low cost and relatively rapid response times to analytes (Hayat and Marty, 2014). Typically, an electrochemical sensor comprises a sensing or working electrode, a counter electrode and a reference electrode, separated by an electrolyte. In recent years, advances in nanomaterials have resulted in significant enhancement in the analytical performance of these electrochemical biosensors and this has, in turn, opened up more possibilities for rapid and *in situ* detection of analytes in biological samples (Beaver et al., 2021). Carbon-based nanomaterials and metallic nanoparticles are known to enhance biosensor performance and sensitivity due to their unique electrocatalytic properties, facilitating increased electron transfer of redox-active species (Shi et al., 2011, 2012).

One such sensing tool is a paper-based electroanalytical device developed for detection of H_2O_2 and salicylic acid (SA) in tomato leaves infected with *Botrytis cinerea* pathogen (Sun et al., 2014, 2020). Out of all the reactive oxygen species (ROS) molecules, H_2O_2 has the longest stability within plant cells (Huang et al., 2019). Hence, H_2O_2 is the key ROS molecule known to participate in cell signaling regulation and induction of plant defense gene expression upon inoculation with bacteria. On the other hand, SA is the main plant hormone involved in plant defense and immunity (Fu and Dong, 2013; Ding and Ding, 2020; Vlot et al., 2021). For detection of H_2O_2 or SA on the paper-based electroanalytical devices, circular tomato leaves samples were punched out of the leaf at different times post infection and transferred onto the surface of their respective working electrodes for measurement (**Figure 1A**). While it provides rapid detection of H_2O_2 and SA, this detection method is invasive and destructive as punching out of leaf samples could cause wounding and tissue senescence.

It remains challenging to achieve online monitoring of electrochemical signals *in situ* without the need to extract or cut up leaf samples. Some researchers have managed to insert electrochemical sensors into fruits for measurement of plant metabolites. For instance, an electrochemical tryptophan (Tryp) sensor was fabricated onto a glass carbon electrode (GCE) for detection in tomato fruit samples (Gao et al., 2021). Tryp is an important precursor for auxin (IAA) biosynthesis and IAA is a plant hormone that plays a crucial role in controlling plant development (Teale et al., 2006). Due to the GCE size, the Tryp electrochemical sensor causes plant tissue damage upon electrode insertion in smaller fruits. Recently, a miniaturized Tryp electrochemical sensor has been constructed using a smaller graphite rod electrode (GRE) (**Figure 1B**) (Yang et al., 2021) which causes less tissue damage during insertion and has successfully detected Tryp levels in smaller fruits such as cherry tomatoes. However, even with the miniaturized GRE, minimizing plant tissue damage when inserting the sensor electrode to other fragile plant parts, such as the leaves or stem, remains complicated.

Microneedle arrays are an attractive option that has been used for construction of minimally invasive electrodes that can be inserted into plant samples. This strategy forms the basis of *in situ* abscisic acid (ABA) (**Figure 1C**) and SA (**Figure 1E**) electrochemical sensors (Liu et al., 2021; Wang et al., 2021). ABA is a plant hormone crucial in plant development processes, such as seed germination, stomato closure and plant adaptation to stresses (Lee and Luan, 2012; Hsu et al., 2021). Both sensors use chronocoulometry as electrochemical sensing strategy, which measures the amperometric response currents of the analytes and generates current-time curves. To minimize damage to plant tissues, the ABA and SA sensors were assembled onto a microneedle and inter-digitated microelectrode (IDME) arrays, respectively to be inserted into plant samples such as cucumber fruit (**Figure 1D**) and leaves (**Figure 1F**) (Liu et al., 2021; Wang et al., 2021). Remarkably, the SA sensor could be attached to cucumber leaves for 1 month, constantly monitoring changes in SA levels without adversely affect plant growth, confirming its reliability and stability. While attaching the IDME array

sensor caused minimal tissue damage to mature cucumber leaves, further work needs to be done to confirm if the same applies to smaller plants or crops.

All in all, electrochemical sensors designed for *in vivo* detection of plant hormones and metabolites are rapid and low-cost. Coupled with novel nanomaterials, the sensors achieved enhanced sensitivities which enable detection of plant hormones and metabolites which are typically present in low quantities. Despite this progress, most electrochemical sensors have been designed to detect biomolecules only in fruit samples with limited applicability to other plant organs. Future approaches include the development of biocompatible nanoelectrodes that could be inserted into the leaves, stem or roots of different plant species with negligible tissue damage.

PLANT NANOBIOTIC SENSORS FOR *IN VIVO* MONITORING OF HORMONES AND SIGNALING MOLECULES

Aside from possessing unique electrocatalytic properties, carbon-based nanomaterials such as single-walled carbon nanotubes (SWNTs) have photostable emission in the near-infrared (nIR) region that does not overlap with chlorophyll autofluorescence (Kwak et al., 2017). This facilitates the application of SWNTs as *in vivo* optical sensors for plant signaling molecules and hormones. The polymer or single-stranded DNA doubles up as a SWNT dispersing agent in aqueous medium and as a synthetic, non-biological antibody for selective recognition and binding to specific plant signaling molecules and hormones. This technique is known as corona phase molecular recognition (CoPhMoRe) whereby different polymer structures or DNA sequences result in the creation of distinct SWNT corona phases that triggers optical modulations such as fluorescence intensity changes or wavelength shifts upon analyte binding (Zhang et al., 2013). Upon syringe infiltration to different plant species, including model species *Arabidopsis thaliana* and non-model plants such as arugula and spinach, these nanosensors could non-destructively monitor the spatiotemporal profile of endogenous signaling molecules and hormones (Lew et al., 2020a). Such information could be captured remotely with portable electronics, providing users with real-time information about plant health. One such nanosensor is designed for *in planta* detection of stress-induced H_2O_2 signaling waves in different plant species, including lettuce (*Lactuca sativa*), arugula (*Eruca sativa*), spinach (*Spinacia oleracea*), strawberry blite (*Blitum capitatum*), sorrel (*Rumex acetosa*) and *Arabidopsis thaliana* (Figure 1G) (Lew et al., 2020b). The sensor utilizes a single-stranded (GT)₁₅ wrapped SWNT suspension that selectively and reversibly binds to H_2O_2 . Different types of stress inflicted onto the plants also resulted in the formation of unique H_2O_2 signaling waveforms varying in amplitude, velocity and full-width-half-maximum (Figure 1H). The specific stress-induced waveforms aids in the elucidation of complex ROS signaling pathways occurring in real-time upon plant acclimation to external stresses.

Plant nanobiotic sensors have also been developed for rapid detection of synthetic auxin plant hormones, used extensively

in plant tissue cultures and as herbicides (Figure 1I) (Ang et al., 2021). Synthetic auxins, 1-naphthalene acetic acid (NAA) and 2,4-dichlorophenoxyacetic acid (2,4-D), are important agricultural and horticultural tools as they mimic natural auxins in influencing various aspects of plant growth and development and are more chemically stable and potent compared to natural auxins (Gianfagna, 1995). Separately, 2 different cationic polymer wrapped SWNTs are reported to selectively detect NAA and 2,4-D in different plant species including spinach, *Arabidopsis thaliana*, *Brassica rapa subsp. chinensis* (pak choi), and *Oryza sativa* (rice) grown in various media, including soil, hydroponic, and plant tissue culture media. The 2,4-D nanosensor also has potential application in rapid testing of 2,4-D herbicide susceptibility as it revealed a discrepancy in uptake and accumulation of supplemented 2,4-D in the leaves of susceptible pak choi vs. resistant rice.

Besides plant hormones and signaling molecules, SWNT-based optical nanosensors have been used in detection of secondary metabolites such as polyphenols. Polyphenols are commonly induced in plants as defense against pathogens or herbivores (Singh et al., 2021). They are prevalent in all plant tissues and organs and are specifically secreted into root exudates to repel pathogenic micro-organisms (Baetz and Martinoia, 2014). Nißler et al. (2022) discovered a selective nanosensor for tannic acid, a key polyphenol using polyethylene glycol phospholipid biopolymer as SWNT wrapping. The optical nanosensor detected tannic acid level changes in *Tococa* leaf methanol extracts challenged with herbivores and in *Glycine max* (soybean) cell culture samples stimulated with a pathogen-derived elicitor, a branched β -glucan cell wall component of the Oomycete fungus *Phytophthora sojae*. It also enabled real-time visualization of polyphenols secreted from the roots of soybean seedlings over a 24 h time-period post elicitor treatment.

By embedding nanosensors into leaves, living plants have also been engineered to detect contaminants that are transported into the plant via the roots and stem. Recently, a plant nanobiotic sensor is developed for detection of arsenite, a toxic heavy metal pollutant predominantly found in anaerobic rice paddy soils taken up through silicon transporters in the roots (Ma et al., 2008). Here, the SWNT is wrapped with single-stranded (GT)₅ which resulted in a strong and selective turn-on response upon detection of arsenite (Figure 1J) (Lew et al., 2021). The sensors were successfully embedded in spinach and rice leaves that detected arsenite that was introduced to the root medium. Further, they were demonstrated in *Pteris cretica* ferns which had the natural ability to hyperaccumulate and tolerate high levels of arsenite (Meharg, 2003). By combining the optical properties of the nanosensor and the intrinsic ability of these ferns to pre-concentrate arsenite, the sensitivity of the nanosensor is enhanced, enabling the detection of 0.6 and 0.2 ppb levels of arsenite after 7 and 14 days, respectively. In another study, peptide-functionalized SWNTs were designed to optically detect picric acid, a common explosive analyte, in spinach plants (Figure 1K) (Wong et al., 2017). In general, the real-time information obtained by these plant nanobiotic sensors could be interfaced with portable and inexpensive electronics such as the

TABLE 1 | Comparison of the various *in vivo* electrochemical and plant nanobionic sensors.

Electrochemical sensors					
Plant analyte	Working electrode	Nanomaterials-based modification	Detection method	Plant species	References
H ₂ O ₂	Indium tin oxide	Nano-gold	Voltammetry	Tomato leaves	Sun et al., 2020
SA	Carbon tape	Multi-walled carbon nanotubes/Nafion	Voltammetry	Tomato leaves	Sun et al., 2014
Tryp	Glass carbon	Polydopamine/reduced graphene oxide/MnO ₂ nanocomposite	Voltammetry	Tomato fruits	Gao et al., 2021
Tryp	Miniaturized graphite rod	Multi-walled carbon nanotubes/poly(sulfosalicylic acid)	Voltammetry	Tomato and cherry tomato fruits	Yang et al., 2021
ABA	Ta wires	Vertical graphene with core-shell Au@SnO ₂ nanoparticles assembled onto microneedle array	Chronocoulometry	Cucumber fruits and juices, grapes and radishes, blended Arabidopsis leaf juices	Wang et al., 2021
SA	Al microelectrodes	Core-shell Au@Cu ₂ O nanoparticles, graphene and polydopamine densely packed into IDME array	Chronocoulometry	Cucumber leaves, juices and stems	Liu et al., 2021
Plant nanobionic sensors					
Plant analyte	SWNT type	SWNT modification	Detection method	Plant species	References
H ₂ O ₂	HiPco SWNT and (6,5)-enriched SWNT	Single-stranded DNA oligomer: (GT) ₁₅	nIR fluorescence quenching	Lettuce, Arugula, Spinach, Strawberry blite, Sorrel, Arabidopsis thaliana leaves	Lew et al., 2020b
NAA	HiPco SWNT	Cationic poly(N-vinyl imidazolium)	nIR fluorescence quenching	Spinach, Arabidopsis thaliana, Pak choi, Rice leaves	Ang et al., 2021
2,4-D	HiPco SWNT	Cationic fluorene-co-phenyl polymer	nIR fluorescence turn-on	Spinach, Arabidopsis thaliana, Pak choi, Rice leaves	Ang et al., 2021
Tannic acid	Monochiral (6,5) SWNT	Polyethylene glycol-phospholipids	nIR fluorescence red-shift and quenching	Soybean Glycine suspension cells, Soybean seedling root exudates, Tococa leaf methanol extracts	Niöbler et al., 2022
As (III)	HiPco SWNT	Single-stranded DNA oligomer: (GT) ₅	nIR fluorescence turn-on	Spinach, Rice and Pteris cretica hyperaccumulator fern leaves	Lew et al., 2021
Picric acid	HiPco SWNT and (6,5)-enriched SWNT	Bombolitin II peptide	nIR fluorescence quenching	Spinach leaves	Wong et al., 2017

Raspberry Pi-based camera module, enabling remote sensing in the field.

In summary, plant nanobionic sensors represent a significant advance in the field of non-destructive sensing in living plants. No pre-treatment, extraction or cutting up of plant samples are required as *in vivo* sensing capabilities are imparted to the plants. They are versatile and have successfully extracted spatiotemporal information about various analytes of interest from a diverse range of plant species that are agriculturally important (Lew et al., 2020d). Plant signaling pathways are however complicated and will require the generation of an integrated response from multiplexing of different nanosensors in order to untangle their intricate interactions. In particular, nanoparticle design principles to localize nanosensors within specific plant organs or compartments will be important to facilitate sensor multiplexing and to illuminate inter-organelle signaling (Lew et al., 2018, 2020c).

NON-DESTRUCTIVE DETECTION OF SURFACE AND AIRBORNE PLANT METABOLITES

Besides internal metabolites, plants also propagate a wide range of signaling molecules along the surface of their organs in response to changing environmental conditions (Mcsteeen and Zhao, 2008; Wong et al., 2017; Lew et al., 2020a). These surface metabolites can be accessed non-destructively to inform the state of plant health and stress conditions. In particular, conductive materials which can conform onto the leaf surface have been engineered to probe electrical signals induced by external stresses. These materials have been shown to adhere onto the leaf surface despite the irregular surface topographies and the existence of trichomes in many plant species. Conductive agar gels, connected to metal wires, can be employed as electrodes to capture the temporal profile of electrical signals elicited upon wounding in *Arabidopsis thaliana* (Mousavi et al., 2013; Nguyen

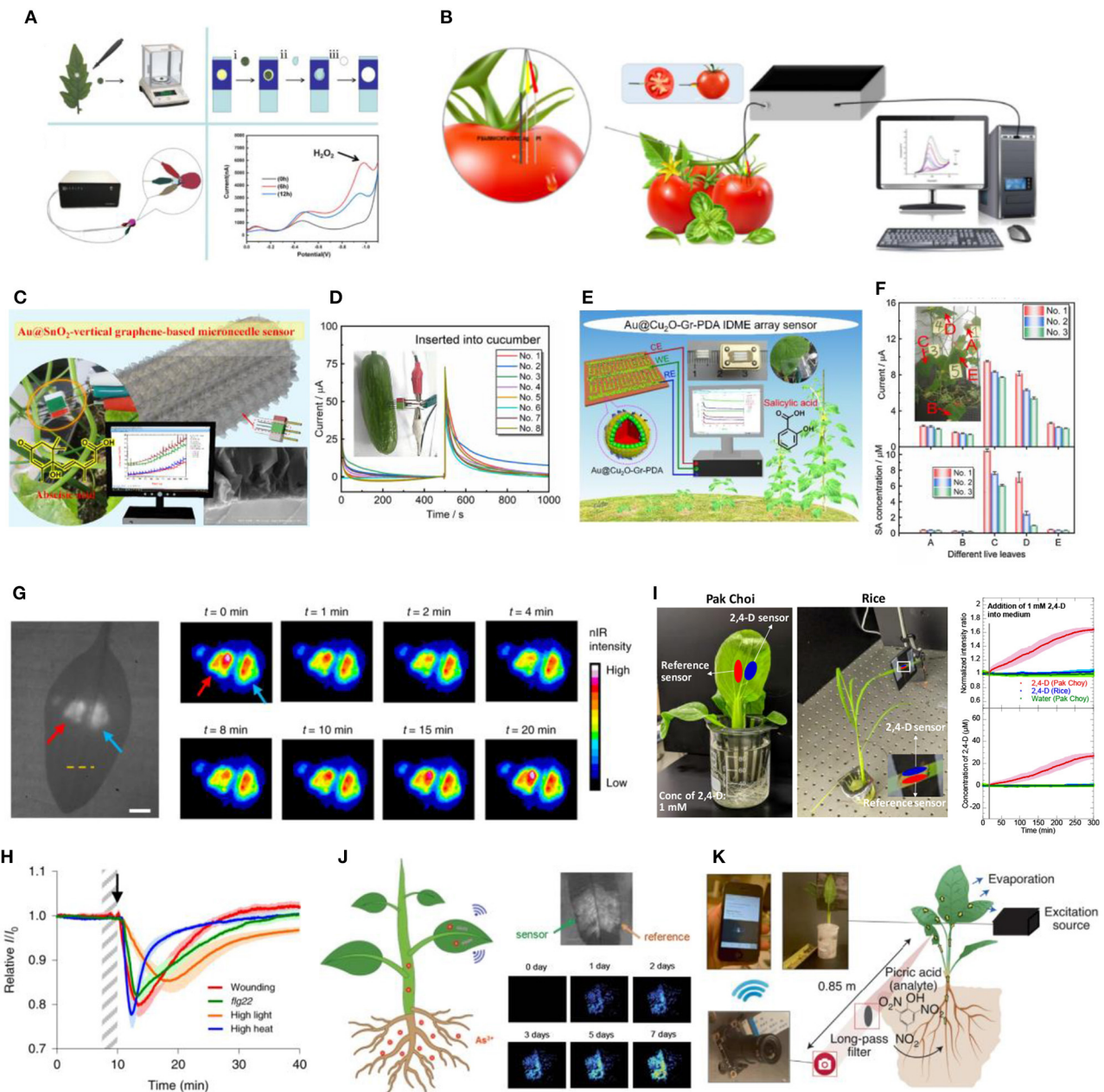


FIGURE 1 | (A) Paper-based electro-analytical device used in detection of H_2O_2 in circular plant samples punched out of the tomato leaves (Sun et al., 2020); (B) Miniaturized electrochemical sensor inserted into tomato fruits for detection of auxin precursor, Tryp (Yang et al., 2021); (C) *in situ* ABA electrochemical sensor assembled onto a microneedle array for detection in fruits (Wang et al., 2021); (D) Current-time curves generated when the ABA microneedle sensor is inserted into cucumber where ABA concentrations is linearly correlated with the step current observed (Wang et al., 2021); (E) *in situ* SA electrochemical sensor arranged in an IDME array for insertion into cucumber leaves (Liu et al., 2021); (F) Response current (top) and derived SA concentration (bottom) obtained from the IDME array sensor in 5 different live cucumber leaves (Liu et al., 2021); (G) Brightfield (left) and corresponding false-colored images (right) of a spinach leaf infiltrated with H_2O_2 (red arrow) and reference (blue arrow) nanosensors on both sides of the leaf mid-vein. False-colored images shows the transient H_2O_2 wave upon mechanical wounding of the leaf at $t = 0$ min (Lew et al., 2020b); (H) H_2O_2 nanosensor response to different types of stress applied to the plant, including mechanical wounding (red), *flg22* treatment (green), high light (orange) and high heat (blue) stresses (Lew et al., 2020b); (I) Real-time sensing of 2,4-D uptake in hydroponically grown pak choi and rice leaves using nanosensors which illustrated a turn-on response observed in pak choi but not in rice over a time-period of 5 h (Ang et al., 2021); (J) Arsenite nanobionic sensor infiltrated into hyperaccumulator plant *Pteris cretica* fern, showing intensity changes corresponding to arsenic accumulation detected over 7-day time period upon arsenite exposure (Lew et al., 2021); (K) Schematic of standoff detection of nitroaromatic compound, picric acid, using nanosensors with real-time information relayed from the nanosensor-infiltrated plant to a portable Raspberry Pi-based electronic device (Wong et al., 2017).

et al., 2018). Recently, the conformability of such hydrogel-based approach was improved by using thermogels as morphable electrodes (Luo et al., 2021). The thermogel solution can undergo *in situ* gelation on hairy leaf surfaces at room temperature to provide higher adhesiveness and improved signal-to-noise ratio for plant electrophysiology (Figure 2A). In another approach, biocompatible polymer electrodes were printed on the leaf surface using the vapor-phase polymerization process (Kim et al., 2019). Stress perception would trigger changes in the electrical conductivity along the surface of plant organs,

which can be monitored with the vapor-deposited polymer electrodes through bioimpedance spectroscopy. Drought and UV photodamage in plants can be monitored over 130 days with this approach. Through non-destructive impedance measurements, these conformal polymer electrodes also enabled early detection of ozone damage in fruiting plants before the manifestation of leaf necrosis (Figure 2B) (Kim et al., 2020). Instead of monitoring electrical signals propagated by plants, Koman et al. developed an innovative approach to monitor the opening and closing of stomata by printing a conductive ink across

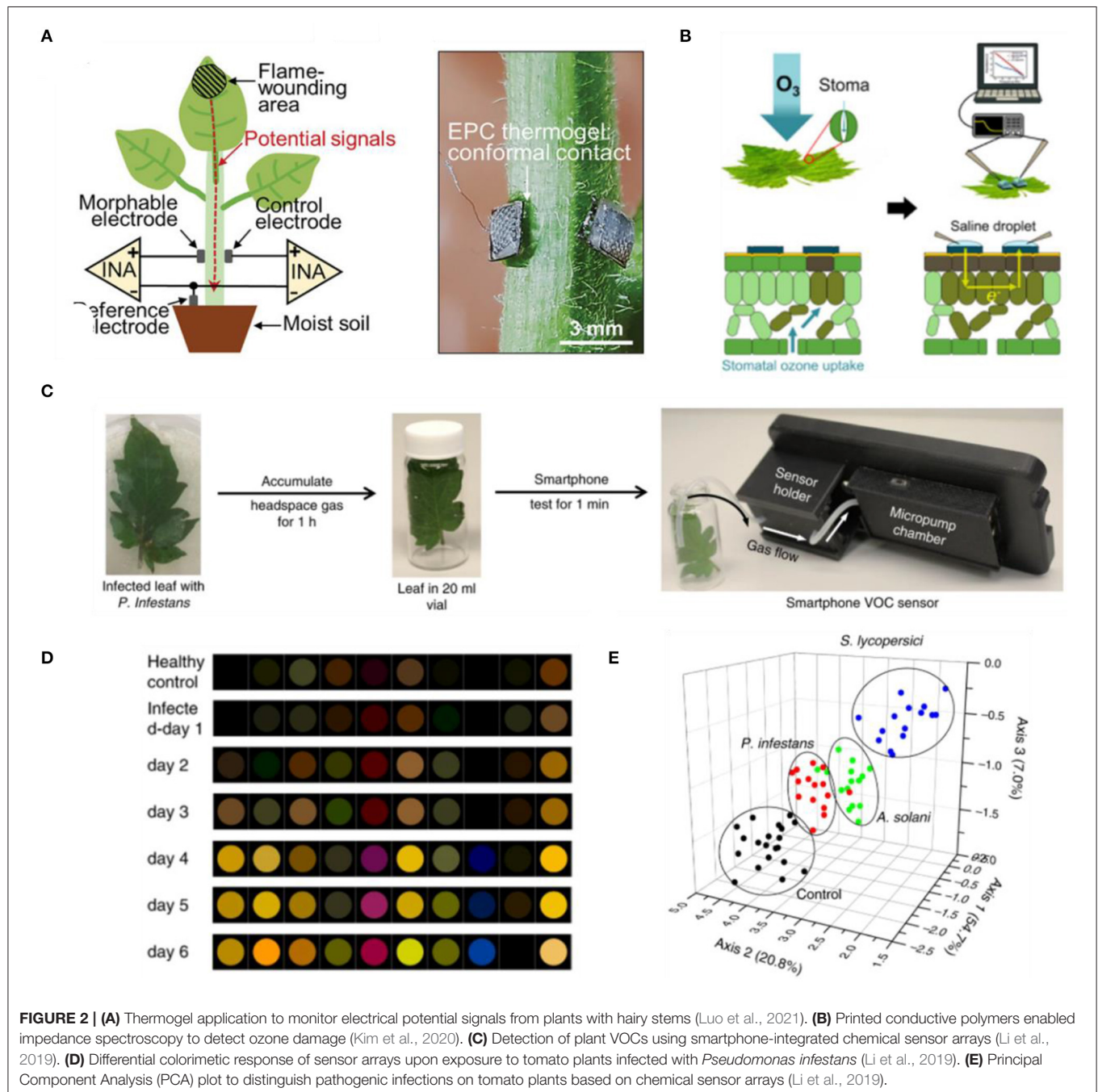


FIGURE 2 | (A) Thermogel application to monitor electrical potential signals from plants with hairy stems (Luo et al., 2021). **(B)** Printed conductive polymers enabled impedance spectroscopy to detect ozone damage (Kim et al., 2020). **(C)** Detection of plant VOCs using smartphone-integrated chemical sensor arrays (Li et al., 2019). **(D)** Differential colorimetric response of sensor arrays upon exposure to tomato plants infected with *Pseudomonas infestans* (Li et al., 2019). **(E)** Principal Component Analysis (PCA) plot to distinguish pathogenic infections on tomato plants based on chemical sensor arrays (Li et al., 2019).

the stomatal apertures (Koman et al., 2017). Stomata opening causes the contact of conductive ink across the guard cells to be broken, leading to an increase in the electrical resistance. The circuit is closed when the aperture closes, lowering the resistance. Hence, this approach enabled monitoring of stomata opening and closing latencies. Stomatal dynamics in response to different light wavelengths and drought conditions could be captured with the printed conductive ink over a period of 7 days. These approaches highlight promising technologies capable of long-term monitoring of plant electrophysiology for stress detection. However, they are labor intensive as their measurements necessitate physical contact with conductive wires to obtain the electrical resistance or impedance values. If the circuit information can be transmitted wirelessly, it will pave way toward wider applications in the field without requiring wired connections or skilled personnel to operate such technology.

There are various types of VOCs that plants employ as communication signals in response to abiotic and biotic stresses (Engelberth et al., 2004; Ton et al., 2006; Erb et al., 2015; Acton et al., 2018). As airborne metabolites, these VOCs serve as signaling molecules between different plant organs and between distant plants (Maffei et al., 2011; Karban, 2017; Cofer et al., 2018). Detection of these VOCs could therefore indicate plant health status non-invasively (Tholl et al., 2021). In general, the detection of VOCs from plants in the field is categorized under two sequential procedures: sampling and analysis. Sampling is required to trap and pre-concentrate VOCs to achieve the detection limit of the analytical instrument. An adsorbent material is typically used to capture VOCs, either through static or dynamic pre-concentration (Jansen et al., 2011). Once trapped, these VOCs can be released upon thermal desorption treatment using a gas chromatography coupled with mass spectrometer (GC-MS). The mixture of VOCs can then be separated and identified with GC-MS analysis. However, this conventional GC-MS-based analysis method requires complex laboratory equipment with substantial time lags between sampling and analysis, limiting on-field analysis of plant VOCs. Portable GC-MS instruments have been developed to accelerate VOCs analysis (Beck et al., 2015; Sharma et al., 2019; Stierlin et al., 2020), but they often require manual sample injection and suffer from poor compound resolution due to limited column length.

Electronic nose-based approach has been demonstrated for a more rapid detection of plant VOCs. This technology leverages changes in the electrical output of a chemical sensor array when a mixture of VOCs flow over the sensor array (Cui et al., 2018; Karakaya et al., 2020). The collective array pattern can then be analyzed to distinguish between different VOCs, enabling non-destructive monitoring of plant VOCs. Analysis of VOCs emitted by diseased plants through this electronic nose approach enabled early identification of bacterial diseases in apple plants before symptom manifestation (Cellini et al., 2016), as well as discrimination of healthy rice plants from those infected with brown planthopper (*Nilaparvata lugens*) (Xu et al., 2014). Building on the electronic nose approach, nanoparticle-based chemical sensor arrays were recently coupled with a smartphone for non-destructive analysis of VOCs from tomato plants (Figure 2C) (Li et al., 2019). The arrays would

change color differently in response to various VOCs, enabling fingerprinting of 10 green leaf volatiles. This concept was then used to detect late blight in tomato as early as the second day of pathogen inoculation (Figures 2D,E). While these are promising developments in sensing plant VOCs, the stability and selectivity of these technologies in response to different stressors and pathogen infections are still to be studied for widespread application in the field.

DISCUSSION

A multitude of advanced materials and novel technologies have been proposed for non-destructive plant health monitoring. These toolsets can be broadly categorized into *in vivo* sensors, which aim to probe the signaling molecules within plant tissues, or platforms to detect surface and airborne metabolites. Monitoring the internal signaling molecules has the advantage of detecting physiological concentrations of plant hormones and small molecules immediately after stress is perceived, enabling real-time plant stress detection. Electrochemical-based microneedle array sensors and fluorescent nanosensors are exciting developments in this area which have been employed to study plant signaling pathways and reveal new mechanistic understandings of plant physiology in response to stresses. While promising, these sensors still need to be introduced manually into the plant tissues, limiting the throughput of such approach for agricultural applications. Non-destructive technologies to detect surface and airborne metabolites include conductive polymers and gels to monitor plant electrophysiology, as well as portable GC-MS and electronic nose approach for VOCs analysis. These platforms do not require access to the internal plant tissues or cells, and thus can be conveniently applied outside of the plant organs for non-invasive monitoring. However, some of these approaches suffer from low sensitivity, bulky form factors and unproven demonstrations in the field. Despite these limitations, non-destructive plant health monitoring has significantly improved our understanding of plant physiological responses to external stresses. Progress in this research area should give rise to more advanced technologies which can be applied to study agriculturally relevant crops in the field, bridging the knowledge gap between model plants commonly used in plant biology and economically important crops.

AUTHOR CONTRIBUTIONS

MA and TL designed the study, generated ideas for discussion, and wrote the manuscript. All authors contributed to the article and approved the submitted version.

ACKNOWLEDGMENTS

TL acknowledges the support by the Agency of Science, Technology and Research (A*STAR) Career Development Fund, Project No. C210812034. MA is grateful for the funding and support from National Research Foundation (NRF), Prime

Minister's Office, Singapore, under its Campus for Research Excellence and Technological Enterprise (CREATE) program. The Disruptive and Sustainable Technology for Agricultural

Precision (DiSTAP) is an interdisciplinary research group of the Singapore-MIT Alliance for Research and Technology (SMART) Center.

REFERENCES

- Acton, W. J. F., Jud, W., Ghirardo, A., Wohlfahrt, G., Hewitt, C. N., Taylor, J. E., et al. (2018). The effect of ozone fumigation on the biogenic volatile organic compounds (BVOCs) emitted from *Brassica napus* above- and below-ground. *PLoS ONE* 13, e0208825. doi: 10.1371/journal.pone.0208825
- Ang, M. C.-Y., Dhar, N., Khong, D. T., Lew, T. T. S., Park, M., Sarangapani, S., et al. (2021). Nanosensor detection of synthetic auxins *in planta* using corona phase molecular recognition. *ACS Sensors* 6, 3032–3046. doi: 10.1021/acssensors.1c01022
- Baetz, U., and Martinoia, E. (2014). Root exudates: the hidden part of plant defense. *Trends Plant Sci.* 19, 90–98. doi: 10.1016/j.tplants.2013.11.006
- Balcke, G. U., Handrick, V., Bergau, N., Fichtner, M., Henning, A., Stellmach, H., et al. (2012). An UPLC-MS/MS method for highly sensitive high-throughput analysis of phytohormones in plant tissues. *Plant Methods* 8, 47. doi: 10.1186/1746-4811-8-47
- Beaver, K., Dantanarayana, A., and Minter, S. D. (2021). Materials approaches for improving electrochemical sensor performance. *J. Phys. Chem. B* 125, 11820–11834. doi: 10.1021/acs.jpcc.1c07063
- Beck, J. J., Porter, N., Cook, D., Gee, W. S., Griffith, C. M., Rands, A. D., et al. (2015). In-field volatile analysis employing a hand-held portable GC-MS: emission profiles differentiate damaged and undamaged yellow starthistle flower heads. *Phytochem. Anal.* 26, 395–403. doi: 10.1002/pca.2573
- Cellini, A., Biondi, E., Blasioli, S., Rocchi, L., Farneti, B., Braschi, I., et al. (2016). Early detection of bacterial diseases in apple plants by analysis of volatile organic compounds profiles and use of electronic nose. *Ann. Appl. Biol.* 168, 409–420. doi: 10.1111/aab.12272
- Cofer, T. M., Seidl-Adams, I., and Tumlinson, J. H. (2018). From Acetoin to (Z)-3-Hexen-1-ol: the diversity of volatile organic compounds that induce plant responses. *J. Agric. Food Chem.* 66, 11197–11208. doi: 10.1021/acs.jafc.8b03010
- Cui, S., Ling, P., Zhu, H., and Keener, H. (2018). Plant pest detection using an artificial nose system: a review. *Sensors* 18, 378. doi: 10.3390/s18020378
- Ding, P., and Ding, Y. (2020). Stories of salicylic acid: a plant defense hormone. *Trends Plant Sci.* 25, 549–565. doi: 10.1016/j.tplants.2020.01.004
- Engelberth, J., Alborn, H. T., Schmelz, E. A., and Tumlinson, J. H. (2004). Airborne signals prime plants against insect herbivore attack. *Proc. Natl. Acad. Sci. U.S.A.* 101, 1781–1785. doi: 10.1073/pnas.0308037100
- Erb, M. (2018). Volatiles as inducers and suppressors of plant defense and immunity—origins, specificity, perception and signaling. *Curr. Opin. Plant Biol.* 44, 117–121. doi: 10.1016/j.pbi.2018.03.008
- Erb, M., Veyrat, N., Robert, C. A. M., Xu, H., Frey, M., Ton, J., et al. (2015). Indole is an essential herbivore-induced volatile priming signal in maize. *Nat. Commun.* 6, 6273. doi: 10.1038/ncomms7273
- Fu, Z. Q., and Dong, X. (2013). Systemic acquired resistance: turning local infection into global defense. *Annu. Rev. Plant Biol.* 64, 839–863. doi: 10.1146/annurev-arplant-042811-105606
- Gao, J., Li, H., Li, M., Wang, G., Long, Y., Li, P., et al. (2021). Polydopamine/graphene/MnO₂ composite-based electrochemical sensor for in situ determination of free tryptophan in plants. *Anal. Chim. Acta* 1145, 103–113. doi: 10.1016/j.aca.2020.11.008
- Gianfagna, T. (1995). Natural and synthetic growth regulators and their use in horticultural and agronomic crops. *Plant Horm.* 751–773. doi: 10.1007/978-94-011-0473-9_34
- Hayat, A., and Marty, J. L. (2014). Disposable screen printed electrochemical sensors: tools for environmental monitoring. *Sensors* 14, 10432–10453. doi: 10.3390/s140610432
- Hsu, P. K., Dubeaux, G., Takahashi, Y., and Schroeder, J. I. (2021). Signaling mechanisms in abscisic acid-mediated stomatal closure. *Plant J.* 105, 307–321. doi: 10.1111/tpj.15067
- Hu, L., Zhang, K., Wu, Z., Xu, J., and Erb, M. (2021). Plant volatiles as regulators of plant defense and herbivore immunity: molecular mechanisms and unanswered questions. *Curr. Opin. Insect Sci.* 44, 82–88. doi: 10.1016/j.cois.2021.03.010
- Huang, H., Ullah, F., Zhou, D.-X., Yi, M., and Zhao, Y. (2019). Mechanisms of ROS regulation of plant development and stress responses. *Front. Plant Sci.* 10:800. doi: 10.3389/fpls.2019.00800
- Jansen, R. M. C., Wildt, J., Kappers, I. F., Bouwmeester, H. J., Hofstee, J. W., and Van Henten, E. J. (2011). Detection of diseased plants by analysis of volatile organic compound emission. *Annu. Rev. Phytopathol.* 49, 157–174. doi: 10.1146/annurev-phyto-072910-095227
- Karakaya, D., Ulucan, O., and Turkan, M. (2020). Electronic nose and its applications: a survey. *Int. J. Autom. Comput.* 17, 179–209. doi: 10.1007/s11633-019-1212-9
- Karban, R. (2017). Tradeoff between resistance induced by volatile communication and over-topping vertical growth. *Plant Signal. Behav.* 12, e1309491. doi: 10.1080/15592324.2017.1309491
- Kim, J. J., Allison, L. K., and Andrew, T. L. (2019). Vapor-printed polymer electrodes for long-term, on-demand health monitoring. *Sci. Adv.* 5, eaaw0463. doi: 10.1126/sciadv.aaw0463
- Kim, J. J., Fan, R., Allison, L. K., and Andrew, T. L. (2020). On-site identification of ozone damage in fruiting plants using vapor-deposited conducting polymer tattoos. *Sci. Adv.* 6, eabc3296. doi: 10.1126/sciadv.abc3296
- Koman, V. B., Lew, T. T. S., Wong, M. H., Kwak, S.-Y., Giraldo, J. P., and Strano, M. S. (2017). Persistent drought monitoring using a microfluidic-printed electro-mechanical sensor of stomata in planta. *Lab Chip* 17, 4015–4024. doi: 10.1039/C7LC00930E
- Kwak, S.-Y., Wong, M. H., Lew, T. T. S., Bisker, G., Lee, M. A., Kaplan, A., et al. (2017). Nanosensor technology applied to living plant systems. *Annu. Rev. Anal. Chem.* 10, 113–140. doi: 10.1146/annurev-anchem-061516-045310
- Lee, S. C., and Luan, S. (2012). ABA signal transduction at the crossroad of biotic and abiotic stress responses. *Plant Cell Environ.* 35, 53–60. doi: 10.1111/j.1365-3040.2011.02426.x
- Lew, T. T. S., Koman, V. B., Gordiichuk, P., Park, M., and Strano, M. S. (2020a). The emergence of plant nanobionics and living plants as technology. *Adv. Mater. Technol.* 5, 1900657. doi: 10.1002/admt.201900657
- Lew, T. T. S., Koman, V. B., Silmore, K. S., Seo, J. S., Gordiichuk, P., Kwak, S.-Y., et al. (2020b). Real-time detection of wound-induced H₂O₂ signalling waves in plants with optical nanosensors. *Nat. Plants* 6, 404–415. doi: 10.1038/s41477-020-0632-4
- Lew, T. T. S., Park, M., Cui, J., and Strano, M. S. (2021). Plant nanobionic sensors for arsenic detection. *Adv. Mater.* 33, 2005683. doi: 10.1002/adma.202005683
- Lew, T. T. S., Park, M., Wang, Y., Gordiichuk, P., Yeap, W.-C., Mohd Rais, S. K., et al. (2020c). Nanocarriers for transgene expression in pollen as a plant biotechnology tool. *ACS Mater. Lett.* 2, 1057–1066. doi: 10.1021/acsmaterialslett.0c00247
- Lew, T. T. S., Sarojam, R., Jang, I.-C., Park, B. S., Naqvi, N. I., Wong, M. H., et al. (2020d). Species-independent analytical tools for next-generation agriculture. *Nat. Plants* 6, 1408–1417. doi: 10.1038/s41477-020-00808-7
- Lew, T. T. S., Wong, M. H., Kwak, S.-Y., Sinclair, R., Koman, V. B., and Strano, M. S. (2018). Rational design principles for the transport and subcellular distribution of nanomaterials into plant protoplasts. *Small* 14, 1802086. doi: 10.1002/smll.201802086
- Li, Z., Paul, R., Ba Tis, T., Saville, A. C., Hansel, J. C., Yu, T., et al. (2019). Non-invasive plant disease diagnostics enabled by smartphone-based fingerprinting of leaf volatiles. *Nat. Plants* 5, 856–866. doi: 10.1038/s41477-019-0476-y
- Li, Z., Zhou, J., Dong, T., Xu, Y., and Shang, Y. (2021). Application of electrochemical methods for the detection of abiotic stress biomarkers in plants. *Biosens. Bioelectron.* 182, 113105. doi: 10.1016/j.bios.2021.113105
- Liu, D., Li, M., Li, H., Li, C., Wang, G., Li, P., et al. (2021). Core-shell Au@Cu₂O-graphene-polydopamine interdigitated microelectrode array sensor for in situ determination of salicylic acid in cucumber leaves. *Sensors Actuators B Chem.* 341, 130027. doi: 10.1016/j.snb.2021.130027

- Luo, Y., Li, W., Lin, Q., Zhang, F., He, K., Yang, D., et al. (2021). A morphable ionic electrode based on thermogel for non-invasive hairy plant electrophysiology. *Adv. Mater.* 33, 2007848. doi: 10.1002/adma.202007848
- Ma, J. F., Yamaji, N., Mitani, N., Xu, X.-Y., Su, Y.-H., McGrath, S. P., et al. (2008). Transporters of arsenite in rice and their role in arsenic accumulation in rice grain. *Proc. Natl. Acad. Sci. U.S.A.* 105, 9931–9935. doi: 10.1073/pnas.0802361105
- Maffei, M. E., Gertsch, J., and Appendino, G. (2011). Plant volatiles: production, function and pharmacology. *Nat. Prod. Rep.* 28, 1359. doi: 10.1039/c1np00021g
- Mcsteen, P., and Zhao, Y. (2008). Plant hormones and signaling: common themes and new developments. *Dev. Cell* 14, 467–473. doi: 10.1016/j.devcel.2008.03.013
- Meharg, A. A. (2003). Variation in arsenic accumulation - hyperaccumulation in ferns and their allies: rapid report. *New Phytol.* 157, 25–31. doi: 10.1046/j.1469-8137.2003.00541.x
- Mousavi, S. A. R., Chauvin, A., Pascaud, F., Kellenberger, S., and Farmer, E. E. (2013). GLUTAMATE RECEPTOR-LIKE genes mediate leaf-to-leaf wound signalling. *Nature* 500, 422–426. doi: 10.1038/nature12478
- Nguyen, C. T., Kurenda, A., Stolz, S., Chételat, A., and Farmer, E. E. (2018). Identification of cell populations necessary for leaf-to-leaf electrical signaling in a wounded plant. *Proc. Natl. Acad. Sci. U.S.A.* 115, 10178–10183. doi: 10.1073/pnas.1807049115
- Nißler, R., Müller, A. T., Dohrman, F., Kurth, L., Li, H., Cosio, E. G., et al. (2022). Detection and imaging of the plant pathogen response by near-infrared fluorescent polyphenol sensors. *Angew. Chem. Int. Ed.* 61, e202108373. doi: 10.1002/anie.202108373
- Pan, X., Welti, R., and Wang, X. (2010). Quantitative analysis of major plant hormones in crude plant extracts by high-performance liquid chromatography-mass spectrometry. *Nat. Protoc.* 5, 986–992. doi: 10.1038/nprot.2010.37
- Qu, C.-C., Sun, X.-Y., Sun, W.-X., Cao, L.-X., Wang, X.-Q., and He, Z.-Z. (2021). Flexible wearables for plants. *Small* 17, 2104482. doi: 10.1002/sml.202104482
- Roper, J. M., Garcia, J. F., and Tsutsui, H. (2021). Emerging technologies for monitoring plant health *in vivo*. *ACS Omega* 6, 5101–5107. doi: 10.1021/acsomega.0c05850
- Sharma, R., Zhou, M., Hunter, M. D., and Fan, X. (2019). Rapid *in situ* analysis of plant emission for disease diagnosis using a portable gas chromatography device. *J. Agric. Food Chem.* 67, 7530–7537. doi: 10.1021/acs.jafc.9b02500
- Shi, J., Claussen, J. C., McLamore, E. S., ul Haque, A., Jaroch, D., Diggs, A. R., et al. (2011). A comparative study of enzyme immobilization strategies for multi-walled carbon nanotube glucose biosensors. *Nanotechnology* 22, 355502. doi: 10.1088/0957-4484/22/35/355502
- Shi, J., Zhang, H., Snyder, A., Wang, M.-x., Xie, J., Marshall Porterfield, D., et al. (2012). An aqueous media based approach for the preparation of a biosensor platform composed of graphene oxide and Pt-black. *Biosens. Bioelectron.* 38, 314–320. doi: 10.1016/j.bios.2012.06.007
- Singh, S., Kaur, I., and Kariyat, R. (2021). The multifunctional roles of polyphenols in plant-herbivore interactions. *Int. J. Mol. Sci.* 22, 1442. doi: 10.3390/ijms22031442
- Stierlin, É., Michel, T., and Fernandez, X. (2020). Field analyses of lavender volatile organic compounds: performance evaluation of a portable gas chromatography-mass spectrometry device. *Phytochem. Anal.* 31, 778–785. doi: 10.1002/pca.2942
- Sun, L., Pan, Y., Wu, J., Zhao, D., Hui, M., Zhu, S., et al. (2020). Paper-based analytical devices for the rapid and direct electrochemical detection of hydrogen peroxide in tomato leaves inoculated with *botrytis cinerea*. *Sensors* 20, 5512. doi: 10.3390/s20195512
- Sun, L.-J., Feng, Q.-M., Yan, Y.-F., Pan, Z.-Q., Li, X.-H., Song, F.-M., et al. (2014). Paper-based electroanalytical devices for *in situ* determination of salicylic acid in living tomato leaves. *Biosensors Bioelectron.* 60, 154–160. doi: 10.1016/j.bios.2014.04.021
- Teale, W. D., Paponov, I. A., and Palme, K. (2006). Auxin in action: signalling, transport and the control of plant growth and development. *Nat. Rev. Mol. Cell Biol.* 7, 847–859. doi: 10.1038/nrm2020
- Tholl, D., Hossain, O., Weinhold, A., Röse, U. S. R., and Wei, Q. (2021). Trends and applications in plant volatile sampling and analysis. *Plant J.* 106, 314–325. doi: 10.1111/tpj.15176
- Ton, J., D'Alessandro, M., Jourdie, V., Jakab, G., Karlen, D., Held, M., et al. (2006). Priming by airborne signals boosts direct and indirect resistance in maize. *Plant J.* 49, 16–26. doi: 10.1111/j.1365-313X.2006.02935.x
- Uzogara, S. G. (2000). The impact of genetic modification of human foods in the 21st century: a review. *Biotechnol. Adv.* 18, 179–206. doi: 10.1016/S0734-9750(00)00033-1
- Vlot, A. C., Sales, J. H., Lenk, M., Bauer, K., Brambilla, A., Sommer, A., et al. (2021). Systemic propagation of immunity in plants. *New Phytol.* 229, 1234–1250. doi: 10.1111/nph.16953
- Wang, Z., Xue, L., Li, M., Li, C., Li, P., and Li, H. (2021). Au@SnO₂-vertical graphene-based microneedle sensor for *in-situ* determination of abscisic acid in plants. *Mater. Sci. Eng. C* 127, 112237. doi: 10.1016/j.msec.2021.112237
- Wang, Z.-G., Jin, X., Bao, X.-G., Li, X.-F., Zhao, J.-H., Sun, J.-H., et al. (2014). Intercropping enhances productivity and maintains the most soil fertility properties relative to sole cropping. *PLoS ONE* 9, e113984. doi: 10.1371/journal.pone.0113984
- Wong, M. H., Giraldo, J. P., Kwak, S.-Y., Koman, V. B., Sinclair, R., Lew, T. T. S., et al. (2017). Nitroaromatic detection and infrared communication from wild-type plants using plant nanobionics. *Nat. Mat.* 16, 264–272. doi: 10.1038/nmat4771
- Xi, L., Zhang, M., Zhang, L., Lew, T.T.S., and Lam, Y.M. (2021). Novel materials for urban farming. *Adv. Mater.* 2105009. doi: 10.1002/adma.202105009
- Xu, S., Zhou, Z., Lu, H., Luo, X., Lan, Y., Zhang, Y., et al. (2014). Estimation of the age and amount of brown rice plant hoppers based on bionic electronic nose use. *Sensors* 14, 18114–18130. doi: 10.3390/s141018114
- Yang, L., Ma, Y., and Ye, J. (2021). *In vivo* detection of L-tryptophan in tomatoes using multi-walled carbon nanotubes and poly (sulfosalicylic acid) film modified graphite rod electrode. *Biosens. Bioelectron.* X 9, 100086. doi: 10.1016/j.biosx.2021.100086
- Yang, T., Siddique, K. H. M., and Liu, K. (2020). Cropping systems in agriculture and their impact on soil health-a review. *Glob. Ecol. Conserv.* 23, e01118. doi: 10.1016/j.gecco.2020.e01118
- Zhang, J., Landry, M. P., Barone, P. W., Kim, J.-H., Lin, S., Ulissi, Z. W., et al. (2013). Molecular recognition using corona phase complexes made of synthetic polymers adsorbed on carbon nanotubes. *Nat. Nanotechnol.* 8, 959–968. doi: 10.1038/nnano.2013.236

Conflict of Interest: The authors declare that the research was conducted in the absence of any commercial or financial relationships that could be construed as a potential conflict of interest.

The handling editor declared a past collaboration with the authors MA and TL.

Publisher's Note: All claims expressed in this article are solely those of the authors and do not necessarily represent those of their affiliated organizations, or those of the publisher, the editors and the reviewers. Any product that may be evaluated in this article, or claim that may be made by its manufacturer, is not guaranteed or endorsed by the publisher.

Copyright © 2022 Ang and Lew. This is an open-access article distributed under the terms of the Creative Commons Attribution License (CC BY). The use, distribution or reproduction in other forums is permitted, provided the original author(s) and the copyright owner(s) are credited and that the original publication in this journal is cited, in accordance with accepted academic practice. No use, distribution or reproduction is permitted which does not comply with these terms.



Raman Spectroscopy Detects Changes in Carotenoids on the Surface of Watermelon Fruits During Maturation

Tushar Dhanani^{1,2†}, Tianyi Dou^{3†}, Kishan Biradar¹, John Jifon^{1,4}, Dmitry Kurouski^{3*} and Bhimanagouda S. Patil^{1,2*}

¹Vegetable and Fruit Improvement Center, Department of Horticultural Sciences, College Station, TX, United States,

²Department of Biochemistry and Biophysics, Texas A&M University, College Station, TX, United States, ³Department of Biochemistry, Texas A&M University, College Station, TX, United States, ⁴Texas A&M AgriLife Research, Weslaco, TX, United States

OPEN ACCESS

Edited by:

Rajeev Ram,
Massachusetts Institute of
Technology, United States

Reviewed by:

Alessandro Natalini,
Unit of Monsampolo del Tronto
(MDT), Italy
Jasenka Gajdoš Kljusurić,
University of Zagreb, Croatia

*Correspondence:

Bhimanagouda S. Patil
b-patil@tamu.edu
Dmitry Kurouski
dkurouski@tamu.edu

[†]These authors have contributed
equally to this work

Specialty section:

This article was submitted to
Technical Advances in Plant Science,
a section of the journal
Frontiers in Plant Science

Received: 09 December 2021

Accepted: 06 May 2022

Published: 31 May 2022

Citation:

Dhanani T, Dou T, Biradar K, Jifon J,
Kurouski D and Patil BS (2022)
Raman Spectroscopy Detects
Changes in Carotenoids on the
Surface of Watermelon Fruits During
Maturation.
Front. Plant Sci. 13:832522.
doi: 10.3389/fpls.2022.832522

A non-invasive and non-destructive technique, Raman spectroscopy, was explored to distinguish different maturity stages (20, 30, 40, and 50 days after anthesis) of watermelon (*Citrullus lanatus*) fruits from four cultivars: Fascination, Orange Crisp, Amarillo and Crimson Sweet. Spectral acquisition from the fruit surface was carried out at the wavelength range of 400–2,000 cm⁻¹ using a handheld Raman spectrometer equipped with 830 nm laser excitation source. The spectra were normalized at 1,438 cm⁻¹ which was assigned to CH₂ and CH₃ vibration. Detecting changes in the spectral features of carotenoids on the surface of watermelon fruits can be used as a marker to monitor the maturity of the fruit. The spectral analysis confirmed the presence of two major carotenoids, lutein and β -carotene, and their intensity decreased upon maturity on the fruit surface. Identification of these pigments was further confirmed by resonance Raman spectra and high-performance liquid chromatography analysis. Results of partial least square discriminant analysis of pre-processed spectra have demonstrated that the method can successfully predict the maturity of watermelon samples with more than 85% accuracy. Analysis of Variance of individual Raman bands has revealed a significant difference among the stages as the level of carotenoids was declined during the ripening of the fruits. Thus, Raman spectral signatures can be used as a versatile tool for the non-invasive determination of carotenoid changes on the watermelon fruits' surface during ripening, thereby enabling effective monitoring of nutritional quality and maturity indices before harvesting the watermelon.

Keywords: Raman spectroscopy, non-invasive, ripeness, carotenoids, external quality

INTRODUCTION

The maturity at harvest significantly affects the quality of fruits and vegetables and the postharvest value chain (Erkan and Dogan, 2019). Non-climacteric fruits such as watermelon (*Citrullus lanatus*) only reach ideal quality for consumption when allowed to ripen on the parent plant (Paul et al., 2012). Usually, the maturity of watermelon fruits is assessed

based on ground spot yellowness, loss of shine, thumping, or the number of senescent tendrils. However, these indicators are highly variable and do not apply uniformly to all genotypes. Furthermore, it is challenging to predict the maturity from rind color pattern, as no color breaks is visible as ripening proceeds (Vinson et al., 2010). It is, therefore, crucial to choose a suitable harvest time for proper postharvest management of watermelon. Non-destructive techniques for appropriate pre- and postharvest handling have received much attention by replacing time-consuming and labor-intensive conventional techniques for monitoring the quality of fruits (Arendse et al., 2021). Several non-destructive methods such as acoustic impulse response (Stone et al., 1996; Diezma-Iglesias et al., 2004; Ke et al., 2009; Zhang et al., 2010; Pintor et al., 2016), dielectric spectroscopy (Nelson et al., 2007a,b), laser Doppler vibrometry (Abbaszadeh et al., 2011a,b, 2013a,b, 2014, 2015a,b), machine vision systems (Ali et al., 2017; Jie and Wei, 2018), surface elastic waves (Stone et al., 1996; Ikeda et al., 2015; Ali et al., 2017), near-infrared and visible spectroscopy (Flores et al., 2008; Jie et al., 2014, 2019) have been studied for internal and external evaluation of watermelon quality.

Among non-destructive techniques, Raman spectroscopy has received increased interest as a promising non-invasive, label-free, and field-based high-throughput phenotyping platform for precision agriculture (Akpolat et al., 2020; Payne and Kurouski, 2020). Raman spectroscopy, which emerged from the discovery of the Raman effect by C. V. Raman in 1928, is a powerful technique that detects characteristic rotational/vibrational energy levels of a molecule. Raman spectroscopy gives spectral fingerprint of the molecules, and the intensity of Raman peak is directly proportional to the molecule's concentration (Hata et al., 2000). Development of portable Raman instruments has enabled rapid in-field measurement of chemical fingerprints and phenotyping of different plant properties (Conrad and Bonello, 2015). Raman spectroscopy has been extensively applied for structural analysis, quality and safety control, classification, and quantification of fruits and vegetables such as apple, avocado, apricot, cabbage, carrot, citrus, cucumber, grape, kiwifruit, mango, citrus, olive, pear, pepper, potato, spinach, and tomato (Liu et al., 2013; Lee and Herrman, 2016; Qin et al., 2019). However, few studies have been examined the internal or external quality attributes of watermelon. Furthermore, the shorter penetration depth of source radiation makes it challenging to study internal quality attributes of fruits with a thick rind, such as watermelon. Regardless, the Raman spectrum from the surface of the watermelon could be used for quality evaluation (Arendse et al., 2018).

The present investigation applied Raman spectroscopy to study the variation of carotenoids in the rind of watermelon fruit during ripening. Carotenoids are common plant pigments and antioxidants with many beneficial properties to plant and human health. Because the Raman spectra of carotenoids vary with minor structural differences, the spectra have been widely used to identify and characterize carotenoids in biological systems. Resonance Raman spectra were acquired from pure

compounds and carotenoid-rich fractions to confirm the presence of individual carotenoids and the results of Raman spectroscopy were compared with those obtained from HPLC analysis. Lastly, partial least squares-discriminant analysis (PLS-DA) was used to couple Raman spectra to the developmental stage, allowing us to predict different development stages of four watermelon cultivars. PLS-DA has been demonstrated to be a more suitable discriminant method comparing to methods like Fisher's linear discriminant analysis or principal component-linear discriminant analysis (Yang and Yang, 2003; Lee et al., 2018).

MATERIALS AND METHODS

Watermelon Samples and Analysis

Raman experiments were conducted using four watermelon varieties: (a) Fascination, (b) Orange Crisp, (c) Amarillo, and (d) Crimson Sweet. Watermelon fruits were harvested at 20 days (Stage A), 30 days (Stage B), 40 days (Stage C), and 50 days (Stage D) after anthesis. Fruits were harvested in the Texas A&M University experimental fields located at the Horticultural Research and Extension Facility near Snook, TX during the harvest season in the year 2020. Fruits were directly transported to the laboratory and washed with water before analysis. Reference compounds lutein, β -carotene and lycopene, reagent-grade acetone, chloroform, HPLC grade methanol, and *tert*-butyl methyl ether were purchased from Sigma-Aldrich, United States. Nanopure water (Barnstead/Thermolyne, Dubuque, IA, United States) was used for HPLC analysis.

Raman Spectrum Acquisition and Data Processing

Three fruit samples at each stage per variety were used for Raman spectrum acquisition. Spectra ranging from the stalk end to the flower end of each fruit's surface were acquired using a hand-held spectrometer (Resolve, Agilent, United States) equipped with a 495 mW laser source with 830 nm excitation wavelength. Spectral acquisition time was set at 1 s. Spectra were acquired using the surface mode setting built into the portable instrument. The barrier scan mode was used, but due to different thicknesses of watermelon rinds, the parameters of the barrier scan varied from scan to scan. Before multivariate analysis, pre-processing such as area normalization, mean centering, a Kruskal–Wallis test was carried out using MATLAB 2020a software. All spectra were normalized to 1,439 cm⁻¹ bands, corresponding to CH₂ and CH₃ vibration, which cannot be assigned to any specific class of biomolecule. Kruskal–Wallis one-way analysis tests if the median in a set of samples is significantly different from other classes in the set. The null hypothesis for Kruskal–Wallis test is that there is no significant difference in the band of interest. The significance level is 0.05. The results report a 95% CI for the true value of median for each compared group. The multi compare function was used to overlap the confidence intervals. Partial least squares

discriminant analysis (PLS-DA) was conducted using MATLAB PLS_Toolbox 8.6.2.

Resonance Raman Study

Resonance Raman spectra of individual carotenoids (pure standards dissolved in extraction solvent) and carotenoid-rich fractions (extracted as described below) were acquired using a confocal inverted microscope (Nikon, Model TE-2000U) with 20x dry Nikon objective (NA=0.45). A solid-state laser (Necsel SLM785.0-FS-01) was used for 485 nm excitation. Lutein, lycopene, and beta-carotene were dissolved in extraction solvent (acetone: chloroform, 7:3), and spectra were collected from solutions individually. The signal was collected in a backscattering geometry and sent to a spectrometer (Princeton Instruments, IsoPlane-320) equipped with a 600 groove/mm grating. Prior to entering the spectrograph, the Rayleigh scattering was filtered with a long-pass filter (Semrock, LP03-785RS-25). The dispersed light was then sent to the CCD (PIX-400BR). All data were processed using GRAMS/AI 7.0 (Thermo Galactic, Salem, NH). Spectra were baselined using multiple-point baseline correction in GRAMS/AI 7.0 (Thermo Galactic, Salem, NH).

Extraction of Carotenoids

After the spectral acquisition, the watermelon rind was separated from the flesh and blended using a laboratory blender (Magic Bullet). Five grams of crushed rind was extracted in dark using extraction solvent (acetone: chloroform, 7:3), vortexed for 1 min at 1814 x g, homogenized (850 Homogenizer, Fisher Scientific, Waltham, Massachusetts, United States) and sonicated (Cole-Parmer Ultrasonic cleaner 8,893) in ice-cold water for 30 min. Sample tubes were centrifuged (Beckman Model TJ-6, Ramsey, Minnesota, United States) at 4480 x g for 10 min. The lower organic layer was collected in another tube and the extraction procedure repeated on the sample to ensure the maximum recovery of analytes. Organic layers from two extractions were pooled together, a 5-ml aliquot was transferred to amber glass vial, and solvent was removed under vacuum at room temperature. The residue was redissolved in 1 ml of extraction solvent. Carotenoid-rich fractions were stored at -80°C until further analysis.

HPLC Profiling of Carotenoids

A Waters 1525 HPLC system (Milford, MA, United States) equipped with 2996 PDA detector, a 717 Plus autosampler was used for quantification. Separation of carotenoids was achieved on YMC carotenoid C₃₀ (250 mm x 4.6 mm) column. The mobile phase constitutes a mixture of (A) *tert*-butyl methyl ether (TBME):methanol:water (85:13:2), and (B) methanol:TBME:water (85:13:2). The gradient was programmed as follows: 0–3 min, 85% (B); then 35%, 33%, 20%, 10%, and 85% B at 6, 12, 19, 23 and 25 min; after that, the initial condition was restored for 3 min. For analysis, 20 μl of each aliquot was injected and the chromatogram was monitored between 210 and 700 nm. Statistical analysis of HPLC results was performed using Microsoft Excel 2019.

RESULTS AND DISCUSSION

Identification of Carotenoids Using Raman Techniques

Raman spectra collected from the surface of four different cultivars of watermelon demonstrated similar profiles. The spectral feature of Fascination type watermelon at four different stages of maturity is shown in **Figure 1**. The bands observed at 1,002, 1,156, 1,186, 1,217, and 1,525 cm^{-1} can be assigned to carotenoids. Carotenoids show two strong Raman bands (1,525 and 1,156 cm^{-1}) due to in-phase $\nu(\text{C}-\text{C})$ and $\nu(\text{C}-\text{C})$ stretching vibrations of the polyene chain (Qin et al., 2011). For instance, β -carotene with 11 conjugated double bonds is characterized by the bands at 1,515 and 1,157 cm^{-1} . Bands at 1,186 and 1,217 can be assigned to C–C stretching vibrations coupled to either C–H in-plane bending or C–CH₃ stretching modes (Grudzinski et al., 2016). A feature of medium intensity occurs at around 1,002–1,008 cm^{-1} , corresponding to the in-phase rocking modes of the CH₃ groups attached to the polyene chain (Schulz et al., 2005; Jehlička et al., 2014). These distinct carotenoid signals also enabled the effective monitoring of four levels of maturity index in hot peppers by Raman spectroscopy (Legner et al., 2021). Raman spectroscopy was recently explored for the *in situ*, non-destructive, and rapid quantitative analysis of photosynthetic pigments, chlorophyll, and carotenoids in tea leaves (Zeng et al., 2021). Other characteristic vibrational bands observed at 520 and 1,047 cm^{-1} can be assigned to cellulose, 915 cm^{-1} to carbohydrates, 747 and 850 cm^{-1} to pectin, 1,267 and 1,606 cm^{-1} to phenylpropanoids or lignin, 1,670 cm^{-1} to protein and 1,286, 1,327, 1,386 and 1,439 cm^{-1} to CH₂/CH₃ vibrations of aliphatic groups (**Supplementary Table S1**).

Resonance Raman

The carotenoid bands observed from the watermelon rind surface using the handheld spectrometer were further confirmed using a confocal microscope at 485 nm excitation. In resonance Raman Spectroscopy, laser excitation frequency is chosen to be close to the frequency of a sample's electronic transition (Merlin, 1985). The resonance Raman spectra of individual carotenoids, β -carotene, lutein, and lycopene exhibited peaks at $\nu \sim 1,527$, $\nu \sim 1,159$ and $\nu = 1,008 \text{ cm}^{-1}$ (**Supplementary Figure S1**). These peaks match the fruit surface spectra of lutein and β -carotene, confirming the presence of these two pigments in the watermelon rind.

However, resonance Raman spectra recorded from pure carotenoids revealed band shifting of assigned wavenumbers. Carotenoids bind biomass, which affects the main polyene chain and thus can cause a significant shift of the band position (1,008–1,002 cm^{-1}) due to changes in electron delocalization. Carotenoids in different solvents can undergo slight band shifts from 1,008 (in extraction solvent) to 1,002 (in watermelon rind) cm^{-1} due to different vibronic coupling in different stages (Yu et al., 2007). Another factor affecting the band shifts is substitution at the terminal end groups of the molecule, resulting in very small wavenumber changes in the solid and liquid states. The band position of carotenoids also depends on the

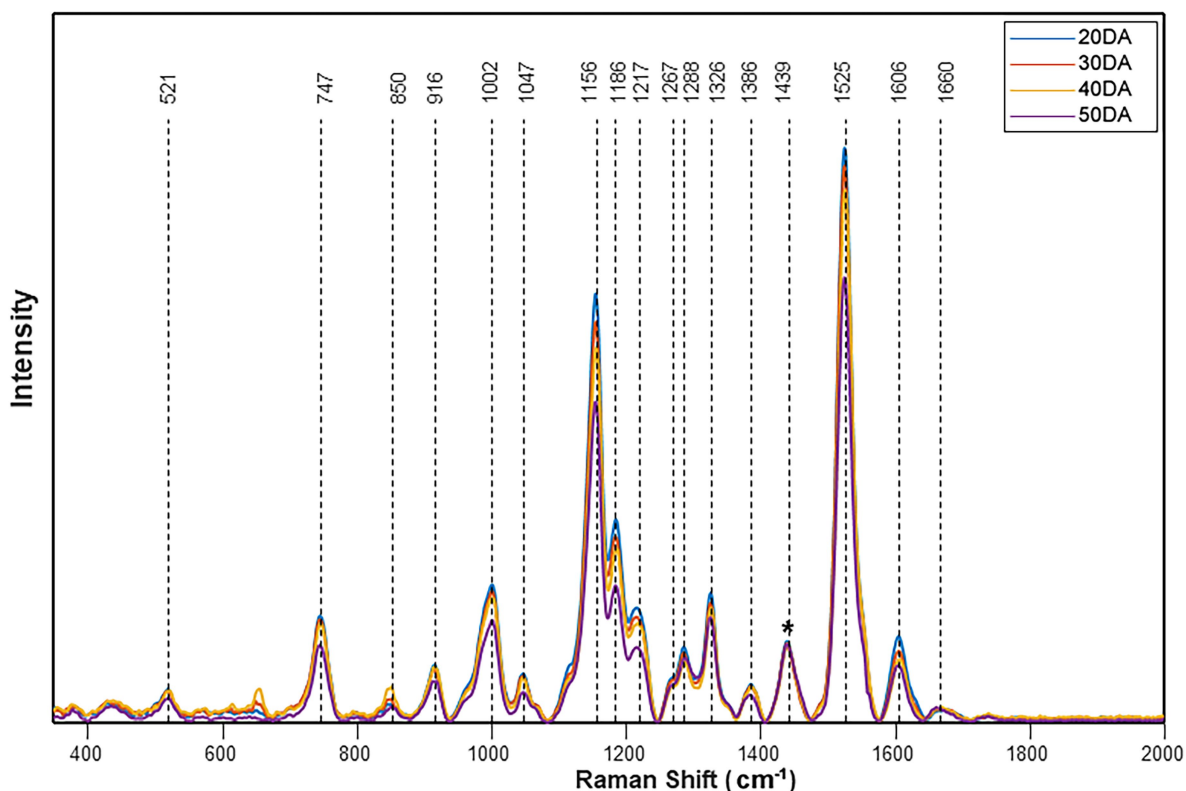


FIGURE 1 | Raman spectra obtained from the surface of the watermelon fruit Fascination cultivar. The stacked spectra represent an average of 20DA=43, 30DA=42, 40DA=42, and 50DA=24. The spectra were normalized at $1,439\text{ cm}^{-1}$ [Marked with an asterisk (*)].

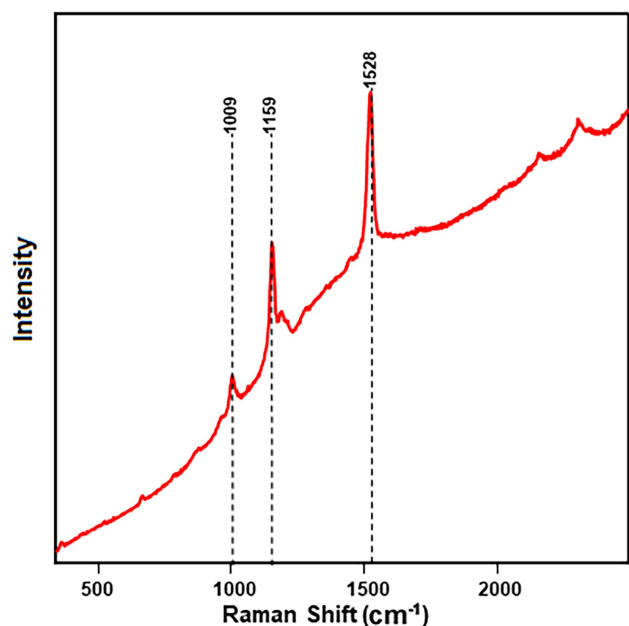


FIGURE 2 | Resonance Raman spectra of carotenoid-rich fraction show prominent bands related to carotenoids obtained from the rind of the Fascination type watermelon.

laser wavelength used for excitation (Jehlička et al., 2014; Harris et al., 2015). Furthermore, resonance Raman spectra of carotenoid-rich fractions of each variety at each stage confirmed the presence of lutein and β -carotene (Figure 2), further authenticated by HPLC analysis. In a previous study, a variety of intact fruits and vegetables and their juices were measured for carotenoids by resonance Raman spectroscopy and compared to concentrations determined by extraction and HPLC (Bhosale et al., 2004).

Raman Spectral Analysis

The spectra obtained from Raman analysis were normalized at $1,438\text{ cm}^{-1}$, which corresponds to CH_2 and CH_3 bending vibrations. Since most organic compounds have these features, it is impossible to attribute these bands to a specific compound. However, normalization allows us to compare the relative intensity of the bands. The watermelon rind showed a trend of decreasing spectral intensity of the main bands from the early stage (A) to the mature stage (D). PLS-DA was conducted to determine whether watermelon maturity stages can be discriminated by using the Raman spectra. Classification results of the PLS-DA model created using Raman spectral data are presented in Table 1. The results table shows that the stage D classification, which determines the full maturity

TABLE 1 | Confusion matrix computed from the PLS-DA model of Raman spectra collected from four watermelon cultivars.

Ripening stage	Total spectra	Predicted as A	Predicted as B	Predicted as C	Predicted as D	Correct (%)
Fascination						
A	43	38	5	0	0	88.4
B	42	8	27	7	0	64.3
C	42	2	11	27	2	64.3
D	24	0	0	1	23	95.8
Orange crisp						
A	43	40	1	2	0	93.0
B	43	0	43	0	0	100
C	39	4	1	32	2	82.1
D	40	0	0	0	40	100
Amarillo						
A	42	42	0	0	0	100
B	42	12	27	3	0	64.3
C	42	0	3	38	1	90.5
D	20	0	0	0	20	100
Crimson sweet						
A	42	36	6	0	0	85.7
B	42	9	31	2	0	73.8
C	42	1	4	37	0	88.1
D	20	0	0	0	20	100

Bold value is the highest number of spectrums predicted according to their ripening stage.

stage, was 100% accurate for three out of four cultivars, while the full maturity stage for the Fascination type watermelon was classified with 95.8% accuracy. 64.3% of spectra identified correctly as stage B and C in Fascination type watermelon, while the rest were incorrectly identified as other stages. Similar accuracy (64.3%) in prediction of stage B of the Amarillo cultivar was also observed. True prediction rates for the remaining stages ranged from 73.8% to 93% for all cultivars. Our results show that PLS-DA is able to differentiate fully matured stages with an accuracy between 95.8% and 100%. Harvesting watermelon fruits at full maturity is critical for the best taste and texture, which determines their market value.

The results obtained from the PLS-DA confusion matrix give an overall view of the classification model, but do not provide information about variation in the individual groups, i.e., the significant differences among maturity stages. Therefore, ANOVA was conducted to determine whether the differences in bands associated with carotenoids were statistically significant (Figure 3). In general, stage A tended to have wider confidence intervals for the true mean intensity of all the bands of carotenoids compared to the later stages (B, C and D). Despite the higher intensity in the Raman spectra, the band at $1,525\text{ cm}^{-1}$ could not accurately differentiate the stages of maturity for all the cultivars. For Fascination type watermelon, all the bands at stage D were significantly lower than in earlier stages. However, stages B and C did not show any significant difference in the spectral intensities. Still, they were distinguished from stages A and D. For the Orange Crisp variety, the intensity of all the studied bands at stages C and D were not significantly different from each other but had a significantly higher intensity compared to stages A and B. The band intensities in stages B and D were similar

in Amarillo type watermelon. As stated earlier, all the bands at stage A were of significantly higher intensity than all other later stages. Finally, in Crimson Sweet, the intensity of bands in stages B and C were similar in Fascination type watermelon and bands in stages B, C, and D were less intense than in stage A. Despite the similarity in the intensities of certain ripening stages, the confidence interval centers for the studied varieties were observed in decreasing order except for Amarillo cultivar during maturity.

The wavenumbers that were mainly accountable for classification could be observed by inspecting the loadings plot for the first three latent variables (LVs), as shown in Figure 4. Those wavenumbers are considered to be important for the differentiation between stages of maturity. Fascination cultivar's loading plot shows that the LV with the highest contribution is at $1,156\text{ cm}^{-1}$ and can be assigned to the carotenoid pigments. Other variables that have the most significant contribution to LV1 correspond to regions of the Raman spectrum at $1,327$ and $1,606\text{ cm}^{-1}$. These characteristic bands can be assigned to the chlorophylls and lignin phenylpropanoids. Investigation of the loading plot of Orange Crisp cultivar indicated that wavenumber at $1,386$ and $1,525\text{ cm}^{-1}$ corresponds to aliphatics and carotenoids were more important for the discrimination of ripening stages. Similarly, Raman's considerable absolute value at $1,386$ and $1,525\text{ cm}^{-1}$ for Amarillo melons had a significant influence on classification. The Crimson Sweet cultivar's loading plot showed that variation associated with carotenoids ($1,156$, $1,186$, and $1,525\text{ cm}^{-1}$) was the most important for this discrimination. Inspection of all the cultivar loading plots showed that the band observed at $1,327\text{ cm}^{-1}$, which was assigned to C–H vibration of aliphatics, also had a remarkable effect on predicting maturity stages.

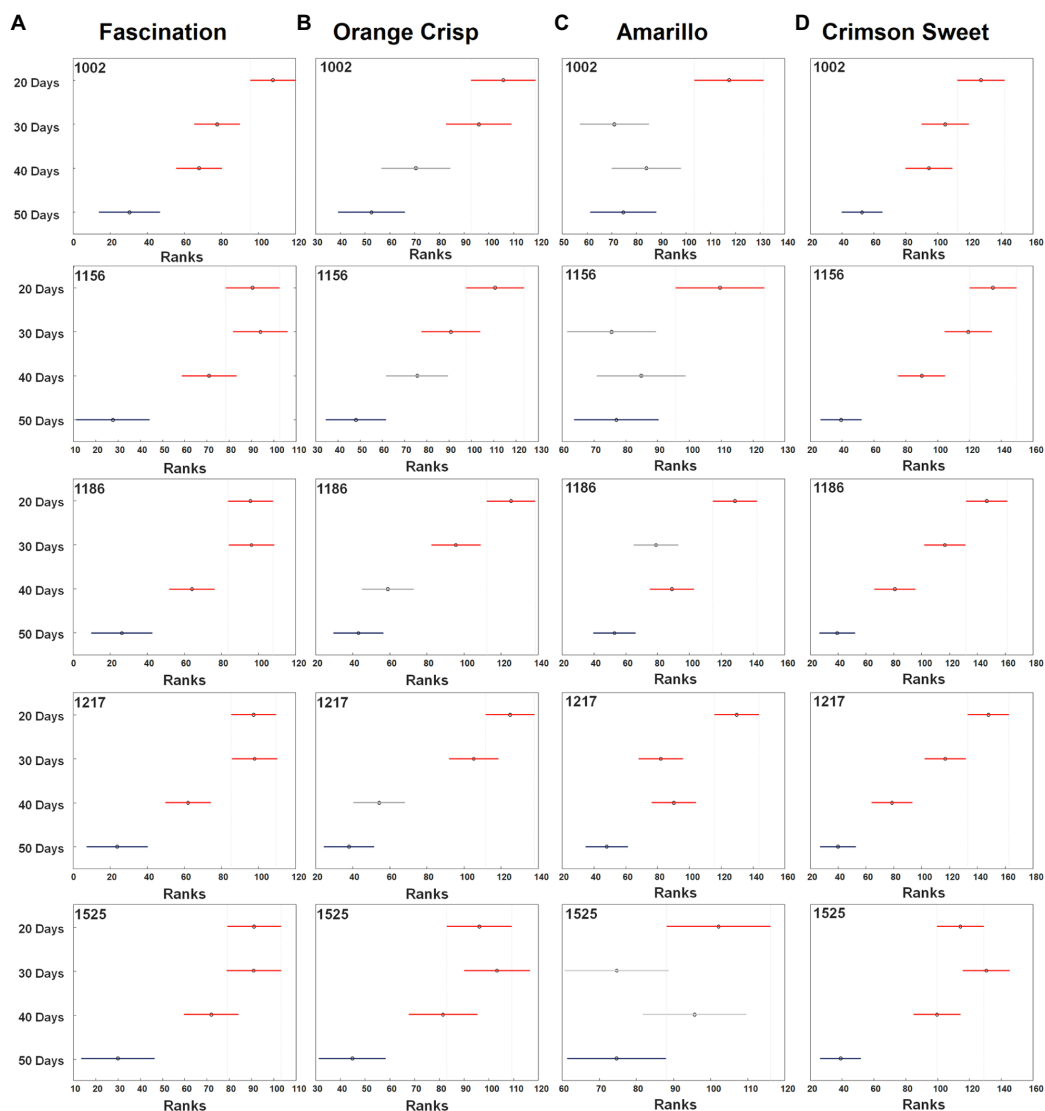


FIGURE 3 | The median (circles) and 95% CI (line) for the relative intensity of bands of carotenoids observed on the surfaces of four watermelon cultivars [Fascination (A), Orange Crisp (B), Amarillo (C), and Crimson Sweet (D)] at four stages of fruit development. For each stage, 20–43 spectra were collected for each cultivar. The confidence intervals were compared to 50 days stage (blue). The separation of different developmental stages is in red and unseparated is in grey. All the spectra analyzed in Kruskal–Wallis test were normalized to $1,439\text{ cm}^{-1}$.

HPLC Analysis

An optimized HPLC method using a C_{30} RP column for the quantification of carotenoids (Supplementary Figure S2) was further used for the analysis of watermelon samples. Lutein and β -carotene were the major carotenoids identified in the watermelon rind extracts and their total concentrations ranged from 1.88 to 14.73 and 0.04 to $0.14\mu\text{g/g}$ fresh weight (FW), respectively (Figure 5). The HPLC analysis did not confirm the presence of lycopene in the extracts congruent with the Raman experiment results. In the Fascination type watermelon, the total carotenoid level varied among ripening stages. However, the intensity of Raman bands for stage B and C were almost similar but lower than stage A and higher than stage D (Figure 3A). HPLC

results show that variation in the total carotenoid level in Orange Crisp cultivar was similar to Fascination variety. ANOVA of Raman bands revealed that stages A and B had a significantly higher rank than stages C and D (Figure 3B). Significant variation in the carotenoid contents in the Amarillo type watermelon was not observed among the maturity stages. Still, an increasing trend was recorded up to stage C. The rank of carotenoid bands at stages B and D was similar from ANOVA results, and stages B to D were significantly lower than stage A (Figure 3C). The highest amount of lutein ($14.73\mu\text{g/g}$ FW) and β -carotene ($6.51\mu\text{g/g}$ FW) representing the total carotenoids ($21.24\mu\text{g/g}$ FW) was recorded in stage B of Crimson Sweet. The level of carotenoids increased from stage A to B, then later showed a decreasing

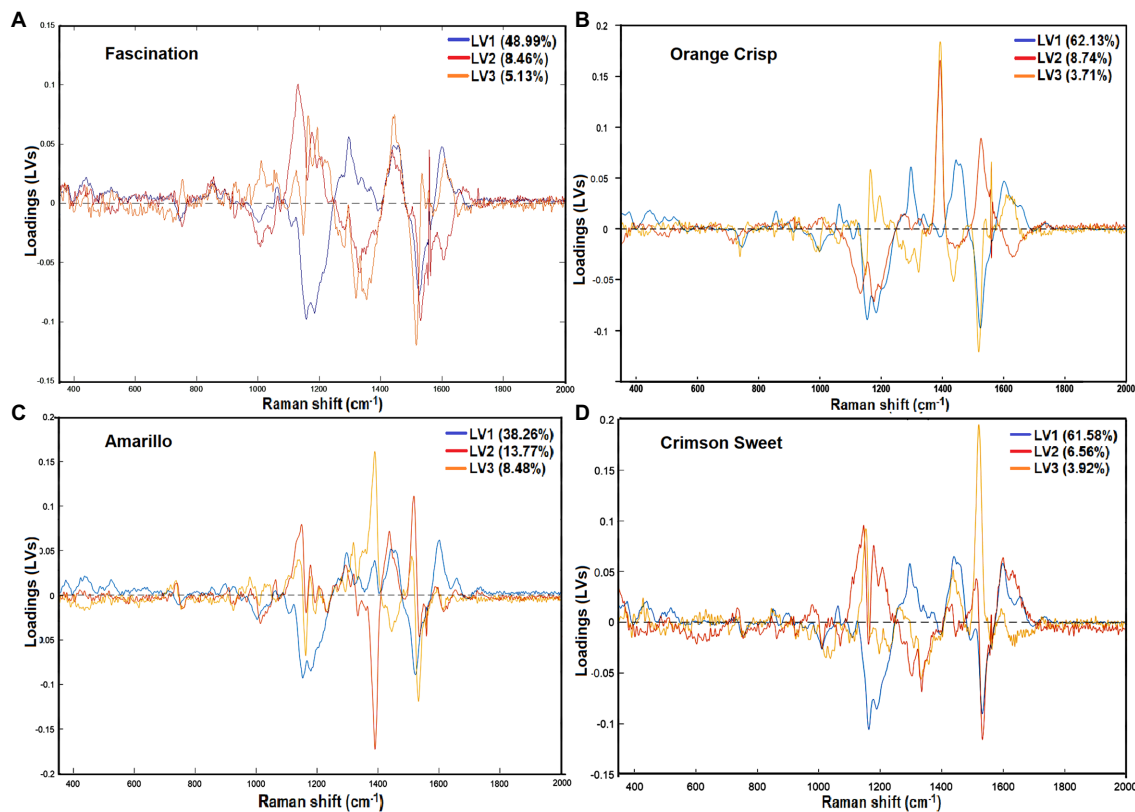


FIGURE 4 | Loading plots for the first three latent variables (LVs) representing wavenumbers having the highest contribution to the maturity prediction model developed from the surface Raman spectra of four watermelon cultivars [Fascination (A), Orange Crisp (B), Amarillo (C), and Crimson Sweet (D)].

trend. The general trend observed in the Kruskal–Wallis and ANOVA results for Fascination cultivar remained true for Crimson Sweet type watermelon (Figure 3D). Further, HPLC results show a decreasing trend for stages B and C for all the cultivars except Amarillo. These trends match the Raman trend analysis results if we look at the confidence interval center in ANOVA.

CONCLUSION

The study confirmed that variation in the carotenoid content measured on the surface of watermelon fruits using a Raman spectrometer can be reliably used for the non-invasive detection of fruit maturity. Raman spectral features for carotenoids were consistent throughout the ripening process with diminishing intensity at full maturity. A fast and sensitive HPLC method for carotenoids was developed using a C₃₀ column with a gradient consisting of TBME, methanol, and water for the validation of Raman spectral analysis. Lutein was a prominent carotenoid followed by β -carotene in the peel of all watermelon varieties. Along with HPLC, resonance Raman confirmed the presence of lutein and β -carotene as major pigments. PLS-DA successfully classified more than 85% of samples with respect to their stage of maturity. ANOVA results of five Raman bands related to carotenoids revealed a significant difference in their

intensities, thereby decreasing the carotenoid level throughout the maturation process. Raman spectroscopy is a prominent technique for identifying and characterizing carotenoids in plant tissues. The Raman bands observed at 1,002, 1,156, 1,186, 1,217, and 1,525 cm⁻¹ corresponding to –C–C– and –C=C– vibrations can be used as fingerprints to characterize the carotenoids. Integrating Raman spectroscopy with other non-destructive techniques such as near-infrared region measurement, Fourier transform infrared spectrophotometry, and chemometric tools could show promising results for online quality assessment of watermelon.

DATA AVAILABILITY STATEMENT

The original contributions presented in the study are included in the article/Supplementary Material, further inquiries can be directed to the corresponding authors.

AUTHOR CONTRIBUTIONS

TDh, JJ, KB, and BP designed the field and lab analysis experiments. TDo and DK designed RS experiment. TD carried out all analytical work. TDh and TDo conducted, collected

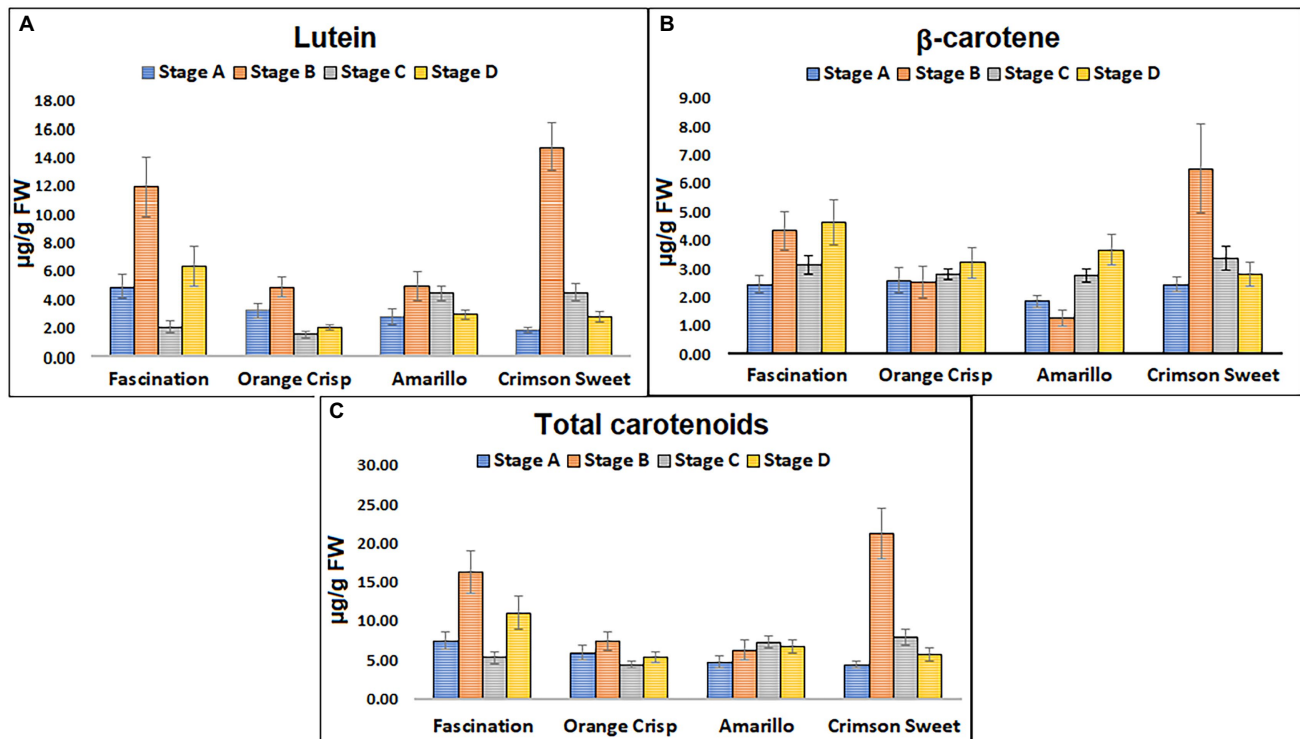


FIGURE 5 | Concentration of individual pigments **(A)** lutein (µg/g FW), **(B)** β-carotene (µg/g FW), and **(C)** total carotenoids detected at different stages of ripening from the fruit rinds of four different cultivars of watermelon. Error bars represent SD from the average ($n = 18$).

and interpreted results, and drafted the manuscript. TDh and TDo have equal contribution. All authors contributed to the article and approved the submitted version.

FUNDING

DK and BP acknowledges the Institute for Advancing Health Through Agriculture for providing financial support. BP also

acknowledges SCRI-Texas Department of Agriculture Block grant 2019-SC-1920-38, USDA-SCRI-2017- 51181-26834.

SUPPLEMENTARY MATERIAL

The Supplementary Material for this article can be found online at: <https://www.frontiersin.org/articles/10.3389/fpls.2022.832522/full#supplementary-material>

REFERENCES

- Abbaszadeh, R., Moosavian, A., Rajabipour, A., and Najafi, G. (2015a). An intelligent procedure for watermelon ripeness detection based on vibration signals. *J. Food Sci. Technol.* 52, 1075–1081. doi: 10.1007/s13197-013-1068-x
- Abbaszadeh, R., Rajabipour, A., Ahmadi, H., Delshad, M., and Mahjoob, M. (2011a). "Assessment of watermelon quality using vibration spectra," in *Innovative Computing Technology. INCT 2011. Communications in Computer and Information Science*. Vol. 241. eds. P. Pichappan, H. Ahmadi and E. Ariwa (Heidelberg, Berlin: Springer), 21–29.
- Abbaszadeh, R., Rajabipour, A., Ahmadi, H., Mahjoob, M., and Delshad, M. (2013a). Prediction of watermelon quality based on vibration spectrum. *Postharvest Biol. Technol.* 86, 291–293. doi: 10.1016/j.postharvbio.2013.07.013
- Abbaszadeh, R., Rajabipour, A., Delshad, M., Mahjub, M., Ahmadi, H., and Lague, C. (2011b). Application of vibration response for the nondestructive ripeness evaluation of watermelons. *Aust. J. Crop. Sci.* 5:920
- Abbaszadeh, R., Rajabipour, A., Mahjoob, M., Delshad, M., and Ahmadi, H. (2013b). Evaluation of watermelons texture using their vibration responses. *Biosyst. Eng.* 115, 102–105. doi: 10.1016/j.biosystemseng.2013.01.001
- Abbaszadeh, R., Rajabipour, A., Sadriana, H., Mahjoob, M. J., Delshad, M., and Ahmadi, H. (2014). Application of modal analysis to the watermelon through finite element modeling for use in ripeness assessment. *J. Food Eng.* 127, 80–84. doi: 10.1016/j.jfoodeng.2013.11.020
- Abbaszadeh, R., Rajabipour, A., Ying, Y., Delshad, M., Mahjoob, M. J., and Ahmadi, H. (2015b). Nondestructive determination of watermelon flesh firmness by frequency response. *LWT* 60, 637–640. doi: 10.1016/j.lwt.2014.08.029
- Akpolat, H., Barineau, M., Jackson, K. A., Akpolat, M. Z., Francis, D. M., Chen, Y.-J., et al. (2020). High-throughput Phenotyping approach for screening major carotenoids of tomato by handheld Raman spectroscopy using chemometric methods. *Sensors* 20:3723. doi: 10.3390/s20133723
- Ali, M. M., Hashim, N., Bejo, S. K., and Shamsudin, R. (2017). Rapid and nondestructive techniques for internal and external quality evaluation of watermelons: a review. *Sci. Hortic.* 225, 689–699. doi: 10.1016/j.scienta.2017.08.012
- Arendse, E., Fawole, O. A., Magwaza, L. S., and Opara, U. L. (2018). Non-destructive prediction of internal and external quality attributes of fruit with thick rind: a review. *J. Food Eng.* 217, 11–23. doi: 10.1016/j.jfoodeng.2017.08.009

- Arendse, E., Nieuwoudt, H., Magwaza, L. S., Ntutumbirwe, J. F. I., Fawole, O. A., and Opara, U. L. (2021). Recent advancements on vibrational spectroscopic techniques for the detection of authenticity and adulteration in horticultural products with a specific focus on oils, juices and powders. *Food Bioprocess Technol.* 14, 1–22. doi: 10.1007/s11947-020-02505-x
- Bhosale, P., Ermakov, I. V., Ermakova, M. R., Gellermann, W., and Bernstein, P. S. (2004). Resonance Raman quantification of nutritionally important carotenoids in fruits, vegetables, and their juices in comparison to high-pressure liquid chromatography analysis. *J. Agric. Food Chem.* 52, 3281–3285. doi: 10.1021/jf035345q
- Conrad, A. O., and Bonello, P. (2015). Application of infrared and Raman spectroscopy for the identification of disease resistant trees. *Front. Plant Sci.* 6:1152. doi: 10.3389/fpls.2015.01152
- Diezma-Iglesias, B., Ruiz-Altisent, M., and Barreiro, P. (2004). Detection of internal quality in seedless watermelon by acoustic impulse response. *Biosyst. Eng.* 88, 221–230. doi: 10.1016/j.biosystemseng.2004.03.007
- Erkan, M., and Dogan, A. (2019). “Harvesting of horticultural commodities,” in *Postharvest Technology of Perishable Horticultural Commodities* (Elsevier: Woodhead Publishing), 129–159.
- Flores, K., Sanchez, M., Perez-Marin, D., Lopez, M., Guerrero, J., and Garrido-Varo, A. (2008). Prediction of total soluble solid content in intact and cut melons and watermelons using near infrared spectroscopy. *J. Near Infrared Spectrosc.* 16, 91–98. doi: 10.1255/jnirs.771
- Grudzinski, W., Janik, E., Bednarska, J., Welc, R., Zubik, M., Sowinski, K., et al. (2016). Light-driven reconfiguration of a xanthophyll violaxanthin in the photosynthetic pigment-protein complex LHCI: a resonance Raman study. *J. Phys. Chem. B* 120, 4373–4382. doi: 10.1021/acs.jpcc.6b01641
- Harris, L. V., McHugh, M., Hutchinson, I. B., Ingley, R., Malherbe, C., Parnell, J., et al. (2015). Avoiding misidentification of bands in planetary Raman spectra. *J. Raman Spectrosc.* 46, 863–872. doi: 10.1002/jrs.4667
- Hata, T. R., Scholz, T. A., Ermakov, I. V., McClane, R. W., Khachik, F., Gellermann, W., et al. (2000). Non-invasive Raman spectroscopic detection of carotenoids in human skin. *J. Invest. Dermatol.* 115, 441–448. doi: 10.1046/j.1523-1747.2000.00060.x
- Ikeda, T., Choi, P.-K., Ishii, T., Arai, I., and Osawa, M. (2015). Firmness evaluation of watermelon flesh by using surface elastic waves. *J. Food Eng.* 160, 28–33. doi: 10.1016/j.jfoodeng.2015.03.020
- Jehlička, J., Edwards, H. G., and Oren, A. (2014). Raman spectroscopy of microbial pigments. *Appl. Environ. Microbiol.* 80, 3286–3295. doi: 10.1128/AEM.00699-14
- Jie, D., and Wei, X. (2018). Review on the recent progress of non-destructive detection technology for internal quality of watermelon. *Comput. Electron. Agric.* 151, 156–164. doi: 10.1016/j.compag.2018.05.031
- Jie, D., Xie, L., Rao, X., and Ying, Y. (2014). Using visible and near infrared diffuse transmittance technique to predict soluble solids content of watermelon in an on-line detection system. *Postharvest Biol. Technol.* 90, 1–6. doi: 10.1016/j.postharvbio.2013.11.009
- Jie, D., Zhou, W., and Wei, X. (2019). Nondestructive detection of maturity of watermelon by spectral characteristic using NIR diffuse transmittance technique. *Sci. Hortic.* 257:108718. doi: 10.1016/j.scienta.2019.108718
- Ke, X., Guandong, G., Guifa, T., Yuxin, Z., and Yuchen, J. (2009). Non-destructive acoustic detection method for maturity of watermelon [J]. *Journal of Agricultural Mechanization Research* 8, 150–154.
- Lee, K.-M., and Herrman, T. J. (2016). Determination and prediction of fumonisin contamination in maize by surface-enhanced Raman spectroscopy (SERS). *Food Bioprocess Technol.* 9, 588–603. doi: 10.1007/s11947-015-1654-1
- Lee, L. C., Liong, C.-Y., and Jemain, A. A. (2018). Partial least squares-discriminant analysis (PLS-DA) for classification of high-dimensional (HD) data: a review of contemporary practice strategies and knowledge gaps. *Analyst* 143, 3526–3539. doi: 10.1039/C8AN00599K
- Legner, R., Voigt, M., Servatius, C., Klein, J., Hambitzer, A., and Jaeger, M. (2021). A four-level maturity index for hot peppers (*Capsicum annum*) using non-invasive automated mobile Raman spectroscopy for on-site testing. *Appl. Sci.* 11:1614. doi: 10.3390/app11041614
- Liu, B., Zhou, P., Liu, X., Sun, X., Li, H., and Lin, M. (2013). Detection of pesticides in fruits by surface-enhanced Raman spectroscopy coupled with gold nanostructures. *Food Bioprocess Technol.* 6, 710–718. doi: 10.1007/s11947-011-0774-5
- Merlin, J. C. (1985). Resonance Raman spectroscopy of carotenoids and carotenoid-containing systems. *Pure Appl. Chem.* 57, 785–792. doi: 10.1351/pac198557050785
- Nelson, S. O., Guo, W.-C., Trabelsi, S., and Kays, S. J. (2007a). Dielectric spectroscopy of watermelons for quality sensing. *Meas. Sci. Technol.* 18, 1887–1892. doi: 10.1088/0957-0233/18/7/014
- Nelson, S. O., Guo, W.-C., Trabelsi, S., and Kays, S. J. (2007b). “Sensing quality of watermelons through dielectric permittivity,” in *2007 IEEE Antennas and Propagation Society International Symposium: IEEE*. 285–288.
- Paul, V., Pandey, R., and Srivastava, G. C. (2012). The fading distinctions between classical patterns of ripening in climacteric and non-climacteric fruit and the ubiquity of ethylene—an overview. *J. Food Sci. Technol.* 49, 1–21. doi: 10.1007/s13197-011-0293-4
- Payne, W. Z., and Kurouski, D. (2020). Raman-based diagnostics of biotic and abiotic stresses in plants. A review. *Front Plant Sci.* 11:616672. doi: 10.3389/fpls.2020.616672
- Pintor, A. L. C., Magpantay, M. A. A., and Santiago, M. R. (2016). Development of an android-based maturity detector mobile application for watermelons [*Citrullus Lanatus* (Thunb.) matsum. & Nakai] using acoustic impulse response. *Small* 200, 44–56.
- Qin, J., Chao, K., and Kim, M. S. (2011). Investigation of Raman chemical imaging for detection of lycopene changes in tomatoes during postharvest ripening. *J. Food Eng.* 107, 277–288. doi: 10.1016/j.jfoodeng.2011.07.021
- Qin, J., Kim, M. S., Chao, K., Dhakal, S., Cho, B.-K., Lohumi, S., et al. (2019). Advances in Raman spectroscopy and imaging techniques for quality and safety inspection of horticultural products. *Postharvest Biol. Technol.* 149, 101–117. doi: 10.1016/j.postharvbio.2018.11.004
- Schulz, H., Baranska, M., and Baranski, R. (2005). Potential of NIR-FT-Raman spectroscopy in natural carotenoid analysis. *Biopolymers* 77, 212–221. doi: 10.1002/bip.20215
- Stone, M., Armstrong, P., Zhang, X., Brusewitz, G., and Chen, D. (1996). Watermelon maturity determination in the field using acoustic impulse impedance techniques. *Trans. ASAE* 39, 2325–2330. doi: 10.13031/2013.27743
- Vinson, E. L., Woods, F. M., Kemble, J. M., Perkins-Veazie, P., Davis, A., and Kessler, J. R. (2010). Use of external indicators to predict maturity of mini-watermelon fruit. *HortScience* 45, 1034–1037. doi: 10.21273/HORTSCI.45.7.1034
- Yang, J., and Yang, J.-Y. (2003). Why can LDA be performed in PCA transformed space? *Pattern Recogn.* 36, 563–566. doi: 10.1016/S0031-3203(02)00048-1
- Yu, M. M. L., Schulze, H. G., Jetter, R., Blades, M. W., and Turner, R. F. B. (2007). Raman microspectroscopic analysis of triterpenoids found in plant cuticles. *Appl. Spectrosc.* 61, 32–37. doi: 10.1366/000370207779701352
- Zeng, J., Ping, W., Sanaeifar, A., Xu, X., Luo, W., Sha, J., et al. (2021). Quantitative visualization of photosynthetic pigments in tea leaves based on Raman spectroscopy and calibration model transfer. *Plant Methods* 17, 1–13. doi: 10.1186/s13007-020-00704-3
- Zhang, Y.-X., Han, J.-L., and Yao, W. (2010). “Non-destructive watermelon maturity detection by acoustic response,” in *2010 2nd International Conference on Information Engineering and Computer Science: IEEE*. December 25–26, 2010; China: Wuhan, 1–4.

Conflict of Interest: The authors declare that the research was conducted in the absence of any commercial or financial relationships that could be construed as a potential conflict of interest.

Publisher’s Note: All claims expressed in this article are solely those of the authors and do not necessarily represent those of their affiliated organizations, or those of the publisher, the editors and the reviewers. Any product that may be evaluated in this article, or claim that may be made by its manufacturer, is not guaranteed or endorsed by the publisher.

Copyright © 2022 Dhanani, Dou, Biradar, Jifon, Kurouski and Patil. This is an open-access article distributed under the terms of the Creative Commons Attribution License (CC BY). The use, distribution or reproduction in other forums is permitted, provided the original author(s) and the copyright owner(s) are credited and that the original publication in this journal is cited, in accordance with accepted academic practice. No use, distribution or reproduction is permitted which does not comply with these terms.



Raman Spectroscopy Applications in Grapevine: Metabolic Analysis of Plants Infected by Two Different Viruses

Luisa Mandrile¹, Chiara D'Errico², Floriana Nuzzo², Giulia Barzan¹, Slavica Matić², Andrea M. Giovannozzi¹, Andrea M. Rossi^{1*}, Giorgio Gambino² and Emanuela Noris^{2*}

¹Istituto Nazionale di Ricerca Metrologica (INRIM), Torino, Italy, ²Institute for Sustainable Plant Protection, National Research Council of Italy (CNR), Torino, Italy

OPEN ACCESS

Edited by:

Nam-Hai Chua,
Temasek Life Sciences Laboratory,
Singapore

Reviewed by:

Dmitry Kourouski,
Texas A&M University, United States
Gajendra Pratap Singh,
Singapore-MIT Alliance for Research
and Technology (SMART), Singapore

*Correspondence:

Emanuela Noris
emanuela.noris@ipsa.cnr.it
Andrea M. Rossi
a.rossi@inrim.it

Specialty section:

This article was submitted to
Technical Advances in Plant Science,
a section of the journal
Frontiers in Plant Science

Received: 10 April 2022

Accepted: 23 May 2022

Published: 14 June 2022

Citation:

Mandrile L, D'Errico C, Nuzzo F,
Barzan G, Matić S, Giovannozzi AM,
Rossi AM, Gambino G and
Noris E (2022) Raman Spectroscopy
Applications in Grapevine: Metabolic
Analysis of Plants Infected by Two
Different Viruses.
Front. Plant Sci. 13:917226.
doi: 10.3389/fpls.2022.917226

Grapevine is one of the most cultivated fruit plant among economically relevant species in the world. It is vegetatively propagated and can be attacked by more than 80 viruses with possible detrimental effects on crop yield and wine quality. Preventive measures relying on extensive and robust diagnosis are fundamental to guarantee the use of virus-free grapevine plants and to manage its diseases. New phenotyping techniques for non-invasive identification of biochemical changes occurring during virus infection can be used for rapid diagnostic purposes. Here, we have investigated the potential of Raman spectroscopy (RS) to identify the presence of two different viruses, grapevine fan leaf virus (GFLV) and grapevine rupestris stem pitting-associated virus (GRSPaV) in *Vitis vinifera* cv. Chardonnay. We showed that RS can discriminate healthy plants from those infected by each of the two viruses, even in the absence of visible symptoms, with accuracy up to 100% and 80% for GFLV and GRSPaV, respectively. Chemometric analyses of the Raman spectra followed by chemical measurements showed that RS could probe a decrease in the carotenoid content in infected leaves, more profoundly altered by GFLV infection. Transcriptional analysis of genes involved in the carotenoid pathway confirmed that this biosynthetic process is altered during infection. These results indicate that RS is a cutting-edge alternative for a real-time dynamic monitoring of pathogens in grapevine plants and can be useful for studying the metabolic changes ensuing from plant stresses.

Keywords: Raman scattering, *Vitis vinifera*, carotenoids, virus, early diagnosis

INTRODUCTION

Grapevine (*Vitis vinifera* L.) is one of the most important fruit crop, with up to 7 million hectares cultivated worldwide in 2020 (FAOSTAT, 2020). Grapevine is mainly grown for wine production and for fresh and dry fruit consumption, but it is also used for seed oil extraction, alcoholic beverage and vinegar production; moreover, several social, touristic, and cultural activities are linked to its cultivation, generating a positive impact on the economy.

Grapevine is affected by several pathogens, including fungi, oomycota, phytoplasmas, and viruses heavily influencing yield and quality of the crop and reducing the economic revenues.

Among grapevine pathogens, viruses are widespread in all cultivated areas, causing different diseases, such as the rugose wood complex, leafroll, infectious degeneration, and fleck disease (Fuchs, 2020). Up to now, more than 80 viruses from 17 families and 34 genera have been identified (Martelli, 2014, 2018), frequently occurring in mixed infection.

Within this large number of viral entities threatening grapevine, grapevine rupestris stem pitting-associated virus (GRSPaV) and grapevine fanleaf virus (GFLV) are two well-known and widespread examples. After its discovery about two decades ago, GRSPaV is nowadays considered one of the most ubiquitous viruses, found in Europe, America, Australia, and Asia (Meng and Rowhani, 2017). GRSPaV belongs to the genus *Foveavirus*, family *Betaflexiviridae*, and it is generally associated to “Rupestris Stem Pitting,” a disorder of the “Rugose Wood complex” (Meng and Gonsalves, 2003). Its presence has been linked to other grapevine diseases, including the vein-clearing complex on cv. Chardonnay (Lunden et al., 2009). Nonetheless, in most cases GRSPaV induces latent infections, with no visible symptoms on infected plants. Despite this, GRSPaV was reported to trigger a number of transcriptional changes on cv. Bosco, mainly regarding photosynthesis and CO₂ fixation, leading to a moderate decrease of the photosynthetic process and an altered reaction of plants to biotic/abiotic stress, underlying possible beneficial effects mediated by this virus toward abiotic factors (Gambino et al., 2012; Pantaleo et al., 2016; Tobar et al., 2020).

GFLV (family *Secoviridae*, genus *Nepovirus*) is a harmful and economically deleterious virus, responsible for the “Grapevine infectious degeneration” complex (Sanfaçon et al., 2009). Symptoms induced by GFLV include vein yellowing, mosaics, internode shortening, typical leaf deformations, smaller and fewer bunches, with irregular ripening. The variability of symptoms observed in vineyards depends on the virus strain, grapevine genotype, cultural practices, and environmental conditions (Martelli, 2017). GFLV is transmitted by the soil-borne ectoparasitic nematode *Xiphinema index* and by infected plant material. Beside phenotypic alterations typical of infectious degeneration, the physiological and molecular changes induced by GFLV can be occasionally associated to an improved tolerance toward fungal infections (Gilardi et al., 2020) and to a moderate water stress (Krebelj et al., 2022). Overall, GRSPaV and GFLV represent two virus models regarding the symptomatology induced on vine plants, which interact with the host in complex and unexpected ways, justifying to more deeply explore the changes occurring during the infection processes.

Early diagnosis of plant pathogens is crucial for a proper disease management, allowing not only to eliminate infected material and reduce further spread of the pathogens, but also to implement clean stock programs useful to preserve the sanitary status of a crop. This is particularly relevant for grapevine, a vegetatively propagated perennial crop, and for viral pathogens which cannot be eliminated with chemical pesticides. For these, in fact, eradication programs are required before the nursery stage and during the clonal selection, currently performed applying sanitation techniques such as meristem culture, thermotherapy, and somatic embryogenesis. Specifically, due to the extensive use

of clonal multiplication of grapevine, many countries have established strict regulations for the grapevine propagation material, in order to verify the presence of viruses and reduce the risk of disease spread (Golino et al., 2017). Plant disease diagnosis is commonly performed using molecular-based procedures (Fang and Ramasamy, 2015; Martinelli et al., 2015), which can be time-consuming, unsuitable for rapidly testing large numbers of samples, require skilled personnel and the availability of pathogen-specific reagents (gene sequences or antibodies), and are not frequently implemented for field application. Indeed, grapevine certification schemes mainly rely on serological and molecular assays, aided by biological indexing, time-consuming and expensive activities often requiring multiple evaluations. In Italy, sanitary schemes dictate that all materials test negative for grapevine virus A (GVA), GFLV, Arabis mosaic virus (ArMV), grapevine leafroll-associated virus-1 and -3 (GLRaV-1, -3), and grapevine fleck virus (GFkV, this only for rootstocks; Italian regulation D.M. 7 July 2006 and D.L. 02 February 2021). Therefore, new diagnostic tools, ideally suitable for field testing of plants by untrained personnel, using friendly and inexpensive equipment and providing results in a short time, with minimal number of steps would be extremely important. Such strategies could allow extensive and fast screening of imported vegetative material, preventing disease spread.

Raman spectroscopy (RS) records the molecular vibrations of cellular metabolites present in a specimen in the absence of labels or reagents and has been recently proposed as a non-destructive and rapid diagnostic procedure for plant pathogens. The spectra obtained from healthy and diseased plant samples are used as specific fingerprints, reflecting changes in cellular metabolites occurring following infection by pathogens or during abiotic stresses. Indeed, several groups including our laboratory have shown that RS can sense the presence of different plant pathogens, among which viruses, in different cultivated crops (Yeturu et al., 2016; Egging et al., 2018; Farber and Kurouski, 2018; Farber et al., 2019a,b; Sanchez et al., 2020). In particular, we showed that specific changes in tomato plants artificially inoculated with two different viruses can be identified by RS, at a stage when visual symptoms were not yet visible (Mandrić et al., 2019).

In the current study, we investigated the potential of RS to determine the occurrence of two different viruses infecting grapevine cv. Chardonnay; the two pathogens were chosen as examples of a latent-asymptomatic virus (GRSPaV) and a dangerous-symptomatic virus (GFLV), whose absence is required in the certification protocols. Plants separately infected by the two viruses were analyzed with a Raman microscope apparatus at different time points during the vegetative season and systemic molecular changes induced by the viruses were analyzed by quantitative reverse transcription-PCR (RT-qPCR).

MATERIALS AND METHODS

Plants

V. vinifera cv. Chardonnay plants infected by either GFLV (cluster IB; NCBI Acc. No. MN889891) or GRSPaV (phylogenetic group GRSPaV-SG1; NCBI Acc. No. MN889892) were previously described in Gilardi et al. (2020). In this work, 2-year-old

infected plantlets and healthy individuals ($n=4$) were maintained in 5-L pots filled with a peat substrate (TS4, Turco Silvestro, Italy). Plants were kept under a gauze greenhouse for the whole duration of the experiment, with constant watering. Each plant represents a biological replica.

RNA Extraction and RT-qPCR

Total RNA was extracted using a rapid CTAB method (Gambino et al., 2008) and its quantity and quality were evaluated with a NanoDrop 1000 spectrophotometer (Thermo Fisher Scientific, Waltham, MA, United States). RNA was then treated with DNase (DNase I, Thermo Fisher Scientific, Waltham, MA, United States) and reverse-transcribed using the High-Capacity cDNA Reverse Transcription Kit (Thermo Fisher Scientific), following manufacturer's instructions.

RT-qPCR reactions were performed in a CFX Connect Real-Time PCR system (Bio-Rad Laboratories, Hercules, CA, United States), using SYBR Green (SensiFAST™ SYBR® No-ROX Kit; Meridian Bioscience, Memphis, Tennessee, United States) with the following cycling conditions: denaturation at 95°C for 2 min, followed by 40 cycles at 95°C for 15 s and 60°C for 30 s. RT-qPCR was conducted for the relative quantification of GFLV and GRSPaV, using primers specific for viral RdRp (Gilardi et al., 2020), and for transcriptional analysis of genes representative of the carotenoid pathway, using Ubiquitin (*VvUBI*) and Actin1 (*VvACT1*) as internal controls. The primers for RT-qPCR are listed in **Supplementary Table S1**. Four independent biological replicates and three technical replicates were run for each RT-qPCR. Gene expression data were subjected to analysis of variance (ANOVA), followed by the Tukey's HSD *post hoc* test ($p \leq 0.05$). The SPSS statistical software package (SPSS Inc., Cary, NC, United States, v.23) was used to run statistical analyses.

Raman Spectroscopic Measurements

Raman spectra were acquired from one half of the fifth leaf counting from the apex, while the other half was used for virus detection and transcript accumulation analysis. Leaf samples for RS analysis were stored in plastic bags and kept on ice until spectra acquisition within the following 4 h. Spectra ($400\text{--}3,100\text{ cm}^{-1}$; 5 cm^{-1} resolution) were acquired using a Dispersive Raman Spectrometer (DRX Thermo Fisher Scientific, Waltham, United States; 785 nm excitation laser, 10× microscope objective, 2 μm laser spot diameter, 10 mW laser power; 20 scans, 1 s each), were collected on the same point of the leaf, taking three points per leaf, on three different leaf lobes.

The spectrometer was weekly calibrated using a certified white light for intensity and neon gas lines for frequency. Moreover, a Si standard was measured before each session, to guarantee consistency within measurements and to avoid differences due to instrument performances. Four different measurements were performed, at monthly intervals, starting in May, until August 2021 (T1 to T4).

Chemometric Analysis of Raman Spectra

Chemometric analysis was conducted using the PLS Toolbox (Eigenvector Research, Inc., Manson, WA) for Matlab R2015a

(Mathworks, Natick, MA). Spectral range between 650 and $3,060\text{ cm}^{-1}$ was considered. Spectra pre-processing consisted in smoothing (Savitzky-Golay filter, 21 pt.), baseline correction (automatic weighted least square regression, second order and Whittaker filter with asymmetry $1e^{-5}$, λ 1,000), and mean centering. Principal Component Analysis (PCA) was used to find non-random data structures attesting non-random variability between groups of spectra. The effect of the different factors of the experimental design was evaluated by analysis of variance simultaneous component analysis (ANOVA-SCA, also known as ASCA), considering the following k factors: (i) "time" (T1, T2, T3, and T4); (ii) "virus" (presence of infection; levels healthy, GRSPaV and GFLV), and (iii) "biological replicates" (levels: different plant specimens).

ASCA was performed considering the two-way correlations between factors. The significance of the experimental factors was quantified determining values of p through a permutation test between the levels of the factors (Zwanenburg et al., 2011). The H_0 hypothesis of no experimental effect, indicating no difference between the levels averages of the effect matrices, with a confidence level of p was tested. Values of p were obtained for the main effects by randomizing the levels of each factor under consideration.

Partial least squares discriminant analysis (PLS-DA) was finally used as a classification method to test the possibility to recognize infected plants. Since an external test set for validation was not available, leave-one plant-out cross validation (CV) was used to determine the classification error (CE).

Sample Extraction and Analysis of Total Carotenoids, Chlorophylls, and Polyphenols

Plant extracts were prepared according to Alrifai et al. (2021), with slight modifications. Grapevine leaves were freeze-dried and maintained at -80°C ; 25–30 mg of powdered material were extracted in 4 ml of an acetone:ethanol (1:1, v/v) solution and extracts were sonicated in a water bath for 15 min and incubated at room temperature for 4 h, with shaking at 400 rpm (Sky4 Shaking Incubator, Argo Lab). After centrifugation ($1,600 \times g$, 5 min), each supernatant was transferred to a clean tube; pellets were re-extracted twice with the same solvent, once using 2 ml for 2 h, followed by 1 ml for 1 h. Supernatants from the same sample were pooled. For total carotenoid and chlorophyll content analysis, a 250-μl aliquot of each extract was added in triplicate to a 96-well microplate. The plate was analyzed immediately using a UV/VIS Varioskan Lux (Thermo Fisher Scientific, Waltham, United States) multi-wells reader, measuring absorbance at 452 nm. A calibration curve was prepared with a β -carotene (Sigma Aldrich, Certified Reference Material, >99%) solution, using at least five concentrations from 2 to 50 μg/ml, $R^2 > 0.99$. Total carotenoid content was expressed as μg of β -carotene equivalents/g of dry weight sample. Absorbance at 666 nm was also recorded to evaluate the chlorophyll content and relative comparison between the tested samples was performed to provide semi-quantitative information.

Total polyphenol content was measured by the Folin-Ciocalteu method, using the same ethanol:acetone (1:1) leaf extracts (see

above). Aliquots of 200 μ l of each extract were added to 15-ml tubes containing 3 ml ultrapure water and 200 μ l Folin–Ciocalteu reagent (Sigma Aldrich). After mixing and incubating the samples for 6 min at room temperature, 200 μ l of 20% (w/v) Na_2CO_3 (Carlo Erba) were added to each tube and vortexed. After 30 min incubation at 37°C, aliquots of 200 μ l of each sample were placed in triplicate in a 96-wells microplate and absorbance at 765 nm was measured with the UV/VIS Varioskan Lux multi-wells reader, by subtracting the absorbance of the blank (ethanol:acetone solution, 1:1). A calibration curve made with gallic acid was used as standard, measuring at least five concentrations from 40 to 200 mg/L. Results were normalized to the weight of the dried leaf sample (mg/L).

EXPERIMENTAL RESULTS AND DISCUSSION

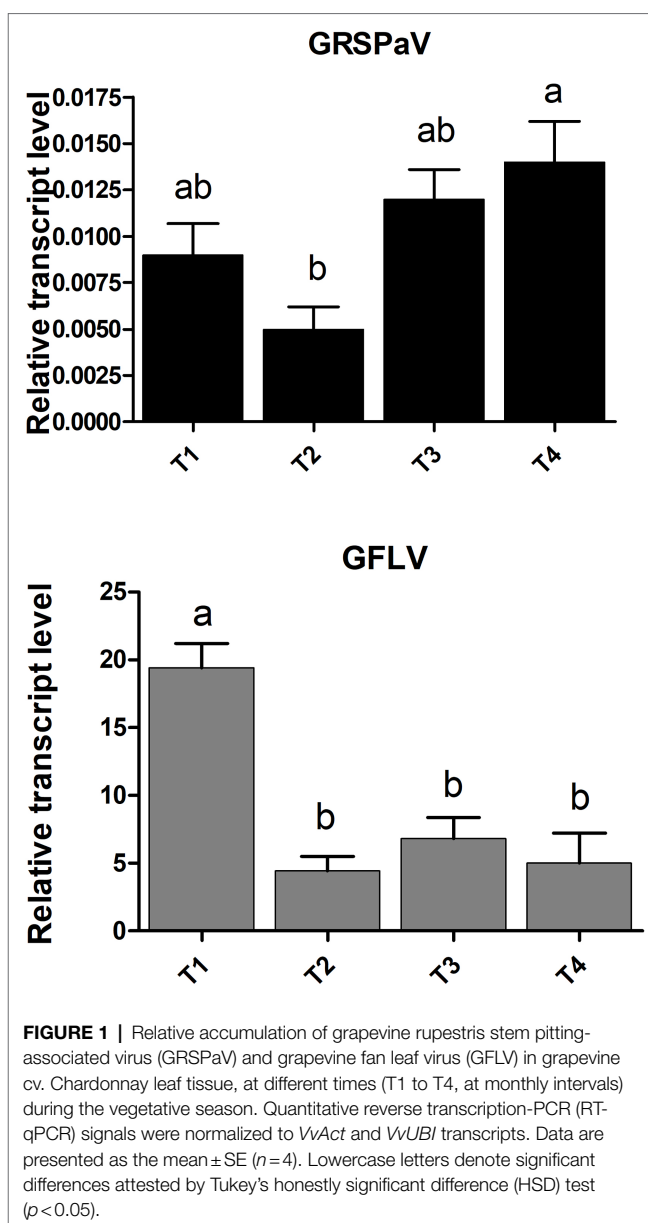
Virus Accumulation in Grapevine Plants Along the Vegetative Season

In this work, we considered grapevine plants cv. Chardonnay infected by either GRSPaV or GFLV, and healthy control individuals (Gilardi et al., 2020). Plants were surveyed along the whole vegetative season from May to August 2021, at four different time points (T1 to T4) at monthly intervals. During the whole season, no visible symptoms could be detected on plants infected by either virus, in agreement with a previous report (Gilardi et al., 2020) and in line with unpublished observations of young plants kept in pots, across several years (G. Gambino, personal observations).

RT-qPCR virus quantification analysis showed an overall stable accumulation of GRSPaV along the whole duration of the experiment, with a slight increase only at the end of the season (Figure 1). In vineyard conditions, the GRSPaV titer in leaves tends to decrease as the season progresses, while no such decrease occurred in the present conditions (Gambino et al., 2012). On the contrary, a remarkable drop in the accumulation of GFLV occurred since the second time point analyzed (T2, June), with no further changes during the vegetative season (Figure 1). The reduction of the GFLV titer along the season is in line with observations recorded in vineyard, where the highest GFLV concentrations in leaves were found in May, i.e., at the beginning of the vegetative period (Krebelj et al., 2015; Gilardi et al., 2020).

Raman Spectra Measurements of Leaves

The Raman spectra of grapevine leaves were collected on intact plant material, focusing the excitation laser directly onto the leaf surface. A near infrared laser wavelength was used to limit the undesired fluorescence effect disturbing Raman signals. Other research paper dealing with Raman measurements on plant tissues report the alternative use of 785 nm (Dou et al., 2021), 830 nm (Farber et al., 2019b; Sanchez et al., 2020; Payne et al., 2022), or 1,064 nm (Yeturu et al., 2016; Farber and Kurouski, 2018; Skoczowski et al., 2022) laser wavelengths to minimize fluorescence interference and increase signal-to-noise



ratio. At the same time, a relatively low laser power and low magnification objective were adopted to avoid thermal stress of the tissue and to collect information from a relatively large area (spot size $>2 \mu\text{m}$). The mean spectra of grapevine leaves showed vibrational bands that were assigned to cellulose, carotenoids, polyphenols, chlorophylls, xylan, lignin, and proteins, being the major components of leaves (Figure 2). The assignment of bands of the most relevant peaks are reported in Table 1. According to previous literature, most of the wavenumbers were related to photosynthetic pigments (Zeng et al., 2021).

Following this analysis, the spectra obtained from healthy plants were compared with those collected from virus-infected plants, at the different time points. Similar spectral profiles were registered among the three different groups of samples, at the different time measurements (Figure 2), indicating that,

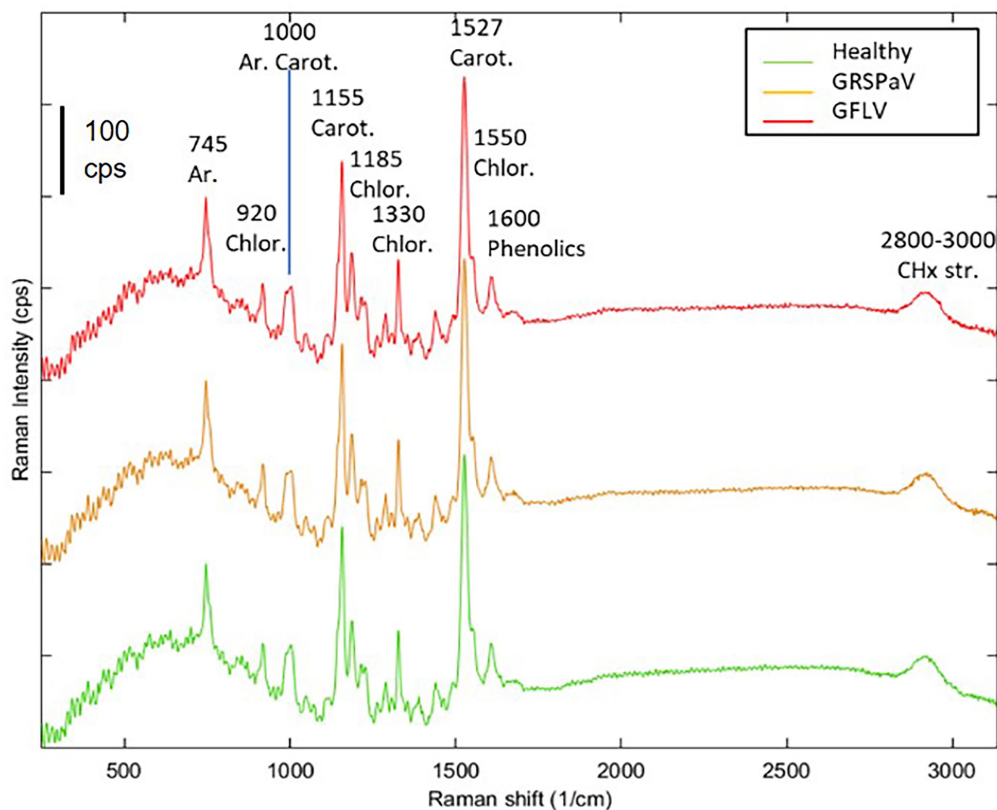


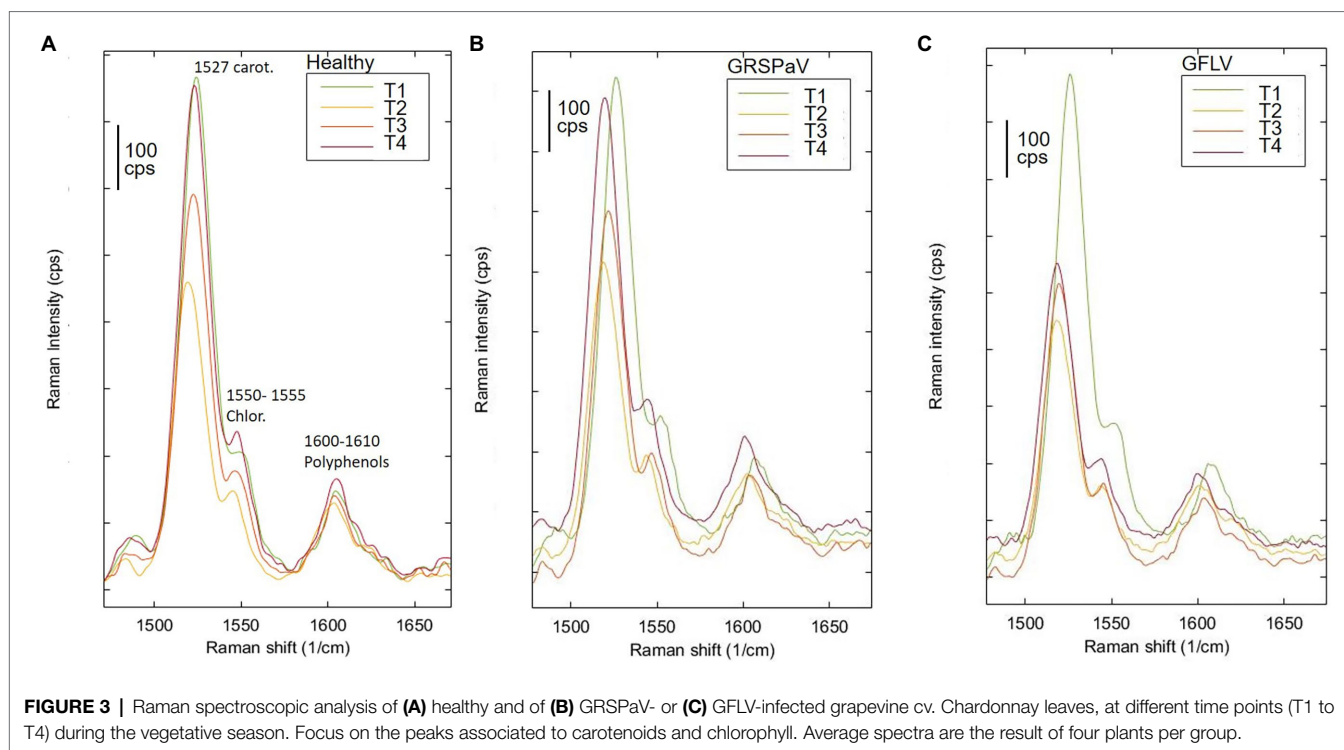
FIGURE 2 | Average Raman spectra of healthy (green), GRSPaV- (yellow), and GFLV- (red)-infected grapevine cv. Chardonnay leaves. Spectra are the result of four plants per group. Representative spectra collected in the first measurement session (T1) are shown.

TABLE 1 | Raman bands assignments for grapevine leaves.

Band (cm ⁻¹)	Vibrational assignment	References
2,800–3,000	CH _x stretching	
1,605	m ν(phenyl ring; phenolics and lignin)	Eravuchira et al., 2012
1,551	m br chlorophyll - central 16-membered-ring vib. + ν(C=C; pyrrole ring)	
1,526	s ν1(C–C; carotenoids)	Koyama et al., 1986
1,483	m δ(CH ₂) and δ(CH ₃)	
1,438	m ν(phenyl ring; phenolics)	Eravuchira et al., 2012
1,370	δCH ₂ bending vibration (aliphatic)	Yu et al., 2007
1,328	m δ(CH) + ν(CN; pyrrole ring br. — chlorophylls)	Boldt et al., 1987
1,320	[δ(C12–H), ν(C11–C12)](β-carotene)	Eravuchira et al., 2012
1,280	m δ(phenyl-OH; phenolics) + – δ(CH). ν(CN; chlorophyll)	Eravuchira et al., 2012; Yeturu et al., 2016
1,215	m δ(CH) + δ(CH ₂ ; chlorophyll)	Boldt et al., 1987
1,180	ms ν(CC) + γ(CH; chlorophylls) + δ(CH phenyl; phenolics)	Boldt et al., 1987; Eravuchira et al., 2012
1,150	s ν2(C\ C; carotenoids)	Gill et al., 1970
1,140	m sh ν(CN). δ(CNC; chlorophyll)	Boldt et al., 1987
1,110	δ(C–OH; carbohydrates)	Farber and Kurouski, 2018
1,050	ν(C–O) + ν(C–C) + ν(C–OH; carbohydrates)	Farber and Kurouski, 2018
1,000	m δ(C–CH ₃ ; carotenoids)	Gill et al., 1970
980	m undefined (chlorophylls)	
909	m undefined (chlorophylls)	
738	ms ring br. mode (aromatics)	

at preliminary observation, the spectral fingerprint of leaves was not severely influenced by the presence of virus infection, but only minimal changes were registered. The entire fingerprint

regions of the mean spectra for the three classes of plants and the four sampling times are shown in supporting information (**Supplementary Figure S1**) for a better comparison. For the



majority of bands, frequency mismatches between healthy and infected plants can be noticed since the third sampling time.

Previous works have determined the assignment of Raman bands obtained from leaf samples which are mostly due to carotenoids, being among the most Raman active classes of compounds present in such tissue (Yeturu et al., 2016). In particular, the most evident peak observed at $1,526\text{ cm}^{-1}$ is assigned to the stretching of the $\text{C}=\text{C}$ double bond in the conjugated chain of carotenoids (Adar, 2017), while the shoulder at $1,550\text{ cm}^{-1}$ is due to chlorophylls. Focusing our attention on this particular band and comparing the mean spectra of healthy and infected plants monitored during the entire vegetative season, a reduced carotenoid concentration in leaves of GFLV-infected plants was noticed since the second measurement (T2). On the contrary, no such tendency occurred in healthy plants or in GRSPaV-infected plants (Figure 3). In addition, a frequency change that exceeds the resolution limit of 5 cm^{-1} , was registered in infected tissues for the carotenoid peak, as well as for other bands in the Raman fingerprint region, since the second sampling (Figure 3). In particular, the $\text{C}=\text{C}$ stretching shifted to a slightly lower frequency in infected plants (from $1,526$ to $1,518\text{ cm}^{-1}$ for GFLV and from $1,526$ to $1,520\text{ cm}^{-1}$ for GRSPaV, at T3), possibly resulting from a modification of the carotenoids profile occurring in these plants (Figure 3). A previous study by Withnall et al. (2003) showed a linear inverse dependency of the frequency location of the band of $\text{C}=\text{C}$ double bonds and the length of the conjugated chain of carotenoids. However, due to the intrinsic limits of Raman measurements on complex biological matrices, the available data do not allow to specifically address the accumulation of carotenoid

molecules of a specific length, an issue which should be investigated with more selective techniques.

Overall, the modification of the Raman peaks, especially those associated to carotenoids, provides an indication that the infection by these two viruses leads to a different metabolic response of infected plants. In particular, a reduced concentration of carotenoids in grapevine suggests a functional link to either a modulation of transcripts involved in carotenoid metabolism or to their degradation and fragmentation or conversion to apocarotenoids, i.e., signaling molecules produced in response to stress. A decrease in carotenoid concentration has been frequently reported when analyzing by Raman spectroscopy plants infected by pathogens (Dou et al., 2021; Farber et al., 2021; Vallejo-Pérez et al., 2021) or subjected to abiotic stresses (Altangerel et al., 2017; Sng et al., 2020), confirming the role of this class of molecules in plant stress responses.

Beside the visual comparison of the average spectra collected from healthy and infected plants over time, a more complete investigation regarding the changes in the Raman profiles was conducted, with a multivariate unsupervised visualization method. This procedure allows to consider the whole spectral information and to test the significance of spectral differences within the groups included in the experimental design. For this, the entire dataset was processed with ASCA using the four plants present in each group (factor “Infection,” levels “healthy,” “GRSPaV,” “GFLV”), considering one leaf per plant, three spectra per leaf, four sampling sessions over four measurements, at monthly intervals (factor “Time,” levels “T1,” “T2,” “T3,” and “T4”). This process is expected to model the effect of each of the factors included in the experimental design and to evaluate

the significance of each effect. At the same time, a PCA model was calculated for each design factor, to help visualizing the results. Then, the significance of each factor was tested by permutation tests within the levels of the factors, providing a $p < 0.5$ value for significant factors. Unfortunately, the ASCA model for the combined dataset showed that no significant spectral variation could be modeled over time to distinguish the three levels of the factor “infection” (Table 2). On the contrary, the factors “time” and “plant specimen” resulted significantly different.

TABLE 2 | Results of ANOVA simultaneous component analysis (ASCA) elaboration on the complete data set of samples.

Factor	No. of principals components	Effect	<i>p</i>
Time	3	39.76	0.001
Plant specimen	11	13.57	0.001
Virus	2	2.77	1.00
Mean	-	0.00	-
Residuals	-	52.28	-

Results were obtained from 144 spectra collected from 12 plants, over 4 months.

These results urged us to consider separately the four sampling sessions and to determine the discrimination ability of RS to detect molecular changes induced in leaves by virus infection, on a temporal basis. For this, in order to obtain data grouping in accordance with the infection, at each sampling time, a PCA was performed, i.e., a common visualization method used to reduce the number of variables and to plot multivariate data as a scatter plot accounting for unsupervised agglomeration of samples due to common features. The PCA score plots obtained are shown in Figure 4, colored according to the infection condition at each sampling time.

In order to elucidate the spectral features driving this unsupervised clustering of spectra, the loadings of the different PCA models were compared. In details, at T3 and T4, the loadings of the first three PCs are very similar (Supplementary Figure S2). Noteworthy, the most important features allowing to separate the different spectra are PC1, which refers to the overall spectral intensity, mainly regarding carotenoid peaks, and PC2, accounting to the band shifts observed at $1,527\text{ cm}^{-1}$ (carotenoids) and 780 cm^{-1} (aromatics, probably mainly phenolics, such as anthocyanin). This analysis confirms that the differences found in the mean spectra are common to all spectra of the same group, albeit with different

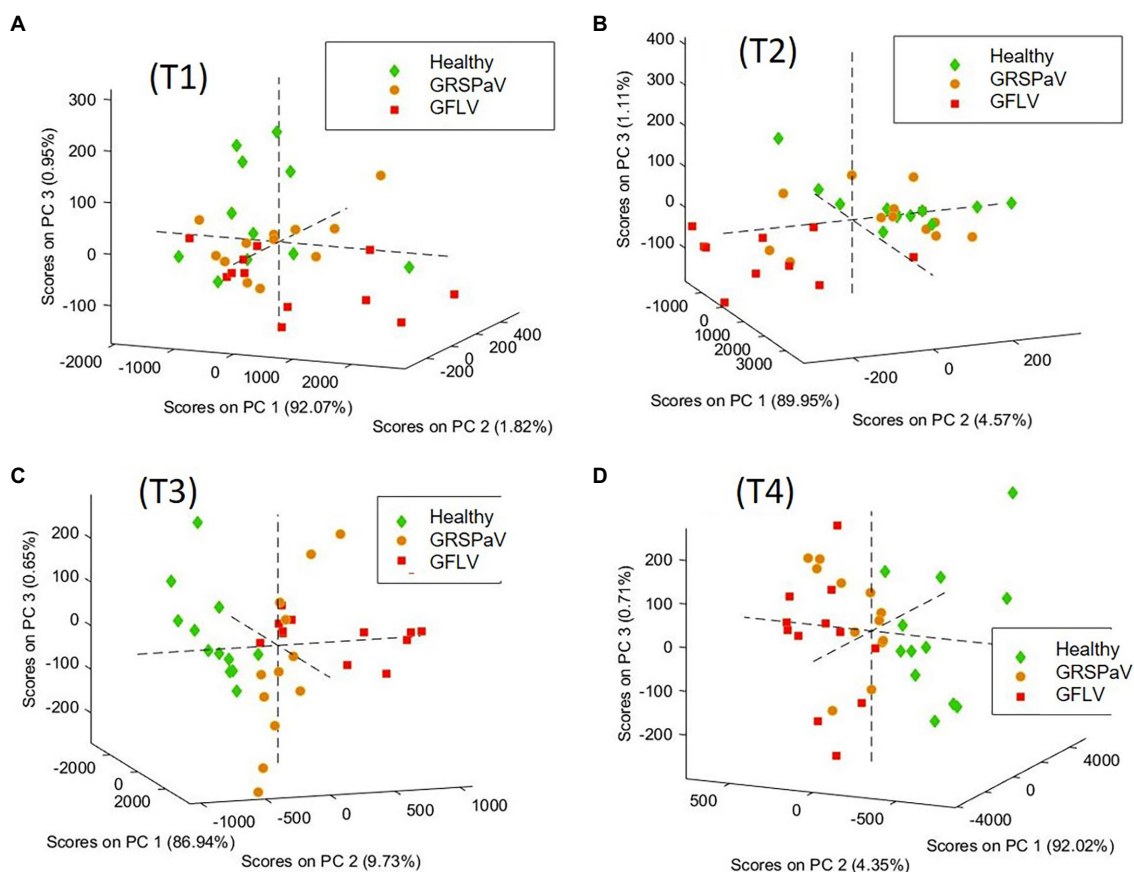


FIGURE 4 | PCA score plots of the spectra of healthy and GRSPaV- or GFLV-infected grapevine cv. Chardonnay plants, calculated at (A) T1, (B) T2, (C) T3, (D) T4, at monthly intervals. 3D graph rotation is set to optimize result visualization.

magnitude. Moreover, this procedure showed that at T3 and T4 it is possible to distinguish healthy plants from those infected by the two different viruses. On the contrary, at T1 and T2, no score grouping could be obtained in the PC1, 2, 3 scores plot, indicating a poor differentiation of spectral profiles of healthy and infected plants. The variance captured at T1 and T2 by the first three PCs, which is mainly related to the fingerprint region between 500 and 1,600 cm^{-1} does not drive clear grouping of scores related to the infection conditions of the samples (Supplementary Figures S2A,B).

Supervised Data Analysis

Considering the absence of visible symptoms induced on grapevine by the two viruses here considered, a major goal of this work was to determine if RS coupled to multivariate statistical methods could discriminate healthy plants from infected individuals. Therefore, PLS-DA was used as a classification method to evaluate the possibility to discriminate healthy from infected plants based on their Raman spectra. Due to the reduced number of plants included in the experimental design which could not be separated into a calibration and a validation set, the Leave-one-group-out cross-validation (CV) method was used; noteworthy, to test the validity of the model with a method more similar to external set testing, full leave-one-out CV was avoided, and the exclusion groups of CV corresponding to “one-plant-out” at a time were set. Therefore, to test the recognition ability of RS, different class vectors were considered, as follows: (1) three class models (healthy, GRSPaV, GFLV) to simultaneously distinguish healthy plants from plants infected by each of the viruses, (2) two class models (healthy vs. infected plants), considering all infected plants together, and (3) two class models (healthy vs. GRSPaV-infected plants or healthy vs. GFLV-infected plants), separately considering the two different viruses. The classification results of such a cross-validation test are reported in Table 3.

Although in the first two measurements (T1 and T2) it was not possible to discriminate the presence of either GRSPaV or GFLV in the plants with a high level of accuracy in CV, infected plants could be distinguished with a classification error (CE) < 20% starting from the T3 measurement. In particular, infected plants (considering GRSPaV and GFLV together) could be distinguished from healthy individuals with CE values of 8% at T3 and T4, a result particularly relevant considering the complete absence of symptoms. Noteworthy, CE 0% were obtained for GFLV-infected tissue in the last two sampling times, probably resulting

from changes in the metabolism of carotenoids occurring in such plants, justifying further investigations, as below described.

The score plots of the two best models in the area defined by the two first latent variables (LVs) of the PLS-DA model and the Receiver Operating Characteristic (ROC) curves are shown in Figure 5, providing a clear visual indication of the model sensitivity and specificity. The two relevant LVs of these models are shown in Supplementary Figure S3, while the model images for the three classes (H,R,G) and for (H,R) at T3 and T4 are reported in Supplementary Figure S4.

Interestingly, the discriminative ability of RS was independent from the amount of virus determined in the leaves and was higher toward the end of the vegetative season (Table 3; Figure 1). This is particularly interesting in the case of GFLV for which the best classification rates in the PLS-DA model were calculated at the T3-T4 measurements against the backdrop of a sharp viral load reduction in the same period. Nonetheless, this result can be assessed in the light of a “load metabolic effect” induced by virus infection in this crop along the seasonal progression (Gambino et al., 2012; Chitarra et al., 2018; Martin et al., 2021). Moreover, the results here reported support previous observations of a higher metabolic impact on grapevine plants exerted by GFLV compared to GRSPaV, corroborating the concept of a co-evolution of GRSPaV with this crop (Gambino et al., 2012) possibly resulting from the long-lasting presence of a hard to eradicate pathogen in grapevine.

Validations via Chemical Analytical Extractions

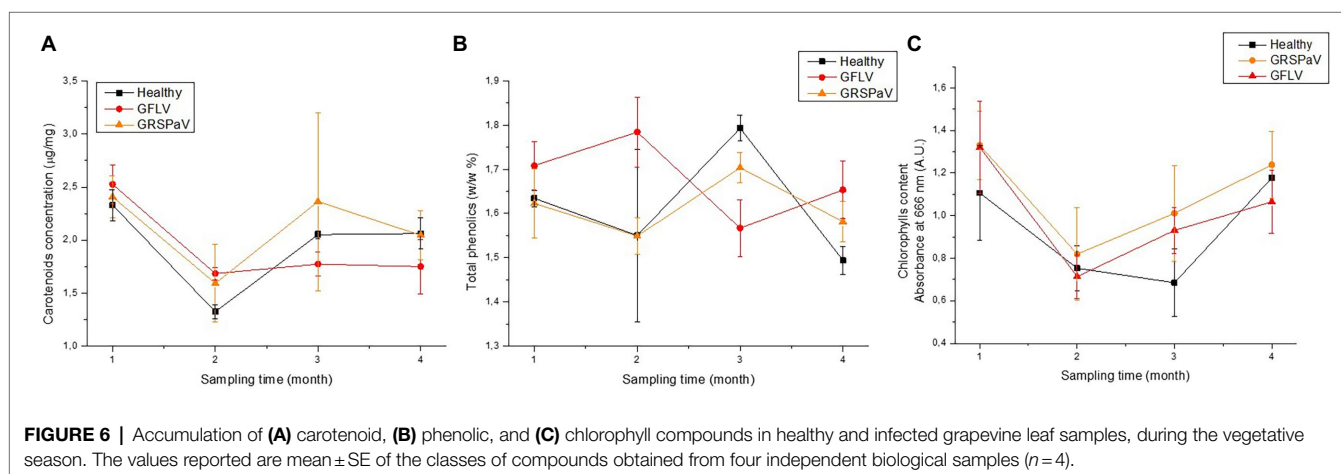
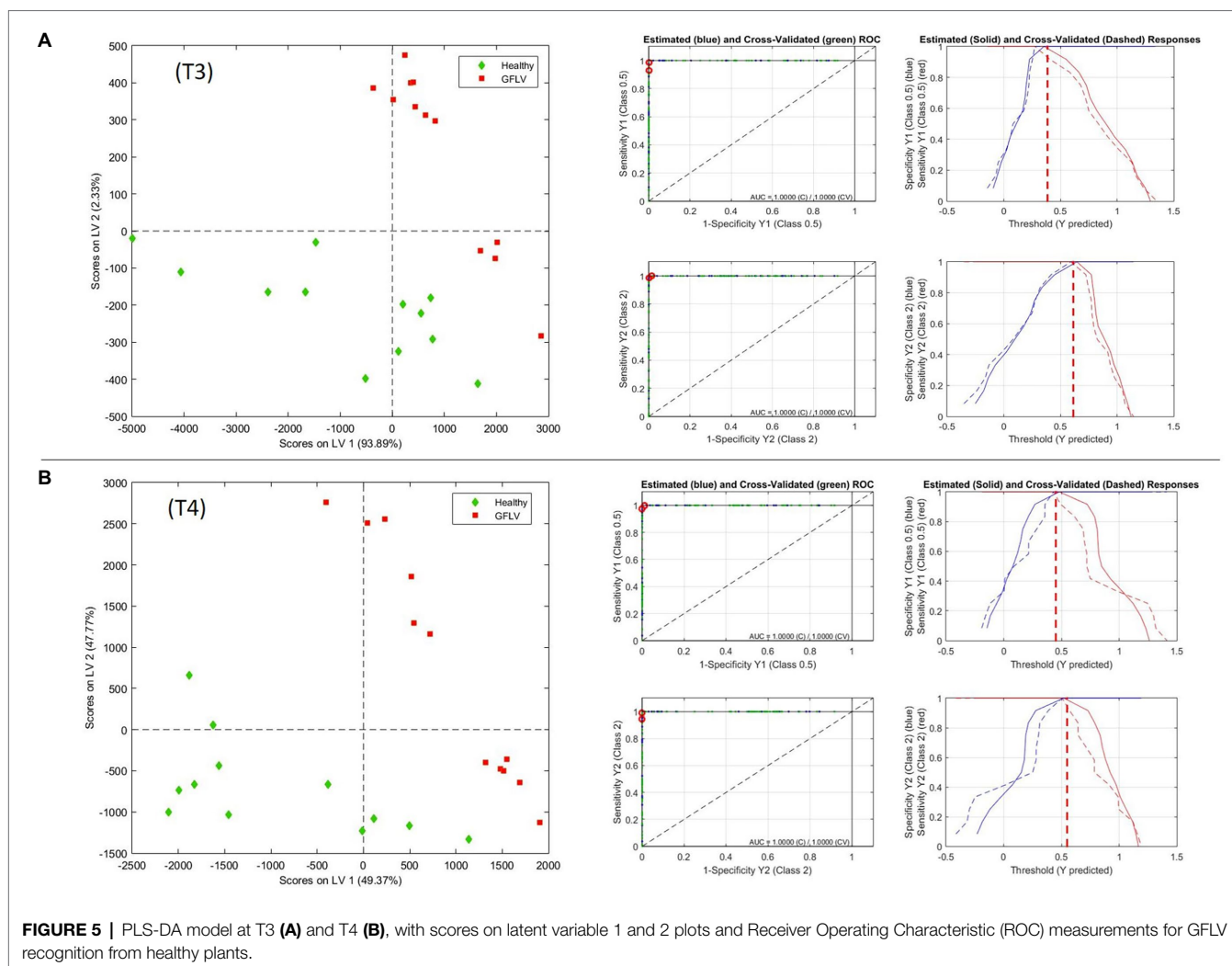
To confirm the results of the RS analyses, the concentration of the three main classes of pigments, i.e., carotenoids, total phenolics, and chlorophylls, were measured by spectrophotometric assays in the same tissues used for RS. As it can be observed in Figure 6, the peculiar trends measured with Raman spectroscopy concerning the concentration of carotenoids were confirmed. In particular, a decrease in carotenoid concentration can be noticed from T1 to T4 in GFLV-infected plants (Figure 6A), in accordance with the RS results (Figure 3). Regarding the other two classes of compounds investigated, i.e., chlorophylls and polyphenols, no significant trends are revealed, in line with the observation that their Raman signals were not relevant for the discrimination between healthy and infected plants. However, interestingly, significant differences in the content of total phenolics compounds between healthy and GFLV-infected plants were recorded at T3 and T4, probably supporting the higher discrimination accuracy for infected plants.

Regarding chlorophylls, a similar trend was detected over time in all groups of plants, independently on the presence of virus infection. Based on these results, the accumulation of chlorophylls does not seem to be influenced by the infection process, rather by the environmental conditions, while the content of carotenoid and phenolic compounds is altered in infected plants. This observation is in line with recent studies highlighting the relevance of secondary metabolites as players in plant defense responses, thus underlying the importance of characterizing the metabolic profiles associated to disease susceptibility traits in grapevine as a promising approach to identify trait-related biomarkers (Maia et al., 2020).

TABLE 3 | PLS-DA classification to distinguish grapevine plants infected by either GFLV or GRSPaV from healthy individuals, over the vegetative season.

Model		T1 (%)	T2 (%)	T3 (%)	T4 (%)
3 Classes	(H,R,G)	50	52	14	19
2 Classes	(H,I), I=R+G	19	36	8	8
2 Classes	(H,R)	25	31	8	12
2 Classes	(H,G)	13	17	0	0

Results are expressed as classification error (CE) and cross validation (CV). H, healthy; R, GRSPaV; G, GFLV; and CE, classification error.



Transcriptional Analysis of Genes Involved in the Carotenoid Pathway

Since the most interesting information related to virus infection determined by RS is linked to the carotenoid content, a

transcriptional study was conducted by RT-qPCR to measure the expression level of a set of target genes involved in carotenoid metabolism (Leng et al., 2017). Carotenoids are mainly synthesized from isopentenyl diphosphate (IPP) and dimethylallyl diphosphate

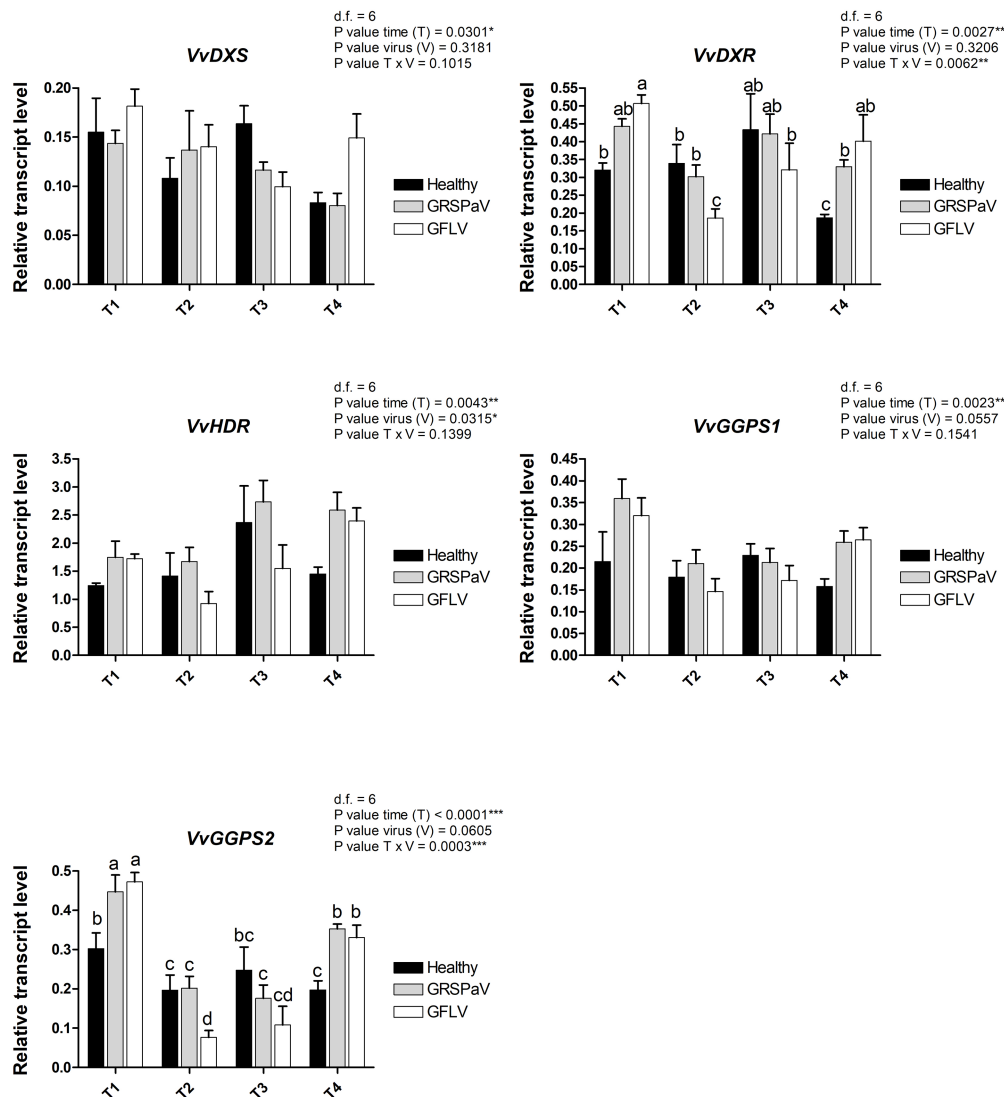


FIGURE 7 | Relative expression levels of *VvDXS* (VIT_05s0020g02130), *VvDXR* (VIT_17s0000g08390), *VvHDR* (VIT_03s0063g02030), *VvGGPS1* (VIT_04s0023g01210), and *VvGGPS2* (VIT_18s0001g12000), measured by RT-qPCR. Samples were collected in four sampling points along the season (May_T1, June_T2, July_T3, and August_T4). RT-qPCR signals were normalized to *VvAct* and *VvUbi* transcripts. Data are presented as the mean \pm SE ($n=4$). Significance of sampling time, virus, and time \times virus ($T \times V$) interaction was assessed by Tukey's HSD test for $p \leq 0.05$ (*), $p \leq 0.01$ (**), $p \leq 0.001$ (***) and the corresponding results are given above each graph in the figure panel. Lower case letters above bars are reported when the $T \times V$ interaction are statistically significant as attested by Tukey's HSD.

(DMAPP) produced through the monoterpene biosynthetic pathway (MEP). In particular, we tested the first two genes of the biosynthetic MEP route, 1-deoxy-D-xylulose-5-phosphate synthase (*VvDXS*) and 1-deoxy-D-xylulose-5-phosphate reductoisomerase (*VvDXR*), and one of the last genes, 1-hydroxy-2-methyl-2-(E)-butenyl-4-diphosphate reductase (*VvHDR*). For these genes, a slight transcript modulation occurred in both healthy and virus-infected plants. While the sampling time (T) was significant for all the three genes, the effect of virus (V) was significant only in the case of *VvDXR*, whose expression increased at T4 in GRSPaV- and GFLV-infected plants. The interaction between virus and time ($V \times T$) was significant only for *VvDXR*, showing a decrease in

GFLV-infected plants at T2, followed by an increase at T4 in both virus-infected samples (Figure 7).

Two isoforms of geranyl pyrophosphate synthase (*VvGPPS*), a gene operating along the MEP pathway, responsible for the production of geranyl pyrophosphate acting as substrate of monoterpenes synthases in the late carotenoid pathway, resulted strongly transcriptionally regulated along with time progression (T), but not by the presence of virus infection (V). In addition, considering the $V \times T$ interaction, a significant downregulation of *VvGPPS2* was recorded in particular in GFLV-infected plants at T2 (Figure 7), mirroring the carotenoid reduction observed by Raman analysis (Figure 3).

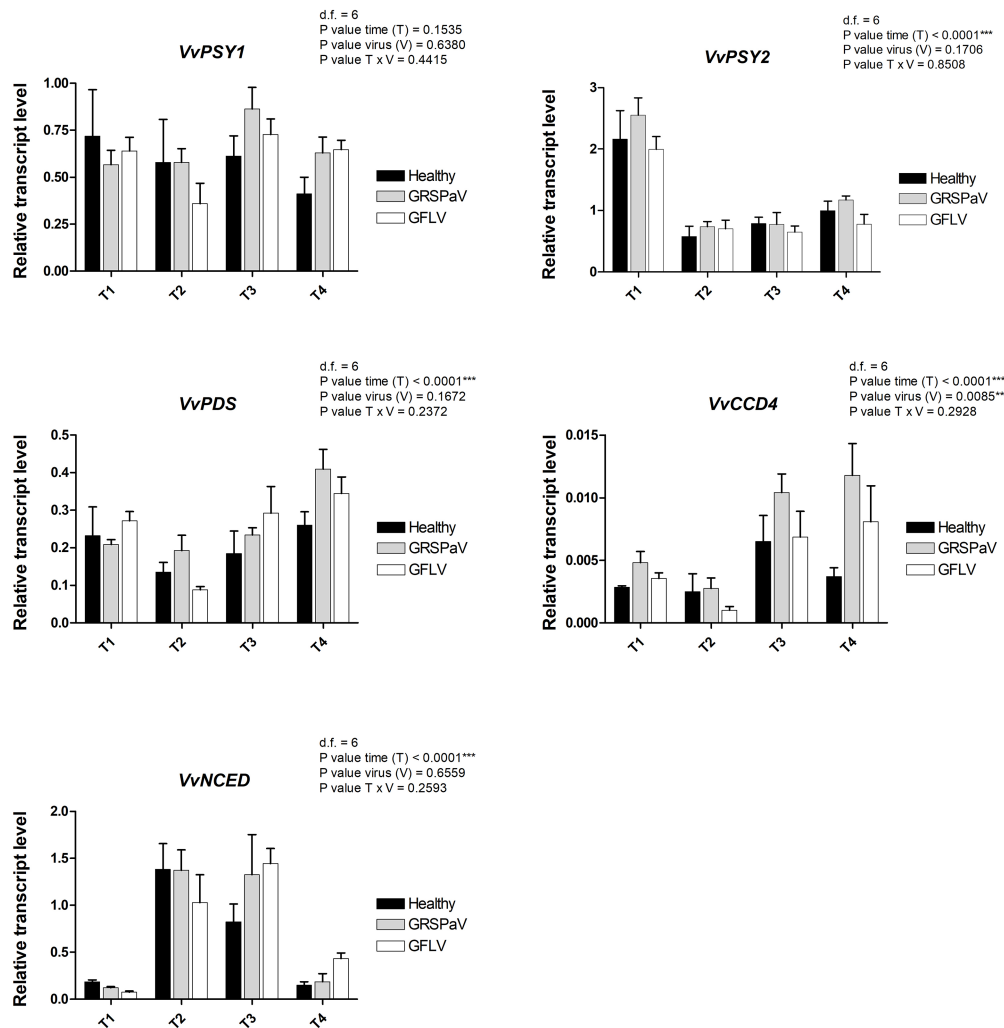


FIGURE 8 | Relative expression levels of *VvPSY1* (MIT_04s0079g00680), *VvPSY2* (MIT_12s0028g00960), *VvPDS* (MIT_09s0002g00100), *VvCCD4* (MIT_02s0087g00930), and *VvNCED* (MIT_19s0093g00550), measured by RT-qPCR. Samples were collected in four sampling points along the season (May_T1, June_T2, July_T3, and August_T4). RT-qPCR signals were normalized to *VvAct* and *VvUBI* transcripts. Data are presented as the mean \pm SE ($n=4$). Significance of sampling time, virus, and time \times virus (T \times V) interaction was assessed by Tukey's HSD test for $p \leq 0.01$ (**), $p \leq 0.001$ (***) and the corresponding results are given above each graph in the figure panel.

Of the two genes encoding the phytoene synthase (*VvPSY*), considered as a bottleneck reaction in the carotenoid pathway, *VvPSY1* did not show any significant modulation regarding the effects of virus infection or time progression, while *VvPSY2* showed a strong T effect (**Figure 8**), indicating its prominent role in the carotenoid reduction occurring after the T1 sampling in the whole set of samples (**Figure 3**). The phytoene produced by *VvPSY* is then desaturated through the action of phytoene desaturase (*VvPDS*) which showed a modulation affected only by T, in particular at T4.

Among the genes involved in carotenoid catabolism, we analyzed a carotenoid cleavage dioxygenase (*VvCCD4*) and a 9-cis-epoxycarotenoid dioxygenase (*VvNCED*). *VvCCD4* is linked to the production of volatile compounds and strigolactones and showed significant V and T effects, with a negative correlation with the accumulation of carotenoids

at T3 and T4. On the other side, *VvNCED*, a key enzyme in the biosynthesis of abscisic acid (ABA), showed a significant T effect with negative correlations with the carotenoids at T2 and T3, and an interesting upregulation in GFLV-infected plants at T4 (**Figure 8**).

Collectively, positive correlations between the reduced accumulation of carotenoids, particularly, in GFLV-infected plants, and the downregulation of transcripts involved in their biosynthesis (i.e., *VvGGPS2* and *VvPSY2*) were detected, accompanied by an upregulation of genes responsible for carotenoid catabolism, i.e., *VvCCD4* and *VvNCED*. This suggests that virus infection, particularly in the case of GFLV, can accelerate the natural reduction of photosynthetic processes mediated by carotenoids occurring across the vegetative season. Moreover, it indicates that RS can sense a metabolic stress response leading to the accumulation

of ABA and strigolactones (Milborrow and Lee, 1998; Auldridge et al., 2006; Havaux, 2013), originating from carotenoid precursors.

CONCLUSION

A growing number of evidences are showing that RS techniques represent a non-invasive, non-destructive analytical approach to monitor the sanitary status of plants (Payne and Kourouski, 2021). Here, we applied RS to grapevine, one of the most economically important crops worldwide, affected by relatively higher number of pathogens compared to other fruit trees and subjected to strict certification programs to guarantee its phytosanitary status. The PLS-DA model here obtained from the RS data demonstrated the suitability of the RS approach to discriminate healthy from infected plants, even in the absence of macroscopic symptoms, with up to 92% accuracy for GRSPaV and 100% accuracy for GFLV, the latter taken as a representative virus that should be absent in certified virus-free plant materials. The Raman spectra allowed to identify the major metabolic changes occurring in this crop in response to virus infection, paving the way to adopt a RS-based approach as a complementary procedure to detect early stages of viral infection not only in vineyards but also in the nurseries. Following proper verification of the congruence of the results, direct evaluation of plants grown in vineyards will be feasible using high-throughput portable Raman spectrometers, as reported by other groups (Farber and Kourouski, 2018; Krimmer et al., 2019; Sanchez et al., 2019; Gupta et al., 2020).

REFERENCES

- Adar, F. (2017). Carotenoids—their resonance Raman spectra and how they can be helpful in characterizing a number of biological systems. *Spectroscopy* 32, 12–20.
- Alrifai, O., Hao, X., Liu, R., Lu, Z., Marcone, M. F., and Tsao, R. (2021). LED-induced carotenoid synthesis and related gene expression in brassica microgreens. *J. Agric. Food Chem.* 69, 4674–4685. doi: 10.1021/acs.jafc.1c00200
- Altangerel, N., Ariunbold, G. O., Gorman, C., Alkahtani, M. H., Borrego, E. J., Bohlmeier, D., et al. (2017). *In vivo* diagnostics of early abiotic plant stress response via Raman spectroscopy. *Proc. Natl. Acad. Sci. U. S. A.* 114, 3393–3396. doi: 10.1073/pnas.1701328114
- Auldridge, M. E., McCarty, D. R., and Klee, H. J. (2006). Plant carotenoid cleavage oxygenases and their apocarotenoid products. *Curr. Opin. Plant Biol.* 9, 315–321. doi: 10.1016/j.pbi.2006.03.005
- Boldt, N. J., Donohoe, R. J., Birge, R. R., and Bocian, D. F. (1987). Chlorophyll model compounds: effects of low symmetry on the resonance Raman spectra and normal mode descriptions of nickel(II) dihydroporphyrins. *J. Am. Chem. Soc.* 109, 2284–2298. doi: 10.1021/ja00242a009
- Chitarra, W., Cuozzo, D., Ferrandino, A., Secchi, F., Palmano, S., Perrone, I., et al. (2018). Dissecting interplays between *Vitis vinifera* L. and grapevine virus B (GVB) under field conditions. *Mol. Plant Pathol.* 19, 2651–2666. doi: 10.1111/mpp.12735
- Dou, T., Sanchez, L., Irigoyen, S., Goff, N., Niraula, P., Mandadi, K., et al. (2021). Biochemical origin of raman-based diagnostics of huanglongbing in grapefruit trees. *Front. Plant Sci.* 12:680991. doi: 10.3389/fpls.2021.680991
- Egging, V., Nguyen, J., and Kourouski, D. (2018). Detection and identification of fungal infections in intact wheat and *Sorghum* grain using a hand-held Raman spectrometer. *Anal. Chem.* 90, 8616–8621. doi: 10.1021/acs.analchem.8b01863
- Eravuchira, P. J., El-Abassy, R. M., Deshpande, S., Matei, M. F., Mishra, S., Tandon, P., et al. (2012). Raman spectroscopic characterization of different regioisomers of monoacyl and diacyl chlorogenic acid. *Vib. Spectrosc.* 61, 10–16. doi: 10.1016/j.vibspec.2012.02.009
- Fang, Y., and Ramasamy, R. P. (2015). Current and prospective methods for plant disease detection. *Biosensors* 5, 537–561. doi: 10.3390/bios5030537
- FAOSTAT (2020). Statistics Division, Food and Agriculture Organization of the United Nations. Available at: <https://www.fao.org/faostat/en/#data/QCL> (Accessed 23 March 2022).
- Farber, C., Bennett, J. S., Dou, T., Abugalyon, Y., Humpal, D., Sanchez, L., et al. (2021). Raman-based diagnostics of stalk rot disease of maize caused by *Colletotrichum graminicola*. *Front. Plant Sci.* 12:722898. doi: 10.3389/fpls.2021.722898
- Farber, C., and Kourouski, D. (2018). Detection and identification of plant pathogens on maize kernels with a hand-held Raman spectrometer. *Anal. Chem.* 90, 3009–3012. doi: 10.1021/acs.analchem.8b00222
- Farber, C., Mahnke, M., Sanchez, L., and Kourouski, D. (2019a). Advanced spectroscopic techniques for plant disease diagnostics. A review. *Trends Analyt. Chem.* 118, 43–49. doi: 10.1016/j.trac.2019.05.022
- Farber, C., Shires, M., Ong, K., Byrne, D., and Kourouski, D. (2019b). Raman spectroscopy as an early detection tool for rose rosette infection. *Planta* 250, 1247–1254. doi: 10.1007/s00425-019-03216-0

DATA AVAILABILITY STATEMENT

The raw data supporting the conclusions of this article will be made available by the authors, without undue reservation.

AUTHOR CONTRIBUTIONS

LM, CDE, SM, FN, and GB performed the experiments. LM, EN, GB, GG, AMG, and FN analyzed the data. LM, GG, and EN wrote the manuscript. LM, GG, AMR, and EN conceived the study and participated in its design. All authors contributed to the article and approved the submitted version.

FUNDING

The present work has been supported by the Fondazione Cassa di Risparmio di Torino, Project VirADEP, ref. no. 2020.0598.

ACKNOWLEDGMENTS

The authors wish to thank Daniele Marian for RNA extraction of leaf samples.

SUPPLEMENTARY MATERIAL

The Supplementary Material for this article can be found online at: <https://www.frontiersin.org/articles/10.3389/fpls.2022.917226/full#supplementary-material>

- Fuchs, M. (2020). Grapevine viruses: a multitude of diverse species with simple but overall poorly adopted management solutions in the vineyard. *J. Plant Pathol.* 102, 643–653. doi: 10.1007/s42161-020-00579-2
- Gambino, G., Cuoizzo, D., Fasoli, M., Pagliarini, C., Vitali, M., Boccacci, P., et al. (2012). Co-evolution between grapevine rupestris stem pitting associated virus and *Vitis vinifera* L. leads to decreased defence responses and increased transcription of genes related to photosynthesis. *J. Exp. Bot.* 63, 5919–5933. doi: 10.1093/jxb/ers244
- Gambino, G., Perrone, I., and Gribaudo, I. (2008). A rapid and effective method for RNA extraction from different tissues of grapevine and other woody plants. *Phytoch. Anal.* 19, 520–525. doi: 10.1002/pca.1078
- Gilardi, G., Chitarra, W., Moine, A., Mezzalama, M., Boccacci, P., Pugliese, M., et al. (2020). Biological and molecular interplay between two viruses and powdery and downy mildews in two grapevine cultivars. *Hortic. Res.* 7:188. doi: 10.1038/s41438-020-00413-x
- Gill, D., Kilponen, R. G., and Rimai, L. (1970). Resonance Raman scattering of laser radiation by vibrational modes of carotenoid pigment molecules in intact plant tissues. *Nature* 227, 743–744. doi: 10.1038/227743a0
- Golino, D. A., Fuchs, M., Al Rwahnih, M., Farrar, K., Schmidt, A., and Martelli, G. P. (2017). “Regulatory aspects of grape viruses and virus diseases: certification, quarantine, and harmonization.” in *Grapevine Viruses: Molecular Biology, Diagnostics and Management*. eds. B. Meng, G. P. Martelli, D. A. Golino and M. Fuchs (Cham, Switzerland: Springer), 581–598.
- Gupta, S., Huang, C. H., Singh, G. P., Park, B. S., Chua, N.-H., and Ram, R. J. (2020). Portable Raman leaf-clip sensor for rapid detection of plant stress. *Sci. Rep.* 10:20206. doi: 10.1038/s41598-020-76485-5
- Havaux, M. (2013). Carotenoid oxidation products as stress signals in plants. *Plant J.* 79, 597–606. doi: 10.1111/tpj.12386
- Koyama, Y., Umemoto, Y., Akamatsu, A., Uehara, K., and Tanaka, M. (1986). Raman spectra of chlorophyll forms. *J. Mol. Struct.* 146, 273–287. doi: 10.1016/0022-2860(86)80299-X
- Krebelj, A. J., Čepin, U., Ravnkar, M., and Novak, M. P. (2015). Spatio-temporal distribution of grapevine fanleaf virus (GFLV) in grapevine. *Eur. J. Plant Pathol.* 142, 159–171. doi: 10.1007/s10658-015-0600-4
- Krebelj, A. J., Rupnik-Gigoj, M., Stele, M., Chersicola, M., Pompe-Novak, M., and Sivilotti, P. (2022). The physiological impact of GFLV virus infection on grapevine water status: first observations. *Plan. Theory* 11:161. doi: 10.3390/plants11020161
- Krimmer, M., Farber, C., and Kurouski, D. (2019). Rapid and noninvasive typing and assessment of nutrient content of maize kernels using a handheld Raman spectrometer. *ACS Omega* 4, 16330–16335. doi: 10.1021/acsomega.9b01661
- Leng, X., Wang, P., Wang, C., Zhu, X., Li, X., Li, H., et al. (2017). Genome-wide identification and characterization of genes involved in carotenoid metabolic in three stages of grapevine fruit development. *Sci. Rep.* 7:4216. doi: 10.1038/s41598-017-04004-0
- Lunden, S., Meng, B., Avery, J., and Qiu, W. (2009). Association of Grapevine fanleaf virus, tomato ringspot virus and grapevine rupestris stem pitting-associated virus with a grapevine vein-clearing complex on var. chardonnay. *Eur. J. Plant Pathol.* 126:135. doi: 10.1007/s10658-009-9527-y
- Maia, M., Ferreira, A. E. N., Nascimento, R., Monteiro, F., Traquete, F., Marques, A. P., et al. (2020). Integrating metabolomics and targeted gene expression to uncover potential biomarkers of fungal/oomycetes-associated disease susceptibility in grapevine. *Sci. Rep.* 10:15688. doi: 10.1038/s41598-020-72781-2
- Mandriale, L., Rotunno, S., Miozzi, L., Vaira, A. M., Giovannozzi, A. M., Rossi, A. M., et al. (2019). Nondestructive Raman spectroscopy as a tool for early detection and discrimination of the infection of tomato plants by two economically important viruses. *Anal. Chem.* 91, 9025–9031. doi: 10.1021/acs.analchem.9b01323
- Martelli, G. P. (2014). Directory of virus and virus-like diseases of the grapevine and their agents. *J. Plant Pathol.* 96, 1–136. doi: 10.4454/JPP.V96I1SUP
- Martelli, G. P. (2017). “An overview on grapevine viruses, viroids, and the diseases they cause,” in *Grapevine Viruses: Molecular Biology, Diagnostics and Management*. eds. B. Meng, G. P. Martelli, D. A. Golino and M. Fuchs (Cham, Switzerland: Springer), 31–46.
- Martelli, G. P. (2018). “Where grapevine virology is heading to,” in *Proc. 19th Congress of International Council for the Study of Viruses and Virus-like Diseases of the Grapevine* (Chile: University of Chile), 10–15.
- Martin, I. R., Vigne, E., Velt, A., Hily, J. M., Garcia, S., Baltenweck, R., et al. (2021). Severe stunting symptoms upon nepovirus infection are reminiscent of a chronic hypersensitive-like response in a perennial woody fruit crop. *Viruses* 13:2138. doi: 10.3390/v13112138
- Martinelli, F., Scalenghe, R., Davino, S., Panno, S., Scuderi, G., Ruisi, P., et al. (2015). Advanced methods of plant disease detection. A review. *Agron. Sustain. Dev.* 35, 1–25. doi: 10.1007/s13593-014-0246-1
- Meng, B., and Gonsalves, D. (2003). Rupestris stem pitting-associated virus of grapevines: genome structure, genetic diversity, detection, and phylogenetic relationship to other plant viruses. *Curr. Opin. Virol.* 3, 125–135.
- Meng, B., and Rowhani, A. (2017). “Grapevine rupestris stem pitting associated virus,” in *Grapevine Viruses: Molecular Biology, Diagnostics and Management*. eds. B. Meng, G. P. Martelli, D. A. Golino and M. Fuchs (Cham, Switzerland: Springer), 257–287.
- Milborrow, B. V., and Lee, H. S. (1998). Endogenous biosynthetic precursors of (+)-abscisic acid. VI. Carotenoids and ABA are formed by the ‘non-mevalonate’ triose-pyruvate pathway in chloroplasts. *Aust. J. Plant Physiol.* 25, 507–512.
- Pantaleo, V., Vitali, M., Boccacci, P., Miozzi, L., Cuoizzo, D., Chitarra, W., et al. (2016). Novel functional microRNAs from virus-free and infected *Vitis vinifera* plants under water stress. *Sci. Rep.* 6:20167. doi: 10.1038/srep20167
- Payne, W. Z., Dou, T., Cason, J. M., Simpson, C. E., McCutchen, B., Burrow, M. D., et al. (2022). A proof-of-principle study of non-invasive identification of peanut genotypes and nematode resistance using raman spectroscopy. *Front. Plant Sci.* 12:664243. doi: 10.3389/fpls.2021.664243
- Payne, W. Z., and Kurouski, D. (2021). Raman spectroscopy enables phenotyping and assessment of nutrition values of plants: a review. *Plant Methods* 17:78. doi: 10.1186/s13007-021-00781-y
- Sanchez, L., Ermolenkov, A., Tang, X. T., Tamborindeguy, C., and Kurouski, D. (2020). Non-invasive diagnostics of Liberibacter disease on tomatoes using a hand-held Raman spectrometer. *Planta* 251:64. doi: 10.1007/s00425-020-03359-5
- Sanchez, L., Pant, S., Xing, Z., Mandadi, K., and Kurouski, D. (2019). Rapid and noninvasive diagnostics of huanglongbing and nutrient deficits in citrus trees with a handheld Raman spectrometer. *Anal. Bioanal. Chem.* 411, 3125–3133. doi: 10.1007/s00216-019-01776-4
- Sanfaçon, H., Wellink, J., Le Gall, O., Karasev, A., van der Vlugt, R., and Wetzel, T. (2009). Secoviridae: a proposed family of plant viruses within the order Picornavirales that combines the families Sequiviridae and Comoviridae, the unassigned genera *Cheravirus* and *Sadwavirus*, and the proposed genus *Torradorvirus*. *Arch. Virol.* 154, 899–907. doi: 10.1007/s00705-009-0367-z
- Skoczowski, A., Oliwa, J., Stawoska, I., Rys, M., Kocurek, M., and Czyczyło-Mysza, I. (2022). The spectral compositions of light changes physiological response of chinese cabbage to elevated ozone concentration. *Int. J. Mol. Sci.* 23:2941. doi: 10.3390/ijms23062941
- Sng, B. J. R., Singh, G. P., Van Vu, K., Chua, N. H., Ram, R. J., and Jang, I. C. (2020). Rapid metabolite response in leaf blade and petiole as a marker for shade avoidance syndrome. *Plant Method* 16:144. doi: 10.1186/s13007-020-00688-0
- Tobar, M., Fiore, N., Pérez-Donoso, A. G., León, R., Rosales, I. M., and Gambardella, M. (2020). Divergent molecular and growth responses of young “cabernet sauvignon” (*Vitis vinifera*) plants to simple and mixed infections with grapevine rupestris stem pitting-associated virus. *Hortic. Res.* 7:2. doi: 10.1038/s41438-019-0224-5
- Vallejo-Pérez, M. R., Sosa-Herrera, J. A., Navarro-Contreras, H. R., Álvarez-Preciado, L. G., Rodríguez-Vázquez, Á. G., and Lara-Ávila, J. P. (2021). Raman spectroscopy and machine-learning for early detection of bacterial canker of tomato: the asymptomatic disease condition. *Plan. Theory* 10:1542. doi: 10.3390/plants10081542
- Withnall, R., Chowdhry, B. Z., Silver, J., Edwards, H. G. M., and de Oliveira, L. F. C. (2003). Raman spectra of carotenoids in natural products. *Spectrochim. Acta A Mol. Biomol. Spectrosc.* 59, 2207–2212. doi: 10.1016/S1386-1425(03)0064-7
- Yeturu, S., Vargas, J. P., Ciobotă, V., Guerrero, R., Garrido, P., and Ramos, L. A. (2016). Handheld Raman spectroscopy for the early detection of plant diseases: abutilon mosaic virus infecting *Abutilon* sp. *Anal. Methods* 8, 3450–3457. doi: 10.1039/C6AY00381H

- Yu, M. M., Schulze, H. G., Jetter, R., Blades, M. W., and Turner, R. F. (2007). Raman microspectroscopic analysis of triterpenoids found in plant cuticles. *Appl. Spectrosc.* 61, 32–37. doi: 10.1366/000370207779701352
- Zeng, J., Ping, W., Sanaeifar, A., Xu, X., Luo, W., Sha, J., et al. (2021). Quantitative visualization of photosynthetic pigments in tea leaves based on Raman spectroscopy and calibration model transfer. *Plant Methods* 17:4. doi: 10.1186/s13007-020-00704-3
- Zwanenburg, G., Hoefsloot, H. C., Westerhuis, J. A., Jansen, J. J., and Smilde, A. K. (2011). ANOVA–principal component analysis and ANOVA–simultaneous component analysis: a comparison. *J. Chemom.* 25, 561–567. doi: 10.1002/cem.1400

Conflict of Interest: The authors declare that the research was conducted in the absence of any commercial or financial relationships that could be construed as a potential conflict of interest.

Publisher's Note: All claims expressed in this article are solely those of the authors and do not necessarily represent those of their affiliated organizations, or those of the publisher, the editors and the reviewers. Any product that may be evaluated in this article, or claim that may be made by its manufacturer, is not guaranteed or endorsed by the publisher.

Copyright © 2022 Mandrile, D'Errico, Nuzzo, Barzan, Matić, Giovannozzi, Rossi, Gambino and Noris. This is an open-access article distributed under the terms of the Creative Commons Attribution License (CC BY). The use, distribution or reproduction in other forums is permitted, provided the original author(s) and the copyright owner(s) are credited and that the original publication in this journal is cited, in accordance with accepted academic practice. No use, distribution or reproduction is permitted which does not comply with these terms.



Novel Vegetation Indices to Identify Broccoli Plants Infected With *Xanthomonas campestris* pv. *campestris*

Mónica Pineda^{1*}, María Luisa Pérez-Bueno^{1,2*} and Matilde Barón¹

¹ Department of Biochemistry and Molecular and Cell Biology of Plants, Estación Experimental del Zaidín, Spanish National Research Council (CSIC), Granada, Spain, ² Department of Plant Physiology, Facultad de Farmacia, University of Granada, Granada, Spain

OPEN ACCESS

Edited by:

Nam-Hai Chua,
Temasek Life Sciences
Laboratory, Singapore

Reviewed by:

Mohsen Yoosefzadeh Najafabadi,
University of Guelph, Canada

Luigi De Bellis,
University of Salento, Italy

*Correspondence:

Mónica Pineda
monica.pineda@eez.csic.es
María Luisa Pérez-Bueno
marisa.perez@ugr.es

Specialty section:

This article was submitted to
Technical Advances in Plant Science,
a section of the journal
Frontiers in Plant Science

Received: 06 October 2021

Accepted: 23 May 2022

Published: 23 June 2022

Citation:

Pineda M, Pérez-Bueno ML and
Barón M (2022) Novel Vegetation
Indices to Identify Broccoli Plants
Infected With *Xanthomonas*
campestris pv. *campestris*.
Front. Plant Sci. 13:790268.
doi: 10.3389/fpls.2022.790268

A rapid diagnosis of black rot in brassicas, a devastating disease caused by *Xanthomonas campestris* pv. *campestris* (Xcc), would be desirable to avoid significant crop yield losses. The main aim of this work was to develop a method of detection of Xcc infection on broccoli leaves. Such method is based on the use of imaging sensors that capture information about the optical properties of leaves and provide data that can be implemented on machine learning algorithms capable of learning patterns. Based on this knowledge, the algorithms are able to classify plants into categories (healthy and infected). To ensure the robustness of the detection method upon future alterations in climate conditions, the response of broccoli plants to Xcc infection was analyzed under a range of growing environments, taking current climate conditions as reference. Two projections for years 2081–2100 were selected, according to the Assessment Report of Intergovernmental Panel on Climate Change. Thus, the response of broccoli plants to Xcc infection and climate conditions has been monitored using leaf temperature and five conventional vegetation indices (VIs) derived from hyperspectral reflectance. In addition, three novel VIs, named diseased broccoli indices (DBI₁-DBI₃), were defined based on the spectral reflectance signature of broccoli leaves upon Xcc infection. Finally, the nine parameters were implemented on several classifying algorithms. The detection method offering the best performance of classification was a multilayer perceptron-based artificial neural network. This model identified infected plants with accuracies of 88.1, 76.9, and 83.3%, depending on the growing conditions. In this model, the three VIs described in this work proved to be very informative parameters for the disease detection. To our best knowledge, this is the first time that future climate conditions have been taken into account to develop a robust detection model using classifying algorithms.

Keywords: biotic stress, climate change, hyperspectral reflectance imaging, machine learning, thermography

INTRODUCTION

The cultivation of broccoli (*Brassica oleracea* var. *italica*) has become increasingly attractive and profitable. It is highly regarded for its nutritional value and also its antioxidant and anticancer properties (Owis, 2015). In Spain, the production of broccoli has increased exponentially in the last decades, and it is expected to continue rising in future. In 2018, broccoli crop yields reached up to

561,000 tons in Spain, and most of them were exported to European countries (latest available data reported by Ministerio de Agricultura, Pesca y Alimentación, www.mapa.gob.es).

Pests and plant diseases are a great challenge in modern agriculture and the main cause of production and economic losses in agriculture worldwide (Savary et al., 2012). Current practices and social activities, such as intensified monoculture in large areas, the use of genetically uniform plant varieties, and international trading of agricultural commodities, contribute largely to the widespread of plant disease epidemics and rapid pathogen evolution (Zhan et al., 2015). Like other Brassica crops, broccoli plants are susceptible to infection by fungi (*Alternaria* leaf spot, anthracnose, blackleg, or mildews), some viruses (virus mosaic), and bacteria (black rot, soft rots, bacterial leaf spots). Among the bacterial pathogens, *Xanthomonas campestris* is one of the most important in brassicas (Mansfield et al., 2012; Ekman et al., 2014; Dep. Primary Industries and Regional Development, Government Western Australia 2018, www.agric.wa.gov.au/broccoli/diseases-vegetable-brassicas).

The most notable pathovar of *X. campestris* is *campestris* (Xcc), which is the causal agent of black rot of crucifers and affects all cultivated brassicas. Indeed, and according to the report elaborated by EIP-AGRI Focus Group for the European Commission, Xcc is a threat to the production of broccoli, cauliflower, and cabbage throughout Europe (2016, Integrated Pest Management for Brassica, <https://ec.europa.eu/eip/agriculture/en/publications/eip-agri-focus-group-ipm-brassica-final-report>). Moreover, Xcc can be subdivided into nine races on the basis of the responses they induce on different cultivars. Among the nine races described for Xcc, races 1 and 4 are considered the most virulent and spread worldwide (Fargier and Manceau, 2007; Tortosa et al., 2018).

Precision agriculture demands the development of imaging sensor-based methods of detection and diagnosis of plant stress, including diseases. Several optical sensors are currently implemented to monitor crop fields (Aasen et al., 2019; Gerhards et al., 2019; Maes and Steppe, 2019; Pérez-Bueno et al., 2019a; Kashyap and Kumar, 2021; Pineda et al., 2021). Their applicability at lab scale and in high-throughput platforms by proximal sensing, and in the field by remote sensing, makes them particularly useful. However, the data provided by imaging sensors are large and complex and, consequently, difficult to interpret. Hence, improving our ability to extract useful information from these vast datasets requires the use of machine learning algorithms (Sperschneider, 2020). Machine learning is a subset of artificial intelligence (AI), consisting of algorithms that are able to learn patterns from a database of known samples and, based on those patterns, identify or categorize new samples. In agriculture, these algorithms can assist in the monitoring and decision-making processes of crop management (Chlingaryan et al., 2018; Golhani et al., 2018; Liakos et al., 2018; Gao et al., 2020). Thus, the implementation of imaging sensors and AI is a pivotal tool for crop management based on digital agriculture (Talaviya et al., 2020; Jung et al., 2021). However, alteration in growth conditions due to climate change imposes an additional challenge to plant disease detection methods based on AI. The expected rises in CO₂ concentration and temperature associated

to climate change would have an impact on agriculture, affecting plants and pathogen physiology (Trivedi et al., 2022) and their geographical distribution (Aidoo et al., 2021). For that reason, potential future climate should be considered as an experimental variable to develop more robust detection methods.

Thermography and multi/hyperspectral reflectance imaging are the most common sensors applied in agriculture (Zarco-Tejada et al., 2018; Maes and Steppe, 2019; Pérez-Bueno et al., 2019b). On the one hand, canopy to air differential temperature (T_C-T_A) is an indirect measurement of the vegetation transpiration rate (Scarth et al., 1948; Milthorpe and Spencer, 1957; Fuchs and Tanner, 1966) and is widely used in proximal and remote sensing for stress detection, as recently reviewed by Pineda et al. (2021). On the other hand, the high spectral resolution of hyperspectral reflectance imaging allows the creation of a growing collection of vegetation indices (VIs). These VIs are transformations of two or more spectral bands which allow reliable temporal and spatial inter-comparisons of vegetation attributes. Thus, VIs are quite simple and effective parameters to quantitatively and qualitatively evaluate vegetation traits such as vigor, fitness, and pigment composition, among other applications (Huete et al., 2002).

In fact, many VIs can be found in the literature. One of the most widely used is the normalized difference vegetation index (NDVI), which is related to vitality of canopies (Tucker, 1979; Pettorelli, 2013). Other VIs correlate with a wide range of plant physiological traits. For example, the photochemical reflectance index (PRI) correlates with photosynthetic activity (Gamon et al., 1992); the carotenoid reflectance index (CRI) (Gitelson et al., 2002) and the anthocyanin reflectance index (ARI) (Gitelson et al., 2001) are related to pigment contents; and the water balance index (WBI) is connected to water content in leaves (Peñuelas et al., 1993). Indeed, recent works have implemented VIs to the study of plants infected by *Xanthomonas* spp. Abdulridha et al. (2019) used a collection of VIs (ARI and NDVI among them) implemented on classifying algorithms to successfully identify tangerine plants infected by *X. citri* pv. *citri*. Similarly, NDVI values correlated well with the extension of the lesions caused by *X. campestris* pv. *oryzae* on rice leaves (Zhang et al., 2022). Moreover, several works have compared the association between climate change and the interannual variability registered on NDVI in several locations around the world (Kalisa et al., 2019; Bagherzadeh et al., 2020; Zhao et al., 2021). Nonetheless, new reflectance parameters could be defined for a given purpose to maximize differences when standard VIs are not sensitive enough (Miao et al., 2007; Mahlein et al., 2013; Zhang et al., 2017; El-Hendawy et al., 2019; Jia et al., 2019; Yuan et al., 2019).

The main aim of this work was to develop an efficient method for the detection of Xcc infection in broccoli plants based on thermal and hyperspectral reflectance imaging on individual leaves. For this purpose, six parameters were recorded: leaf temperature (particularly T_C-T_A) and five already known VIs. Moreover, three novel VIs specifically designed for detecting the Xcc infection were extracted from the reflectance spectra of healthy and diseased broccoli leaves. They were named diseased broccoli indices (DBI₁-DBI₃). This set of nine parameters were implemented on a selection of algorithms widely used on

TABLE 1 | Climatic conditions assessed for broccoli growth: CCC (current climate conditions), RCP 4.5, and RCP 8.5 (Representative Concentration Pathways 4.5 and 8.5) regionalized for Region of Murcia for years 2081–2100.

Climate Scenario	Temperature (°C)		CO ₂ (ppm)
	Day	Night	
CCC	31	17	408
RCP 4.5	34	20	650
RCP 8.5	37	23	1000

precision agriculture for their success in classifying infected plants: the multilayer perceptron-based artificial neural network (MLP), the support vector machine (SVM), and the k-nearest neighbor (kNN). Finally, the suitability of the trained models was evaluated by comparing their performances in correctly classifying new samples as healthy or diseased leaves under a range of climate conditions, including intermediate and extreme climate change scenarios, as well as current climate conditions. Furthermore, the relevance of every input parameter for the detection of Xcc infection in broccoli plants was evaluated.

MATERIALS AND METHODS

Plant Growth at Different Climate Conditions

Growth conditions under two possible future climate change scenarios were chosen taking into account the 5th Assessment Report by the Intergovernmental Panel on Climate Change (AR5; IPCC, 2014). In that assessment, a range of projections of greenhouse gases emissions responding to both socio-economic development and climate policy was considered. Future climate conditions were estimated based on representative concentration pathways (RCPs), depending on potential scenarios of greenhouse gases emissions and their atmospheric concentrations, air pollutant emissions, and land use for the year 2100. Thus, current climate conditions (CCC) were compared to future scenarios, being RCP 8.5 the most extreme scenario, meaning most dramatic increase in CO₂ levels and subsequent global warming. In turn, the so called RCP 4.5 would represent an intermediate scenario between CCC and RCP 8.5 and was considered by the AR5 as the most probable scenario by 2100.

The C₃ broccoli plants (*Brassica oleracea* var. *italic* cv. *calabrese natalino*) were grown in a growth chamber in a 16/8-h day/night regime with 60% relative humidity, 200 mol photon m⁻² s⁻¹ of PAR light. The ambient temperature and CO₂ concentrations (Table 1) were chosen according to the data regionalized by the Spanish State Meteorology Agency (AEMet) for Region of Murcia (largest Spanish broccoli producer) for current climate conditions and those corresponding to RCP 4.5 and RCP 8.5 in years 2081–2100. Day and night temperatures correspond to the average values in Region of Murcia during the growing season. For each experiment, plants were sown and grown at the corresponding CCC, RCP 4.5, or RCP 8.5 conditions.

Bacterial Growth and Inoculation

Xanthomonas campestris pv *campestris* (Xcc) race 1 and race 4 were grown for 24 h at 28°C in LB (Luria-Bertani) plates. Bacterial suspensions were prepared in sterile 10 mM MgCl₂ at 10⁸ colony-forming units per ml (cfu mL⁻¹) by adjusting the optical density at 600 nm to 0.1.

The third leaf of four-week-old plants (under CCC or RCP 4.5) or five-week-old plants (in case of RCP 8.5) was mock-inoculated with sterile 10 mM MgCl₂ or inoculated with bacterial suspension by clipping four secondary veins per leaf with rat tooth tweezers previously dipped in the corresponding solution (Figure 1). For each experiment, twelve plants per treatment (CCC and RCP 4.5) and four plants per treatment (RCP 8.5) were inoculated. Leaves were imaged at 1, 2, 3, 6, and 9 days post-inoculation (dpi). At least two experiments per climate condition were carried out, providing similar results.

Thermal Imaging

Thermal images of whole leaves were recorded using a FLIR A305sc camera (FLIR Systems, Wilsonville, OR, USA) vertically positioned 30 cm above the leaf, according to Pérez-Bueno et al. (2016). For each measurement, 10 thermal images were collected in the plant growth chamber over 10 s. These images were averaged to extract temperature values for whole leaves. Image processing was carried out using the FLIR ResearchIR v. 3.4 software.

Hyperspectral Reflectance Imaging

Reflectance spectra (400–1,000 nm) of broccoli leaves were recorded using a Pika L hyperspectral imaging camera (Resonon, Bozeman, MT, USA) in the visible (400–700 nm) to near-infrared spectral range (700–1,000 nm), with a spectral sampling at 2.1 nm and a spectral resolution (full width at half maximum) of 3.7 nm. The camera was positioned vertically 45 cm over the sample, which was placed on a translation stage. Thus, a datacube with 281 images was built for each attached leaf.

Leaves were illuminated with four calibrated xenon lamps with homogeneous light intensity between 400 and 1,000 nm, positioned above the samples and around the camera. Previous to leaf measurements, dark and light corrections were made in darkness and illuminating a white homogenous calibration tile provided by Resonon, respectively. Dark and light corrections, build-up of datacubes and analysis, were carried out with the software Spectronon v. 2.134 (Resonon).

Reflectance spectra averaged for whole leaves were obtained and used to calculate images corresponding to several widely used VIs, as summarized in Table 2. To avoid overfitting of machine learning models, only not redundant VIs were selected.

Data Analysis

Numerical data obtained from thermal and reflectance images (including reflectance spectra and VIs) were managed using Microsoft Office Excel 2016 (Microsoft Corporation, Redmond, WA, USA). Aiming to design a simple method of detection,

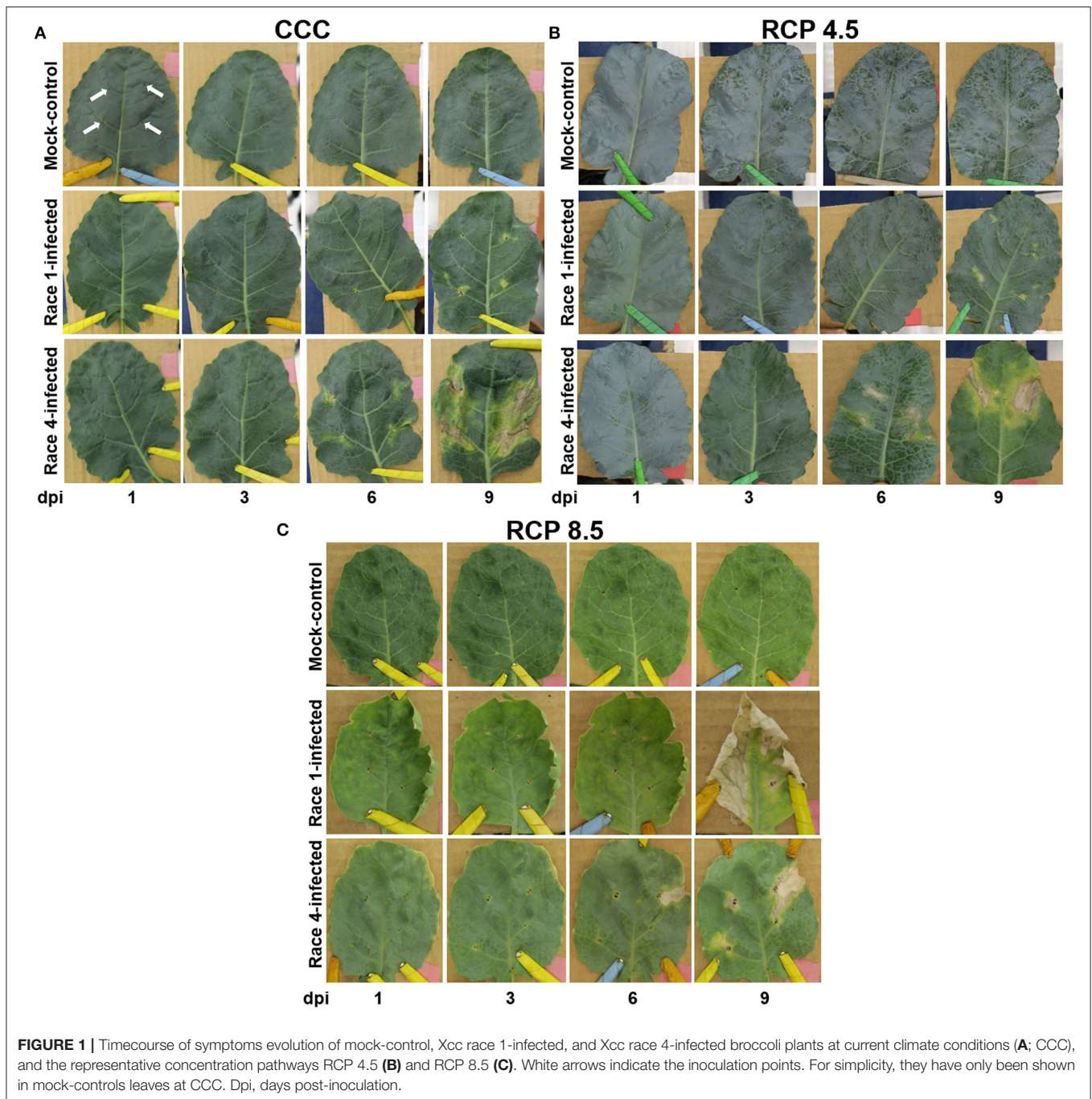


FIGURE 1 | Timecourse of symptoms evolution of mock-control, Xcc race 1-infected, and Xcc race 4-infected broccoli plants at current climate conditions (A: CCC), and the representative concentration pathways RCP 4.5 (B) and RCP 8.5 (C). White arrows indicate the inoculation points. For simplicity, they have only been shown in mock-controls leaves at CCC. Dpi, days post-inoculation.

values were averaged from whole leaves rather than regions of interest.

Two-tailed Student's *t*-test (Microsoft Excel) was performed to compare, for every treatment and at every dpi assayed: (a) spectra reflectance profiles; (b) values of novel VIs (DBIs). The null hypothesis was that there were no differences between treatments. This hypothesis was considered false at $p < 0.05$, and variables were treated as different when *p*-value was below this value. Figure graphs were plotted using Microsoft Excel.

Classification Analysis by Machine Learning

Data collected through whole experiments were organized in databases (Microsoft Excel), one per climate condition. Each database contained values of selected parameters (T_C - T_A , NDVI, PRI, ARI, CRI, WBI, DBI₁, DBI₂, and DBI₃) at every dpi (1–9 dpi) and treatment (mock-control, Xcc race 1-, and Xcc race 4-infected plants). In addition, data were rescaled from zero to one to ensure comparison between treatments and days, according

TABLE 2 | Common vegetation indices (VIs) from the literature that were used in this work.

VIs name	Related to	Equation	References
Anthocyanins reflectance index 1	Anthocyanins	$ARI = \frac{1}{R_{550}} - \frac{1}{R_{700}}$	Gitelson et al., 2001
Carotenoids reflectance index 2	Carotenoids	$CRI = \frac{1}{R_{510}} - \frac{1}{R_{700}}$	Gitelson et al., 2002
Normalized difference vegetation index	Vigor	$NDVI = \frac{R_{800} - R_{670}}{R_{800} + R_{670}}$	Tucker, 1979
Photochemical reflectance index	Photosynthesis	$PRI = \frac{R_{531} - R_{570}}{R_{531} + R_{570}}$	Gamon et al., 1992
Water balance index	Water	$WBI = R_{900} - R_{970}$	Peñuelas et al., 1993

TABLE 3 | Sample size (n) of the training and test databases created for each growth condition.

Treatment	Training dataset (n)	Test dataset (n)
CCC	98	41
RCP 4.5	84	39
RCP 8.5	42	18

to the equation: *rescaled value* = (*x*-minimum)/maximum. Then, the three databases were randomly partitioned into training and test datasets, in a proportion of 7:3, respectively (Table 3). This partition was carried out using a seed that ensured that every category (treatment and dpi) was well represented in both datasets. The experimental data were analyzed by the free version of KNIME v. 4.3.2 (KNIME AG, Zurich, Switzerland; www.knime.com; Berthold et al., 2008).

Three models were built for each one of the three growing conditions by analyzing the corresponding databases with three supervised classifying algorithms: MLP, SVM, and kNN. MLP is a network inspired by biological neural networks in which different interconnected nodes (called neurons) organized in layers transmit information to each other, learning from both input and output data (Hahn, 2009; Behmann et al., 2015). In contrast, SVM distributes samples in a high-dimensional feature space defined by support vectors. In this case, new samples are categorized based on what side of hyperplanes they fall on (Behmann et al., 2015). Finally, kNNs assign proportional weights to the contributions of the sample neighbors based on distances. These weights determine to what category a new sample would most likely belong to (Blanzieri and Melgani, 2008).

Broccoli leaves were categorized into mock-control, Xcc race 1-, and Xcc race 4-infected plants using the classifying algorithms MLP, SVM, and kNN. The performance of classification was evaluated in terms of (i) sensitivity (true positive rate); (ii) specificity (true negative rate); (iii) accuracy (percentage of right guesses); and (iv) *F*-measure (harmonic mean of precision and sensitivity; where precision is the number of correct control samples divided by the number of all plants classified as “control”). All the three feedforward backpropagation MLPs tested were designed to have one hidden layer with four neurons (half the number of variables used to feed them). Higher number of hidden layers or their neurons did not result in an improvement of the performance. A polynomial kernel was used

for the SVMs, with bias = 1 and gamma = 1. More complex spatial kernels did not improve the performance of the algorithm. Finally, the optimal number of neighbors for the kNN algorithm was *k* = 5 using the Euclidean distance. Regarding SVM and kNN libraries, we have used the basic nodes (SVM learner and K nearest neighbor, respectively) implemented on Knime software v. 4.3.2. This process was performed independently for each of the three climate conditions under study.

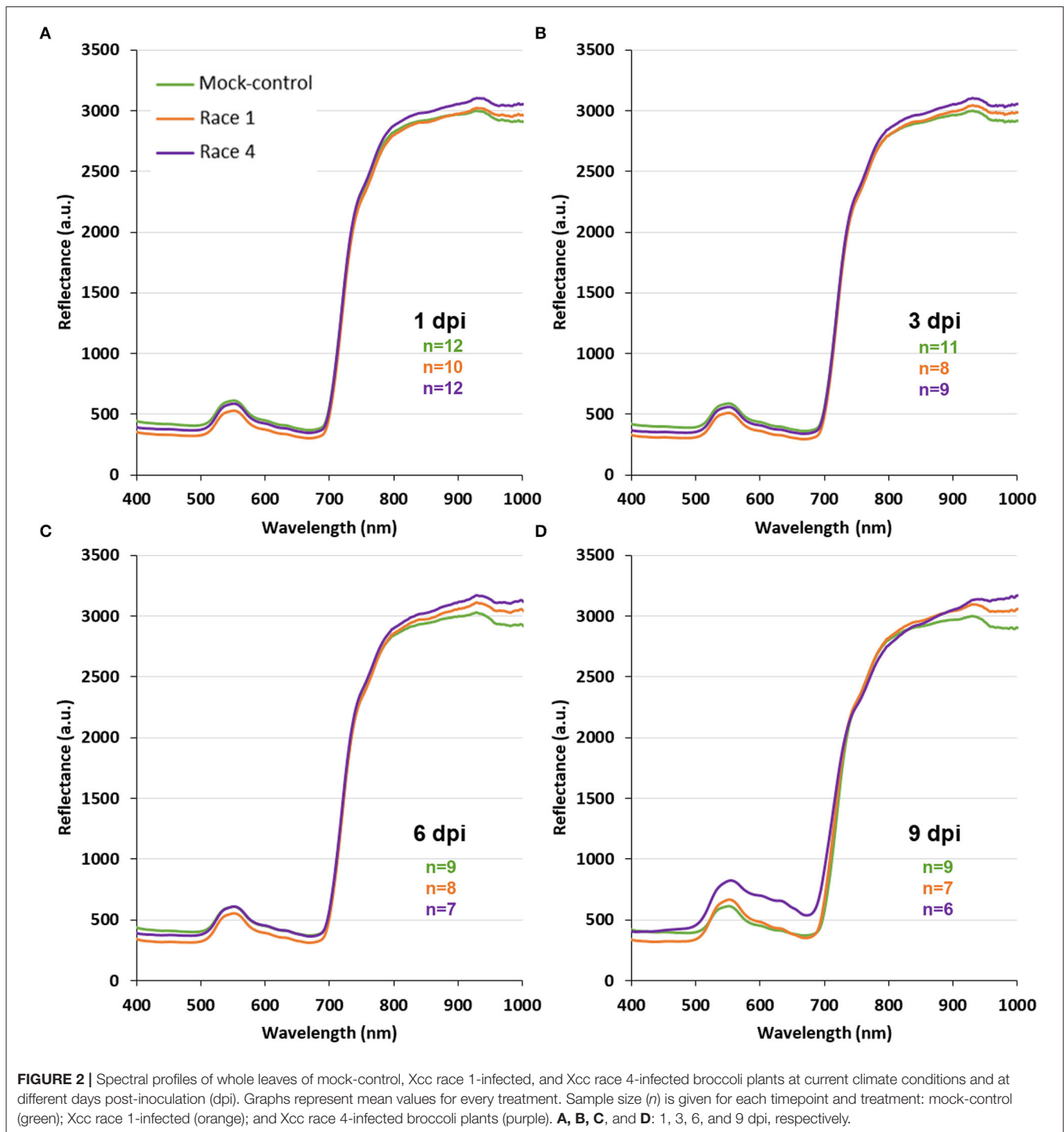
Finally, the global variable importance was calculated for each parameter (T_C - T_A , NDVI, PRI, ARI, CRI, WBI, DBI₁, DBI₂, and DBI₃), that is, how informative was a given parameter for the model to make a correct decision. For such a purpose, global surrogate random forest (RF) models were trained to estimate the variable importance using the Global Feature Importance component developed for Knime software (https://hub.knime.com/knime/spaces/Examples/latest/00_Components/Model%20Interpretability/Global%20Feature%20Importance%20sim%20R90ymhRbHOc78Z). RF was trained on the standardly pre-processed input data. Feature importance was then calculated by counting how many times it had been selected for a split and at which rank (level) among all available features (candidates) in the trees of the RF.

RESULTS

Evolution of Symptoms Under a Range of Growth Conditions

Plants grown from sowing under CCC, RCP4.5, or RCP8.5 conditions were inoculated with Xcc race 1 or 4, and the evolution of symptoms was followed up to 9 dpi. At CCC and RCP 4.5, Xcc infection on broccoli plants consisted in chlorosis followed by a progressive necrosis of the tissue surrounding the inoculation site to finally reach the V-shaped lesions typical of this bacterial infection (Figure 1). Xcc race 4 caused the most severe symptoms, with necrosis at the clipping point starting at 3 dpi and evident at 6 dpi; chlorosis surrounded the inoculated area at 6 dpi, and V-shaped lesions were patent at 9 dpi. In contrast, Xcc race 1 produced similar symptoms in a slower time course, with a delay of 3 days. Mock-control leaves only displayed the actual lesions. It is worth noticing that there was no evolution in symptoms from 0 to 1 dpi under any of the assayed growth conditions.

The RCP 8.5 conditions affected the growth of broccoli plants, which displayed stunting and early senescence. Moreover, leaves were smaller and thicker than those of plants grown at CCC or RCP 4.5 conditions. At RCP 8.5, the evolution of the infection by



either race resembled that described for Xcc race 4 under CCC. Moreover, Xcc race 1 was more virulent than Xcc race 4 at 9 dpi.

Novel VIs Could Discriminate Between Healthy and Xcc-Infected Broccoli Leaves

For every treatment (mock-control, Xcc race 1-, and Xcc race 4-infected), whole leaf reflectance spectra were registered at 1, 2, 3,

6, and 9 dpi. Those profiles revealed specific spectral patterns for each treatment, showing clear differences between them from the first timepoint measured (Figure 2; Supplementary Figures 1, 2). Thus, the use of VIs based on hyperspectral reflectance measurements seemed to be useful to distinguish between control and Xcc (race 1 or 4)-infected plants. The common VIs ARI, CRI, PRI, NDVI, and WBI were obtained from the spectra for every

TABLE 4 | Novel vegetation indices (VIs) firstly described in this work.

VIs name	Related to	Equation
Diseased broccoli index 1	Xcc infection	$DBI_1 = \frac{R_{400} - R_{690}}{R_{850}}$
Diseased broccoli index 2	Xcc infection	$DBI_2 = \frac{R_{400}}{R_{850}}$
Diseased broccoli index 3	Xcc infection	$DBI_3 = \frac{R_{578}}{R_{529}}$

treatment and dpi measured and recorded in a database for each climate condition.

In addition, novel VIs were designed, based on spectral differences between healthy and Xcc-infected broccoli leaves. Reflectance spectra were compared by Student's *t*-test in order to determine at which wavelengths reflectance values were statistically different (at least $p < 0.05$) between treatments. Thus, three spectral ranges were found to show maximal differences between treatments at every dpi tested: 400–500, 600–700, and 900–1000 nm. On the contrary, the regions 520–570 and 730–890 nm were very stable and not affected by the infection until 9 dpi. For this reason, they were selected for “normalization” of the designed parameters. Several wavelengths were chosen within these spectral regions of interest. To avoid redundancy of adjacent wavelengths in the reflectance spectra, only wavelengths separated by at least 40 nm were used in this process. Finally, the selected wavelengths were combined by different mathematical calculations (additions, subtractions, divisions, or combinations thereof) in order to find novel VIs showing statistical differences ($p < 0.05$ according to Student's *t*-test) between treatments along entire experiments at each climate condition. Among the large collection of proposed VIs, three of them, named diseased broccoli indices 1–3 (DBI_{1-3} ; **Table 4**), offered maximum significant differences between mock-control and Xcc-infected broccoli plants. It is worth noticing that DBI_{1-3} did not show statistically significant correlation with each other, meaning that DBI_{1-3} did not provide redundant information to the classifiers.

Identification of Xcc-Infected Leaves by Classificatory Algorithms

For each experimental condition, an independent database was built containing the values of selected parameters (T_C - T_A , NDVI, PRI, ARI, CRI, WBI, DBI_1 , DBI_2 , and DBI_3) for every treatment and dpi assayed. The three databases were normalized and then randomly split in two datasets: training (70%) and testing (30%). Each of the three training dataset was used to feed supervised classifying algorithms (MLP, SVM, and kNN) to classify samples into the following categories: mock-control, Xcc race 1-, and Xcc race 4-infected leaves; each of the three testing dataset was used to calculate their performance of classification.

The MLPs provided the highest accuracy for every climate condition (**Figure 3**). They also provided the highest *F*-measure under every condition and, in general terms, the highest sensitivity. In contrast, SVM and kNN showed similar accuracies

for CCC; however, these two algorithms were not able to identify control and infected samples at RCP 4.5 or RCP 8.5, with accuracies of 45–50% and rather low specificity. Moreover, any attempt of classification by MLP, SVM, or kNN into two categories (mock-control vs Xcc-infected) was inefficient. This was probably due to the underrepresentation of mock-control samples in the datasets (1/3 healthy vs. 2/3 of infected), whereas in three-category models, every group had the same size.

The suitability of the designed VIs for the identification of Xcc-infected leaves was evaluated in terms of global variable importance in the classifiers, calculated by a surrogate RF algorithm (**Figure 4**). The accuracies obtained for the fit of each RF were 85.7%, 87.2%, and 88.9% for CCC, RCP 4.5, and RCP 8.5, respectively. Under CCC, the most informative parameters were DBI_1 , DBI_2 , and WBI. In contrast, under RCP 4.5 conditions, T_C - T_A , DBI_3 , and PRI obtained the highest global variable importance. Finally, under RCP 8.5 conditions, DBI_2 , CRI, and NDVI were the most instructive parameters.

DISCUSSION

Imaging techniques appear to be essential for precision agriculture due to their fast time-spatial response to biotic and abiotic stress in a non-destructive manner (Barón et al., 2016; Mahlein, 2016). In the last years, thermal and (multi- or hyper-) reflectance imaging sensors have been broadly used for monitoring stress in crop fields. Furthermore, sustainable agriculture is increasingly relying on AI (such as classifying algorithms) coupled with computer vision, to solve farming issues and to promote the automation of decision-making process (Tian et al., 2020; Nabwire et al., 2021). However, these methods require basic research to define informative parameters that efficiently report the health state and fitness of a particular crop. This work aims to define optimal VIs and classifiers for the detection of Xcc-infected broccoli leaves. Furthermore, the robustness of those models was analyzed under climate conditions mimicking those expected for Region of Murcia in years 2081–2100.

According to Fargier and Manceau (2007), when a cultivar of a brassica is infected by Xcc, a collection of polymorphisms is obtained depending on the race inoculated. In the case of broccoli plants used for this study (*B. oleracea* var. *italic* cv. *calabrese natalino*), the symptoms developed under CCC triggered by races 1 and 4 were similar. However, Xcc race 1 showed a slower timecourse than race 4 under the same ambient conditions. The process of undergoing climate change could affect considerably plant biochemistry and therefore plant defense responses. For this reason, it is relevant to include future climate conditions in disease detection studies. Indeed, each disease may respond differently to these variations, and thus, climate change would cause neutral, positive, or negative effects on plant responses to diseases (Trebecki et al., 2017; Velásquez et al., 2018; Cheng et al., 2019). According to the results reported here, symptoms caused by Xcc on susceptible broccoli plants would not be altered on an intermediate climate change scenario like RCP 4.5. These results are in accordance

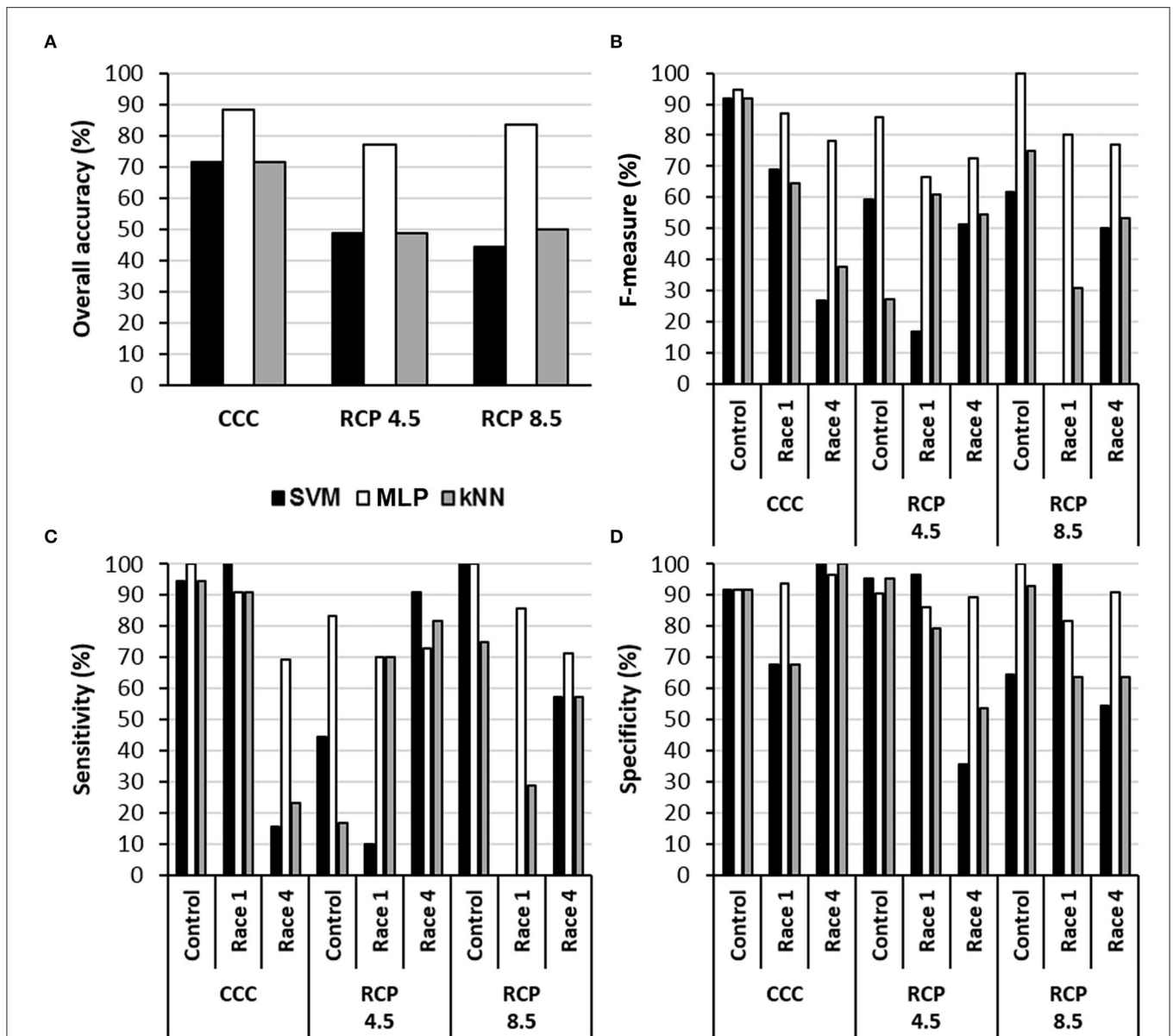


FIGURE 3 | Performance of three algorithms for the classification of samples into the categories control, Xcc race 1-infected, and Xcc race 4-infected leaves in terms of overall accuracy (A), *F*-measure (B), sensitivity (C), and specificity (D) for each climate scenario. SVM, support vector machine; MLP, multilayer perceptron-based artificial neural network; kNN, k-nearest neighbors ($k = 5$ neighbors). CCC, current climate conditions; RCP 4.5 and 8.5, representative concentration pathways 4.5 and 8.5.

with previous works, as extensively reviewed by Gullino et al. (2018). However, the RCP 8.5 imposed a stress condition limiting or slowing down plant growth. It will be of particular interest to gain knowledge about the impact of combined high temperature and high CO_2 on photosynthetic processes of the broccoli plant which, as a C_3 species, is well adapted to mild temperatures. Nevertheless, further research would be needed to fully understand the impact of climate change on broccoli plant physiology (particularly on photosynthesis), as well as on the physiology of Xcc races, and/or their interaction with host plants.

In literature, a number of classic VIs derived from multispectral (and hyperspectral) imaging can be found. This VIs can be used to detect, classify, and quantify specific diseases with varying degrees of success (Lowe et al., 2017). However, high-resolution spectra recorded with hyperspectral imaging sensors allow the selection of an optimized set of wavelengths to maximize differences between healthy and infected plants. Those wavelengths can be used to create novel parameters specific for a given host–pathogen system or stress factor. This approach has already been demonstrated to be suitable to detect diseased plants when combined with AI algorithms. Thus, Mahlein et al. (2013)

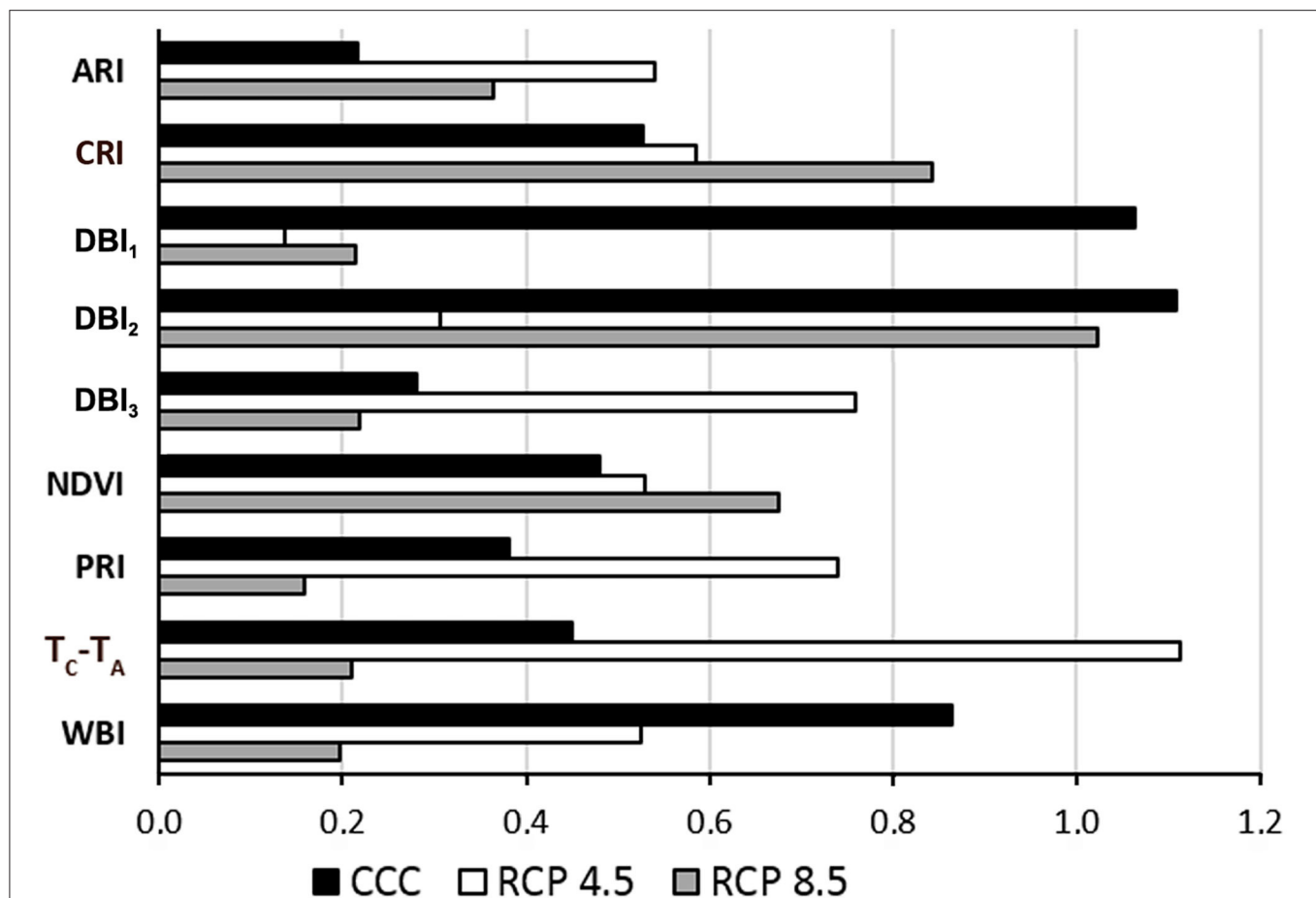


FIGURE 4 | Global variable importance calculated using a global surrogate random forest (RF) model. CCC, current climate conditions; RCP 4.5 and 8.5, representative concentration pathways 4.5 and 8.5; ARI, anthocyanin reflectance index; CRI, carotenoid reflectance index; DBI_{1–3}, disease broccoli index 1–3; NDVI, normalized difference vegetation index; PRI, photochemical reflectance index; T_C-T_A, normalized temperature; WBI, water balance index.

reported specific spectral disease indices for the detection of sugar beet plants infected with *Cercospora* leaf spot, sugar beet rust, or powdery mildew. Those indices improved disease detection and identification when implemented on classifiers. Similarly, Yuan et al. (2019) proposed a novel method for detecting anthracnose in tea plants based on hyperspectral imaging that included two new disease indices in the classificatory models. Moreover, the analysis of reflectance spectral data of healthy and diseased wheat ears allowed the creation of a novel index that demonstrated a stronger ability to determine the severity of the *Fusarium* head blight compared with other sixteen existing spectral indices (Zhang et al., 2020).

In this work, three novel VIs have been developed to successfully distinguish between healthy and Xcc-infected broccoli plants (Table 4). Leaf reflectance is a complex phenomenon dependent on biochemical and biophysical properties of the canopy leaves, which in turn are affected by growth conditions and diseases. Thus, the visible reflectance range (400–700 nm) is mostly influenced by the leaf pigment

content; the reflectance in the near-infrared range (700–1100 nm) depends on water content and leaf structure, or internal scattering processes; and the short-wave infrared (1,100–2,500 nm) is influenced by the composition of leaf chemicals and water, as reviewed by Mahlein (2016). Since chlorophylls are the main pigments influencing reflectance spectrum at 400 and 690 nm, both DBI₁ and DBI₂ indices could be indicative of the severity of chlorosis. Moreover, DBI₃ could be also related to the contents on chlorophylls and carotenes (Carter and Knapp, 2001).

DBI₁, DBI₂, and DBI₃, together with thermal (T_C-T_A) and other common hyperspectral reflectance parameters (NDVI, PRI, ARI, CRI, and WBI), were implemented in three different supervised classifiers (MLP, SVM, and kNN) for each experimental condition. Since the learning process of each algorithm differs from each other, so will the quality of its predictions on the new samples. In this sense, it is a common procedure to compare the performance of several algorithms when sorting new samples (the validation datasets) after training

on the same dataset. Metrics such as specificity (true negative rate), sensitivity (true positive rate), accuracy (percentage of right guesses), or *F*-measure (harmonic mean of precision and sensitivity) evaluate the performance of classification, that is, the estimation of the true risk of error of the output prediction of a machine learning algorithm (Shalev-Shwartz and Ben-David, 2014; Liakos et al., 2018). The MLPs were the most effective classifier, with the highest overall accuracy and *F*-measure under the three growing conditions assayed. The performance of the MLP models was comparable to that reported by other authors for disease detection classifiers. Indeed, an increasing number of studies apply classifiers to spectral data (including or not thermal parameters) to identify infected plants at conditions resembling CCC. For example, Sankaran et al. (2013) reported an accuracy of 87% when classifying citrus trees infected by *Candidatus Liberibacter* spp, a bacteria causing Huanglongbing disease. Zarco-Tejada et al. (2018) obtained accuracies of disease detection exceeding 80% when classifying *Xylella fastidiosa*-infected olive trees. This pathogen, alike Xcc, is a xylem bacterium. Abdulridha et al. (2020a,b) identified tomato plants infected with tomato yellow leaf curl virus, *Xanthomonas perforans*, or *Corynespora cassiicola* (a fungus) with 94–100% accuracy depending on the pathogen. Pérez-Bueno et al. (2019b) detected avocado trees suffering white root rot (caused by the fungus *Rosellinia necatrix*) with accuracies up to 82.5%. Nguyen et al. (2021) achieved accuracies ranging from 82 to 96.75% when identifying vines affected by the Grapevine vein-clearing virus. Similarly to the results here reported, Yuan et al. (2019) designed novel hyperspectral reflectance indices which help to identify *Gloeosporium theae-sinesis* Miyake-infected tea plants with 94 and 98% accuracies at pixel and leaf levels, respectively.

The performance of the models was affected differentially by growing conditions, depending on the classifier. In both RCPs, the accuracy of the classifiers decreased in all cases. However, the accuracy of models based on MLP only decreased from 88.1% at CCC to 76.9 and 83.3% for RCP 4.5 and RCP 8.5, respectively. This advantage of MLPs against SVM and kNN models could be related to the fact that MLPs are less affected by noise factors (compared to other algorithms), which in turn reduces significantly the influence of the unknown variability. Therefore, MLPs are usually more robust models that often outperform other classifying algorithms in solving a variety of classification problems (Basheer and Hajmeer, 2000; Bala and Kumar, 2017). To our best knowledge, this is the first time that machine learning classifiers have been applied to hyperspectral and thermal data taken under climate conditions mimicking those projected for the future in order to classify healthy and infected plants.

DBI₁, DBI₂, and DBI₃ proved to be important features for plant classification according to a surrogate RF used for testing the global importance of variables. Overall, DBI₁ and DBI₂ were the most informative parameters of the set for CCC. However, the global variable importance varied for each parameter depending on the climate conditions. Under RCP 4.5 conditions, T_C-T_A and DBI₃ were the most informative parameters. In contrast, DBI₂

was the parameter with the highest global variable importance at RCP 8.5. This effect may be due to the impact of growing conditions on the symptomatology (degree of chlorosis and/or necrosis) of the infections, as discussed above.

CONCLUSION

The parameters DBI₁, DBI₂, and DBI₃ here presented are good reporters for Xcc infection in broccoli leaves. Furthermore, the model based on MLP and the set of parameters DBI₁, DBI₂, and DBI₃ along with common VIs (ARI, CRI, NDVI, PRI, and WBI) and T_C-T_A would be an effective procedure for the identification of Xcc-broccoli infected plants. In addition, this model proved to be robust regardless of the climate conditions.

DATA AVAILABILITY STATEMENT

The original contributions presented in the study are included in the article/**Supplementary Material**. Further inquiries can be directed to the corresponding authors.

AUTHOR CONTRIBUTIONS

MP, MLP-B, and MB conceived and designed the experiments and wrote the manuscript. MP and MP-B conducted the experiments. MP analyzed the data, interpreted the results, and mounted images. MB contributed to the materials, equipment, and analysis tools. All the authors reviewed it and approved the final version.

FUNDING

This work was supported by grant RTI2018-094652-B-I00 funded by MCIN/AEI/10.13039/501100011033 and by “ERDF: A way of making Europe”. The free open access publication was partially funded by Consejo Superior de Investigaciones Científicas (CSIC) through the Unidad de Recursos de Información Científica para la Investigación (URICI).

SUPPLEMENTARY MATERIAL

The Supplementary Material for this article can be found online at: <https://www.frontiersin.org/articles/10.3389/fpls.2022.790268/full#supplementary-material>

Supplementary Figure 1 | Spectral profiles of whole leaves of mock-control, Xcc race 1-infected, and Xcc race 4-infected broccoli plants at RCP 4.5 and at different days post-inoculation (dpi). Graphs represent mean values for every treatment. Sample size (*n*) is given for each timepoint and treatment: mock-control (green); Xcc race 1-infected (orange); and Xcc race 4-infected broccoli plants (purple).

Supplementary Figure 2 | Spectral profiles of whole leaves of mock-control, Xcc race 1-infected, and Xcc race 4-infected broccoli plants at RCP 8.5 and at different days post-inoculation (dpi). Graphs represent mean values (*n* = 4) for every treatment and timepoint.

REFERENCES

- Aasen, H., Van Wittenberghe, S., Medina, N. S., Damm, A., Goulas, Y., Wieneke, S., et al. (2019). Sun-induced chlorophyll fluorescence II: review of passive measurement setups, protocols, and their application at the leaf to canopy level. *Remote Sens.* 11, 33. doi: 10.3390/rs11080927
- Abdulridha, J., Ampatzidis, Y., Kakarla, S. C., and Roberts, P. (2020a). Detection of target spot and bacterial spot diseases in tomato using UAV-based and benchtop-based hyperspectral imaging techniques. *Precis. Agric.* 21, 955–978. doi: 10.1007/s11119-019-09703-4
- Abdulridha, J., Ampatzidis, Y., Qureshi, J., and Roberts, P. (2020b). Laboratory and UAV-based identification and classification of tomato yellow leaf curl, bacterial spot, and target spot diseases in tomato utilizing hyperspectral imaging and machine learning. *Remote Sens.* 12, 2732. doi: 10.3390/rs1212732
- Abdulridha, J., Batuman, O., and Ampatzidis, Y. (2019). UAV-based remote sensing technique to detect citrus canker disease utilizing hyperspectral imaging and machine learning. *Remote Sens.* 11, 1373. doi: 10.3390/rs11111373
- Aidoo, O. F., Cunze, S., Guimapi, R. A., Arhin, L., Ablormeti, F. K., Tettey, E., et al. (2021). Lethal yellowing disease: insights from predicting potential distribution under different climate change scenarios. *J. Plant Dis. Prot.* 128, 1313–1325. doi: 10.1007/s41348-021-00488-1
- Bagherzadeh, A., Hoseini, A. V., and Totmaj, L. H. (2020). The effects of climate change on normalized difference vegetation index (NDVI) in the Northeast of Iran. *Model. Earth Syst. Environ.* 6, 671–683. doi: 10.1007/s40808-020-00724-x
- Bala, R., and Kumar, D. (2017). Classification using ANN: a review. *Int. J. Comput. Intell. Res.* 13, 1811–1820.
- Barón, M., Pineda, M., and Pérez-Bueno, M. L. (2016). Picturing pathogen infection in plants. *Z. Naturforsch. C* 71, 355–368. doi: 10.1515/znc-2016-0134
- Basheer, I. A., and Hajmeer, M. (2000). Artificial neural networks: fundamentals, computing, design, and application. *J. Microbiol. Methods* 43, 3–31. doi: 10.1016/S0167-7012(00)00201-3
- Behmann, J., Mahlein, A.-K., Rumpf, T., Römer, C., and Plümer, L. (2015). A review of advanced machine learning methods for the detection of biotic stress in precision crop protection. *Precis. Agric.* 16, 239–260. doi: 10.1007/s11119-014-9372-7
- Berthold, M. R., Cebon, N., Dill, F., Gabriel, T. R., Kötter, T., Meinel, T., et al. (2008). *KNIME: The Konstanz Information Miner*. Freiburg: Springer Berlin Heidelberg, 319–326.
- Blanzieri, E., and Melgani, F. (2008). Nearest neighbor classification of remote sensing images with the maximal margin principle. *IEEE Trans. Geosci. Remote* 46, 1804–1811. doi: 10.1109/TGRS.2008.916090
- Carter, G. A., and Knapp, A. K. (2001). Leaf optical properties in higher plants: linking spectral characteristics to stress and chlorophyll concentration. *Am. J. Bot.* 88, 677–684.
- Cheng, Y. T., Zhang, L., and He, S. Y. (2019). Plant-microbe interactions facing environmental challenge. *Cell Host Microbe* 26, 183–192. doi: 10.1016/j.chom.2019.07.009
- Chlingaryan, A., Sukkari, S., and Whelan, B. (2018). Machine learning approaches for crop yield prediction and nitrogen status estimation in precision agriculture: a review. *Comput. Electron. Agric.* 151, 61–69. doi: 10.1016/j.compag.2018.05.012
- Ekman, J., Tesoriero, L., and Grigg, S. (2014). *Pests, Diseases and Disorders of Brassica Vegetables: A Field Identification Guide*. North Sydney, NSW: Horticulture Australia.
- El-Hendawy, S. E., Al-Suhaibani, N. A., Elsayed, S., Hassan, W. M., Dewir, Y. H., Refay, Y., et al. (2019). Potential of the existing and novel spectral reflectance indices for estimating the leaf water status and grain yield of spring wheat exposed to different irrigation rates. *Agric. Water Manag.* 217, 356–373. doi: 10.1016/j.agwat.2019.03.006
- Fargier, E., and Manceau, C. (2007). Pathogenicity assays restrict the species *Xanthomonas campestris* into three pathovars and reveal nine races within *X. campestris* pv. *campestris*. *Plant Pathol.* 56, 805–818. doi: 10.1111/j.1365-3059.2007.01648.x
- Fuchs, M., and Tanner, C. B. (1966). Infrared thermometry of vegetation. *Agron. J.* 58, 597–601. doi: 10.2134/agronj1966.00021962005800060014x
- Gamon, J. A., Peñuelas, J., and Field, C. B. (1992). A narrow-waveband spectral index that tracks diurnal changes in photosynthetic efficiency. *Remote Sens. Environ.* 41, 35–44. doi: 10.1016/0034-4257(92)90059-S
- Gao, Z., Luo, Z., Zhang, W., Lv, Z., and Xu, Y. (2020). Deep learning application in plant stress imaging: a review. *AgriEngineering* 2, 430–446. doi: 10.3390/agriengineering2030029
- Gerhards, M., Schlerf, M., Mallick, K., and Udelhoven, T. (2019). Challenges and future perspectives of multi-/hyperspectral thermal infrared remote sensing for crop water-stress detection: a review. *Remote Sens.* 11, 1240. doi: 10.3390/rs11101240
- Gitelson, A. A., Merzlyak, M. N., and Chivkunova, O. B. (2001). Optical properties and nondestructive estimation of anthocyanin content in plant leaves. *Photochem. Photobiol.* 74, 38–45. doi: 10.1562/0031-8655(2001)074<0038:opane>2.0.co;2
- Gitelson, A. A., Zur, Y., Chivkunova, O. B., and Merzlyak, M. N. (2002). Assessing carotenoid content in plant leaves with reflectance spectroscopy. *Photochem. Photobiol.* 75, 272–281. doi: 10.1562/0031-8655(2002)0750272ACCIPL2.0.CO2
- Golhani, K., Balasundram, S. K., Vadmalai, G., and Pradhan, B. (2018). A review of neural networks in plant disease detection using hyperspectral data. *Inf. Process. Agric.* 5, 354–371. doi: 10.1016/j.inpa.2018.05.002
- Gullino, M. L., Pugliese, M., Gilardi, G., and Garibaldi, A. (2018). Effect of increased CO₂ and temperature on plant diseases: a critical appraisal of results obtained in studies carried out under controlled environment facilities. *J. Plant Pathol.* 100, 371–389. doi: 10.1007/s42161-018-0125-8
- Hahn, F. (2009). Actual pathogen detection: sensors and algorithms – a review. *Algorithms* 2, 301–338. doi: 10.3390/a2010301
- Huete, A., Didan, K., Miura, T., Rodriguez, E. P., Gao, X., and Ferreira, L. G. (2002). Overview of the radiometric and biophysical performance of the MODIS vegetation indices. *Remote Sens. Environ.* 83, 195–213. doi: 10.1016/S0034-4257(02)00096-2
- IPCC (2014). *AR5. Climate Change 2014: Synthesis Report. Contribution of Working Groups I, II and III to the Fifth Assessment Report of the Intergovernmental Panel on Climate Change*. Geneva: IPCC. Available online at: <https://www.ipcc.ch/report/ar5/syr/>
- Jia, M., Wang, Z., Wang, C., Mao, D., and Zhang, Y. (2019). A new vegetation index to detect periodically submerged mangrove forest using single-tide Sentinel-2 imagery. *Remote Sens.* 11, 2043. doi: 10.3390/rs11172043
- Jung, J., Maeda, M., Chang, A., Bhandari, M., Ashapure, A., and Landivar-Bowles, J. (2021). The potential of remote sensing and artificial intelligence as tools to improve the resilience of agriculture production systems. *Curr. Opin. Biotechnol.* 70, 15–22. doi: 10.1016/j.copbio.2020.09.003
- Kalisa, W., Igbawua, T., Hanchiri, M., Ali, S., Zhang, S., Bai, Y., et al. (2019). Assessment of climate impact on vegetation dynamics over East Africa from 1982 to 2015. *Sci. Rep.* 9, 16865. doi: 10.1038/s41598-019-53150-0
- Kashyap, B., and Kumar, R. (2021). Sensing methodologies in agriculture for monitoring biotic stress in plants due to pathogens and pests. *Inventions* 6, 29. doi: 10.3390/inventions6020029
- Liakos, K. G., Busato, P., Moshou, D., Pearson, S., and Bochtis, D. (2018). Machine learning in agriculture: a review. *Sensors* 18, 2674. doi: 10.3390/s18082674
- Lowe, A., Harrison, N., and French, A. P. (2017). Hyperspectral image analysis techniques for the detection and classification of the early onset of plant disease and stress. *Plant Methods* 13, 80. doi: 10.1186/s13007-017-0233-z
- Maes, W. H., and Steppe, K. (2019). Perspectives for remote sensing with unmanned aerial vehicles in precision agriculture. *Trends Plant Sci.* 24, 152–164. doi: 10.1016/j.tplants.2018.11.007
- Mahlein, A.-K. (2016). Plant disease detection by imaging sensors – parallels and specific demands for precision agriculture and plant phenotyping. *Plant Dis.* 100, 241–251. doi: 10.1094/pdis-03-15-0340-fe
- Mahlein, A. K., Rumpf, T., Welke, P., Dehne, H. W., Plümer, L., Steiner, U., et al. (2013). Development of spectral indices for detecting and identifying plant diseases. *Remote Sens. Environ.* 128, 21–30. doi: 10.1016/j.rse.2012.09.019
- Mansfield, J., Genin, S., Magori, S., Citovsky, V., Sriariyanum, M., Ronald, P., et al. (2012). Top 10 plant pathogenic bacteria in molecular plant pathology. *Mol. Plant Pathol.* 13, 614–629. doi: 10.1111/j.1364-3703.2012.00804.x
- Miao, X., Gong, P., Swope, S., Pu, R., and Carruthers, R. (2007). Detection of yellow starthistle through band selection and feature extraction from hyperspectral imagery. *Photogramm. Eng. Remote Sensing* 73, 1005–1015.
- Milthorpe, F. L., and Spencer, E. J. (1957). Experimental studies of the factors controlling transpiration. *J. Exp. Bot.* 8, 413–437. doi: 10.1093/jxb/8.3.413

- Nabwire, S., Suh, H.-K., Kim, M. S., Baek, I., and Cho, B.-K. (2021). Review: application of artificial intelligence in phenomics. *Sensors* 21, 4363. doi: 10.3390/s21134363
- Nguyen, C., Sagan, V., Maimaitiyiming, M., Maimaitijiang, M., Bhadra, S., and Kwasniewski, M. T. (2021). Early detection of plant viral disease using hyperspectral imaging and deep learning. *Sensors* 21, 742. doi: 10.3390/s21030742
- Owis, A. (2015). Broccoli; The green beauty: a review. *J. Pharm. Sci. Res.* 7, 696.
- Peñuelas, J., Filella, I., Biel, C., Serrano, L., and Savé, R. (1993). The reflectance at the 950–970 nm region as an indicator of plant water status. *Int. J. Remote Sens.* 14, 1887–1905. doi: 10.1080/01431169308954010
- Pérez-Bueno, M. L., Pineda, M., and Barón, M. (2019a). Phenotyping plant responses to biotic stress by chlorophyll fluorescence imaging. *Front. Plant Sci.* 10:1135. doi: 10.3389/fpls.2019.01135
- Pérez-Bueno, M. L., Pineda, M., Cabeza, F., and Barón Ayala, M. (2016). Multicolor fluorescence imaging as a candidate for disease detection in plant phenotyping. *Front. Plant Sci.* 7:1790. doi: 10.3389/fpls.2016.01790
- Pérez-Bueno, M. L., Pineda, M., Vida, C., Fernández-Ortuño, D., Torés, J. A., De Vicente, A., et al. (2019b). Detection of white root rot in avocado trees by remote sensing. *Plant Dis.* 103, 1119–1125. doi: 10.1094/PDIS-10-18-1778-RE
- Pettorelli, N. (2013). *The Normalized Difference Vegetation Index*. Oxford: Oxford University Press.
- Pineda, M., Barón, M., and Pérez-Bueno, M.-L. (2021). Thermal imaging for plant stress detection and phenotyping. *Remote Sens.* 13, 68. doi: 10.3390/rs13010068
- Sankaran, S., Maja, J. M., Buchanon, S., and Ehsani, R. (2013). Huanglongbing (citrus greening) detection using visible, near infrared and thermal imaging techniques. *Sensors* 13, 2117–2130. doi: 10.3390/s130202117
- Savary, S., Ficke, A., Aubertot, J.-N., and Hollier, C. (2012). Crop losses due to diseases and their implications for global food production losses and food security. *Food Secur.* 4, 519–537. doi: 10.1007/s12571-012-0200-5
- Scarth, G. W., Loewy, A., and Shaw, M. (1948). Use of the infrared total absorption method for estimating the time course of photosynthesis and transpiration. *Can. J. Res.* 26c, 94–107. doi: 10.1139/cjr48c-010
- Shalev-Shwartz, S., and Ben-David, S. (2014). *Understanding Machine Learning: From Theory to Algorithms*. Cambridge: Cambridge University Press.
- Sperschneider, J. (2020). Machine learning in plant–pathogen interactions: empowering biological predictions from field scale to genome scale. *New Phytol.* 228, 35–41. doi: 10.1111/nph.15771
- Talaviya, T., Shah, D., Patel, N., Yagnik, H., and Shah, M. (2020). Implementation of artificial intelligence in agriculture for optimisation of irrigation and application of pesticides and herbicides. *Artif. Intell. Agric.* 4, 58–73. doi: 10.1016/j.aiia.2020.04.002
- Tian, H., Wang, T., Liu, Y., Qiao, X., and Li, Y. (2020). Computer vision technology in agricultural automation—a review. *Inf. Process. Agric.* 7, 1–19. doi: 10.1016/j.inpa.2019.09.006
- Tortosa, M., Cartea, M. E., Rodríguez, V. M., and Velasco, P. (2018). Unraveling the metabolic response of *Brassica oleracea* exposed to *Xanthomonas campestris* pv. *campestris*. *J. Sci. Food Agric.* 98, 3675–3683. doi: 10.1002/jsfa.8876
- Trebicki, P., Däder, B., Vassiliadis, S., and Fereres, A. (2017). Insect–plant–pathogen interactions as shaped by future climate: effects on biology, distribution, and implications for agriculture. *Insect Sci.* 24, 975–989. doi: 10.1111/1744-7917.12531
- Trivedi, P., Batista, B. D., Bazany, K. E., and Singh, B. K. (2022). Plant–microbiome interactions under a changing world: responses, consequences and perspectives. *New Phytol.* 234, 1951–1959. doi: 10.1111/nph.18016
- Tucker, C. J. (1979). Red and photographic infrared linear combinations for monitoring vegetation. *Remote Sens. Environ.* 8, 127–150. doi: 10.1016/0034-4257(79)90013-0
- Velásquez, A. C., Castroverde, C. D. M., and He, S. Y. (2018). Plant–pathogen warfare under changing climate conditions. *Curr. Biol.* 28, R619–R634. doi: 10.1016/j.cub.2018.03.054
- Yuan, L., Yan, P., Han, W., Huang, Y., Wang, B., Zhang, J., et al. (2019). Detection of anthracnose in tea plants based on hyperspectral imaging. *Comput. Electron. Agric.* 167, 105039. doi: 10.1016/j.compag.2019.105039
- Zarco-Tejada, P. J., Camino, C., Beck, P. S. A., Calderon, R., Hornero, A., Hernández-Clemente, R., et al. (2018). Prevalent symptoms of *Xylella fastidiosa* infection revealed in spectral plant-trait alterations. *Nat. Plants* 4, 432–439. doi: 10.1038/s41477-018-0189-7
- Zhan, J., Thrall, P. H., Papaix, J., Xie, L., and Burdon, J. J. (2015). Playing on a pathogen's weakness: using evolution to guide sustainable plant disease control strategies. *Annu. Rev. Phytopathol.* 53, 19–43. doi: 10.1146/annurev-phyto-080614-120040
- Zhang, C., Ren, H., Qin, Q., and Ersoy, O. K. (2017). A new narrow band vegetation index for characterizing the degree of vegetation stress due to copper: the copper stress vegetation index (CSVVI). *Remote Sens. Lett.* 8, 576–585. doi: 10.1080/2150704X.2017.1306135
- Zhang, D., Wang, Q., Lin, F., Yin, X., Gu, C., and Qiao, H. (2020). Development and evaluation of a new spectral disease index to detect wheat fusarium head blight using hyperspectral imaging. *Sensors* 20, 2260. doi: 10.3390/s20082260
- Zhang, J., Feng, X., Wu, Q., Yang, G., Tao, M., Yang, Y., et al. (2022). Rice bacterial blight resistant cultivar selection based on visible/near-infrared spectrum and deep learning. *Plant Methods* 18, 49. doi: 10.1186/s13007-022-00882-2
- Zhao, W., Yu, X., Jiao, C., Xu, C., Liu, Y., and Wu, G. (2021). Increased association between climate change and vegetation index variation promotes the coupling of dominant factors and vegetation growth. *Sci. Total Environ.* 767, 144669. doi: 10.1016/j.scitotenv.2020.144669

Conflict of Interest: The authors declare that the research was conducted in the absence of any commercial or financial relationships that could be construed as a potential conflict of interest.

Publisher's Note: All claims expressed in this article are solely those of the authors and do not necessarily represent those of their affiliated organizations, or those of the publisher, the editors and the reviewers. Any product that may be evaluated in this article, or claim that may be made by its manufacturer, is not guaranteed or endorsed by the publisher.

Copyright © 2022 Pineda, Pérez-Bueno and Barón. This is an open-access article distributed under the terms of the Creative Commons Attribution License (CC BY). The use, distribution or reproduction in other forums is permitted, provided the original author(s) and the copyright owner(s) are credited and that the original publication in this journal is cited, in accordance with accepted academic practice. No use, distribution or reproduction is permitted which does not comply with these terms.



Physiological Responses Manifested by Some Conventional Stress Parameters and Biophoton Emission in Winter Wheat as a Consequence of Cereal Leaf Beetle Infestation

Helga Lukács[†], Ildikó Jócsák[†], Katalin Somfalvi-Tóth and Sándor Keszthelyi^{*}

Institute of Agronomy, Hungarian University of Agriculture and Life Sciences, Kaposvár, Hungary

OPEN ACCESS

Edited by:

Nam-Hai Chua,
Temasek Life Sciences Laboratory,
Singapore

Reviewed by:

Szilvia Veres,
University of Debrecen, Hungary
Anabela Bernardes Da Silva,
Universidade de Lisboa, Portugal

*Correspondence:

Sándor Keszthelyi
keszthelyi.sandor@uni-mate.hu

[†]These authors have contributed
equally to this work

Specialty section:

This article was submitted to
Technical Advances in Plant Science,
a section of the journal
Frontiers in Plant Science

Received: 20 December 2021

Accepted: 09 May 2022

Published: 06 July 2022

Citation:

Lukács H, Jócsák I,
Somfalvi-Tóth K and Keszthelyi S
(2022) Physiological Responses
Manifested by Some Conventional
Stress Parameters and Biophoton
Emission in Winter Wheat as
a Consequence of Cereal Leaf Beetle
Infestation.
Front. Plant Sci. 13:839855.
doi: 10.3389/fpls.2022.839855

Oulema melanopus L. (Coleoptera: Chrysomelidae) is one of the most serious pests of winter wheat that causes peeling of the epidermis and tissue loss. The complex mapping of the physiological responses triggered by *O. melanopus* as a biotic stressor in winter wheat has not been fully explored with the help of non-invasive imaging and analytical assays, yet. The aim of the present work was to study the effect of *O. melanopus* on the physiological processes of winter wheat, especially on the extent of lipid peroxidation and antioxidant activity derived from tissue destruction, as well as photosynthetic ability. The results of the measurements enabled the identification of the antioxidant and lipid-oxidation-related physiological reactions, and they were reflected in the dynamics of non-invasive biophoton emissions. Our non-invasive approach pointed out that in the case of *O. melanopus* infestation the damage is manifested in tissue loss and the systemic signaling of the biotic stress may have reached other plant parts as well, which was confirmed by the results of antioxidant capacity measurements. These results indicate that the plant reacts to the biotic stress at a whole organizational level. We identified that the antioxidant and lipid-oxidation-related physiological reactions were reflected in the dynamics of two aspects of biophoton emission: delayed fluorescence and ultra-weak bioluminescence. Our research further supported that the non-invasive approach to stress assessment may complete and detail the traditional stress indicators.

Keywords: biotic stress, delayed fluorescence, leaf damage, lipid oxidation, non-invasive imaging, *Oulema melanopus*, *Triticum aestivum*, ultra-weak photon emission

INTRODUCTION

The cereal leaf beetle, *Oulema melanopus* L. (Coleoptera: Chrysomelidae) is one of the most serious pests of cereals, especially winter wheat. The species is originally a Mediterranean fauna element, but it has been introduced in the whole Palearctic and Nearctic regions (Lesage et al., 2007). The presence and damages of this pest are very significant due to the extended distributions of it and its host plants, which is confirmed by in-crop pesticide treatments against it by means of some residual (Tanaskovic et al., 2012) and other biological in-crop applications (Mazurkiewicz et al., 2021).

The typical symptoms of both adults and larvae on the host plant caused by cereal leaf beetle are thin and long lines, where initially the epidermis of the leaf has been peeled. Under uncontrolled circumstances, these damages can aggravate in several cases even when the majority part of photosynthetic surfaces could also impair (Bieńkowski, 2010). A field of cereals looks weathered and chloritized, but is never completely destroyed. First and second leaves of plants are mostly inhabited by larvae (Groll and Wetzel, 1984), where damage is usually no more than 40% of the total (Philips et al., 2011). In case the leaves of cereals are damaged by some biotic or abiotic factors, they generally lag behind in their development and have a decreased nutrient integration, occurred water management disturbance which eventually leads to quantitative and qualitative yield loss (Steinger et al., 2020).

The *in vivo* and non-invasive approach in plant stress detection has been considered to be of high importance, and the biophoton emission measurement is one of these techniques whose application has gained attention in the last two decades (Bodemer et al., 2000; Birtic et al., 2011; Kobayashi et al., 2014; Rui-Rui et al., 2015; Kamal and Komatsu, 2016; Kan et al., 2017; Prasad et al., 2017; Oros and Alves, 2018; Zhou et al., 2019; Jócsák et al., 2020; Chen et al., 2021; Pónya et al., 2021). Plants emit photons under certain circumstances, such as energy release from the photosynthetic apparatus of the non-utilized photons in the electron transport chain of photosystem II (PSII). This phenomenon is the delayed fluorescence (DF) that reflects the integrity state of the photosynthetic apparatus. DF only occurs in photosynthetic tissues with decay times from milliseconds to minutes (Bodemer et al., 2000). At this point, some of the electrons in the photosynthetic electron transport chain flow back to the reaction center, where the chlorophyll molecules reach an excited state and emit photons, such as red luminescence. Research revealed that DF decay kinetics are suitable for the *in vivo* determination of the homeostatic state of plants, nevertheless the extent of DF and its decay dynamics are suitable for stress assessment purposes (Goltsev et al., 2009; Sánchez-Moreiras et al., 2020). Bodemer et al. (2000) found that DF decay differs in 3-(3,4-dichlorophenyl)-1,1-dimethylurea (DCMU)-poisoned *Chlorella* spp. culture compared with healthy culture. Zhou et al. (2019) used DF to assess the effects of drought stress and salinity on barley, but to our knowledge, not for biotic stressors.

Another source of photon emission is related to the mitochondrial processes, the electron transport chain which emits photons through the relaxation of its excited components. Furthermore, the oxidation of lipids (Zhou et al., 2019) produces photon-emitting reactive oxygen species (ROS), such as triplet carbonyls and singlet oxygen, as well as reactive nitrogen species (RNS) (Bennett et al., 2005), the detection and visualization of which is possible with a highly sensitive charge-coupled device (CCD) (Jócsák et al., 2020).

These processes can be utilized in stress-related researches in plants since the strength of the signals of both DF and ultra-weak bioluminescence (UWLE) differ under the metabolic and tissue structure alterations triggered by stressors of either abiotic. UWLE was formerly used for the characterization of heat

stress (Kobayashi et al., 2014), flood (Kamal and Komatsu, 2016), osmotic stress (Rui-Rui et al., 2015), or cadmium (Jócsák et al., 2020), similarly to biotic stressors, such as leaf wound in *Spathiphyllum* (Oros and Alves, 2018) and *Arabidopsis* (Prasad et al., 2017), or the infestation of two spotted-spider mite (*Tetranychus urticae* L.) (Pónya et al., 2021). These investigations commonly utilize the possibility to differentiate among the effects of stressors *via* imaging and parameterizing of the bioluminescence measurements, but to this date there were no studies on the tissue alterations of *O. melanopus* on winter wheat.

Several studies carried out research on the effects of leaf impairment triggered by various factors on reproductive traits (Macedo et al., 2007; Shao et al., 2010; Steinger et al., 2020), nutrient content (Buráňová et al., 2015; Hamnér et al., 2017), and adaptive ability (Chen et al., 2016) of winter wheat. Nevertheless, the complex mapping of the physiological responses triggered by this biotic stressor in winter wheat has not been fully explored with the help of non-invasive imaging and analytical assays, yet. In this context, the aim of the present work was to study the effect of *O. melanopus* on the physiological processes of winter wheat, especially on the extent of lipid peroxidation and antioxidant activity derived from tissue destruction, as well as photosynthetic ability. In addition, we were also aimed to identify whether these physiological reactions are reflected in the dynamics of the non-invasive measurement, imaging, and analysis of biophoton emission.

MATERIALS AND METHODS

Sampling and Experimental Setting

To determine the physiological response of winter wheat caused by *O. melanopus*, mixed-gender adults were collected from an insecticide-free environment. The collection was carried out in early April 2021 in the Zselicszentpál area (Hungary, Somogy county, GPS coordinates: 46°30'84"N, 17°82'08"E). Adults were collected using an entomological sweeping net. The temperature range during the rearing of insects in the climate chamber was 20 ± 1°C. Relative humidity was maintained at 60 ± 5%, and photoperiodic setting was 18L:6D, corresponding to the insect vitality optimum (Mazurkiewicz et al., 2019).

In parallel, healthy, damage-free winter wheat seeds were sown in 19-cm diameter plastic pots (80 seeds/pot), which were placed in a Pol-Eco Apartura KK 1450 climate chamber (POL-EKO-APARATURA sp.j. ul. Kokoszycka 172C 44–300 Wodzisław Śląski, Poland) at 20°C, 120 μM m⁻² s⁻¹ light intensity for 16 h as daylight conditions and 16°C; 0 μM m⁻² s⁻¹ light intensity for 8 h as night conditions. When seedlings reached the 2–3 leaved stage, 5 pots continued to grow without changing their conditions, and 5 pots were treated with 20 images of the model beetles (*O. melanopus*) per pot under the isolator covered with well-ventilated textiles. Subsequently, after leaf damage, stress analytical evaluation and non-invasive imaging were taken on the sixth day of insect application to determine the extent of oxidative stress and its visual display. First, the non-invasive type of the measurements were conducted starting with ultra-weak photon emission (UPE). After the completion of the UPE measurement,

the soil plant analysis development (SPAD) measurement was done. The sequential order of the measurement was chosen to avoid any potential stress on the plants including even the light pressure that the usage of SPAD equipment poses on the leaf blades of the seedlings. Subsequently, the seedlings were sampled for the fresh/dry weight (DW) determination, ferric reducing antioxidant power (FRAP), and malondialdehyde (MDA) measurements when the whole above-ground part of the plants was used. The sampling method was the following: the above-ground part of the seedlings was cut into ~0.5-cm pieces. After that the pieces were mixed thoroughly to create an average sample for the fresh DW and for antioxidant capacity and lipid peroxidation measurement. The measurements were repeated three times per pot and the chemical analyses were measured in three parallels per each pot.

Tissue Damage Determination

Similar to other leaf analysis-based experiments (Sorgini et al., 2019; Zhang et al., 2019; Wang et al., 2020), damaged leaves were scanned to objectively determine leaf surface destruction. Five leaves were scanned and the number of pixels per each image were determined and the pixel number of the white background was subtracted, resulting in the pixel number of the whole leaf. Then, pixel points of differently colored areas were designated using the GIMP 2.10.8 software, and thus the pixels of damaged leaves were determined in the percentage of reduction of the photosynthesizing surface (**Figure 1**).

Determination of Fresh/Dry Weight Ratio

A total of 1 g of leaves were measured by an Ohaus Discovery DV215CDM (Ohaus Corporation 1.800.672.7722 7 Campus Drive, Suite 310 Parsippany, NJ 07054, United States) analytical scale weighing up to 5 decimal places. Subsequently, leaves were dried in a drying cabinet (Mettler SLE 600, Mettler GmbH + Co. KG, Aeussere Rittersbacher Strasse 38, D-91126 Schwabach, Germany) at 60°C for 24 h. Then the weight of the dried samples was recorded. Fresh/DW ratio was expressed as % and it was calculated by $[(w_x - w_0)/w_x] \times 100$, where the w_x is the DW and w_0 is the fresh weight.

Measurement of Lipid Peroxidation

Malondialdehyde content was determined by the thiobarbituric acid (TBA) reaction with some modifications to the original method of Heath and Packer (1968). Samples of 0.5 g were homogenized with 2 mL of 0.1% trichloroacetic acid (TCA) in cold mortars from which 1.8 mL was transferred to 2 mL microtubes with automatic pipettes. To this solution, 40 μ L of 20% butylated hydroxytoluene (BHT) in absolute ethanol was added to stop further lipid oxidation. The solutions were vortexed for 15 s and centrifuged at $18,600 \times g$ for 10 min at 4°C. From the clear supernatant, 0.25 mL was added to 1 mL of 20% TCA containing 0.5% TBA, gently mixed, and briefly centrifuged for 5 s. The solutions were incubated in a water bath (Julabo ED-5M) for 30 min at 96°C. The reactions were stopped by cooling the solutions immediately on ice followed by centrifugation at 10,000 rpm for 5 min. Absorbance at 532 and 600 nm was recorded using a SmartSpec™ Plus spectrophotometer,

and MDA concentration was calculated by subtracting the non-specific absorption at 600 nm from the absorption at 532 nm using an absorbance coefficient of extinction, $156 \text{ mM}^{-1} \text{ cm}^{-1}$. The results were expressed as nmol g^{-1} in DW.

Ferric Reducing Antioxidant Power Assay

Total antioxidant activity is measured by the modified assay of FRAP of Benzie and Strain (1999). The constituents of the FRAP reagent were the following: acetate buffer (300 mM pH 3.6), 2,4,6-tripyridyl-*s*-triazine (TPTZ) 10 mM in 40 mM HCl, and $\text{FeCl}_3 \cdot 6\text{H}_2\text{O}$ (20 mM). The working FRAP reagent was prepared by mixing acetate buffer, TPTZ, and $\text{FeCl}_3 \cdot 6\text{H}_2\text{O}$ in the ratio of 10:1:1 at the time of use. The standard solution was 10 mM ascorbic acid (AA) prepared freshly at the time of measurement. To 0.1 mL of the supernatant was added 2.9 mL of FRAP reagent in 5-mL screw cap centrifuge tubes, vortexed in a 37°C water bath (Julabo ED-5M, JULABO GmbH 77960 Seelbach/Germany) for 4 min, and the absorbance was measured at 593 nm against a blank with a BIORAD SmartSpec™ Plus spectrophotometer (Bio-Rad Ltd., 1000 Alfred Nobel Drive Hercules, CA 94547, United States). The FRAP values of the samples were determined were of AA equivalent ($\text{mmol AA equivalent g}^{-1} \text{ DW}$) based on the AA calibration curve, as the averages of three independent measurements (Benzie and Strain, 1999; Szöllösi and Szöllösi Varga, 2002).

Determination of Relative Chlorophyll Content

The SPAD index, a non-invasive measurement for relative chlorophyll content, was measured by reading 10 individual points on 10 seedlings of each treatment with SPAD (Soil Plant Analysis Development–SPAD-502; Konica Minolta Sensing Inc., Japan) equipment. In a wheat leaf with ~10–15 cm long, measurements were taken along the full length of each leaves approximately every 1–1.5 cm.

Non-invasive Imaging of Stress Reactions in Plant: Delayed Fluorescence and Ultra-Weak Photon Emission

For measuring UPE, the NightShade LB 985 In Vivo Plant Imaging System (Berthold Technologies GmbH & Co. KG, 75323 Bad Wildbad, Germany) equipped with a sensitive, thermoelectrically cooled slow-scan NighOwlcam CCD device has been employed. The instrument was controlled by the IndiGo™ 2.0.5.0. software. Intensities of light were converted into counts per second (cps) by using the controlling software. The exposure time was kept at 60 s using a pixel binning of 2×2 . During the duration of taking the images both the “background correction” and the “cosmic suppression” options were enabled to ensure the elimination of high-intensity pixels potentially caused by cosmic radiation. One pot for each treatment of the seedlings to be imaged was placed into the dark imaging box. In the first part of the measurement, DF signal was measured immediately after placing the pots in the dark chamber for



FIGURE 1 | Leaf surface destruction caused by *O. melanopus*. Five leaves were scanned and the pixels of damaged leaves were determined in the percentage of reduction of the photosynthesizing surface.

10 min. Thereafter, the samples were continued to be kept in dark to provide sufficient time for dark adaptation, and from the 30th minute, for the pots spent in the dark, bioluminescence data was also acquired for 10 min.

Statistical Analysis

One-way ANOVA was assumed to be applied to determine the differences between samples. To do so, two conditions must be fulfilled. Firstly, the samples must be normally distributed, secondly the samples must have homoscedasticity. Shapiro–Wilks test was used to determine the distribution. The null hypothesis was that the sample is normally distributed, which was accepted when the *p*-value exceeded 0.05. Depending on the distribution, i.e., the sample is normally or not-normally distributed, two methods were applied to calculate the homogeneity of variances: Bartlett test for normal distributions and Flinger–Killeen non-parametric test for non-normal distributions. When the distribution of the two samples was different, the less robust Flinger–Killeen test was used to determine homoscedasticity. Since the results of testing conditions supported the application of one-way ANOVA only in the case of fresh/DW data, Wilcoxon-test was used to prove the differences between samples for the rest of the measured parameters. When both samples (control + infested) have the same distribution, the type of homoscedasticity test is unequivocal. In the case of MDA, the Flinger–Killeen test was chosen with higher reliability for determining the homogeneity of variance.

Statistical Outputs of Homogenous Distribution and Significant Differences of the Examined Stress Indices

Table 1 presents the results of the statistical analysis of the measured physiological parameters, such as relative chlorophyll content, antioxidant capacity, and lipid oxidation; and biophoton emission-related parameters: DF and UPE.

The results of the Shapiro–Wilks test indicated that UPE and MDA values showed normal distribution but the test of the parameters (SPAD, FRAP, and DF) did not. Furthermore since the variance of the samples was so pronounced, the ANOVA was only applicable for the statistical analysis of

the fresh/DW ratio values. According to the results for one-way ANOVA and Wilcoxon tests, all parameters showed significant differences (Table 1; more detailed results in Supplementary Material 1).

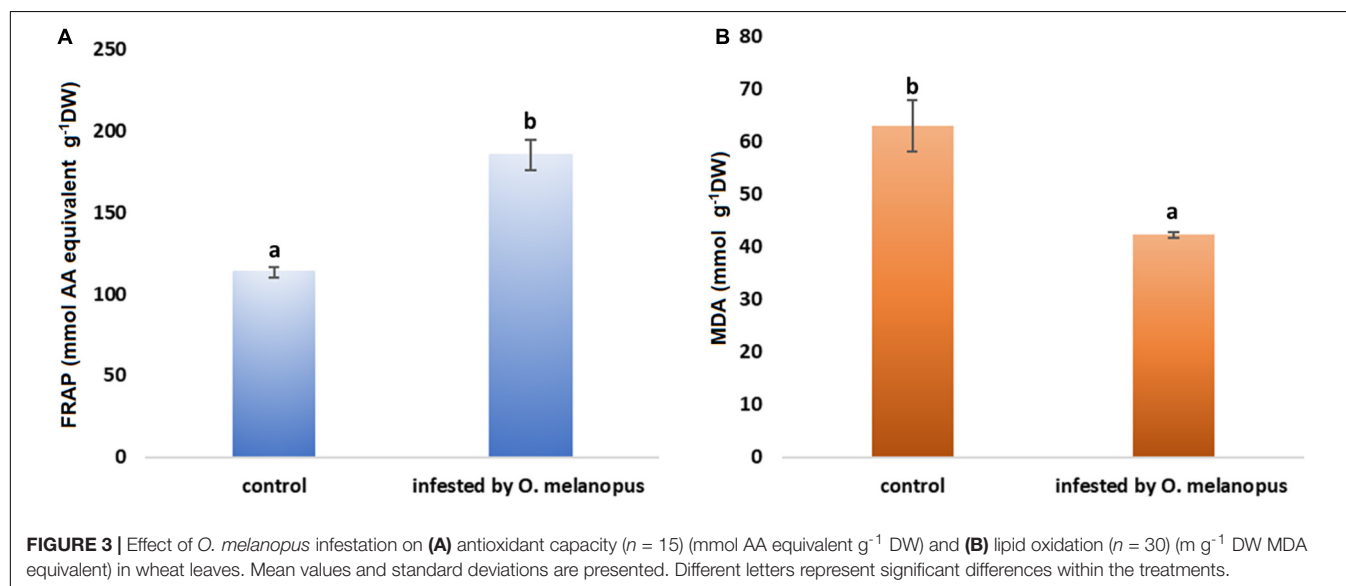
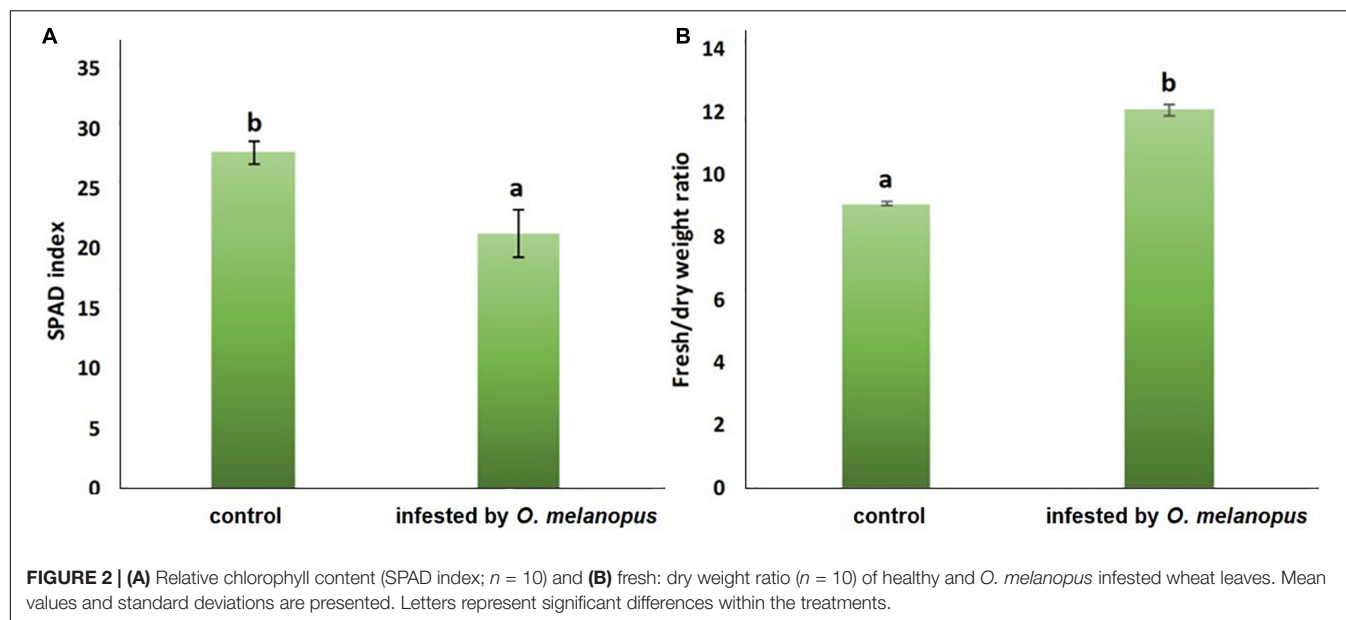
RESULTS

Changes in the Photosynthetic Tissue and Relative Chlorophyll Content

The damage of *O. melanopus* showed serious tissue damage during the 6 days of infestation. Mean of leaf surface destruction caused by *O. melanopus* was $12.280 \pm 1.323\%$, the average of five investigated leaves (Figure 1). The results of the relative chlorophyll content (SPAD index) and fresh/DW ratio are presented in Figure 2. The infestation of *O. melanopus* manifested as a significant decrease in the SPAD index

TABLE 1 | Statistical analysis of the examined stress parameters in damaged wheat caused by *O. melanopus*: ANOVA analysis of fresh/dry weight ratio and Wilcoxon tests of relative chlorophyll content (SPAD), antioxidant capacity (FRAP), lipid oxidation (MDA), delayed fluorescence (DF), and ultra-weak photon emission (UPE).

Summary		Results of ANOVA for fresh/dry weight ratio				
Groups	Count	Sum	Average	Variance		
Control	5	45.318	9.063	0.017		
<i>O. melanopus</i> infested	5	60.354	12.071	0.106		
Analysis of variance						
Source of variation	SS	df	MS	F	p-value	F critical value
Between groups	22.608	1	22.608	384.891	5.8×10^{-8}	5.317
Within groups	0.495	8	0.061			
Total	23.104	9				
p-value		Results of Wilcoxon test				
MDA	1.478×10^{-7}	There are significant differences between groups				
FRAP	3.383×10^{-6}					
SPAD	2.200×10^{-16}					
UPE	2.200×10^{-17}					
DF	1.520×10^{-3}					



from 28.2 to 20.6. The Shapiro–Wilks normality test showed that the SPAD data did not show normal distribution ($p > 0.05$), and thus was analyzed with the Wilcoxon test (Table 1) and revealed a significant ($p = 2.2 \times 10^{-16}$) 27% decrease in total (Figure 2). The normality test resulted in normal distribution for fresh/dry mass ratio, and consequently the one-way ANOVA was used and proved a significant ($p = 5.84 \times 10^{-16}$) increase of *O. melanopus* infested wheat: 24.9%, from 9.064 to 12.071.

Changes in Antioxidant Capacity and Lipid Oxidation

The FRAP values reflect that part of the overall antioxidant state of plant tissues that is possible to determine with the

method of ferric reducing antioxidant capacity. The Shapiro–Wilks normality test resulted that the antioxidant capacity data did not show normal distribution ($p > 0.05$), and the Wilcoxon test (Table 1) was used which showed that the increase was significant ($p = 3.383 \times 10^{-6}$) in the FRAP values of the *O. melanopus*-infested wheat samples (11.43 μg AA equivalent g⁻¹ FW) compared with the healthy leaves (6.92 μg AA equivalent g⁻¹ FW; Figure 3).

Lipid oxidation is a stress indicator of membrane structure- and function-related processes, such as the damage caused by *O. melanopus*. The results of MDA level measurement showed the decrease in MDA content in the tissues of *O. melanopus*-infested wheat. The Shapiro–Wilks normality test resulted that the lipid oxidation data did not show normal distribution ($p > 0.05$), thus the data were analyzed with the Wilcoxon test (Table 1),

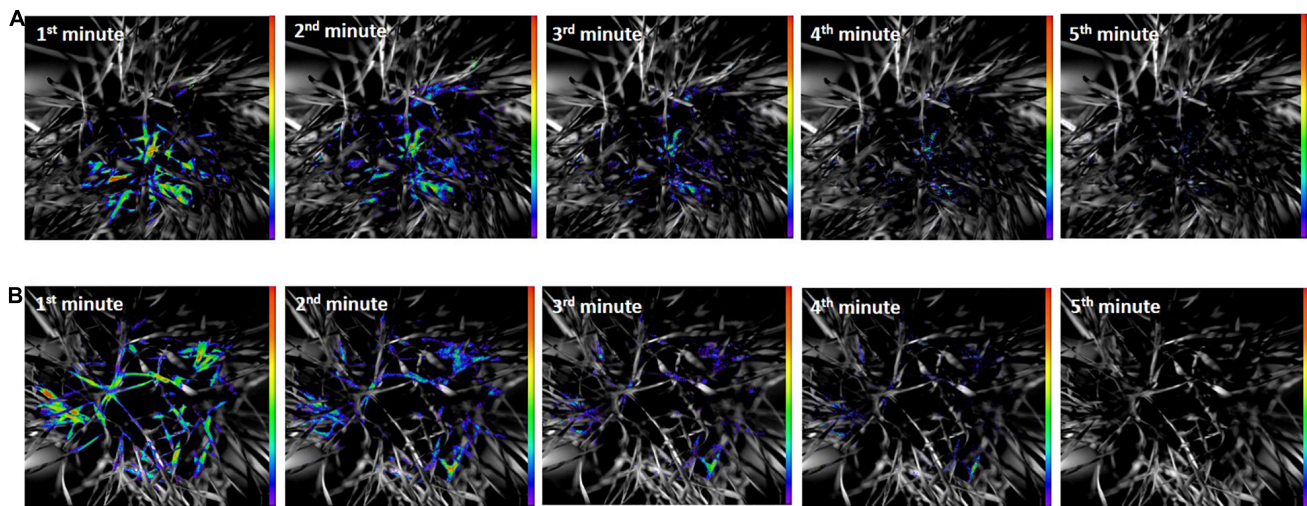


FIGURE 4 | (A) Delayed fluorescence decay of healthy and **(B)** *O. melanopus* infested leaves during the first 5 min of the measurement. The intensity of color bar shows signal intensity detected by the equipment and converted into a scale of color intensity via IndiGo™ 2.0.5.0. software.

which proved that the decrease in MDA content was significant ($p = 1.478 \times 10^{-7}$). The control MDA level was $16.91 \text{ nM g}^{-1} \text{ FW}$ and the *O. melanopus*-infested level dropped to $14.87 \text{ nM g}^{-1} \text{ FW}$, i.e., 13%, which is a statistically significant ($p \leq 0.05$) decrease induced by the biotic stressor: *O. melanopus*.

Changes in the Sum of Overall Count per Second Values of Delayed Fluorescence and Lipid Oxidation Related Bioluminescence

The results of DF decay of healthy and *O. melanopus* infested leaves during the first 5 min of the measurement are presented in **Figure 4**. The images reveal a distinct difference between the healthy and stressed samples. The DF signal of the healthy plants was highly intensive during the first minute of the measurement in both sample types, which was depicted as intensive orange and red pseudocolors in the images. A decreasing tendency of signals was obtained from the second minute of the measurement in healthy plants; however, the photon emission signals arising from the *O. melanopus* infested leaves were lower as it was indicated by the pseudocolors. This tendency continued during the fourth minute and the photon emission reached low intensity by the end of the fifth minute.

Figure 5 shows the results of UPE both in the original size and due to UPE in an enlarged version of typical areas with considerable UPE signals. The images of UPE signals showed differences between the healthy and *O. melanopus*-infested samples, and according to the pseudocolor intensity, it indicated an increase of stressed plants in all the first 5 min of the measurement compared to that of the healthy samples.

Besides the acquisition of images, the fluorescence data were also analyzed to derive objective parameters for a precise evaluation of the putative trends and tendencies depicted by the images. DF measurements were followed consecutively by UWLE

data acquisition after a completed dark adaptation period of 30 min (**Figure 6**). This measurement setup enabled a distinction between photosynthetic- and lipid-oxidation-related processes. The Shapiro–Wilks normality test resulted that the both DF and UPE data did not show normal distribution ($p > 0.05$), and thus was analyzed with Wilcoxon test.

The presented data are the summary of all photon counts during 10 min of data acquisition for both DF and UPE (**Figure 6**). The results show an opposite trend of the changes in DF and UPE indicated before in the presented images (**Figures 4, 5**), but both types of measurements resulted in a significant difference in the sum of overall photon count per second values. However, in the case of DF, the infestation of *O. melanopus* resulted in a 250% significant decrease ($p = 0.001152$) compared to the control plants from 1.72×10^6 to 6.88×10^5 . On the contrary, the direction of the changes of UPE was opposite to that of the DF values and resulted in a significant ($p = 2.2 \times 10^{-17}$) increase (**Table 1**). UPE was more than 300% higher than in the case of the control from 7499.688 to 2197.424 (**Figure 6**).

Changes of Overall Count per Second Values of Delayed Fluorescence and Lipid Oxidation-Related Bioluminescence

To identify the temporal dynamics of *O. melanopus*-induced changes in photon emission, the time-course analysis of the detected photon signals was also conducted besides the evaluation of the sum of the overall cps values. Therefore, both DF and the consequent UPE were measured for 10 min.

The results show a distinctive trend in both the phenomena. DF has a highly sharp decreasing tendency in first few minutes of the measurement, and from the fifth minute the data decays toward zero, but does not reach it. After dark adaptation was

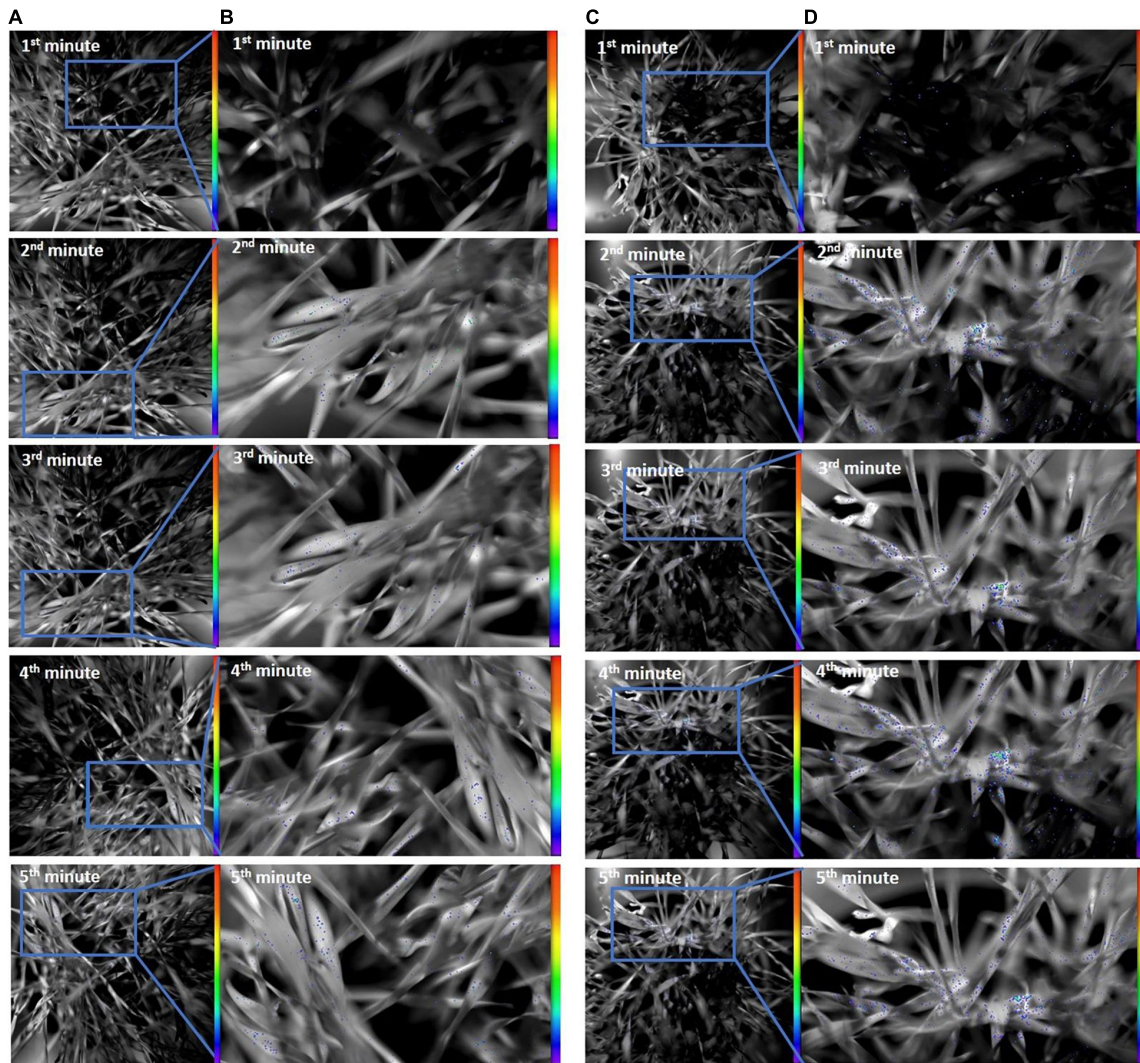


FIGURE 5 | Ultra-weak photon emission of (A: original; B: enlarged) healthy and (C: original; D: enlarged) *O. melanopus*-infested leaves during the first 5 min of measurement. The intensity of color bar shows signal intensity detected by the equipment and converted into a scale of color intensity via IndiGo™ 2.0.5.0. software.

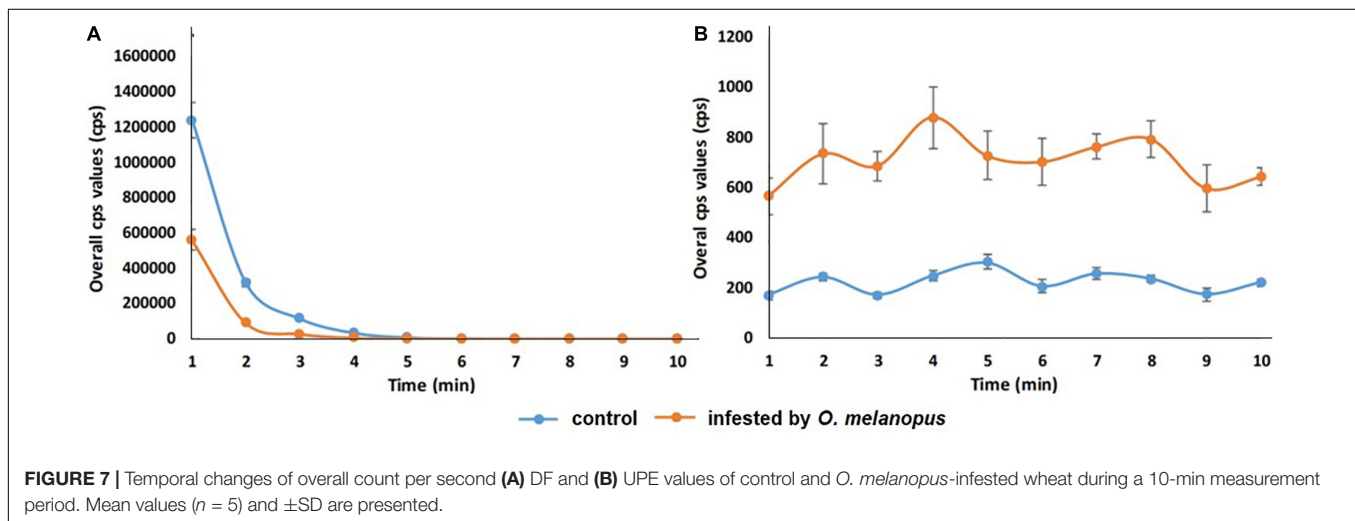
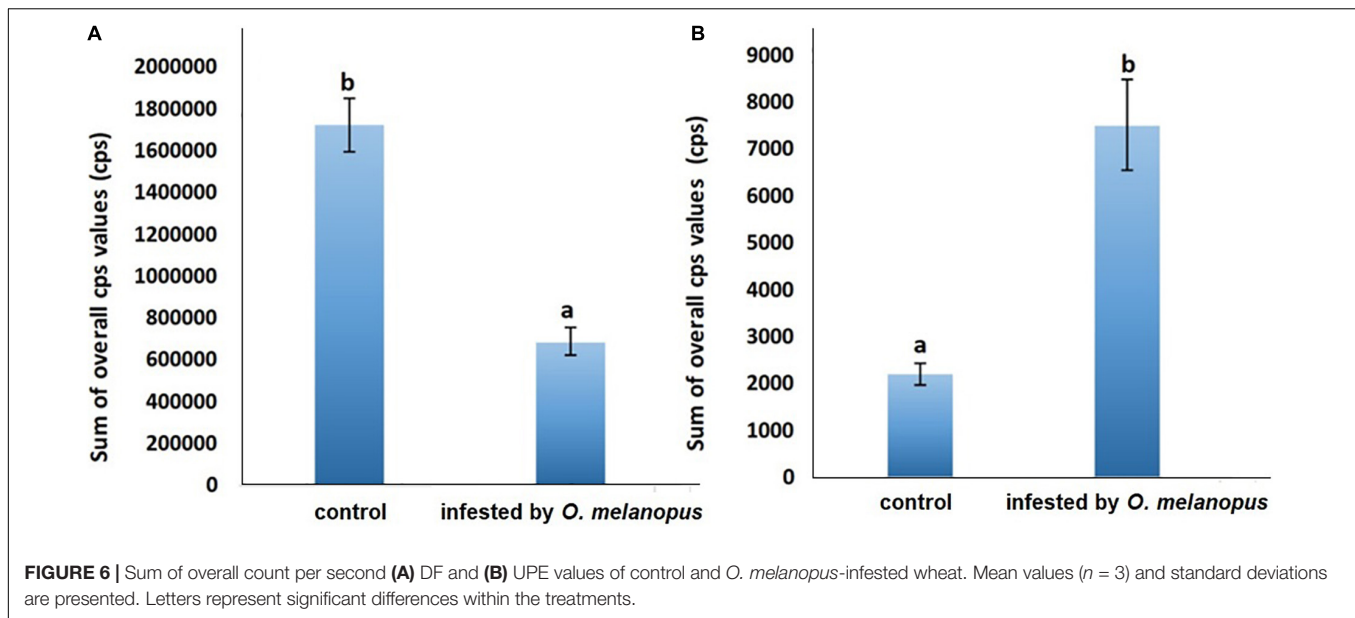
completed, the UPE values reached a quasi-steady state that significantly differed according to the sample types for the whole duration of our observations (Figure 7).

DISCUSSION

The indication of this research was to visualize and gain parameters of the physiological effects regarding key metabolic pathways, such as photosynthesis and lipid oxidation affected by a biotic stressor, *O. melanopus*. Firstly, the tissue structure disruption was determined and analyzed by pixel distinction, and the damage was objectively determined as it was done several times before (Bieńkowski, 2010; Philips et al., 2011). After 6 days of *O. melanopus* infestation, there was tissue loss that was manifested in the decrease of chlorophyll content, which

was indicated by the SPAD index and increased fresh/dry ratio values. The phenomenon of tissue loss is a typical symptom of *O. melanopus* infestation and it has been documented that the extent of the loss of photosynthetic tissue could be so pronounced that photosynthetic efficiency drops (Olfert et al., 2004). The results of relative chlorophyll content and fresh/DW ratios indicate mechanisms of altered photosynthetic system and tissue integrity.

The analytical investigations of antioxidant capacity and lipid oxidation, along with the measurements of DF and UPE, provided a deeper insight not only into the underlying mechanisms, but in the case of the two latter to the temporal dynamics as well. The dynamics of DF and UPE were opposite in their trends and the scale of the emitted photons were distinct. These changes and differences originated from the distinct nature of the underlying processes.



In the initial phase of photon emission measurement right after the placement of the plants into the dark chamber, the processes of the photosynthesis started to gradually cease, resulting in DF. It is well-known that dark-adaptation-related phenomenon of photosynthesizing tissues, the decay of which takes more time, if the plant is in an intact and healthy condition. However, DF ceases more rapidly if the plant is under the effect of a stressor of any kind, in our case a biotic one: *O. melanopus*. DF decay kinetics were proved to be proper tools for stress assessment purposes, mostly in the case of abiotic stressors (Bodemer et al., 2000; Kan et al., 2017; Zhou et al., 2019; Chen et al., 2021), and according to our results, for a biotic stressor as well. In accordance to the findings of Hennecke and Br  x (2012), our results also point to a relationship between UPE and the oxidation state. These authors showed that a healthy plant emits DF considerably more intensively, than a stressed one as opposed to the phenomenon of UPE; when the photon-emission

is a sign of the presence of stressors, and thus stressed plants emit photons more intensively than non-stressed ones (Hennecke and Br  x, 2012; J  cs  k et al., 2020).

The results of tissue loss quantification showed the destructive effect of *O. melanopus* infestation, which obviously included the loss of membrane system as well, that consequently reflected as a decrease in the colorimetric oxidative stress assessment assay. That is why according to our results, MDA content, as an indicator of lipid oxidation processes, did not completely prove to be suitable for the proper characterization of the degree of stress induced by *O. melanopus*. This phenomenon can be explained by the type of damage because the investigated impairment was triggered by a pest, which typically causes direct destruction of plant tissues. As opposed to some hiding lifestyle, arthropod pests, such as cereal leaf miner (*Agromyza nigrociliata* Hendel, 1931), which trigger an indirect covertly damage which will not occurred on the host plant (not directly affecting the examined

photosynthetic tissues, Roik and Walczak, 2012). The reason for this may lie in the fact that the chewing action leads to tissue loss, which may interfere with the results of the analytical measurement. The formation of TBA reactive substances that are possible to detect *via* the formation of malondialdehyde are mostly linked to membrane lipids, the degradation of which leads to an accelerating reaction of oxidized forms of lipid membranes. In the case of *O. melanopus*, however, it was not possible to properly quantify as a consequence of tissue loss.

Nevertheless, the results of UPE enlightened this problem from a different angle. Until recently, the recognition of ROS as detrimental products of plant metabolism has been toned since it was confirmed that ROS act as signaling molecules with the capability of mediating environmental signals toward the genetic functionality of the cells leading to stress-responsive alteration of gene expression (Sewelam et al., 2016). These environmental signals include both abiotic stressors and biotic ones, such as pathogens, herbivores, and wounding, as we have experienced during our research work, since ROS are curial components of host defense responses leading to the increased synthesis of antioxidants (Bhatia et al., 2004), as indicated in our research work by the increased FRAP values. Different kinds of ROS, such as hydrogen peroxide, superoxide, or singlet oxygen combined with their production sites, such as plastids, cytosol, peroxisome, or apoplast, trigger distinctive physiological and molecular responses (Gadjev et al., 2006). One way of fulfilling these signaling roles is that ROS such as H_2O_2 is able to diffuse through cells *via* aquaporin (Borisova et al., 2012), leading to systemic responses (Sewelam et al., 2016). Although in the case of *O. melanopus* infestation, the damage is manifested in tissue loss, the systemic signaling of the biotic stress may reach other plant parts as well, which led to increased UPE signals. The results of antioxidant capacity measurements further strengthen this idea, since, despite the tissue loss, the non-enzymatic ferric reducing antioxidant capacity significantly increased, indicating that the plant reacts to the biotic stress on a whole organizational level.

Based on the present results, the changes of the healthy and *O. melanopus* infested wheat showed that the insect causes severe damage to wheat that was visualized (Figure 4) and parametrized (Figure 5) through the detection of photon signals emitted by the plants. Furthermore, our results indicate the possibility to capture the signaling mechanisms of infestation, since despite the lowered MDA values, the overall photon emission increased in *O. melanopus* infested leaves. However, the specific nature of the formed ROS will be a consequent step on the path of elucidating the concrete signaling pathways of *O. melanopus* infestation, some of which are independent of the direct lipid oxidation processes that the decrease of MDA level indicated along with the increase of overall biophoton emission signals. As a consequence of the investigations, it was confirmed that DF and UPE are both suitable for non-invasive way of biotic stress detection, triggered by *O. melanopus*. We identified that the antioxidant and lipid-oxidation-related physiological reactions were reflected in the dynamics of non-invasive biophoton emissions: both in the decay of DF and the consequent differences in UPE signals. Our research further supported that the non-invasive approach of stress assessment may complete and detail the traditional stress

indicators, leading to a more precise estimation of the outcome of biotic stressors, even on a large scale.

Moreover, the physiological response of the damaged target organisms triggered by various stressors can be objectively judged by the application of this non-destructive imaging, which at the same time creates further research opportunities for the cognition of the inner stress advancement in the later vegetation stage of the same living plant material. In additional future perspectives, these non-destructive methods should play an increasingly determinative role in the research of plant-arthropod interaction to the more perfect discovery of hidden biological progressions. Eventually, the results originating from these methods can unequivocally contribute to both the development of integrated plant protection and the realization of reasonable pesticide utilization.

DATA AVAILABILITY STATEMENT

The raw data supporting the conclusions of this article will be made available by the authors, without undue reservation.

AUTHOR CONTRIBUTIONS

SK and IJ designed the methodology and wrote the manuscript. SK collected the research materials and set the experimental insect–host samples. IJ, KS-T, and HL performed the laboratory experiments, served the research, and performed the data evaluation. All authors read and approved the manuscript.

FUNDING

This research was funded by projects of the European Union, the European Social Fund: EFOP-3.6.3.-VEKOP-16-2017-00008 and EFOP-3.6.3.-VEKOP-16-2017-00005, as well as competition (ÚNKP/2020/2021) of the New National Excellence Program of the Ministry for Innovation and Technology from the source of the National Research, Development and Innovation Fund.

ACKNOWLEDGMENTS

We are thankful to Krisztián Lukács for his kind editing advice and help during manuscript preparation. We are also thankful for the Molecular Biology Laboratory of HUAL Institute of Animal Sciences, Kaposvár Campus, where the stress analytical measurements were completed.

SUPPLEMENTARY MATERIAL

The Supplementary Material for this article can be found online at: <https://www.frontiersin.org/articles/10.3389/fpls.2022.839855/full#supplementary-material>

REFERENCES

- Bennett, D. M., Mehta, M., and Grant, M. (2005). Biophoton imaging: a non-destructive method for assaying R gene responses. *Mol. Plant Microbe Interact.* 18, 95–102. doi: 10.1094/MPMI-18-0095
- Benzie, I. F. F., and Strain, J. J. (1999). Ferric reducing/ antioxidant power assay: direct measure of total antioxidant activity of biological fluids and modified version for simultaneous measurement of total antioxidant power and ascorbic acid concentration. *Meth. Enzymol.* 299, 15–23. doi: 10.1016/S0076-6879(99)99005-5
- Bhatia, S., Kapoor, H. C., and Lodha, M. L. (2004). Modification of antioxidant status of host cell in response to bougainvillea antiviral proteins. *J. Plant Biochem. Biotechnol.* 13, 113–118. doi: 10.1007/BF03263204
- Bieńkowski, A. O. (2010). Feeding behaviour of leaf beetles (Coleoptera, Chrysomelidae). *Entomol. Rev.* 90, 1–10. doi: 10.1134/S001387381001001X
- Birtic, S., Ksas, B., Genty, B., Mueller, M. J., Triantaphylidēs, C., and Havaux, M. (2011). Using spontaneous photon emission to image lipid oxidation patterns in plant tissues. *Plant J.* 67, 1103–1115. doi: 10.1111/j.1365-313X.2011.04646.x
- Bodemer, U., Gerhardt, V., Yacobi, Y. Z., Zohary, Z., Friedrich, G., and Pohlmann, M. (2000). Phytoplankton abundance and composition of freshwaters systems determined by DF excitation spectroscopy and conventional methods. *Arch. Hydrobiol. Spec. Issues Adv. Limnol.* 55, 101–120.
- Borisova, M. M., Kozuleva, M. A., Rudenko, N. N., Naydov, I. A., Klenina, I. B., and Ivanov, B. N. (2012). Photosynthetic electron flow to oxygen and diffusion of hydrogen peroxide through the chloroplast envelope via aquaporins. *Biochim. Biophys. Acta* 1817, 1314–1321. doi: 10.1016/j.bbabi.2012.02.036
- Buránová, Š., Černý, J., Kulhanek, M., Vašák, F., and Balík, J. (2015). Influence of mineral and organic fertilizers on yield and nitrogen efficiency of winter wheat. *Int. J. Plant Prod.* 9, 257–272. doi: 10.22069/IJPP.2015.2047
- Chen, W., Jia, B., Chen, J., Feng, Y., Li, Y., Chen, M., et al. (2021). Effects of different planting densities on photosynthesis in maize determined via prompt fluorescence, delayed fluorescence and P700 signals. *Plants Basel* 10:276. doi: 10.3390/plants10020276
- Chen, Y., Zhang, Z., Wang, P., Song, X., Wei, X., and Tao, F. (2016). Identifying the impact of multi-hazards on crop yield – a case for heat stress and dry stress on winter wheat yield in northern China. *Eur. J. Agron.* 73, 55–63. doi: 10.1016/j.eja.2015.10.009
- Gadjev, I., Vanderauwera, S., Gechev, T. S., Laloi, C., Minkov, I. N., Shulaev, V., et al. (2006). Transcriptomic footprints disclose specificity of reactive oxygen species signaling. in *Arabidopsis*. *Plant Physiol.* 141, 436–445. doi: 10.1104/pp.106.078717
- Goltsev, V., Zaharieva, I., Chernev, P., and Strasser, R. (2009). Delayed chlorophyll fluorescence as a monitor for physiological state of photosynthetic apparatus. *Biotechn. Biotechn. Equip.* 23, 452–457. doi: 10.1080/13102818.2009.10818461
- Groll, E., and Wetzl, T. (1984). Studies on population structure of cereal leaf beetle (*Oulema* spp.). *J. Appl. Entomol.* 97, 113–124.
- Hamner, K., Weih, M., Eriksson, J., and Kirchmann, H. (2017). Influence of nitrogen supply on macro- and micronutrient accumulation during growth of winter wheat. *Field Crops Res.* 213, 118–129. doi: 10.1038/s41598-018-37838-3
- Heath, R. L., and Packer, L. (1968). Photoperoxidation in isolated chloroplasts. I. Kinetics and stoichiometry of fatty acid peroxidation. *Arch. Biochem. Biophys.* 125, 189–198. doi: 10.1016/0003-9861(68)90654-1
- Hennecke, M., and Brück, A. (2012). *Measurement of Biophoton Emission in Plants – An Alternative Monitoring System for Stress Factors*. Berthold Technologies, AN985_005v1. Baden Württemberg: Berthold Technologies GmbH & Co.KG.
- Jócsák, I., Malgwi, I., Rabnec, G., Szegő, A., Varga-Visi, É., Végvári, G., et al. (2020). Effect of cadmium stress on certain physiological parameters, antioxidative enzyme activities and biophoton emission of leaves in barley (*Hordeum vulgare* L.) seedlings. *PLoS One* 15:e0240470. doi: 10.1371/journal.pone.0240470
- Kamal, A. H. M., and Komatsu, S. (2016). Proteins involved in biophoton emission and flooding-stress responses in soybean under light and dark conditions. *Mol. Biol. Rep.* 43:73. doi: 10.1007/s11033-0153940-4
- Kan, X., Ren, J. J., Chen, T. T., Cui, M., Li, C. L., Zhou, R. H., et al. (2017). Effects of salinity on photosynthesis in maize probed by prompt fluorescence, delayed fluorescence and P700 signals. *Environ. Exp. Bot.* 140, 56–64. doi: 10.1016/j.envexpbot.2017.05.019
- Kobayashi, K., Okabe, H., Kawano, S., Hidaka, Y., and Hara, K. (2014). Biophoton emission induced by heat shock. *PLoS One* 9:e105700. doi: 10.1371/journal.pone.0105700
- Lesage, L., Dobesberger, E. J., and Majka, C. G. (2007). Introduced leaf beetles of the Maritime provinces, 2: the cereal leaf beetle *Oulema melanopus* (Linnaeus) (Coleoptera: Chrysomelidae). *Proc. Entomol. Soc. Wash.* 109, 286–294.
- Macedo, T. B., Peterson, R. K., Dausz, C. L., and Weaver, D. K. (2007). Photosynthetic responses of wheat, *Triticum aestivum* L., to defoliation patterns on individual leaves. *Environ. Entomol.* 36, 602–608. doi: 10.1603/0046-225x(2007)36[602:prowta]2.0.co;2
- Mazurkiewicz, A., Jakubowska, M., Tumialis, D., Bocianowski, J., and Roik, K. (2021). Foliar application of entomopathogenic nematodes against cereal leaf beetle *Oulema melanopus* L. (Coleoptera: Chrysomelidae) on wheat. *Agronomy* 11:1662. doi: 10.3390/agronomy11081662
- Mazurkiewicz, A., Jakubowska, M., Tumialis, D., Skrzecz, I., Roik, K., Pezowicz, E., et al. (2019). Laboratory bioassay of selected entomopathogenic nematodes as mortality factors of *Oulema melanopus* (Coleoptera: Chrysomelidae). *J. Entomol. Sci.* 54, 390–400. doi: 10.18474/JES18-118
- Olfert, O., Weiss, R. M., Woods, S., Philip, H., and Dosdall, L. (2004). Potential distribution and relative abundance of an invasive cereal crop pest, *Oulema melanopus* L. (Coleoptera: Chrysomelidae). *Can. Entomol.* 36, 277–287. doi: 10.4039/N03-073
- Oros, C. L., and Alves, F. (2018). Leaf wound induced ultraweak photon emission is suppressed under anoxic stress: observations of under aerobic and anaerobic conditions using novel in vivo methodology. *PLoS One* 13:e0198962. doi: 10.1371/journal.pone.0198962
- Philips, C. R., Herbert, D. A., Kuhar, T. P., Reisig, D. D., Thomason, W. E., and Malone, S. (2011). Fifty years of cereal leaf beetle in the U.S.: an update on its biology, management, and current research. *J. Integr. Pest Manag.* 2, 1–5. doi: 10.1603/ipm11014
- Pónya, Z., Jócsák, I., and Keszthelyi, S. (2021). Detection of ultra-weak photon emission in sunflower (*Helianthus annuus* L.) infested by two spotted-spider mite, *Tetranychus urticae* Koch-research note. *Phytoparasitica* 50, 43–50. doi: 10.1007/s12600-021-00938-4
- Prasad, A., Sedláčková, M., Kale, R. S., and Pospíšil, P. (2017). Lipoxxygenase in singlet oxygen generation as a response to wounding: in vivo imaging in *Arabidopsis thaliana*. *Sci. Rep.* 7:9831. doi: 10.1038/s41598-017-09758-1
- Roik, K., and Walczak, F. (2012). Harmfulness of leaf miners (Agromyzidae) on winter wheat plantations in Poland. *J. Agric. Sci. Technol.* A 2:417.
- Rui-Rui, H., Gang, X., Kai, L., and Yan-Yan, Z. (2015). Effect of extremely low frequency pulsed electric field on delayed biophoton emission of cells in maize seedling root under osmotic stress. *Acta Photon. Sin.* 44:0517003. doi: 10.3788/gzxb20154405.0517003
- Sánchez-Moreiras, A. M., Graña, E., Reigosa, M. J., and Araniti, F. (2020). Imaging of chlorophyll a fluorescence in natural compound-induced stress detection. *Front. Plant Sci.* 11:583590. doi: 10.3389/fpls.2020.583590
- Sewelam, N., Kazan, K., and Schenk, P. M. (2016). Global Plant stress signaling: reactive oxygen species at the cross-road. *Front. Plant Sci.* 7:187. doi: 10.3389/fpls.2016.00187
- Shao, L., Zhang, X., Hideki, A., Tsuji, W., and Chen, S. (2010). Effects of defoliation on grain yield and water use of winter wheat. *J. Agric. Sci.* 148, 191–204. doi: 10.1017/S0021859609990542
- Sorgini, C. A., Barrios-Perez, I., Brown, P. J., and Ainsworth, E. A. (2019). Examining genetic variation in maize inbreds and mapping oxidative stress response QTL in B73-Mo17 nearly isogenic lines. *Front. Sustain. Food Syst.* 3:51. doi: 10.3389/fsufs.2019.00051
- Steinger, T., Klotzli, F., and Ramseier, H. (2020). Experimental assessment of the economic injury level of the cereal leaf beetle (Coleoptera: Chrysomelidae) in winter wheat. *J. Econ. Entomol.* 113, 1823–1830. doi: 10.1093/jeet/toaa080
- Szöllösi, R., and Szöllösi Varga, I. (2002). Total antioxidant power in some species of Labiatae. (Adaptation of FRAP method). *Acta Biol. Szeged.* 46, 125–127.
- Tanaskovic, S., Madic, M., Durovic, D., Knezavic, D., and Vukajlovic, F. (2012). Susceptibility of cereal leaf beetle (*Oulema melanopa*) in winter wheat to various foliar insecticides in Western Serbia Region. *Rom. Agric. Res.* 29, 361–366.
- Wang, X., Li, Z., Liu, B., Zhou, H., Elmongy, M. S., and Xia, Y. (2020). Combined proteome and transcriptome analysis of heat-primed azalea reveals new insights into plant heat acclimation memory. *Front. Plant Sci.* 11:1278. doi: 10.3389/fpls.2020.01278

- Zhang, Y., Fu, Y., Fan, J., Li, Q., Francis, F., and Chen, J. (2019). Comparative transcriptome and histological analyses of wheat in response to phytotoxic aphid *Schizaphis graminum* and non-phytotoxic aphid *Sitobion avenae* feeding. *BMC Plant Biol.* 19:547. doi: 10.1186/s12870-019-2148-5
- Zhou, R., Kan, X., Chen, J., Hua, H., Li, Y., Ren, J., et al. (2019). Drought-induced changes in photosynthetic electron transport in maize probed by prompt fluorescence, delayed fluorescence, P700 and cyclic electron flow signals. *Environ. Exp. Bot.* 158, 51–62. doi: 10.1016/j.envexpbot.2018.11.005

Conflict of Interest: The authors declare that the research was conducted in the absence of any commercial or financial relationships that could be construed as a potential conflict of interest.

Publisher's Note: All claims expressed in this article are solely those of the authors and do not necessarily represent those of their affiliated organizations, or those of the publisher, the editors and the reviewers. Any product that may be evaluated in this article, or claim that may be made by its manufacturer, is not guaranteed or endorsed by the publisher.

Copyright © 2022 Lukács, Jócsák, Somfalvi-Tóth and Keszthelyi. This is an open-access article distributed under the terms of the Creative Commons Attribution License (CC BY). The use, distribution or reproduction in other forums is permitted, provided the original author(s) and the copyright owner(s) are credited and that the original publication in this journal is cited, in accordance with accepted academic practice. No use, distribution or reproduction is permitted which does not comply with these terms.



OPEN ACCESS

EDITED BY
Dimitrios Koutsouras,
Max Planck Institute for Polymer
Research, Germany

REVIEWED BY
Zhonglin Shang,
Hebei Normal University, China
Alessia Candeo,
Politecnico di Milano, Italy

*CORRESPONDENCE
Eleni Stavrinidou
eleni.stavrinidou@liu.se

SPECIALTY SECTION
This article was submitted to
Technical Advances in Plant Science,
a section of the journal
Frontiers in Plant Science

RECEIVED 08 April 2022
ACCEPTED 30 June 2022
PUBLISHED 22 July 2022

CITATION
Armada-Moreira A, Diacci C, Dar AM,
Berggren M, Simon DT and
Stavrinidou E (2022) Benchmarking
organic electrochemical transistors
for plant electrophysiology.
Front. Plant Sci. 13:916120.
doi: 10.3389/fpls.2022.916120

COPYRIGHT
© 2022 Armada-Moreira, Diacci, Dar,
Berggren, Simon and Stavrinidou. This
is an open-access article distributed
under the terms of the [Creative
Commons Attribution License \(CC BY\)](#).
The use, distribution or reproduction in
other forums is permitted, provided
the original author(s) and the copyright
owner(s) are credited and that the
original publication in this journal is
cited, in accordance with accepted
academic practice. No use, distribution
or reproduction is permitted which
does not comply with these terms.

Benchmarking organic electrochemical transistors for plant electrophysiology

Adam Armada-Moreira ¹, Chiara Diacci ¹,
Abdul Manan Dar ¹, Magnus Berggren ^{1,2},
Daniel T. Simon ¹ and Eleni Stavrinidou ^{1,2,3*}

¹Laboratory of Organic Electronics, Department of Science and Technology, Linköping University, Norrköping, Sweden, ²Wallenberg Wood Science Center, Department of Science and Technology, Linköping University, Norrköping, Sweden, ³Umeå Plant Science Centre, Department of Forest Genetics and Plant Physiology, Swedish University of Agricultural Sciences, Umeå, Sweden

Plants are able to sense and respond to a myriad of external stimuli, using different signal transduction pathways, including electrical signaling. The ability to monitor plant responses is essential not only for fundamental plant science, but also to gain knowledge on how to interface plants with technology. Still, the field of plant electrophysiology remains rather unexplored when compared to its animal counterpart. Indeed, most studies continue to rely on invasive techniques or on bulky inorganic electrodes that oftentimes are not ideal for stable integration with plant tissues. On the other hand, few studies have proposed novel approaches to monitor plant signals, based on non-invasive conformable electrodes or even organic transistors. Organic electrochemical transistors (OECTs) are particularly promising for electrophysiology as they are inherently amplification devices, they operate at low voltages, can be miniaturized, and be fabricated in flexible and conformable substrates. Thus, in this study, we characterize OECTs as viable tools to measure plant electrical signals, comparing them to the performance of the current standard, Ag/AgCl electrodes. For that, we focused on two widely studied plant signals: the Venus flytrap (VFT) action potentials elicited by mechanical stimulation of its sensitive trigger hairs, and the wound response of *Arabidopsis thaliana*. We found that OECTs are able to record these signals without distortion and with the same resolution as Ag/AgCl electrodes and that they offer a major advantage in terms of signal noise, which allow them to be used in field conditions. This work establishes these organic bioelectronic devices as non-invasive tools to monitor plant signaling that can provide insight into plant processes in their natural environment.

KEYWORDS

plant electrophysiology, organic electrochemical transistor (OECT), organic electronics, Venus flytrap, *Arabidopsis thaliana*

Introduction

Plants are the most widespread organisms on the planet, representing the majority of Earth's biomass (Bar-On et al., 2018). These organisms, the product of millions of years of evolution, are highly developed biosensors, capable of monitoring a myriad of external stimuli such as water availability, temperature, and soil composition, among

many others (Yu et al., 2021). The stimuli sensed by plants are transduced *via* different signaling pathways, including hydraulic, chemical, and electrical signals (Choi et al., 2016). While the importance of electrical signals for plant signaling has been widely reported, it is a very complex phenomenon, as recently reviewed by Klejchova et al. (2021). Indeed, when considering biological signaling, electrical signals do not occur isolated. Instead, they are intrinsically related to ionic transients and plant hormonal responses (Farmer et al., 2020; Suda et al., 2020; Grenzi et al., 2021). Monitoring plant responses to various stimuli in high resolution will not only advance our knowledge on basic plant science, which can be used to improve plant acclimation to biotic and abiotic stress, but also provide a handle for interfacing plants with technology, aiding the development of advanced and green technology.

A notable example of plant electrical signaling is the Venus flytrap (VFT) action potential. These fast action potentials are one of the most well-known plant signals, having been first described in the 19th century (Burdon-Sanderson, 1873). These electrical signals, characterized by an “all-or-nothing” response, fast propagation, and constant amplitude (Gilroy and Trewavas, 2001), are elicited by the activation of mechanosensitive trigger cells and lead to the sudden closure of the trap, allowing for the digestion of small insects and arachnids (Hedrich and Neher, 2018).

In another relevant example, a different and slower type of plant signals is the slow wave potential. This signal, induced by external stressors, consists of a transient depolarization of irregular shape and duration (Vodeneev et al., 2015), and has been associated with the activation of cellular defense mechanisms, such as the synthesis of the defense-related hormone jasmonate (Mousavi et al., 2013; Nguyen et al., 2018) and ethylene (Marhavý et al., 2019). While these signals have an intracellular origin, it is possible to monitor them by changes in the leaf surface potential, which are called wound-activated surface potential changes (WASPs) (Mousavi et al., 2013).

Overall, even though this signaling mechanism is quite widespread and carries an enormous amount of information, the field of plant electrophysiology is still in its infancy when compared to its animal counterpart. Most common techniques in this field are restricted to cumbersome data acquisition setups and laboratory conditions, requiring the use of Faraday cages and physical immobilization of plants (Dufil et al., 2021). Other techniques, especially applied to intracellular recordings, are not suitable for monitoring environmental electrophysiological responses, since they wound the plant and consequentially alter their electrical behavior (Salvador-Recatalà et al., 2014). Thus, there is a need to develop new tools that allow *in situ* monitoring in a non-invasive manner.

Recent reviews in plant electrophysiology highlight the need for this field to be considered as an interdisciplinary challenge in order to attain significant knowledge (Li et al., 2021). Indeed, the development of devices and materials capable of interfacing with

plants, for a myriad of functions, has been increasing, bringing together material science and plant biology (Lew et al., 2020; Dufil et al., 2021). A new contender to advance this effort is the field of organic electronics.

While the current standard for plant electrophysiology remains Ag/AgCl electrodes (Volkov et al., 2011, 2019), or other metal inorganic electrodes (Rhodes et al., 1996; Brette and Destexhe, 2012; Chatterjee et al., 2015, 2017; Ríos-Rojas et al., 2015; Kim et al., 2018; Chong et al., 2019), novel approaches from the realm of organic electronics are now being explored. These include self-adhering poly(3,4-ethylenedioxythiophene) polystyrene sulfonate (PEDOT:PSS)-based surface electrodes, which are flexible and can thus conform to plant anatomy (Meder et al., 2021), as well as the development of an ionic electrode capable of interfacing hairy plant tissues with metal electrodes that allows for a significant improvement in signal-to-noise ratio (SNR) and maintains signal stability regardless of plant movements (Luo et al., 2021).

Among organic electronic devices, the organic electrochemical transistor (OECT) represents an optimal platform for interfacing living systems (Nawaz et al., 2021) as it operates at low voltages and has an electrolyte as an integral part of the device. The OECT is a three terminal device where source and drain electrodes are connected by a thin layer of an organic (semi) conductor, while the gate electrode is separated by an electrolyte. Typically, in OECTs, organic mixed-ionic electronic conductors (OMIECs), such as the conjugated polymer PEDOT:PSS, are used as the channel material (Stavriniidou et al., 2013; Paulsen et al., 2020). Upon bias application between gate and source, ions are driven from the electrolyte into the channel resulting in doping or dedoping of the OMIEC layer and therefore changing the channel conductivity (Rivnay et al., 2018). The ions can penetrate throughout the OMIEC layer volume, giving rise to a volumetric capacitance, which allows high signal amplification, and thus operation in low voltage regime (Proctor et al., 2016; Volkov et al., 2017). Additionally, OECTs can be fabricated on ultra-thin, flexible and conformable substrates (Khodagholy et al., 2013; Cea et al., 2020). They are miniaturized devices with high amplification and ensure high SNR, essential characteristics for *in vivo* recording.

One of the first uses of OECTs as tools for electrophysiology was described by Malliaras and colleagues the authors developed OECT arrays to successfully measure epileptiform discharges in rat brain, demonstrating higher SNR compared to surface electrodes (Khodagholy et al., 2013). The application of OECTs as tools for mammalian electrophysiology has become increasingly widespread and validated, with several innovations in both surface and implantable technologies in the last years (Bai et al., 2019). On the other hand, reports on the use of OECTs for plant monitoring and electrophysiology are much sparser in literature. Two notable examples focus on the successful use of enzymatically functionalized OECTs for long-term monitoring of glucose and sucrose in trees (Diaci et al., 2021) and on a first

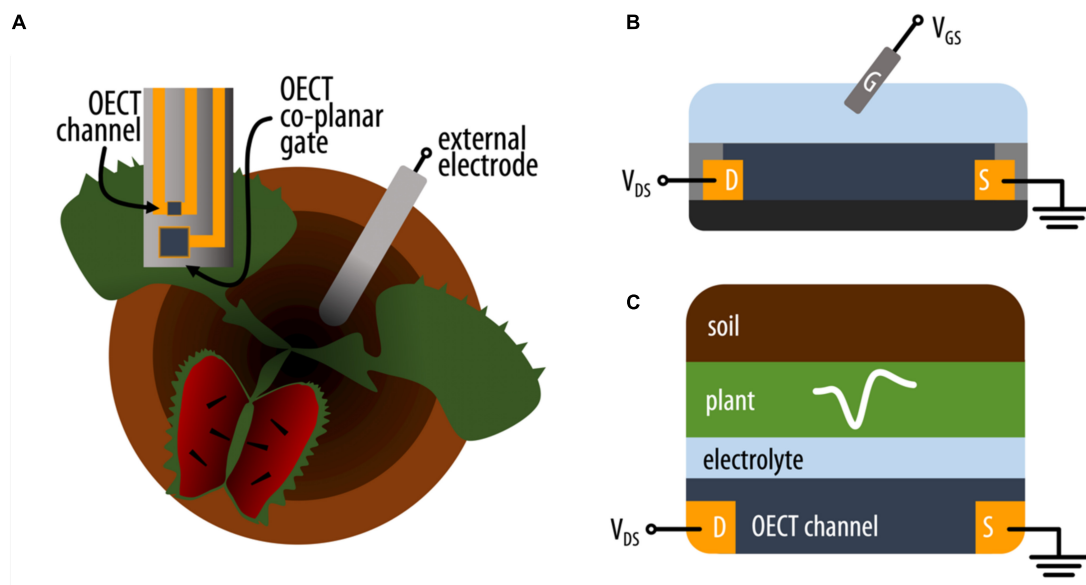


FIGURE 1

(A) Schematic representation of the experimental setup where an OECT (top view) with channel and co-planar gate electrode is attached on the lobe of the VFT and an external electrode is placed in the soil. (B) Schematic (side) representation of an OECT where the current in the conducting polymer channel between source (S) and drain (D) electrodes is modulated by a voltage applied between the electrolyte and channel via a gate electrode (G). (C) Simplified schematic of the various electrolytic components interfacing with the OECT channel on the VFT lobe (side view).

demonstration of OECTs as tools for plant electrophysiology, where these devices were able to record the action potential of the carnivorous VFT, with increased SNR compared to Ag/AgCl electrodes (Bischak et al., 2020). However, this last example is only a demonstration that does not fully characterize these devices as electrophysiological tools.

Thus, we aimed to benchmark OECTs for plant electrophysiology (Figure 1) using two well-known plant electrical signals as biological models: action potential of VFT and wound response of *Arabidopsis thaliana*. In this work, we compare OECTs to a PEDOT:PSS electrode (equivalent in size and composition) and to a Ag/AgCl electrode (the current gold standard for plant electrophysiology). We also compare the performance of the different devices in less controlled conditions, where a Faraday cage is not used to minimize external noise.

Materials and methods

Organic electrochemical transistor fabrication

A 125 μm -thick polyethylene naphthalate foil (PEN, Teonex Q65HA, Peutz Folien GmbH, Germany) was cut in a circular substrate with 10.2 cm diameter. The substrate was cleaned with water and acetone, then vacuum baked for 90 s at 120°C.

Layers of 2 nm of chromium (Cr), for a better metal adhesion, and 50 nm gold (Au) were evaporated onto the clean surface. Photolithography (MA/BM6 Mask Aligner, SUSS MicroTec SE, Germany) and a Shipley 1805 positive resist were used to pattern the gold contacts, wiring, channel and gate/s. The substrate was then wet etched in I_2/KI solution for Au, and with a chromium etcher for the chromium layer while the remaining resist was stripped with acetone. A thin film of PEDOT:PSS (Clevios PH1000) mixture with 5% (v/v) ethylene glycol (EG), 1% (v/v) (3-Glycidyloxypropyl)trimethoxysilane (GOPS), and dodecylbenzenesulfonic acid (1 drop per 5 ml) was deposited by spin-coating and patterned using a Shipley 1813 positive resist. The PEDOT:PSS layer was then dry etched with CF_4/O_2 reactive ions, in order to create channels and gates. The remaining resist was stripped again with acetone. In the end, the substrate was encapsulated, to ensure wire insulation with SU-8 2010 (MicroChem) and openings on the active areas were created by wet etching with developer mr-Dev 600 (Microresist Technology). Chemicals were used as received from Sigma-Aldrich unless stated otherwise.

Plant material

Venus flytrap plants were acquired from Plantagen (Sweden) and kept in a greenhouse with controlled temperature and humidity (22/18°C light/dark, 12 h photoperiod, 60%

relative humidity), and watered with DI water. *A. thaliana* were seeded and grown in a controlled growth chamber (IntellusUltra Connect, Percival Scientific, IA, United States), with a 12 h photoperiod, at 18°C and 80% relative humidity.

Electrophysiological recording of Venus flytrap action potentials

Venus flytrap plants were removed from the greenhouse and left to acclimate to the experimental room for at least 10 min before experiments were performed. For Ag/AgCl and PEDOT:PSS electrode recordings, the electrode was placed on a trap, using Signa gel as an electrolyte, and a Ag/AgCl electrode in the soil was used as a reference electrode. One trigger hair was touched using a wooden stick after acquiring 20 s of baseline recording (no activity). Data was acquired using a InfiniiVision 3000A X-Series digital oscilloscope (Keysight Technologies, CA, United States). For OECT recordings, the source-drain channel of the OECT was placed on a trap, using Signa gel as an electrolyte, and a Ag/AgCl electrode in soil was used as the gate electrode. The device was biased with $V_{DS} = -0.4$ V and $V_{GS} = 0.3$ V. Data was recorded using a Keithley SourceMeter 2612B (Tektronix, OR, United States) and custom Labview software. For recordings inside the Faraday cage, an extra Ag/AgCl electrode was placed in soil and connected to the Faraday cage, in order to ground the whole system.

Electrophysiological recording of *Arabidopsis thaliana* laser-induced wound response

Five-week-old *A. thaliana* plants were removed from the growth chamber and left to acclimate in the recording setup for c. 20 min. At this point, a Ag/AgCl electrode was placed in the damp soil and one of the recording devices was interfaced with one of the leaves, using a 10 mM KCl and 20 wt% PVA in DI water solution as an electrolyte. For Ag/AgCl and PEDOT:PSS electrode recordings, the Ag/AgCl electrode in soil was used as the reference electrode. For OECT recordings, this electrode was used as the gate electrode and the device was biased with $V_{DS} = -0.4$ V and $V_{GS} = 0.3$ V, which resulted in the highest signal amplification (Supplementary Figure 1). For recordings inside the Faraday cage, an additional Ag/AgCl electrode was placed in the soil, and used to ground the whole system. A 7 W laser (450 nm, Sainsmart, KA, United States) was focused on the main vein 1 cm distally away from the recording device, in order to induce a wound with 1 mm diameter. Baseline activity was recorded for at least 20 s before the laser was triggered. The laser was active for 1 s at 50% laser power, which was sufficient to burn through the leaf. Wound response was recorded for at least 100 s following the laser action, using a Keithley SourceMeter

2612B for OECT or a ME2100-System (Multichannel Systems, Germany) for the Ag/AgCl or PEDOT:PSS electrodes.

Data analysis

All experiments were performed with at least three different plants. A detailed characterization of the full datasets can be found in Supplementary Table 1. Data acquired from the digital oscilloscope and the ME2100-System were downsampled to 100 Hz to match that acquired by the Keithley SourceMeter. For VFT action potentials, data were filtered with an analog Bessel highpass filter (0.01 Hz, order 2) to remove baseline wandering. The different action potentials were aligned by their steepest deflection point (local minima of the first temporal derivative). If more than one action potential was recorded in one trap, these were averaged and considered to be $N = 1$. For *A. thaliana* data, the different WASPs were aligned by the timing of laser on. For parameter quantification, all waveforms were smoothed with a gaussian averaging filter, with window size of 200 ms and 500 ms, for VFT and *A. thaliana*, respectively. Data were analyzed with custom Matlab code and GraphPad Prism.

Results

Organic electrochemical transistor configuration for plant electrophysiology

The motivation of using OECTs as plant electrophysiological tools relies in the inherent amplification of the OECT device where small changes on the gate voltage are translated as larger changes in the OECT channel current. We hypothesize that the plant signals can act as voltage modulators at the gate electrode. In order to optimize the electrophysiology recordings with OECTs, different OECT configurations were tested using the VFT as the model system. In all configurations, the OECT channel was placed on a lobe of one of the traps, using the commercially available Signa gel as the interfacing electrolyte. However, we explored three different ways to interface the gate electrode: (i) a PEDOT:PSS electrode was placed on the same lobe with the OECT channel and was electrolytically connected to plant and channel (Figure 2A and Supplementary Figure 2 for alternative representation); (ii) a Ag/AgCl electrode was attached on a non-electrically active plant surface (Figure 2B); and (iii) a Ag/AgCl electrode was immersed in the soil (Figure 2C). In order to study the modulation of the OECT channel current via the gate electrode, we measured the transfer curve in the various configuration ($V_{DS} = -0.4$ V and V_{GS} from -0.2 to 0.6 V). The transfer curves showed that efficient modulation of the channel current occurs in all configurations with slightly improved modulation when the gate electrode is

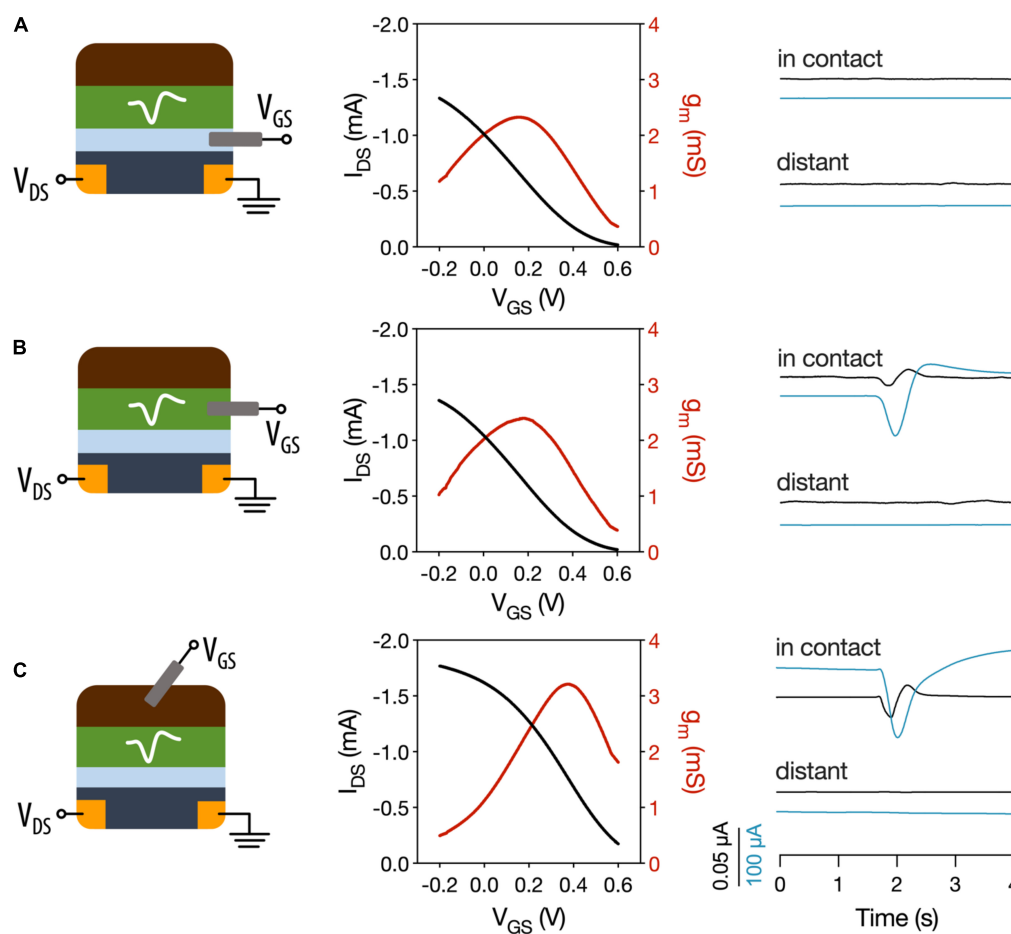


FIGURE 2

Different OECT configurations for plant electrophysiology. OECT transfer curves and transconductance and VFT action potentials recorded with (A) OECT co-planar PEDOT:PSS gate electrode. (B) Ag/AgCl electrode in a non-electrically active plant tissue as the gate electrode. (C) Ag/AgCl electrode in soil used as gate electrode. In contact refers to a recording of the trap where the OECT channel is attached. Distant corresponds to recordings in which a different trap was stimulated. Black trace: gate current. Blue trace: drain current.

placed in the soil. Quantitatively, this is shown by the maximum transconductance value that corresponds to the derivative of the transfer curve and hence the change on the channel current due to a change on the gate potential.

Then, action potentials were recorded in the different configurations, by stimulating either the trap in which the OECT channel was attached or a distant trap. First, we observed that when a co-planar gate electrode is used, we were not able to record the action potential. In contrast when the gate electrode is placed on the plant or in the soil the action potential can be recorded as a change in the OECT channel current. These results show that, in order to efficiently record the plant signals, the plant must be part of the OECT circuit with gate voltage being applied between plant and OECT channel either *via* soil or a non-electrically active plant tissue. Furthermore, the action potential was recorded only when the OECT channel was attached on the stimulated trap and not at a distant one. This shows that the plant signal is local and does not travel across the

whole plant, which is in line with previous reports (Volkov et al., 2007; Suda et al., 2020) that show that the signal does not travel beyond the petiole.

Thus, for the following experiments, a Ag/AgCl electrode placed in the soil was used as the gate electrode of the device, which is in line with previous studies of OECTs as electrophysiological tools in plants (Bischak et al., 2020) and in mammalian brain (Khodagholy et al., 2013).

Fast plant signals: Venus flytrap action potentials

Given their importance in the field of plant electrophysiology, the VFT action potentials were chosen to first investigate the use of OECTs as tools in plant electrophysiology. The OECT channel was placed on a trap, using the commercially available Signa gel as the interfacing electrolyte and a Ag/AgCl

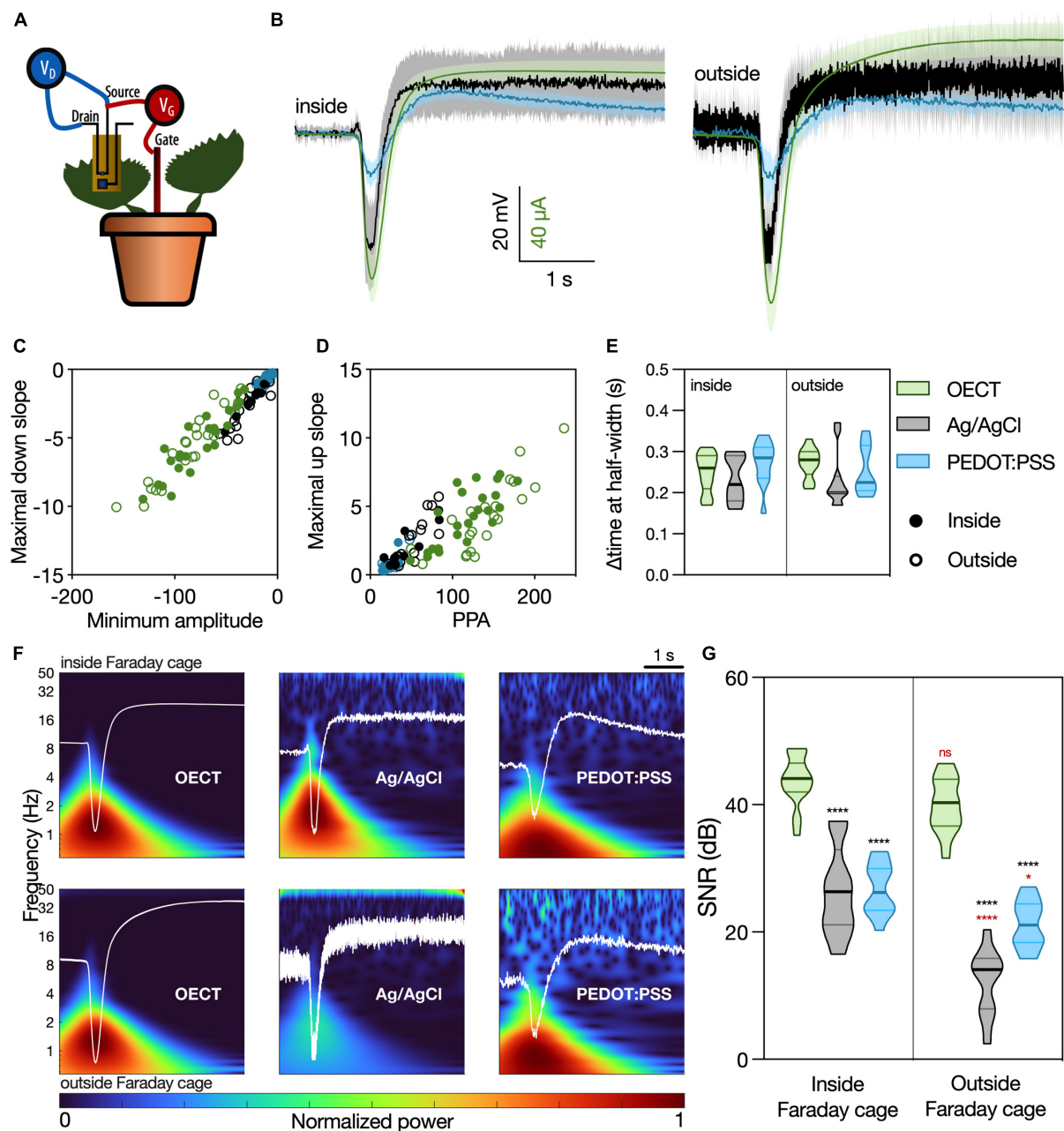


FIGURE 3

Venus flytrap (VFT) action potentials recorded with different devices. (A) Schematic representation of the recording setup. The OECT channel was attached to a lobe of a VFT trap, using a commercially available electrophysiology gel as an electrolyte. Gate voltage (V_{GS}) was applied between source and a Ag/AgCl electrode in the soil. Drain voltage (V_{DS}) was applied across the OECT channel. For recordings with Ag/AgCl or PEDOT:PSS electrodes, the recording electrodes were attached on the trap, and a Ag/AgCl electrode in soil was used as reference. For the recordings inside of the Faraday cage, an extra Ag/AgCl electrode was placed in the soil and used to ground the whole system. (B) Average waveform acquired with the different devices: OECT (green trace), Ag/AgCl electrode (black trace), and PEDOT:PSS electrode (blue trace). Data represented as mean \pm 95% CI. $N = 9-24$ traps from 4 to 10 independent plants. Quantification of the (C) linear relationship between the maximal down slope and minimum amplitude; (D) linear relationship between the maximal up slope and the peak-to-peak amplitude of the action potential; (E) duration of action potential, characterized by the delta time at half-width. No significant differences were found in any of the considered parameters, using a simple linear regression and statistical comparison of slopes [for panels (C,D)] or a two-way ANOVA considering the parameters "device" and "Faraday cage" [for panel (E)]. (F) Time-frequency domain normalized magnitude scalograms of the average waveform acquired with the different devices, inside and outside of the Faraday cage. The average waveform is overlaid in white. (G) Quantification of SNR for the different waveforms, $N = 9-20$. * $p < 0.05$, **** $p < 0.0001$ using a two-way ANOVA considering the parameters "device" and "Faraday cage," followed by Tukey's multiple comparison test. In black, differences within the same "cage" condition; in red, differences in the same "device" condition. In (E,G), data are represented in violin plots, where the width of the shaded area represents the proportion of data points at any given zone, with lines at median and quartiles.

electrode in the soil as the gate electrode (Figure 3A) as described in the previous section. For recordings with Ag/AgCl and PEDOT:PSS electrodes, the recording electrode was placed on the trap and a Ag/AgCl electrode in soil as the reference electrode. The average waveforms recorded with the different devices (Figure 3B) show high correlation among themselves (Supplementary Table 2), which implies that the OECT performed similarly to the electrodes in recording this phenomenon. Importantly, three different OECTs were used to record these signals, to ensure proper reproducibility among devices. The waveforms obtained from the different OECTs were equivalent (Supplementary Figure 3).

Different waveform parameters were quantified in order to compare in detail the similarity of the different devices in resolving this signal (Supplementary Figure 4). The relationship between the peak signal amplitude and slope (Figure 3C), as well as the relationship between the peak-to-peak amplitude (PPA) and the slope between signal minimum and maximum (Figure 3D), showed similar behavior for all considered devices, both inside and outside of the Faraday cage (Supplementary Table 3). Furthermore, the time interval at half-width was considered to quantify the temporal component of the action potential (Figure 3E). Again, no differences were found between the different devices. Taking all these quantifications into account, we conclude that the OECT is as efficient in recording the VFT action potentials as the current standard for plant electrophysiology (Ag/AgCl electrode) and the similar in size and composition PEDOT:PSS electrode.

Signal-to-noise ratio of the different devices was then calculated as the peak amplitude of the waveform (current or voltage) divided by the standard deviation of the baseline recording (no stimulation), a widely used method of computing SNR found in literature (Khodagholy et al., 2013; Bischak et al., 2020). In Figure 3F, the time-frequency domain of the average waveforms, a visual representation of the signal power at each frequency band and timepoint, shows a much clearer signal resolution for OECT compared to other devices, especially outside of the Faraday cage. This finding is then quantified in Figure 3G, where the OECT shows a higher SNR compared to the other devices, either inside or outside of the Faraday cage. Additionally, the signal recorded with the OECT does not get disrupted outside of the Faraday cage, unlike those recorded with the Ag/AgCl and PEDOT:PSS electrodes.

Slow plant signals: *Arabidopsis thaliana* wound-activated surface potential changes

As previously mentioned, slow wave potentials and, more specifically, wound-induced potential changes, are also relevant plant electrical signals. However, when studying wounding responses, it is very common to find signal artifacts that arise

from the movement induced by the wounding stimulus and not the wounding itself (Degli Agosti, 2014; Luo et al., 2021). Thus, to avoid such artifacts, we chose to study a laser-induced wound response. Since WASP intensity weakens with increasing distance from site of wounding (Stahlberg et al., 2006), we chose to record 1 cm away, in the proximal direction, from the laser and keep that distance constant. Furthermore, it is also known that WASP amplitude depends on the intensity of the stimulus (Vodeneev et al., 2015), which led us to set the 7 W laser at a constant intensity of 50% of laser power for 1 s.

The different devices were then interfaced with an *A. thaliana* leaf, using a solution of 10 mM KCl and 20 wt% PVA in DI water as electrolyte. Similarly to the experimental setup for recording the VFT action potential, a Ag/AgCl electrode in the soil was used as the gate electrode for OECT recordings or as the reference electrode for PEDOT:PSS and Ag/AgCl electrode recordings. For recordings inside of the Faraday cage, an additional Ag/AgCl electrode was placed in the soil and used to ground the system. The average waveform recorded with the different devices (Figure 4A) is similar to those found in literature (Mousavi et al., 2013; Nguyen et al., 2018). Additionally, as previously described in literature, we did not find any spontaneous electrical activity unrelated to the wounding signal (Mousavi et al., 2013). All the obtained waveforms share a high correlation between the different devices and also between different Faraday cage conditions (Supplementary Table 2), implying that the OECT can resolve this biological signal as efficiently as the other electrodes. While the signals are similar, the WASPs present an increased variability in their response tail. This was already expected since WASP architecture is known to be quite variable, even within the same plant species (Mousavi et al., 2013; Farmer et al., 2020), which accounts for the increased error associated with the duration/recovery of the recorded WASPs.

In order to finely quantify the waveform similarity between the different devices, two different WASP parameters were considered, as depicted in Figure 4B. These were latency (Figure 4C, the time interval between wounding and reaching half peak amplitude) and duration (Figure 4D, the time interval between wounding and recovery, measured as the zero in the signal's first temporal derivative). Using a two-way ANOVA considering the parameters "device" and "Faraday cage," no statistically significant differences were found between the different samples. Considering the waveform and parameter similarity, it is possible to conclude that the OECT is able to record this biological signal in a manner comparable to the current gold standard.

Finally, the frequency content of the different waveforms was investigated (Figure 4E) and a SNR analysis was performed (Figure 4F). When the recordings were performed inside of the Faraday cage, all the devices show a similar time-frequency spectrum, although it is possible to observe some noise at around 40 Hz caused by the laser in the spectrums of the

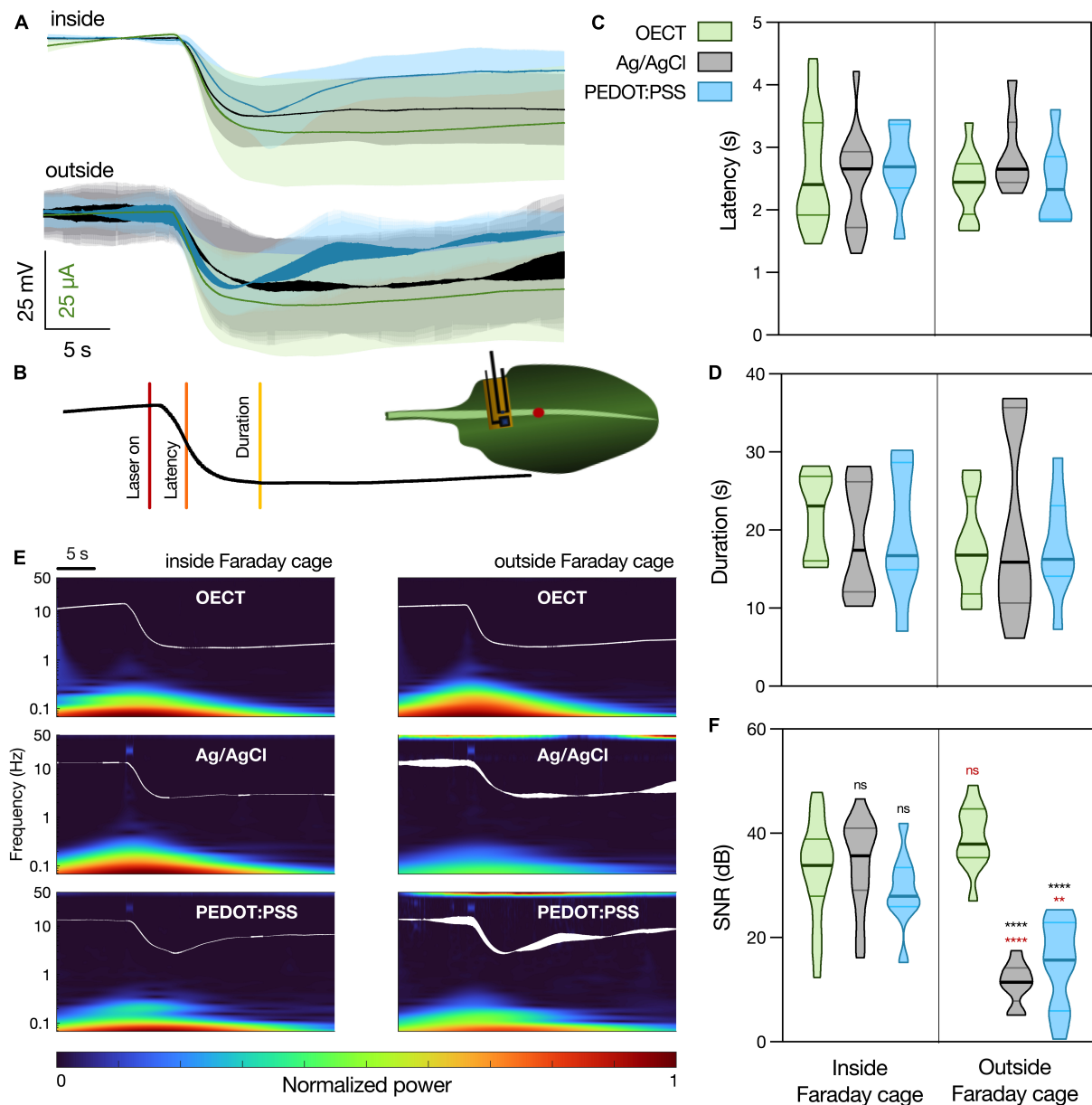


FIGURE 4

Arabidopsis thaliana WASP triggered by laser recorded with different devices. **(A)** Average waveform recorded with the different devices, inside and outside the Faraday cage: OECT (green trace), Ag/AgCl electrode (black trace), and PEDOT:PSS electrode (blue trace). Data represented as mean \pm 95% CI. $N = 10$ –20 leaves from 3 to 5 different plants. **(B)** Schematic representation of experimental setup. Laser was shined on a leaf for 1 s at 50% laser power and the different devices were in contact with the leaf less than 1 cm away, in a proximal direction, from the laser. The parameters considered for the characterization of the WASP were latency (time to reach half of maximal amplitude) and duration (time from laser on to recovery). **(C)** Quantification of latency and **(D)** duration of WASPs recorded with the different devices. No statistically significant differences were found. $N = 7$ –18. **(E)** Time-frequency analysis of the average waveform acquired with the different devices, inside and outside of the Faraday cage. **(F)** Quantification of SNR for the different waveforms, $N = 9$ –19. $**p < 0.01$, $****p < 0.0001$ using a two-way ANOVA considering the parameters “device” and “Faraday cage,” followed by Tukey’s multiple comparison test. In black, differences within the same “cage” condition; in red, differences in the same “device” condition. In **(C,D,F)**, data are represented in violin plots, where the width of the shaded area represents the proportion of data points at any given zone, with lines at median and quartiles.

PEDOT:PSS and Ag/AgCl electrodes. This is then translated into similar values of SNR between the different devices. However, when the recordings were performed outside of the Faraday

cage, it is possible to observe an increase in noise levels (50 Hz) in both PEDOT:PSS and Ag/AgCl electrode recordings. Similarly, this is translated into a significant decrease in the SNR

for these devices, while the OECT maintains a high SNR, which highlights an advantage of using this latter device for plant electrophysiology, especially outside of laboratory conditions.

Discussion

In this work, we set out to benchmark OECTs for plant electrophysiology, comparing their performance to that of PEDOT:PSS and Ag/AgCl electrodes. We were able to conclude that OECTs can resolve the biological signals as efficiently as the tested electrodes and that these organic electronic devices offer a significant improvement in the SNR of the recordings, especially when moving away from laboratory conditions. This is, to our knowledge, the first report that thoroughly characterizes these devices for plant electrophysiology, in a controlled and quantified manner, considering two different types of electrical signals. Importantly, while surface electrical recordings do not allow for the determination of the cellular origin of the signals, this approach represents a compromise between spatial resolution and invasiveness and remains a relevant method to extract meaningful information about plant electrophysiology.

Regarding the VFT action potential, while the waveforms attained are similar to some found in literature (Bischak et al., 2020), there is a large variability in action potential shape reported over the years (de Bakker et al., 2021; Meder et al., 2021). While a more comprehensive study on the origin of this variability remains to be conducted, special attention should be paid to the experimental setup and data filtering in plant electrophysiology. Indeed, since electrophysiology has been developed for mammalian systems, most commercially available electrophysiology systems are not suitable for plant signal recording. For this application, it is required that the employed system has the capacity to record high amplitude signals and has no hardware highpass filter (such as the commonly used 0.1 Hz highpass filter). Along the same line, data filtering can deeply impact the recorded signal. For example, for neuronal signals, it is possible to bandpass them to extract different components only because a great deal of research was devoted to isolate and quantify the different frequency contents of those signals. Such knowledge does not yet exist for plant electrical signals. Thus, even seemingly innocuous data treatment can mask some aspects of these signals. In practical terms, while data acquisition and treatment in plant electrophysiology still needs to be further elucidated and optimized, this discussion brings to light the need to create field-wide standards and analyses.

Regarding the values found for SNR, our study is in line with previous reports that state that VFT action potentials recorded with OECTs have a SNR of 1250, compared to that of Ag/AgCl of 11 (Bischak et al., 2020), which corresponds to a difference of around 40 dB between the devices. While these findings are

in line with our results, this study does not mention if the recordings were performed inside a Faraday cage nor does it mention if data filtering was performed.

Regarding *A. thaliana* WASPs, there is less variability in signal shape found in literature, with our waveforms matching those previously reported. Still, when studying wound response in plants, some aspects must be considered. Firstly, surface recordings are more suitable for this end than intracellular approaches, since they are non-invasive and thus do not elicit wound responses caused by insertion. However, they do not allow for the identification of the cellular identity of these signals (Farmer et al., 2020). This leads to a very relevant conundrum in the study of plant wound response: not being able to identify cellular origins without invasive techniques; but also changing the wound response by using said techniques. This problem is now starting to be surmounted by the use of voltage-sensitive dyes and genetic mutants (Zhao et al., 2015; Farmer et al., 2020; Rigoulot et al., 2021). Nonetheless, a better integration of molecular-based approaches and electrophysiological techniques still needs to be developed.

Our study, albeit not tackling the issue of the cellular origin of plant electrical signals, was still able to show that, for *A. thaliana* WASPs, the OECT offers the advantage of a higher SNR when not in laboratory conditions compared to the used electrodes.

Overall, this study validates OECTs as viable tools for plant electrophysiology, with the clear advantage of maintaining signal integrity outside of laboratory conditions. The application of untethered OECT-based sensors *in situ* using Arduino devices with WiFi modules (Diaci et al., 2021) further corroborates this conclusion. Additionally, previous work on OECTs as mammalian electrophysiological tools employed multi-OECT arrays (Khodagholy et al., 2013), which implies that this technology can be used to resolve spatial and temporal signals in field conditions. A final advantage of OECTs is the possibility for their low-cost fabrication, using screen-printing technology (Zabihpour et al., 2020).

Alas, the validation of new tools for plant electrophysiology is only a small fraction of much needed innovation. Recent reviews cover the advances in plant-inspired biomimetic soft robotics and machines (Esser et al., 2020; Mazzolai et al., 2020), as well as the developments in plant biohybrid devices and bioelectronic applications (Dufil et al., 2021), highlighting the immense possibilities for interaction of plants with technology. However, without better and more diverse tools to study plant phenomena, these possibilities cannot be reached.

Data availability statement

The raw data supporting the conclusions of this article will be made available by the authors, without undue reservation.

Author contributions

AA-M designed and performed the experiments, analyzed the data, and wrote the manuscript. CD fabricated the OECTs, optimized the parameters for their use in these plant applications, and wrote the manuscript. AMD optimized the experimental setup and aided in the experimental design. MB and DTS contributed to the development of OECTs. ES conceived the project, designed, and supervised the research. All authors reviewed the manuscript.

Funding

This work was supported by the Swedish Foundation For Strategic Research (FFL18-0101), the European Union's Horizon 2020 Research and Innovation Programme under Grant Agreement No. 800926 (FET-OPEN-HyPhOE), the Knut and Alice Wallenberg Foundation and the Wallenberg Wood Science Center, and by the Swedish Government Strategic Research Area in Materials Science on Advanced Functional Materials at Linköping University (Faculty Grant SFO-Mat-LiU No. 2009-00971).

Acknowledgments

We thank Dion Khodagholy, Columbia University, for fruitful discussions on electrophysiology and Bernhard

Burtscher for his input in the development of programs to run equipment and troubleshooting of the OECT recording setup.

Conflict of interest

The authors declare that the research was conducted in the absence of any commercial or financial relationships that could be construed as a potential conflict of interest.

Publisher's note

All claims expressed in this article are solely those of the authors and do not necessarily represent those of their affiliated organizations, or those of the publisher, the editors and the reviewers. Any product that may be evaluated in this article, or claim that may be made by its manufacturer, is not guaranteed or endorsed by the publisher.

Supplementary material

The Supplementary Material for this article can be found online at: <https://www.frontiersin.org/articles/10.3389/fpls.2022.916120/full#supplementary-material>

References

- Bai, L., Elósegui, C. G., Li, W., Yu, P., Fei, J., and Mao, L. (2019). Biological applications of organic electrochemical transistors: electrochemical biosensors and electrophysiology recording. *Front. Chem.* 7:313. doi: 10.3389/FCHEM.2019.00313/BIBTEX
- Bar-On, Y. M., Phillips, R., and Milo, R. (2018). The biomass distribution on Earth. *Proc. Natl. Acad. Sci. U.S.A.* 115, 6506–6511. doi: 10.1073/pnas.1711842115
- Bischak, C. G., Flagg, L. Q., and Ginger, D. S. (2020). Ion exchange gels allow organic electrochemical transistor operation with hydrophobic polymers in aqueous solution. *Adv. Mater.* 32:e2002610. doi: 10.1002/adma.202002610
- Brette, R., and Destexhe, A. (2012). "Intracellular recording," in *Handbook of Neural Activity Measurement*, eds A. Destexhe and R. Brette (Cambridge: Cambridge University Press).
- Burdon-Sanderson, J. S. (1873). I. Note on the electrical phenomena which accompany irritation of the leaf of *Dionaëa muscipula*. *Proc. R. Soc. Lond.* 21, 495–496. doi: 10.1098/rsp1872.0092
- Cea, C., Spyropoulos, G. D., Jastrzebska-Perfect, P., Ferrero, J. J., Gelinas, J. N., and Khodagholy, D. (2020). Enhancement-mode ion-based transistor as a comprehensive interface and real-time processing unit for in vivo electrophysiology. *Nat. Mater.* 19, 679–686. doi: 10.1038/s41563-020-0638-3
- Chatterjee, S. K., Das, S., Maharatna, K., Masi, E., Santopolo, L., Colzi, I., et al. (2017). Comparison of decision tree based classification strategies to detect external chemical stimuli from raw and filtered plant electrical response. *Sensors Actuators B Chem.* 249, 278–295. doi: 10.1016/j.snb.2017.04.071
- Chatterjee, S. K., Das, S., Maharatna, K., Masi, E., Santopolo, L., Mancuso, S., et al. (2015). Exploring strategies for classification of external stimuli using statistical features of the plant electrical response. *J. R. Soc. Interface* 12:20141225. doi: 10.1098/rsif.2014.1225
- Choi, W.-G., Hilleary, R., Swanson, S. J., Kim, S.-H., and Gilroy, S. (2016). Rapid, Long-Distance Electrical and Calcium Signaling in Plants. *Annu. Rev. Plant Biol.* 67, 287–307. doi: 10.1146/annurev-arplant-043015-112130
- Chong, P. L., Singh, A. K., and Kok, S. L. (2019). Characterization of Aloe Barbadensis Miller leaves as a potential electrical energy source with optimum experimental setup conditions. *PLoS One* 14:e0218758. doi: 10.1371/journal.pone.0218758
- de Bakker, J. M. T., Belterman, C. N. W., and Coronel, R. (2021). Excitability and propagation of the electrical impulse in Venus flytrap; a comparative electrophysiological study of unipolar electrograms with myocardial tissue. *Bioelectrochemistry* 140:107810. doi: 10.1016/J.BIOELECHEM.2021.107810
- Degli Agosti, R. (2014). Touch-induced action potentials in *Arabidopsis thaliana*. *Arch. Des. Sci.* 57, 125–138. doi: 10.1093/aob/mcx155
- Diacci, C., Abedi, T., Lee, J. W., Gabrielson, E. O., Berggren, M., Simon, D. T., et al. (2021). Diurnal in vivo xylem sap glucose and sucrose monitoring using implantable organic electrochemical transistor sensors. *iScience* 24:101966. doi: 10.1016/j.isci.2020.101966
- Dufl, G., Bernacka-Wojcik, I., Armada-Moreira, A., and Stavrinidou, E. (2021). Plant Bioelectronics and Biohybrids: the Growing Contribution of Organic Electronic and Carbon-Based Materials. *Chem. Rev.* 122, 4847–4883. doi: 10.1021/ACS.CHEMREV.1C00525

- Esser, F. J., Auth, P., and Speck, T. (2020). Artificial venus flytraps: a research review and outlook on their importance for novel bioinspired materials systems. *Front. Robot. AI* 7:75. doi: 10.3389/FROBT.2020.00075/BIBTEX
- Farmer, E. E., Gao, Y.-Q., Lenzoni, G., Wolfender, J.-L., and Wu, Q. (2020). Wound- and mechanostimulated electrical signals control hormone responses. *New Phytol.* 227, 1037–1050. doi: 10.1111/nph.16646
- Gilroy, S., and Trewavas, A. (2001). Signal processing and transduction in plant cells: the end of the beginning? *Nat. Rev. Mol. Cell Biol.* 2, 307–314. doi: 10.1038/35067109
- Grenzi, M., Bonza, M. C., Alfieri, A., and Costa, A. (2021). Structural insights into long-distance signal transduction pathways mediated by plant glutamate receptor-like channels. *New Phytol.* 229, 1261–1267. doi: 10.1111/nph.17034
- Hedrich, R., and Neher, E. (2018). Venus flytrap: How an excitable, carnivorous plant works. *Trends Plant Sci.* 23, 220–234. doi: 10.1016/j.tplants.2017.12.004
- Khodagholy, D., Doublet, T., Quilichini, P., Gurfinkel, M., Leleux, P., Ghestem, A., et al. (2013). In vivo recordings of brain activity using organic transistors. *Nat. Commun.* 4:1575. doi: 10.1038/ncomms2573
- Kim, J. Y., Lee, C., Jeon, M. S., Park, J., and Choi, Y.-E. (2018). Enhancement of microalga *Haematococcus pluvialis* growth and astaxanthin production by electrical treatment. *Bioresour. Technol.* 268, 815–819. doi: 10.1016/j.biortech.2018.08.014
- Klejchova, M., Silva-Alvim, F. A. L., Blatt, M. R., and Alvim, J. C. (2021). Membrane voltage as a dynamic platform for spatiotemporal signaling, physiological, and developmental regulation. *Plant Physiol.* 185, 1523–1541. doi: 10.1093/PLPHYS/KIAB032
- Lew, T. T. S., Koman, V. B., Gordiichuk, P., Park, M., and Strano, M. S. (2020). The Emergence of Plant Nanobionics and Living Plants as Technology. *Adv. Mater. Technol.* 5:1900657. doi: 10.1002/ADMT.201900657
- Li, J. H., Fan, L. F., Zhao, D. J., Zhou, Q., Yao, J. P., Wang, Z. Y., et al. (2021). Plant electrical signals: a multidisciplinary challenge. *J. Plant Physiol.* 261:153418. doi: 10.1016/j.jplph.2021.153418
- Luo, Y., Li, W., Lin, Q., Zhang, F., He, K., Yang, D., et al. (2021). A Morphable Ionic Electrode Based on Thermogel for Non-Invasive Hairy Plant Electrophysiology. *Adv. Mater.* 33:2007848. doi: 10.1002/ADMA.202007848
- Marhavý, P., Kurenda, A., Siddique, S., Dénervaud Tendon, V., Zhou, F., Holbein, J., et al. (2019). Single-cell damage elicits regional, nematode-restricting ethylene responses in roots. *EMBO J.* 38:e100972. doi: 10.15252/EMBJ.2018100972
- Mazzolai, B., Tramacere, F., Fiorello, I., and Margheri, L. (2020). The Bio-Engineering Approach for Plant Investigations and Growing Robots, A Mini-Review. *Front. Robot. AI* 7:573014. doi: 10.3389/FROBT.2020.573014/BIBTEX
- Meder, F., Saar, S., Taccola, S., Filippeschi, C., Mattoli, V., and Mazzolai, B. (2021). Ultraconformable, Self-Adhering Surface Electrodes for Measuring Electrical Signals in Plants. *Adv. Mater. Technol.* 6:2001182. doi: 10.1002/admt.202001182
- Mousavi, S. A. R., Chauvin, A., Pascaud, F., Kellenberger, S., and Farmer, E. E. (2013). GLUTAMATE RECEPTOR-LIKE genes mediate leaf-to-leaf wound signalling. *Nature* 500, 422–426. doi: 10.1038/nature12478
- Nawaz, A., Liu, Q., Leong, W. L., Fairfull-Smith, K. E., and Sonar, P. (2021). Organic Electrochemical Transistors for In Vivo Bioelectronics. *Adv. Mater.* 33:2101874. doi: 10.1002/ADMA.202101874
- Nguyen, C. T., Kurenda, A., Stolz, S., Chételat, A., and Farmer, E. E. (2018). Identification of cell populations necessary for leaf-to-leaf electrical signaling in a wounded plant. *Proc. Natl. Acad. Sci. U.S.A.* 115, 10178–10183. doi: 10.1073/pnas.1807049115
- Paulsen, B. D., Tybrandt, K., Stavrinidou, E., and Rivnay, J. (2020). Organic mixed ionic–electronic conductors. *Nat. Mater.* 19, 13–26. doi: 10.1038/s41563-019-0435-z
- Proctor, C. M., Rivnay, J., and Malliaras, G. G. (2016). Understanding volumetric capacitance in conducting polymers. *J. Polym. Sci. Part B Polym. Phys.* 54, 1433–1436. doi: 10.1002/POLB.24038
- Rhodes, J. D., Thain, J. F., and Wildon, D. C. (1996). The pathway for systemic electrical signal conduction in the wounded tomato plant. *Planta* 200, 50–57. doi: 10.1007/BF00196648
- Rigoulot, S. B., Schimel, T. M., Lee, J. H., Sears, R. G., Brabazon, H., Layton, J. S., et al. (2021). Imaging of multiple fluorescent proteins in canopies enables synthetic biology in plants. *Plant Biotechnol. J.* 19, 830–843. doi: 10.1111/PBI.13510
- Ríos-Rojas, L., Morales-Moraga, D., Alcalde, J. A., and Gurovich, L. A. (2015). Use of plant woody species electrical potential for irrigation scheduling. *Plant Signal. Behav.* 10:e976487. doi: 10.4161/15592324.2014.976487
- Rivnay, J., Inal, S., Salleo, A., Owens, R. M., Berggren, M., and Malliaras, G. G. (2018). Organic electrochemical transistors. *Nat. Rev. Mater.* 3:17086. doi: 10.1038/natrevmats.2017.86
- Salvador-Recatalà, V., Tjallingii, W. F., and Farmer, E. E. (2014). Real-time, in vivo intracellular recordings of caterpillar-induced depolarization waves in sieve elements using aphid electrodes. *New Phytol.* 203, 674–684. doi: 10.1111/nph.12807
- Stahlberg, R., Cleland, R. E., and Van Volkenburgh, E. (2006). “Slow Wave Potentials — a Propagating Electrical Signal Unique to Higher Plants,” in *Communication in Plant*, eds F. Baluška, S. Mancuso, and D. Volkmann (Berlin: Springer).
- Stavrinidou, E., Leleux, P., Rajaona, H., Khodagholy, D., Rivnay, J., Lindau, M., et al. (2013). Direct Measurement of Ion Mobility in a Conducting Polymer. *Adv. Mater.* 25, 4488–4493. doi: 10.1002/ADMA.201301240
- Suda, H., Mano, H., Toyota, M., Fukushima, K., Mimura, T., Tsutsui, I., et al. (2020). Calcium dynamics during trap closure visualized in transgenic Venus flytrap. *Nat. Plants* 6, 1219–1224. doi: 10.1038/s41477-020-00773-1
- Vodeneev, V., Akinchits, E., and Sukhov, V. (2015). Variation potential in higher plants: mechanisms of generation and propagation. *Plant Signal. Behav.* 10:e1057365. doi: 10.1080/15592324.2015.1057365
- Volkov, A. G., Adesina, T., and Jovanov, E. (2007). Closing of Venus Flytrap by Electrical Stimulation of Motor Cells. *Plant Signal. Behav.* 2, 139–145. doi: 10.4161/psb.2.3.4217
- Volkov, A. G., Toole, S., and WaMaina, M. (2019). Electrical signal transmission in the plant-wide web. *Bioelectrochemistry* 129, 70–78. doi: 10.1016/j.bioelechem.2019.05.003
- Volkov, A. G., Wooten, J. D., Waite, A. J., Brown, C. R., and Markin, V. S. (2011). Circadian rhythms in electrical circuits of *Clivia miniata*. *J. Plant Physiol.* 168, 1753–1760. doi: 10.1016/j.jplph.2011.03.012
- Volkov, A. V., Wijeratne, K., Mitraka, E., Ail, U., Zhao, D., Tybrandt, K., et al. (2017). Understanding the Capacitance of PEDOT:PSS. *Adv. Funct. Mater.* 27:1700329. doi: 10.1002/ADFM.201700329
- Yu, R., Wu, Y., and Xing, D. (2021). Can Electrophysiological Parameters Substitute for Growth, and Photosynthetic Parameters to Characterize the Response of Mulberry and Paper Mulberry to Drought? *Plants* 10:1772. doi: 10.3390/PLANTS10091772
- Zabhipour, M., Lassnig, R., Strandberg, J., Berggren, M., Fabiano, S., Engquist, I., et al. (2020). High yield manufacturing of fully screen-printed organic electrochemical transistors. *npj Flex. Electron.* 4:15. doi: 10.1038/s41528-020-0078-9
- Zhao, D. J., Chen, Y., Wang, Z. Y., Xue, L., Mao, T. L., Liu, Y. M., et al. (2015). High-resolution non-contact measurement of the electrical activity of plants in situ using optical recording. *Sci. Rep.* 5:13425. doi: 10.1038/SREP13425

Frontiers in Plant Science

Cultivates the science of plant biology and its applications

The most cited plant science journal, which advances our understanding of plant biology for sustainable food security, functional ecosystems and human health.

Discover the latest Research Topics

[See more →](#)

Frontiers

Avenue du Tribunal-Fédéral 34
1005 Lausanne, Switzerland
frontiersin.org

Contact us

+41 (0)21 510 17 00
frontiersin.org/about/contact

